Late Miocene and Early Pliocene Palaeoceanography at the Eastern Equatorial Pacific IODP Site U1338: Implications for Climate Evolution and Stability

Anna Joy Drury

A thesis submitted in fulfillment of the requirements for the degree of
Doctor of Philosophy and the Diploma of Imperial College

December 2013

Imperial College London
Department of Earth Science and Engineering

Declaration of Originality

I hereby declare that all presented in this thesis is my own or else is appropriately referenced.

Anna Joy Drury

December 2013

Copyright Declaration

Acknowledgements

I would like to say a big thank you to the following people:

- To my supervisor, Cédric John, for his support and advice and for the opportunities I've had during my PhD. To the department for the Janet Watson Studentship that gave me the chance to do this PhD in the first place.
- To Amelia Shevenell, Tom Dunkley Jones and David Hodell for their fruitful discussions and advice on different aspects of this PhD project. To Geoff Lee for his effort and the enjoyment of working together on the planktic foraminiferal project. To Will Gray for his help with the trace element project. To Bridget Wade for her help with planktic foraminiferal taxonomy. To Gill Pennock and Martyn Drury for their help with the scanning electron microscopy work.
- To Simon Davis for his lab help and helping me nurse the Kiel Devise through endless hiccups. To Rindy Ostermann, Tobias Kluge, John MacDonald, Annabel Dale, Claire Huck, Will Gray and Katy Prentice for teaching me the lab-ropes.
- To Tobias Kluge, Geoff Lee, Peter Fitch and my parents for casting their critical eyes over my thesis. To my examiners, Tina van de Flierdt and Bridget Wade for providing constructive and critical feedback that has improved this work.
- To all of the Carbonate Group members, including those I have not yet thanked (Veerle Vandeginste, Claire Sena, Sunshine Abbott, Martin Hönig, Manuela Stehle, Anne-Lise Jourdan, Julia Beckert, Kimberley Johnston and Carl Jacquemyn) for making my time here educational, enjoyable and full of giggles.
- To the London Palaeoclimate Network and its members, and to the friends and colleagues from USSP'11, for advice, discussions and a regular palaeoclimate fix.
- To Jan Cilliers, Lorraine Craig and the lecturers for whom I demonstrated in class and field, for the chance to expand my experience beyond solely researching.
- To my friends Hayley, Martin, Nick, Dave, Pete, Barry, Geoff, Claire, Tina, Spenny, Barbara, Aislinn, Suzanne, Jake, Matt and our Crabtree Pub Quiz Team for their endless support and for making my time in London fantastic.
- And of course to my family for their love and support throughout my PhD.

  To my grandparents, June and Ralph, for making Windy Ridge a peaceful, relaxing and enjoyable home from home.

  To my parents Gill and Martyn, for their endless patience, advice and support over the past few years. Thank you.

Abstract

The short-term background climate variability during the climatically stable latest Miocene to early Pliocene (LM-EP) is not well understood, owing to the lack of continuous, high-resolution climate records. Assessing variability during an interval of long-term climatic stability will constrain how sensitivity of major Earth's system components (Earth system response - ESR) to external radiative forcing has changed through time.

This study investigated LM-EP climate, focussing on changes in ESR, El-Niño-Southern-Oscillation state, glacio-eustacy and the Messinian Salinity Crisis (MSC), and the origin of the Late Miocene Carbon Isotope Shift (LMCIS). This project produced the first high-resolution benthic foraminiferal $\delta^{18}O$ and $\delta^{13}C$ record in the eastern equatorial Pacific (IODP Site U1338) from 8.0-3.5 Ma that resolves all Milankovitch cyclicities. A high-resolution, orbitally-based age model, planktic foraminiferal $\delta^{18}O$, $\delta^{13}C$ and Mg/Ca, coccolith-rich 'clumped isotopes' Δ_{47}, spectral analyses and multi-site benthic foraminiferal isotope compilations were also produced.

Planktic foraminiferal Mg/Ca sea surface temperatures (SSTs) were ~25 °C. Coccolith-rich Δ_{47} temperatures were unrealistically cold at ~10-15 °C, reflecting moderate coccolith preservation and vital effects that cause higher Δ_{47}.

Site U1338 and 982 combined benthic foraminiferal ($\delta^{18}O$; $\delta^{13}C$) wavelet analyses show moderate ESR from 6.3–4.7 Ma and after 3.7 Ma, but lower ERS from 7.0–6.3 Ma. The $\delta^{18}O$-minimum stage ~5.33 Ma, during long-term minimum $\delta^{18}O$, suggests that glacio-eustacy played a role in the MSC termination. The benthic foraminiferal $\delta^{13}C$ compilation confirms that the LMCIS was globally synchronous and caused by a negative shift in oceanic reservoir $\delta^{13}C$, driven by changes in the continental carbon flux (increased sea-floor-spreading / C_4-grass expansion).

Data syntheses show that global warmth, dominant El-Niño state, high cryosphere sensitivity, lower ice volume and short-term ice sheet variations characterised the LM-EP pre-7.0 and post-5.7 Ma. Stable conditions occurred ~7.0-5.7 Ma, with dominant La-Niña, higher ice volume, low cryosphere sensitivity and lower SSTs.

Table of Contents

List of Figures

List of Tables

Chapter 1.

Introduction

1.1. Thesis Rationale:

Late Miocene and Early Pliocene Climate Stability and Threshold Events

The latest Miocene to early Pliocene is one of the most climatically stable periods of the Cenozoic (Zachos et al., 2001). However, the state of the short-term background climate variability in this interval is not well understood. It is important to assess short-term climate variability during an interval of long-term climatic stability because this helps us understand how the response of the major Earth's climate system to external radiative forcing has changed over time.

The prolonged climatic stability of the latest Miocene (LM: 8.0 – 5.33 Ma) until the earliest Pliocene (EP: 5.33 – 3.50 Ma) occurs between two intervals of large-amplitude long-term climatic change. The late Miocene is preceded by a

major cooling episode in the middle Miocene (~14 Ma) (Flower and Kennet, 1993) and the early Pliocene is succeeded by the mid Pliocene warm period (~ 3 Ma) (Haywood and Valdes, 2004) and further cooling during intensification of Northern Hemisphere Glaciations (~2.7 Ma) (Shackleton and Opdyke, 1977). Superimposed on this stable background, a number of threshold events, including the late Miocene Carbon Isotope Shift (7.6 – 6.6 Ma) and the Messinian Salinity Crisis (5.96 – 5.33 Ma) occurred. Constraining changes in natural background climate variability could contribute to explaining the occurrence of such threshold events during periods of relative climatic stability.

1.2. Aims

The aims of this PhD thesis are twofold:

1. To investigate the evolution of natural background climate variability in the late Miocene to early Pliocene, and how this translates to changes in the major Earth systems response to solar forcing during an extended period of climatic stability.
2. To explore the evolution of late Miocene to early Pliocene climate in respect to important climatic changes occurring from 8.0 – 3.5 Ma. Specifically,
   a) to explore the changes to equatorial Pacific sea surface conditions, and to evaluate the state of the El-Niño-Southern-Oscillation (ENSO) and the correlation between the ENSO state and the Biogenic Bloom;
   b) to explore the role of glacio-eustatic variation in the onset and termination of the Messinian Salinity Crisis (MSC);
   c) to explore the nature and forcing mechanisms behind the late Miocene Carbon Isotope Shift (LMCIS);

The eastern equatorial region of the vast Pacific Ocean is an important component of the global climate system and is crucial for understanding climate evolution. As such, it forms the location selected for this study. The Pacific currently covers a staggering 50% of the Earth's surface and is the largest ocean basin and reservoir of nutrients, heat and water storage on Earth (Lyle et al., 2008). As a result of the large size of the Pacific reservoir, geochemical records from the Pacific are thought to approximate global mean changes accurately. Furthermore, the eastern equatorial Pacific is dominated by high surface water productivity and sedimentation rates, which is ideal for high-resolution palaeoceanography studies (Lyle et al., 2010). The recent IODP Expeditions 320/321 "Pacific Equatorial Age Transect" (PEAT) programme recovered extensive and continuous Cenozoic carbonate-rich sediments from eight sites in the eastern equatorial Pacific (Palike et al., 2010). Due to the combination continuous sedimentation, the generally good preservation of calcareous nanno- and microfossils, and the drilling of multiple holes using advanced piston coring techniques, sediments recovered at Site U1338 provides an expanded record of late Miocene and early Pliocene sediments that are ideally suited for the high-resolution foraminiferal geochemical studies required for this study.

1.3. Detailed Objectives and Approach

To achieve the aims presented above, multi-proxy geochemistry records and complimentary spectral analyses were generated from deep-sea pelagic sediments from IODP Site U1338, and compared to published records. To accomplish this, the following detailed objectives were addressed:

1. *Assess foraminiferal preservation using scanning electron microscopy (SEM) and percentage coarse fraction records (%CF), before generating two sets of foraminiferal stable $\delta^{18}O$ and $\delta^{13}C$ isotope records at Site U1338:*
   a) *High-resolution benthic foraminiferal $\delta^{18}O$ and $\delta^{13}C$ records (8.0 – 3.5 Ma, at ~ 3.5 kyr temporal resolution).*
   b) *Planktic foraminiferal $\delta^{18}O$ and $\delta^{13}C$ records (8.0 – 3.5 Ma, at ~ 16 kyr resolution).*
2. *Create a high-resolution age model for IODP Site U1338 by stratigraphically correlating benthic $\delta^{18}O$ and $\delta^{13}C$ records from deep-sea Site U1338 and ODP Site 982 (N. Atlantic).*
3. *Use planktic and benthic foraminiferal $\delta^{13}C$, sedimentation rates, and published bulk $\delta^{13}C$, % $CaCO_3$ and SiO_2 records to establish the extent of the Biogenic Bloom at Site U1338.*
4. *Combine planktic foraminiferal $\delta^{18}O$ and Mg/Ca ratios from Site U1338 with published equatorial Pacific records to establish the state of El-Niño-Southern-Oscillation.*
5. *Generate a novel 'clumped isotope' Δ_{47} record from the coccolith-rich sediments from Site U1338 to evaluate this approach as an independent sea surface temperature (SST) proxy.*
6. *Compare the U1338 and 982 benthic $\delta^{18}O$ and $\delta^{13}C$ wavelet analyses to external radiative forcing to reconstruct cryosphere and carbon cycle sensitivity and Earth system response.*
7. *Create benthic $\delta^{18}O$ and $\delta^{13}C$ compilations from Atlantic, Southern and Pacific Oceans.*
8. *Use the $\delta^{18}O$ compilation, cryosphere sensitivity and published data to estimate global ice volume change and assess its importance in the Messinian Salinity Crisis.*
9. *Combine the $\delta^{13}C$ compilation, together with carbon cycle sensitivity and a conceptual carbon-cycle model to assess the origins of the late Miocene Carbon Isotope Shift.*

1.4. Thesis Outline

This thesis consists of seven chapters, with additional appendices and references. Chapters 1 and 2 contain introductory and further background information. Chapters 3 to 6 achieve the aims and objectives discussed above. Chapter 7 brings together the main conclusions and outcomes from this PhD study and discusses future avenues for research. A more detailed description of each chapter is given below.

In **chapter 2** the importance and global climatic history of the late Miocene and early Pliocene is explored, particularly focusing on the evolution of the eastern equatorial Pacific region and climate. A detailed description of IODP Site U1338 is also provided.

The main aim of **chapter 3** is to evaluate the preservation of the benthic and planktic foraminifera selected for geochemical analysis at IODP Site U1338, and to assess whether the planktic and high-resolution benthic foraminiferal $\delta^{18}O$ and $\delta^{13}C$ records from Site U1338 are suitable for palaeoclimate research.

In **chapter 4**, an improved high-resolution, astronomically based age model is established for the U1338 splice from 8.0 – 3.5 Ma. This is achieved by stratigraphically correlating the benthic $\delta^{18}O$ and $\delta^{13}C$ records from deep-sea sites U1338 and 982 using auto-correlation software. The age model strength is discussed and spectral analyses of the U1338 isotope records are used to assess whether stratigraphic correlation to an orbitally tuned target has induced artificial variability. The late Miocene to early Pliocene $\delta^{18}O$ and $\delta^{13}C$ isotope stratigraphy is discussed and if possible, marine isotope stages are identified.

Chapter 5 combines the planktic and benthic foraminiferal $\delta^{18}O$ and $\delta^{13}C$ records with planktic foraminiferal Mg/Ca ratios and published geochemical records, to investigate the state and evolution of surface conditions in the equatorial Pacific between 8.0 and 4.4 Ma. This compilation aims to reconcile the state of the El-Niño-Southern-Oscillation and the Biogenic Bloom during the late Miocene to early Pliocene in the equatorial Pacific. Finally, this chapter explores the application of 'clumped isotope' measurement on coccolith-rich sediments as a novel SST proxy.

The evolution of global climate in the late Miocene to early Pliocene is discussed in **chapter 6**. Firstly, cryosphere and carbon cycle sensitivity and Earth system response to external forcing are reconstructed using wavelet analyses on high-resolution benthic $\delta^{18}O$ and $\delta^{13}C$ records. Secondly, a benthic $\delta^{18}O$ compilation is used to assess variations in global ice volume and to constrain the role of glacio-eustacy at the onset and termination of the Messinian Salinity Crisis. The benthic $\delta^{13}C$ compilation is used to establish changes in inter-ocean $\delta^{13}C$ gradients and to guide a discussion into the origins of the late Miocene Carbon Isotope Shift.

Chapter 7 contains a summary of the key findings, conclusions and wider implications resulting from the research projects presented in this thesis. This concluding chapter also contains a section exploring the potential avenues for future research that this project has bought to light.

Chapter 2.

Late Miocene to Early Pliocene Climate and the Eastern Equatorial Pacific

2.1. Late Miocene and Early Pliocene

Cenozoic climate change is characterised by the long-term transition from the warm, greenhouse climates of the Palaeocene and Eocene to the long-term cooling trends seen in the icehouse world of the Oligocene and the Neogene (Figure 2.1) (Zachos et al., 2001). The latest Miocene (8.0 – 5.33 Ma) through early Pliocene (5.33 – 3.50 Ma) period is considered one of the more climatically stable of the last 65 Ma. The following two sections explore the general global climate trends, as well as look at the various threshold events that occurred during the late Miocene to early Pliocene.

2.1.1. Climate Stability

During the late Miocene to early Pliocene, long-term climate is considered to be relatively stable (Hodell et al., 2001). Comparisons between spectral analyses of benthic foraminiferal oxygen isotopes $\delta^{18}O$ records and insolation forcing indicate that the late Miocene was a time of decreased climate sensitivity before 4.5 Ma (Pisias et al., 1995; Hodell et al., 2001; LaRiviere et al., 2012). Long-term benthic foraminiferal $\delta^{18}O$ vary minimally (~ 0.25 – 0.5 ‰) and overall the long-term $\delta^{18}O$ trend hardly changes (Figure 2.1.a) (Shackleton et al., 1995b; Shackleton and Hall, 1997; Hodell et al., 2001; Billups et al., 2008), which has been interpreted as a lack of large long-term changes in ice volume (Hodell et al., 2001). This lack of change in long-term late Miocene benthic foraminiferal $\delta^{18}O$ contrasts with the preceding middle Miocene cooling trend of 1 – 1.3 ‰ (Flower and Kennet, 1993) and the later drop in benthic foraminiferal $\delta^{18}O$ of ~ 1 - 1.5 ‰ at the onset of the Northern Hemisphere Glaciations in the Pleistocene (Shackleton and Opdyke, 1977; Shackleton et al., 1983). Superimposed on the long-term late Miocene to early Pliocene benthic foraminiferal $\delta^{18}O$ trends, there are short-term fluctuations in $\delta^{18}O$ of ~ 0.5 ‰, indicating that the size of the west and east Antarctic ice sheets were fluctuating (Shackleton et al., 1995b), and that there were ephemeral ice sheets present in the Northern Hemisphere (Hodell et al., 2001). Ephemeral Arctic ice is supported by ice rafted debris (IRD) reaching the Fram Strait as early as 14 Ma, which has been interpreted as evidence for seasonal ice sheets (Wolf-Welling et al., 1996). Increased IRD from offshore Greenland from about 10 Ma onwards has been interpreted as the occurrence of small permanent ice sheets on mainland Greenland (Wolf and

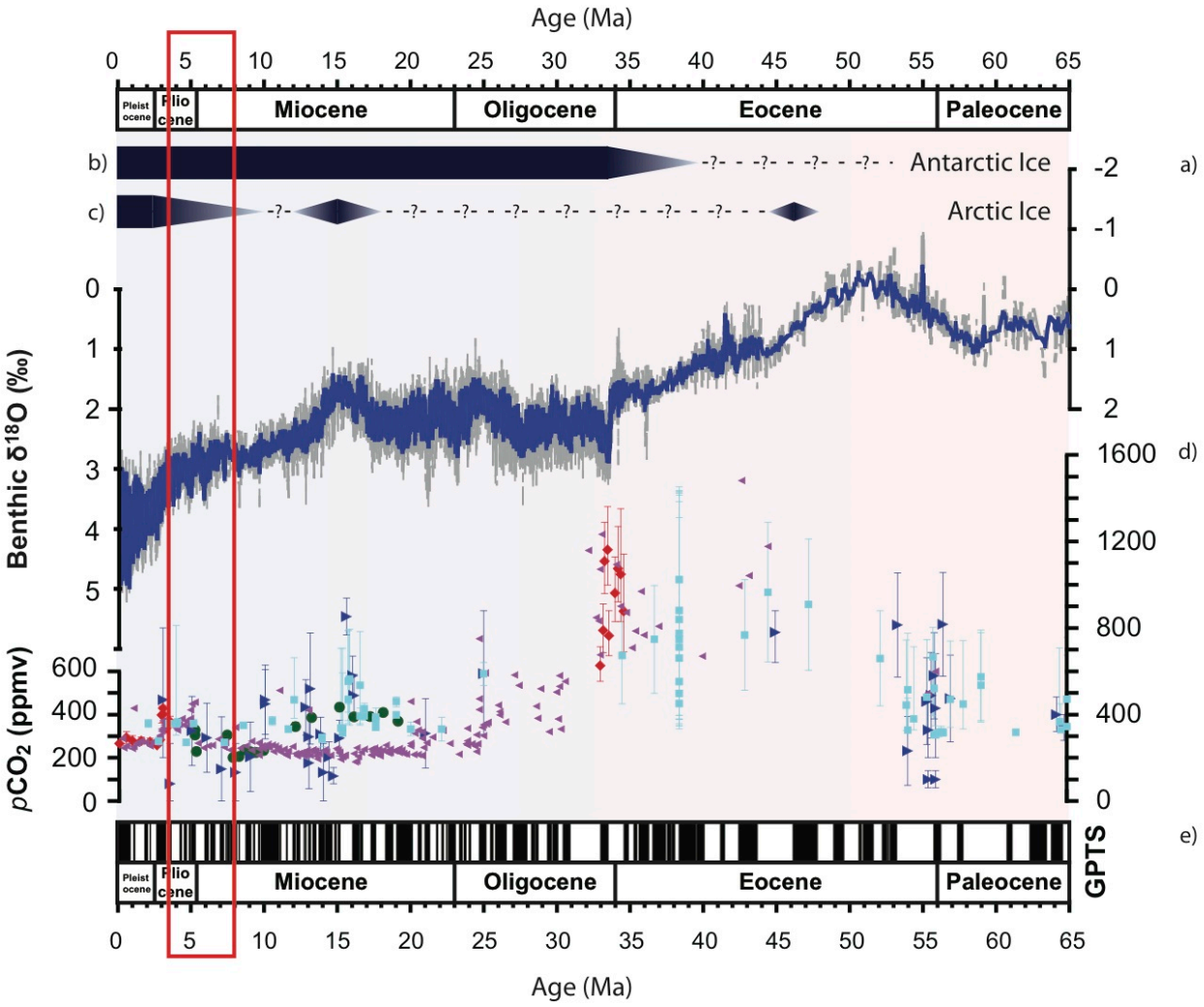

Figure 2.1. Overview of changes in Cenozoic climate. The focus interval of this study, late Miocene to early Pliocene, is highlighted with the red box.

(a) Benthic foraminiferal $\delta^{18}O$ stack (dark blue = average; grey = spread of individual data points) highlighting the change from a warm, ice free world during the Palaeocene and much of the Eocene, to the constant presence of large ice sheets from the late Eocene/Oligocene onwards. The cooling trend from the early Eocene onwards is also clear (Zachos et al., 2001, 2008).

(b) Estimates of Antarctic ice sheets. Permanent ice sheets have been present from the Oligocene onwards, although there is evidence for ephemeral ice sheets in the latest Eocene. The earliest evidence for Antarctic ice sheets is still debated, but the earliest ice on Antarctica is thought to have originated in the Eocene (Zachos et al., 2008).

(c) Estimates of Arctic, Northern Hemisphere ice sheets. Large, permanent ice sheets, such as those seen on Greenland today, have only been present from the late Pliocene/Pleistocene onwards. There is evidence for small-scale and ephemeral ice sheets present on Greenland from 10 Ma onwards, with some seasonal ice as early as 14 Ma (Backman and Moran, 2009).

(d) Cenozoic CO_2 estimates with published uncertainties where available with error bars from a range of CO_2 proxies: B/Ca ratios (dark green circles), $\delta^{11}B$ (red diamonds), palaeosols (dark blue triangles), phytoplankton (purple triangles), stomata (light blue squares) (Beerling and Royer, 2011 and the references therein). Although the degree of agreement between the proxies is not always great, it is clear that CO_2 was much higher than modern in the early Cenozoic. During the late Miocene and early Pliocene, CO_2 was lower than modern for an extended interval.

(e) Ages for palaeomagnetic reversals (Cande and Kent, 1995)

Thiede, 1991; Jansen and Sjøholm, 1991; Larsen et al., 1994; Fronval and Jansen, 1996; O'Connell et al., 1996; Thiede and Myhre, 1996; Backman and Moran, 2009). Although the this Arctic IRD could also originate from changes in mountain glacier extent and does not confirm the existence of continental ice sheets, it does confirm ice volume in the northern hemisphere was present and variable at this time. Proximal records from around Antarctica have also shown that both the East and West Antarctic ice sheets were behaving dynamically for at least parts of the late Miocene to early Pliocene (Robin, 1988; Talarico and Sandroni, 2009; Naish et al., 2009; Mckay et al., 2009; Monien et al., 2012; Cook et al., 2013) (Figure 2.1.b and c). Global ice volume variability will be discussed in greater detail in Chapter 6.

Continental configurations in the late Miocene to early Pliocene were comparable to today, however a number of oceanic gateways were at a different stage during this period. The Indonesian Throughflow was less restricted than it is today (Lyle et al., 2008) (Figure 2.2) and the Central American Seaway still connected the Atlantic and Pacific Oceans at the equator (Haug and Tiedemann, 1998). This topic is discussed further in Section 2.2.1. The Arctic Ocean remained largely isolated from the Pacific Ocean, as the Bering Strait remained closed until ~ 5.3 Ma (Lyle et al., 2008). The sill of the Greenland-Scotland Ridge, which separates the Arctic and Atlantic Oceans, was deepened sufficiently in the early Oligocene to allow deep-water formation in the north Atlantic (Davies et al., 2001; Via and Thomas, 2006). However, some studies have suggested that the sill depth may have varied during the late Miocene to early Pliocene, as a result of changing mantle plume activity below the Greenland-Scotland Ridge (Wright and Miller, 1996; Thomas and Via, 2007).

By the mid to late Miocene, the global deep-ocean circulation patterns have closely resembled the modern thermohaline circulation (Wright et al., 1991) (Figure 2.2). In the present day deep-water formation occurs in the North Atlantic (North Atlantic Deep Water). This NADW flows southward through the Atlantic, where it partially upwells and mixes with circumpolar water. This mixed water mass then sinks to form Antarctic Bottom Water (AABW), which flows northward into the Atlantic, Pacific and Indian Oceans. The AABW eventually upwells in areas of the northern Indian and Pacific Oceans, where it eventually returns to join the circumpolar waters as intermediate water masses (Broecker, 1991; Schmitz, 1996; Marshall and Speer, 2012). Increases in benthic foraminiferal faunal assemblages, which are characteristic of oxygenated environments, indicate that the start of deep-water formations in the North Atlantic from the mid to late Miocene (Woodruff and Savin, 1989). Dissolved silica and nutrients progressively accumulate in deep waters as it travels away from the source region due to dissolution and/or oxidation of particles sinking from the surface oceans (Woodruf and Savin, 1989). An increase in the silica deposition in the Indian and Pacific Oceans, concurrent with a decrease in silica deposition in the North Atlantic between 14 and 10 Ma, has been attributed to the start of NADW formation (Woodruff and Savin, 1989). The establishment of modern carbon ($\delta^{13}C$) and neodymium (ε_{Nd}) isotope gradients between the North Atlantic, Southern Ocean and the Pacific supports that the onset of proto-NADW formation occurred from the mid to late Miocene onwards, (Wright et al., 1991; Billups et al., 1998, Billups, 2002; van de Flierdt et al., 2004; Hodell and Venz-Curtis, 2006; Martin and Scher, 2006; Thomas and Via, 2007; Klevenz et al., 2008). Consensus on the variation in proto-NADW strength throughout the late

Miocene to early Pliocene has not yet been reached, however, most records indicate that the proto-NADW export was as strong, if not stronger than modern between 8.0 and 3.5 Ma, with a possible short-term reduction in proto-NADW strength between 5.0 and 4.0 Ma (Hodell and Venz-Curtis, 2006; Klevenz et al., 2008).

The late Miocene is thought to be a period of low atmospheric CO_2 concentrations (Figure 2.1.d). CO_2 reconstructions from alkenones (Pagani et al., 1999a, b; Tipple and Pagani 2010), planktic foraminiferal boron isotopes ($\delta^{11}B$) (Pearson and Palmer, 2000) and B/Ca ratios (Tripati et al., 2009) indicate late Miocene atmospheric CO_2 was ~250 ppmv, similar to pre-industrial Holocene values. Reconstructions using stomatal indices also indicate CO_2 was low (~300 ppmv) but variable during the late Miocene (Kürschner et al., 2008). Long-term trends indicate that CO_2 increased slightly towards the Miocene-Pliocene boundary, with early Pliocene CO_2 values being higher than pre-industrial Holocene, but lower than modern levels (Pagani et al., 2010; Seki et al., 2010) (Figure 2.1.d).

Despite the low CO_2 concentrations of the late Miocene to early Pliocene, model output (Micheels et al., 2011) and proxy data (LaRiviere et al., 2012) from the terrestrial and oceanic realms all indicate that the climate was far warmer than the Pliocene Warm Period and the present day. Tortonian (early late Miocene) vegetation reconstructions show that continental temperatures were up to 4.5 °C warmer than the modern day, particularly in the low to mid latitudes, thereby reducing the terrestrial latitudinal gradient (Pound et al., 2011). Oceanic latitudinal temperature gradients were also reduced compared to the present day during Tortonian (Moore and Lombari, 1981; Williams et al.,

2005; LaRiviere et al., 2012). Sea surface temperature (SST) reconstructions from TEX_{86} (Rommerskirchen et al., 2011), $U^{k'}_{37}$ (Herbert and Schuffert, 1998; Rommerskirchen et al., 2011; LaRiviere et al., 2012), radiolarian assemblages (Moore and Lombari, 1981), planktic foraminiferal $\delta^{18}O$ compilations (Williams et al., 2005) and bottom water temperature (BWT) reconstructions from benthic foraminiferal Mg/Ca ratios (Lear et al., 2002) show a cooling trend throughout the late Miocene to early Pliocene. By the end of the Messinian (latest Miocene), best-fit modelled vegetation reconstructions based on palaeobotanical and palaeoecological proxy data indicate that the world remained 2 to 2.5 °C warmer than present, and that the latitudinal temperature gradient increased throughout this period and approached the modern gradient (Pound et al., 2012). The weaker equator-to-pole temperature gradient in the late Miocene and its progressive strengthening throughout the late Miocene to early Pliocene has been attributed to the presence and then gradual closure of the Central American Seaway (Micheels et al., 2011; LaRiviere et al., 2012).

Many authors have argued that CO_2 and climate were decoupled in the late Miocene and early Pliocene due to the discrepancy between a visible global cooling trend superimposed on warmer than modern global temperatures (Kurschner et al., 2008; Tripati et al., 2009; LaRiviere et al., 2012). Other authors have attributed this apparent decoupling to the presence of a negative feedback related to the C_4 grass expansion in the late Miocene (Pagani et al., 2009). Between 8 – 6 Ma, a large shift was observed in the terrestrial realm from a C_3 to a C_4 dominated biomass (Cerling et al., 1997; Matson and Fox, 2010). The C_4 expansion is generally attributed to the presence of widespread aridity in the late Miocene, coupled with the very low CO_2 levels (Pagani et al., 1999b; Tipple

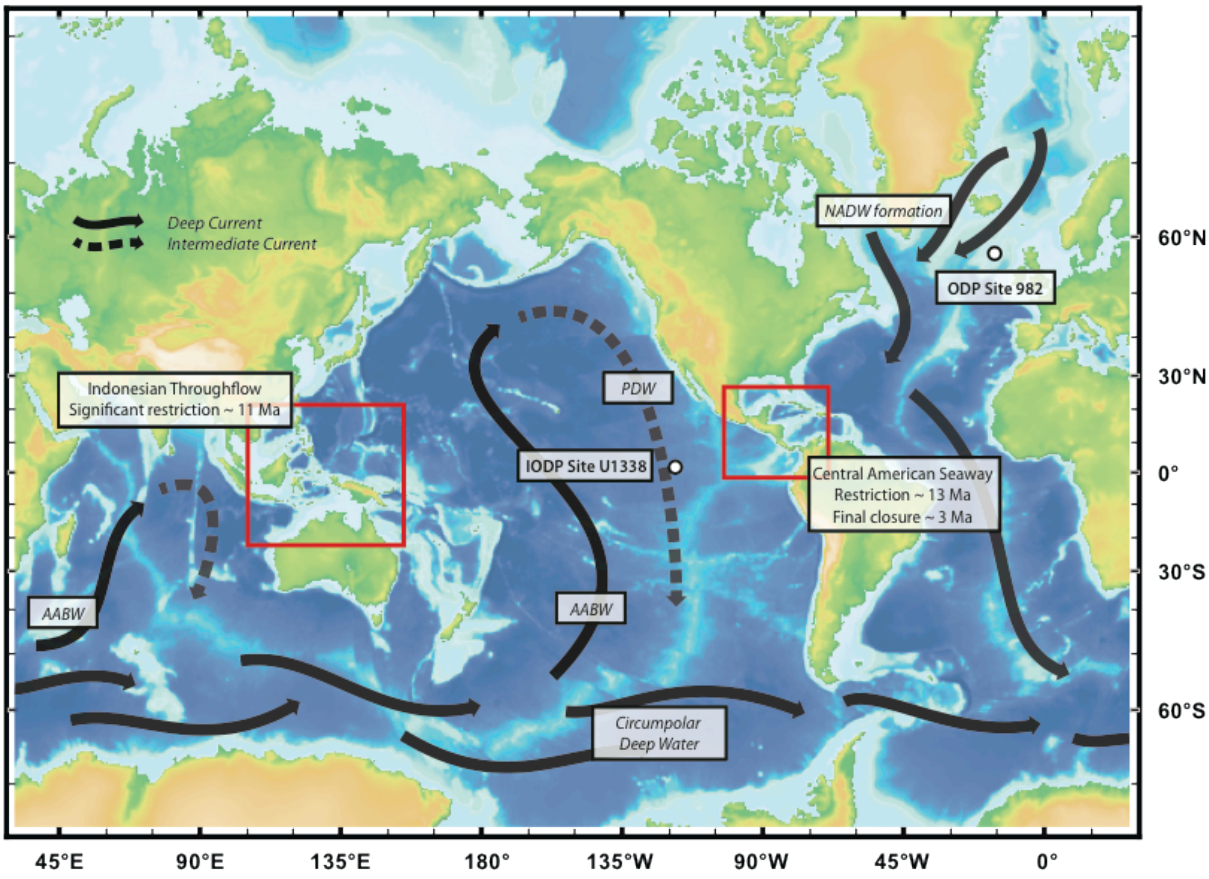

Figure 2.2. Overview of the locations where oceanic gateway changes occurred that affected surface and deep-water circulation in the equatorial Pacific during the late Miocene and early Pliocene. The Indonesian Throughflow (left hand red box) experienced a considerable restriction about 11 Ma (Lyle et al., 2008). Deep-water flow through in the Central American Seaway (right hand red box) was restricted about 11 Ma, whereas the final closure did not occur until about 3 Ma (Haug and Tiedemann, 1998).

The arrows provide a schematic representation of the modern thermohaline circulation pattern, with North Atlantic Deep Water (NADW) forming around Greenland, flowing south to join the Circumpolar deep waters around Antarctica. NADW then sinks to form Antarctic Bottom Water (AABW), which flows into the Atlantic, Indian and Pacific. The Pacific and Indian components of AABW upwell and return towards Antarctica as intermediate waters.

The location of IODP Site U1338 and ODP Site 982 are also shown on this Figure. (Ryan et al., 2009; Made in GeoMapApp using a modern basemap).

and Pagani, 2010). C_3 plants, in particular trees, can increase chemical weathering in the soil, which in turn draws down CO_2 from the atmosphere. It has been suggested that the decrease in C_3 biomass due to the C_4 expansion acted as a negative feedback on CO_2 drawdown, and stopped atmospheric CO_2 from decreasing below pre-industrial Holocene values (Pagani et al., 2009; Beerling et al., 2012).

2.1.2. Threshold events

During the comparatively stable climatic period of the late Miocene and early Pliocene, a number of large shifts occurred in both the terrestrial and ocean realms. The climatic perturbations discussed in the paragraphs below include the C_3 to C_4 expansion (~ 8 – 6 Ma), the biogenic bloom (~ 8 – 4.5 Ma), the late Miocene carbon isotope shift (~ 8 – 6 Ma) and finally, the Messinian salinity crisis (5.96 – 5.33 Ma).

Between 8 and 6 Ma, the C_4 grass expansion marked a shift from a C_3 to a C_4 dominated biomass, driven by a rise in aridity in the middle late Miocene in conjunction with low atmospheric CO_2 levels (Pagani et al., 1999b). Overlapping with the C_3:C_4 shift, rapid increases in the mass accumulation rates of sedimentary components related to primary productivity (carbonate, silica and phosphorous) in addition to increases in various palaeoproductivity proxies were recognised broadly in sites in the Atlantic (Hermoyian and Owen, 2001; Diester-Haass et al., 2002, 2004, 2005, 2006) Indian (Dickens and Owen, 1994, 1999; Hermoyian and Owen, 2001) and Pacific Ocean (van Andel et al., 1975;

Lyle et al., 1995; Farrell et al., 1995; Li et al., 2002; Grant and Dickens, 2002; Wang et al., 2004). This widespread high productivity event, which broadly occurs between 8.0 and 4.5 Ma, is referred to as the Biogenic Bloom (Farrell et al., 1995; Grant and Dickens, 2002). Although the Biogenic Bloom was originally recognised in upwelling areas in the Indian and Pacific oceans (Farrell et al., 1995; Dickens and Owen, 1999), it has since also been recognised in upwelling areas in the Atlantic (Diester-Haass et al., 2002, 2004) and in oligotrophic, non-upwelling areas of the Atlantic and Indian oceans (Hermoyian and Owen, 2001; Diester-Haass et al., 2005). There is some variation in the exact timing and duration of the Biogenic Bloom between sites; however, generally the peak in the biogenic bloom is considered around 7.6 to 6.0 Ma, with a further secondary peak around 5 Ma (Lyle et al., 1995; Grant and Dickens, 2002; Lyle, 2003).

The forcing of the late Miocene to early Pliocene Biogenic Bloom has been attributed to an overall increase of nutrient supply to the ocean and/or a change in the nutrient distribution patterns between the different ocean basins (Grant and Dickens, 2002; Diester-Haass et al., 2004). The correlation between aeolian deposits at marine sites and productivity proxies indicates that increasing atmospheric circulation strength during this time may have increased the supply in nutrients to the oceans (Diester-Haass et al., 2006). In response to changes in atmospheric circulation pattern driven by the Himalayan uplift between 10 – 8 Ma (An et al., 2001), increased low-latitude aridity and a correspondingly larger dust flux into the oceans has also been proposed as a mechanism to increase both nutrient supply and change nutrient delivery patterns (Filippelli, 1997; Diester-Haass et al., 2006). The forcing of the Biogenic Bloom at Site U1338 will be explored in more detail in Chapter 5 (section 5.5.2).

Between 8 – 6 Ma, marine carbon isotope ($\delta^{13}C$) records from planktic and benthic foraminifera show a large long-term negative shift of almost 1 ‰, frequently referred to as the late Miocene carbon isotope shift (LMCIS) (Haq et al., 1980). Because the LMCIS coincides with the peak of the biogenic bloom (~ 7.6 – 6.0 Ma – Lyle et al., 1995), some authors have suggested that the LMCIS could reflect changes in surface water productivity (Diester-Haass et al., 2006). However, a surface productivity driven $\delta^{13}C$ shift would be expected to lead to a divergence of planktic and benthic foraminiferal $\delta^{13}C$ records (see section 3.2.1.2), which is not observed (Grant and Dickens, 2002). An alternative hypothesis is that the LMCIS was driven by changes in the overall $\delta^{13}C$ value of the oceanic reservoir, as this would affect surface and deep-water $\delta^{13}C$ in all ocean basins equally (Hodell et al., 1994) (see section 3.2.1.2). A decrease in overall organic matter deposition on the seafloor and/or an increase in the transfer of organic matter from the land to the sea could cause a negative shift in the overall oceanic reservoir $\delta^{13}C$ (Hodell and Venz-Curtis, 2006). Considering the concurrent nature of the LMCIS and the C_3 to C_4 shift, it could be that the C_4 grass expansion partially drove the LMCIS. However, this hypothesis still needs to be explored fully, and is investigated using the benthic and planktic $\delta^{13}C$ foraminiferal records from Site U1338 produced in this study (see Chapter 3, 5 and 6).

The Messinian Salinity Crisis is an interesting climatic perturbation that occurred towards the end of the late Miocene between 5.96 and 5.33 Ma. During the Crisis, from the onset around 5.96 ± 0.02 Ma the Mediterranean basin became progressively isolated from the Atlantic Ocean, resulting in gypsum deposition between 5.96 – 5.59 Ma and complete isolation from the Atlantic by

5.59 Ma (Krijgsman et al., 1999, 2010). The MSC was brought to an abrupt end when re-flooding from Atlantic waters at 5.33 Ma re-established open marine conditions in the Mediterranean (Krijgsman et al., 2010). Spectral analyses of evaporite sequences in the Mediterranean have shown that the internal cyclical deposition of evaporites was driven by precession-controlled African continental hydrological cycles (Krijgsman et al., 1999). However, the relative role of tectonic uplift and sea level fall in the onset and termination of the MSC is not yet fully constrained. Although tectonic uplift was probably the main driving force of the initial isolation, there is still uncertainty surrounding the exact contribution of glacio-eustatic change during the crisis (Krijgsman et al., 2010).

The effect of the MSC on global climate is relatively unknown. Some authors have suggested that the isolation of the Mediterranean from the Atlantic could have affected the stratification in the Atlantic, as saline warm waters would no longer flow from the Mediterranean into the Atlantic, which could have affected the strength and/or the isotopic composition of the proto-NADW flowing southward (Billups, 2002). The full effects of the MSC on global climate require further work. Past investigations into Messinian glacio-eustacy have not established whether there was a direct causal relationship between the onset of the Messinian Salinity Crisis and global sea level fall (Hodell et al., 2001; Vidal et al., 2002). The combination of the high-resolution benthic foraminiferal $\delta^{18}O$ record from Site U1338 produced in this study, together with additional published data are used to explore the role of glacio-eustacy further (Chapter 6).

2.2. Palaeoceanographical Setting

2.2.1. Eastern Equatorial Pacific

The main study site used in this project is located in the eastern equatorial region of the Pacific Ocean. Past studies have highlighted the importance of the Pacific Ocean in the evolution of climate during the Cenozoic (van Andel et al., 1975; Pisias et al., 1995). The equatorial Pacific comprises 50% of Earth's tropical ocean and plays an essential role in global heat transport, carbon cycling, and the hydrologic cycle. In addition, the equatorial Pacific is a principal zone of primary production (Lyle et al., 2010), which makes it an important region for deposition and burial of calcium carbonate-rich sediments (Pisias et al., 1995). The equatorial region is furthermore a major zone of heat gain through the trapping of incoming solar radiation (Bryden and Brady, 1985). The eastern equatorial cold tongue, located in the central and eastern equatorial Pacific, is an important region for CO_2 exchange, with a large CO_2 flux going from the CO_2-rich upwelled waters to the atmosphere (Takahashi et al., 1997, 2002, 2009). The high biogenic sedimentation rates that are characteristic of this region make the equatorial Pacific an ideal location for high-resolution physical, biological and chemical studies on pelagic sediments, especially studies that aim to further understanding of the cause-and-effect relationship between surface water processes and climate change.

In the early Cenozoic, all major ocean basins were connected by a series of circumequatorial gateways, including the Tethyan Seaway and the Central American Seaway (CAS). By the late Miocene, the Tethyan Seaway had largely disappeared, and the Indonesian Throughflow (ITF) remained as the last

significant connection between the Indian and Pacific Basins (Figure 2.2). The ITF became significantly restricted about 11 Ma, and has continued shoaling up to the present day. There is still considerable flow of water from the Pacific into the Indian Ocean (10^6 m^3/s) (Lyle et al., 2008). As the ITF was deeper during the late Miocene and early Pliocene, the Pacific-to-Indian flow must have been larger than the present day flow (Billups, 2002). The Pacific and Atlantic basins remained connected by the CAS throughout the late Miocene and early Pliocene (Figure 2.2). However, the exact timing of the progressive separation of the two basins is not yet fully constrained. The CAS started shoaling around 13 Ma, restricting deep-water flow from the Pacific to the Atlantic (Haug and Tiedemann, 1998). Evidence for shoaling of the calcite compensation depth (CCD – the depth in the water column below which the seawater is under-saturated with respect to $CaCO_3$; below the CCD the rate of calcite dissolution is greater than or equals the rate of calcite accumulation) in the easternmost Pacific has been linked to further restriction of the deep-water connection between the two basins at about 10 Ma (Lyle et al., 1995). Progressive flow restriction through the CAS would have continued throughout the late Miocene. Various authors have interpreted changes in water mass tracers ($\delta^{13}C$ and Mg/Ca) between the two basins around 6.6 to 5 Ma as evidence for further CAS closure (Billups, 2002; Lear et al., 2003). Although the formation of a land bridge did not occur until about 2.7 Ma, the shoaling of the CAS to depths less than 100 m occurred after 4.6 Ma and caused a major reorganisation of surface ocean circulation in the Atlantic (Haug and Tiedemann, 1998).

Between 4.6 – 3.2 Ma the on-going restriction of surface current exchange between the Atlantic and Pacific is associated with an increase of salinity in the

Atlantic and the establishment of the modern Atlantic-Pacific salinity gradients (Haug et al., 2001). Effects of the CAS restriction on the surface circulation patterns in the Pacific are thought to be fewer, as the flow went from the Pacific to the Atlantic (Haug and Tiedemann, 1998). Although full-scale Northern Hemisphere glaciations did not occur until ~ 3.1 – 2.5 Ma, surface water changes caused by the restriction of shallow-water exchange through CAS were a crucial pre-condition to the establishment of large scale continental ice sheet growth (Haug and Tiedemann, 1998).

As described in Section 2.1.1, the late Miocene to early Pliocene deep-water circulation patterns closely resembled the modern thermohaline conveyor belt circulation. The largest changes that occurred in Pacific Deep Water (PDW) circulation were the cessation of flow from the Pacific into the Atlantic and Indian basins through the respective restriction of the CAS around 13 Ma (Haug and Tiedemann, 1998) and of the ITF around 11 Ma (Lyle, 2003). In the modern thermohaline circulation pattern, the PDW are seen as the end of the deep-water conveyor belt system. AABW flows into the deepest Pacific, collecting nutrients and carbon released from the oxidation of organic matter in the water column above as it flows further north (Wright et al., 1992). This nutrient rich deep-water progressively mixes with overlying PDW (van der Flierdt, 2004). Pacific Deep Water eventually exports deep water back into the Southern Ocean (Schmitz, 1996; Marshall and Speer, 2012). Before 7.5 Ma, the late Miocene $\delta^{13}C$ gradient between the North Atlantic and Pacific Oceans ranged from 0.5 to 0.8 ‰ (Wright et al., 1991), slightly less than the modern gradient of 1 ‰ (Kroopnick, 1985). This gradient increased to the modern value after 7 Ma, and

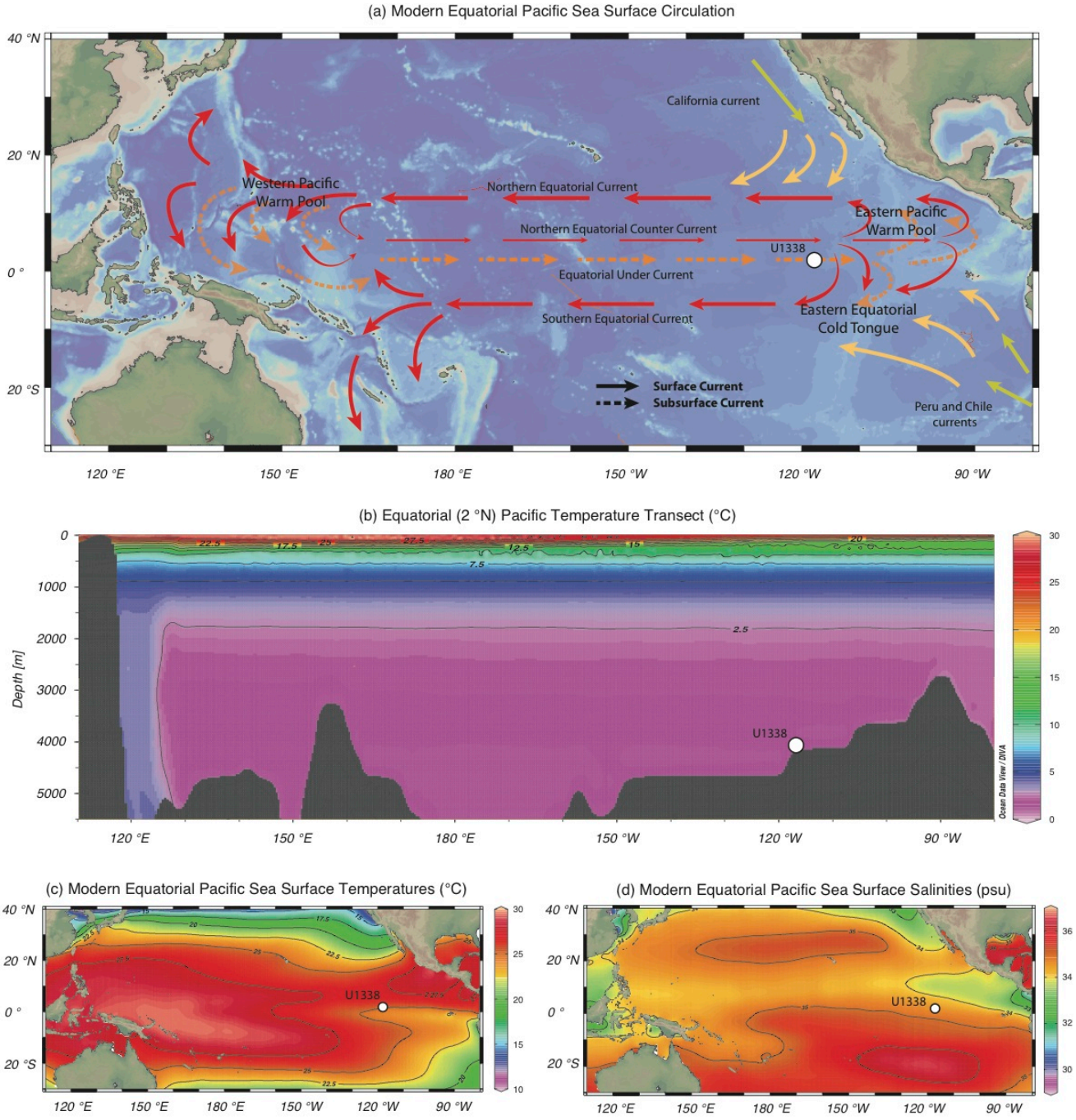

Figure 2.3. Modern equatorial Pacific region, showing the location of IODP Site U1338.

(a) Modern equatorial Pacific sea surface circulation, showing the wind-driven circulation pattern with the Northern and Southern Equatorial Currents driving warm water westward towards the Western Pacific Warm Pool. The warm Northern Equatorial Counter Current and the cooler Equatorial Undercurrent return waters to the eastern Pacific, respectively supplementing the Eastern Pacific Warm Pool and the Eastern Equatorial Cold Tongue. The cool Peru and Chile currents also join the Eastern Equatorial Cold Tongue. The colour of the arrow

denotes the approximate temperature of each of the currents. Modern circulation patterns adapted from Pisias et al. (1995) and Rousselle et al. (2013).

(b) Modern distribution of temperature with water depth along a 2 °N latitudinal transect. Interesting features include the progressive shoaling of the thermocline from west to east, and modern bottom water temperatures at IODP Site U1338 of ~ 1.5 °C (data from Locarnini et al., 2010). Depth is shown on the left vertical axis. Thermocline depth in eastern Pacific (118 °W - Site U1338) = ~ 100 m water depth. Thermocline depth in western Pacific (160 °E) = ~ 190 m water depth.

(c) Modern sea surface temperatures: temperatures are warmer in the western Pacific due to the build up of warm waters by trade winds. Cooler temperatures are found in the eastern Pacific because of the influx of cooler currents originating off South America combined with the influx of the Equatorial Undercurrent (see also Figure 2.3. a); Surface waters at Site U1338 are about 25 °C (data from Locarnini et al., 2010).

(d) Modern sea surface salinity: Pacific equatorial waters are less saline than Atlantic ones. Surface waters at Site U1338 have a salinity of around 34.6 psu (data from Antonov et al., 2010).

All maps were made using ODV4 (Schlitzer, 2010) with data from the World Ocean Atlas 2009 database (Levitus, 2010). The temperature and salinity maps were interpolated using DIVA gridding.

remained at ~ 1 ‰ for the remainder of the late Miocene and early Pliocene (Wright et al., 1991; Billups et al., 1998; Hodell and Venz-Curtis, 2006).

Reconstructions of equatorial Pacific bottom water temperatures (BWT) are limited for the late Miocene to early Pliocene. Mg/Ca measurements on benthic foraminifera from western equatorial Pacific ODP Site 806 indicate BWT were approximate 5.5 °C (Lear et al., 2003), which agrees with Mg/Ca estimates for this period from the South Atlantic (Billups and Schrag, 2002). This suggests that Pacific BWT were warmer than the present day Pacific BWT of ~ 1.5 °C (Locarnini et al., 2010), which agrees with temperature estimates from $\delta^{18}O$ (Billups et al., 1998). Recent reconstructions, which compiled data from a wide range of sites in the equatorial Pacific, show that the CCD recovered and deepened after the late Miocene carbonate crash (~10 Ma), which was a major dissolution event in the late Miocene when the CCD shoaled in most of the equatorial Pacific (Lyle et al., 1995, 2003). Since ~ 10 Ma, the CCD has remained at a depth of around 4.5 km for the remainder of the late Miocene and early Pliocene (Palike et al., 2012).

The state of equatorial Pacific surface water circulation during the late Miocene and early Pliocene is not well known, but is thought to broadly resemble modern circulation patterns in this region. The present day surface circulation pattern in the equatorial Pacific is complicated (Figure 2.3.a), but largely reflects tropical atmospheric circulation patterns and the change in the direction of the Coriolis effect across the equator (Pisias et al., 1995). Currently, the convergence zone of the northeast and southwest trade winds, referred to as the Intertropical Convergence Zone (ITCZ), generally lies just to the north of the equator in the eastern equatorial Pacific. Driven by trade winds along the ITCZ, the Northern

and Southern Equatorial currents (NEC, SEC) drive warm waters towards the west, causing a build-up of waters in the Western Pacific Warm Pool (WPWP). The build-up of water in the west creates a pressure gradient that both drives the North Equatorial Counter Current (NECC), which carries warm waters from west to east to feed the Eastern Pacific Warm Pool (EPWP), and drives the cooler Equatorial Undercurrent (EUC) from east to west. In the east, the EUC combines with the cool Peru and Chile currents to form the Eastern Equatorial Cold Tongue (EECT). The combination of the build-up of warm water in the WPWP and cool EUC flowing towards the eastern equatorial Pacific, leads to an asymmetrical thermocline, which is deeper in the west Pacific compared to the east (Figure 2.3.b).

The exact time when the modern distribution of surface currents in the equatorial Pacific was established is relatively unknown. The WPWP is thought to have first appeared around 11.6 Ma, following the initial, significant restriction of the ITF. Mixed layer and thermocline reconstructions from multi-species planktic foraminiferal isotope and assemblage studies from ODP Site 806 (western equatorial Pacific) indicate that a proto WPWP and EUC were present between 11.6 – 9.6 Ma, with surface circulation patterns resembling normal to 'La Niña'-like conditions (Nathan and Leckie, 2009). The authors suggest that between 9.6 and 6.5 Ma the WPWP and EUC were weakened, and more 'El Niño' like conditions dominated. Thermocline reconstructions that combined the foraminiferal thermocline reconstructions from Site 806 with a radiolarian diversity study from ODP Site 1241 (eastern equatorial Pacific) indicate that the thermocline was deeper across the equator during the late Miocene, and shoaled progressively leading into the early Pliocene (LaRiviere et al., 2012), which

would fit a scenario of dominant 'El Niño' conditions for this period. Evidence for active 'El Niño'-like conditions during the late Miocene have also been found in the inter-annual variability recorded by evaporite varve thickness as far away as the Mediterranean (Galeotti et al., 2010). The foraminiferal studies at Site 806 indicate that the WPWP and EUC strengthened again after 6.5 Ma, leading to a reestablishment of normal to 'La Niña'-like conditions (Nathan and Leckie, 2009; LaRiviere et al., 2012). Alkenone studies at IODP Site U1338 also indicate a shoaling of the thermocline in the late Miocene, and suggest that the eastern equatorial cold tongue first appeared in the early Pliocene around 4.8 – 4.0 Ma (Rousselle et al., 2013). All three studies cite the gateway restrictions of the ITF and the CAS as a dominant driving force for these circulation and thermocline changes.

Modern sea surface temperatures (SST) and sea surface salinities (SSS) for the equatorial Pacific region are shown in Figure 2.3c and d respectively. SST reconstructions of the equatorial Pacific during the late Miocene to early Pliocene period reflect the globally warmer temperatures. Summer and winter temperatures estimated from radiolarian assemblages from DSDP Sites 158 and 77 and alkenone $U^{k'}_{37}$ records from IODP Site U1338 all show late Miocene climate was warmer than modern (Moore and Lombari, 1981; Rousselle et al., 2013). Temperatures in the easternmost Pacific, in the EPWP, were as high as 30 °C compared to ~28 °C today (Moore and Lombari, 1981), whilst temperatures in the central-eastern Pacific reached around 28-29 °C compared to modern temperatures of around 25 °C (Moore and Lombari, 1981; Rousselle et al., 2013) (Figure 2.3c). All datasets also reflect the general cooling trend seen in surface waters elsewhere on the globe (*North Pacific:* Moore and Lombari, 1981 and

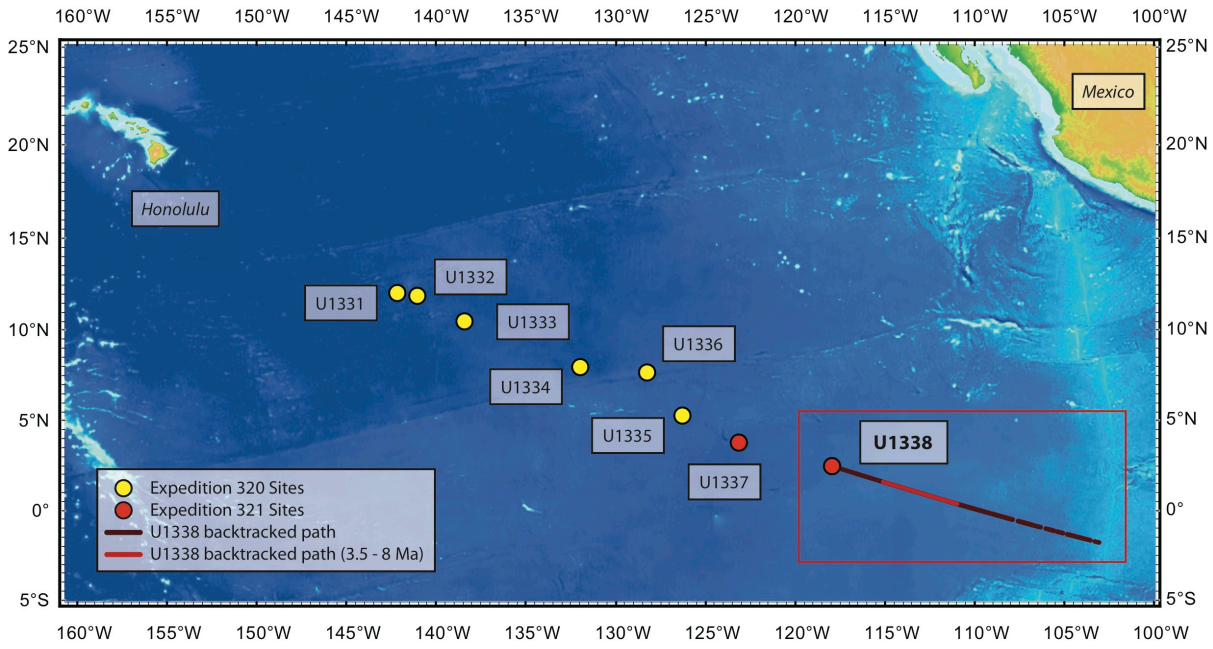

Figure 2.4. Showing the location of the IODP PEAT Expedition 320 and 321 sites. To account for plate movement, the backtracked location of Site U1338 from its formation until the present day (dark red) is shown, with the interval between 8.0 and 3.5 Ma highlighted (bright red). (Made using GeoMapApp – Ryan et al., 2009).

U1338 First Order Age Model			
Event	**Type**	**Depth** *(m CCSF-A)*	**Age** *(Ma)*
C2An.3/C2Ar	*Magnetochron*	49.13	3.596
T *Reticulofenestra pseudoumbilicus* (NN16)	*Nannofossil*	51.86	3.7
T *Ceratolithus acutus* (NN13)	*Nannofossil*	75.49	5.04
B Ceratolithus acutus	*Nannofossil*	84.6	5.35
T *Discoaster quinqueramus* (NN12)	*Nannofossil*	93.38	5.58
T *Nicklithus amplificus*	*Nannofossil*	107.12	5.98
B *Nicklithus amplificus*	*Nannofossil*	133.68	6.91
B *Discoaster berggrenii* (NN11)	*Nannofossil*	177.01	8.29
T = Top Occurance; B = Bottom Occurance			

Table 2.1.

Overview of the shipboard palaeomagnetic and nannofossil datums, their depth along the U1338 splice (m CCSF-A; Wilkins et al., 2013) and their respective age. These datums form the basis for the first-order age model used for Site U1338. All shipboard nannofossil and palaeomagnetic data comes from (Palike et al., 2010) and (Expedition 320/321 Scientists, 2010).

LaRiviere et al., 2012; *Equatorial Atlantic:* Herbert and Schuffert, 1998; *South Atlantic:* Rommerskirchen et al., 2011; *Global SST reconstruction:* Williams et al., 2005). Sea surface salinity (SSS) is not well constrained for the late Miocene and early Pliocene. Modern SSS near Site U1338 is ~ 34.6 psu. Rousselle et al., (2013) combine alkenone $U^{k'}_{37}$ temperatures and $\delta^{18}O$ from coccolithophores to reconstruct the $\delta^{18}O$ of seawater, which predominantly reflects local salinity and global ice volume changes (see Section 3.2.1.1). The authors attribute changes between 6.8 and 6.0 Ma in their reconstructed $\delta^{18}O_{seawater}$ as a freshening of the surface waters by ~ 2 psu (Rousselle et al., 2013).

2.2.2. Site Description: IODP Site U1338

Our study utilises late Miocene through early Pliocene sediments recovered at Integrated Ocean Drilling Program (IODP) Site U1338 (2°30.469'N, 117°58.178'W; water depth 4200 m, palaeo depth ~3850 – 4050 m (Palike et al., 2012), drilled during IODP Expeditions 320/321 "Pacific Equatorial Age Transect". Sailing in 2009, the PEAT programme was designed to further understanding of how the equatorial Pacific evolved during the Cenozoic and how this major oceanic region interacted with the global climate system. The PEAT cruises drilled a NW-SE transect of eight sites, which each targeted a period between 52 – 0 Ma when the respective sites moved across the equator in a NW direction (Figure 2.4). Past expeditions in this region, ODP Exp. 199 (Paleogene) and ODP Exp. 138 (Neogene) did not recover sufficient carbonate rich sediment to splice together sections that were longer than 10 Myr suitable

for cyclostratigraphy (Lyle et al., 2010). An important goal of the PEAT programme was to augment existing drilling records and work towards a continuous high-resolution composite record of environmental change in the equatorial region between 56 Ma and the present (Lyle et al., 2010). Detailed information about the PEAT programme and Site U1338 can be found in the 320/321 Expedition Summary (Palike et al., 2010) and the Site U1338 Summary (Expedition 320/321 Scientists, 2010).

Four holes (A-D) were cored at Site U1338 using a combination of advanced piston corer and extended core barrels techniques. Combining segments from holes A-C, Wilkens et al. (2013) constructed a composite section, with an approximate length of 400 m core composite depth below seafloor (CCSF-A), which is equivalent to meters composite depth below seafloor (mcd) (IODP-MI, 2011).

Using the shipboard nannofossil and palaeomagnetic datums available for the interval between 8.0 and 3.5 Ma provided the shipboard splice with first-order age control (Table 2.1). Figure 2.5 shows the shipboard biostratigraphic and palaeomagnetic datums available for the late Miocene and early Pliocene interval. Unfortunately, only one palaeomagnetic reversal datum was measured between 8.0 and 3.5 Ma. Seven coccolithophore nannofossil datums were chosen to supplement the palaeomagnetic datum. The coccolith nannofossil datums were preferentially selected as these datums had good coverage across the relevant interval and approximated the linear regression through all other biostratigraphic datasets well (Figure 2.5). Two coccolithophore nannofossil datums (~ 7.0 and 7.2 Ma) were not included in the first-order age model, as these distorted the long-term trend isolated in Chapter 4 (see section 4.3.1).

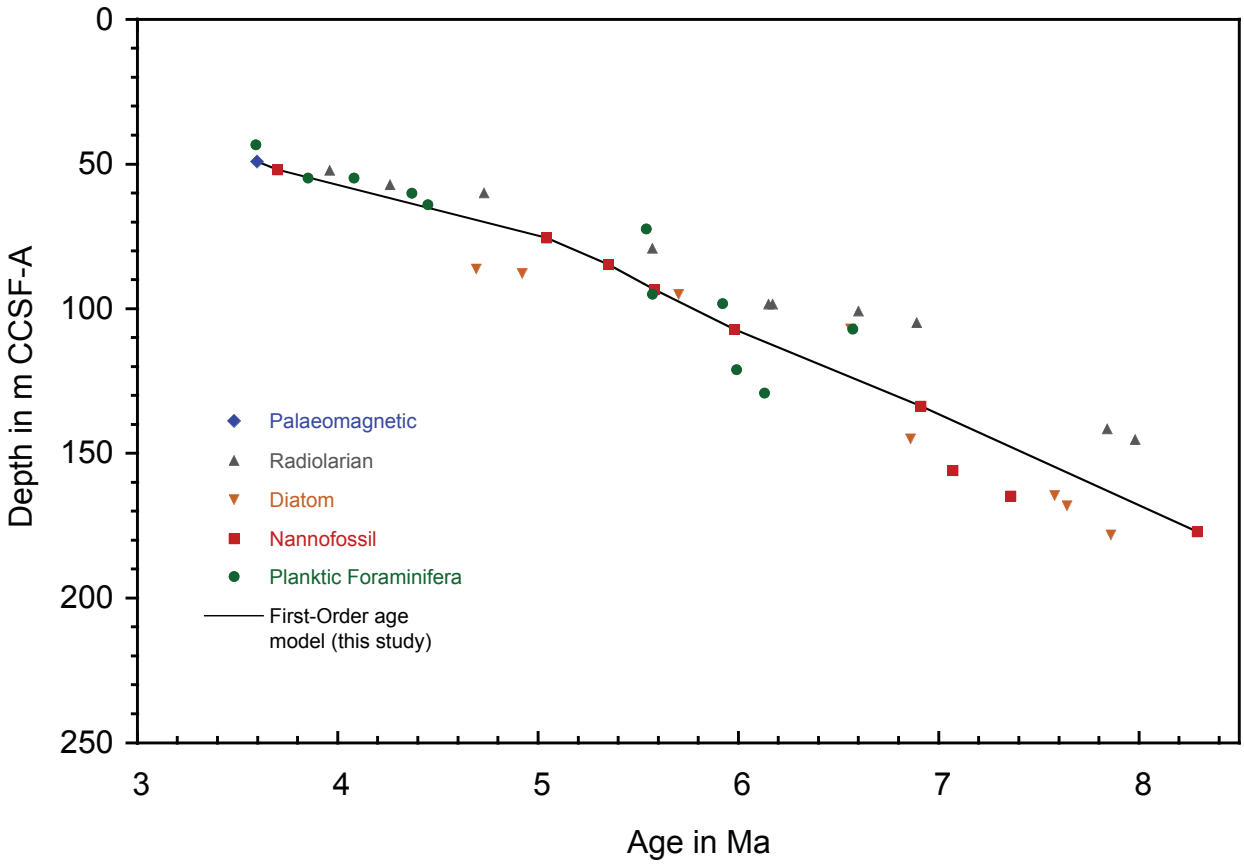

Figure 2.5. Overview of the shipboard biostratigraphic and palaeomagnetic datums for Site U1338 between 8.0 and 3.5 Ma (Expedition 320/321 Scientists, 2010). The first-order age model compiled for this study, using linear interpolation between the 1 palaeomagnetic and 7 nannofossil datums, is shown with a black line.

Between 48 and 180 m CCSF-A, the composite splice provides an expanded, continuous sedimentary record spanning the late Miocene to early Pliocene, with high sedimentation rates during both periods (shipboard estimates: late Miocene = 28.7 m/Myr; early Pliocene = 12.7 m/Myr) (Expedition 320/321 Scientists, 2010). During this target period, Site U1338 was located between 0 – 2 °N in the equatorial Pacific, underneath the main equatorial productivity zone (Palike et al., 2012) (Figure 2.4). The main lithology constitutes varying light green to light grey nannofossil ooze, with occasional darker intervals containing abundant siliceous microfossils (predominantly diatoms) (Expedition 320/321 Scientists, 2010).

Site U1338 remained above the CCD from the initial formation of the oceanic crust to today, although reconstructions of the CCD (Palike et al., 2012) show decreases in the carbonate accumulation rate when the CCD briefly shoaled around 4 Ma. Weight % $CaCO3_3$ reconstructions, from discrete measurements and x-ray fluorescence (XRF) data, show that between 48 and 180 m CCSF-A average %$CaCO_3$ remains high at around 70 – 80 %, although there are a few intervals where %$CaCO_3$ drops to around 40 – 60% (Lyle et al., 2012; Lyle and Backman, 2013).

Benthic foraminifera occur continuously throughout the record, and are generally well preserved. Assemblage composition indicates a bathyal to abyssal palaeoenvironment (Expedition 320/321 Scientists, 2010). Planktic foraminifera generally make up >80% of the >63 μm fraction of shipboard samples, with the preservation varying from poor to very good (Hayashi et al., 2013). Planktic foraminifer assemblages are characteristic of tropical to subtropical surface conditions (Expedition 320/321 Scientists, 2010).

Chapter 3.

Planktic and Benthic Foraminiferal Stable Isotope Records from IODP Site U1338: Preservation and Stratigraphy

3.1. Foraminifera: Isotopes and Preservation

Foraminiferal tests are frequently used as geochemical and micropalaeontological archives in many palaeoceanographical and biostratigraphical studies. Foraminifera are particularly popular as geochemical proxies, as different aspects of the chemical composition of their calcite shells, otherwise known as tests, are used as palaeoclimate proxies. However, with geochemical proxies, it is crucial that the calcite test is well preserved. Later recrystallisation or overgrowth with a calcite that was precipitated at a different temperature in water with a different chemistry can considerably alter the average chemical composition of the foraminiferal test (Pearson et al., 2001).

Likewise, dissolution can remove primary calcite, thereby altering the average chemical composition of the foraminiferal test (Edgar et al., 2013).

The main focus of chapter 3 is to evaluate the preservation of both the benthic and planktic foraminifera selected for geochemical analysis at IODP Site U1338. Section 3.2 presents a brief overview of the use of foraminifera as geochemical proxies in palaeoceanography, focussing particularly on the use of $\delta^{18}O$ and $\delta^{13}C$ measured on foraminifera, and the effects of diagenesis on foraminiferal calcite. Section 3.2 will also review previous work on early Pliocene to late Miocene isotope stratigraphy. An overview of the analytical methods used in this chapter can be found in section 3.3. In section 3.4, the $\delta^{18}O$ and $\delta^{13}C$ stable isotope measurements are presented, together with back-scattered electron images (BSE) collected using scanning electron microscopy (SEM) from *Cibicidoides mundulus* and *Globigerinoides sacculifer*. Finally, in section 3.5, the relative influence of primary factors on the benthic foraminiferal stable isotopes, such as changes in seawater $\delta^{18}O$ and $\delta^{13}C$, versus secondary factors, such as dissolution, are assessed by comparing the stable isotope, SEM images and % coarse fraction (%CF) measurements with published records of weight% $CaCO_3$ and SiO_2. These comparisons will also test whether or not the benthic foraminiferal stable isotope records are suitable for stratigraphic correlation. Finally, the broad trends of the planktic and benthic foraminiferal stable isotopes are discussed with respect to the known early Pliocene to late Miocene stratigraphy.

3.2. Background and Previous Work

3.2.1. Foraminifera in Palaeoceanography

Foraminifera are unicellular marine microorganisms, which generally precipitate their calcitic shells directly from seawater over a life span of ~ 2 weeks for some planktic species (Spero, 1998) and up to five years of more for some benthic species (Hemleben and Kitazato, 1995). These microfossils are popular palaeo-archives, as firstly, both planktic and benthic species are widespread and often diverse throughout the Cenozoic and Mesozoic (Morkhoven et al., 1986; Wade et al., 2011). In addition, planktic species generally evolve rapidly, making them ideal organisms for biostratigraphy (Wade et al., 2011). Both planktic and benthic foraminifera further exhibit a wide geographic distribution, with species found from the Polar Regions to the tropics (Kennet and Srinivasan, 1983; Morkhoven et al., 1986). Finally, characteristic foraminiferal species can be found throughout the water column. Photic zone mixed layer and thermocline-dwelling planktic foraminifera are common in all ocean basins (Kennet and Srinivasan, 1983), whereas benthic species can both live in the top 2-20 cm of sediment column (infaunal benthic foraminifera) and at the sediment-water interface (upper 1 cm of sediment column – epifaunal benthic foraminifera) (Morkhoven et al., 1986). As foraminifera record the chemical composition of the seawater in which they lived in their tests, they are particularly popular as geochemical archives. The following sections explore the use of $\delta^{18}O$ and $\delta^{13}C$ measured on planktic and benthic foraminiferal calcite, followed by a section discussing the impact of diagenesis on these proxies.

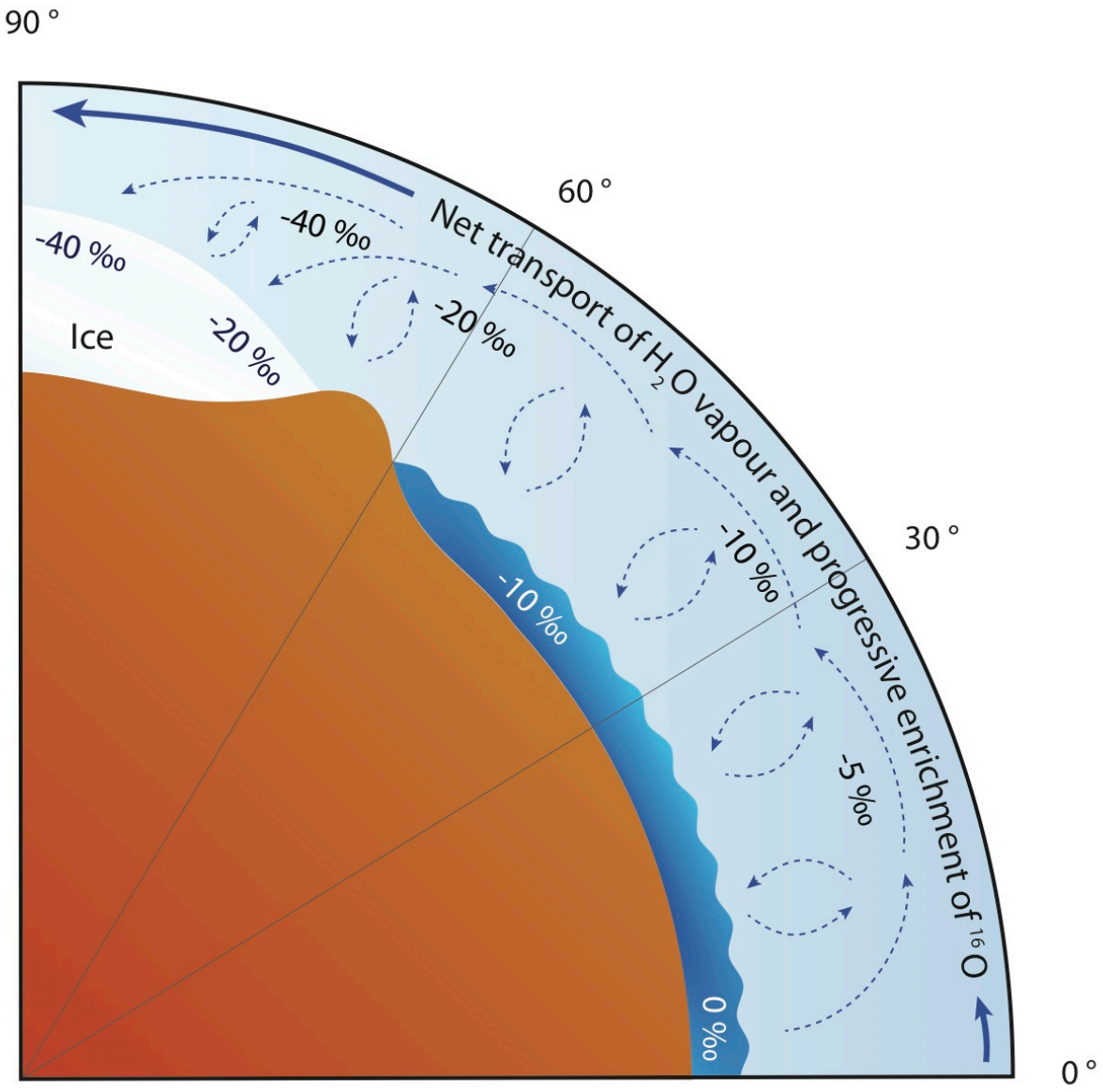

Figure 3.1. Schematic diagram showing cross section of the Earth and indicating how the $\delta^{18}O_{sw}$ becomes progressively enriched in ^{16}O as it moves from low to higher latitudes, leading to very isotopically ^{16}O enriched ice sheets (adapted from Ruddiman, 2001). Values are chosen to represent the progressive fractionation and are not based on published or measured values.

3.2.1.1. Stable Oxygen Isotopes in foraminifera ($\delta^{18}O$)

The stable oxygen isotope composition of foraminiferal calcite ($\delta^{18}O$) is a function of the original oxygen isotopic composition of seawater ($\delta^{18}O_{sw}$) and the foraminifera's calcifying temperature (Urey, 1947; Emiliani, 1954; Duplessy et al., 1970). Species-specific temperature calibrations exist for both planktic and benthic foraminiferal $\delta^{18}O$. These calibrations are generally based upon the original calibration for organically precipitated calcite (Epstein et al., 1953):

$$T = 16.5 - 4.3 \times (\delta^{18}O_{calcite} - \delta^{18}O_{sw}) + 0.14 \times (\delta^{18}O_{calcite} - \delta^{18}O_{sw})^2$$

In this calibration, when $\delta^{18}O_{sw}$ increases, $\delta^{18}O$ increases proportionately. When temperature increases by 1°C, $\delta^{18}O$ decreases by ~0.23‰. The dominant global control on $\delta^{18}O_{sw}$ is the amount of ^{16}O-enriched freshwater stored in ice sheets, which is related to global ice volume (Figure 3.1). Local influences, such as river influx and the evaporation/precipitation balance, both affect local salinity and $\delta^{18}O_{sw}$, particularly in surface waters (Rohling and Bigg, 1998).

Benthic foraminiferal $\delta^{18}O$

Benthic foraminiferal $\delta^{18}O$ reflects bottom water temperature (BWT) and deep-water $\delta^{18}O_{sw}$ (Shackleton and Opdyke, 1973). Changes in salinity do not affect deep-water $\delta^{18}O_{sw}$ much, as deep-waters are isolated from the effects of evaporation, river discharge and freshwater runoff (Katz et al., 2010). Therefore variations in deep-water $\delta^{18}O_{sw}$ mainly reflect variations in global ice volume (Miller et al., 2005). This relationship has been much utilised to reconstruct glacio-eustacy during the Cenozoic (65.5-0 Ma) (Shackleton and Opdyke, 1973;

Miller et al., 1991; Holbourn et al., 2005; John et al., 2011). The benefit of glacio-eustatic reconstructions, which use benthic foraminiferal $\delta^{18}O$ to approximate $\delta^{18}O_{sw}$ and sea level, is that these reconstructions can estimate glacio-eustacy at orbital timescales (~3-4 kyr resolution) (Shackleton and Opdyke, 1973; Miller et al., 1991; Holbourn et al., 2005; Westerhold et al., 2005; Holbourn et al., 2007). The main issue with this approach is that benthic foraminiferal $\delta^{18}O$ is also influenced by temperature, which masks $\delta^{18}O_{sw}$ and corresponding ice volume signal. More recent approaches have used independent temperature proxies, such as Mg/Ca (Lear et al., 2000; Billups and Schrag, 2002), or a combination of Li/Ca and Mg/Ca (Lear et al., 2010) to deconvolve the relative contributions of calcification temperature and $\delta^{18}O_{sw}$ on benthic foraminiferal $\delta^{18}O$.

Planktic foraminiferal $\delta^{18}O$

Planktic foraminiferal $\delta^{18}O$ reflects the $\delta^{18}O_{sw}$ and temperature of the surface water, and can be used as a guide towards sea surface temperature (SST). Shallow water $\delta^{18}O_{sw}$ is controlled by salinity (Rohling and Bigg 1998) and sea-water acidity (pH) (Spero et al., 1997), as well as ice volume. An increase in salinity leads to an increase in $\delta^{18}O_{sw}$ (0.5‰ psu^{-1}; psu = practical salinity unit), as evaporation favours the uptake of ^{16}O-enriched water (Maslin and Swann, 2005). Furthermore, planktic foraminifera are a diverse group, with different species found living within specific depth ranges (Emiliani, 1954; Spero and Lea, 1993). The range in depth habitat of different planktic species (surface/mixed layer/thermocline/deep thermocline dwellers) can be utilised to reconstruct surface waters structure, as the main changes in this region are related to temperature and nutrient availability (Elderfield et al., 2002).

Successfully interpreting planktic foraminiferal $\delta^{18}O$ requires a good understanding of the ecology of both extant and extinct species (Thunell and Belyea, 1982). Certain planktic and benthic species do not precipitate their shells in equilibrium with surrounding seawater, which can lead to a constant offset between the $\delta^{18}O$ and $\delta^{18}O_{sw}$. These 'vital effects' or disequilibrium effects have to be taken into account when looking at biogenic calcite (Spero and Williams, 1988; Shackleton et al., 1995b), and is an important reason for using species-specific calibrations when relating $\delta^{18}O$ to $\delta^{18}O_{sw}$ or temperature.

3.2.1.2. Stable Carbon Isotopes in foraminifera ($\delta^{13}C$)

The carbon isotope composition of foraminiferal calcite ($\delta^{13}C$) reflects the original $\delta^{13}C$ of the dissolved inorganic carbon (DIC) of seawater ($\delta^{13}C_{DIC}$) (Epstein et al., 1953). Because the residence time of carbon is about 180 kyrs, variations in $\delta^{13}C_{DIC}$ on longer timescales reflect changes in the $\delta^{13}C$ of the oceanic carbon reservoir (Broecker and Peng, 1982).

Benthic foraminiferal $\delta^{13}C$

Benthic foraminiferal $\delta^{13}C$ is controlled by 1) the initial $\delta^{13}C_{DIC}$ of the source water, 2) the time since the deep water sank below the surface, and 3) changes in overlying surface water productivity. Processes such as surface water productivity, gas exchange at the atmosphere-ocean interface and mixing of water masses with different $\delta^{13}C_{DIC}$ values all affect the source water $\delta^{13}C_{DIC}$

(Hodell and Venz-Curtis, 2006). As the water mass sinks and travels away from the source region, progressive amounts of ^{12}C-rich particulate organic matter oxidises in the overlying water column, thereby releasing its constituents to the bottom water, and subsequently gradually enriching the deep-waters with ^{12}C and nutrients (e.g. water mass 'aging') (Broecker and Peng, 1982). Changes in surface water productivity also affect deep-water $\delta^{13}C_{DIC}$, because, in areas of high surface productivity, the organic matter flux to the seafloor is greater, and more ^{12}C is released during oxidation, thereby decreasing deep-water $\delta^{13}C_{DIC}$ (Katz et al., 2010). Comparing benthic foraminiferal $\delta^{13}C$ gradients between basins, and between locations with different water depths has often been applied as a method for reconstructing deep-ocean circulation (Woodruff and Savin, 1989; Wright et al., 1991/1992; Hodell and Venz-Curtis, 2006).

Planktic foraminiferal $\delta^{13}C$

Planktic $\delta^{13}C$ reflects variations in $\delta^{13}C_{DIC}$, although many species show constant offsets from the $\delta^{13}C_{DIC}$ due to vital effects. Surface $\delta^{13}C_{DIC}$ predominantly varies with surface productivity, as marine phytoplankton, which are the main surface waters producers, have an average $\delta^{13}C_{org}$ between -17 and -22‰. In areas with high nutrient flux and high productivity, the $\delta^{13}C_{DIC}$ becomes depleted in ^{12}C (Maslin and Swann, 2005). Comparing interspecies $\delta^{13}C$ values can be used to reconstruct changes in nutrient distribution within the surface water column (Katz et al., 2010). Vital effects are often used as an umbrella-term that includes species-specific offsets from equilibrium-precipitation of calcite from seawater. This is because many planktic foraminifera have photosymbionts living in the microenvironment surrounding

the foraminifera (Bé et al., 1982). These symbionts preferentially take up the ^{12}C in $\delta^{13}C_{DIC}$, which enriches the local seawater further with ^{13}C (Spero and Lea, 1993). Because the planktic foraminifera precipitate their tests from this further ^{13}C-enriched seawater, the foraminiferal $\delta^{13}C$ becomes further depleted in ^{12}C (Spero and William, 89; Spero 1998). By controlling the habitat and life cycle of the photosymbionts, pH and light-dark cycles affect $\delta^{13}C$ by altering the microenvironment from which the foraminifera precipitates its shell (Spero, 1998). As these effects are different between species, they may contribute to the differences in vital effects.

Planktic – benthic foraminiferal $\Delta\delta^{13}C$

Comparing benthic and planktic foraminiferal $\delta^{13}C$ can help to reconstruct the relative importance of changes in productivity, versus changes in the average oceanic reservoir $\delta^{13}C$ (Figure 3.2). Intensification of surface productivity increases the difference between benthic and planktic foraminiferal $\delta^{13}C$, whereas this difference decreases during low productivity (Maslin and Swann, 2005) (Figure 3.2.a). A co-variation of benthic and planktic foraminiferal $\delta^{13}C$, can reflect a change in the global carbon budget (Hodell et al., 1994) (Figure 3.2.b), such as changes in the terrestrial biomass input flux, changes in the $\delta^{13}C$ of the terrestrial biomass, or changes in the ratio of carbon removed by deposition of organic matter over carbonates in deep marine sediments (Hodell and Venz-Curtis, 2006).

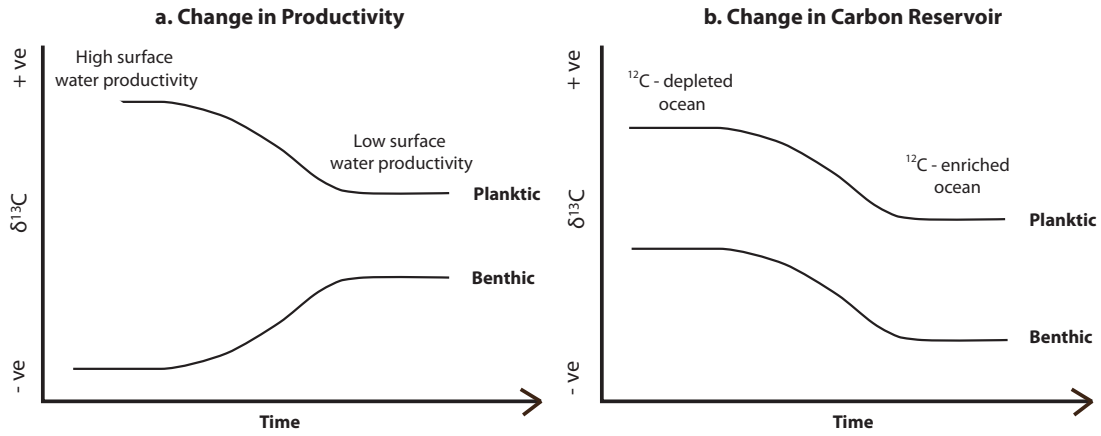

Figure 3.2. Showing relative planktic and benthic foraminiferal $\delta^{13}C$ during:

(a) Changes in productivity. Benthic and planktic foraminiferal $\delta^{13}C$ records converge during times of low surface water productivity, and diverge during times of high surface water productivity (Maslin and Swann, 2005).

(b) Changes in the carbon reservoir. Benthic and planktic foraminiferal $\delta^{13}C$ records co-vary if driven by reservoir-wide changes in $\delta^{13}C$ (Maslin and Swann, 2005).

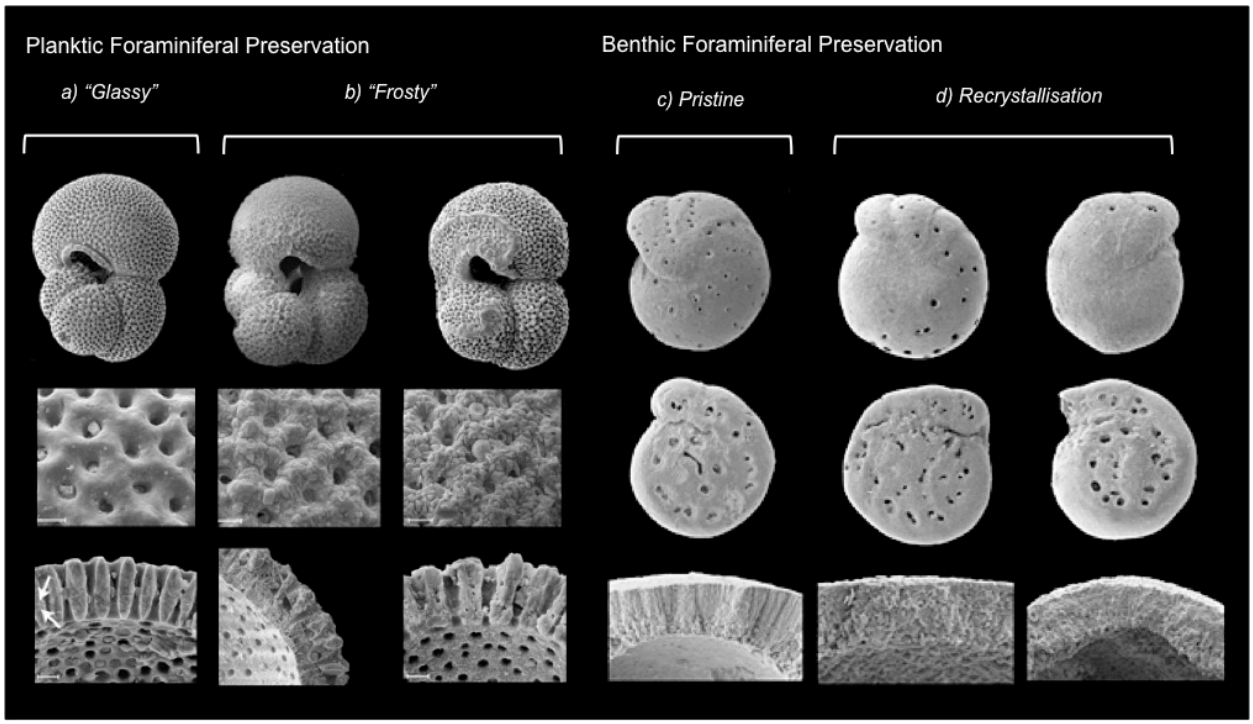

Figure 3.3. Planktic (left) and benthic (right) foraminiferal preservation:

a) SEM images of pristine, "glassy" planktic foraminifera (various species). From top to bottom: the whole foraminiferal test showing a well-defined pore structure and aperture; high-resolution image of the outer test wall, showing the smooth

original texture made up of microgranular calcite; high-resolution image of the test wall cross section, showing the original microgranular calcite, and well-defined pore channels. Images are adapted from Sexton et al., 2006.

b) SEM images of diagenetically altered "frosty" planktic foraminifers (various species). From top to bottom: the whole foraminiferal tests, with the pore-structure less visible, and the aperture less well-preserved; high-resolution image of the outer test wall, showing varying degrees of overgrowth with blocky inorganic calcite; high-resolution image of the test wall cross section, showing that the original microgranular calcite has been recrystallised into large inorganic calcite crystals. Images are adapted from Sexton et al., 2006.

c) SEM images of pristine, benthic foraminifera. The top two images show the spiral and umbilical sides of the benthic foraminifera. There is no visible sign of inorganic calcite overgrowth, and the pore structure has been retained. The lower image shows a cross-section of the test wall. The microgranular texture of the calcite is retained, and there is no sign of recrystallisation in the test wall or overgrowth on the interior or exterior test walls. Images are adapted from Edgar et al., 2013.

d) SEM images of recrystallised, benthic foraminifera. The top two images show the spiral and umbilical sides of the benthic foraminifers. As with the pristine example, there is no visible sign of inorganic calcite overgrowth on either specimen, and the pore structure has been retained. However, differences are visible when looking at the lower images, which show cross-sections of the test walls. The microgranular texture of the calcite is no longer intact, but has been replaced by blocky, inorganic calcite crystals. Images are adapted from Edgar et al., 2013.

3.2.1.3. Effect of Preservation in Sediments on Foraminiferal $\delta^{18}O$ and $\delta^{13}C$

Post-depositional dissolution and re-precipitation of foraminiferal calcite can diagenetically overprint the original biogenic $\delta^{18}O$ and $\delta^{13}C$ signals with inorganic calcite that has the same chemical composition as the pore water $\delta^{18}O_{sw}$ and $\delta^{13}C_{DIC}$, with the surrounding water temperature placing an additional control on the precipitated $\delta^{18}O$ (Pearson et al., 2001).

Planktic foraminiferal preservation

Much research has been done into the effects of the preservation state of planktic foraminifera on $\delta^{18}O$ and $\delta^{13}C$ (Pearson et al., 2001; Williams et al., 2005; Sexton et al., 2006; Pearson and Burgess, 2008). The preservation of planktic foraminifera has been described as gradationally varying between pristine 'glassy' preservation, to 'frosty', and eventually 'chalky' preservation (Sexton et al., 2006). Glassy planktic foraminifera (Figure 3.3.a) appear as translucent under a reflective light microscope (RLM) and are generally found in clay-rich sediments. The glassy specimens retain the original precipitated microstructure, which is made up of calcitic microgranules (~ 0.1 μm diameter) that are laterally fused together (Pearson and Burgess, 2008). The outer and inner test walls of glassy planktic foraminifera are smooth on a sub-micron scale, and cross sections of the test walls show a pervasive microgranular structure (Sexton et al., 2006). Frosty planktic foraminifera appear opaque when viewed under RLM and are often recovered from biogenic oozes and chalky deep-sea deposits (Pearson and Burgess, 2008). With increasing opaqueness, frosty

specimens frequently show increasing overgrowth on the interior and exterior test walls, and the cross sections of test walls show widespread recrystallisation of the microgranular calcite into large inorganic calcite crystals (Figure 3.3.b) (Sexton et al., 2006; Pearson and Burgess, 2008). The widespread recrystallisation also causes the foraminifera to become mechanically weaker (Pearson and Burgess, 2008), thereby increasing the chance of fragmentation during deposition or sample processing.

The diagenetic alteration of the foraminiferal calcite is thought to affect the foraminiferal $\delta^{18}O$ values more than their $\delta^{13}C$ values. Pearson et al. (2001) suggested that the recrystallisation of the calcite occurred along a mixing line between the original primary planktic foraminiferal calcite and the diagenetic inorganic calcite end member. As planktic foraminifera undergo diagenesis on the sea floor, recrystallisation and overgrowth with inorganic calcite causes an increase in the $\delta^{18}O$ values of the foraminiferal calcite. If used for temperature reconstructions, recrystallised frosty planktic foraminiferal calcite will provide lower temperature than pristine glassy planktic foraminiferal calcite (Sexton et al., 2006). No significant offset was seen between glassy and frosty $\delta^{13}C$ values (Sexton et al., 2006).

Despite the effects of diagenesis on planktic foraminiferal calcite, examination of frosty specimens can still be of great use in sites where pristine glassy foraminifera are not available. At any single site, the inter-species offsets of both $\delta^{18}O$ and $\delta^{13}C$ remain constant (Sexton et al., 2006). Furthermore, when comparing sites of a similar latitude and preservation, $\delta^{18}O$ values were found to be very similar (Williams et al., 2005; Sexton et al., 2006). Frosty foraminiferal

calcite can still be very useful as a palaeoceanographic proxy when interpreting temporal trends and rates of change (Williams et al., 2005; Sexton et al., 2006).

Benthic foraminiferal preservation

Research into the extent of diagenesis in benthic foraminifera, and the effects of diagenesis on the stable isotopic composition of benthic species has been far less extensive. Generally, benthic foraminifera are considered less receptive to diagenetic processes such as dissolution, recrystallisation and overgrowth (Sexton and Wilson, 2009; Edgar et al., 2013). Firstly, any recrystallisation that occurs will occur in pore waters of a similar temperature and chemical composition to the bottom waters where the original benthic foraminiferal calcite precipitated. Secondly, benthic foraminifera generally have more calcified tests than planktic foraminifera, and are therefore thought to be more resistant to both dissolution and recrystallisation (Sexton and Wilson, 2009). Finally, the similarity in Cenozoic benthic foraminiferal isotope records from a range of sites in different ocean basins, with varying depositional settings and burial histories, suggest that the benthic foraminiferal calcite must retain a strong primary signal (Edgar et al., 2013). However, recent studies applying high-resolution SEM studies to benthic foraminifera have shown that similar levels of recrystallisation have been seen at micron and sub-micron scale in benthic species as it has in planktic species (Sexton and Wilson, 2009; Edgar et al., 2013). The outer test microstructure of various frosty specimens showed similar degrees of overgrowth (Figure 3.3.c & d). However, when a cross-section of the test wall was investigated on the same specimen, the microgranular structure was only preserved in some specimens (Figure 3.3.c), with other

specimens showing considerable recrystallisation (Figure 3.3.d) (Edgar et al., 2013). In contrast to the effects of diagenesis on planktic foraminiferal calcite, neither dissolution, recrystallisation nor overgrowth seem to create any offset in benthic foraminiferal $\delta^{18}O$ and $\delta^{13}C$ values compared to $\delta^{18}O$ and $\delta^{13}C$ from pristine specimen (Edgar et al., 2013).

3.2.2. Early Pliocene to Late Miocene Benthic Foraminiferal Isotope Stratigraphy

The late Miocene to early Pliocene benthic and planktic foraminiferal oxygen $\delta^{18}O$ isotope stratigraphy is predominantly characterised by low amplitude long-term variation (~ 0.25 – 0.5 ‰), reflecting the long-term stability in global ice volume. Superimposed on these long-term trends, the $\delta^{18}O$ isotope stratigraphy records higher-frequency variations with an amplitude of ~ 0.5 ‰ (Shackleton et al., 1995b; Shackleton and Hall, 1997; Billups et al., 1998/2002; Hodell et al., 2001; Hodell and Venz-Curtis, 2006) (see section 2.1.1 for a more information). There is some debate as to the exact shape of the global $\delta^{18}O$ isotope stratigraphy, as the current benthic foraminiferal isotope records reflect both global ice volume changes, and more local influences, such as changes in temperature (Hodell and Venz-Curtis, 2006).

The carbon $\delta^{13}C$ isotope stratigraphy shows more distinct long-term variation than the $\delta^{18}O$ record. The most distinctive change in the $\delta^{13}C$ is the globally synchronous late Miocene Carbon Isotope Shift (LMCIS), which characterises the late Miocene $\delta^{13}C$ record between 7.6 and 6.6 Ma (Haq et al.,

1980; Hodell and Venz-Curtis, 2006) (see Figure 3.4 for indication of size an extent of LMCIS at Site U1338). The exact cause of the LMCIS has not yet been constrained, but has been associated with either a change in the $\delta^{13}C$ composition of the global oceanic reservoir, or to a widespread, global increase in surface productivity (see section 2.1.2 for more details).

3.3. Methodology

3.3.1. Sediment processing and Sampling Strategy

A total of 1330 samples were taken every 10 cm between 48 and 185 m CCSF-A along the composite splice at Site U1338 (Wilkens et al., 2013). Visible core disturbances due to mechanical drilling processes or bioturbation were avoided, as these processes can cause sediments of different ages to mix together. Sampling resolution corresponds to 1 sample per ~3.5 kyr throughout the late Miocene and 1 sample per ~7.9 kyr in the early Pliocene based on the shipboard sedimentation rate estimates (Section 2.2.2 – Site Description). Each 20 cc sample was freeze-dried, weighed, and 5 cc was kept as an archive. 15 cc were washed through a 63 μm sieve to separate the fine (<63 μm) and coarse (>63 μm) fractions. Both fractions were oven-dried at 45 °C, and the coarse fraction dry-weight recorded to calculate the weight percentages of the fine (%FF) and coarse fractions %CF.

3.3.2. Stable Isotope Measurements

Oxygen and carbon isotope ratios ($\delta^{18}O$; $\delta^{13}C$) were measured on the epifaunal benthic foraminifera *Cibicidoides mundulus* (*C. mundulus*) and the mixed layer planktic foraminifera *Globigerinoides sacculifer* (*Gs. sacculifer*). The benthic species *C. mundulus* was selected because it is a widespread epifaunal species, which generally live in the upper 1 cm of the sediment-water interface, and is frequently used in palaeoceanographic studies. An epifaunal species was chosen over an infaunal species, as the water properties at the sediment-water interface are thought to better reflect the water chemistry at the sea floor, whereas the water properties of the infaunal environment is thought to better reflect pore water chemistry. The planktic species *Gs. sacculifer* was chosen because it is a widespread and commonly used mixed-layer species that is abundant throughout the studied interval. A mixed-layer, or euphotic species was chosen as it best approximates conditions found at the sea surface.

Where possible, well-preserved specimens were selected using RLM by choosing translucent specimens (predominantly the case with the benthic foraminiferal specimens), and by avoiding specimens that showed visible signs of inorganic calcite overgrowth and/or dissolution. Fragmented specimens were avoided. Subsequent SEM studies were used for a higher resolution assessment of the preservation of the foraminiferal calcite (see section 3.3.3). After selection, each sample was ultra-sonicated in methanol to remove any fine-grained particles.

All planktic measurements and the majority of benthic analyses (93% of the dataset) were performed in the Qatar Stable Isotope laboratory at Imperial College London (ICL) using a Kiel IV – Thermo Mat 253 combination in dual inlet

mode. All samples were reacted with 105% orthophosphoric acid at 70 °C. The remaining 7% of benthic analyses were run on a continuous flow GasBench II – Thermo DeltaPLUS XP combination in the Bloomsbury Environmental Isotope Facility at University College London (UCL), where samples were reacted with 100% orthophosphoric acid at 70 °C.

All isotope results are reported against the Vienna Peedee Belemnite standard (VPDB) using the standard δ notation expressed in per mille (‰) as defined by McKinney et al. (1950):

$$\delta^{18}O_{sample}(in\ ‰) = \frac{(^{18}O/^{16}O)_{Sample} - (^{18}O/^{16}O)_{Standard}}{(^{18}O/^{16}O)_{\ Standard}} \cdot 1000$$

Analytical precision (1 standard deviation = 1σ), calculated from replicates of NBS-19 and ICL's internal Carrera Marble standard (ICM), is 0.04 ‰ for $\delta^{13}C$ and 0.07 ‰ for $\delta^{18}O$ on the Kiel-MAT 253 combination, and 0.02 ‰ for $\delta^{13}C$ and 0.09 ‰ for $\delta^{18}O$ on the GasBench-Delta combination. Replicates of ICM run at both laboratories ensure good inter-laboratory reproducibility. All benthic and planktic foraminiferal data produced in this study can be found Appendix A.1., together with a more detailed discussion on the corrections applied to the data.

3.3.2.1. Benthic Foraminiferal Stable Isotopes

3-6 specimens *C. mundulus* specimens were selected from the 250-500 μm size fraction from 1330 samples. Between 48 and 180 m CCSF-A, the average sampling resolution is ~ 10 cm; between 180 and 186 m CCSF-A, the average sampling resolution is ~ 50 cm. Occasionally, further *C. mundulus* were selected from the 125-250 size fraction if insufficient specimens were found in the 250-

500 μm fraction to ensure a sufficiently high sample weight was achieved. This was the case for approximately 14% of samples. Replicate analyses of benthic foraminiferal samples on ~ 12% of the data indicate that sample reproducibility (1 standard deviation = 1σ) is better than 0.08 ‰ for $\delta^{13}C$ and 0.07 ‰ for $\delta^{18}O$ on samples run at ICL, and equal or better than the reproducibility of the standards for samples run at UCL. $\delta^{18}O$ values of *C. mundulus* were further corrected to equilibrium by adding 0.64 ‰ (Shackleton et al., 1995b).

3.3.2.2. Planktic Foraminiferal Stable Isotopes

Between 62 and 186 m CCSF-A, 2-8 *Gs. sacculifer* were selected from the 250 to 355 μm size fraction from a total of 212 samples at an average sampling resolution of 50 cm. Replicate analyses of planktic foraminiferal samples (~ 10% of the data) indicate that sample reproducibility (1 standard deviation = 1σ) is better than 0.1 ‰ for both $\delta^{13}C$ and $\delta^{18}O$ on samples run at ICL.

3.3.3. Scanning Electron Microscopy

Multiple *C. mundulus* and *Gs. sacculifer* were selected from the 250 – 500 μm and 250 – 355 μm size fractions respectively for scanning electron microscopy (SEM) to assess the general preservation of these species throughout the U1338 splice. A total of 14 benthic foraminiferal specimens from 8 samples and 16 planktic foraminiferal specimens from 16 samples were selected at a range of depths throughout the sampled interval. The specimens were mounted onto sticky carbon tape on a stub and were imaged using the Leo 1455 VP

(variable pressure) SEM at the Natural History Museum (London, United Kingdom). The images were made at low vacuum using back-scattered electrons in topography mode (BSE-TOPO), and therefore the samples were not coated. The working distance for all images was set to 15 – 16 mm, with a spot size of 500 (Leo-specific setting) and an acceleration voltage of 15 kV. High-resolution versions of the images can be found in the appendix: benthic foraminifera – Appendix A.2; planktic foraminifera – Appendix A.3.

3.4. Results

Figure 3.4 shows the spliced core photo from Site U1338 (Figure 3.4.a**,** Wilkens et al., 2013) and the high-resolution benthic foraminiferal $\delta^{18}O_{CM}$ and $\delta^{13}C_{CM}$ (Figure 3.4.b, c & d), as well as the planktic foraminiferal $\delta^{18}O_{GS}$ and $\delta^{13}C_{GS}$ (Figure 3.4.e & f) and the weight % coarse fraction$_{>63}$ (>63 μm) (Figure 3.4.g). All records have been plotted against depth in metres CCSF-A (see section 2.2.2 for CCSF-A definition).

3.4.1. Benthic Foraminiferal Results

3.4.1.1. $\delta^{13}C$ from *Cibicidoides mundulus* ($\delta^{13}C_{CM}$)

The carbon isotope record measured on the benthic foraminifera *Cibicidoides mundulus* ($\delta^{13}C_{CM}$) displays considerable long-term variation (Figure 3.4.b). There is a major decrease in $\delta^{13}C_{CM}$ values of almost 1 ‰ between

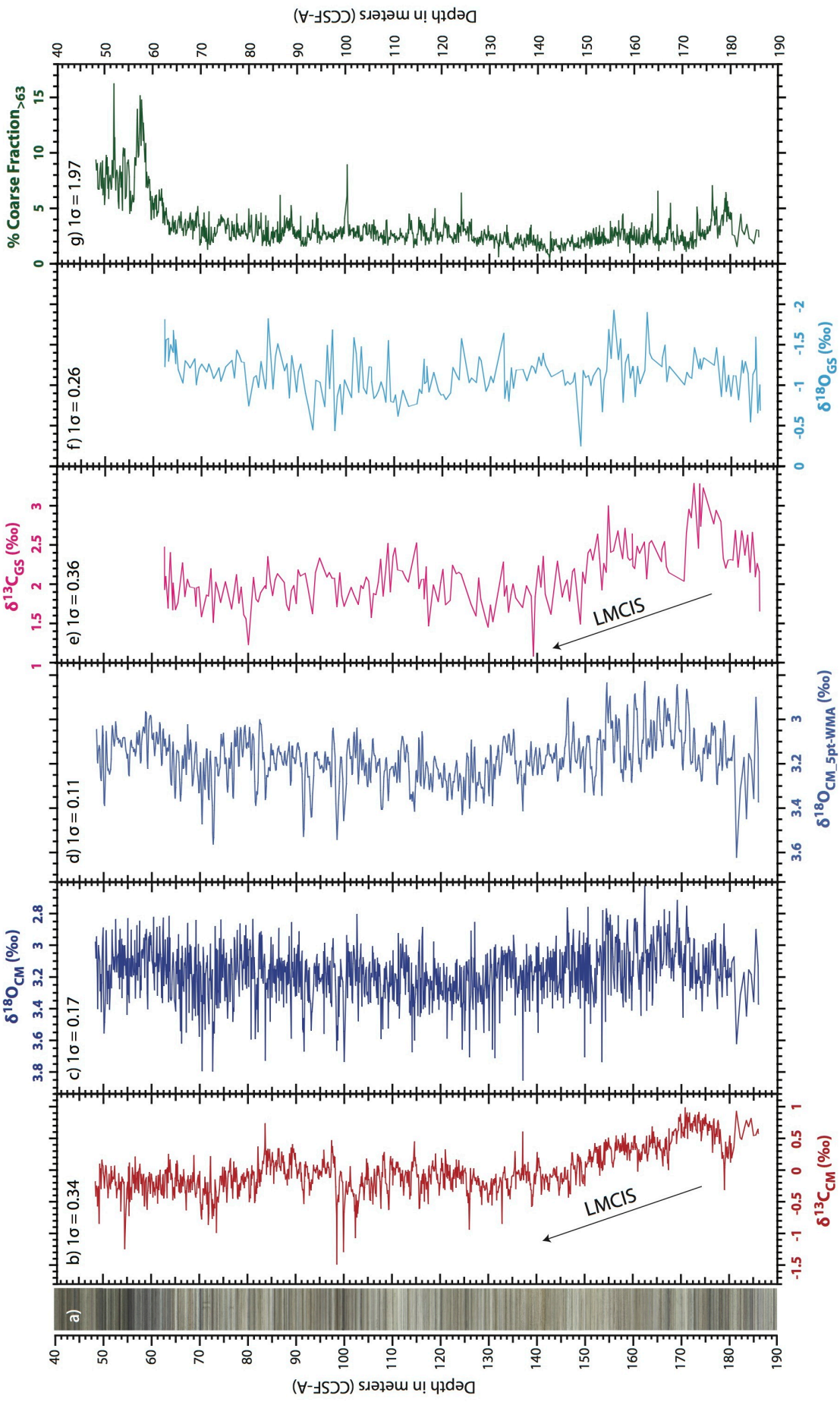
a)
b) 1σ = 0.34
c) 1σ = 0.17
d) 1σ = 0.11
e) 1σ = 0.36
f) 1σ = 0.26
g) 1σ = 1.97
LMCIS
LMCIS
δ13CCM (‰)
δ18OCM (‰)
δ18OCM_5pt-WMA (‰)
δ13CGS (‰)
δ18OGS (‰)
% Coarse Fraction>63
Depth in meters (CCSF-A)
Depth in meters (CCSF-A)

Figure 3.4:
Overview of benthic (*Cibicidoides mundulus*) and planktic (*Globigerinoides sacculifer*) foraminiferal stable isotopes and %coarse fraction from Site U1338. All data is plotted against depth in meters CCSF-A.

a) Core photo of the spliced section of U1338 (Wilkens et al., 2013).

b) Benthic foraminiferal $\delta^{13}C_{CM}$ record from Site U1338. Samples are taken every 10 cm between 48 and 181 m CCSF-A. Below 181 m samples were taken every 50 cm. Average = -0.01 ‰, 1 standard deviation = 1σ = 0.34 ‰.

c) Benthic foraminiferal $\delta^{18}O_{CM}$ record from Site U1338. Samples are taken every 10 cm between 48 and 181 m CCSF-A. Below 181 m samples were taken every 50 cm. Average = 3.17 ‰, 1σ = 0.17 ‰.

d) 5 point weighted moving average (5pt WMA) of the $\delta^{18}O_{CM}$ record shown in b). The following weighting was applied to smooth the record = 1st point = 30%; 2nd point = 70%; 3rd point = 100%; 4th point = 70%; 5th point = 30%. Average = 3.17 ‰, 1σ = 0.11 ‰.

e) Planktic foraminiferal $\delta^{13}C_{GS}$ record from Site U1338. Samples are taken approximately every 50 cm between 62 and 186 m CCSF-A. Average = 2.09 ‰, 1σ = 0.36 ‰.

f) Planktic foraminiferal $\delta^{18}O_{GS}$ record from Site U1338. Samples are taken approximately every 50 cm between 62 and 186 m CCSF-A. Average = -1.14 ‰, 1σ = 0.26 ‰.

g) % coarse fraction (> 63 μm; $\%CF_{>63}$) record from Site U1338. Samples are taken every 10 cm between 48 and 181 m CCSF-A. Below 181 m samples were taken every 50 cm. Average = 3.23 %, 1σ = 1.97 %.

approximately 170 and 130 m CCSF-A. This change marks a permanent, negative shift in average $\delta^{13}C_{CM}$ values. From the base of the record to 170 m CCSF-A, $\delta^{13}C_{CM}$ values are frequently as high as 0.7 to 1.0 ‰, with a brief interval of $\delta^{13}C_{CM}$ values around – 0.3 ‰ around 180 m CCSF-A. Above 130 m CCSF-A to the top of the record, long-term $\delta^{13}C_{CM}$ oscillates by ~ 0.2 ‰ around a mean of 0.15 ‰.

Short-term $\delta^{13}C_{CM}$ values oscillate by about 0.3 to 0.5 ‰ in relatively well-defined cycles throughout the record. The variability in the $\delta^{13}C_{CM}$ record increases slightly between approximately 115 and 90 m CCSF-A. Particularly between 105 and 95 m CCSF-A there are $\delta^{13}C_{CM}$ excursions of 1 ‰ or more. In the uppermost part of the record (48 – 70 m CCSF-A) the cycles are less pronounced.

3.4.1.2. $\delta^{18}O$ from *Cibicidoides mundulus* ($\delta^{18}O_{CM}$)

The oxygen isotope record measured on the benthic foraminifera *Cibicidoides mundulus* ($\delta^{18}O_{CM}$) (Figure 3.4.c) shows far less long-term variation than the $\delta^{13}C_{CM}$ record. Across the whole record, the average $\delta^{18}O_{CM}$ is ~3.2 ‰. Long-term $\delta^{18}O_{CM}$ decreases from ~ 3.2 ‰ at the base of the record to ~3.0 ‰ at 175 m CCSF-A. A slow, long-term increase from ~3.0 to 3.3 ‰ follows between 175 and 125 m CCSF-A. Long-term $\delta^{18}O_{CM}$ then slowly decreases towards 3.1 ‰ at the top of the record. The short-term variations in the $\delta^{18}O_{CM}$ record are considerably noisier than in the $\delta^{13}C_{CM}$ record. Applying a 5-pt weighted moving average (weighting = 1st point = 30%; 2nd point = 70%; 3rd point = 100%; 4th point = 70%; 5th point = 30%) reduces the noise and improves

the signal-to-noise ratio: the short-term cycles present in the $\delta^{18}O_{CM}$ record are highlighted, without losing the main long and short term characteristics of the dataset (Figure 3.4.d). In the lowermost section of the record (180 – 150 m CCSF-A), there are clearly defined cycles present in the $\delta^{18}O_{CM}$ record, with $\delta^{18}O_{CM}$ oscillating by ~ 0.3 ‰. These short-term oscillations are not exceptionally well defined throughout most of the remainder of the record, with the exception of the interval between ~ 110 and 80 m CCSF-A, where a number of clear cycles can be identified with $\delta^{18}O_{CM}$ excursions of ~ 0.5 ‰.

3.4.1.3. Secondary Electron Imaging (SEM_{CM})

Figure 3.5 shows BSE-TOPO SEM images of 14 *Cibicidoides mundulus* selected from 8 samples between 87.13 and 176.60 m from the U1338 splice.

The SEM images show that the benthic foraminifera from Site U1338 generally show good preservation. The umbilical and spiral sides of the specimens from 87.13, 129.17, 148.20 and 164.93 m CCSF-A (Figures 3.5.a, e, f & g respectively) show only very minor calcite overgrowth. For these specimens, the original pores are still well preserved and the apertures and individual chambers are well defined. The specimens from samples at depth 89.53 and 101.38 m CCSF-A (Figures 3.5.b & c respectively) show very similar levels of overgrowth as the specimens in Figure 3.5 a, e, f and g. However, these specimens have possibly experienced very minor dissolution (red arrows – Figure 3.5.b and c) around some of the edges of a few pores on the umbilical side.

The only samples where preservation was not good were the specimen from 115.49 m CCSF-A and the specimen examined on its umbilical side form

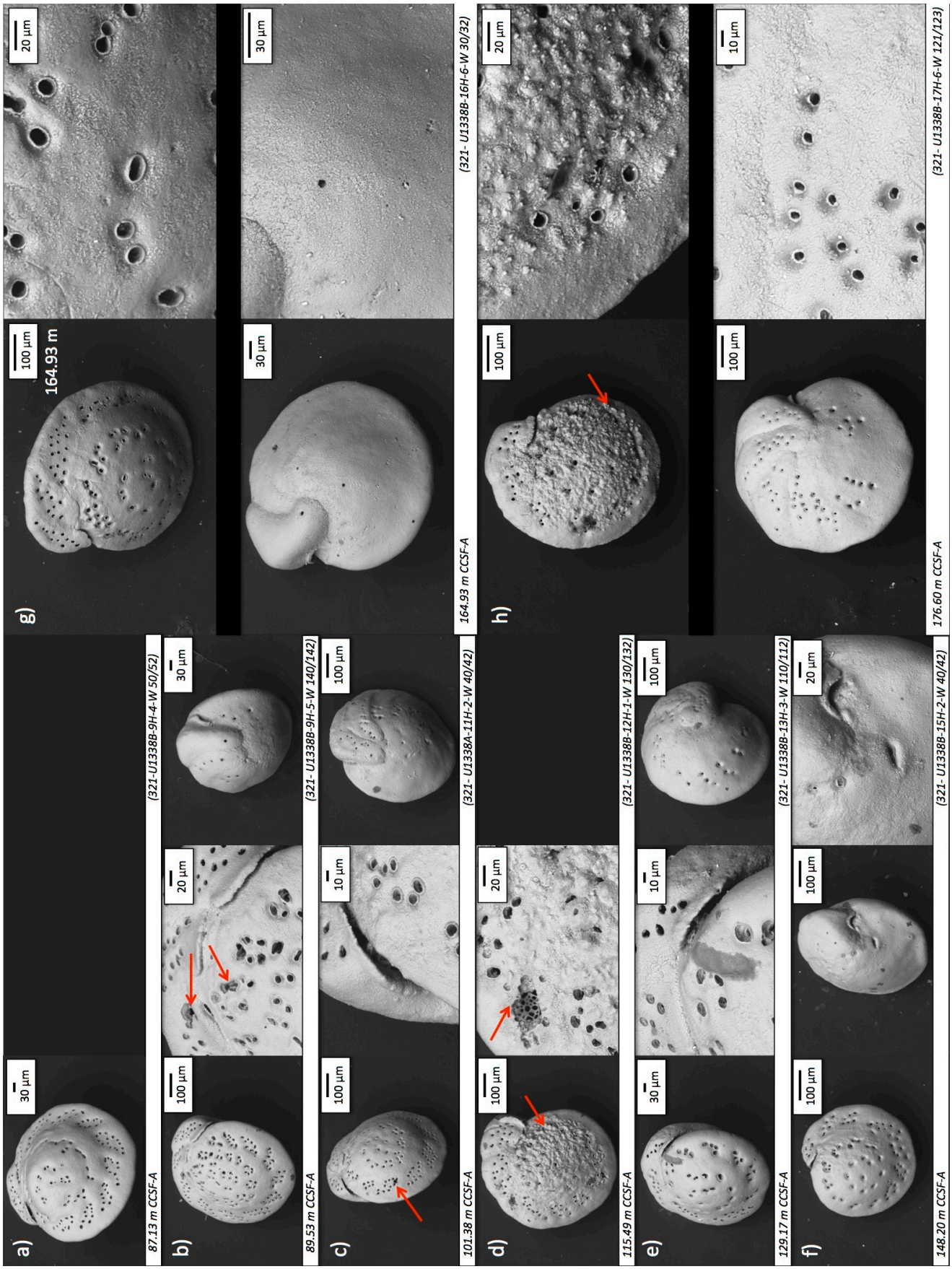
a)
b)
c)
d)
e)
f)
g)
h)
87.13 m CCSF-A
(321-U1338B-9H-4-W 50/52)
89.53 m CCSF-A
(321- U1338B-9H-5-W 140/142)
101.38 m CCSF-A
(321- U1338A-11H-2-W 40/42)
115.49 m CCSF-A
(321- U1338B-12H-1-W 130/132)
129.17 m CCSF-A
(321- U1338B-13H-3-W 110/112)
148.20 m CCSF-A
(321- U1338B-15H-2-W 40/42)
164.93 m CCSF-A
(321- U1338B-16H-6-W 30/32)
176.60 m CCSF-A
(321- U1338B-17H-6-W 121/123)
164.93 m
30 µm
20 µm
10 µm
100 µm

Figure 3.5. BSE-TOPO SEM images of 14 benthic *Cibicidoides mundulus* from 8 samples selected between 87.13 and 176.60 m CCSF-A on the Site U1338 splice:
Generally, specimens a), e), f) and g) show only minor calcite overgrowth, and the pore structures are still very well preserved.

Specimens b) and c) generally show similar preservation levels shown in a and e to g, although there is some evidence of minor dissolution around some of the pores (red arrows).

Specimen d) and the umbilical specimen shown in h) show greater degrees of diagenetic alteration than the other specimens. Both specimens show evidence of dissolution, as well as large calcite overgrowths (red arrows). The spiral samples in d) and h) do not show much overgrowth, or any signs of dissolution.

176.60 m CCSF-A (Figures 3.5.d & h umbilical side respectively). Both these specimens show some evidence of dissolution, as well as large calcite overgrowths, which disguise the original pores and chamber structure (red arrows Figure 3.5d and h umbilical side). The specimens examined on their spiral sides from both 115.49 and 176.60 m CCSF-A shows similar levels of overgrowth as the well-preserved specimens discussed above (Figure 3.5.d & h spiral side respectively).

3.4.2. Planktic Foraminiferal Results

The planktic foraminiferal stable isotope results ($\delta^{18}O_{GS}$ and $\delta^{13}C_{GS}$) are shown in Figure 3.4 ($\delta^{18}O$ in e; $\delta^{13}C$ in f). On average, the planktic foraminiferal $\delta^{18}O_{GS}$ and $\delta^{13}C_{GS}$ records have a spatial resolution of 50 cm between 42 and 186 m CCSF-A. All records have been plotted against depth in meters CCSF-A (see section 2.2.2 for CCSF-A definition).

3.4.2.1. $\delta^{13}C$ from *Globigerinoides sacculifer* ($\delta^{13}C_{GS}$)

Similar to the $\delta^{13}C_{CM}$ record, the carbon isotope record measured on the mixed-layer planktic foraminifera *Globigerinoides sacculifer* ($\delta^{13}C_{GS}$) displays substantial long-term variation (Figure 3.4.e). Between 175 and 135 m CCSF-A there is a long-term shift of ~1 ‰ in the $\delta^{13}C$ from ~2.8 to 1.9 ‰. From 135 m until the top of the record at ~ 60 m CCSF-A, the long-term $\delta^{13}C$ trend oscillates by about 0.2 ‰ around a mean of 2.0 ‰.

The resolution is not sufficiently high to resolve the same short-term variation as in the benthic foraminiferal $\delta^{13}C_{CM}$ record, however the $\delta^{13}C_{GS}$ record displays slightly larger short-term oscillations of ~ 0.5 – 0.7 ‰ throughout the record compared to the $\delta^{13}C_{CM}$ record.

3.4.2.2. $\delta^{18}O$ from *Globigerinoides sacculifer* ($\delta^{18}O_{GS}$)

The oxygen isotope record measured on the planktic foraminifera *Globigerinoides sacculifer* ($\delta^{18}O_{GS}$) (Figure 3.4.f) shows less long-term variation than the $\delta^{13}C_{GS}$ record, yet more than the benthic foraminiferal $\delta^{18}O_{CM}$ record. From the base to the top of the $\delta^{18}O_{GS}$ record, long-term $\delta^{18}O_{GS}$ decreases from ~ – 1.00 to ~ – 1.50 ‰. Between 185 and 155 m CCSF-A, long-term $\delta^{18}O_{GS}$ initially decreases by 0.4 ‰ from – 1 to – 1.4 ‰. Long-term $\delta^{18}O_{GS}$ then increases between 155 and 115 m CCSF-A by ~ 0.5 ‰ from – 1.4 to – 0.9 ‰. Finally, between 115 and 60 m CCSF-A, long-term $\delta^{18}O_{GS}$ decreases by ~ 0.6 ‰ from – 0.9 to – 1.5 ‰.

As with the $\delta^{13}C_{GS}$ record, the resolution of the $\delta^{18}O_{GS}$ is not sufficiently high to resolve the same short-term variation as in the benthic foraminiferal $\delta^{18}O_{CM}$ record. However, the $\delta^{18}O_{GS}$ record displays short-term oscillations of ~ 0.6 to 0.9 ‰ compared to the $\delta^{18}O_{CM}$ record.

3.4.2.3. Secondary Electron Imaging (SEM_{GS})

Figure 3.6 shows BSE-TOPO SEM images of 15 *Globigerinoides sacculifer* selected from various samples between 63.64 and 178.70 m from the U1338 splice.

In general, unlike the SEM images of the benthic foraminifera, the SEM images of the planktic foraminifera indicate that the specimens are not pristine and that the preservation is variable. All specimens show some levels of recrystallisation, ranging from very minor (Figure 3.6.f and k) to high (Figure 3.6.i and j). However, even in the worst recrystallisation cases, the original pore structure remains visible, occasionally with the spine bases intact.

On the basis of the SEM images, specimens from 105.50 and 117.87 m CCSF-A (Figures 3.6.f & k respectively) show the best preservation. The latter specimen was mechanically broken to expose the wall structure and the inside of the test. Both specimens show minor recrystallisation of the outer test, and many spine bases remain visible. The inner wall of the specimen at 117.87 m CCSF-A equally only shows minor overgrowth, and generally has retained a smooth surface (Figure 3.7). The cross-section of the test wall shows that the internal growth structure is still largely retained. However, the microgranular texture of the test wall has recrystallised throughout, as large calcite crystals can be seen throughout the wall (Figure 3.7). Nonetheless, there is also clear evidence that there is no infilling seen in the specimen, as the internal wall has remained smooth.

Specimens from 63.64, 96.73, 111.70, 125.74, 171.51 and 178.70 m CCSF-A (Figures 3.6.a, e, h, m, n & o respectively) have experienced more recrystallisation than the specimens discussed above, with the recrystallized calcite formed in larger crystals. However the spine bases are still frequently visible. The recrystallisation is worse, and masks most of the spine bases in the specimens from 74.58, 87.35, 91.23, 110.70 and 118.87 m CCSF-A (Figures 3.6.b, c, d, g & l respectively). The worst recrystallisation was found on specimens from

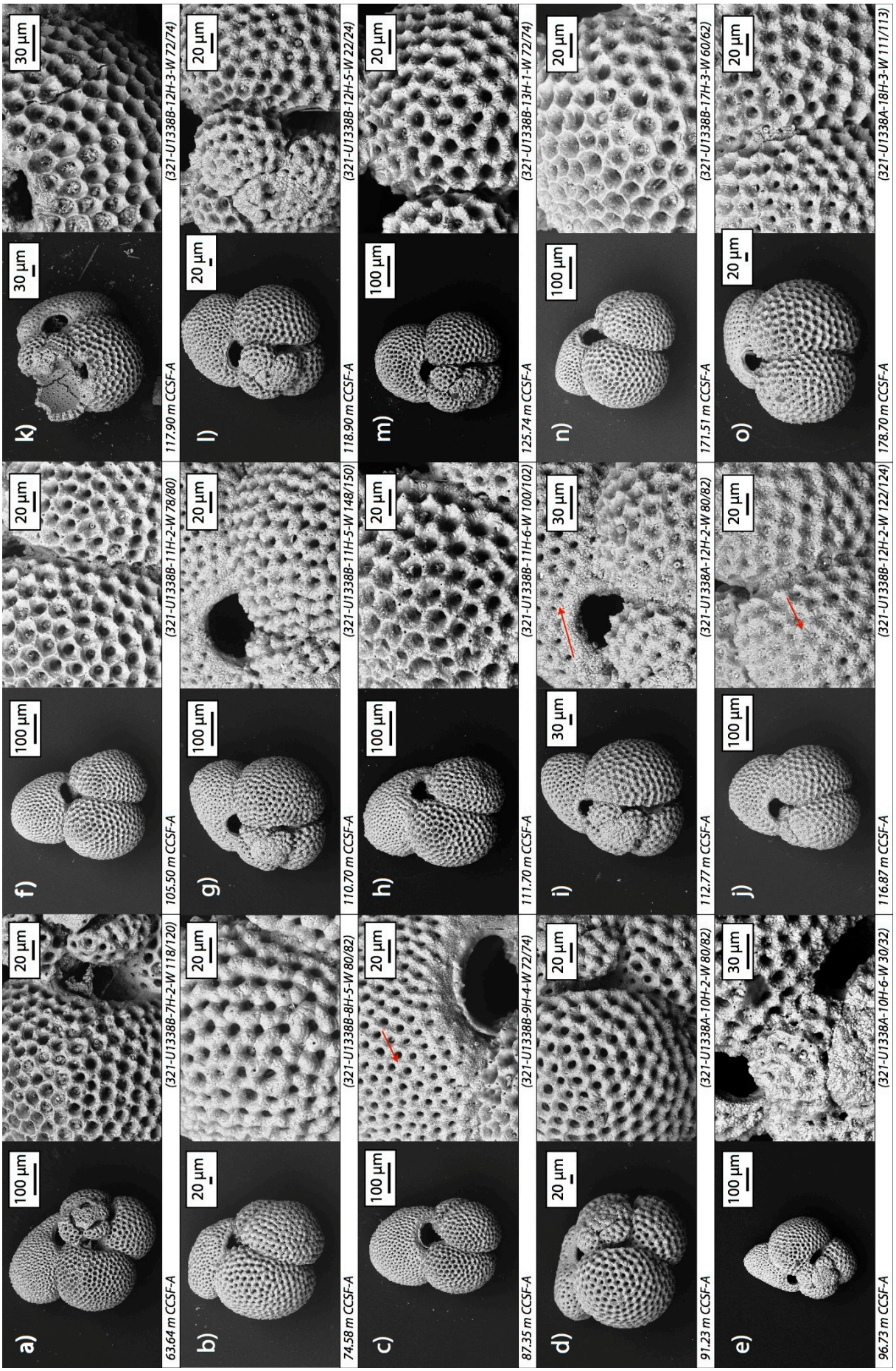
a)
63.64 m CCSF-A
(321-U1338B-7H-2-W 118/120)
b)
74.58 m CCSF-A
(321-U1338B-8H-5-W 80/82)
c)
87.35 m CCSF-A
(321-U1338B-9H-4-W 72/74)
d)
91.23 m CCSF-A
(321-U1338A-10H-2-W 80/82)
e)
96.73 m CCSF-A
(321-U1338A-10H-6-W 30/32)
f)
105.50 m CCSF-A
(321-U1338B-11H-2-W 78/80)
g)
110.70 m CCSF-A
(321-U1338B-11H-5-W 148/150)
h)
111.70 m CCSF-A
(321-U1338B-11H-6-W 100/102)
i)
112.77 m CCSF-A
(321-U1338A-12H-2-W 80/82)
j)
116.87 m CCSF-A
(321-U1338B-12H-2-W 122/124)
k)
117.90 m CCSF-A
(321-U1338B-12H-3-W 72/74)
l)
118.90 m CCSF-A
(321-U1338B-12H-5-W 22/24)
m)
125.74 m CCSF-A
(321-U1338B-13H-1-W 72/74)
n)
171.51 m CCSF-A
(321-U1338B-17H-3-W 60/62)
o)
178.70 m CCSF-A
(321-U1338A-18H-3-W 111/113)

Figure 3.6. BSE-TOPO SEM images of 16 mixed-layer planktic *Globigerinoides sacculifer* from 15 samples selected between 87.13 and 176.60 m CCSF-A on the Site U1338 splice:

Generally, the SEM images show that none of the specimens are pristine, and that the preservation is variable.

Specimens f) and k) show the best preservation, with only minor recrystallisation and overgrowth on the outer test, and many pores and spine bases still well defined.

Specimens a), e), h), m), n) and o) show evidence of greater recrystallisation than specimens f) and k), with more widespread recrystallisation and overgrowth. Despite this, many pores and spine bases still remain visible.

Specimens b), c), d), g) and l) show a greater degree of alteration, as most of the spine bases are no longer visible, and the pores have been considerable narrowed by the calcite overgrowth.

The worst recrystallisation is found on specimens i) and j), where the spine bases are almost entirely overgrown, and the original pore structure is almost completely obscured by recrystallisation and overgrowth.

Gametogenic calcite is indicated with red arrows.

112.77 and 116.87 m CCSF-A (Figures 3.6.i and j respectively). Here the spine bases have almost entirely disappeared and the original pore structure is almost entirely obscured by recrystallisation.

It is worth noting that all specimens show the presence of fine carbonaceous and siliceous material of generally biogenic origin attached to the foraminifera's tests. Normally, sonication prior to stable isotope analysis would be used to dislodge most of this material. This was not done to the specimens examined in the SEM. Also, it is worth noting that blockier, gametogenic calcite is present on the final chamber of all imaged specimens (red arrows – Figure 3.6).

3.4.3. % Coarse Fraction$_{>63}$ (%CF$_{>63}$)

Figure 3.4.g shows the weight % of the >63 μm coarse fraction$_{>63}$ (%CF$_{>63}$). The %CF$_{>63}$ remains very low throughout most of the record. At the base of the record, %CF$_{>63}$ decreases from around 5 % to ~ 2.5 % by about 170 m CCSF-A. For the remaining part of the record, the long-term average remains around 2.5 % until 65 m CCSF-A, with a brief excursion to ~ 10% at 100 m CCSF-A. %CF$_{>63}$ then rapidly increases to ~ 7.5 % at the top of the record, with a broad peak around 12.5 % between 60 and 55 m CCSF-A. The short-term variability in the %CF$_{>63}$ is generally quite low (around 1 – 2 %) from the base of the record until about 60 m CCSF-A. The short-term variability then increases to nearer to 5% from 60 m CCSF-A to the top of the record.

3.5. Discussion

3.5.1. Foraminiferal Preservation:

Implications for the Robustness of Geochemical Proxies

Evaluating the preservation of both the benthic and planktic foraminiferal specimens from IODP Site U1338 is important in order to understand the robustness of the stable isotope records. The BSE-TOPO SEM images of foraminifera from this site show that both the benthic and planktic foraminiferal specimens have undergone some alteration, which was not easily visible under RLM. Generally, the benthic foraminifera have only been slightly affected (Figure 3.5). Out of the 8 imaged specimens, 6 showed good preservation with only very minor overgrowth. The other 2 specimens showed considerable overgrowth on the umbilical side. Considering Edgar et al.'s (2013) work on the influence of recrystallisation and overgrowth on the $\delta^{18}O$ value of benthic foraminiferal calcite, this suggests that the $\delta^{18}O_{CM}$ and $\delta^{13}C_{CM}$ records from the benthic foraminifera are minimally affected by diagenesis.

The BSE-TOPO images of the planktic foraminiferal specimens show that the specimens have undergone far more alteration (Figure 3.6 and 3.7). Preservation is highly variable, with all specimens showing evidence of some overgrowth and recrystallisation. The degree of preservation ranges from fair to poor. The variability of the preservation is interesting, particularly when comparing specimens that are only separated by ~ 1 m in depth. Between these specimens (Figure 3.6.h compared to i, and j to k), the difference in recrystallisation and overgrowth is large. Compared to examples from Sexton et

al. (2006) and Pearson and Burgess (2008), none of the planktic foraminiferal specimens at Site U1338 show the same degree of preservation as the glassy foraminifera presented in both articles. However, the worst recrystallised specimens from this study show somewhat better preservation than the worst examples shown in both Sexton et al. (2006) and Pearson and Burgess (2008). The range of preservation seen in the U1338 planktic foraminifera supports the assertion that the transition from 'glassy' to 'frosty' and 'chalky' specimens is a gradational one. A recent study of planktic foraminifera in the mid Miocene section of the Site U1338 site shows that the preservation of the planktic foraminifera investigated is generally good (Fox and Wade, 2013). Generally, the specimens have not undergone substantial recrystallisation, with the original submicron microgranular wall texture remaining intact (Fox and Wade, 2013). The difference in preservation between the foraminifera investigated by Fox and Wade (2013) and the foraminifera investigated in this study is unexpected, as the specimens in Fox and Wade (2013) have undergone greater burial depths (an additional 200 m or more) than the specimens in this study. This suggests that burial depth was not the main control on diagenetic alteration at this site.

Unlike the benthic foraminiferal stable isotopes, the planktic foraminiferal $\delta^{18}O_{GS}$ have most likely been affected by the poor preservation. The recrystallisation and overgrowth will have most likely increased planktic foraminiferal $\delta^{18}O_{GS}$ from the original biogenic calcite $\delta^{18}O$ value. The diagenetic effect on $\delta^{18}O_{GS}$ will need to be considered when interpreting the $\delta^{18}O_{GS}$ in terms of equatorial surface water conditions. However, the planktic foraminiferal $\delta^{18}O_{GS}$ and $\delta^{13}C_{GS}$ results will still provide useful insights about the evolution of climate in this region, as past research has shown that the temporal trends are

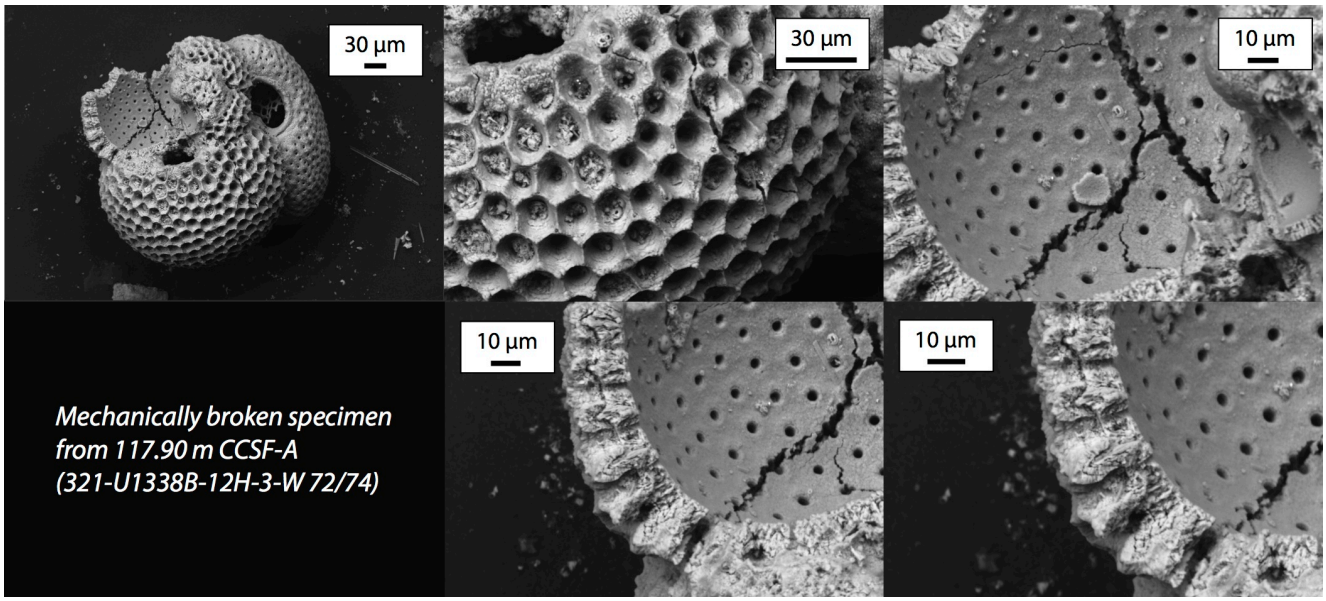

Figure 3.7. More detailed BSE-TOPO SEM images of the mechanically broken mixed-layer planktic *Globigerinoides sacculifer* from 117.90 m CCSF-A on the Site U1338 splice (*cf.* Figure 3.6.k):

This specimen was one of the better-preserved *Gs. sacculifer* imaged. There is only minor overgrowth on the outer test wall, and the original pores remain clear, with many of the spine bases still visible.

The inner test wall only shows minor overgrowth, and has generally retained the smooth texture, which is characteristic for the internal wall of many planktic species (Pearson and Burgess, 2008).

The test-wall cross-section shows that the internal growth structure is still largely retained. However, the microgranular texture that would have originally made up the test wall has been recrystallised and replaced with large calcite crystals.

still preserved (Williams et al, 2005; Sexton et al., 2006). Furthermore, absolute comparisons of the planktic foraminiferal $\delta^{18}O_{GS}$ and $\delta^{13}C_{GS}$ can be made to records from sites with similar preservation states and depositional settings (Sexton et al., 2006). Finally, the $\delta^{13}C$ values in planktic foraminifera do not seem to be affected as much by recrystallisation (Sexton et al., 2006).

Indirect indicators, such as the co-variation of the weight % of the >63 μm coarse fraction$_{>63}$ ($\%CF_{>63}$) to the weight% carbonate ($\%CaCO_3$) can also be used to assess the diagenetic history of a site. $\%CF_{>63}$ is considered to be a good proxy for carbonate dissolution, with the $\%CF_{>63}$ decreasing as dissolution increases, since dissolution weakens and aids fragmentation of planktic foraminifera particularly (Haug and Tiedemann, 1998; Bickert et al., 1994). A decrease in $\%CaCO_3$ can indicate either an influx of other sedimentary components, such as SiO_2, or an increase in dissolution. Combining $\%CF_{>63}$ and$\%CaCO_3$ can also often reveal much about the potential presence of dissolution at a site. A decrease in both proxies would most likely be driven by dissolution (Bickert et al., 1994; Lyle et al., 2012).

Figure 3.8 shows an overview of silica content (weight % SiO_{2_XRF}) (d), estimated from XRF measurements (Lyle et al., 2012), together with the core photo (a), $\%CaCO_{3\_BULK/XRF}$ (b) and the $\%CF_{>63}$ records (c) (see Appendix A.4. for a combination of Figures of 3.4 and 3.8). The weight% calcium carbonate$_{_BULK/XRF}$ ($CaCO_{3\_BULK/XRF}$) from the IODP Site U1338 splice obtained from a combination of $CaCO_3$ estimates based on XRF measurements and discrete $CaCO_3$ measurements on bulk sediment (Lyle et al., 2012; Lyle and Backman, 2013). Generally, weight% $CaCO_{3\_BULK/XRF}$ remains between 60 to 80 % throughout most of the record, although there are some intervals where percentages drop to as low as

20 %. Between 180 and 145 m CCSF-A, the $CaCO_3$ content is high, ranging between 60-80 %. From 145 to 140 m there is a sharp decrease of 40 %, where the $CaCO_3$ content is halved from 80 to 40 %. $CaCO_3$ content recovers at 140 m and remains between 60 to 80 % until 55 m CCSF-A, although there are a few short intervals around 100 m, 85 m and 68 m where the % $CaCO_{3\_BULK/XRF}$ drops to 40%. Between 55 and 50 m, % $CaCO_{3\_BULK/XRF}$ drops to values between 20 to 40 %, which are the lowest values seen in the whole section. After this low $CaCO_3$ content interval, % $CaCO_{3\_BULK/XRF}$ recovers to around 60 % at the top of the record.

A co-varying decrease in the $\%CF_{>63}$ and $\%CaCO_{3\_BULK/XRF}$ records from U1338 could indicate that dissolution affected the site. However, a decrease of $\%CaCO3_{\_BULK/XRF}$ concurring with an increase in $\%CF_{>63}$ is more likely to be caused by an influx of other sedimentary particles that are not calcite, for instance an increase of terrigenous material, or biogenic silica (SiO_2), depending on the site location. During the late Miocene through to early Pliocene**,** large blooms of siliceous phytoplankton, in particular of diatoms, have been reported in the equatorial Pacific**,** (Palike et al., 2010; Expedition 320/321 Scientists, 2010; Lyle et al., 2012), so an increase in biogenic SiO_2 deposition compared to biogenic $CaCO_3$ deposition would lead to a decrease in overall $\%CaCO_{3\_BULK/XRF}$, but would not necessarily drive a change or decrease in $\%CF_{>63}$.

Using co-varying $\%CaCO_{3\_BULK/XRF}$ and $\%CF_{>63}$ as an indicator for dissolution, there are a number of intervals where the primary drivers of change on benthic foraminiferal $\delta^{13}C_{CM}$ and $\delta^{18}O_{CM}$ isotopes (see section 2.3) might have been influenced by other processes, such as dissolution. Between 145 to 140 m CCSF-A, a significant decrease occurs in the $\%CaCO_{3\_BULK/XRF}$ record. At the same

time, a very slight decrease in the $\%CF_{>63}$ to ~0.7 % occurs, which is barely discernible, as the $\%CF_{>63}$ is low throughout most of the record. A co-varying decrease occurring in $\%CaCO_{3\_BULK/XRF}$ and $\%CF_{>63}$, indicates that the benthic foraminiferal $\delta^{13}C_{CM}$ and $\delta^{18}O_{CM}$ isotopes in this interval are slightly affected by dissolution. However, there are no large excursions in the isotopes in this interval that can be directly tied to the decrease in the other records. Around 100 m, several considerable negative excursions of around 30% occur in the $\%CaCO_{3\_BULK/XRF}$ record, which coincide with a single extraordinarily large singular increase in the $\%CF_{>63}$ record, and slightly precede a double peak in both the benthic foraminiferal $\delta^{13}C_{CM}$ and $\delta^{18}O_{CM}$ isotopes. As there is no co-varying decrease of $\%CF_{>63}$ and $\%CaCO_{3\_BULK/XRF}$, it is possible that this excursion is not due to a dissolution event. The upper interval of this section is a particularly variable part of the section. Firstly, $\%CF_{>63}$ progressively increases from a stable average value of ~3% to 15 % between 65 to 58 m, and then decreases to about 7.5 %, and remains around this mean until the top of the record. The decrease in %CF around 58 m, precedes a large drop in $CaCO_3$ from ~ 70 % to ~ 35 % at 58 m, which lasts until 54 m (Figure 3.8).

When comparing the three intervals discussed above to SiO_2 records from the same site (Lyle et al., 2012), there are similar increases seen in the SiO_2 records simultaneous to the decreases in $CaCO_3$. The antipathetic correlation between the SiO_2 and $CaCO_3$ suggests that the decreases in the $CaCO_3$ are probably mainly caused by influxes of biogenic silica, rather than a dissolution effect. This antipathetic correlation provides additional evidence that the main variations in these records reflect primary factors, such as variations in temperature and in seawater $\delta^{18}O$ and $\delta^{13}C$, rather than secondary factors, such

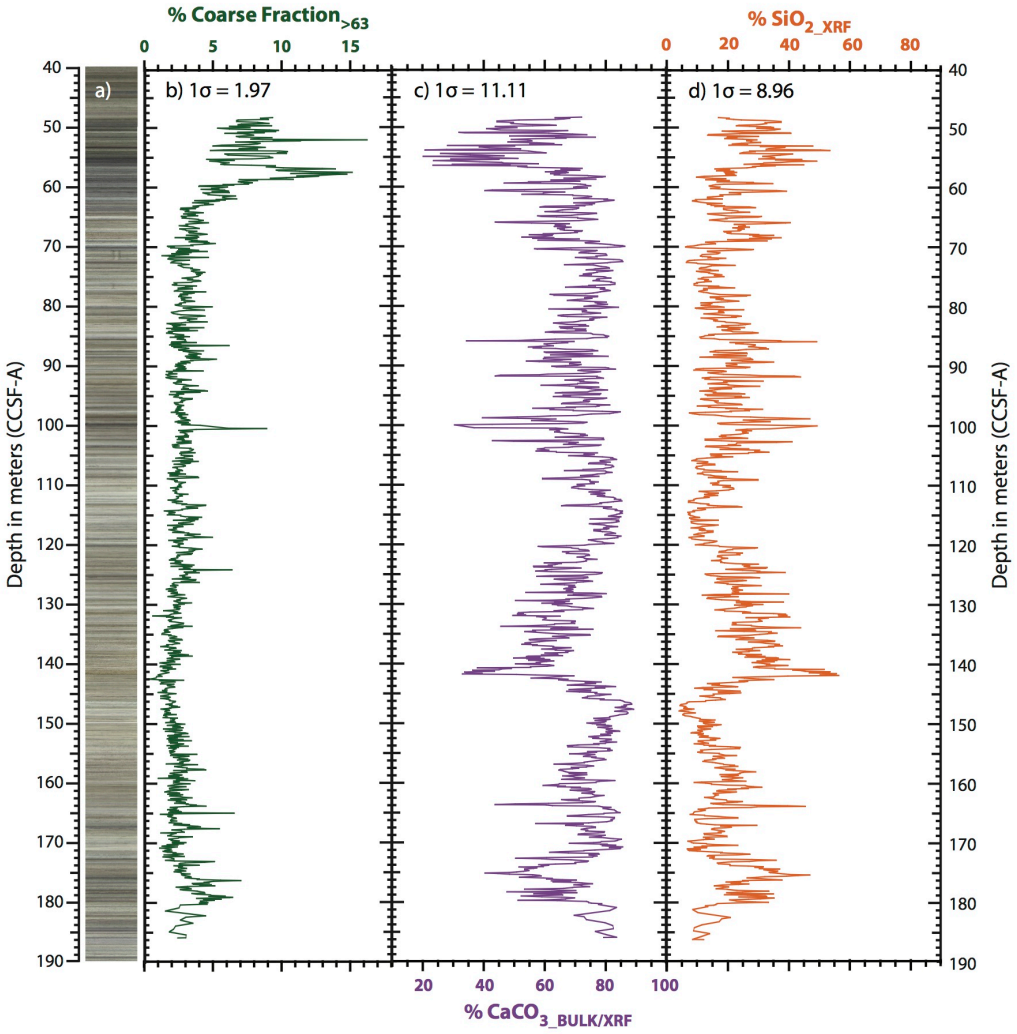

Figure 3.8: Comparison of %CF record, and silica (SiO_2) and carbonate ($CaCO_3$) content.

a) Core photo of the U1338 splice (Wilkens et al., 2013).

b) % coarse fraction (> 63 µm; $\%CF_{>63}$) record from Site U1338. Samples are taken every 10 cm between 48 and 181 m CCSF-A. Below 181 m samples were taken every 50 cm. Average = 3.23 ‰, 1 standard deviation = 1σ = 1.97 ‰.

c) Carbonate content (weight% $CaCO_{3\_BULK/XRF}$) record from Site U1338. This record is a composite of $CaCO_3$ estimates from XRF measurements, and discrete measurements of $CaCO_3$ on bulk sediment samples (Lyle et al., 2012 and Lyle and Backman, 2013 respectively). Data points were resamples from a larger dataset, at the same frequency as the original isotope records. Average = 69.78 %, 1σ = 11.11 %.

d) Silica content (weight% SiO_{2_XRF}) record from Site U1338. This record is a composite of SiO_2 estimates from XRF measurements (Lyle et al., 2012). Data points were resamples from a larger dataset, at the same frequency as the original isotope records. Average = 20.33 %, 1σ = 8.96 %.

as dissolution. In general, the lack of correlation between the planktic and benthic foraminiferal isotopes and the sedimentary properties at Site U1338, support the contention that external processes, such as dissolution, changes in $CaCO_3$ deposition and changes in the influx of other materials, such as dust and SiO_2, are unlikely to have directly affected the benthic and planktic foraminiferal isotopes directly.

In addition to the SEM images and the lack of correlation between the isotopes and the sedimentary properties, another indication that the stable isotope records at IODP Site U1338 faithfully record a climate history is the fact that the general shape of the long-term trends in both the benthic and planktic foraminiferal $\delta^{13}C_{CM}$ and $\delta^{18}O_{CM}$ isotopes matches the shape of published late Miocene to early Pliocene isotope records. This implies that the benthic foraminiferal stable isotopes can be used for stratigraphic correlation to other sites, particularly because of the high-resolution nature of the records (discussed further in section 3.5.2).

3.5.2. Early Pliocene and Late Miocene Isotope Stratigraphy at IODP Site U1338

The long-term trends and variability of the benthic foraminiferal $\delta^{18}O_{CM}$ record (Figure 3.4.c) correspond well to findings from other records, which show that the late Miocene was a period of relative stability in long-term ice volume (See section 2.1.1 and 3.2.1) (Shackleton et al., 1995b; Shackleton and Hall, 1997; Billups et al., 1998; Hodell et al., 2001; Billups, 2002; Hodell and Venz-Curtis,

2006). Likewise, the planktic foraminiferal $\delta^{18}O_{GS}$ record shows similar low-amplitude variability as the benthic foraminiferal $\delta^{18}O_{CM}$ record. The planktic foraminiferal $\delta^{18}O_{GS}$ record shows slightly more long-term variation, which is most likely due to changes in sea surface temperatures and salinity. Palaeoclimate and palaeoceanographical interpretations are discussed in more detail in Chapter 5.

The major decrease in $\delta^{13}C_{CM}$ values of almost 1 ‰ between approximately 170 and 130 m CCSF-A is also an interesting stratigraphic marker. In terms of shape, extent and position within the record, this shift most likely corresponds to the late Miocene Carbon Isotope Shift (LMCIS – section 2.1.2). The LMCIS has been documented as a widespread and synchronous event (Keigwin, 1979; Haq et al., 1980; Hodell and Venz-Curtis, 2006), with the cause of the crisis suggested as both a large-scale productivity event in the surface regions, or a shift in the average $\delta^{13}C$ signature of the global ocean from a ^{12}C-depleted ocean to a more ^{12}C-enriched ocean (see section 2.1.2 and section 3.2.1.2 for details). Despite the presence of a large-scale biogenic bloom in the equatorial Pacific and other oceanic regions during the time of the LMCIS (Palike et al., 2010; Expedition 320/321 Scientists, 2010; Lyle et al., 2012; section 2.1.2), the presence of the LMCIS in records from around the globe suggests that a change in the average oceanic reservoir $\delta^{13}C$ is more likely to explain the LMCIS than regional changes in surface water productivity. This is furthermore supported by the fact that the planktic foraminiferal $\delta^{13}C_{GS}$ shows a remarkable resemblance to the benthic foraminiferal $\delta^{13}C_{CM}$ record. As briefly discussed in section 3.2.1.2, a productivity-driven negative shift in benthic foraminiferal calcite would lead to a divergence in benthic and planktic foraminiferal records (Figure 3.2a). A change

in the $\delta^{13}C$ of the oceanic reservoir however, would lead to a concurrent shift in the planktic and benthic foraminiferal records, as is graphically represented in Figure 3.2b. The exact nature and origins of the LMCIS is explored in more detail in Chapter 6, where the benthic and planktic foraminiferal records from Site U1338 are placed in a global context and compared to other published stable isotope records from this period.

Because of the broad similarities between the U1338 benthic foraminiferal $\delta^{13}C_{CM}$ and $\delta^{18}O_{CM}$ isotopes and the global late Miocene to early Pliocene stable isotope stratigraphy, it is reasonable to assume that the predominant variation in these records reflect global changes driving variations in seawater $\delta^{13}C$ and $\delta^{18}O$. The most important global forcing are changes in total ocean reservoir $\delta^{13}C$ and global ice volume. However, the relative contribution of global forcing (reservoir $\delta^{13}C$; global ice volume) versus local or regional forcing (temperature or productivity changes, or influxes of a water mass from a different source region) cannot yet be determined. This contribution of local, regional and global forcing is explored in following chapters by comparing the U1338 benthic and planktic foraminiferal $\delta^{13}C$ and $\delta^{18}O$ isotopes to additional isotopic records to determine which changes may reflect global forcings, and which are potentially due to regional changes (Chapter 6). The fact that the benthic foraminiferal $\delta^{13}C_{CM}$ and $\delta^{18}O_{CM}$ isotopes from Site U1338 seem to be minimally affected by dissolution make these records suitable for correlation to the isotopic records from Site 982, situated in the North Atlantic. This correlation method is explored in the Chapter 4. However, even though the benthic foraminiferal $\delta^{18}O_{CM}$ and $\delta^{13}C_{CM}$ isotopes predominantly seem to reflect primary forcing factors, the sample reproducibility is only better than 0.1 ‰. Considering the signal of the

benthic foraminiferal $\delta^{18}O_{CM}$ and $\delta^{13}C_{CM}$ records is only 0.3 to 0.5 ‰, caution should be exercised when interpreting both records.

3.6. Conclusion

The BSE-TOPO SEM images of multiple benthic and planktic foraminiferal specimens from Site U1338 show that both sets of foraminifera have undergone some alteration. The SEM investigation of the benthic foraminifera show that the majority of the specimens have only slightly been affected by minor calcite overgrowth. There is also only very minor evidence for dissolution in a couple of the specimens. A quarter of the specimens investigated show a reasonable amount of overgrowth. However, as diagenetic alteration is not thought to greatly alter the original isotopic composition of the benthic foraminiferal calcite, the alteration of the primary benthic foraminiferal calcite is unlikely to have influenced the $\delta^{18}O_{CM}$ and $\delta^{13}C_{CM}$ significantly.

The BSE-TOPO images of the planktic foraminiferal specimens show signs of far greater alteration than found in the benthic foraminiferal specimens. The preservation state ranges from specimens with some overgrowth and internal recrystallisation, but which retain original features such as pores, spine pits and internal test-wall growth structure, to specimens where recrystallisation and overgrowth disguise many of the original features. Preservation state is also highly variable, with specimens that are less than a metre apart showing considerably different levels of alteration. The planktic foraminiferal $\delta^{18}O_{GS}$ were probably altered, with precipitation in pore waters most likely causing an

increase in $\delta^{18}O_{GS}$ from the original planktic foraminiferal value. Despite this, considering the planktic foraminiferal $\delta^{18}O_{GS}$ and $\delta^{13}C_{GS}$ results in a palaeoceanographical context is still valuable. The $\delta^{13}C_{GS}$ record was most likely far less affected than the $\delta^{18}O_{GS}$ record, and the temporal trends in both records are most likely still valid.

The comparison between the sedimentary properties $\%CF_{>63}$, $\%CaCO_{3\_BULK/XRF}$ and $\%SiO_{2\_XRF}$ from Site U1338, and the lack of correlation between these records and the benthic and planktic foraminiferal stable isotope records, further indicate that the isotope records from this site predominantly reflect primary factors, and are minimally influenced by dissolution. This minimal influence is also supported by the general similarity between the benthic and planktic foraminiferal $\delta^{13}C$ and $\delta^{18}O$ isotopes and the late Miocene to early Pliocene isotope stratigraphy, with low amplitude, long-term variation in the $\delta^{18}O_{CM}$ isotopes, and the LMCIS visible at the end of the of the $\delta^{13}C_{CM}$ record.

Chapter 4.

Site U1338: Stratigraphic Correlation and High-Resolution Age Model Generation

4.1. Objectives and Existing Age Constraints at Site U1338

Having strong age constraints on any palaeoceanographic record is important, as it enables the timing, rate and duration of changes in the record to be determined. Good age control also enables meaningful comparison to other records and separation of global and regional trends in palaeoclimate. The first-order age model for IODP Site U1338 based on shipboard palaeomagnetic and nannofossil datums (Table 2.1; see section 2.2.2 in Chapter 2) provides good initial age constraints on the upper section of the U1338 splice, placing the age of the sediments between 8.5 and 3.5 Ma. The single shipboard palaeomagnetic measurement in the studied interval firmly places the age of the top of the record

at ~ 3.5 Ma. However, the further seven nannofossil datums, which place the top of the record at ~ 3.7 Ma and the base of the record at around 8.2 Ma, have associated depth errors of 0.6 – 0.8 m (equivalent to up to ± 45 kyr) (Table 2.1). Furthermore, in the first-order age model (see section 2.2.2.) only eight datums for a core length of ~ 138 m were selected: for any region between the eight shipboard datums, the age constraint is solely provided by linear interpolation between adjacent nannofossil datums. An improved, higher-resolution age model for IODP Site U1338 is vital for later investigation of regional and global climate change, background climate variability and Earth system sensitivity using various geochemical proxy records from this site (Chapters 5 and 6).

On timescales relevant to the late Miocene and early Pliocene, a wide range of dating techniques have been applied to provide strong age constraints on sedimentary records from deep-sea drill sites or outcrops. Absolute age models are based on radiometric dating techniques, such as uranium series dating (U-Pb – Denniston et al., 2008) and argon-argon measurements ($^{40}Ar/^{39}Ar$ – Kuiper et al., 2004). Although radiometric age datums are ideal and provide an absolute age value, radiometric dating requires suitable and sufficient material to be present, which is not always the case in deep ocean cores. $^{40}Ar/^{39}Ar$ can be measured on minerals such as biotite and sanidine, and U-Pb ages can be obtained from zircons (Kuiper et al., 2004; Cole et al., 2005), however these minerals are generally only present in deep marine sites that contain volcanic ash layers. U-Pb is measured on corals and other calcitic material; however, this application is complicated because calcite contains lower levels of uranium and lead than, for instance, found in minerals such as zircon. Therefore measurements of U-Pb on calcite require large sample sizes (Cole et al., 2005).

Also to obtain the original deposition age, the calcite cannot have undergone any diagenetic alteration (Cole et al., 2005; Denniston et al., 2008).

Relative dating techniques, including magnetostratigraphy (Cande and Kent, 1995), chemostratigraphy (Woodruff and Savin, 1989) and biostratigraphy (Wade et al., 2011), are often used to derive age models for older deep-sea cores by interpolating between datums, such as with the shipboard age model for Site U1338. Magneto-, chemo- and biostratigraphies can be calibrated relative to each other, and ultimately to absolute age datums. More recently, magneto-, chemo- and biostratigraphies have been calibrated using orbital tuning (Lourens et al., 2004; Wade et al., 2011). Orbital tuning involves aligning dominant cycles isolated from variations in chemical proxies (e.g. Shackleton et al., 1995a, b) or sedimentary properties (e.g. Hilgen, 1991) to mathematically calculated astronomical solutions for past variations in solar insolation that the Earth receives (e.g. Laskar et al., 1993), thereby providing a best-fit solution to constrain the age of the record (e.g. Lourens et al., 2004). The main benefit of orbital tuning is that it provides high-resolution age constraints on data points in between palaeomagnetic and biostratigraphic datums (Lourens et al., 2004).

Stratigraphic correlation between records can provide consistent relative age constraints on two or more records. Oxygen isotope records from benthic foraminifera have frequently been used as a method to establish age models for deep ocean sites, where well-defined isotope stages identified in one record are correlated with similar isotopic stages in other records, thereby placing the records on a common age scale (Woodruff and Savin, 1989; Hodell et al., 2001; Hodell and Venz-Curtis, 2006; John et al., 2011). Benthic foraminiferal $\delta^{18}O$ is used as a correlation tool between sites, as the $\delta^{18}O$ partially records a signal

that reflects changes in global ice volume (Shackleton and Opdyke, 1973) (see also section 3.2.1.1). Benthic foraminiferal $\delta^{18}O$ records are generally preferred over planktic foraminiferal $\delta^{18}O$ records, as the seawater $\delta^{18}O$ component of benthic foraminiferal $\delta^{18}O$ records is often less masked by local effects, such as regional salinity variations (Maslin and Swann, 2005). Reflecting a combination of surface water $\delta^{18}O$ and calcification temperature, planktic foraminiferal $\delta^{18}O$ are considered more susceptible to the variable conditions found at the surface (Katz et al., 2010) (see section 3.2.1.1). Benthic foraminiferal $\delta^{13}C$ has also been previously used as a stratigraphic correlation tool, as changes in benthic foraminiferal $\delta^{13}C$ frequently reflect changes in ocean reservoir $\delta^{13}C_{DIC}$ (Hodell and Venz-Curtis, 2006) (see section 3.2.1.2). As the mixing time of the ocean is currently around 1000 years (Broecker and Peng, 1985), and the oceanic configuration in the late Miocene to early Pliocene is similar to today, it is reasonable to suggest that changes at timescales longer than 1 kyr in global seawater $\delta^{18}O$ and $\delta^{13}C$ can be considered as simultaneous between the major oceanic basins.

The main objective of this chapter is to establish an improved high-resolution age model on the investigated interval of the U1338 splice. This is achieved by stratigraphically correlating the high-resolution benthic foraminiferal isotope records from Site U1338 to comparable high-resolution benthic foraminiferal stable isotope records from ODP Site 982 in the North Atlantic (the benthic foraminiferal U1338 $\delta^{18}O_{CM}$ and $\delta^{13}C_{CM}$ are presented versus depth in Chapter 3). Site 982 was chosen, as there are published benthic foraminiferal isotope records from this location covering the interval of interest (8.0 – 3.5 Ma) that have orbitally tuned (Hodell et al., 2001). The choice of Site

982 as a correlation target is further explored in section 4.2.2. The stratigraphic correlation between Sites U1338 and 982 is facilitated by using the automated stratigraphic correlation tool 'Match' (Lisiecki and Lisiecki, 2002), discussed in section 4.3.1. The reliability of the improved high-resolution age model is also critically assessed. Finally, a comparison is made of all age and depth records: the B-Tukey and wavelet analyses of the U1338 benthic foraminiferal $\delta^{18}O_{CM}$ and $\delta^{13}C_{CM}$ records on the depth and the shipboard and Match-generated age models. This comparison helps to assess what, if any, influence there is on the spectra of Site U1338 $\delta^{18}O$ and $\delta^{13}C$ when these records are stratigraphically correlated to an orbitally tuned target.

4.2. Background and Previous Work

4.2.1. Milankovitch Cycles, Astronomical Solutions and Orbital Tuning

The amount of external solar radiation, or insolation (W/m^2), that any point on the Earth's surface receives, depends on the shape of the Earth's orbit around the sun, and the orientation of the Earth's axis in relation to the Earth's orbital plane (Laskar, 1999). Due to the chaotic nature of the universe and changes in the gravitational pull between the various planetary bodies in the solar system, the shape of Earth's orbit and the axis orientation changes through time (Laskar et al., 1993). The amount and spatial distribution of insolation received on Earth is therefore not constant through time. Milankovitch (1941)

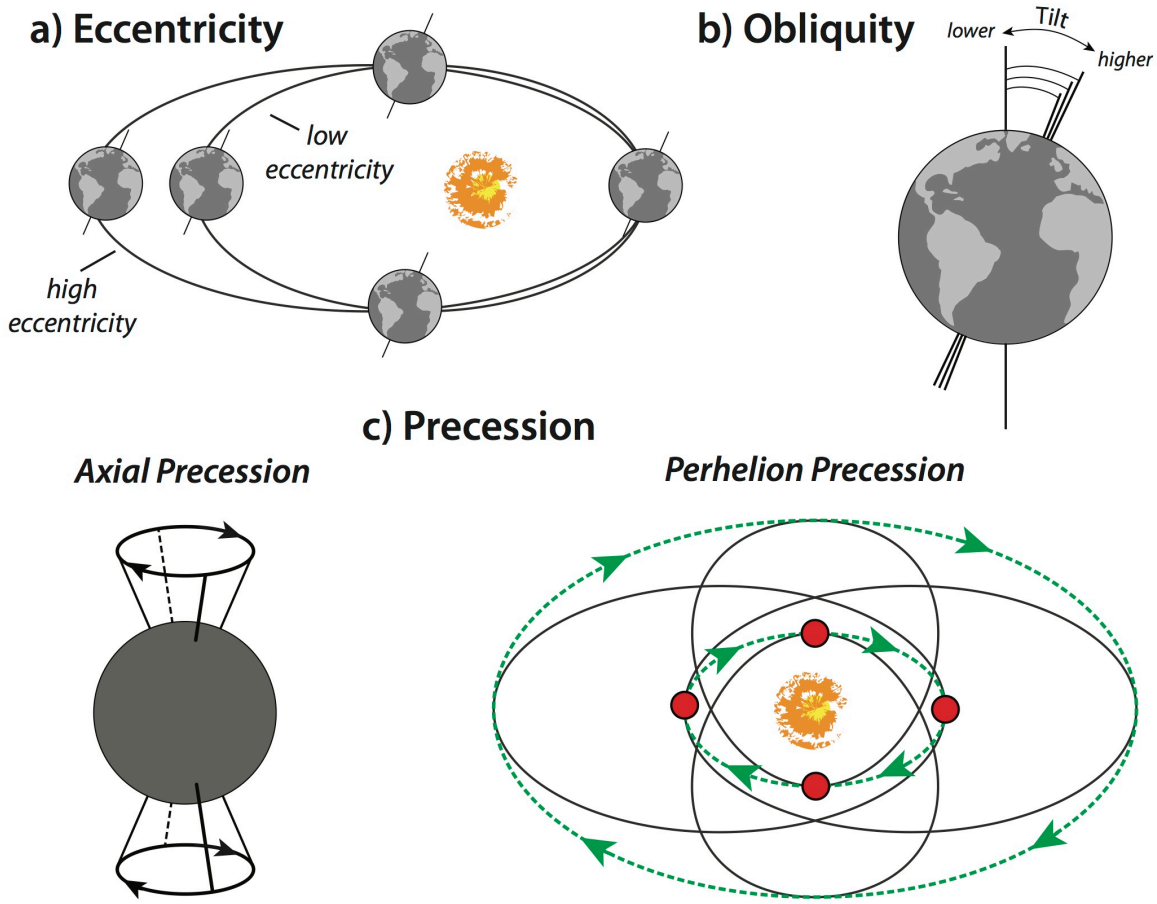

Figure 4.1. Overview of the orbital parameters that define Milankovitch cycles, adapted from Palike, 2005.

a) Shows the difference between low and high eccentricity. A low eccentricity orbit is more circular, and the amount of insolation delivered globally is more equal around the orbit. Because a high eccentricity orbit is more elliptical, the Earth receives increasingly different amounts of insolation depending on where the Earth is in its orbit.

b) Shows the difference between low and high obliquity, or axial tilt. High tilt denotes periods when the Earth's rotation axis is angled further away from the theoretical axis that is perpendicular to the orbital plane. Low tilt means that the axis is closer to perpendicular to the orbital plane.

c) Shows the two components of precession: 1) axial precession and 2) precession of the perihelion (also referred to as precession of the equinoxes). Axial precession describes the rotation of the Earth's axis towards and away from the sun relative to the same point on the Earth's orbit around the sun, for instance the perihelion. The precession of the perihelion describes the rotation of the perihelion, or orientation of the elliptical orbit relative to the sun.

first proposed the parameters now used to describe variations in Earth's orbit and axis orientation (eccentricity, obliquity and precession), and coupled past glacial-deglacial cycles on timescales of 10^4-10^6 years to variations in the amount and distribution of solar insolation that the Earth received. Milakovitch showed that each of these parameters cause cyclical variations in the Earth's orbit.

A schematic overview of the three Milankovitch cycles is shown in Figure 4.1 (adapted from Palike, 2005). Eccentricity controls the amount of solar radiation received by the Earth, averaged over a whole year, whereas obliquity and precession control the seasonal contrasts and global distribution of solar radiation on Earth (Palike, 2005). Eccentricity (Figure 4.1.a) describes the variations in solar radiation induced by changes in the shape of the orbit of the Earth around the Sun, from more elliptical (high eccentricity) to more circular (low eccentricity). Eccentricity generally contains a periodic variation around 400 kyr ('long' eccentricity cycle), as well as around 127 and 96 kyr ('short' eccentricity cycles) (Palike, 2005). Obliquity, or tilt, describes the angle between the Earth's spin axis, and the Earth's orbital plane around the sun (Figure 4.1.b). High obliquity induces a stronger seasonal contrast than low obliquity. The variation in obliquity shows strong oscillation at a ~ 41 kyr period, with additional periods around 54 kyr, and potentially 29 kyr (Palike, 2005; Lourens et al., 2010). Finally, precession (Figure 4.1.c) describes the rotation of the Earth's spin axis relative to the stars. The rotation of the spin axis essentially controls when the Earth passes through the perihelion (closest point to the sun on Earth's orbit) with respect to the different seasons. As the position of the perihelion also rotates relative to the stars, these two precession components (precession of the Earth's spin axis and precession of the perihelion) induce

several periodicities into the variation of incoming solar radiation, namely ~ 19, 22 and 24 kyr (Palike, 2005).

The initial relationship between variations in eccentricity, obliquity and precession (Milankovitch cycles), incoming solar radiation and climate change, was confirmed by Hays et al., (1976), who correlated glacial-interglacial cycles to early solutions of past orbital variations for the last 500 kyr. More recent calculations have provided precise astronomical solutions back to 20 to 10 Ma (La93 – Laskar et al., 1993) and 50 to 40 Ma (La2004 – Laskar et al., 2004). These solutions provide a crucial method of astronomical age calibration for many sedimentary records through the process of orbital tuning, where sedimentary cycles (Hilgen, 1991; Krijgsman et al., 1999), or cyclical variations in chemical climate proxies (Shackleton and Crowhurst, 1997; Lourens et al., 2004; Westerhold et al., 2005), are aligned with orbital solutions. For instance, the La2004 astronomical solution (Laskar et al., 2004) has been used in the creation of the astronomically tuned Neogene timescale (ATNTS2004 – Lourens et al., 2004). Many high-resolution isotopic records published before the ATNTS2004 were orbitally tuned to the La93 astronomical solution (also sometimes referred to as La90), including the records from Sites 926 (Shackleton and Hall, 1997) and 982 (Hodell et al., 2001), and the global isotope stack for 5 to 0 Ma (Lisiecki and Raymo, 2005). Fortunately, the La93 and La2004 solutions are practically indistinguishable for the first 10 Ma and do not differ significantly between 10 and 20 Ma (Laskar et al., 2004; Lourens et al., 2004), so records calibrated to either of these orbital solutions can be considered comparable within the interval studied in this thesis.

4.2.2. Correlation Target: ODP Site 982

ODP Site 982 (57°30.992'N, 15°52.001'W – Figure 4.2.a; see Figure 2.2 for location compared to Site U1338) was drilled as part of Expedition 162 in the North Atlantic (Shipboard Scientific Party, 1996; Jansen and Raymo, 1996). The site was drilled as a shallow water site, in 1134 m water depth on the Rockall Plateau. The benthic foraminiferal stable isotope records from Site 982 ($\delta^{18}O_{BF\_5pt}$ and $\delta^{13}C_{BF}$; Figure 4.2.b and c) were chosen as a correlation target for a number of reasons. Firstly, the high-resolution Site 982 isotope records are continuous throughout the 8.0 to 3.5 Ma interval and have been placed on an astronomically based time scale (see section 4.2.1) (Hodell et al., 2001; Hodell and Venz-Curtis, 2006). The stable isotope records from Site 982 cover the interval 9.0 to 3.5 Ma (sampled every 2.5 kyr between 4.6 – 3.5 Ma - Hodell and Venz-Curtis, 2006; sampled every 10 kyr between 9.0 – 4.6 Ma - Hodell et al., 2001). The section from Hodell et al. (2001) was orbitally tuned between 9.0 to 4.6 Ma to the astronomical solution La93 (Laskar et al., 1993) using the gamma ray attenuation (GRA) bulk density and the benthic foraminiferal oxygen isotopes. The orbitally tuned time scale from Shackleton et al. (1995a) (based on the astronomical solution from Berger and Loutre, 1991) was used as an age model for stable isotope records between 4.6 and 3.5 Ma (Hodell and Venz-Curtis, 2006). Orbitally deep-sea benthic foraminiferal $\delta^{18}O$ records exist in the Pacific covering sections of the interval of interest at Site U1338, for instance the 6 – 0 Ma record from Site 846 in the eastern equatorial Pacific (Shackleton et al., 1995b). However, no high-resolution or orbitally tuned record extends beyond 6 Ma in the equatorial Pacific. This was a further reason to choose Site 982 as a correlation target.

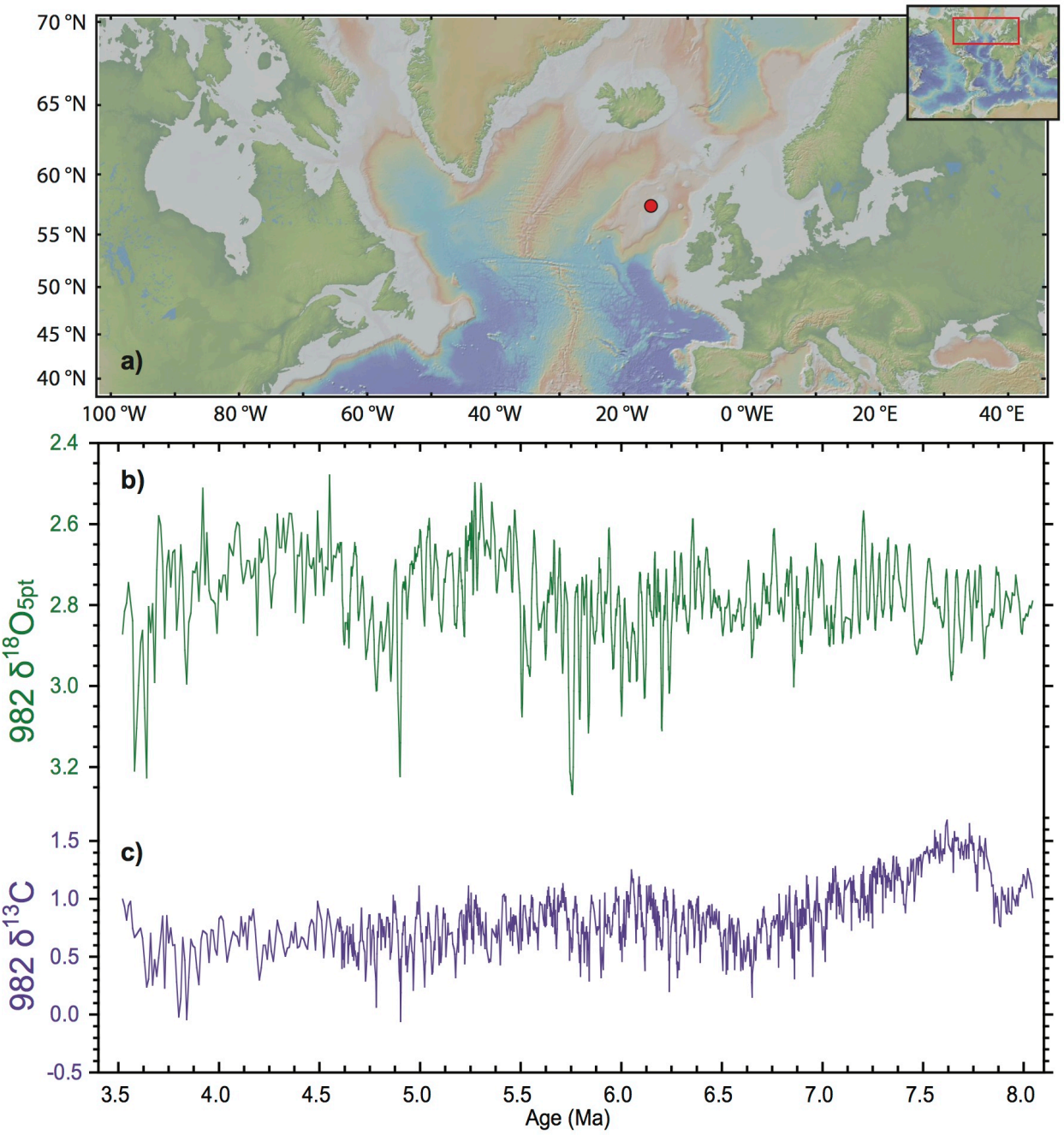

Figure 4.2. Overview of the data available from ODP Site 982.

a) Map showing the location of ODP Site 982 in the North Atlantic. (The map was produced using GeoMappApp – Ryan et al., 2009).

b) Benthic $\delta^{18}O$ and (c) $\delta^{13}C$ isotopes from ODP Site 982. The interval 4.6 to 3.5 Ma has a temporal sampling resolution of 10 kyr and was published in Hodell and Venz-Curtis (2006). The interval between 8.1 and 4.6 Ma is from the 9.0 to 3.5 Ma record initially published in Hodell et al., 2001, with a temporal resolution of 2.5 kyr.

Stratigraphically correlating the records from U1338 and 982 using the benthic foraminiferal isotope records is beneficial, as any future improvements on either the Site 982 age model or the U1338 age model can easily be translated to the other site, so that any comparisons between the two sites remain valid. Finally, the Site 982 isotope records were selected as a target records, because Hodell and Venz-Curtis (2006) correlated the isotope records from Site 982 to five additional DSDP and ODP sites across the late Miocene to early Pliocene interval (DSDP Site 607 in the North Atlantic, ODP Sites 704, 1088 and 1090 in the South Atlantic, and ODP Site 849 in the equatorial Pacific). A correlation between U1338 and Site 982 enables easy inter-site comparisons between the records from U1338 and records from the above-mentioned sites, which will help when deciphering the local, regional and global influences on the U1338 stable isotope records (these multi-site compilations are made and discussed in Chapters 5 and 6).

4.3. Analysis Techniques and Methods

4.3.1. Stratigraphic Correlation using Match

Chronostratigraphic correlation is a powerful approach, which not only enables direct comparison between records from different locations, but can also be used to provide age constraints for one location by transferring the age model from another location. Visually correlating recognisable events between chemical proxy records is a well-established, albeit time-consuming, method

(Shackleton et al., 1995a, b). Manual correlation could also induce error, based on the bias of the operator. Past attempts at automating this process were hampered by the need for a good initial fit (Martinson et al., 1982). The Match software package is a recent development that uses dynamic programming, constrained by a number of penalty functions, to provide the optimal solution for alignment of up to four pairs of records from different locations (initial software by Lisiecki and Lisiecki, 2002; expanded by Lisiecki and Herbert, 2007; downloaded on 01.04.2013 from http://lorraine-lisiecki.com/match.html). Dynamic programming encompasses a group of algorithms that divide a single problem into multiple subproblems and saves each subproblem solution separately to reduce computation time. The Match technique divides the target and signal data sets into a large number of equally spaced intervals, and then calculates a score for each possible alignment of the two datasets. The numbers of intervals are user-defined for each site. The total score is calculated as Σ^2, where Σ is the absolute difference between each pair of aligned intervals. The best-fit alignment by Match has the lowest score. This technique allows the short- and long-term variations in the selected records to be correlated simultaneously.

The main benefits of the Match software are the penalty functions that help constrain the alignment to represent realistic geological and palaeoceanographical settings. The penalty functions, which include an 'endpoint', 'speed', 'speed change', 'tie point' and 'gap' penalties, help counter problems that occur with noise, record gaps and changes in accumulation rate. These functions enable Match to process 'real' datasets and still provide realistic alignment solutions. Furthermore the software does not require the input of an

Match Autocalculate Penalty functions	
Variables	**definition**
s	*square(larger of two series standard deviations)*
m	*square(mean_targetseries - mean_signalseries)*
d	*(begin value_targetseries - end value_targetseries)*
Penalty	**Autocalculate function**
Endpoint / NoMatch	*15 (s + 4m)*
Speed	*1.5 (0.2s + 4m)*
Speed Change	*3.5 * (0.15s + 4m)*
Tie Point	*5000 (s/d + 4m)*
Gap	*1000 (s/d + 3.2m)*

Table 4.1.

Overview of the auto-calculate functions supplied to calculate an estimate for the various Match penalty functions.

initial alignment guess, although tie points can be included to guide the Match. The software was expanded in Lisiecki and Herbert (2007) to allow the programme to ignore specified intervals suspected of containing gaps in the record. The 'endpoint' or 'no-match' penalty tells the Match software how well the two datasets are known to align. A high endpoint value will force the start and end point of both datasets to align, whereas a low no-match penalty will allow Match the flexibility to not force the start and end points of both series to match precisely. The 'speed' penalty constrains the range of accumulation rates the programme chooses to align the records, and the 'speed change' defines how quickly (e.g. by what increment) the program can increase or decrease an accumulation rate. This allows geologically realistic sedimentation rates and rate changes to be included. Finally, the 'tie point' and 'gap' penalties respectively indicate how strictly the software must align any tie points, and by how much the size of the specified gaps can be stretched or compressed during the alignment process. Although the authors suggest varying all of the parameters, including penalties and interval size to find the best configuration, they also provide an auto-calculate method for the penalties, as a guideline for the ideas penalty-configuration for the alignment process. An overview of the functions needed to obtain auto-calculate values for the Match penalties is given in Table 4.1.

The process of creating a stratigraphic correlation between Sites U1338 and 982 was iterative. Firstly, the age constraint provided by first-order shipboard age model for Site U1338 (Table 2.1) was used to isolate the long-term cycles (long-term eccentricity at 400-kyr) from the U1338 benthic foraminiferal $\delta^{18}O_{CM}$ and $\delta^{13}C_{CM}$ records. The first-order shipboard age model was also used to provide some initial tie points for Match to use as guides in the alignment

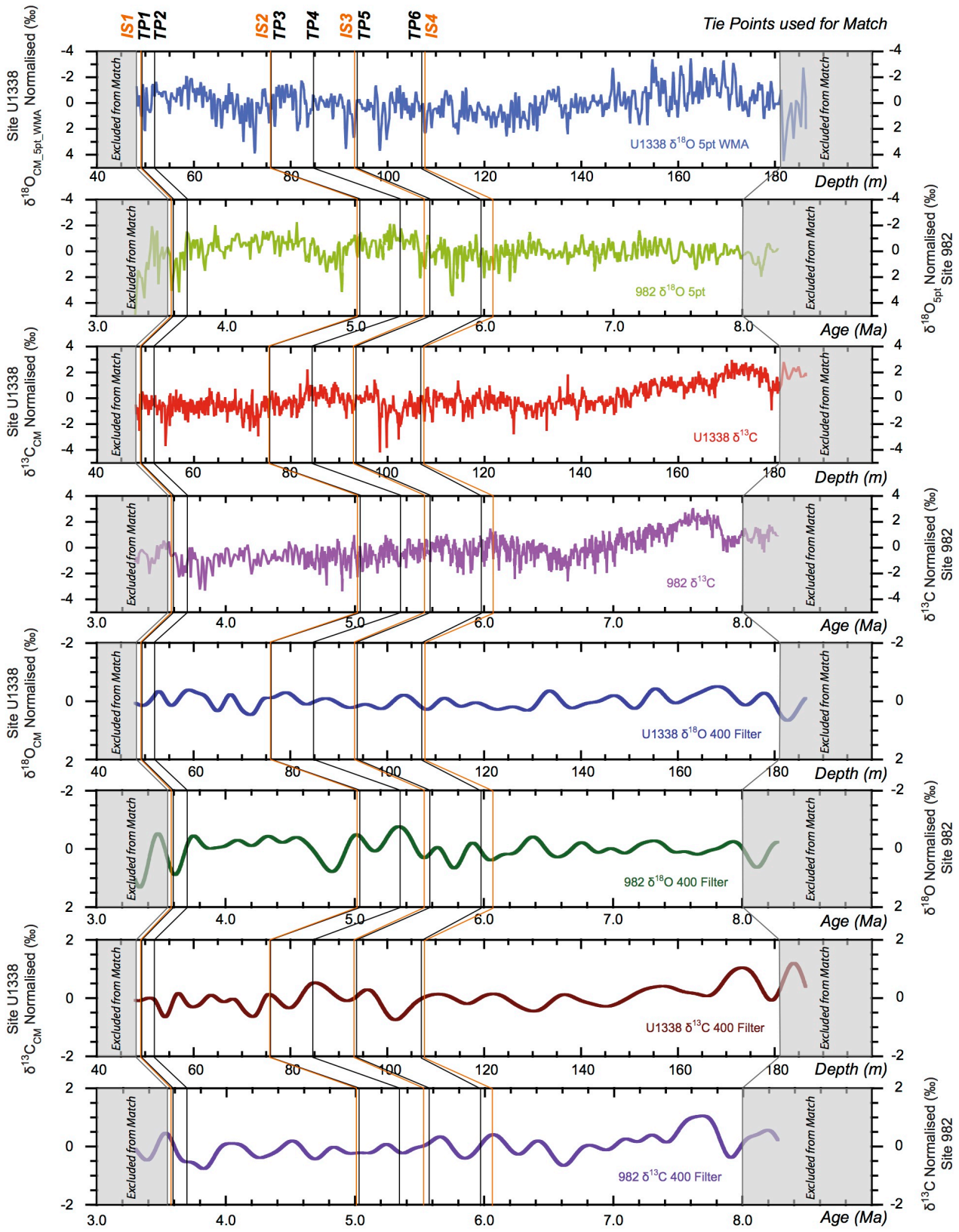
IS1
TP1
TP2
IS2
TP3
TP4
IS3
TP5
TP6
IS4
Tie Points used for Match
Site U1338 δ18OCM_5pt_WMA Normalised (‰)
U1338 δ18O 5pt WMA
Depth (m)
δ18O5pt Normalised (‰) Site 982
982 δ18O 5pt
Age (Ma)
Site U1338 δ13CCM Normalised (‰)
U1338 δ13C
δ13C Normalised (‰) Site 982
982 δ13C
Site U1338 δ18OCM Normalised (‰)
U1338 δ18O 400 Filter
δ18O Normalised (‰) Site 982
982 δ18O 400 Filter
Site U1338 δ13CCM Normalised (‰)
U1338 δ13C 400 Filter
982 δ13C 400 Filter
Excluded from Match

Figure 4.3:

Overview of all the data set pairs used in both the first- and second-generation Match alignment. From top to bottom, the order is as follows: benthic $\delta^{18}O$ 5pt WMA (weighted moving average) from U1338 and 982; benthic $\delta^{13}C$ from U1338 and 982; benthic $\delta^{18}O$ 400-kyr filter from U1338 and 982; benthic $\delta^{13}C$ 400-kyr filter from U1338 and 982. The 982 isotope data comes from Hodell et al., 2001 and Hodell and Venz-Curtis, 2006.

The grey shaded areas at the start and end of the plots indicate the intervals that were excluded from the Match correlation.

The black lines highlight the relative position of the tie points used in the first-generation Match alignment (TP 1 – 6; for details see Table 4.3). The orange lines indicated the position of the tie points that replaced TP 1, 3, 5 and 6 in the second-generation Match alignment (IS 1 – 4; for details see Table 4.3).

process. The isotope data from both Sites U1338 and 982 were normalised by subtracting the respective time series means, and followed by division with the standard deviation. With the stable isotope datasets from both sites converted, the 400-kyr long-term trends of $\delta^{18}O_{CM}$ and $\delta^{13}C_{CM}$ were isolated in Analyseries (Paillaird et al., 1996 - version 2.0.4.2) using a broad Gaussian filter, centred on the frequency of 0.0025 with a bandwidth of 0.002. A broad filter was selected to isolate the 400-kyr trend, as a too narrow filter would ignore much of the long-term trend. This is particularly important with the U1338 datasets, as the first-order age model is fairly low-resolution. The stable isotope data from U1338 was replotted on the depth scale to enable direct depth-age correlation between Sites U1338 and 982 during the Match alignment.

Following isolation of the 400-kyr trend, the first Match (G1) alignment was generated using four pairs of data from Sites U1338 and 982: 1) the benthic foraminiferal $\delta^{18}O$ 5pt-averaged datasets; 2) the benthic foraminiferal $\delta^{13}C$ datasets; 3) the benthic foraminiferal $\delta^{18}O$ 400-kyr filtered datasets and 4) the benthic foraminiferal $\delta^{13}C$ 400-kyr filtered datasets (See Chapter 3 for a description of the $\delta^{18}O$ 5pt and $\delta^{13}C$ datasets from Site U1338; see Hodell et al., 2001 for a description of the $\delta^{18}O$ 5pt and $\delta^{13}C$ datasets from Site 982). Figure 4.3 gives an overview of the dataset pairs used for the Match alignment. The first and last (approximately) 200 kyr of all Site 982 datasets were excluded from the Match alignment process, as the start was beyond the age range of the U1338 records constrained by the palaeomagnetic reversal at 3.5 Ma, and the end was constrained by the presence of the late Miocene CIS in both records. The low-resolution data in the last 5 m CCSF-A of Site U1338 were also excluded because the sampling resolution was too low to fully resolve cycles that could be

Match Tie Point Overview						
a) First Order Age Model Tie Points						
ID	***Based on***	***Age (Ma)***	***Depth (m CCSF-A)***	***Error (m CCSF-A)***		
TP1	C2An.3/C2Ar	3.596	49.13	0		
TP2	T Reticulofenestra pseudoumbilicus (NN16)	3.70	51.86	0.8		
TP3	T Ceratolithus acutus (NN13)	5.04	75.49	0.615		
TP4	B Ceratolithus acutus	5.35	84.6	0.75		
TP5	T Discoaster quinqueramus (NN12)	5.58	93.38	0.75		
TP6	T Nicklithus amplificus	5.98	107.12	0.685		
b) Adapted Age Model Tie Points						
ID	***Based on***	***Age (Ma)***	***Depth (m CCSF-A)***	***Age Shift (kyr)***	***Depth Shift (m)***	***Within Original Tie Point Error***
IS1	Isotope Event Correlation near TP1	3.58	49.12	-16	-0.01	Yes
TP2	T Reticulofenestra pseudoumbilicus (NN16)	3.70	51.86	*n/a*	*n/a*	*n/a*
IS2	Isotope Event Correlation near TP3	5.019	75.58	-21	0.09	Yes
TP4	B Ceratolithus acutus	5.35	84.6	*n/a*	*n/a*	*n/a*
IS3	Isotope Event Correlation near TP5	5.542	93.02	-38.1	-0.36	Yes
IS4	Isotope Event Correlation near TP6	6.073	107.61	92.5	0.49	Yes

Table 4.2.

Overview of the tie points used in both the first- (a) and second-generation (b) Match alignments. Note that the alternative tie points for TP 1 (IS1), TP3 (IS2), TP5 (IS3) and TP6 (IS4) all fall within the depth error of the original datums (*n/a* = not applicable).

correlated. Figure 4.3 also shows the relative position of the tie points used in the first Match alignment, denoted by the black markers TP1 through to TP6 (a tie point overview can be found in Table 4.2). All tie points have a depth-error associated with them, associated with the sampling interval the shipboard magneto- and biostratigraphies were originally done at (Palike et al., 2010). The ages do not have errors associated with them, as this is already incorporated within the number of decimal places the age is reported against (Palike et al., 2010).

Table 4.3 provides an overview of the configuration used for the first-generation Match alignment. The start and end values for all datasets were chosen to exclude the grey areas shown on Figure 4.3. The no-match/endpoint penalty was kept low, set at 0.01. A low no-match penalty allows Match software the flexibility with placing the start and end points of both series to improve the match. The number of intervals for datasets from Sites U1338 and 982 were set to 1010, following guidelines in Lisiecki and Lisiecki, 2002. Initial tests, where the speed and speed change were varied, showed that the autocalculate values provided the best possible setting and gave the lowest Match alignment score. For this reason the autocalculate values for the speed and speed change penalties were used. The tie point penalty was also left at the autocalculate value of 1, as this allows Match some flexibility with assigning the exact position of the tie points selected (Figure 4.3 and Table 4.3). The first-generation (G1) Match alignment was visually inspected to assess the quality of the correlation. Where isotopic events seemed to be offset between the U1338 and 982 records, tie points were adjusted to try to reduce the offset (Table 4.2). The second-generation Match (G2) alignment has an identical configuration to the first-

Match Configuration Overview			
First Generation Match (G1)		**Second Generation Match (G2)**	
Dataset parameters		Dataset parameters	
Site U1338		*Site U1338*	
Datasets	d18O 5pt	Datasets	d18O 5pt
	d13C		d13C
	d18O 400 kyr filter		d18O 400 kyr filter
	d13C 400 kyr filter		d13C 400 kyr filter
Start point	48.2 m CCSF-A	Start point	48.2 m CCSF-A
End point	181 m CCSF-A	End point	181 m CCSF-A
# intervals	1010	# intervals	1010
Site 982		*Site 982*	
Datasets	d18O 5pt	Datasets	d18O 5pt
	d13C		d13C
	d18O 400 kyr filter		d18O 400 kyr filter
	d13C 400 kyr filter		d13C 400 kyr filter
Start point	3560 kyr	Start point	3550 kyr
End point	8000 kyr	End point	8000 kyr
# intervals	1010	# intervals	1010
Penalties		Penalties	
No Match penalty	0.01	No Match penalty	0.01
Speed penalty	0.78	Speed penalty	0.78
Speed Change penalty	0.59	Speed Change penalty	0.59
Tie point penalty	1.00	Tie point penalty	1.00
Gap penalty	0.00	Gap penalty	0.00
Speed parameters		Speed parameters	
Target speed	1:1	Target speed	1:1
Available speeds	1:3, 2:5, 1:2, 3:5, 2:3, 3:4, 4:5, 1:1, 5:4, 4:3, 3:2, 5:3, 2:1, 5:2, 3:1	Available speeds	1:3, 2:5, 1:2, 3:5, 2:3, 3:4, 4:5, 1:1, 5:4, 4:3, 3:2, 5:3, 2:1, 5:2, 3:1
Score and Breakdown		Score and Breakdown	
Points	3569.70	Points	3425.26
No Match Penalty Points	0.93	No Match Penalty Points	0.93
Speed Penalty Points	167.38	Speed Penalty Points	192.46
Speed Change Penalty Points	251.93	Speed Change Penalty Points	271.99
Tie Point Penalties	4.10	Tie Point Penalties	6.53
Gap Point Penalties	0.00	Gap Point Penalties	0.00
Total Score	3994.04	Total Score	3897.18

Table 4.3.

Overview of the configuration settings used for the first- (G1) and second- (G2) generation Match alignments. See main text (section 4.3.1) for a more detailed discussion of the parameters and penalties.

generation Match alignment (Table 4.3), with the exception of the adapted tie points (Table 4.2), and a slightly adapted start point on both U1338 and 982 datasets to accommodate the change of the uppermost tie point. The final age model produced from the final alignment is shown in Appendix B.1.

4.3.2. Blackman-Tukey Spectral Analysis

A power spectrum estimates the spectral density of a time-series (Weedon, 2005). This group of spectral analysis techniques essentially characterises which frequencies are present, and determines their dominance within the time-series. Power spectra are generally reported in frequency, or period, on the x-axis versus power density on the y-axis. If the power spectrum shows higher power at a given frequency, this indicates that the original time-series contains dominant cycles with that frequency.

Blackman-Tukey (B-Tukey) spectral analysis with a Bartlett window was performed on the benthic foraminiferal U1338 and 982 $\delta^{18}O$ and $\delta^{13}C$ records, and the reconstructed sedimentation rates. Spectral plots were produced in the depth, the first-order age model and second-generation Match age model time domains. The B-Tukey spectra were generated using the Analyseries program (Paillaird et al., 1996 - version 2.0.4.2). Equally spaced datasets were created in Analyseries using linear interpolation between data points. To enable the shorter-term frequencies in the datasets to be investigated more easily, the long-term frequencies were removed from each dataset using a Gaussian notch filter (depth-domain: filter centred at 0.00, with bandwidth of 0.07; time domain: filter centred at 0.00, with bandwidth of 0.00175). This process removed all cycles

above 14 m in the depth-spectra and above 570 kyr in the time-spectra. Before the B-Tukey power spectral method was applied using a Bartlett window, all datasets were linearly detrended, normalised to unit variance and prewhitening (weak form of filtering where high frequencies are enhanced and low frequencies are suppressed – Weedon, 2005) was applied.

4.3.3. Wavelet Analysis

Simple power spectra as discussed above provide information about the relative power of different frequencies averaged across the whole dataset. However, to establish whether different frequencies dominate during different intervals, another form of time-series analysis is needed. A windowed power spectra, or evolutionary spectra could be applied, where a fixed window size is slid along the time series with a power spectra being measured at regular intervals (Torrence and Compo, 1998). However, the selection of a suitable window size causes complications for evolutionary spectra: a too narrow window would often fail to capture the true power at low frequencies, whereas a too broad filter would likewise not capture the power in the higher frequencies (Weedon, 2005). A technique that bypasses the window-size issue is wavelet analysis. In wavelet analysis, the simple window of an evolutionary spectrum is replaced by a wavelet. The most common wavelet is a Morlet wavelet, which is a combination of a sine wave and a Gaussian filter (Torrence and Compo, 1998) (Figure 4.4). This wavelet can be scaled depending on the frequency to which it is applied: the largest scale wavelet is used for the lowest frequencies, and then

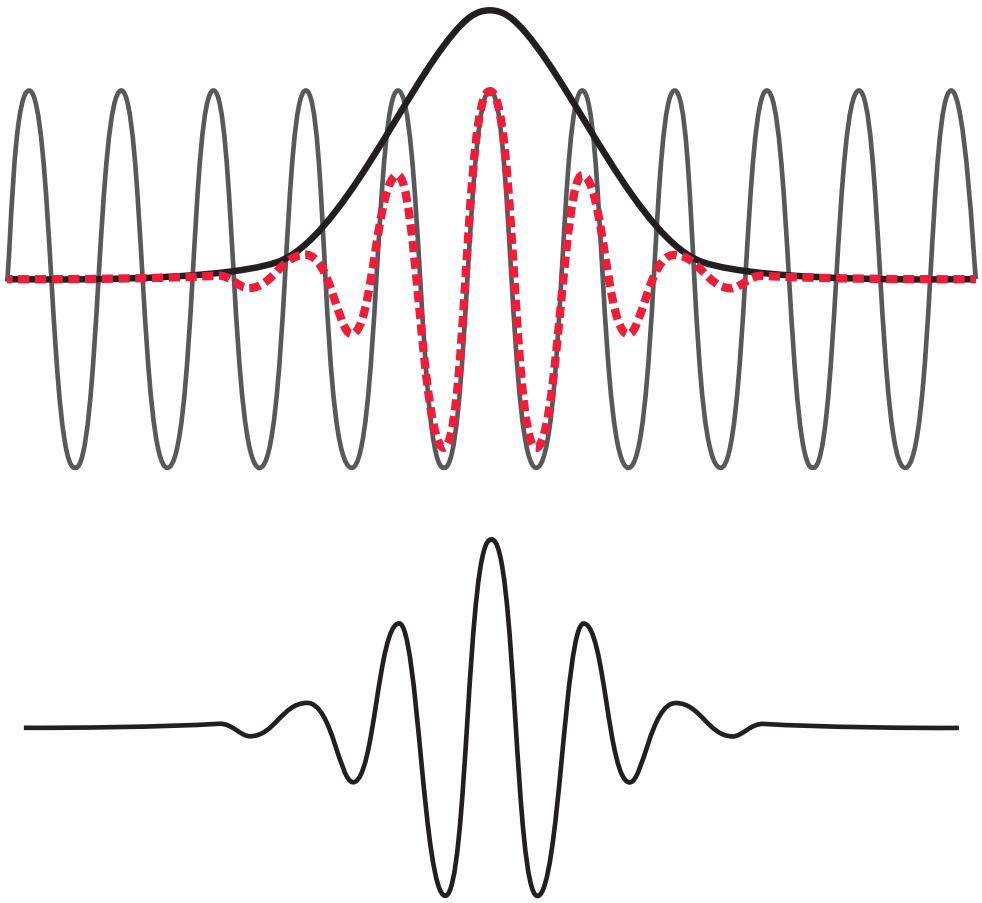

Figure 4.4. Example of a Morlet Wavelet.

The upper schematic shows how a Gaussian envelope (black) and a sine wave (grey) combine to form a Morlet wavelet (red), which is one of the most commonly applied wavelets. The lower schematic shows the Morlet wavelet on its own.

reduced step-wise in size, with the smallest wavelet applied to the highest frequencies (Weedon, 2005). The difference between an evolutionary spectrum and a wavelet analysis is schematically represented in Figure 4.5.

Wavelet analyses were performed on the benthic foraminiferal $\delta^{18}O$ and $\delta^{13}C$ records from U1338 and 982, as well as on the reconstructed sedimentation rates from Site U1338. Wavelet plots were produced in both the depth, and the first-order model and second-generation Match model time domains. The wavelet analyses were made using a programme initially designed by Torrence and Compo (1998) to allow easy use of the wavelet analysis method on a variety of datasets. The version of this software used in this thesis is an expanded version of the Torrence and Compo (T&C) wavelet programme, which was published by Grinsted et al. in 2004 (downloaded from http://noc.ac.uk/using-science/crosswavelet-wavelet-coherence in July 2013). This updated software package, which can be run in Matlab, has included 95% confidence limits on the original T&C wavelet package to highlight areas of significant power, as well as cross-wavelet and wavelet coherence packages. The wavelet plots were generated using the Grinsted software package in Matlab (version 2012a) on equally spaced datasets, which were created in Analyseries using linear interpolation between data points. The software automatically pads the datasets with zeros to make the total number of data points up to the power of two, which makes the analysis process quicker. Cone of influences are included on all plots (opaque area), within which edge effects due to the individual dataset lengths exist and should be considered during interpretation (Grinsted et al., 2004).

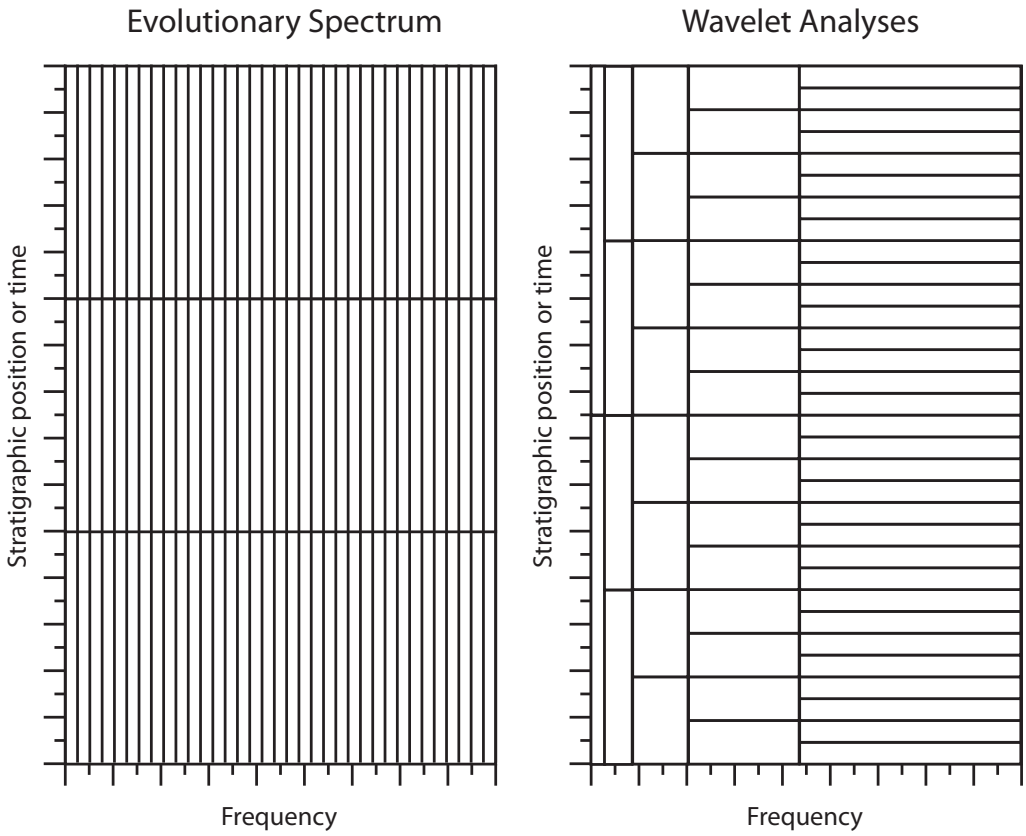

Figure 4.5. Overview of an evolutionary spectrum and a wavelet analysis.
This figure schematically represents the difference between an evolutionary spectrum (left) and a wavelet analysis (right). In an evolutionary spectrum, a window of a fixed size is applied at regular steps in the frequency domain to resolve the changes in power at the different frequencies throughout the record. In a wavelet analysis, a different scale of wavelet is applied to increasingly smaller intervals on time or depth domain, encompassing increasingly larger areas in the frequency domain.

4.4. Results

4.4.1. Age Model Generation

Figure 4.6 shows the normalised full resolution stable isotope records from Sites U1338 (a) and 982 (b) with their respective 400-kyr filtered datasets. The filtered 400-kyr datasets clearly represent the long-term changes in the high-resolution datasets well. Furthermore, there are clear similarities between the long-term benthic foraminiferal $\delta^{13}C$ trends of Sites U1338 and 982, particularly in the lower section of the record.

The results from the first-generation Match (G1) alignment are shown in Figure 4.7. The alignment score is given in Table 4.3. The long-term trends show good agreement, particularly between the two benthic foraminiferal $\delta^{13}C$ 400-kyr records in the bottom half of the record, and between the two benthic foraminiferal $\delta^{18}O$ 400-kyr records in the top half of the record (Figure 4.7 c and d). To evaluate the quality of the Match alignment of short-term variations, the benthic foraminiferal $\delta^{18}O$, $\delta^{18}O$ 5pt and $\delta^{13}C$ from Sites U1338 and 982 were compared in 1 Myr intervals ($\delta^{18}O$ 5pt - Figure 4.8; $\delta^{18}O$ and $\delta^{13}C$, - Appendix B.2. a and b respectively). On close inspection, the first-generation Match (G1) alignment has generally correlated Sites U1338 and 982 fairly well. This is particularly visible in large parts of the comparison between the two benthic foraminiferal $\delta^{18}O_{CM}$ 5pt records (Figure 4.8), as the signal to noise ratio is larger compared to the un-averaged benthic foraminiferal $\delta^{18}O$ records (Appendix B.2.a).

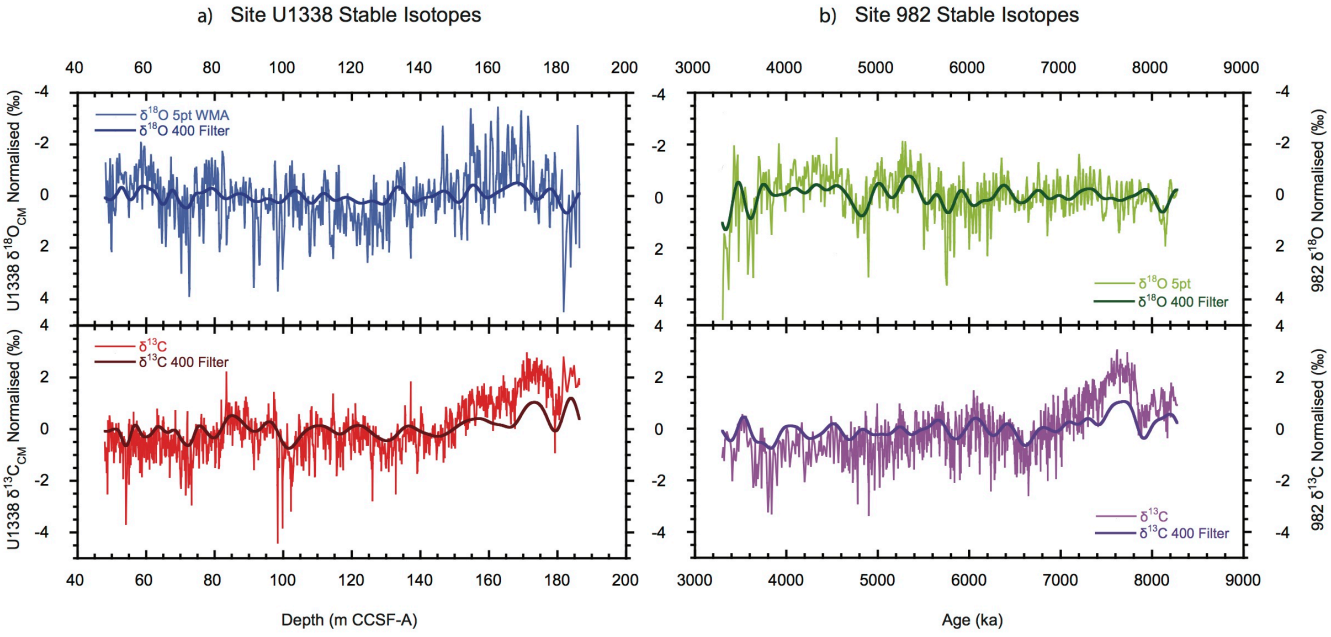

Figure 4.6. Overview of complete and filtered isotopic records used for the first- and second-generation Match alignments.

a) Depth profile overview of the normalised complete $\delta^{13}C_{CM}$ and the $\delta^{18}O_{CM}$ 5pt WMA, and the respective 400 kyr filtered trends from Site U1338.

b) Age profile overview of the normalised complete $\delta^{13}C$ and the $\delta^{18}O_{CM}$ 5pt, and the respective 400 kyr filtered trends from Site 982 (Hodell et al., 2001; Hodell and Venz-Curtis, 2006).

Generally, the long-term trends of the high-resolution records are reflected well in the filtered 400-kyr records.

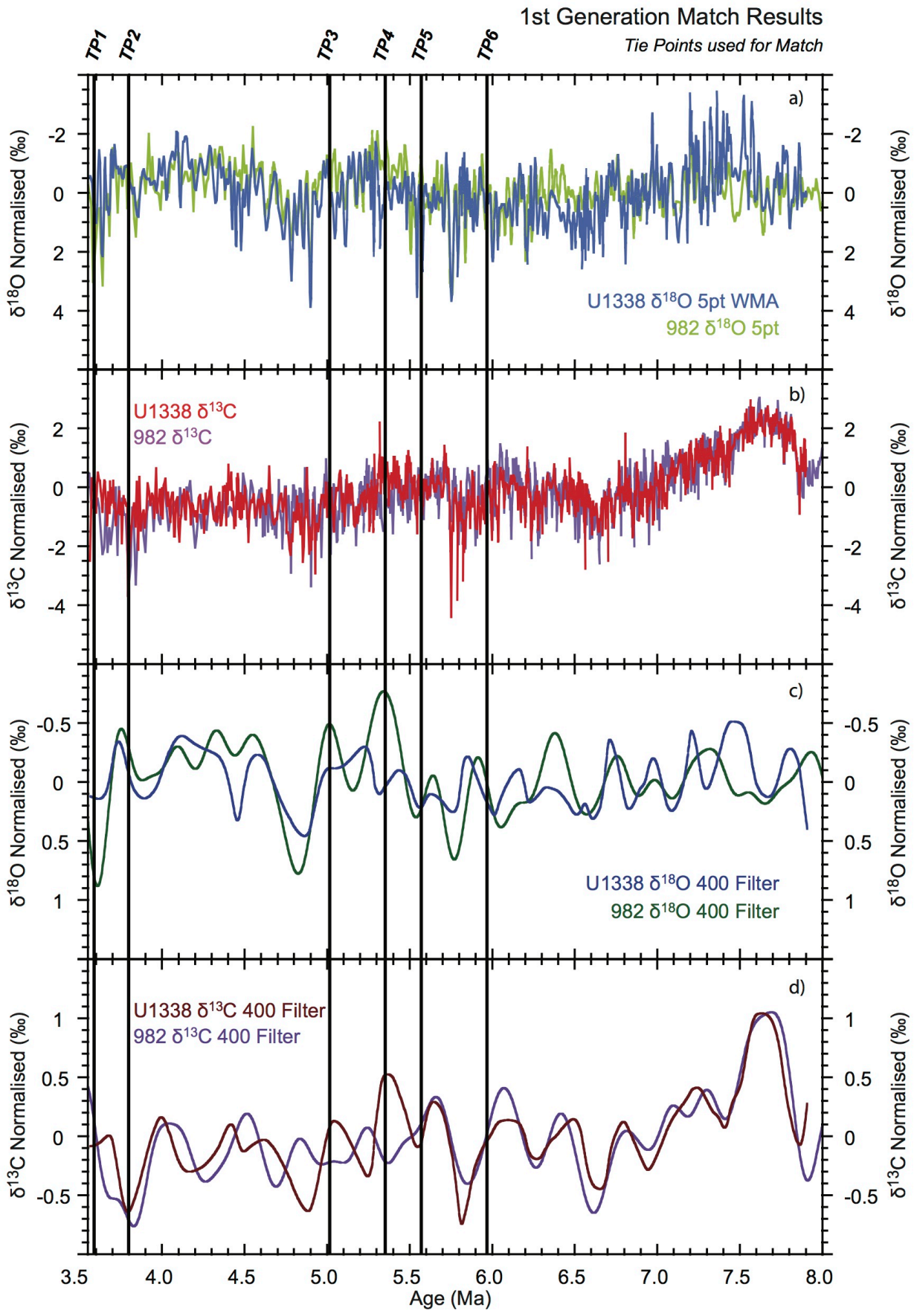
1st Generation Match Results
Tie Points used for Match
TP1
TP2
TP3
TP4
TP5
TP6
a)
U1338 δ18O 5pt WMA
982 δ18O 5pt
b)
U1338 δ13C
982 δ13C
c)
U1338 δ18O 400 Filter
982 δ18O 400 Filter
d)
U1338 δ13C 400 Filter
982 δ13C 400 Filter
δ18O Normalised (‰)
δ13C Normalised (‰)
Age (Ma)
3.5
4.0
4.5
5.0
5.5
6.0
6.5
7.0
7.5
8.0

Figure 4.7.

Overview of the first-generation Match (G1) results, with the U1338 and 982 benthic $\delta^{18}O$ and $\delta^{13}C$ (original and filtered) records.

It is difficult to evaluate the alignment of the high-resolution records in these diagrams, but in terms of the long-term trend alignment, the $\delta^{13}C$ records align well at the base of the record, whereas the $\delta^{18}O$ records align better at the top of the record. Note that these panels only include the sections of the U1338 and 982 records actually included in the Match correlation.

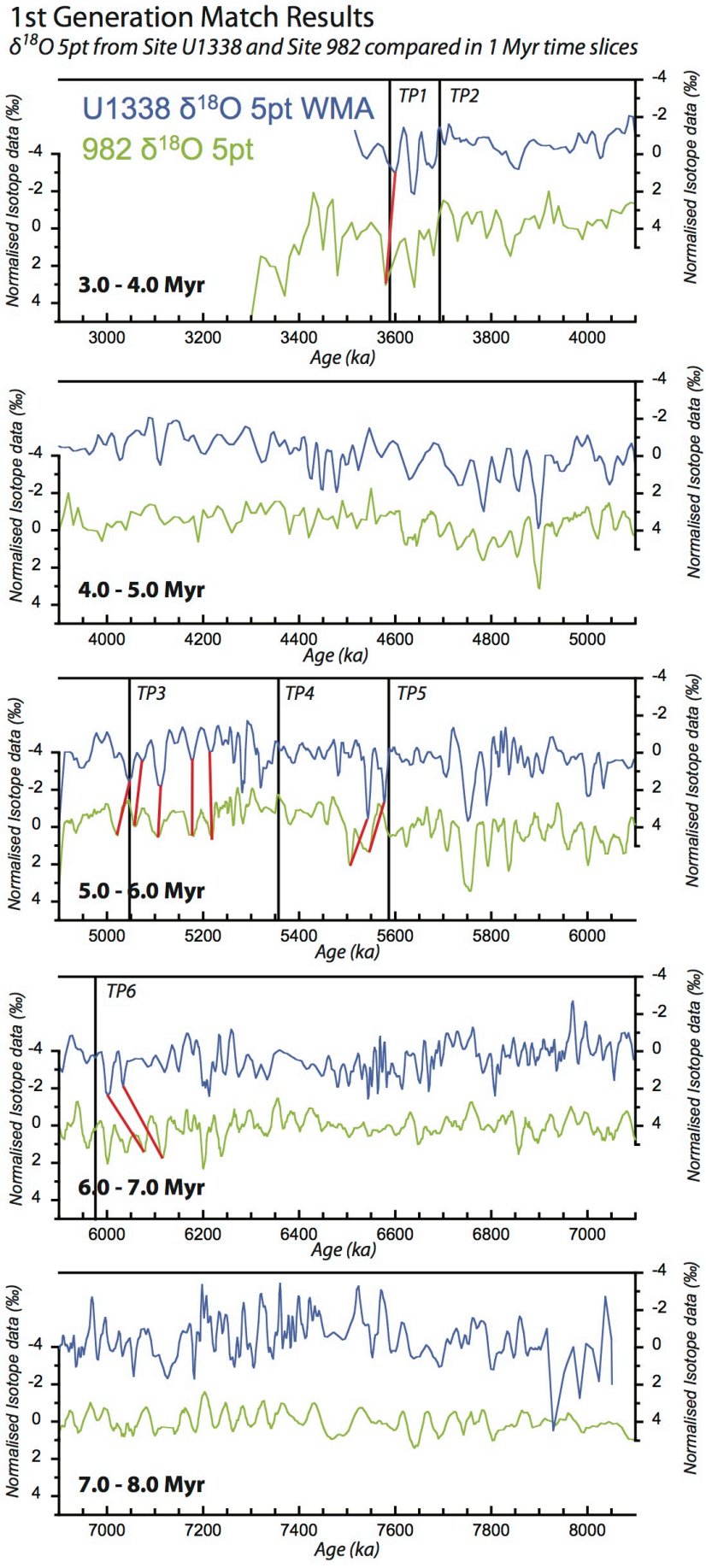
1st Generation Match Results
δ18O 5pt from Site U1338 and Site 982 compared in 1 Myr time slices
U1338 δ18O 5pt WMA
982 δ18O 5pt
TP1
TP2
3.0 - 4.0 Myr
4.0 - 5.0 Myr
TP3
TP4
TP5
5.0 - 6.0 Myr
TP6
6.0 - 7.0 Myr
7.0 - 8.0 Myr
Normalised Isotope data (‰)
Age (ka)

Figure 4.8.

Detailed overview of the benthic $\delta^{18}O_{\_5pt}$ from Sites U1338 and 982 aligned using the first-generation Match (G1) alignment to evaluate how well the records align in terms of short-term fluctuations. The positions of the tie points used to guide the alignment are highlighted with black lines.

Generally, the alignment is good throughout most of the record. The exceptions are highlighted using red lines. Here the location of TP1, 3, 5 and 6 respectively have seemingly forced an offset between isotopic events of a similar nature.

There are a number of sections where there is an offset between the alignments of isotopic events of a similar nature (see red lines in Figures 4.8 and Appendix B.2). Interestingly, these occur at the relative position of four out of the six tie points that were based on shipboard datums: tie points TP1, TP3, TP5 and TP6. If these tie points are adjusted so that the isotopic events align, the depth offset between the original shipboard TP tie point and the new isotope IS tie point is always less than the depth error on the original shipboard TP tie point (Table 4.2). This small offset suggests that these isotopic events are probably the same, and that TP1, 3, 5 and 6 can be exchanged for isotopic event based tie points IS1, 2, 3 and 4 respectively for the second-generation Match alignment.

The results of the second Match (G2) alignment are shown in Figure 4.9, and the alignment score is a slight improvement on the alignment score for the first-generation Match (G1) alignment (Table 4.3). Comparing the long-term trends, generally, the two records agree fairly well and there is not much difference between the first and second-generation Match alignment. When comparing 1 Myr sections of the benthic foraminiferal $\delta^{18}O$, $\delta^{18}O$ 5pt and $\delta^{13}C$ records ($\delta^{18}O$ 5pt - Figure 4.10; $\delta^{18}O$ and $\delta^{13}C$, - Appendix B.3. a and b respectively), the sections with good alignment in the first-generation Match (G1) correlation remain unchanged. However, there is distinct improvement in the intervals where the TP tie points were adjusted to the IS tie points. In these intervals, there is no longer an offset between comparable isotopic events (see red lines in Figure 4.10 and Appendix B.3).

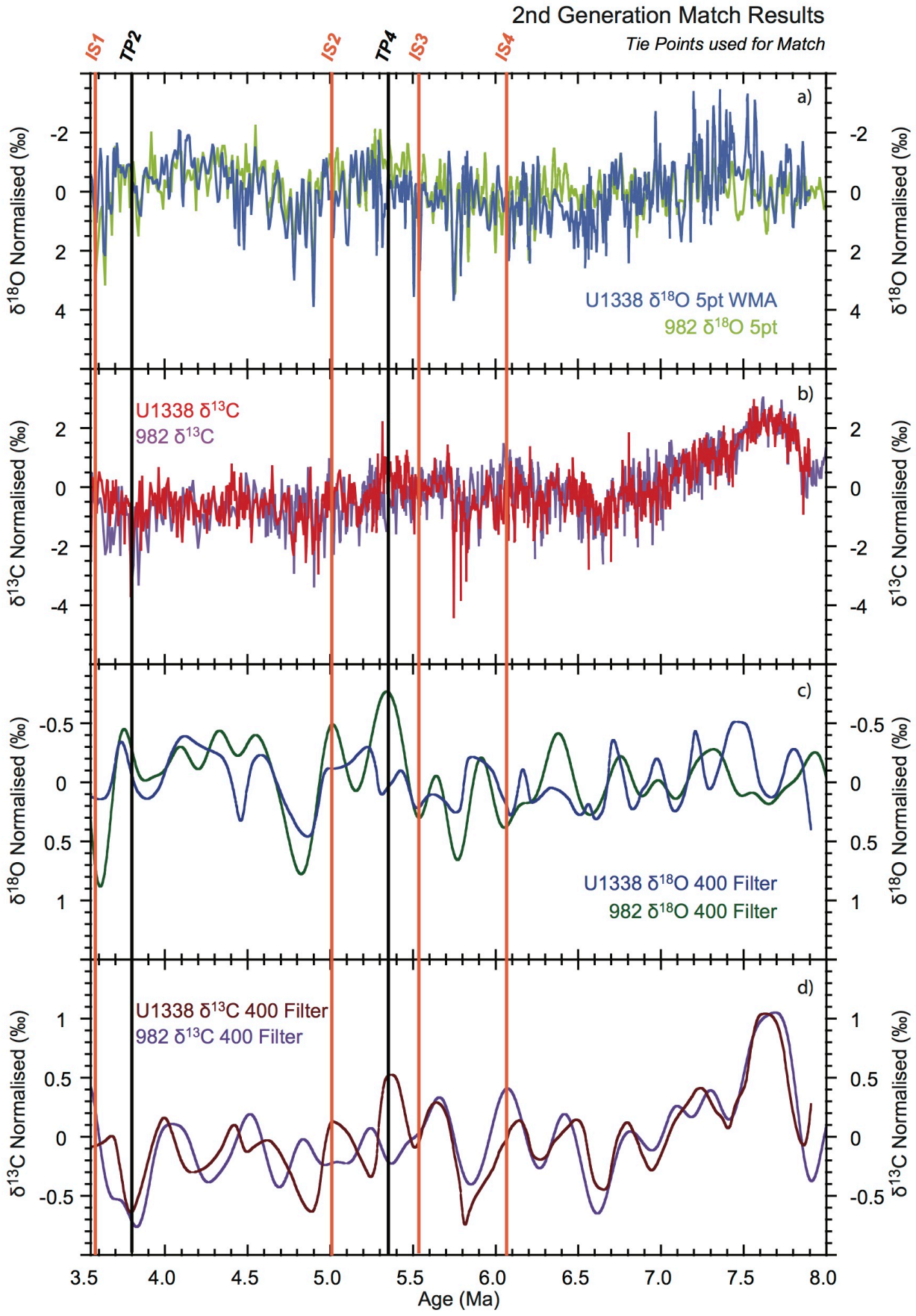
2nd Generation Match Results
Tie Points used for Match
IS1
TP2
IS2
TP4
IS3
IS4
a)
U1338 δ18O 5pt WMA
982 δ18O 5pt
b)
U1338 δ13C
982 δ13C
c)
U1338 δ18O 400 Filter
982 δ18O 400 Filter
d)
U1338 δ13C 400 Filter
982 δ13C 400 Filter
δ18O Normalised (‰)
δ13C Normalised (‰)
Age (Ma)
3.5
4.0
4.5
5.0
5.5
6.0
6.5
7.0
7.5
8.0

Figure 4.9.

Overview of the second-generation Match (G2) results, with the benthic U1338 and 982 $\delta^{18}O$ and $\delta^{13}C$ (original and filtered) records.

The long-term results look similar to the results from the first-generation alignment, so the reassignment of the tie points has not altered the long-term trend alignment. Note that these panels only include the sections of the U1338 and 982 records actually included in the Match correlation.

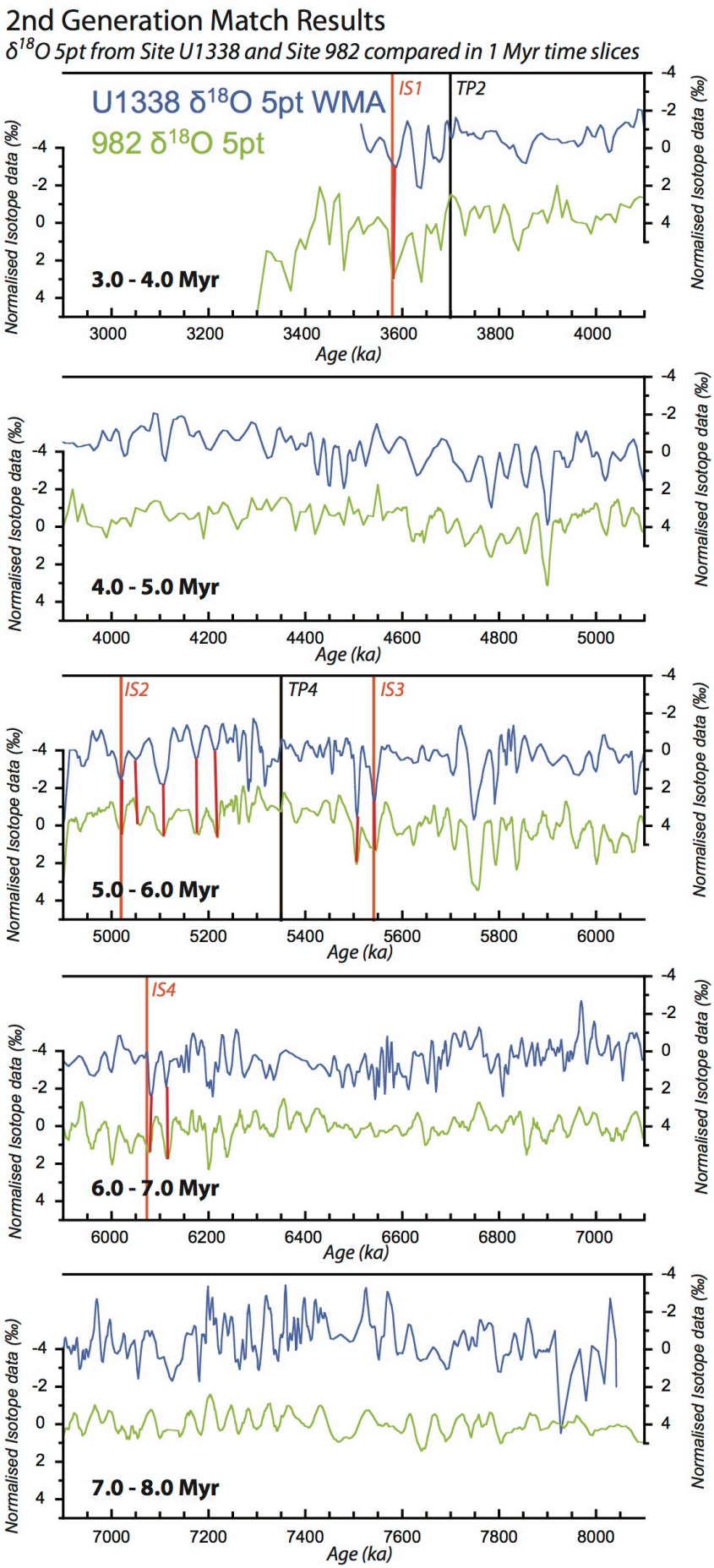
2nd Generation Match Results
δ18O 5pt from Site U1338 and Site 982 compared in 1 Myr time slices
U1338 δ18O 5pt WMA
982 δ18O 5pt
IS1
TP2
3.0 - 4.0 Myr
4.0 - 5.0 Myr
IS2
TP4
IS3
5.0 - 6.0 Myr
IS4
6.0 - 7.0 Myr
7.0 - 8.0 Myr
Normalised Isotope data (‰)
Age (ka)

Figure 4.10.

Detailed overview of the benthic $\delta^{18}O_{\_5pt}$ from Sites U1338 and 982 aligned using the second-generation Match alignment (G2) to evaluate how well the records align in terms of short-term fluctuations. The positions of the tie points used to guide the alignment are highlighted with black and orange lines.

The red lines highlight the areas that were initially badly aligned in the second-generation Match alignment. Simply by adjusting four tie points, the alignment is much improved. Other areas that already had good alignment are now equally well aligned.

4.4.2. Sedimentation Rate Results

4.4.2.1. Time Series

Figure 4.11 a and b shows the age-depth relationships and sedimentation rates of the first-order shipboard age model and the second-generation Match (G2) age model for Site U1338. The age-depth relationships (Figure 4.11 a) look similar in the younger and middle section of the record, with a shallower age-depth relationship during the early Pliocene than during the latest Miocene. The decrease in the age-depth relationship occurs earlier in the G2 age model (around 5.25 Ma) than it does in the shipboard age model (around 5.1 Ma). A notable difference is that the G2 age model displays a steeper age-depth relationship than the shipboard age model in the oldest section of the record, from 8.0 – 6.25 Ma.

The sedimentation rates (m/Myr) derived from the shipboard and G2 age models again show similar patterns from about 6.5 – 3.5 Ma (Figure 4.11 b). The G2 sedimentation rates fluctuate far more than the shipboard age model sedimentation rates, however the averages are similar. The fact that the G2 sedimentation rates vary more is to be expected, as the age model has a higher resolution than the shipboard model. In the base section of the record, between 8.0 and 6.5 Ma, the variation in the G2 sedimentation rates is similar to the remainder of the record. However, the mean G2 sedimentation rates in this interval are higher than any other section, and higher than any shipboard sedimentation rates seen at Site U1338. An overview of average sedimentation rates is given in Table 4.4, based on shipboard and second-generation Match age model data.

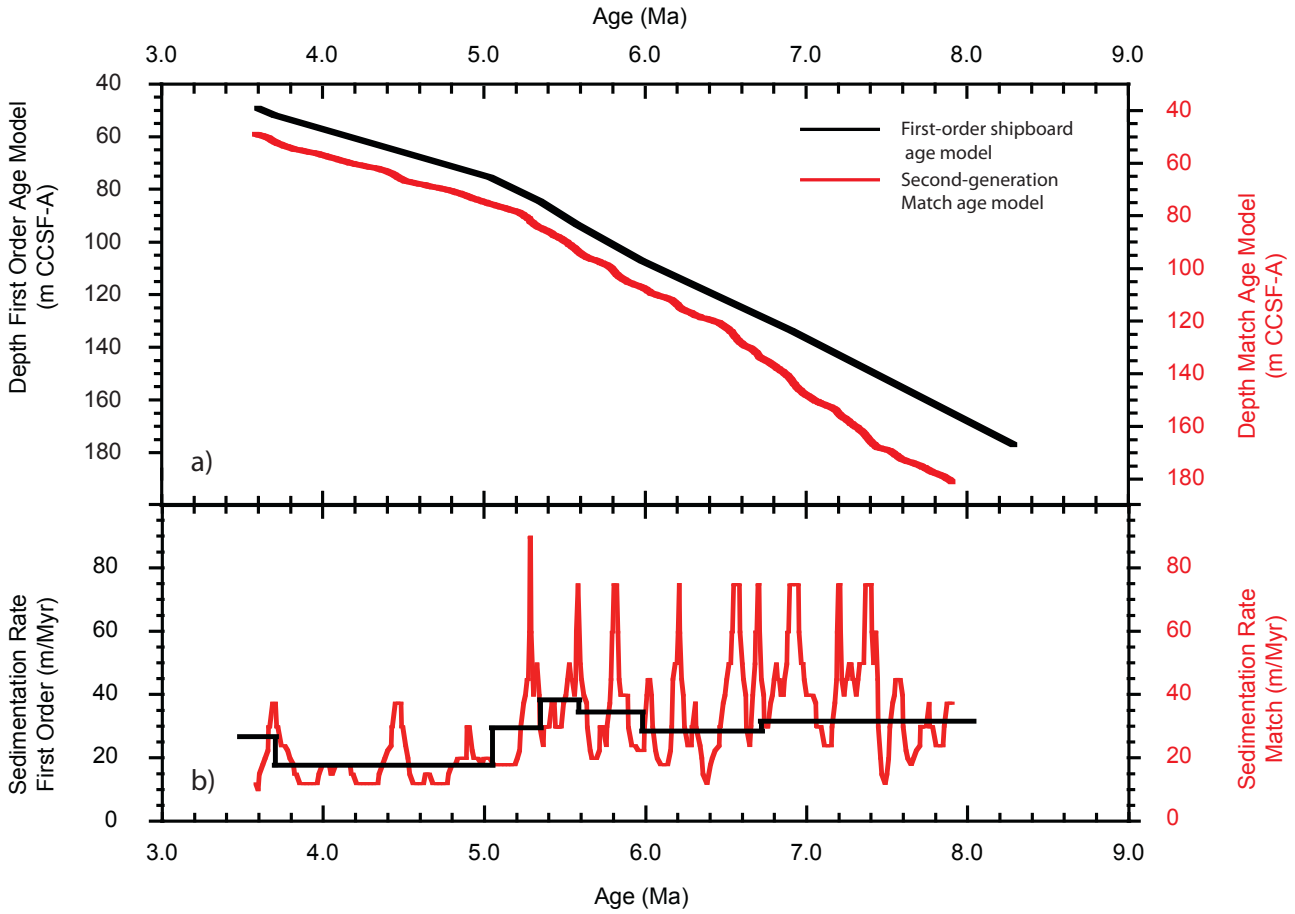

Figure 4.11.

a) Age-depth relationships for the first-order shipboard age model (black) and the second-generation Match age model (red).

b) Sedimentation rates reconstructed using the age depth relationships for both the first-order (black) and second-generation Match (red) age models.
Sedimentation rates were calculated by dividing the U1338 depth steps by the assigned 982 age steps to get to meters / millions of years.

Average Sedimentation Rates		
First-Order age model sedimentation rates		
(a)	***Age Interval***	***Average Sedimentation Rates***
	(Myr)	(m/Myr)
	3.5 - 5.1	18
	5.1 - 8.3	31
Second-generation Match age model sedimentation rates		
(b)	***Age Interval***	***Average Sedimentation Rates***
	(Myr)	(m/Myr)
	3.5 - 5.25	19
	5.25 - 6.25	36
	6.25 - 8.0	39

Table 4.4. Overview of average sedimentation rates calculated for both (a) the first-order age model based on shipboard age datums, and (b) the second-generation Match (G2) age model.

4.4.2.2. Sedimentation Rate B-Tukey Spectral Analysis

Figure 4.12 shows the B-Tukey spectrum (a) and the wavelet analysis (b) of the reconstructed sedimentation rates on the G2 age model. The B-Tukey spectra of the sedimentation rates show a strong power in the 380 and 180 kyr bands (Figure 4.12.a). The wavelet analysis of the G2 sedimentation rates (Figure 4.12.b) shows high power in the 1.0 Myr band throughout the record, and in the 580 kyr band between 7.0 and 5.75 Ma. There is significantly high power in the 400 kyr band from 7.5 to ~ 4.5 Ma. After 4.5 Ma, the power remains high, albeit not significant. The 200 – 250 kyr band also displays high power throughout much of the record, although it weakens between 7.0 and 6.0 Ma, and after 5.0 Ma. Interestingly, every 250 kyr, there is significant power band that covers all frequencies. For a more detailed discussion, see section 4.5.3.

4.4.3. U1338 Benthic Foraminiferal $\delta^{18}O_{CM}$ Time Series Analysis

Figure 4.13 compares the depth, first order shipboard and second generation Match age model B-Tukey spectra and wavelet analyses of the U1338 $\delta^{18}O_{CM}$ dataset.

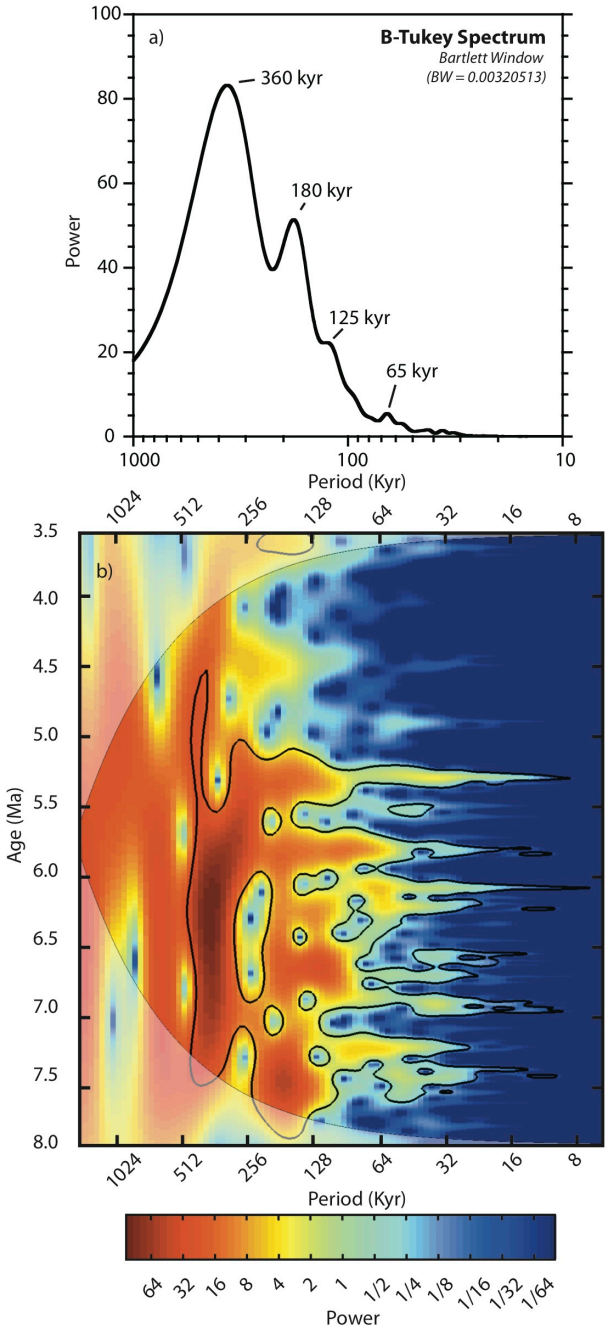

Figure 4.12.

Spectral analyses of reconstructed sedimentation rates at Site U1338 using the second generation Match (G2) age model. (a) B-Tukey and (b) wavelet analyses both highlight the strength of a 360 and 180 kyr cycle in the G2 sedimentation rates.

The B-Tukey spectrum was calculated using Analyseries (Paillaird et al., 1996 - version 2.0.4.2), using a Bartlett window (bandwidth = 0.00320513). The wavelet analysis was calculated in Matlab using the Torrence and Compo, 1998 protocol, republished by Grinsted et al., 2004. Regions outlined with a black line show 95% confidence limits on the original T&C wavelet package to highlight areas of significant power.

4.4.3.1. Depth Domain U1338 $\delta^{18}O_{CM}$ Spectral Analysis

The U1338 $\delta^{18}O_{CM}$ B-Tukey spectrum on the depth scale (Figure 4.13.a) shows high power around the 7.5 m band. There is a further set of high power peaks around the 1.5 – 2.0 m band. Below 1.5 meters the spectra is noisy, indicating that there are various sub-meter scale cycles present, which do not remain constant through time.

The U1338 $\delta^{18}O_{CM}$ depth wavelet (Figure 4.13.b) shows high power in the 30 m band. This is only significant (black outline shows 95 % confidence limit – see section 4.3.3) between about 95 and 80 m CCSF-A, but remains strong throughout the record. There is a high power present in the 10 m band between 170 and 130 m CCSF-A, as well as high power in the 6 – 8 m band from the base of the record until about 90 m CCSF-A. The most significant power is seen in the 1.5 – 2 m band between 160 and 180 m CCSF-A, and again between 110 and 80 m CCSF-A. There is significant power in the 0.5 to 1 m band throughout most of the record, with the exception of the spectra below 165 m CCSF-A, and between 130 and 150 m CCSF-A.

4.4.3.2. Shipboard Time Domain U1338 $\delta^{18}O_{CM}$ Spectral Analysis

The U1338 $\delta^{18}O_{CM}$ B-Tukey spectrum on the shipboard timescale (Figure 4.13.c) shows a high power around 250 kyr band. There is a further set of high power peaks around 55 – 65 kyr, as well as around 40 kyr. The final distinct peak occurs at 27 kyr. There are higher frequency peaks present, but these are quite noisy, although these could be related to precession.

The U1338 $\delta^{18}O_{CM}$ shipboard timescale wavelet (Figure 4.13.d) shows a strong, albeit not significant power in the 1.0 – 1.2 Myr band, possibly related to obliquity. There is a strong power around 450 kyr from about 5.0 Ma until the top of the record. Between the base of the record and ~ 6.8 Ma, there is a strong power in the 385 kyr band. There is also a fairly consistent high power throughout the record around 200 - 250 kyr bands. As in the depth wavelet, the most significant power is found in the higher frequency cycles. Between 8.5 and 7.8 Ma, there is a strong cyclicity in the 50 kyr band. This is absent between 7.8 and 5.8 Ma, but reappears after 5.8 Ma in the 40 – 60 kyr bands. Finally, there is a fairly consistent high power in the 16 kyr band throughout most of the record.

4.4.3.3. Match (G2) Time Domain U1338 $\delta^{18}O_{CM}$ Spectral Analysis

The U1338 $\delta^{18}O_{CM}$ B-Tukey spectrum on the G2 Match timescale (Figure 4.13.e) shows a high power around the 225 kyr period, followed by two smaller peaks around 120 and 70 – 80 kyr. The highest power can be found in a group of peaks at 50 and 40 kyr, followed by a smaller peak around 30 kyr. The noise in the higher frequency seems reduced, focussing the bands in peaks around 24 and 22 kyr.

The U1338 $\delta^{18}O_{CM}$ G2 timescale wavelet (Figure 4.13.f) shows a strong, albeit mostly not significant power in the 1.0 – 1.2 Myr band, possibly related to long-term obliquity. There is high power in the 200 kyr band, particularly at the base of the record up to 6.5 Ma, and between 6.0 and 5.0 Ma. There is evidence for power in the 125 kyr band between 7.8 and 7.0 Ma, as well as around 6.0 Ma and between 5.0 and 4.5 Ma. As with both previous U1338 $\delta^{18}O_{CM}$ wavelets, the

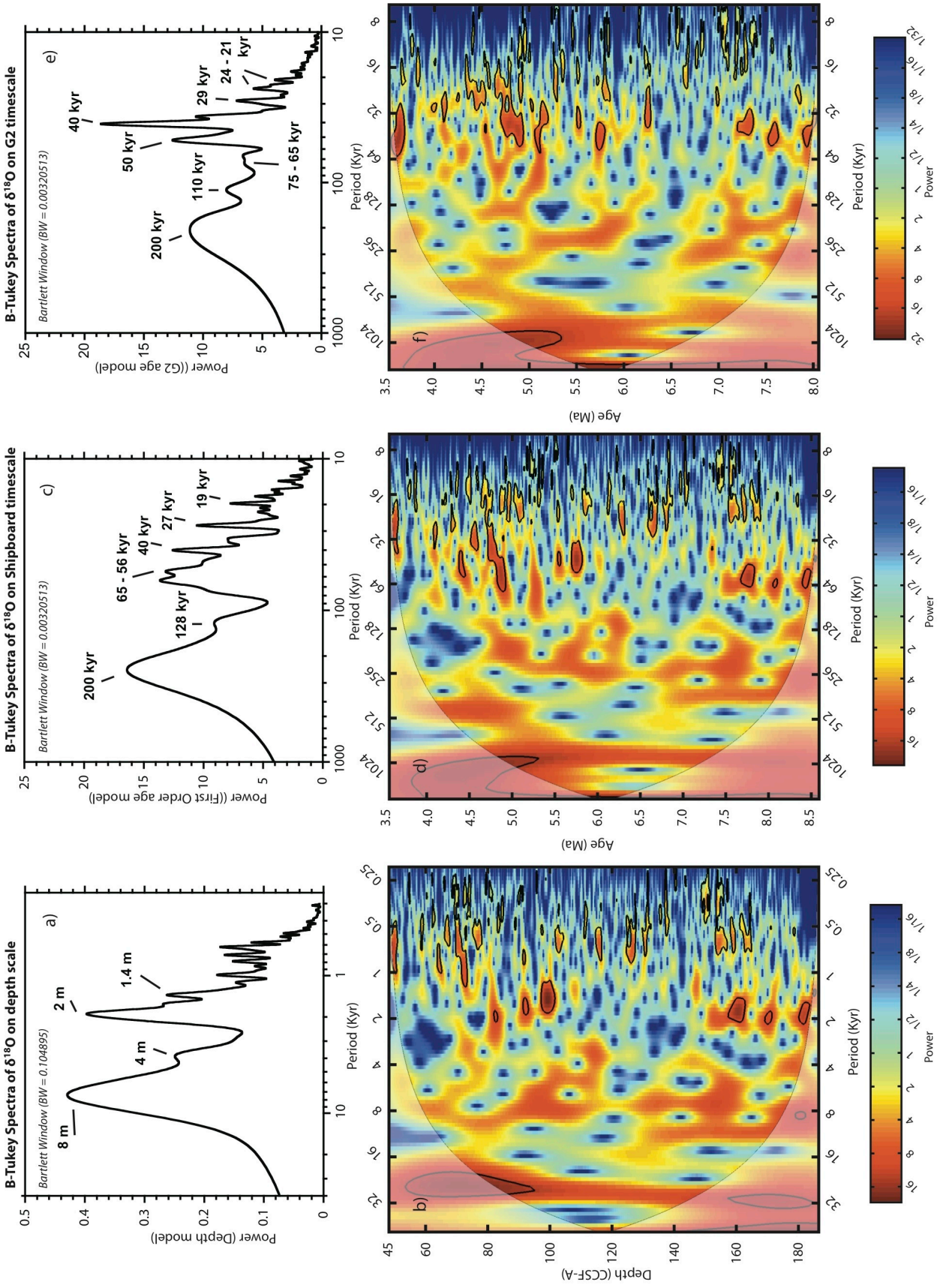
B-Tukey Spectra of δ18O on depth scale
Bartlett Window (BW = 0.104895)
a)
8 m
4 m
2 m
1.4 m
Power (Depth model)
Period (Kyr)
b)
Depth (CCSF-A)
Power
B-Tukey Spectra of δ18O on Shipboard timescale
Bartlett Window (BW = 0.00320513)
c)
200 kyr
128 kyr
65 - 56 kyr
40 kyr
27 kyr
19 kyr
Power ((First Order age model)
d)
Age (Ma)
B-Tukey Spectra of δ18O on G2 timescale
e)
200 kyr
110 kyr
50 kyr
40 kyr
29 kyr
24 - 21 kyr
75 - 65 kyr
Power ((G2 age model)
f)

Figure 4.13.

B-Tukey and wavelet analyses of the $\delta^{18}O_{CM}$ records from U1338:

a) and b) on the CCSF-A depth scale.

c) and d) using the first order age model created using shipboard palaeomagnetic and biostratigraphic datums.

e) and f) using the second generation Match age model created using shipboard palaeomagnetic and biostratigraphic datums.

All three B-Tukey/wavelet couples show the presence of strong short-term variation around the 1 – 2 m / 30 – 60 kyr bandwidth. There is also strong long-term variation in the 8 m / 200 kyr bandwidth.

The B-Tukey spectra were calculated using Analyseries (Paillaird et al., 1996 - version 2.0.4.2), using a Bartlett window (depth bandwidth = 0.104895; time bandwidth = 0.00320513). The wavelet analysis was calculated in Matlab using the Torrence and Compo, 1998 protocol, republished by Grinsted et al., 2004.

most significant power is found in the higher frequency bands. There is strong power throughout the record in the 30 – 60 kyr band, frequently centred around 40 kyr. The power drops in this band between 7.0 and 6.5 Ma. There is also some significant power in the 18 – 25 kyr band, particularly between 5.8 and 4.0 Ma.

4.4.4. U1338 Benthic Foraminiferal $\delta^{13}C_{CM}$ Time Series Analysis

Figure 4.14 compares the depth, first order and second generation Match age model B-Tukey spectra and wavelet analyses of the $\delta^{13}C_{CM}$ dataset.

4.4.4.1. Depth Domain U1338 $\delta^{13}C_{CM}$ Spectral Analysis

The U1338 $\delta^{13}C_{CM}$ B-Tukey spectrum on the depth scale (Figure 4.14.a) shows a high power around 12.5 and 7.5 m bands. There is further high power around 3.5 meters, as well as a set of high power peaks ~ the 1.2 – 2.1 m band.

The U1338 $\delta^{13}C_{CM}$ depth wavelet (Figure 4.14.b) shows that there is a high, but not significant power around the 30 m band. Between 160 and 70 m CCSF-A, a high power band slowly moves from 16 m to 8 m. The most significant power is found in the 1.5 to 1 m band between about 120 to 48 m CCSF-A. The 0.5 m band also shows significant power in this same interval. In general, the U1338 $\delta^{13}C_{CM}$ depth wavelet displays less significant power than the $\delta^{18}O_{CM}$ depth wavelet.

4.4.4.2. Shipboard Time Domain U1338 $\delta^{13}C_{CM}$ Spectral Analysis

The U1338 $\delta^{13}C_{CM}$ B-Tukey spectrum on the shipboard timescale (Figure 4.14.c) shows high power in the 380 kyr band, followed by a weak peak around 180 m. There is also clear power in the 100, 70 and 50 kyr bands, with some power in the 40 and 35 kyr bands.

The U1338 $\delta^{13}C_{CM}$ the shipboard timescale wavelet (Figure 4.14.d) shows a strong, albeit not significant power in the 1000 kyr band throughout the record. Between 7.8 and 4.8 Ma there is also high power in a shifting band from ~ 500 to 250 kyr. The most significant power is found in the 30 – 60 kyr band from ~ 6.5 to 3.5 Ma. There is also significant power in the 15 to 25 kyr band throughout the same interval.

4.4.4.3. Match (G2) Time Domain U1338 $\delta^{13}C_{CM}$ Spectral Analysis

The U1338 $\delta^{13}C_{CM}$ B-Tukey spectrum on the G2 Match timescale (Figure 4.14.e) shows a high power around the 360 kyr period. There is a weak peak around 125 kyr, followed by a more dominant peak at 80 kyr. Below 80 kyr there are few larger peaks. There is a small peak distinguishable around 40 kyr.

As with the depth and shipboard timescale wavelets, the U1338 $\delta^{13}C_{CM}$ G2 Match timescale wavelet (Figure 4.14.f) shows high, albeit not significant power around the 1000 kyr band throughout the whole record. There is also high power in the 380 kyr band from about 7.5 to 4.8 Ma. The most significant power can be found in the highest frequency bands. There is some significant power in the 30 – 60 kyr band around 6.0, 5.0 and 4.0 Ma. Significant power is also seen in the 16 – 25 kyr band, particularly between 6.5 and 5.0 Ma, and after 4.0 Ma.

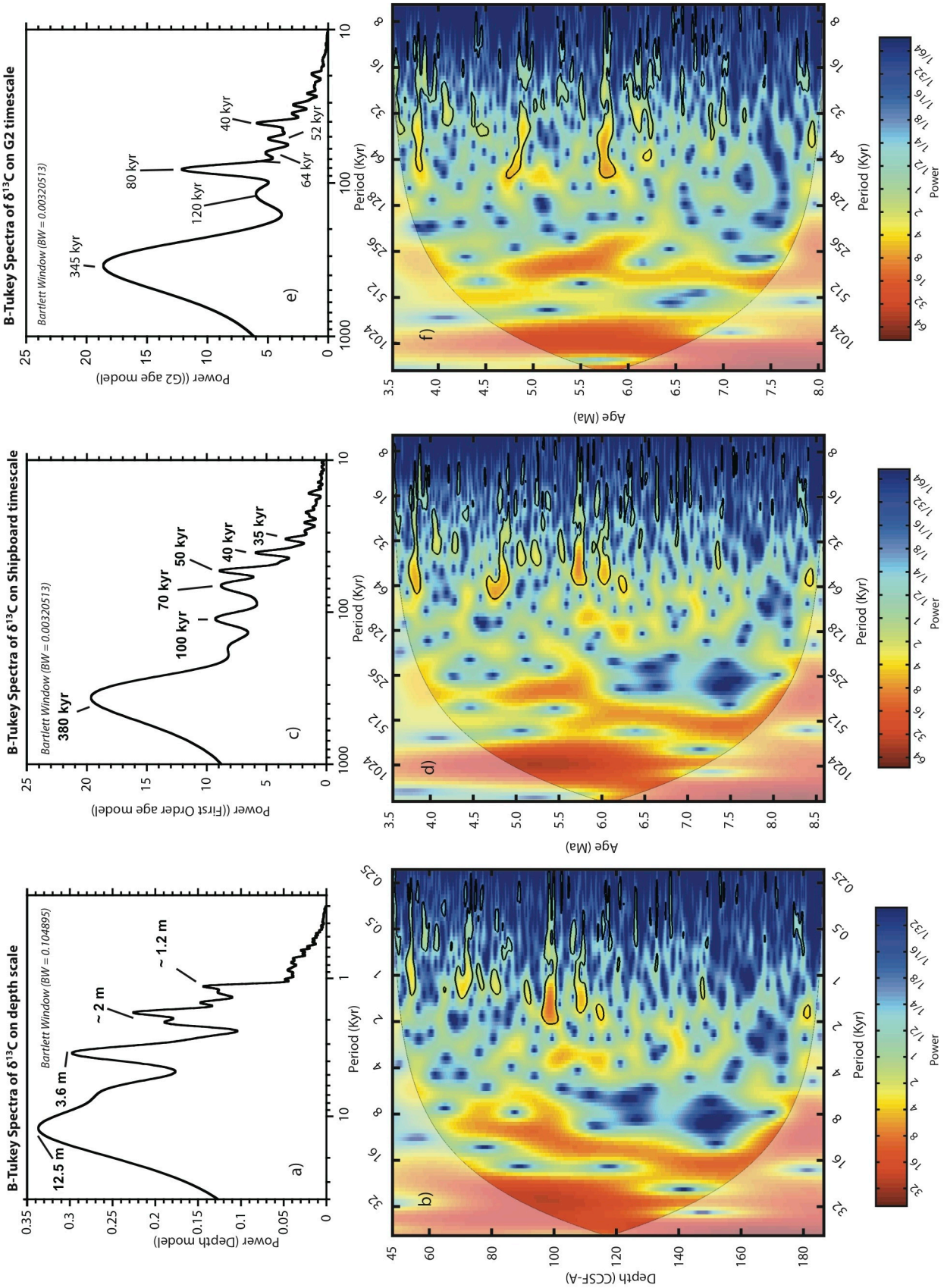
B-Tukey Spectra of δ13C on depth scale
Bartlett Window (BW = 0.104895)
12.5 m
3.6 m
~ 2 m
~ 1.2 m
Power (Depth model)
a)
B-Tukey Spectra of δ13C on Shipboard timescale
Bartlett Window (BW = 0.00320513)
380 kyr
100 kyr
70 kyr
50 kyr
40 kyr
35 kyr
Power ((First Order age model)
c)
B-Tukey Spectra of δ13C on G2 timescale
Bartlett Window (BW = 0.00320513)
345 kyr
120 kyr
80 kyr
64 kyr
40 kyr
52 kyr
Power ((G2 age model)
e)
Depth (CCSF-A)
b)
Age (Ma)
d)
Age (Ma)
f)
Period (Kyr)
Power

Figure 4.14.

B-Tukey and wavelet analyses of the $\delta^{13}C_{CM}$ records from U1338 on:

a) and b) the U1338 depth scale.

c) and d) the first order age model created using shipboard palaeomagnetic and biostratigraphic datums.

e) and f) the second generation Match age model created using shipboard palaeomagnetic and biostratigraphic datums.

All three B-Tukey/wavelet couples show the presence of strong short-term variation around the 1 – 2 m / 30 – 60 kyr bandwidth. There is also strong long-term variation in the 12.5 m / 400 kyr bandwidth.

The B-Tukey spectra were calculated using Analyseries (Paillaird et al., 1996 - version 2.0.4.2), using a Bartlett window (depth bandwidth = 0.104895; time bandwidth = 0.00320513). The wavelet analysis was calculated in Matlab using the Torrence and Compo, 1998 protocol, republished by Grinsted et al., 2004.

4.5. Discussion

4.5.1. Assessing the G2 Age Model

The second generation Match (G2) age model, which is high-resolution and astronomically based, was created using the best alignment between the benthic foraminiferal stable isotope records from Sites U1338 and 982 using Match (Lisiecki and Lisiecki, 2002). Records from IODP Site U1338 can now be compared to a wide range of sites in the North Atlantic, Southern Ocean and Pacific, to examine the relative contribution of regional versus global factors on the U1338 records (see Chapters 5 and 6).

When using the G2 age model, the alignment between the benthic foraminiferal isotope records from U1338 and 982 is generally very good. Many glacial and interglacial cycles are visible throughout both records, and the late Miocene Carbon Isotope Shift (LMCIS) has been correlated in the oldest section of the record (Figure 4.15). However, in certain sections of Site U1338 record, the high-resolution nature of the correlation-based age model should be treated cautiously. Although it has been placed on an astronomically based timescale, the 4.6 to 3.5 Ma section of Site 982 has not been orbitally tuned. Furthermore, due to the original sampling strategy, the temporal resolution of the 982 records is reduced to approximately a fifth of the rest of the record between 4.6 and 3.5 Ma. The benthic foraminiferal stable isotope records from Sites U1338 and 982 align fairly well during this period, although this could also be an artefact of the lower resolution of the target record. The interval between 7.0 and 6.5 Ma should also be treated with caution, as the variation and signal-to-noise ratio in the U1338

oxygen isotope record is smaller here than in other sections of the record, so it is more difficult to evaluate the alignment (Figure 4.10 and Appendix B.3).

Match has provided a realistic correlation between Sites U1338 and 982, however the programme is not ideal. The Match penalty functions constrain the realism of the generated alignment, but Match does not produce any measure of alignment error, unlike the Monte-Carlo method suggested by Malinverno, (2012). In the Monte-Carlo approach, 1000 alignments are made, and the final alignment is given as the mean of all the calculated alignments. Taking the standard deviation or the variability of all the alignments provides an error estimate for the correlation. Applying the Monte-Carlo approach to the correlation between Sites U1338 and 982 was beyond the scope of this project. However, future work may elucidate how well these two alignment methods compare to each other and to see whether they both produce similar results (Malinverno, 2012).

4.5.2. Age Model influence on Spectral Analyses

As the 982 timescale is predominantly orbitally tuned, this section discusses whether correlating the benthic foraminiferal stable isotopes from U1338 and 982 have artificially induced any cyclicity into the site U1338 records. This is tested by comparing the power distribution pattern of B-Tukey spectra and wavelet analysis of the U1338 stable isotopes on the original depth-scale, and on the shipboard and G2 timescales.

The patterns of the U1338 $\delta^{18}O_{CM}$ B-Tukey spectra on the depth, shipboard and G2 scales the patterns are remarkably similar (Figure 4.13.a, c and e). All

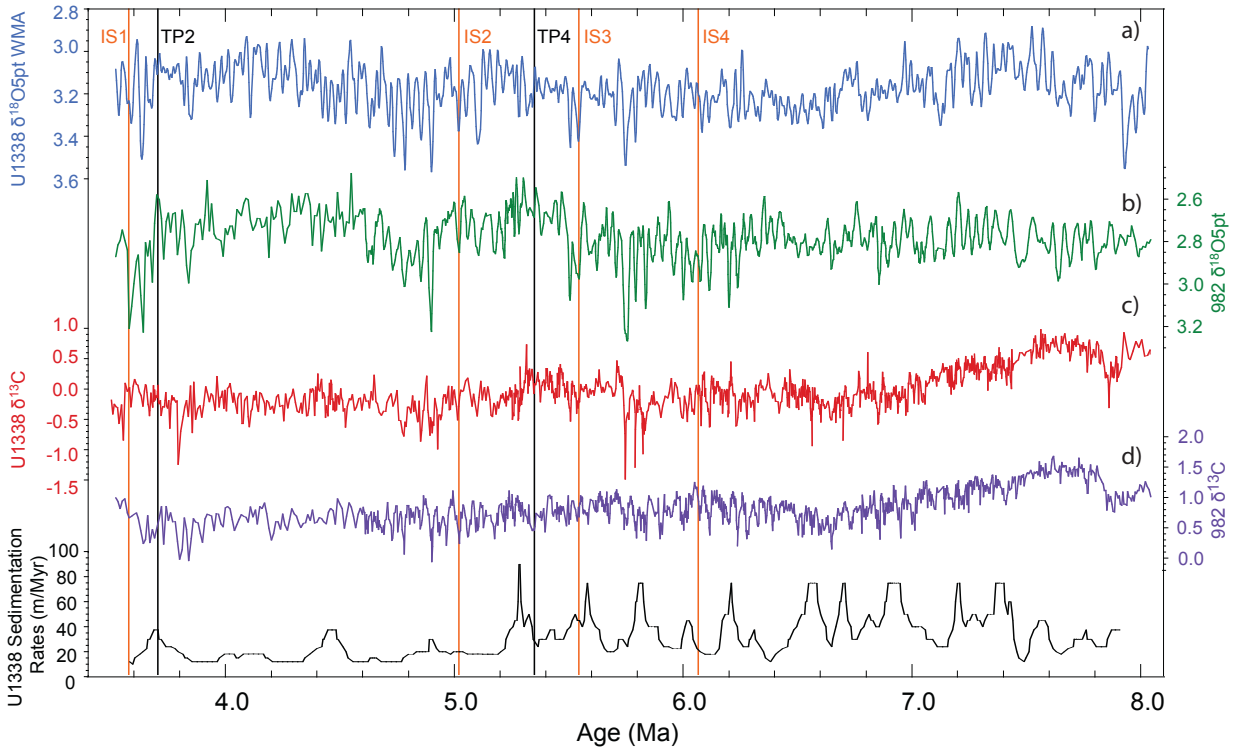

Figure 4.15.

Overview of the benthic foraminiferal U1338 and 982 stable isotope records and U1338 sedimentation rates on the second generation (G2) timescale. The orange and black markers indicate the locations of the tie points used in this alignment to guide the Match software (see Table 4.3 for tie point overview).

a) Shows the benthic $\delta^{18}O_{CM\_5pt\_WMA}$ from Site U1338 on the G2 timescale.

b) Shows the benthic $\delta^{18}O_{\_5pt}$ from Site 982 on the G2 timescale.

c) Shows the benthic $\delta^{13}C_{CM}$ from Site U1338 on the G2 timescale. The late Miocene Carbon Isotope Shift is clearly visible between 7.6 and 6.6 Ma.

d) Shows the benthic $\delta^{13}C$ from Site 982 on the G2 timescale. The late Miocene Carbon Isotope Shift is clearly visible between 7.6 and 6.6 Ma.

e) Shows the sedimentation rates reconstructed using the G2 age depth relationships.

three spectra show a clear long-term response around 7.5 m in the depth domain, corresponding to 250 and 225 kyr respectively in the shipboard and G2 age model spectra. Dominant peaks are found in the 1.5 – 2.0 m band in the depth spectra, which corresponds to a broad set of peaks between 65 – 40 kyr in the shipboard timescale spectra, and to a triple set of peaks around 50 – 40 kyr in the G2 timescale spectra. These peaks are probably the same and most likely reflect obliquity forcing (see section 4.2.1); however, the power has been focussed to a narrower bandwidth in the G2 spectra. Similarly, all three spectra show the presence of high frequency peaks in the sub-meter scale in the depth domain, or below 25 kyr in the time domain spectra, possibly relating to precession (see section 4.2.1). However, these peaks are far more focussed in the G2 spectra than they are in either the depth, or the shipboard timescale spectra.

When comparing the $\delta^{18}O_{CM}$ wavelet analyses on the depth, shipboard and G2 scales (Figure 4.13.b, d and f), it is apparent that there are clear distinguishable patterns shared by the three wavelets, irrespective of scale or domain. The U1338 $\delta^{18}O_{CM}$ depth wavelet shows a high power in the 30 m band, which corresponds to a high power in the 1000 – 1200 kyr band in both the shipboard and G2 time domain wavelets. All records also show high power in the deepest/oldest parts of the record, broadly spread in the 5 – 10 m or 150 – 250 kyr bands, although the power in the 200 kyr band is more concentrated in the G2 wavelet. In the higher frequencies, the time domain records show significant power in the 30 – 50 kyr band, corresponding to a similar power distribution in the 1 – 2 m cycles in the depth wavelet. The pattern in the high power intervals is comparable between the two time-domain wavelets with the strongest power in the 40 kyr band, which strongly suggests obliquity has a strong influence on the

$\delta^{18}O$ records. The power is again more focussed in the 40 kyr band in the G2 wavelet compared to the shipboard wavelet.

Comparing the U1338 $\delta^{13}C_{CM}$ B-Tukey spectra on the depth, shipboard and G2 scales (Figure 4.14.a, c and e), all three spectra show a clear long-term response at 12.5 m in the depth spectra, corresponding to 380 and 360 kyr in the shipboard and G2 spectra. Both the shipboard and G2 spectra show high power around 100 and 70 kyr (shipboard spectra) or 125 and 80 kyr (G2 spectra), which most likely corresponds to the 3.5 m peak seen in the depth spectra. The broad features of the U1338 $\delta^{13}C_{CM}$ wavelet analyses on the depth, shipboard and G2 scales remain similar (Figure 4.14.b, d and f). All three wavelets display very strong long-term (> 1000 kyr or > 30 m / cycle) trends. All three wavelets also display a fairly strong trend around 8 – 16 m in the depth wavelet, and between 250 and 500 kyr in both age wavelets. This trend seems more continuous and linear in response in the G2 wavelet concentrated in the 385 kyr band, whereas it drifts from the 500 kyr band around 7.5 Ma to the 250 kyr by 4.5 Ma in the shipboard wavelet, and between the 16 m and 8 m band in the depth wavelet. This implies that the shipboard and depth wavelets do not properly represent the trend through time. In the higher frequency bands, there is power around the 30 – 50 kyr band in both the shipboard and the G2 age wavelets, which corresponds to 1 to 2 m band in the depth wavelet. None of the U1338 $\delta^{13}C_{CM}$ wavelets have much significant power below about 120 m CCSF-A, or before 6.3 Ma.

The comparison above shows that the power distribution pattern remains similar between the depth, shipboard and G2 U1338 $\delta^{18}O_{CM}$ and $\delta^{13}C_{CM}$ wavelets. The similarity in power distribution between all records indicates that

correlating to an orbitally tuned target does not induce any artificial cyclicity into the G2 wavelet. The comparison provides good evidence that the primary signals seen in the G2 wavelet reflect a true response of the isotope records. In addition, the U1338 $\delta^{18}O_{CM}$ and $\delta^{13}C_{CM}$ G2 wavelets focus power into narrower bands than the shipboard wavelet. This implies that the G2 wavelets can be successfully applied to reconstructing background variability and climate response to changes in Earth's system sensitivity to external radiative forcing (see Chapter 6, section 6.4.1). A more detailed discussion of the orbital influence on the benthic foraminiferal $\delta^{18}O_{CM}$ and $\delta^{13}C_{CM}$ records can be found in section 6.4.1.1.

4.5.3. Sedimentation Rates

The reconstructed sedimentation rates at Site U1338 vary considerably (Figure 4.11 b). The range of sedimentation rates (12 – 89 m/Myr) is similar to the range of sedimentation rates reconstructed at Site 982 (10 – 150 m/Myr) (Hodell et al., 2001). The average sedimentation rates reconstructed for Site U1338 using the second-generation Match age model generally agree well with the preliminary shipboard estimates (Figure 4.11 b; Table 4.4). There are, however, two main differences between the model and the shipboard estimates. The first difference between the two is that the changeover from low to high sedimentation rates in the early Pliocene occurs ~ 150 kyr earlier in the second-generation Match age model compared to the first-order age model. Secondly, in the oldest part of the records, the G2 sedimentation rates are higher than the

shipboard rates. This higher sedimentation rate is largely due to the alignment of the LMCIS between 7.8 and 6.6 Ma in the correlation between Sites 982 and U1338. The LMCIS was considered as a valid correlation target, as it has been shown to be a globally synchronous event. However, it does not agree with the final shipboard nannofossil datum (B *Discoaster berggrenii* – *NN11*) (Table 2.1), which places the base of the record around 177 m CCSF-A as early as 8.3 Ma. If the sediments at 177 m were as old as 8.3 Ma, the placement of the LMCIS at Site U1338 would be completely offset with the LMCIS at Site 982, which is not in agreement with past literature stating that the LMCIS is a globally synchronous event. Therefore, the final shipboard nannofossil datum was not included in the G2 Match age model alignment.

4.5.4. Marine Isotope Stage (MIS) Identification

Many glacial and interglacial stages have been identified in late Miocene to early Pliocene benthic foraminiferal $\delta^{18}O$ records. These marine isotope stages (MIS) are named according to a scheme first suggested by Shackleton et al. (1995b). In this scheme, each MIS is identified using a combination of letters and numbers depending on which palaeomagnetic subchron the MIS occurs in. The letter(s), for instance N for Nunivak, indicate which subchron the isotopic event occurs in, and the numbers indicate whether the event is an interglacial (odd numbers increasing from 1) or a glacial (even numbers increasing from 2) stage. Lisiecki and Raymo (2005) expanded the Shackleton-scheme and defined 24 new isotopic stages between 5.0 and 3.4 Ma. To incorporate these new stages, the

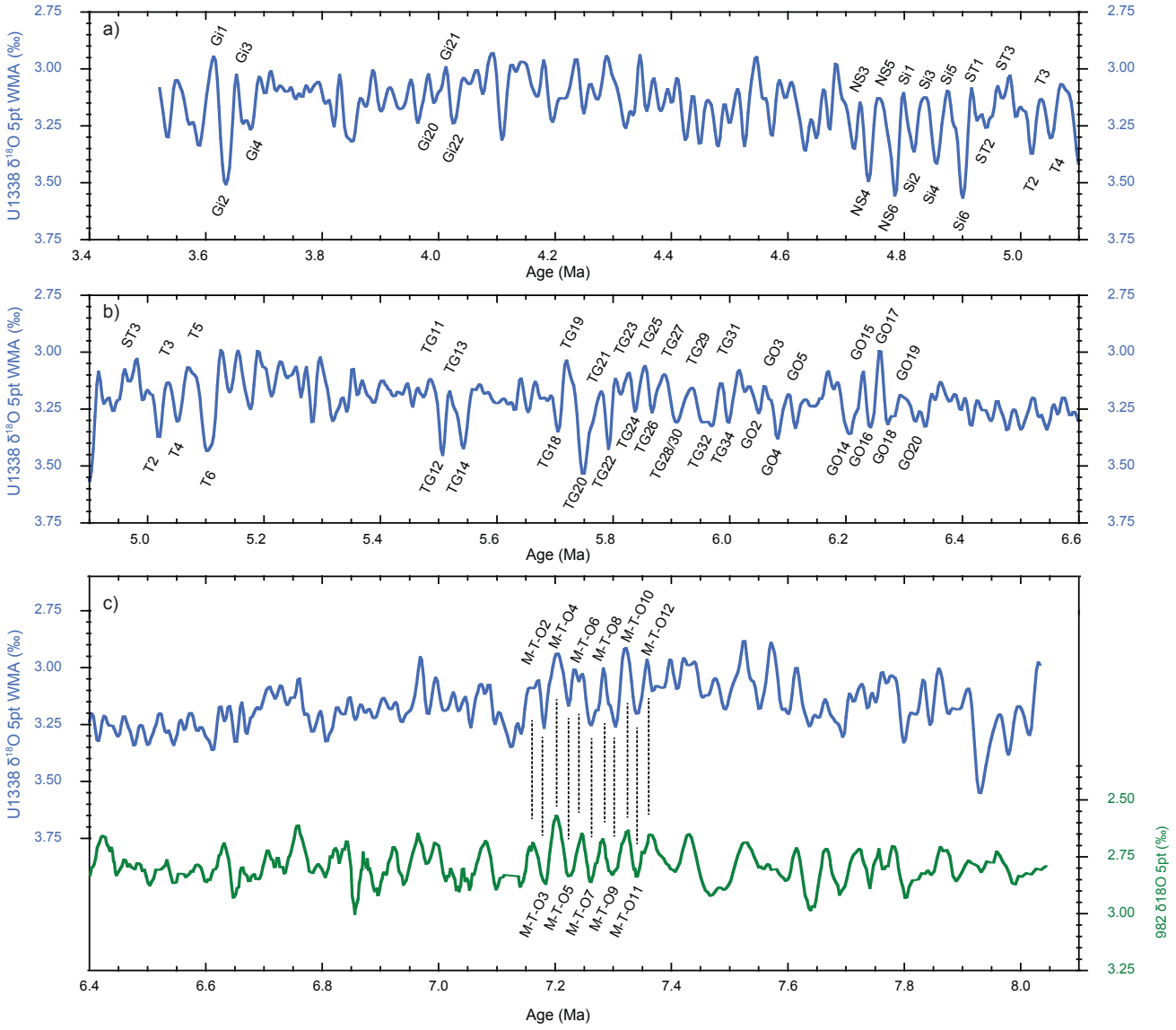

Figure 4.16.

Overview of the identification of marine $\delta^{18}O$ isotope stages (MIS):

a) and b) Age profile of the benthic $\delta^{18}O_{\_5pt\_WMA}$ from U1338 with 30 MIS from the Shackleton-scheme identified between 6.5 and 3.5 Ma (Shackleton et al., 1995b). MIS names come from Shackleton et al. (1995b), Lisiecki and Raymo (2005) and van der Laan et al. (2005). Stages identified by van der Laan et al. (2005) as C3An.18O have been given the prefix GO. The $\delta^{18}O$ 5pt WMA record is a five point weighted moving average of an equally resampled (every 3 kyr) version of the original $\delta^{18}O_{CM}$ record. For the original $\delta^{18}O_{CM}$ dataset, see Appendix A.1. For the resampled $\delta^{18}O_{CM}$ dataset and the resampling process, see Appendix B.4.

c) Age profile of the benthic foraminiferal $\delta^{18}O$ records from Sites U1338 982 with the identification of 11 new stages between 7.4 and 7.1 Ma. These MIS have been identified with the prefix M-T-O.

original stages identified by Shackleton et al. (1995b) were occasionally subdivided and/or renamed. Between 6.5 and 5.8 Ma, van der Laan et al. (2005) identified additional stages. Currently, the Shackleton scheme has not been extended beyond 6.5 Ma for the late Miocene, and no globally recognised stages have been classified between 6.5 Ma and the identification of the Mi-1 through 7 glacial stages between 24 and 9 Ma (Miller et al., 1991; Westerhold et al., 2005).

Based on the new high-resolution G2 timescale, many interglacial/glacial cycles can be identified in the Site U1338 benthic foraminiferal $\delta^{18}O_{CM\_5ptWMA}$ record (Figure 4.16.a). The LMCIS remains a key marker in the benthic foraminiferal $\delta^{13}C_{CM}$ record, with the broad maximum occurring between 7.8 and 7.5 Ma, followed by the negative shift between 7.5 and 6.6 Ma (Figure 4.16.c). The new high-resolution age model enables the identification of 30 MIS from the Shackleton-scheme in the benthic foraminiferal $\delta^{18}O_{CM\_5pt\_WMA}$ record between 6.5 and 3.5 Ma (Figure 4.16.a and b). For simplicity, stages originally identified by van der Laan et al. (2005) as C3An.18O have been given the prefix GO on Figure 4.16.b. The most important and prominent glacial stages identified before 6.5 Ma in the U1338 benthic foraminiferal $\delta^{18}O_{CM\_5pt\_WMA}$ record are NS4, NS6 and Si6 between 4.9 and 4.7 Ma, T6 around 5.1 Ma, TG12 and TG14 around 5.5 Ma, and TG18, TG20 and TG22 between 5.8 to 5.7 Ma.

In addition to the 30 Shackleton-scheme MIS, a total of 11 new marine isotope stages (6 interglacials; 5 glacials) are identified between 7.4 and 7.1 Ma in both the U1338 and 982 benthic foraminiferal $\delta^{18}O$ records (Figure 4.16 c). As this interval is characterised by the Tortonian – Messinian boundary (~ 7.249 Ma) and the MIS are identified in the benthic foraminiferal $\delta^{18}O$ records, the prefix M-T-O has been chosen to identify the MIS. Stages were only defined and

named if the isotopic stage was recognisable in both the U1338 and 982 records, and if the isotopic excursion had comparable amplitudes to neighbouring stages. Table 4.5 provides an overview of the ages of the newly defined stages. No stages were defined in the 7.0 – 6.5 Ma interval, as the amplitude of variations in the U1338 record in particular were too low to identify any clear stages. Even though there are clear excursions in both the U1338 and 982 records, no new stages were identified before 7.4 Ma, because the agreement between the individual excursions in the benthic foraminiferal U1338 and 982 $\delta^{18}O$ records was reduced in this interval.

In future, with the existence of more high-resolution stable isotope records such as those from Sites U1338, 982, 926 (equatorial Atlantic – Shackleton and Hall, 1997) and Sites 704, 1088 and 1090 in the South Atlantic (Hodell and Venz-Curtis, 2006), the newly defined CIS stages could be tied in successfully to the Shackleton-scheme. Future work could potentially advance the identification of global marine isotope stages between 6.9 and 6.5 Ma and beyond 7.4 Ma. An interesting approach would be to extend the MIS identification in a similar way as Lisiecki and Raymo (2005), where they classified global MIS when they appeared in ~ 80 % of the records included in their isotopic stack. Incorporating the new CIS stages identified here, and extending the Shackleton identification scheme to further back into the late Miocene, will better constrain the isotope stratigraphy in the late Miocene. This will facilitate any studies using isotopic correlation as a method for inter-site comparison or age model generation.

Marine Isotope Stage Identification - 7.1 to 7.4 Ma			
	Identifier	**Type**	**Age (Ma)**
	M-T-O2	*Interglacial*	7.163
	M-T-O3	*Glacial*	7.181
	M-T-O4	*Interglacial*	7.205
	M-T-O5	*Glacial*	7.223
	M-T-O6	*Interglacial*	7.241
	M-T-O7	*Glacial*	7.262
	M-T-O8	*Interglacial*	7.283
	M-T-O9	*Glacial*	7.304
	M-T-O10	*Interglacial*	7.322
	M-T-O11	*Glacial*	7.340
	M-T-O12	*Interglacial*	7.358
Age (Ma) is reported on timescale from Site 982 (Hodell et al., 2001), based on the La93 astronomical solution			

Table 4.5.

Overview of the 11 newly identified MIS in the U1338 and 982 benthic foraminiferal $\delta^{18}O$ records between 7.4 and 7.1 Ma. The prefix M-T-O is given to all stages, as the stages are identified in the $\delta^{18}O$ record during the interval is characterised by the Tortonian – Messinian boundary. The age is reported on the 982 age model (Hodell et al., 2001), which is based on the La93 astronomical solution (Laskar et al., 1993).

4.6. Conclusions

The stratigraphic correlation between the benthic foraminiferal isotope records from Sites U1338 in the equatorial Pacific and 982 in the North Atlantic provides Site U1338 with a high-resolution, orbitally based age model. The alignment between the records is generally good, although it is difficult to evaluate from 4.6 – 3.5 Ma and 7.0 – 6.5 Ma. The age model should be treated cautiously in these sections. The similarity between the reconstructed shipboard and G2 Match sedimentation rates and age-depth relationships offers further support that the G2 age model is realistic.

The pattern of spectral power in the B-Tukey and wavelet analyses is similar between the analyses of the G2 U1338 $\delta^{18}O_{CM}$ and $\delta^{13}C_{CM}$ records on the depth, shipboard and G2 scales. This indicates that correlating the U1338 stable isotope records to an orbitally tuned target did not induce any artificial cyclicity into the records.

Clear cycles between 6.4 – 3.5 Ma enabled identification of 30 marine isotope stages from the Shackleton-scheme in the $\delta^{18}O$ 5pt-WMA record. The most important and prominent of these cycles were NS4, NS6 and Si6 (4.7 – 4.9 Ma), T6 (~ 5.1 Ma), TG12 and TG14 (~ 5.5 Ma) and TG18, TG20 and TG22 (between 5.7 – 5.8 Ma). In addition 11 preliminary new MIS were identified between 7.4 and 7.1 Ma in both the U1338 and 982 benthic foraminiferal $\delta^{18}O$ records. These MIS have been identified with the prefix M-T-O.

Chapter 5.

Evolution of Equatorial Pacific Sea Surface Conditions: Potential for a New Multi-proxy Approach

5.1. Introduction and Aims

The establishment of modern circulation patterns and sea surface temperature (SST) distribution in the equatorial Pacific (see section 2.2.1) is thought to have occurred sometime during the late Miocene to early Pliocene (Pisias et al., 1995; Rousselle et al., 2013) and is frequently linked to the progressive isolation of the Pacific and Atlantic surface oceans through the closure of the Central American Seaway (CAS) (Haug et al., 2001). However, the exact evolution of the modern SST and sea surface currents in this region is not

yet fully understood. An important component of the modern Pacific sea surface system is the El-Niño-Southern-Oscillation (ENSO). ENSO describes the atmosphere-ocean system that drives a sea surface temperature phenomenon in the Pacific Ocean, which displays interannual variation between two main phases: El Niño (the warm phase) and La Niña (the cold phase) (Trenberth, 1997). A complete El Niño – La Niña cycle occurs approximately every 3 – 7 years (Goddard et al., 2001). Modern day 'normal' sea surface conditions show east-west gradients in both sea surface temperatures (SST) and thermocline depth: the east Pacific generally has cooler temperatures and a shallower thermocline, whereas the west Pacific is generally warmer, with a deeper thermocline (Figure 5.1 a; see also section 2.2.1). During an El Niño state, the equatorial Pacific experiences reduced SST and thermocline gradients and displays uniform, warm temperatures and a deep thermocline across the basin (Figure 5.1 b) (Alexander et al., 2002). During a La Niña, the equatorial Pacific develops into a more exaggerated version of the normal sea surface distribution: SST and thermocline gradients are exaggerated, with further thermocline shoaling and SSTs cooling in the eastern equatorial Pacific (Figure 5.1 c) (Alexander et al., 2002). Although ENSO is a Pacific Ocean phenomenon, the ENSO state is thought to affect global atmospheric, terrestrial and marine systems (see Goddard et al., 2001 and Alexander et al., 2002 and the references therein).

a)

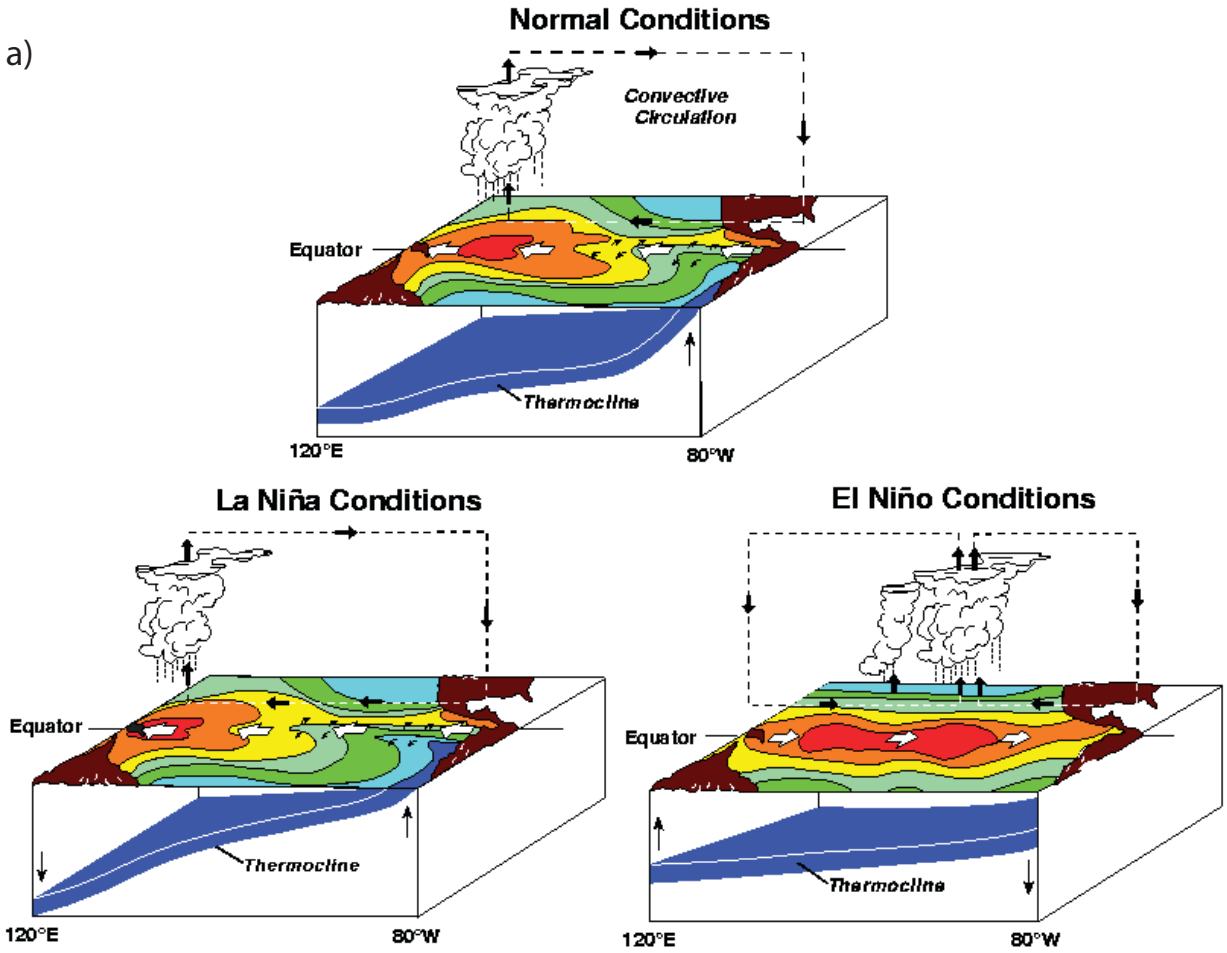
Normal Conditions
Convective Circulation
Equator
Thermocline
120°E
80°W
La Niña Conditions
Equator
Thermocline
120°E
80°W
El Niño Conditions
Equator
Thermocline
120°E
80°W

b)

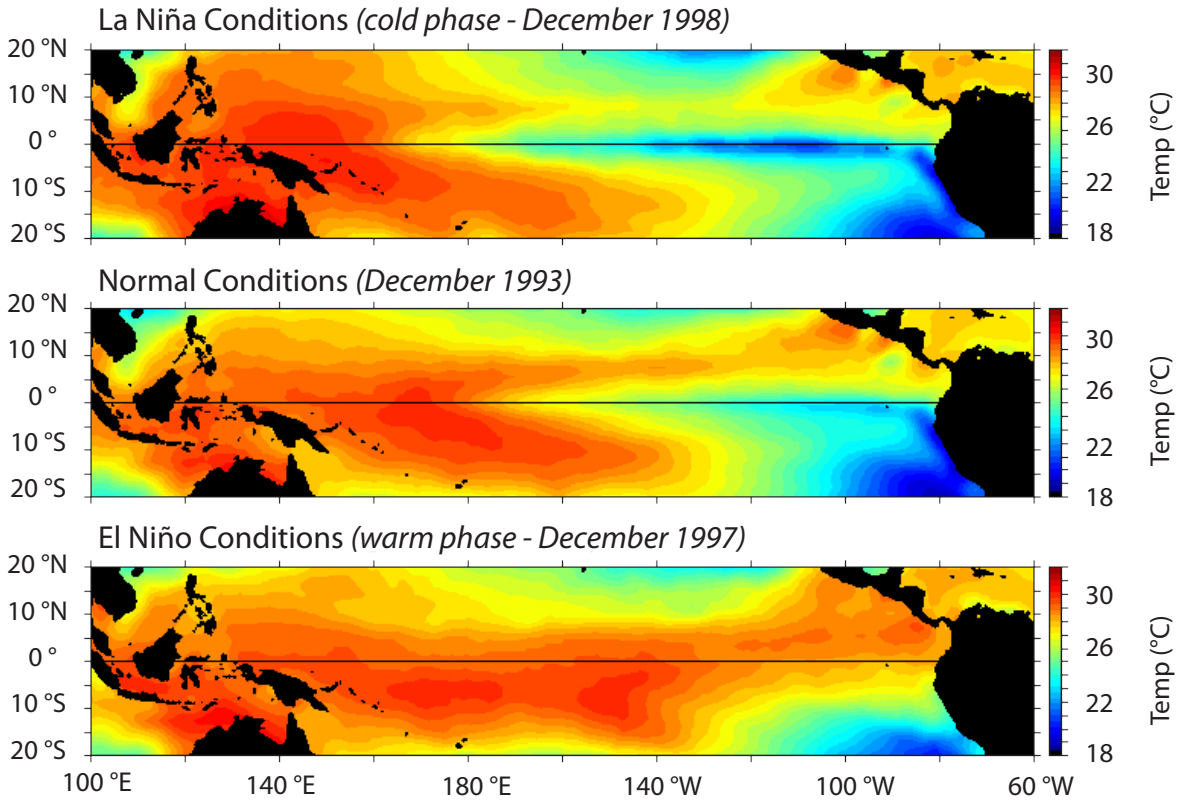
La Niña Conditions (cold phase - December 1998)
Normal Conditions (December 1993)
El Niño Conditions (warm phase - December 1997)
20 °N
10 °N
0 °
10 °S
20 °S
100 °E
140 °E
180 °E
140 °W
100 °W
60 °W
30
26
22
18
Temp (°C)

Figure 5.1. Overview of the El-Niño-Southern-Oscillation (ENSO) phases:

a) Cartoon representation of sea surface temperatures (SST) and thermocline depth across the equatorial Pacific during normal, El Niño and La Niña phases (taken from National Oceanic and Atmospheric Administration El Niño theme page).

b) Reynolds Sea Surface Temperature Analysis from the National Centre for Environmental Prediction showing the differences in SST between La Niña, normal and El Niño phases in more detail (Reynolds et al., 2007; graphics adapted from an image supplied on the National Oceanic and Atmospheric Administration El Niño theme page).

Past studies have suggested that during the late Miocene to early Pliocene, the equatorial Pacific climate was in a permanent El-Niño-like state, with a deep thermocline across the equatorial region (LaRiviere et al., 2012). The thermocline in the eastern equatorial Pacific gradually shoaled, whilst the thermocline in the western equatorial Pacific gradually deepened, thereby slowly increasing the east-west thermocline depth gradient towards a La Niña-like state (LaRiviere et al., 2012). The modern El-Niño-Southern-Oscillation is thought to have developed by the late Pliocene (LaRiviere et al., 2012). The shoaling of the thermocline in the eastern equatorial Pacific has been linked to thermocline shoaling driven by the closure of the CAS (Zhang et al., 2012; LaRiviere et al., 2012). However, the Biogenic Bloom, which occurred between ~ 8 to 4.5 Ma in all oceanic basins (Diester-Haass et al., 2002; Grant and Dickens, 2002) (see section 2.1.2) has been associated with nutrient delivery to the surface ocean through increased upwelling of cool nutrient-rich waters and shoaling of the thermocline in the Tasman Sea (Grant and Dickens, 2002). Studies have found both evidence for thermocline shoaling and cooling for brief intervals during the late Miocene, associated with the establishment of the Equatorial Undercurrent (EUC) and the Peru and Chile Currents (PCC) during a La Niña-like climate state (Nathan and Leckie, 2009; Rousselle et al., 2013). The increased upwelling suggested as a mechanism for the Biogenic Bloom (Grant and Dickens, 2002) is difficult to reconcile with the permanent El Niño-state suggested to be dominant throughout the late Miocene and early Pliocene (LaRiviere et al., 2012).

The main aim of this chapter is to investigate the state and evolution of surface-water conditions in the equatorial Pacific between 8.0 and 4.4 Ma, and the implications these conditions might have for the ENSO state and the Biogenic Bloom during the late Miocene to early Pliocene. To achieve this main aim, three objectives are chosen. Firstly, the development of sea surface temperature evolution at Site U1338 in the eastern equatorial Pacific is established by combining multiple SST proxies, including planktic foraminiferal $\delta^{18}O$ and Mg/Ca ratios and published $U^{k'}_{37}$ records. In addition to the conventional SST proxies, a novel approach, which applies 'clumped isotope' geochemistry to coccolith-rich sediments as a potential approach to SST reconstruction, is explored (section 5.2.2, 5.3.3 and 5.5.1). The second objective is to assess the state of productivity and upwelling at Site U1338 by combining spectral analysis on sedimentation rates, $CaCO_3$ and SiO_2 records, with bulk sediment, planktic and benthic foraminiferal $\delta^{13}C$ records. The third objective is to reconstruct equatorial east-west planktic foraminiferal $\delta^{18}O$ and SST gradients and the state of the ENSO during the late Miocene and early Pliocene by combining multi-proxy records from Site U1338 compiled for objective 1 and 2 with published planktic foraminiferal $\delta^{18}O$ and $U^{k'}_{37}$ records from the western and far-eastern equatorial Pacific. Combining the outcomes of objectives 2 and 3 will help identify any interplay between equatorial Pacific Ocean circulation, the ENSO state and the origins of the Biogenic Bloom: any interplay might be useful in reconciling the current contradiction of a permanent late Miocene El Niño-state with the presence of potentially upwelling-driven productivity.

5.2. Background and Previous Work

5.2.1. Established Sea Surface Temperature (SSTs) Proxies: Planktic Foraminiferal $\delta^{18}O$ and Mg/Ca

As discussed in more detail in section 3.3.1.1, $\delta^{18}O$ in planktic foraminifera is partially controlled by calcification temperature. However, using planktic foraminiferal $\delta^{18}O$ as a sea surface temperature proxy is complicated by the fact that planktic foraminiferal $\delta^{18}O$ is also controlled by the original $\delta^{18}O$ composition of seawater ($\delta^{18}O_{sw}$) (Epstein et al., 1953). However, assuming constant $\delta^{18}O_{sw}$, planktic foraminiferal $\delta^{18}O$ will decrease by ~ 0.23 ‰ with a temperature increase of 1 °C, which means a 1 ‰ change approximately equates to a 4 °C temperature change (Epstein et al., 1953).

An alternative, frequently applied geochemical proxy for sea surface temperatures (SST) is the Mg/Ca ratio of planktic foraminiferal calcite (for instance Ravelo et al., 2005; Wara et al., 2005; Groeneveld et al., 2008). Mg is incorporated into biogenic calcite during $CaCO_3$ precipitation (Nurnberg, 1995). Mg^{2+} is generally substituted directly with Ca^{2+} into the $CaCO_3$ lattice, but can also be taken up at defect/interstitial sites (Nurnberg, 1995). The partitioning coefficient for Mg in biogenic calcite is mainly controlled by temperature (Rosenthal et al., 1997). The original Mg/Ca composition of seawater, which is known to change through time, affects both benthic and planktic foraminiferal Mg/Ca (Broecker and Peng, 1982). The residence times for Mg (~ 10 Myr) and Ca (~ 1 Myr) in the ocean mean that seawater Mg/Ca can be seen as constant

when looking at changes on timescales < 10^6 years (Broecker and Peng, 1982). By assuming that the seawater Mg/Ca ratio has remained constant, for records that are less than 1 Myr long planktic foraminiferal Mg/Ca ratios can be used to reconstruct relative changes in calcification temperatures (Lear et al., 2003). However, long-term (> 1 Myr) variations in foraminiferal Mg/Ca may reflect a combination of changes in seawater Mg/Ca and water temperature (Billups and Schrag, 2002; Medina-Elizalde et al., 2008). Modelling studies have attempted to predict past seawater Mg/Ca composition (Berner, 2004; Fantle and DePaolo, 2006), and found a general agreement between the model output and Mg/Ca values of fluid inclusions: however, there is still considerable uncertainty associated with these reconstructions, as fluid inclusion data is sparse.

Planktic foraminiferal Mg/Ca ratios strongly reflect the temperature of the water in which the foraminifera calcify (Nurnberg et al., 1996). There are many calibrations between temperature and planktic foraminiferal Mg/Ca (Nurnberg et al., 1996; Hastings et al., 1998; Elderfield and Ganssen, 2000), which follow a general exponential formula: $Mg/Ca = B \times e^{(0.9 \pm 0.2 \times T)}$, where B is a species-specific factor (Katz et al., 2010). In surface waters, depth-habitat and water-temperature are closely related; therefore, Mg/Ca uptake decreases with increasing depth and decreasing temperature (Elderfield et al., 2002). This complicates studies of planktic foraminiferal Mg/Ca if the depth habitat of the investigated species is not well constrained, or if it is unknown how different species migrate through the water column during their life cycle (Spero, 1998; Elderfield et al., 2002). Without careful selection, there is a risk that the Mg/Ca ratio measured reflects a combination of the temperature at a range of different depths (Rosenthal et al., 1997; Katz et al., 2010). Research has also shown that

for some planktic species, the larger planktic foraminifera also have higher Mg/Ca ratios than smaller specimens (Elderfield et al., 2002). The increasing Mg/Ca with increasing size has been attributed to smaller individuals calcifying faster than larger individuals, thereby having less time to incorporate Mg^{2+} (Elderfield et al., 2002). Within shells, Mg/Ca content can also vary considerably (Nurnberg, 1995). Changes in seawater salinity and acidity (pH) can also affect planktic foraminiferal Mg/Ca uptake (Lea et al., 1999). Changes in seawater pH cause a 7±5% increase in Mg/Ca per 0.1 pH unit (~0.8±0.5 °C), and changes in seawater salinity cause a 5±3% increase in Mg/Ca per psu (~0.5±0.3 °C) (Lea et al., 1999). Similar to planktic foraminiferal $\delta^{18}O$ and $\delta^{13}C$, post-depositional diagenesis should also be taken into consideration when applying planktic foraminiferal Mg/Ca ratios as a SST proxy (Hastings et al., 1998). However, Sexton et al. (2006) showed that diagenesis does not affect planktic foraminiferal Mg/Ca as much as it affects planktic foraminiferal $\delta^{18}O$.

5.2.2. Novel approach to SST reconstruction: Clumped Isotope Thermometry on Coccolith-rich sediments

'Clumped isotope' geochemistry is a recent development in the field of stable isotope geochemistry that is based on the abundance of bonds between rare, heavy isotopes within a molecule (Eiler and Schauble, 2004). Due to a lower vibrational energy between two rare, heavy isotopes (for CO_2: ^{13}C; ^{17}O and ^{18}O),

these heavy-heavy bonds will preferentially form at lower temperatures, as this is a more thermodynamically favoured option (Schauble et al., 2006). At higher temperatures, the distribution of bonds that form from all available isotopes approaches a completely random (stochastic) distribution (for CO_2: ^{12}C and ^{13}C; ^{16}O, ^{17}O and ^{18}O) (Schauble et al., 2006). This 'clumped isotope' principle has been applied as a palaeothermometer in carbonates, where the abundance of bonds between rare carbon and oxygen isotopes (for instance ^{13}C – ^{18}O bonds) within the crystal lattice of a carbonate mineral shows an inverse relationship with temperature (Ghosh et al., 2006; Schauble et al., 2006; Eiler, 2007). After acid digestion, the CO_2 released from carbonates has 12 different isotopologues (molecules that differ solely in their isotopic composition, e.g. isotopologues of hydrogen are H^2, HD and D^2), of which eight isotopologues contain two or three heavy isotopes. These eight isotopologues, which are otherwise referred to as multiply substituted isotopologues, will be preferentially formed at lower temperatures, as heavy-heavy isotope bonds have a greater thermodynamic stability than light-heavy isotope bonds. The most abundant multiply substituted isotopologue of CO_2 is ^{13}C-^{18}O-^{16}O, which has a mass of 47 (Ghosh et al., 2006). There are other CO_2 isotopologues with a mass of 47; however, ~ 97 % of the total mass 47 is constituted by the ^{13}C-^{18}O-^{16}O isotopologue.

The 'clumped isotope' thermometer is defined by the Δ_{47} parameter, which quantifies the amount of multiply substituted mass 47 isotopologues compared to a stochastic distribution (Eiler and Schauble, 2004; Huntington et al., 2009):

$$\Delta_{47} = \left[\left(\frac{R^{47}_{sample}}{R^{47*}_{stochastic}} - 1\right) - \left(\frac{R^{46}_{sample}}{R^{46*}_{stochastic}} - 1\right) - \left(\frac{R^{45}_{sample}}{R^{45*}_{stochastic}} - 1\right)\right] \cdot 1000$$

where sample R^{47}, R^{46} and R^{45} are respectively the sample ratios of mass 47, 46 and 45 signal voltage over mass 44 signal voltage (e.g. R^{47} = mass 47 signal voltage / mass 44 signal voltage) and stochastic R^{47*}, R^{46*} and R^{45*} are respectively the ratios of mass 47, 46 and 45 over mass 44 for a gas with the same bulk composition but a stochastic distribution of heavy isotope bonds. The stochastic distribution is calculated for each bulk composition using the abundance ratios $^{13}C/^{12}C$, $^{17}O/^{16}O$ and $^{18}O/^{16}O$, which are derived from the measured $\delta^{13}C_{VPDB}$ and $\delta^{18}O_{VPDB}$ from each sample (Eiler, 2007).

The main benefit of 'clumped isotope' Δ_{47} thermometry is that Δ_{47} is independent of the original bulk isotopic ($\delta^{18}O$ and $\delta^{13}C$) composition of the material being measured (Schauble et al., 2006; Eiler, 2007). This independence arises because the carbonate Δ_{47} thermometer is based on a homogeneous equilibrium reaction, which has a temperature-dependent equilibrium constant:

$$M^{12}C^{18}O^{16}O_2 + M^{13}C^{16}O_3 = M^{13}O^{18}O^{16}O_2 + M^{12}C^{16}O_3$$

M denotes the cation position in the carbonate crystal lattice. With low temperatures, the reaction is driven to the right, as this is more thermodynamically stable. With higher temperatures, it goes towards a more stochastic distribution (Eiler, 2007). The independence of Δ_{47} from original fluid composition circumvents the major issues with conventional stable isotope thermometers, such as foraminiferal calcite $\delta^{18}O$. Foraminiferal $\delta^{18}O$ is affected by changes in temperature, changes in the original fluid $\delta^{18}O$ composition from which the test precipitated and species-specific vital effects (see sections 3.2.1 and 5.2.2). Ghosh et al. (2006) provided the first inorganic calcite calibration for Δ_{47} at temperatures between 1 and 50 °C. This calibration has since been extended to temperatures relevant for diagenetic carbonate studies (Passey and

Henkes, 2012). Many studies on individual biogenic carbonates have shown that most biogenic Δ_{47}-temperature relationships fall within the 95 % confidence limits of the inorganic calcite calibration (inorganic calcite – Ghosh et al., 2006; coccolithophores and foraminifera – Tripati et al., 2010; foraminifera - Grauel et al., 2013; corals – Thiagarajan et al., 2011; mollusks and brachiopods – Henkes et al., 2013; overview – Eiler, 2011). Some studies suggest that certain biogenic calcites may show offsets from the inorganic Δ_{47}-temperature relationships (Henkes et al., 2013). However, in general, Δ_{47} does not seem to be affected by vital effects that can greatly alter the bulk $\delta^{18}O$ and $\delta^{13}C$ composition of a species shell.

Tripati et al. (2010) showed that the relationship between cultured coccoliths and bulk coccolith-rich sediments show a similar Δ_{47}-temperature relationship as inorganic calcite, so that Δ_{47} on coccoliths may be an interesting surface environment proxy in the future. A preliminary study was carried out to assess the feasibility of using Δ_{47} as a temperature proxy (John et al., 2012). In this study, four bulk (< 63 μm) fine fraction sediment samples from the late Miocene at Site U1338 were measured for clumped isotope Δ_{47} to see whether the Δ_{47} temperatures were applicable as a sea surface temperature proxy (John et al., 2012). The average Δ_{47} values for the four < 63 μm samples ranged between 0.712 and 0.729 ‰, which, using the Passey and Henkes (2012) calibration, equate to temperatures between 13.6 and 9.5 °C. As modern SSTs in this region are above 25 °C, the reconstructed Δ_{47} temperatures are very cold. This was interpreted as probably being due to the presence of thermocline and benthic foraminiferal calcite fragments or juveniles with calcite precipitated at lower temperatures mixing with the warm coccolith calcite, thereby giving an

average lower Δ_{47} temperature (John et al., 2012; Drury et al., 2012). With the study presented in this chapter, separation of smaller size fractions from the original < 63 μm sediment was made to isolate a size fraction containing predominantly coccolithophore calcite on which to measure the Δ_{47}. If the low temperatures seen in the John et al. (2012) and Drury et al. (2012) studies were due to mixing of multiple calcite components, isolating a small size fraction is more likely to exclude foraminiferal fragments and juveniles.

5.2.3. Coccolithophores and Coccolith Preservation

Coccolithophores are small (2 – 20 μm) unicellular marine phytoplankton, which generally live in the mixed layer/photic zone (Young et al., 2005; Schmidt et al., 2006). These marine phytoplankton have calcitic exoskeletons (coccospheres) that are made up of many small platelets (coccoliths) with a typical size of 1 – 15 μm (Schmidt et al., 2006; James and Austin, 2008). Coccolith calcite is generally less receptive to dissolution than planktic foraminiferal calcite (Schmidt et al., 2006), which has made coccoliths popular geochemical archives and biostratigraphical proxies, especially in locations and intervals where the CCD is too shallow to preserve planktic foraminifera (e.g. Bown and Dunkley Jones, 2012; Prentice et al., in prep). The preferential preservation of coccoliths compared to planktic foraminifera is predominantly due to a difference in calcite crystal size, with smaller crystals being more susceptible to dissolution than larger crystals (Adelseck et al., 2013; Hover et al., 2001). As discussed in section 3.2.1.3, foraminiferal tests are made up of calcitic

microgranules ~ 0.1 μm in diameter (Pearson and Burgess, 2008), which makes the calcite susceptible to dissolution and recrystallisation because of the small crystal size (Sexton et al., 2006; Schmidt et al., 2006). Coccolithophores precipitate the coccoliths from an internal vesicle, and form two main types of coccolith: holococcoliths and heterococcoliths (Young et al., 2005). Holococcoliths are made up of 0.1 μm euhedral calcite crystals (Schmidt et al., 2006). Holococcoliths are therefore very susceptible to dissolution and are rarely well preserved in deep-sea sediments (Bown et al., 2008). Heterococcoliths are made up of larger, more complexly shaped, single crystals of calcite (Schmidt et al., 2006), which makes them far less susceptible to dissolution (Bown et al., 2008).

Although it is well established that coccoliths preserve better than planktic foraminifera, coccolith preservation has not yet been as well defined as the preservation of planktic or benthic foraminifera (Bown et al., 2008). The two main concerns with coccolith calcite are dissolution and overgrowth (Su et al., 2000). Recrystallisation of coccolith calcite is not common, as holococcoliths mostly dissolve, and the large crystal size of the heterococcoliths makes overgrowth more thermodynamically favourable (Adelseck et al., 1973; Hover et al., 2001). Holococcoliths rarely preserve outside of clay-rich sediments, as they are very susceptible to dissolution (Bown et al., 2008). Dissolution (also referred to as etching) of heterococcoliths can range from slight etching (affects delicate structures; creates a serrated edge of coccolith), moderate (delicate structures destroyed; causes coccolith outlines to become irregular) to strong etching (delicate taxa are rare; coccolith fragments are abundant) (Roth and Thierstein, 1972; Roth, 1973; Roth, 1983; Blechschmidt, 1979; Su et al., 2000). Overgrowth

of heterococcoliths can also range from slight (some irregular secondary growth; slight thickening of central coccolith areas), to moderate (common irregular secondary growth; delicate structures overgrown and difficult to recognise), to strong overgrowth (overgrowth hinders identification) (Roth and Thierstein, 1972; Roth, 1973; Roth, 1983; Su et al., 2000). Based on shipboard investigations, the coccolith preservation at Site U1338 is generally moderate in the late Miocene to early Pliocene (Expedition 320/321 Scientist).

5.3. Analytical Techniques and Methods

5.3.1. Planktic Foraminiferal Trace Element Analysis

A total of 12 samples were selected from the U1338 splice between 6.5 and 5.5 Ma for planktic foraminiferal Mg/Ca analyses. Samples were chosen on the basis that sufficient *Globigerinoides sacculifer* were present to provide large enough samples for ICP-OES (inductively coupled plasma optical emission spectroscopy). Because Mg/Ca should increase with increasing planktic foraminiferal test size (see Section 5.2.1.1), foraminifera were picked for Mg/Ca analysis from multiple size fractions of the same sample (250 – 355 μm; 355 – 425 μm; 425 – 500 μm). This was done to see whether the original positive test size – Mg/Ca relationship is retained. For each Mg/Ca measurement, approximately 250 – 400 μg of foraminiferal calcite was required. On average, this equated to ~ 18 *Gs. sacculifer* for the 250 – 355 μm fraction, ~ 10 *Gs.*

Overview of samples selected for planktic Mg/Ca analysis								
Sample ID	***Sample depth*** *in m CCSF-A*	***Sample age*** *in ka*	***Size fraction*** *in µm*	***Replicated***	***Average # foraminifera***	***Average Sample weight*** *in µg*	***Contamination***	***Core Depth Correction*** *in km*
GS3	92.83	5537	250-355		20	304		3.97
GS6	95.93	5641	250-355		17	356		3.96
GS7	98.40	5748	250-355		18	310		3.96
			355-425		10	372		3.96
			425-500		5	344		3.96
GS8	99.47	5788	250-355		20	384		3.96
			355-425		12	338		3.96
			425-500		6	326		3.96
GS9	100.96	5806	250-355		16	328		3.96
GS19	112.75	6180	250-355		19	330		3.95
			355-425		10	314		3.95
GS20	112.97	6184	250-355	Yes	20.5	318		3.94
			355-425		10	320		3.94
GS12	113.35	6193	250-355	Yes	16	322		3.94
			355-425		10	368		3.94
			425-500		5	378		3.94
GS13	113.55	6196	250-355	Yes	21	315	Both replicates contaminated - excluded	3.94
			355-425		10	326		3.94
GS15	115.29	6221	355-425		10	390		3.94
			425-500		7	334		3.94
GS16	117.69	6319	250-355		20	440		3.94
GS17	119.99	6431	250-355		16	252		3.93

Table 5.1. Overview of the samples selected for Mg/Ca analysis of the planktic foraminifera *Globigerinoides sacculifer*. For the IODP code of the Sample ID, see appendix C.1.

sacculifer for the 355 – 425 μm fraction and ~ 6 *Gs. sacculifer* for the 425 – 500 μm fraction. An overview of the measured samples, including the number (#) of foraminifera and sample weight, is provided in Table 5.1.

Prior to ICP-OES analysis, all samples were cleaned using the Cd-cleaning protocol adapted from Boyle and Keigwin (1985). For each sample, all selected foraminifera were crushed between two glass slides and visually inspected under a light microscope. Any non-foraminiferal material (pyrite or discoloured fragments) was removed using a picking brush, leaving only visually clean *Gs. sacculifer* fragments behind. The foraminiferal fragments were then sonicated in DI water to remove clays, followed by a reduction step to remove metal oxides. All samples underwent a final oxidative step to remove any organic matter before being dissolved in a HNO_3 acid solution (0.1 M) in final preparation for liquid acquisition analysis using ICP-OES.

The dissolved samples were measured for calcium (Ca), magnesium (Mg), strontium (Sr), iron (Fe), aluminium (Al) and manganese (Mn) on the Varian ICP-OES at University College London, using the intensity ratio calibration method published by de Villiers et al. (2002). In this method, all samples are initially measured for calcium only, to establish each sample's Ca concentration. Because the ICP-OES is sensitive to Ca, when the Ca concentration is too high, the plasma can semi-de-energise, thereby making it less effective. In addition, if the Ca concentration is too high, the ions can reabsorb their own emissions, and the amount of Ca in the sample is underestimated. These effects are referred to as matrix effects, and to avoid these as much as possible, each sample was diluted to a similar 60-ppm Ca concentration. When sample concentration was < 60 ppm, an in-house Mg/Ca standard was diluted to a comparable [Ca]. The low-

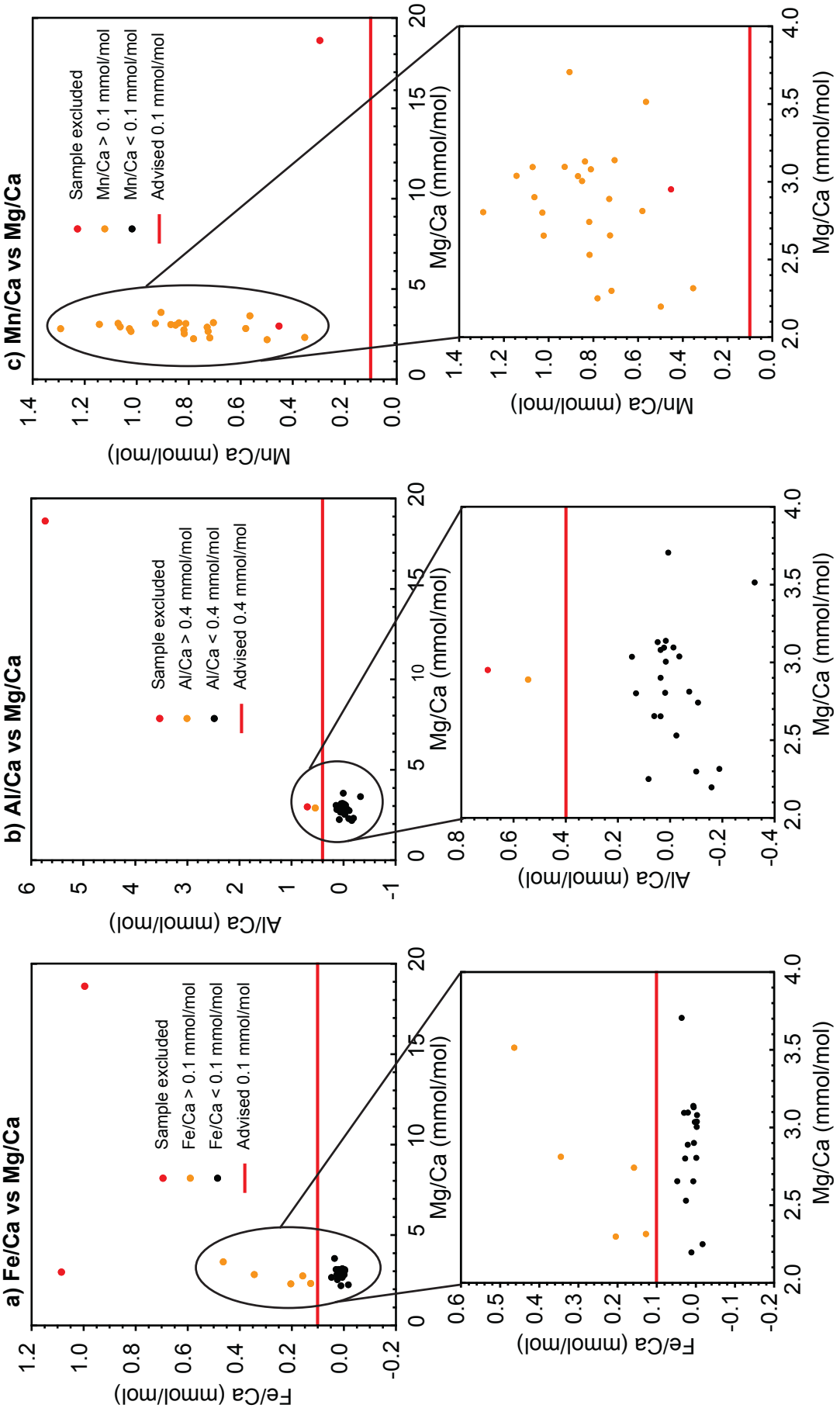
a) Fe/Ca vs Mg/Ca
Sample excluded
Fe/Ca > 0.1 mmol/mol
Fe/Ca < 0.1 mmol/mol
Advised 0.1 mmol/mol
Fe/Ca (mmol/mol)
Mg/Ca (mmol/mol)
b) Al/Ca vs Mg/Ca
Sample excluded
Al/Ca > 0.4 mmol/mol
Al/Ca < 0.4 mmol/mol
Advised 0.4 mmol/mol
Al/Ca (mmol/mol)
Mg/Ca (mmol/mol)
c) Mn/Ca vs Mg/Ca
Sample excluded
Mn/Ca > 0.1 mmol/mol
Mn/Ca < 0.1 mmol/mol
Advised 0.1 mmol/mol
Mn/Ca (mmol/mol)
Mg/Ca (mmol/mol)

Figure 5.2. Overview of Mg/Ca vs Fe, Al, Mn/Ca scatter plots to assess contamination on the trace element samples.

a) Fe/Ca versus Mg/Ca, showing the excluded samples (red), as well as the included samples that were above (orange) and below (black) the advised Fe/Ca levels of 0.1 mmol/mol (red line) (Elderfield et al., 2010).

b) Al/Ca versus Mg/Ca, showing the excluded samples (red), as well as the included samples that were above (orange) and below (black) the advised Al/Ca levels of 0.4 mmol/mol (red line) (Elderfield et al., 2010).

c) Mn/Ca versus Mg/Ca, showing the excluded samples (red), as well as the included samples that were above (orange) the advised Mn/Ca levels of 0.1 mmol/mol (red line) (Elderfield et al., 2010).

[Ca] standards were run alongside the low-[Ca] samples to allow potential matrix effects to be quantified, and if necessary, corrected for. Standards with known elemental concentrations were simultaneously measured with the samples to allow for conversion from intensity to element concentration.

Although Mg/Ca ratios were the only desired element ratio for proxy purposes, Fe/Ca, Al/Ca and Mn/Ca ratios were used to establish whether any contamination remained after the Cd-cleaning procedure (Boyle and Keigwin, 1985). Barker et al. (2003) and Elderfield et al. (2010) suggest excluding all data with Al/Ca ratios above 0.4 mmol/mol if the corresponding Mg/Ca is also high. In addition, results with > 0.1 mmol/mol Fe/Ca and > 0.1 mmol/mol Mn/Ca should be treated with caution (Barker et al., 2003; Elderfield et al., 2010). In this studies' dataset one sample was excluded because the Mg/Ca value was almost an order of magnitude larger than all other measured samples (Figure 5.2). The sample furthermore had higher Al/Ca and Fe/Ca ratios than recommended (Figure 5.2.a and b). One additional sample was excluded because it showed higher-than-recommended Al/Ca and Fe/Ca coupled with high Mg/Ca ratios (Figure 5.2.a and b). In addition to the excluded data points, five additional samples show higher Fe/Ca values (Figure 5.2.a). All Mn/Ca values are higher than first advised by Barker et al. (2003). However, a further study by Pena et al. (2005) showed that different species have different absolute values of Mn/Ca. Although *Gs. sacculifer* was not analysed in that study, it is feasible that *Gs. sacculifer* takes up relatively higher Mn/Ca. Pena et al. (2005) also showed that the main contaminant phase that has both a high Mn concentration and a high Mg concentration, is a Mn-Mg-carbonate coating on the inside of the foraminiferal test. The Mn/Ca of this coating is 400 mmol/mol and the Mg/Ca

ratio is 50 mmol/mol (Pena et al., 2005), which is far higher than the range of 0.3 – 1.1 mmol/mol for Mn/Ca and 2.2 – 3.7 mmol/mol for Mg/Ca seen in the U1338 samples. A further explanation of the higher Mn/Ca values at Site U1338 could be related to differential seawater Mn concentrations between the Pacific Ocean and the Altantic Ocean, where the Barker et al. (2003) study was based, as a strong control on the uptake of Mn^{2+} into the calcite lattice is the original Mn^{2+} concentration of the seawater (Pena et al., 2005). Most importantly, the higher Mn/Ca ratios for all samples, and the higher Fe/Ca ratios for five samples do not show a significant trend with Mg/Ca (lower insets Figure 5.2.a and c). For this reason in particular these samples were not excluded from the following study. Finally, after contamination analysis, Mg/Ca ratios were compared to sample [Ca] to see whether any matrix effect was observed (Figure 5.3). As no trend was observed between [Ca] and sample Mg/Ca, no additional correction for [Ca] was applied.

Based on replicate analyses of an in-house standard of known elemental composition, analytical Mg/Ca reproducibility is 0.02 mmol/mol. Duplicate analyses of two samples (~ 14 % of the data) indicate that natural Mg/Ca sample variability is 0.18 mmol/mol. Results from samples where Mg/Ca ratios were measured on more than one size fraction (250 – 355, 355 – 425 and 425 – 500 μm samples) show a positive correlation between size and Mg/Ca ratio (Figure 5.2.a). As samples with sufficient *Gs. sacculifer* to measure Mg/Ca ratios were scarce in the studied interval, a size-correction-factor was introduced. For each sample with multiple size fractions, Mg/Ca ratios were normalised by division to the smallest size fraction Mg/Ca. A linear regression was then placed through the normalised size fraction Mg/Ca ratios to provide a size correction factor for the

larger size fractions (Figure 5.2.b). When applied, Mg/Ca ratios are divided by a correction factor of 1.132 for the 355 – 425 μm fraction, and by 1.249 for the 425 – 500 μm fraction. The effect of the size correction on the Mg/Ca ratios is shown in the results section (section 5.4.1). Correction for size fraction induces a variability of 0.16 mmol/mol. Therefor, for samples that were size-corrected, overall variability is 0.24 mmol/mol ($\sqrt{sample\ variability^2 + size\ variability^2}$ = $\sqrt{0.18^2 + 0.16^2}$). Based on replicate analyses of an in-house standard of known elemental composition, analytical Sr/Ca reproducibility is 0.007 mmol/mol. Duplicate analyses of two samples (~ 14 % of the data) indicate that natural Sr/Ca sample variability is 0.01 mmol/mol, far lower than the variability seen in the Mg/Ca sample variability. Sr/Ca was measured on the same range of size fractions as Mg/Ca. *Globigerinoides sacculifer* is expected to display a negative trend in Sr/Ca with increasing size fraction, related to the decreased uptake of Sr^{2+} with the slower calcification of larger specimen compared to smaller specimen (Elderfield et al., 2002). Because the Sr/Ca in planktic foraminifera show no strong temperature dependence (Elderfield et al., 2002), the Sr/Ca records produced in this study are solely considered as an additional measure of whether the primary Mg/Ca signal is preserved (see discussion in section 5.5.1.1). Therefore no size fraction correction was applied to the Sr/Ca data.

To convert the Mg/Ca ratios to sea surface temperatures, the Dekens et al., (2002) calibration, which incorporates a correction factor for dissolution due to overlying water column depth, was used: $Mg/Ca = 0.37\ e^{0.09[\,T\,-\,0.36\,(depth)\,-\,2.0]}$. The core depth correction factor is designed to account for Mg/Ca removal due to dissolution in the water column. The core depth correction factor in this equation is specific to the Pacific Ocean basin. This calibration was also chosen as

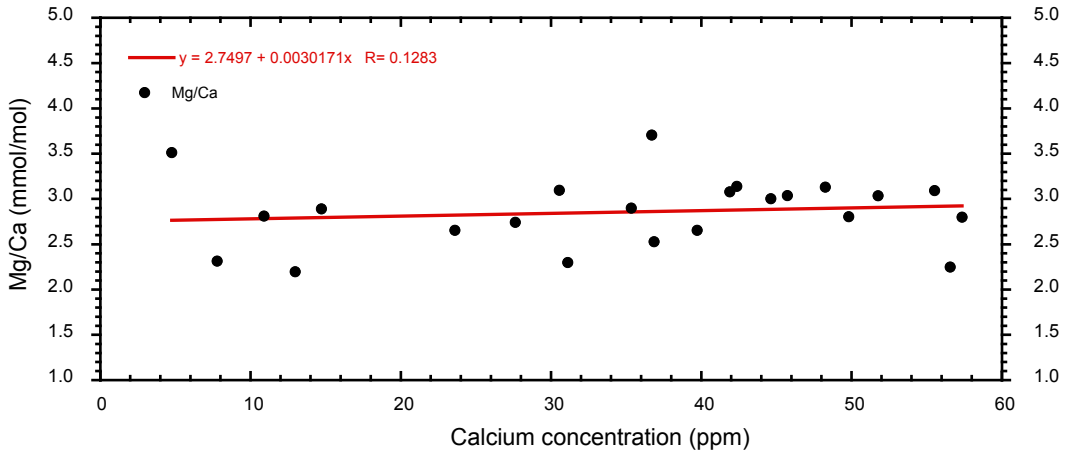

Figure 5.3. Scatter plot of the relationship between sample Mg/Ca ratio and the sample Ca concentration.

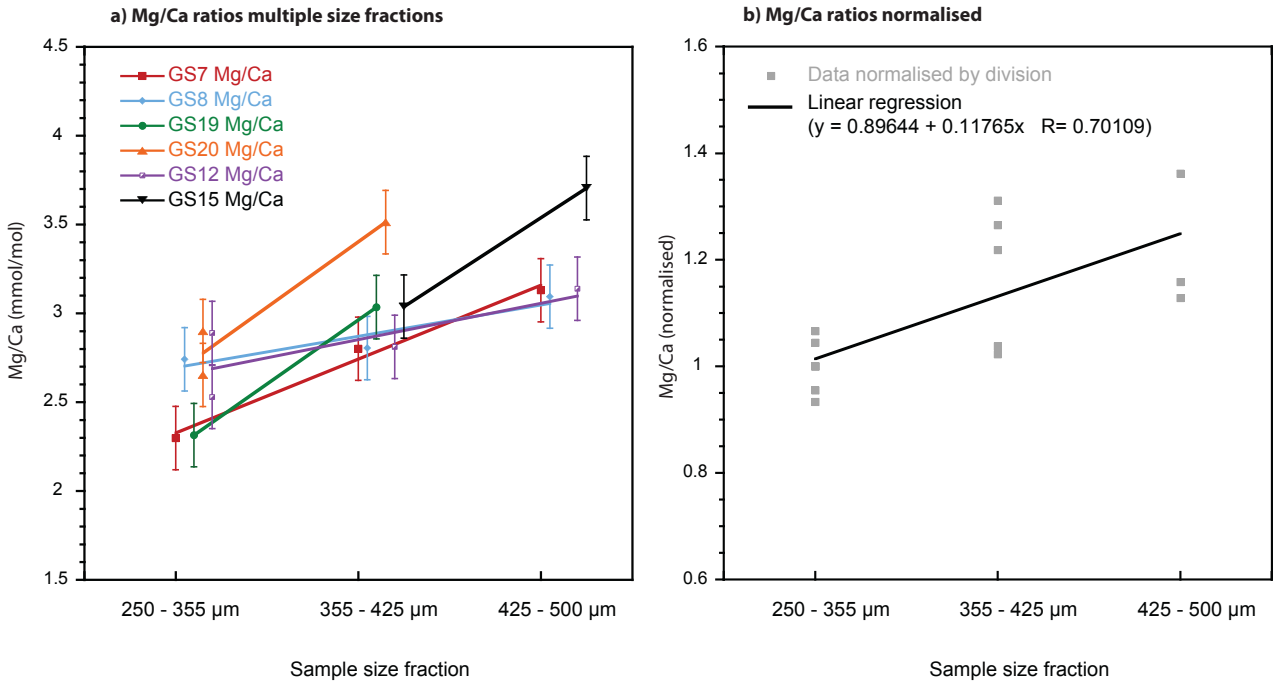

Figure 5.4. Overview of the size correction applied to the Mg/Ca data from the larger size fractions.

a) Shows the positive relationship between Mg/Ca and test size for the six samples for which Mg/Ca was measured on multiple size fractions.

b) Shows the normalised Mg/Ca data, with the linear regression that was used to correct the larger size fractions back to the 250 – 355 µm size fraction. Normalisation was done by dividing each size fraction Mg/Ca by the smallest size fraction Mg/Ca for each sample.

it is species specific for *Gs. sacculifer* and it was based on core top specimens, which are more comparable to the fossil samples used in this study than calibrations based on plankton tows or cultures. The palaeocore depth was calculated for each measured sample based on the U1338 palaeodepth reconstructions in Palike et al. (2012) (Table 5.1). For these samples the core correction adds the equivalent Mg/Ca-temperature of between 3.42 and 3.43 °C to all samples to account for dissolution. The trace element and temperature dataset produced for Site U1338 in this study, is displayed in Appendix C.1.

5.3.2. Fine Fraction Separation

Two < 63 μm fine fraction samples (c1 and c2), separated during the sediment processing for foraminiferal selection (see section 3.3.1) were chosen for clumped isotope Δ_{47} analysis (Table 5.2). These two samples were specifically chosen to be less than 1 cm along the U1338 splice from two samples on which Rousselle et al. (2013) measured $U^{k'}_{37}$ temperatures, bulk $\delta^{18}O$ and $\delta^{13}C$ and 2 – 5 μm fraction $\delta^{18}O$. Because Rousselle et al. (2013) also worked on samples from IODP Site U1338, choosing contemporaneous samples provides a unique opportunity to compare proxies on very proximal samples. The depth and age offsets between the selected c1 and c2 samples and the Rousselle et al. samples are shown in Table 5.2.

Initially, 1 g of each < 63 μm sample was mixed with DI water and wet sieved through a 20 μm steel-mesh sieve to isolate the < 20 μm fraction. The < 20 μm fraction was split, and half was washed through a 10 μm stainless steel mesh

sieve to isolate the < 10 μm fraction. A centrifugation-aided settling technique base on Stokes law was chosen to isolate the 2 – 5 μm fraction. This particle separation technique applies Stokes law: $V = \frac{g\,(\rho_p - \rho_l)\,D^2}{1.8\,\eta}$, where V (m/s) is the terminal settling velocity of a particle, g is the gravitational constant (9.8 m/s^2), ρ_p and ρ_l (kg/m^3) are respectively the particle and liquid density, D is the spherical particle diameter in cm and η (kg/(s · m)) is the liquid viscosity (Moore and Reynolds, 1997). Particle centrifugation is frequently used to separate fine clay particles (Moore and Reynolds, 1997). Unfortunately there was insufficient remaining sample in the < 10 μm fraction to successfully apply centrifugation. Therefore, a further 1 g of the original < 63 μm fraction was placed in de-ionised water, and centrifuged to collect the > 5 μm fraction in the substrate/pellet in the bottom of the centrifuge tube. The supernatant fluid containing the < 5 μm particles was transferred to clean centrifuge tubes, and centrifugation was again applied to collect particles between 2 and 5 μm in the substrate at the base of the centrifuge tube. Each centrifugation step was repeated 8 times, each time removing the supernatant fluid (< 2 μm particles), in order to concentrate enough material in the 2 – 5 μm fraction. Sufficient material was recovered after each step to measure around six replicates of 5 – 6 mg each.

5.3.3. Clumped Isotope (Δ_{47}) Analysis

The four size fraction from samples c1 and c2 (see section 5.3.2) were each analysed for Δ_{47} between three and four times to provide accurate and precise Δ_{47} measurements (Table 5.2). The carbonate-rich sediment samples were

reacted with acid to convert them to CO_2, which was cleaned using the online-reaction, manual vacuum line method of Dennis and Schrag (2010). Per replicate, 5 – 6 mg of the sediment fraction was reacted with 104 % orthophosphoric acid at 90 °C for 10 minutes. The released CO_2 was trapped continuously in a liquid nitrogen (LN_2) trap at – 192 °C, which freezes both the CO_2 and H_2O released during the reaction. After the reaction was complete, the LN_2 trap was replaced with a slush trap (a mix of ethanol and LN_2 with a temperature of ~ – 80 °C) so the CO_2 is released, but the H_2O is kept trapped. The CO_2 was then transferred through a Poropak Q trap set at – 35 °C into another LN_2 trap for 40 minutes. This stage is designed to remove any halide or hydrocarbon contamination, which could interfere with accurate measurements of Δ_{47} in the mass spectrometer. After completing the Poropak Q cleaning stage, the clean CO_2 was transferred to a cold finger, ready for mass spectrometer analysis. For each replicate, the sample CO_2 was measured on a duel inlet Thermo MAT 253 isotope ratio mass spectrometer in the Qatar Stable Isotope laboratory at Imperial College London, using the analysis method of Huntington et al. (2009). The sample CO_2 is measured against a working reference gas of known composition (Oztech; $\delta^{13}C$ = – 3.63 ‰ vs VPDB; $\delta^{18}O$ = 25.020 vs VSMOW). The measurement process consists of 8 runs of 7 cycles each, with the initial beam size of both sample and working gas set at 15000 mV.

To account for acid fractionation, the raw data was corrected as follows: $\delta^{18}O$ was corrected using the fractionation factor for calcite from Kim et al. (2007); Δ_{47} was corrected using the fractionation factor from Wacker et al., (2013) adjusted for a calcite reaction at 90 °C. An overview of correction factors is given in Table 5.3. The data was then corrected for mass spectrometer-specific

Overview of clumped isotope measurements and comparable Uk37 data																	
Sample ID	Depth in m CCSF-A	Age in ka	Size fraction in µm	Replicate	δ18O in ‰	δ18O average in ‰	δ18O stdev in ‰	δ13O in ‰	δ13O average in ‰	δ13O stdev in ‰	Δ47 in ‰	Δ47 average in ‰	Δ47 standard error in ‰	T (°C) average	T (°C) standard error	Uk37 T (°C)	Depth offset in m CCSF-A	Age offset in ka
Sample c1	76.18	5055	< 63	1	-0.17	-0.17	0.01	1.38	1.36	0.02	0.735	0.729	0.011	9.5	1.9	27.68	0.03	1.87
				2	-0.16			1.37			0.717							
				3	-0.16			1.34			0.736							
			< 20	1	0.08	-0.14	0.19	1.40	1.37	0.04	0.729	0.724	0.004	11.1	0.7			
				2	-0.29			1.39			0.722							
				3	-0.22			1.32			0.721							
			< 10	1	-0.38	-0.23	0.12	1.44	1.41	0.04	0.723	0.730	0.005	9.3	0.7			
				2	-0.19			1.43			0.732							
				3	-0.25			1.41			0.730							
				4	-0.11			1.36			0.735							
			2 - 5	1	-0.12	-0.10	0.07	1.49	1.43	0.07	0.717	0.712	0.007	14.8	1.0			
				2	-0.06			1.49			0.709							
				3	-0.02			1.39			0.718							
				4	-0.18			1.34			0.704							
Sample c2	105.32	5999	< 63	1	-0.23	-0.12	0.09	0.62	0.60	0.03	0.735	0.727	0.013	10.2	2.0	26.35	0.04	2.42
				2	-0.16			0.60			0.740							
				3	-0.04			0.56			0.723							
				4	-0.05			0.62			0.710							
			< 20	1	-0.14	-0.14	0.04	0.53	0.55	0.03	0.723	0.729	0.005	9.6	0.7			
				2	-0.13			0.54			0.735							
				3	-0.08			0.60			0.729							
				4	-0.19			0.56			0.728							
			< 10	1	-0.21	-0.27	0.05	0.50	0.51	0.03	0.765	0.747	0.016	4.2	2.2			
				2	-0.31			0.48			0.740							
				3	-0.28			0.55			0.736							
			2 - 5	1	-0.22	-0.26	0.09	0.70	0.62	0.06	0.735	0.728	0.013	10.0	2.2			
				2	-0.20			0.58			0.735							
				3	-0.37			0.59			0.713							

Table 5.2. Overview of the sample information and resulting data of the individual replicates of each clumped isotope measurement. The final columns also provide the information about the depth and age offset between the samples measured in this study, and the contemporaneous samples from the Rousselle et al. (2013) study. The $U^{k'}_{37}$ temperatures for the samples from Rousselle et al. (2013) are also provided.

IODP Core information: Sample c1 = 321-U1338B-8H-4-W 50/52; Sample c2 = 321-U1338B-11H-2-W 60/62.

effects. Sample $\delta^{13}C$ and $\delta^{18}O$ were corrected by addition of a correction factor based on the offset between the 2-week measured average of the carbonate standards ETH3 and Carrara marble and their universally accepted values (Carrara marble – published value from Dennis et al., 2011; ETH – university accepted value determined by multiple analyses in six clumped isotope labs, including Imperial College – Bernasconi et al., in prep). To obtain a correction for Δ_{47}, heated gases (CO_2 heated to ~ 1000 °C to obtain a stochastic distribution of the rare, heavy isotopes) with a range of bulk $\delta^{18}O$ and $\delta^{13}C$ composition were cleaned and measured regularly using the same methodology applied to the samples. The resulting heated gas data should all have the same stochastic Δ_{47} value, but a range of bulk $\delta^{18}O$ and $\delta^{13}C$ compositions. However, due to inherent non-linearity and fragmentation and recombination of analyte CO_2 in the mass spectrometer during the measurement, there are always slight variations in the heated gas Δ_{47} with bulk composition, which causes a gradient in the heated gas Δ_{47} – bulk composition relationship, generally referred to as the 'non-linearity effect'. This effect can be corrected for using the slope and intercept of the heated gas line. To ensure that the Δ_{47} data from this study can be compared to Δ_{47} data from other laboratories, all data was transferred into the universal reference frame (URF) outlined by Dennis et al., (2011). In this method at least three standards, with a known value within the reference frame, were measured regularly on each machine used for Δ_{47} measurement. A transfer function was calculated by applying a linear regression to the measured versus universally accepted or published values of these three standards. Data was transferred into the URF by applying the transfer function. For this study, the transfer function was based on repeated measurements of heated gases (published value from

Wang et al., 2004), and the two carbonate standards run in the Imperial College lab: ETH3 and Carrara Marble.

Two additional parameters were applied to monitor for contamination. In addition to the collector installed in the Thermo MAT 253 to detect isotopologues of mass 47, the Thermo MAT 253 also has collectors to detect mass 48 and 49. CO_2 has multiply-substituted isotopologues of both mass 48 and 49, however, these are far less abundant than the multiply-substituted isotopologues with mass 47. Δ_{47} values can be artificially increased if contaminants such as halides and hydrocarbons are present in the sample gas. If present, contaminants such as halides and hydrocarbons will also be registered on both the mass 48 and 49 collectors. For this reason, the mass 48 and 49 properties of a sample measurement can be used to assess contamination (Huntington et al., 2009). Firstly, samples with a δ^{48} and Δ_{48} values that do not fall within 1 ‰ of the δ^{48} and Δ_{48} values of the heated gas line were excluded. In addition, samples with a 49 parameter greater than 0.2 were also excluded:
49 parameter = $(V^{49}_{sample} / V^{44}_{sample} - V^{49}_{standard} / V^{44}_{standard}) \cdot 1000$ (V = voltage)

The final, corrected Δ_{47} replicates were averaged per size fraction to get an average Δ_{47} ± 1 standard error (1 S.E.) in ‰, which was then converted to temperature. The Δ_{47} – temperature calibration from Passey and Henkes, 2012 was used, with an additional – 0.011 ‰ correction factor to adjust for a difference in the acid fractionation used between this study and Passey and Henkes (2012):

$$\Delta^{47} = \frac{-3.407 \cdot 10^9}{T^4} + \frac{2.365 \cdot 10^7}{T^3} - \frac{2.607 \cdot 10^3}{T^2} - \frac{5.880}{T} + 0.280 - 0.011$$

This calibration was chosen over calibrations from Tripati et al. (2010) and Grauel et al. (2013), despite the fact that these two calibrations incorporate a large amount of data on the Δ_{47} – temperature relationship of both planktic foraminifera and coccolithophores. However, neither of these calibrations are reported in the URF, which means the results cannot directly be compared to the results from this study. The Passey and Henkes (2012) calibration was also chosen as the Δ_{47} measurements used in this calibration were measured using the same analytical method as this study, which ensures comparability. In addition, the internal calibration from the Qatar Stable Isotope laboratory at Imperial College London (Kluge et al., 2013; Kluge et al., in prep-a) agrees well with the Passey and Henkes (2012) calibration.

5.3.4. High Resolution Secondary Electron Microscopy

5.3.4.1. Backscatter and Secondary Electron Imaging

All four size fractions from sample c1 and c2 were mounted on sticky carbon tape on individual stubs. The uncoated samples were initially imaged using the Leo 1455 VP (variable pressure) SEM at the Natural History Museum (London, United Kingdom). The images were made at low vacuum using back-scattered electrons in topography mode (BSE-TOPO), with a working distance of 15 – 16 mm, a spot size setting of 500 (Leo 1455 VP specific setting) and an acceleration voltage of 15 kV.

As this approach was insufficient in spatial resolution to resolve all components in the sediment, the 2 – 5 µm fraction of sample c2 was coated with

platinum and imaged using the JEOL JCM-6000 NeoScope Benchtop SEM in high vacuum mode at Utrecht University (the Netherlands). To resolve the smaller scale features of the sediments, images were taken in secondary electron mode at a working distance of 19 mm. The filament and probe currents were set to high. The acceleration voltage was set at 10 or 15 kV, depending on the resolution required.

5.3.4.2. EDS elemental mapping and area analysis

To determine the chemical composition of the different sedimentary components, four energy-dispersive X-ray spectroscopy (EDS) area maps were made of different sections of sample c2. The EDS maps were all made with an acceleration voltage of 15 kV using high filament and probe currents.

The EDS map of calcium can be used to highlight of the amount of calcite present in the c2 sample. Visually assessing and analysing the EDS Ca map in Adobe Illustrator CS5 can further help determine the ratio of coccolith versus non-coccolith calcite. First, the total calcite area of each Ca-EDS map was estimated by using the live-trace function in Illustrator CS5. The total area of the trace was calculated using the Telegraphics Patharea Filter plugin (downloaded on 07.11.2013 from http://telegraphics.com.au/sw/product/patharea). Clearly identifiable coccoliths and coccolith fragments were then traced by hand. The traced area was then estimated, again using the Patharea Filter. To calculate the ratio of non-coccolith to coccolith calcite, the total area of calcite was compared to the area identifiable as coccoliths. To account for the different scale of each EDS map, the coccolith and non-coccolith calcite areas are presented in %.

Oveview of calcite acid fractionation factors		
Type	*Acid fractionation correction factor*	*Reference*
δ18O calcite at 90 °C	1.008128581	Kim et al., 2007
Δ47 calcite at 90 °C	0.075	Wacker et al., 2013

Table 5.3. Overview of the different fractionation factors applied in this study.

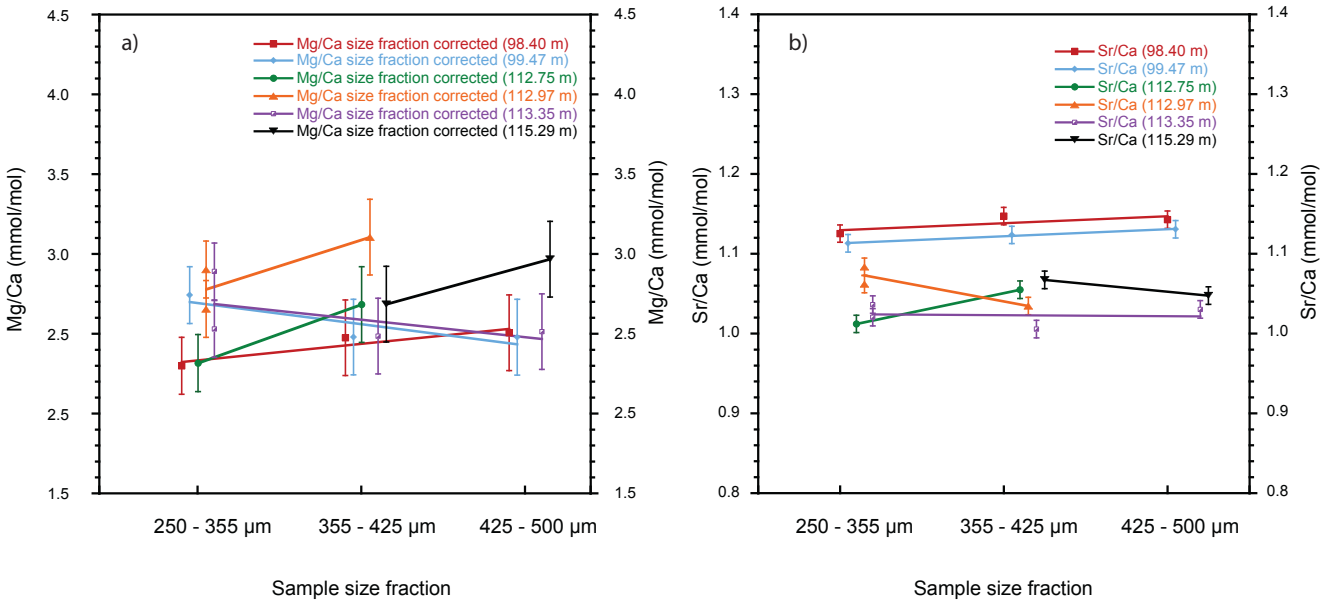

Figure 5.5. Overview of size corrected Mg/Ca_{GS} ratios and uncorrected Sr/Ca_{GS} ratios. A version of this figure including the uncorrected Mg/Ca_{GS} can be found in Appendix C.2.

a) Shows Mg/Ca ratios after size fraction correction from the three different size fractions. The Mg/Ca ratios from the different size fractions from the same sample are now within error of each other. Error bars are 0.24 mmol/mol (1 σ) for data in the 355 – 500 µm size fractions and 0.18 mmol/mol (1 σ) for data in the 250 – 355 µm size fraction. 1 σ = 1 standard deviation.

b) Shows original Sr/Ca ratios from the three different size fractions. Error bars are 0.01 mmol/mol (1 σ = 1 standard deviation).

5.4. Results

5.4.1. Planktic Foraminiferal Mg/Ca_{GS} and Sr/Ca_{GS}

Figure 5.5 shows (a) the size-corrected Mg/Ca_{GS} and (b) uncorrected Sr/Ca_{GS} ratios (mmol/mol) of the three size fractions measured on six different samples (see section 5.3.1). Before correction for size, the increasing trend with increasing test size is clearly visible in all samples (Figure 5.3.a). After size fraction correction, the Mg/Ca_{GS} measurements on samples in the 355 – 425 and 425 – 500 µm fractions are on average reduced by 0.35 ± 0.03 and 0.65 ± 0.06 mmol/mol. After size fraction correction the Mg/Ca values are similar within error (Figure 5.5.a). Appendix C.2. shows a compilation of the uncorrected and size corrected Mg/Ca_{GS}, together with the uncorrected Sr/Ca_{GS}.

Unlike the Mg/Ca_{GS}, the uncorrected Sr/Ca_{GS} data shows unanimous trend with increasing size fraction (Figure 5.5.b). The samples at 98.40, 99.47 and 113.35 m CCSF-A show no significant change across the three size fractions. The samples at 112.97 and 115.29 m show a decrease of Sr/Ca_{GS} with increasing size fraction, however, the sample at 112.75 m shows an increase of Sr/Ca_{GS} with increasing size fraction. It is notable to see that the Sr/Ca_{GS} record displays far less variability overall than the Mg/Ca_{GS} record.

Including all size-corrected data, the Mg/Ca_{GS} measurements from Site U1338 range between 2.20 and 3.10 mmol/mol, equating to a temperature range of 23.2 to 27.1 °C (Figure 5.6). In the oldest part of the record, around 6.4 – 6.3 Ma, the temperatures are the coolest around 23.5 °C. By the end of the record, between 5.7 and 5.5 Ma, temperatures have increased to 25 – 27 °C. However,

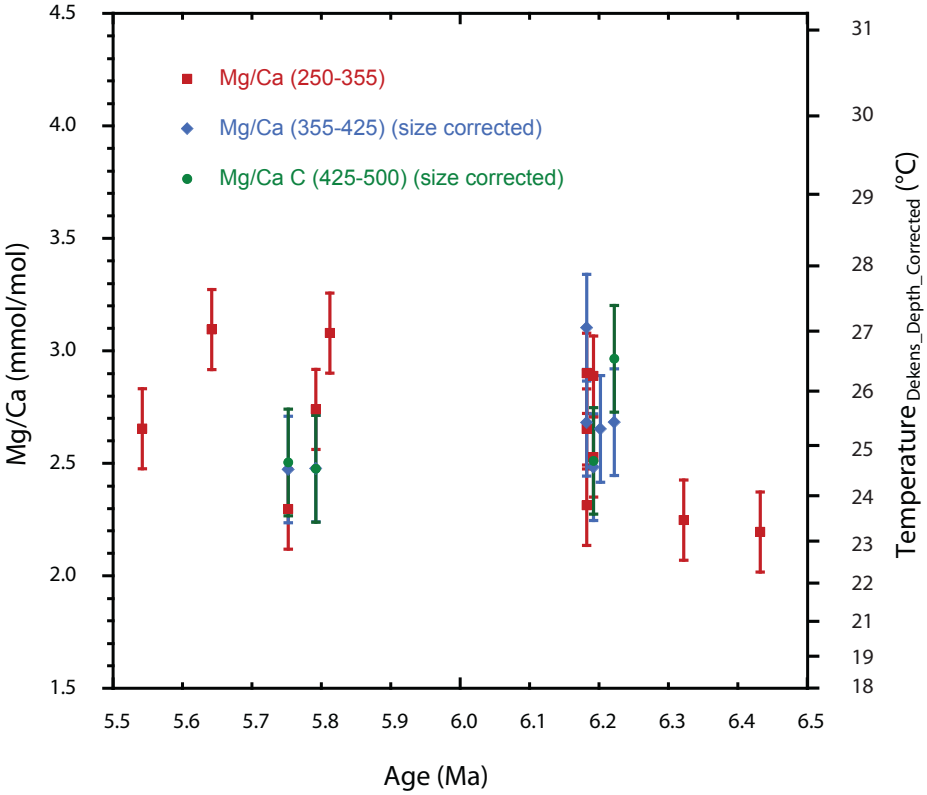

Figure 5.6. Mg/Ca ratios and the temperatures (using Dekens et al., 2002) on age. All Mg/Ca ratios from the 355 – 425 µm and 425 and 500 µm size fractions have been size corrected.

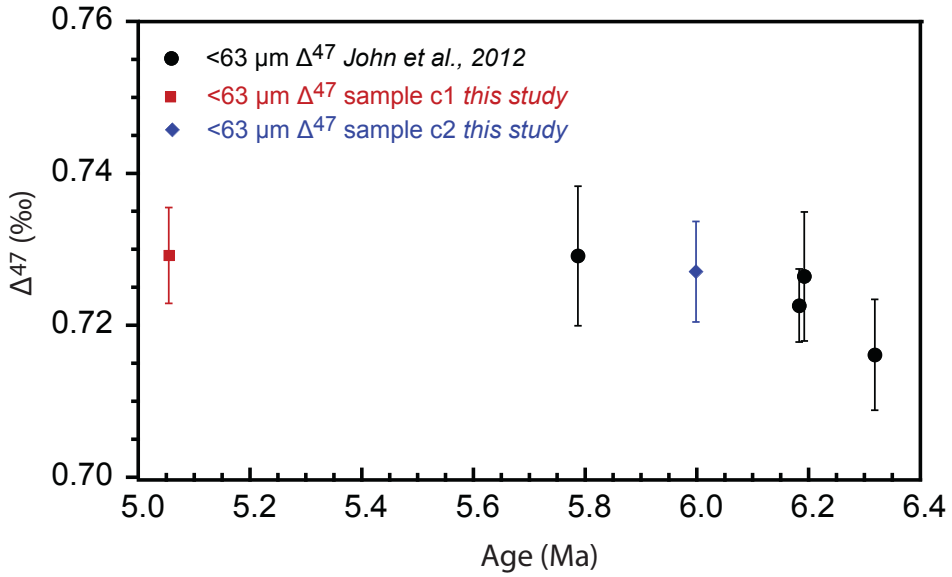

Figure 5.7. Clumped isotope Δ^{47} results on age from the bulk fine fraction (<63 µm) from this study (red and blue data points), and from John et al., (2012) (black data points).

the short-term variability of the Mg/Ca_{GS} and respective temperatures is large. The short-term variability between samples (averaged across size fractions) equates to a range of 0.39 mmol/mol (1.6 °C) around 6.2 Ma, and 0.65 mmol/mol (2.7 °C) around 5.8 Ma.

5.4.2. Fine Fraction Geochemistry: Clumped (Δ_{47}) and Conventional ($\delta^{18}O$, $\delta^{13}C$) Isotopes

The bulk (< 63 μm) fine fraction clumped Δ_{47} values for samples c1 and c2 are respectively 0.729 ± 0.006 ‰(1 S.E.) and 0.727 ± 0.007 ‰ (1 S.E.), which agrees with earlier measurement on the bulk fine fraction material from this site (John et al., 2012) (Figure 5.7). Figure 5.8 and Table 5.2 provide an overview of the Δ_{47}, temperature, $\delta^{18}O$ and $\delta^{13}C$ values and errors for the size fractions < 63 μm, < 20 μm, < 10 μm and 2 – 5 μm. There is no strong increasing or decreasing trend in Δ_{47} with smaller size fractions in either sample c1 or c2 (Figure 5.8.a). For sample c1, the Δ_{47} measurements of the < 63 μm (0.729 ‰; 9.5 °C), <20 μm (0.724 ‰; 11.1 °C) and <10 μm (0.730 ‰; 9.3 °C) size fractions are within error of each other (Figure 5.8.a; Table 5.2). For the smallest size fraction, 2-5 μm, the Δ_{47} decreases by almost 0.02 ‰ to 0.712 ‰ (14.8 °C) compared to larger size fractions. For sample c2, the Δ_{47} values for the < 63 μm and < 20 μm fractions are again within error of each other (< 63 μm: 0.727 ‰ or 10.2 °C; < 20 μm: 0.729 ‰ or 9.6 °C) (Figure 5.8.a; Table 5.2). However the Δ_{47} value for the < 10 μm fraction is considerably higher at 0.747 ‰ (4.2 °C) compared to the larger size fractions. The sample c2 2 – 5 μm fraction Δ_{47} also shows a decrease of about

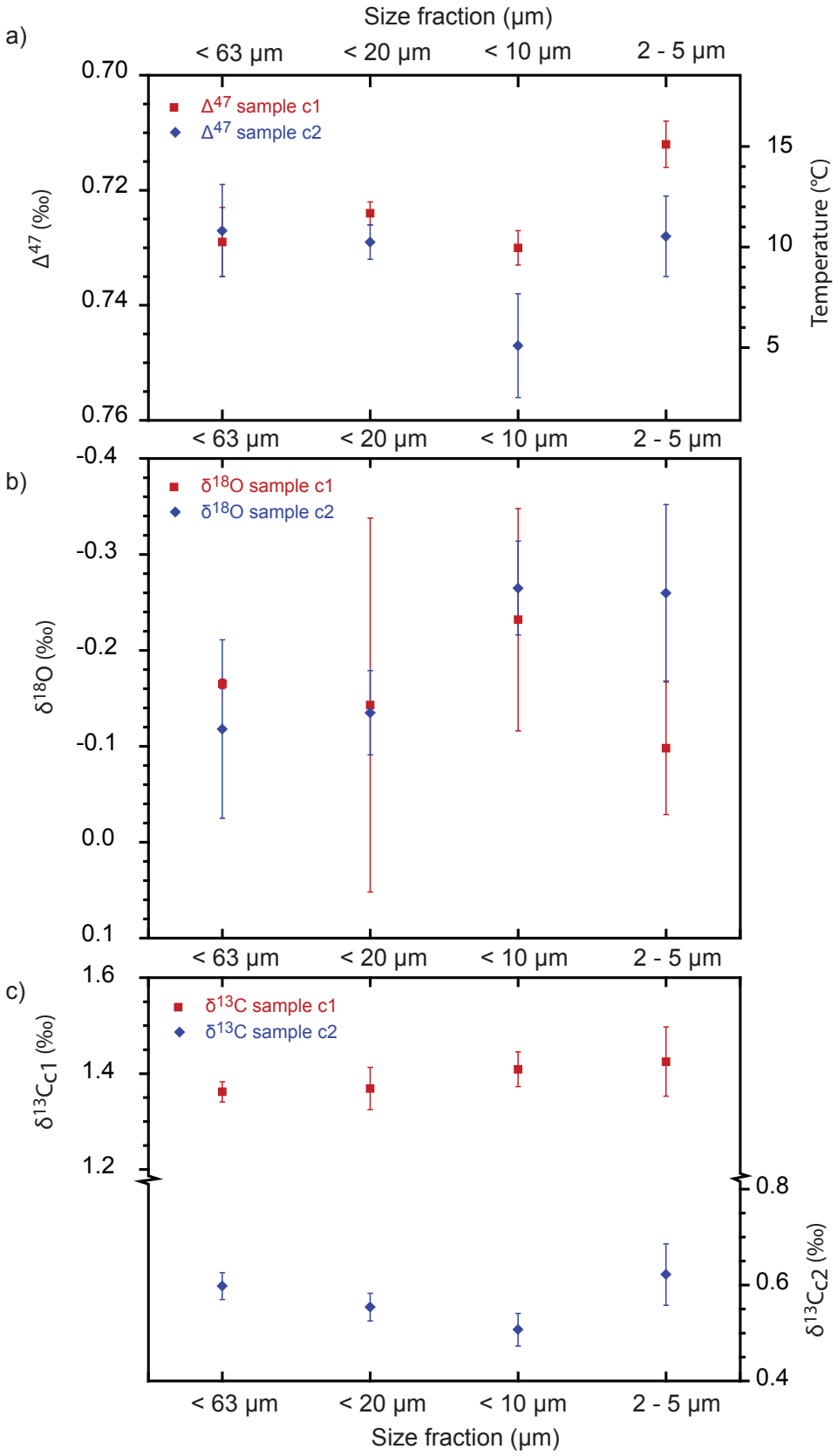

Figure 5.8. Overview of the geochemical (Δ^{47} – a; $\delta^{18}O$ – b; $\delta^{18}O$ – c) results for all four size fractions (< 63 µm; < 20 µm; < 10 µm; 2 – 5 µm) of the c1 (red) and c2 (blue) samples analysed for clumped isotopes.

0.02 ‰ to 0.728 (10.0 °C), which is similar to the Δ_{47} values for the < 63 μm and < 20 μm fraction of sample c2.

The sample c2 $\delta^{18}O$ averages show an overall increasing trend from the largest (< 63 μm) to the smallest (2 – 5 μm) size fractions (Figure 5.8.b; Table 5.2). The sample c1 $\delta^{18}O$ averages show a slight decrease between the <63 μm and 2 – 5 μm samples, however again the values are within error of each other (Figure 5.8.b; Table 5.2). For both sample c1 and c2, the average $\delta^{13}C$ value is comparable between the four different size fractions, although there is approximately a 0.8 ‰ offset between the average $\delta^{13}C$ value for sample c1 and c2. Both samples show a slight increase in $\delta^{13}C$ between the < 63 and 2 – 5 μm fractions, however the measurements are within error of each other (Figure 5.8.c; Table 5.2). Although the average $\delta^{18}O$ from the c1 and c2 size fractions show some differences, the measurements are within errors of each other.

5.4.3. Fine Fraction SEM

5.4.3.1. BSE- and SE-SEM

Figure 5.9 shows an overview of BSE-SEM images of the four different size fractions of sample c1 and c2. The images of the sample c1 and c2 < 63 μm fractions show the presence of many heterococcolith plates, as well as large fragments of radiolarians and foraminifera. There are also large numbers of whole diatoms present (Figure 5.9.a and e). The sample c1 and c2 < 20 μm fractions show a reduction in the number of large radiolarian fragments. There

are still some diatoms present, however the amount is greatly reduced compared to the < 63 μm fraction (Figure 5.9.b and f). Again, the <10 μm fraction for both sample c1 and c2 shows almost no large fragments and diatoms (Figure 5.9.c and g). The 2 – 5 μm fractions from samples c1 and c2 again show the presence of many heterococcoliths (Figure 5.9.d and h). However, there is also evidence that larger diatom particles were not successfully removed during the centrifugation.

In addition to the high concentration of heterococcoliths in all samples, all BSE-SEM images indicate that there are also large numbers of smaller particulates (< 2 μm) present in all size fractions (Figure 5.9). Higher resolution SE-SEM images of the sample c2 2 – 5 μm size fraction show that the dominant components are coccoliths, coccolith plate and diatom fragments and small fragments (Figure 5.10). The small fragments are sometimes distinguishable as very small coccolith or foraminiferal fragments (Figure 5.10). However, the fragments are frequently too small to accurately distinguish their origin, but could potentially be fragmented holo- and heterococcoliths.

Higher resolution imaging was used to assess the preservation of the coccoliths (Figure 5.11). No holococcoliths are identifiable, although some of the smaller fragments of calcite may be disintegrated holococcoliths. The central structures of the most of the heterococcoliths have not been retained, which would suggest slight to moderate dissolution/etching has occurred. Most imaged heterococcoliths possibly also show some minor overgrowths of single calcite cells (red arrows – Figure 5.11 a, b, e, f). However, as there is a large amount of small fragments present, some of this potential overgrowth could simply be a small fragment attached to the coccolith surface (Figure 5.11.b,c). The resolution of the SE-SEM micrographs is not sufficiently high to judge whether there is any

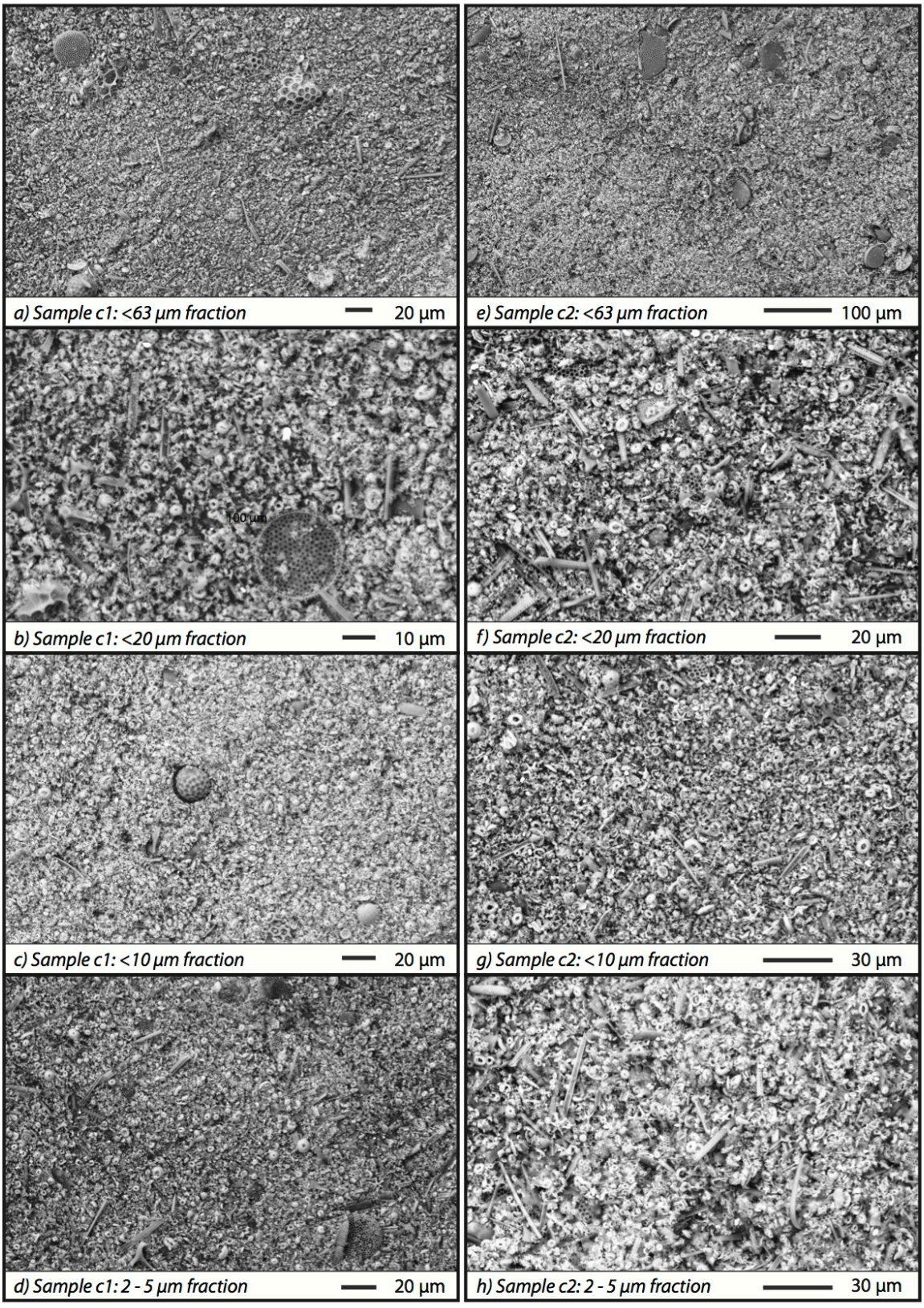

Figure 5.9. Overview of BSE-SEM images of the c1 (a – d) and c2 (e – h) samples. Each size fraction was imaged separately, and show that the size fraction separation was generally successful at removing most large fragments. For larger versions of this image, please see Appendix C.3.

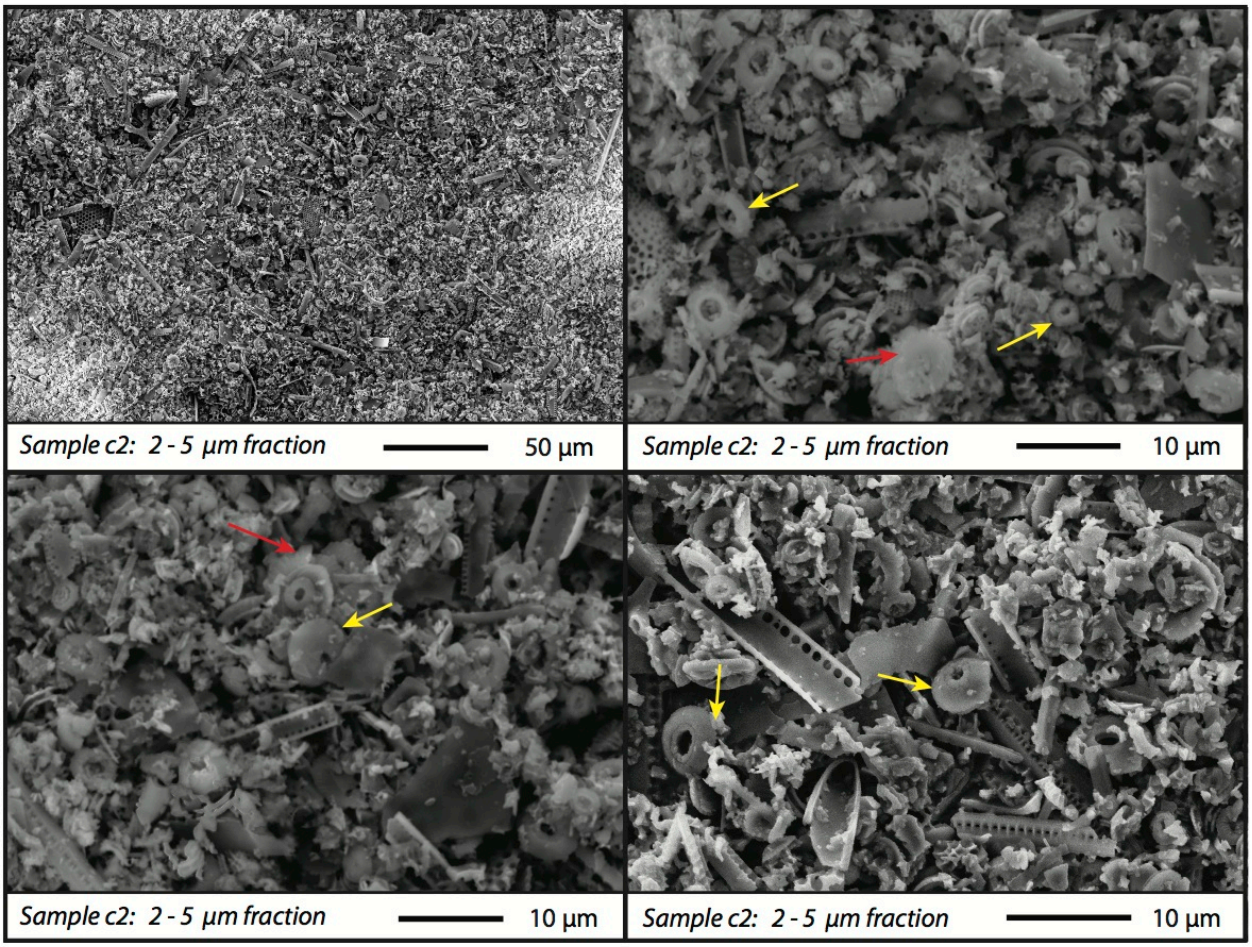

Figure 5.10. High-resolution SE-SEM images of the c2 sample 2 – 5 µm size fraction, showing the presence of large numbers of coccoliths (green arrows). The images also show the presence of small fragments that are partially made up of foraminiferal and coccolith fragments (red arrows). For larger versions of this image, please see Appendix C.4.

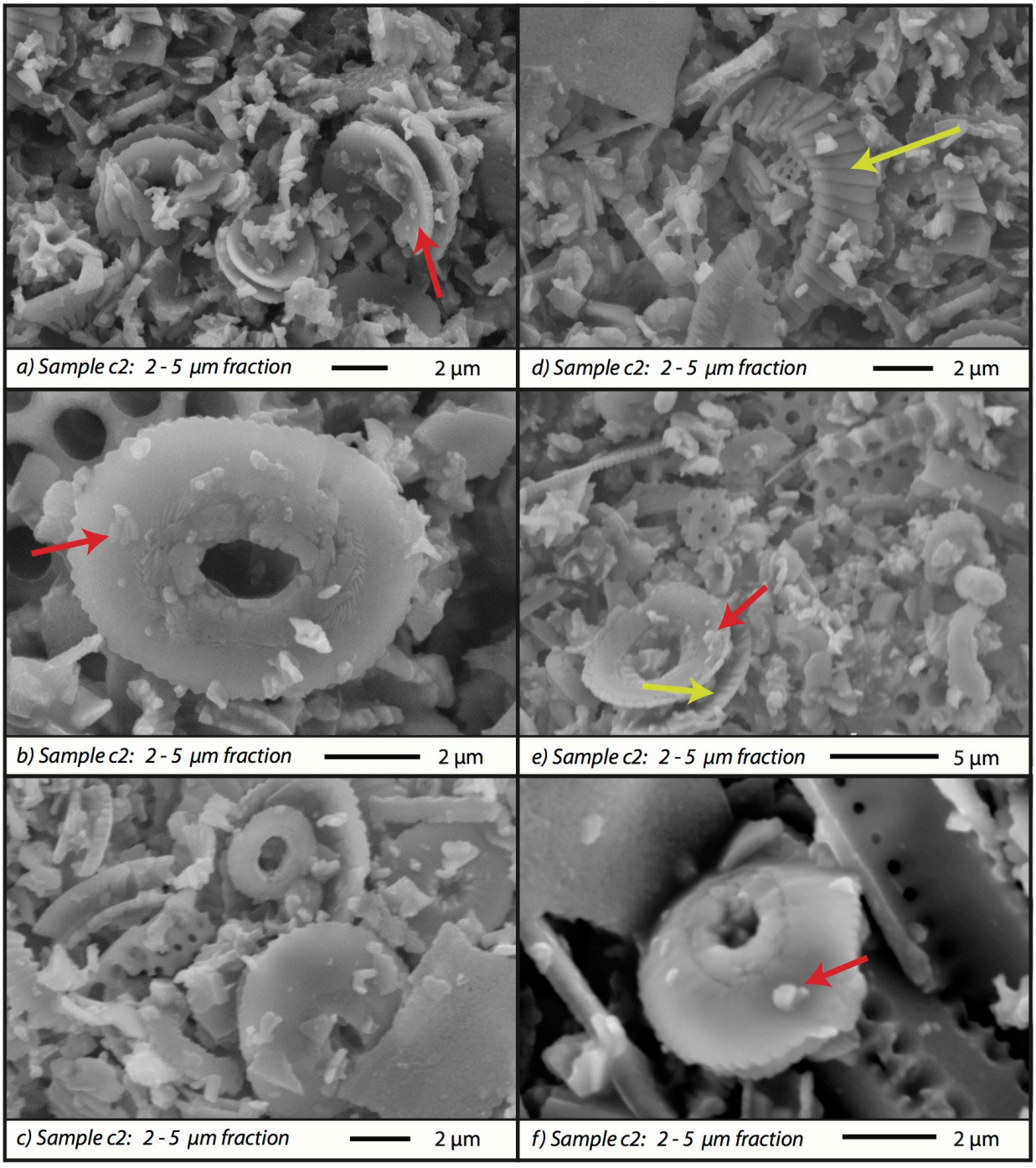

Figure 5.11. High resolution SE-SEM images of sample c2 showing the preservation of the coccoliths. Generally, there slight to minor etching, although there is considerable fragmentation. Original microstructures are retained (green arrows), but there is some evidence of calcite overgrowths (red arrows).

recrystallisation. The original structure of the coccolith is also retained in some of the heterococcoliths (green arrows – Figure 5.11. d and e). However, the absence of holococcoliths and clear original structures in all heterococcoliths, together with the minor overgrowths and large number of fragments would suggest that the preservation of these samples is moderate, potentially moderate to poor.

5.4.3.2. Elemental EDS maps and area analysis

To assess the predominant chemical composition of the different fragments in all size fractions of both sample c1 and c2, four EDS maps were taken of the 2 – 5 μm fraction of sample c2 (Figure 5.12 – split over two pages). Although the EDS analysis is not quantitative, the maps show that the main chemical components are calcite ($CaCO_3$ – represented by calcium) and silica (SiO_2 – represented by silicon) (Figure 5.12. a, c, e, g). Three of the four EDS maps also show some presence of barite ($BaSO_4$ – represented by barium) (Figure 5.11.a, c and e). Figure 5.11.a shows clear evidence of large barite crystals. The shape of the crystals is euhedral to subspherical, which shows it is marine barite, not diagenetic or hydrothermal barite (Paytan et al., 2002).

Overlays of the calcium (Ca), silicon (Si) and barium (Ba) EDS maps over the SE-SEM image of the mapped area, confirm that the SiO_2 present in the sample is predominantly biogenic fragments of diatoms and radiolarians (green are Figure 5.11.b, d, f and h). In addition, apart from the occasional marine barite crystal (blue area – Figure 5.11.b, d, f and h), the remaining components of the sediment fraction are all calcite (red area – Figure 5.11.b, d, f and h). The red

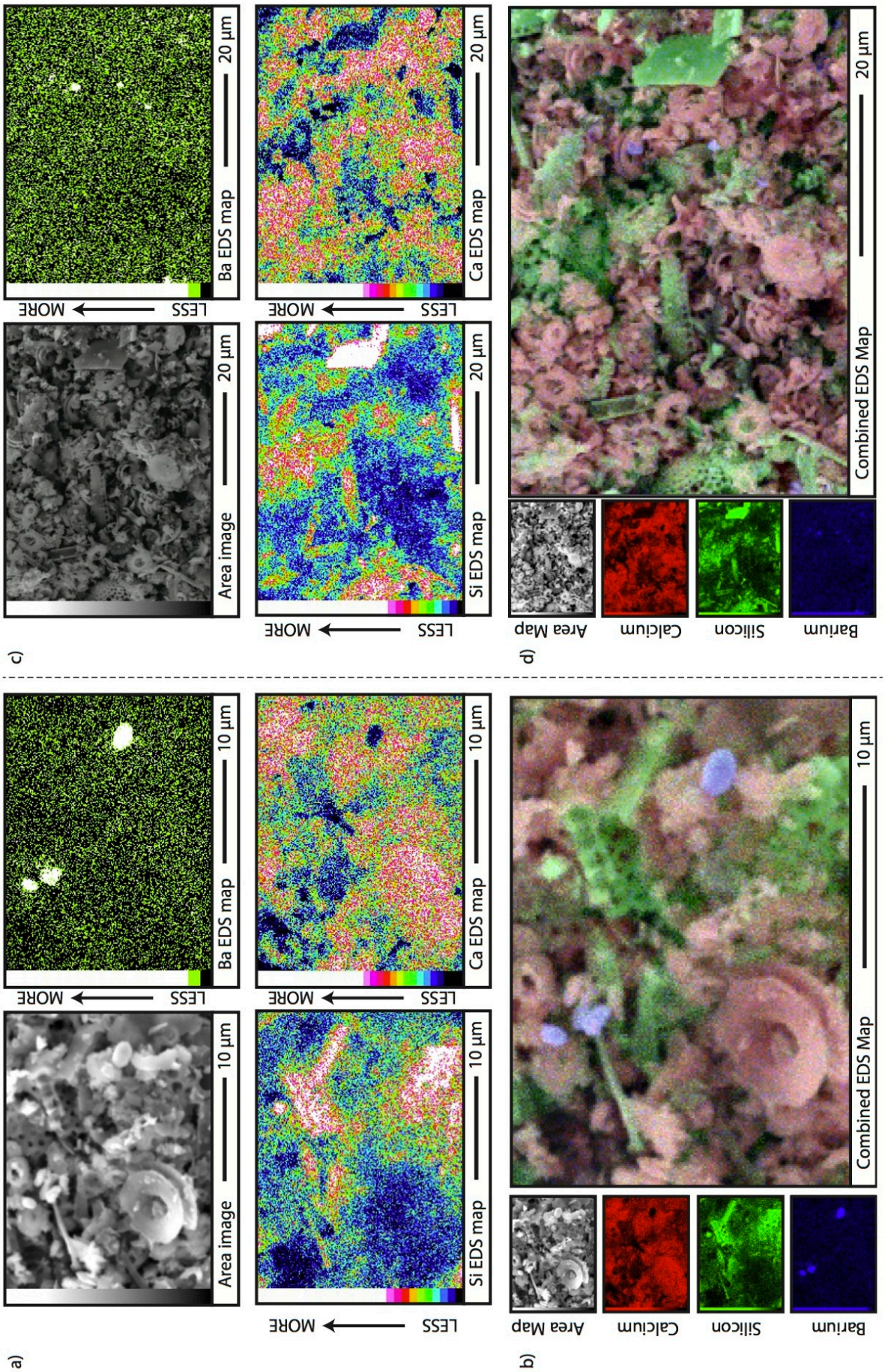
a)
Area image
Ba EDS map
Ca EDS map
Si EDS map
LESS
MORE
10 µm
b)
Area Map
Calcium
Silicon
Barium
Combined EDS Map
c)
20 µm
d)

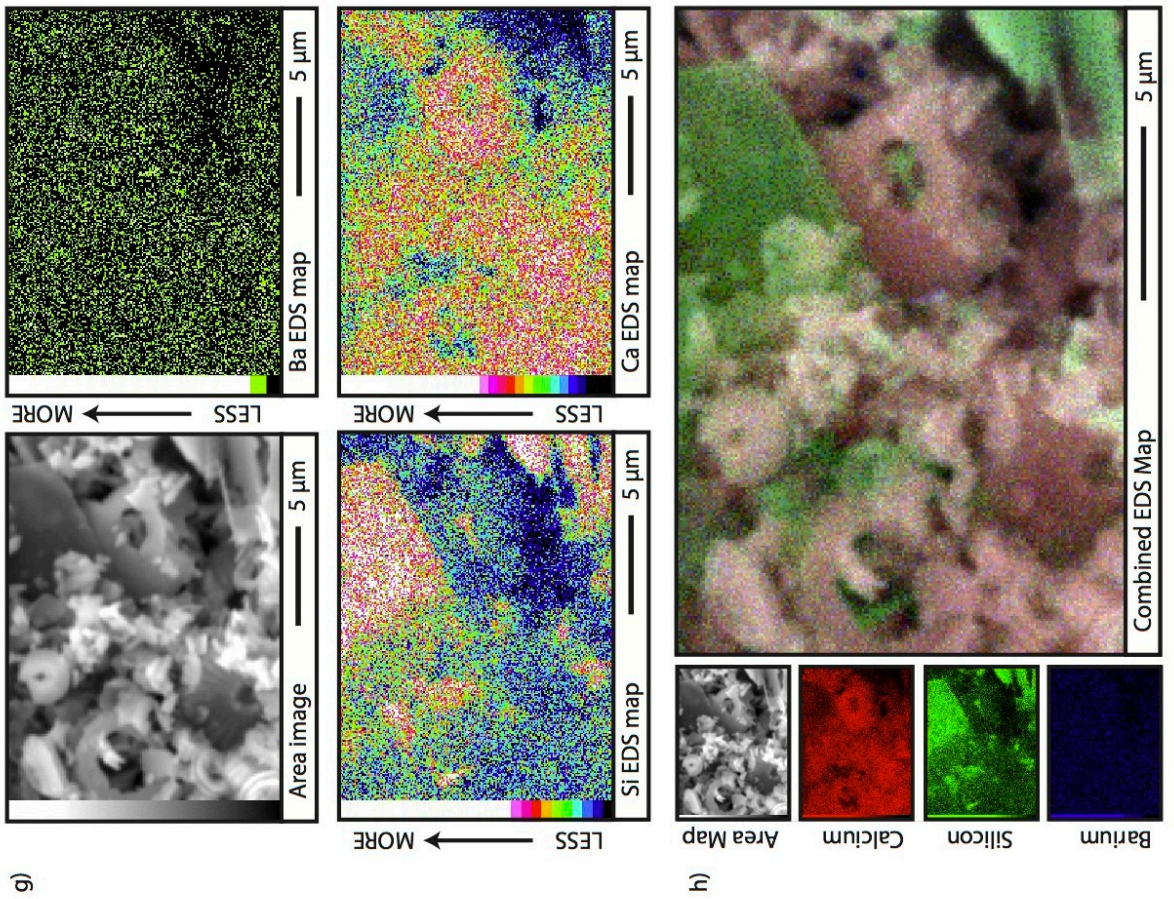
g)
Area image
5 µm
Ba EDS map
LESS
MORE
Ca EDS map
Si EDS map
h)
Barium
Silicon
Calcium
Area Map
Combined EDS Map

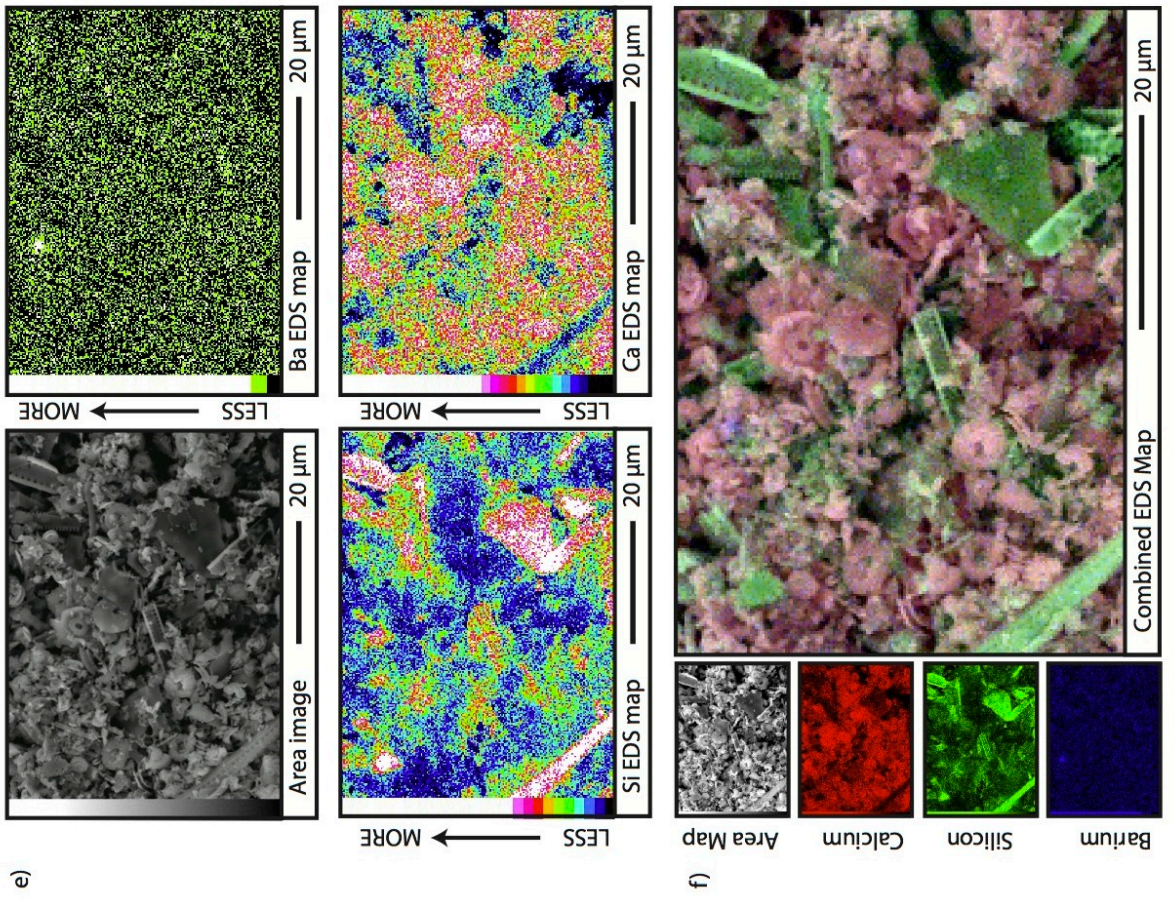
e)
Area image
20 µm
Ba EDS map
LESS
MORE
Ca EDS map
Si EDS map
f)
Barium
Silicon
Calcium
Area Map
Combined EDS Map

Figure 5.12. Overview of the four areas mapped elementally using EDS on sample c2.

The individual area image, barium (Ba), calcium (Ca) and silicon (Si) EDS maps are shown in a, c, e and g. An overlay of the Ba, Ca and Si over the area image are shown in b, d, f and h.

These EDS maps show that the main two components are biogenic SiO_2 and $CaCO_3$, although there is also some marine barite present in two maps (a and c).
For larger images, please see Appendix C.5.

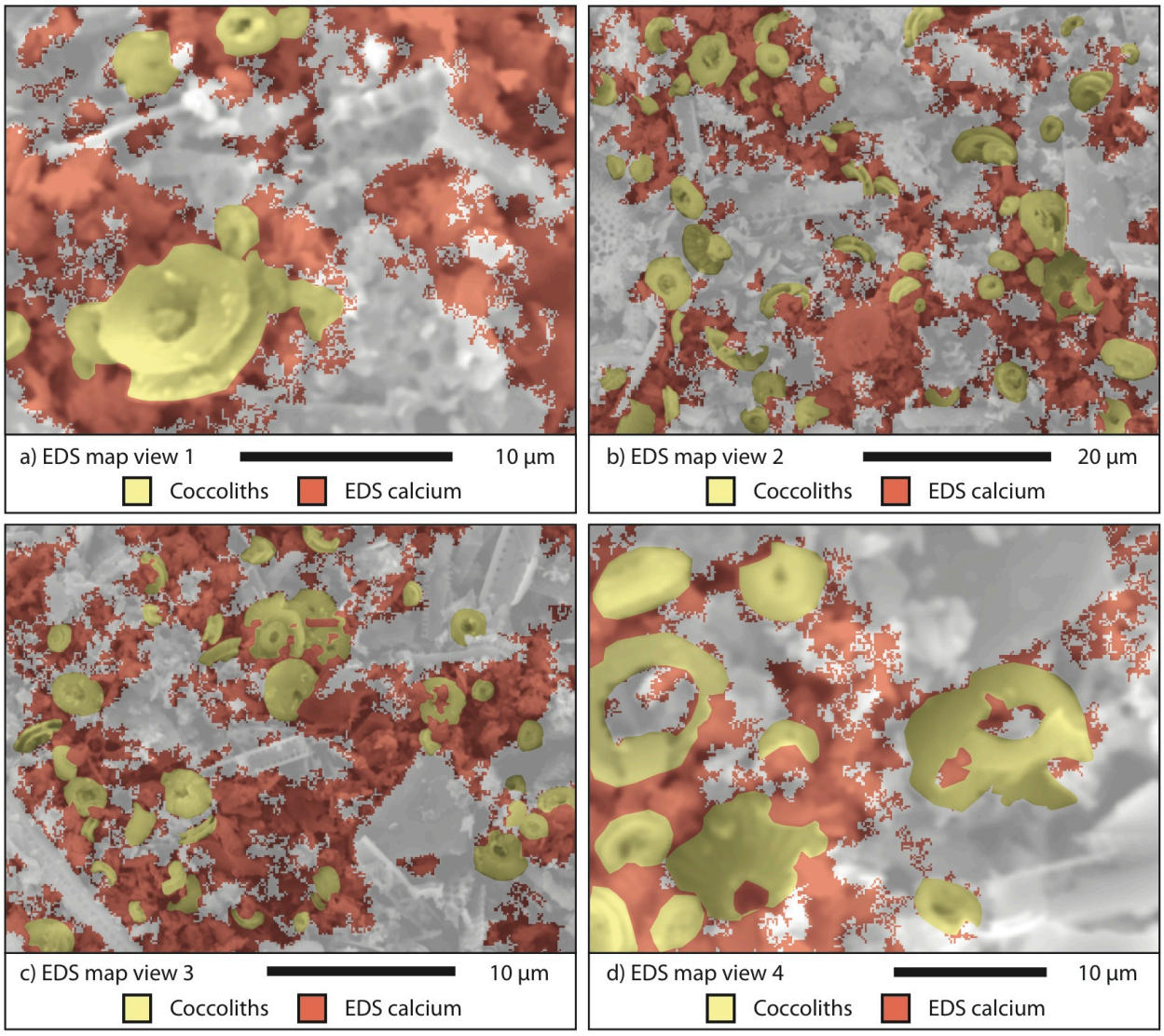

Figure 5.13. Overview of area analysis using the EDS-SEM Ca element map. The red area of each map is the traced extent of calcium in the area. The yellow areas are the particles clearly identifiable as coccolith calcite or fragments. For larger images, please see Appendix C.6.

areas of the four EDS overlays show that much of the smaller (<2 μm) fragments and particles, which were sometimes distinguishable as coccolith plate fragments, are all calcite.

Figure 5.13 shows the four images of sample c2 originally mapped using EDS in Figure 5.11. However, here only calcium (Ca – representing $CaCO_3$) EDS map is overlain in transparent red (Figure 5.13 – red areas). In addition, the areas that are clearly identifiable as heterococcoliths are highlighted in transparent yellow (Figure 5.13 – yellow areas). The proportion of red non-coccolith to yellow heterococcolith calcite is shown in Table 5.4. For three of the four maps, more than 50 % of the sample area is composed of heterococcolith calcite (Figure 5.13 b, c and d). Only the map shown in Figure 5.13.a. has around 25% coccolith calcite.

5.5. Discussion

5.5.1. Sea Surface Temperatures (SSTs) at Site U1338

5.5.1.1. Comparison of SSTs from Δ_{47}, Mg/Ca_{GS} and $U^{k'}_{37}$

The various sea surface temperature (SST) proxies measured at U1338 are shown in Figure 5.14. The fine fraction Δ_{47} measurements (2 – 5 μm fraction: this study; < 63 μm: John et al., 2012) record temperatures around 10 – 15 °C, which is on average ~ 12 to 16 °C cooler than both the planktic foraminiferal Mg/Ca_{GS} (~25 °C) and $U^{k'}_{37}$ (~ 27 °C) (Rousselle et al., 2013) SSTs. This temperature

Ratio Coccolith : Non Coccolith Calcite		
Area	*Coccolith calcite*	*Non-coccolith calcite*
Map 1	25%	75%
Map 2	52%	48%
Map 3	57%	43%
Map 4	55%	45%
Average	47%	53%

Table 5.4. Overview of the per cent coccolith versus non-coccolith calcite identified in Figure 5.12. The proportion of coccolith : non-coccolith calcite is given for each map and as an average of all four mapped areas.

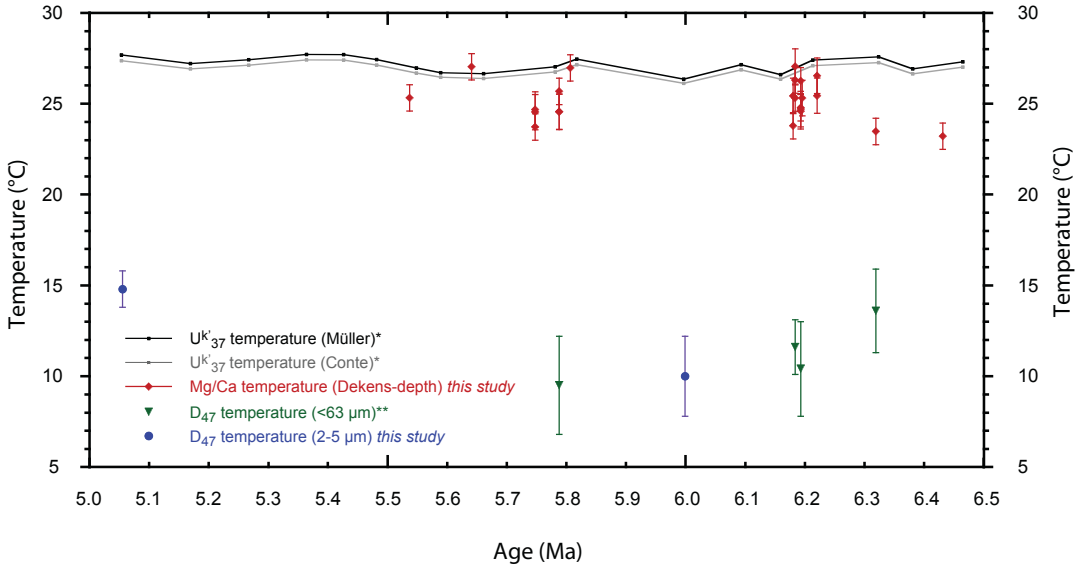

Figure 5.14. Comparison of all sea surface temperature proxies measured at Site U1338, including clumped isotope Δ^{47}, planktic foraminiferal Mg/Ca and $U^{k'}_{37}$.

Data sources: Mg/Ca ratios from planktic foraminiferal calcite – this study; clumped isotope measurements on the 2 – 5 µm fraction – this study; clumped isotope measurements from the < 63 µm fraction come from ** - John et al., 2012; Alkenone $U^{k'}_{37}$ temperatures are shown using two different calibrations (Müller et al., 1998; Conte et al., 2006), originally published by Rousselle et al., 2013.

difference is substantial. The potential reasons for the much cooler 2 – 5 μm fraction Δ_{47} temperatures are discussed in section 5.5.1.2. The Mg/Ca_{GS} and $U^{k'}_{37}$ records show better agreement in SSTs. The Mg/Ca_{GS} SSTs (25 ± 1.1 °C) are on average ~ 2 °C cooler than the $U^{k'}_{37}$ SSTs (~ 27 ± 0.4 °C), and also show a greater degree of variability than the alkenone SSTs (Figure 5.14).

The 2 °C negative offset and greater variability seen in the Mg/Ca_{GS} record could be caused by a number of factors. Firstly, the preservation of the planktic foraminifera *Globigerinoides sacculifer* (*Gs. sacculifer*) at Site U1338 is poor to fair (Figure 3.6 and section 3.5.1 Chapter 3). Both the preferential dissolution of Mg/Ca rich calcite, or recrystallisation at lower temperatures with calcite with a lower Mg/Ca value, could lower the measured Mg/Ca_{GS} at Site U1338. However, the Dekens et al., (2002) calibration used to convert the Mg/Ca_{GS} to SSTs, already takes dissolution in the water column into account by including a core-depth dependent correction factor (see section 5.3.1 for more information). Furthermore, Sexton et al. (2006) showed that the effect of diagenetic alteration of frosty planktic foraminifera on the measured Mg/Ca values was far lower than the effect seen on the $\delta^{18}O$ values. Unlike the increasing trend with increasing size seen in the Mg/Ca_{GS} ratios, which supports the retention of a primary Mg/Ca signal, the Sr/Ca_{GS} ratios show an ambiguous response with increasing size fraction. Elderfield et al. (2002) showed that Sr/Ca should show a comparable decreasing trend with increasing size fraction as the increasing trend seen in Mg/Ca. The absence of this negative trend could indicate some diagenetic influence on the trace element ratios. The Sr/Ca values of diagenetic calcite are very low, generally below 0.3 mmol/mol, whereas modern foraminiferal Sr/Ca generally lies above 1.3 mmol/mol (Kozdon et al., 2013). The fact that the

absolute Sr/Ca_{GS} values at Site U1338 are closer to modern foraminiferal Sr/Ca than they are to diagenetic Sr/Ca values, would suggest that diagenesis is of minimal influence. However, the slightly lower Sr/Ca_{GS} values compared to modern, and the lack of negative trend in the Sr/Ca could indicate some minor dissolution effects. This would concur with the dissolution of Mg/Ca expected with increasing water column depth, which is corrected for by using the Dekens et al. (2002) calibration.

An additional factor that could partially explain the increased variability in the Mg/Ca_{GS} record compared to the $U^{k'}_{37}$ values is that the sampling resolution of the Mg/Ca_{GS} record is higher across short intervals than the $U^{k'}_{37}$ record. The Mg/Ca_{GS} variability may therefore just reflect shorter-term variations that are not captured by the $U^{k'}_{37}$ record. Finally, the absolute differences between the Mg/Ca_{GS} and $U^{k'}_{37}$ values could arise because the planktic foraminifera *Gs. sacculifer* records the lower temperature of a slightly deeper water mass in the mixed layer compared to the alkenone producers. Although young *Gs. sacculifer* is thought to live in the upper 0 – 10 m (upper euphotic zone) (Bé, 1980; Spero and Lea, 1993), older specimens that have undergone gametogenesis are thought to calcify in the 50 – 75 m (Sadekov et al., 2009). Although care was taken to select specimen in narrow size fractions, the possibility that each size fraction included a range of *Gs. sacculifer* that calcified at different depths, cannot be excluded. Note that the inclusion of the larger size fractions samples (355 – 425 and 425 – 500 μm) after size fraction correction does not change the average or standard deviation of the complete Mg/Ca_{GS} dataset compared to the Mg/Ca_{GS} dataset including only the 250 – 355 μm Mg/Ca_{GS} data (all data – size corrected = 25.2 ± 1.1 °C; only 250 – 355 μm data = 25.3 ± 1.4 °C).

5.5.1.2. Evaluation of clumped isotope Δ_{47} SSTs

The comparison of the three SST proxies from Site U1338 highlighted that the temperatures calculated using Δ_{47} are unrealistically low for equatorial Pacific sea surface temperatures. The lower temperature obtained from Δ_{47} analyses of the < 63 μm fraction was attributed to the potential presence of thermocline and benthic foraminiferal fragments. Because these fragments precipitated at lower (thermocline or deep water) temperatures compared to mixed layer/sea surface temperatures, the fragments will have higher Δ_{47}. When mixed with the lower Δ_{47} from coccolith calcite, the overall sample Δ_{47} will increase, thereby giving artificially cold temperatures. The initial aim of measuring clumped isotope Δ_{47} on progressively smaller size fractions was to remove the foraminiferal fragments and concentrate the coccoliths, thereby obtaining a more accurate SST proxy. However, as is shown in Figure 5.8.a, there is no consistent trend of decreasing Δ_{47} with decreasing size fraction.

Because the samples selected for Δ_{47} analysis (c1 and c2) were chosen to be in close proximity to samples measured by Rousselle et al., 2013, direct comparison of SST and stable isotope results between the two studies is possible, and might help explain the low Δ_{47} temperatures. Figure 5.15.a shows the Δ_{47} measurements from the four separate size fractions from samples c1 and c2 compared to the nearest-sample $U^{k'}_{37}$ temperatures from Rousselle et al., 2013. All eight data points are lower than the $U^{k'}_{37}$ SSTs, although both sample c1 and c2 show a comparable temperature increase of almost 5 °C from the < 10 μm to the 2 – 5 μm fractions. For sample c1, there is also an overall significant temperature increase from the < 63 μm to the 2 – 5 μm fraction, which could

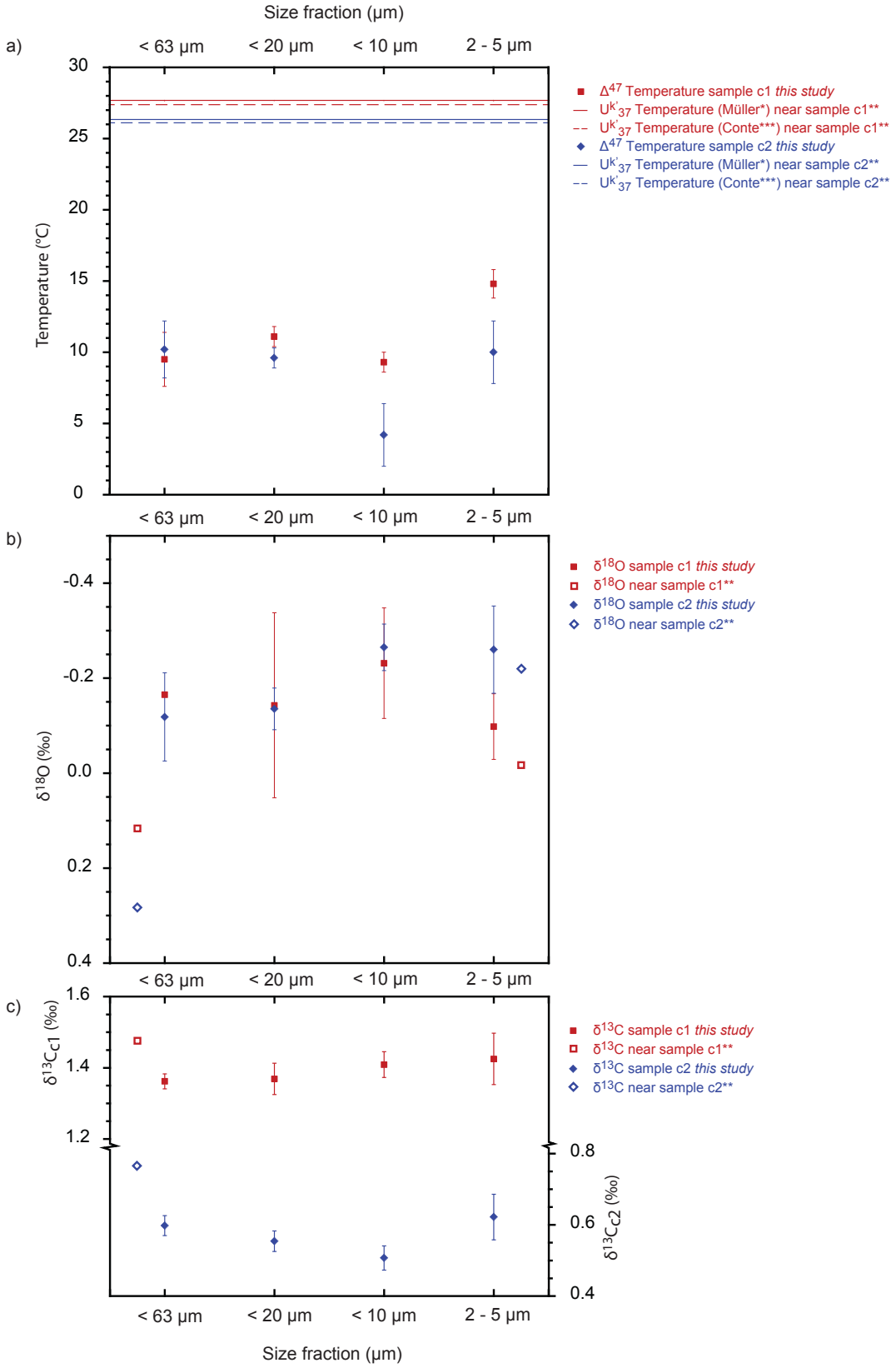

Figure 5.15. Comparing the a) Δ^{47} temperatures, b) $\delta^{18}O$ and c) $\delta^{13}C$ results from the four size fractions from sample c1 (red) and c2 (blue) to the a) $U^{k'}_{37}$ temperatures, b) bulk and 2 – 5 µm $\delta^{18}O$, and c) bulk $\delta^{13}C$ from contemporaneous samples from Rousselle et al., 2013.

reflect a reduction in the amount of benthic foraminiferal fragments present in the 2 – 5 μm fraction. However, this trend is not reproduced in sample c2.

Figure 5.15.b and c respectively show the < 63 μm $\delta^{18}O$ and $\delta^{13}C$ from samples c1 and c2 compared to the contemporaneous bulk $\delta^{18}O$ and $\delta^{13}C$ from the Rousselle et al. (2013). Both the bulk $\delta^{18}O$ and $\delta^{13}C$ are higher than the sample c1 and c2 < 63 μm fraction $\delta^{18}O$ and $\delta^{13}C$ values (0.3 – 0.4 ‰ for $\delta^{18}O$; 0.1 – 0.2 ‰ for $\delta^{13}C$). The higher bulk $\delta^{18}O$ could reflect the presence of a larger portion of benthic or thermocline planktic foraminifera, which precipitate at lower temperatures (higher $\delta^{18}O$), and which would, on average, increase the overall $\delta^{18}O$. However, the positive offset between the bulk and < 63 μm $\delta^{13}C$ values would not be explained by physical mixing of surface water calcite with benthic or thermocline foraminiferal calcite, as benthic foraminiferal $\delta^{13}C$ is normally lower than planktic foraminiferal mixed layer $\delta^{13}C$. Figure 5.15.b also shows the $\delta^{18}O$ values from the 2 – 5 μm fractions from samples c1, c2 and the Rousselle et al. (2013) dataset. Interestingly, the $\delta^{18}O$ values from the contemporaneous 2 – 5 μm fractions are very similar, with the c1 and c2 $\delta^{18}O$ being slightly lower than the Rousselle $\delta^{18}O$ values. The similarity of the 2 – 5 μm $\delta^{18}O$ values between this study and Rousselle et al. (2013) implies that both datasets are recording a higher than expected $\delta^{18}O$. This suggest that the offset between the Δ_{47} and $U^{k'}_{37}$ SSTs might be associated with the origin of the calcite in the 2 – 5 μm fraction.

As previously mentioned, the Δ_{47} measurements on coccolith-rich 2 – 5 μm material produced results unexpectedly low for sea surface temperatures. There are a number of factors and mechanisms that may have affected the Δ_{47} values of

the isolated 2 – 5 μm calcite fraction. These include the effectiveness of the size fraction separation, the presence of abiotic/diagenetic cements, coccolith preservation and coccolith vital effects. These factors will be discussed in the following paragraphs to determine whether they can account for the high Δ_{47}.

Size fraction separation

The BSE, SE and EDS analyses of the different size fractions of samples c1 and c2 show that the majority of the sediment is made up of calcite and silica (Figure 5.9, 5.10 and 5.12), supporting the sedimentary composition suggested by bulk and XRF measurements of the U1338 splice (Lyle et al., 2012; Lyle and Backman, 2013). The BSE SEM images show that the sieve-based separation method successfully removes the larger fragments from the smaller fractions (Figure 5.9. a, b, c, e, f and g), however the images also show that the centrifugation does not remove all larger diatom fragments (Figure 5.9. d and h). This is most likely because the centrifugation-separation methodology is based on Stokes' law, which assumes that the to-be-separated particles are spherical and have identical density. This is not the case for diatoms, as these are not always spherical, and are also hollow. Furthermore, the densities used to calculate the settling time were based on calcite, not silica. The BSE and SE images of the 2 – 5 μm fraction also show that the centrifugation technique does not successfully remove the < 2 μm particles (Figure 5.10). The origin of the high Δ_{47} may lie in the presence of these small particles, which will be discussed in the following paragraphs.

Abiotic/Diagenetic calcite

The EDS maps show that a large component of these small < 2 μm particles is made up of calcite (Figure 5.12). Although some of the particles are identifiable as heterococcolith or foraminiferal fragments, large numbers of the fragments are not definitively identifiable as biogenic (Figure 5.10). A proportion of these < 2 μm fragments could be disintegrated holococcoliths (Bown et al., 2008). However, a portion of this < 2 μm particles could be abiotic/diagenetic in origin. Considering the proportion of < 2 μm particles, if these particles were formed as micritic cements from cold pore waters during early diagenesis, the contribution of higher Δ_{47} to the overall sample could account for the offset between Δ_{47}- and $U^{k'}_{37}$-based SSTs. Even if a proportion of the < 2 μm particles consist of fragmented holococcoliths, it is possible that these could have undergone recrystallisation during early diagenesis at lower temperatures, thereby also contributing higher Δ_{47} to the overall sample. If the input of higher Δ_{47} and cold temperature calcite originates from the smallest particles in the sediment, this would also explain the lack of decreasing Δ_{47} with decreasing size fraction, as removing the larger sedimentary components does not affect the composition of the smaller components.

Area analysis of the Ca EDS maps (Figure 5.13) show that the proportion of coccolith calcite in the c2 sample is ~ 47 ± 15 % on average. Three maps show more than 50% coccolith calcite (Figure 5.13. b, c and d), whereas the fourth map shows there is only 25% coccolith calcite (Figure 5.13.a) (Table 5.4). The calcification temperature of this non-coccolith calcite can be approximated to see whether the mixing of the coccolith and non-coccolith calcite can account for the

Overview of calculated temperatures						
Area	*% Coccolith Calcite*	*Calculated BWT*	*Preditcted BWT (benthic Mg/Ca)*	*Temp Offset to benthic Mg/Ca*	*Preditcted BWT (benthic Mg/Ca including δ18O offset)*	*Temp offset to benthic Mg/Ca with δ18O offset*
Map 1	25%	3.5 °C	5.7 °C	2.2 °C	3.6 °C	0.1 °C
Map 2	52%	- 3.7 °C	5.7 °C	9.4 °C	3.6 °C	7.3 °C
Map 3	57%	- 5.0 °C	5.7 °C	10.6 °C	3.6 °C	8.6 °C
Map 4	55%	- 4.5 °C	5.7 °C	10.2 °C	3.6 °C	8.1 °C
Average	47%	- 2.4 °C	5.7 °C	8.1 °C	3.6 °C	6.0 °C

Table 5.5. Overview of the predicted temperatures based on estimated area using the EDS Ca maps from Figure 5.12. Predicted bottom water temperatures (BWT) using benthic foraminiferal Mg/Ca comes from Lear et al., 2003 (see Table 5.6).

Overview of parameters used for non-coccolith calcite temperature calculation			
Data	*Age*	*Value*	*Source*
Site U1338 modern T	present day	1.45 °C	World Ocean Database 2009 (Locarnini et al., 2010)
Site U1338 Late Miocene benthic δ18O	5999 ka	3.36 ‰	This study
Site U1338 Uk'37	5997 ka	26.34 °C	Rousselle et al., 2013
Site 806 modern T	present day	1.87 °C	World Ocean Database 2009 (Locarnini et al., 2010)
Site 806 Mg/Ca	6056 ka	5.67 °C	Lear et al., 2003
Site 806 Late Miocene benthic δ18O	5950 ka	2.84 ‰	Nathan and Leckie, 2009
Site 806 - U1338 inferred benthic δ18O T °C offset	offset 47 ka	2.08 °C	

Table 5.6. Overview of all data used to estimate the required temperature of the non-coccolith calcite to achieve the temperatures from the Δ_{47} measurements.

observed temperature offset. The complete sample c2 calcite from the 2 – 5 μm fraction has a temperature of 10.0 °C (Table 5.2). The coccolith calcite precipitation temperature can be inferred from the contemporaneous $U^{k'}_{37}$ temperature, which is 26.3 °C (Table 5.2). As the ratio of non-coccolith to coccolith calcite is known for sample c2, the calcification temperature of the non-coccolith calcite needed to obtain the measured Δ_{47} temperature can be calculated (Table 5.5).

For the areas with more than 50% coccolith calcite, the non-coccolith calcite would have had to precipitate between – 5 and – 3.5 °C (Table 5.6). It is immediately clear that the approximate non-coccolith calcite precipitation temperatures are unfeasibly cold. In addition, considering that modern bottom water temperatures at Site U1338 are already 1.5 °C (Table 5.6; also see section 2.2.1 in chapter 2, and Figure 2.3), such low temperatures are unrealistic. The only late Miocene estimates for deep-sea temperatures in this region come from ODP Site 806 in the Western equatorial Pacific, where Mg/Ca measurements on benthic foraminifera indicate bottom water temperatures of 5.6 °C (Lear et al., 2002; Table overview) at the same time as sample c2 was deposited at Site U1338. The offset between the inferred non-coccolith temperatures and the Site 806 temperature is equally unrealistic, with Site U1338 being colder by a range between 9 and 11 °C for the samples with more than 50 % coccolith calcite. However, the non-coccolith temperature from the EDS map of sample c2 with only 25 % coccolith calcite shows only a 2 °C offset with the Site 806 deep-water temperatures. Site 806 is a lot shallower than Site U1338 (2500 m compared to 4200 m current water depth), which is reflected in an offset of ~ 0.5 ‰ between the benthic foraminiferal $\delta^{18}O$ values at both sites and equates to a temperature

difference of ~ 2 °C (Table 5.6). Even incorporating this additional 2 °C decrease in potential bottom water temperature at Site U1338 (3.6 °C), there is still a 7 – 9 °C offset between this temperature and the calculated non-coccolith temperatures for the areas with more than 50 % coccolith calcite. However, the calculated non-coccolith temperature for the area with only 25% coccolith calcite is nearly identical as the calculated Site U1338 bottom water temperature (See Table 5.5).

The above discussion about possible processes to explain the low Δ_{47} contains a number of assumptions, both about the inferred SST and bottom water temperatures at Site U1338, and about relating proportions in surface area of two components to volume. However, the approach does indicate that the presence of the small non-coccolith fragments could account for part of the Δ_{47}-based SSTs offset from the $U^{k'}_{37}$-based SSTs. For this mechanism to account for the complete offset, ~ 75 % of the calcite would have to be bottom water in origin, even when taking the implied East – West temperature gradient into account. This coccolith – non-coccolith calcite ratio is present in one map (Figure 5.13). However, the average non-coccolith proportion is ~ 20 % lower than required, although it is possible that the amount of coccoliths were overestimated in the tracing process (yellow areas – Figure 5.13). In addition, the above area analysis also assumes that most of the < 2 μm calcite particles were abiotic in origin. This assumption excludes the possibility that any disintegrated holococcoliths are present and preserve their primary calcite signal.

Coccolith preservation

Because of the difference between the observed and required proportion of non-coccolith calcite in the fine fraction sediment, it is likely that additional mechanisms are contributing to the overall Δ_{47}- $U^{k'}_{37}$ based SSTs offset. The preservation state of the coccolith calcite could affect the overall sample Δ_{47} value, as both overgrowth and recrystallisation at bottom water temperatures could have reduced the proportion of surface-water calcite contributing to the overall Δ_{47}. The SE-SEM study could not resolve sufficiently high spatial resolution to determine whether any of the large or complete heterococcolith fragments had undergone recrystallisation. However, recrystallisation is not often seen in heterococcolith calcite, because of the large crystal size of the individual calcite crystals. For this reason, overgrowth with secondary diagenetic calcite is more likely to be a concern for heterococcolith preservation. As shown in the SE-SEM results in section 5.4.3.1, the coccoliths investigated only show moderate, or poor to moderate preservation. Many heterococcoliths show evidence for secondary calcite overgrowth (Figure 5.11. d and f), and the proportion of coccolith to non-coccolith calcite, this could have contributed further diagenetic calcite to the overall signal. In addition, as none of the heterococcoliths have central structures that are preserved (Figure 5.11), slight to moderate etching must have occurred, which could have further decreased the proportion of surface water calcite present in the sample.

Coccolith vital effects

A further mechanism that may affect the average Δ_{47} of the coccolith-calcite is the presence of 'vital effects' that occur due to the way coccolithophores

precipitate their calcite exoskeletons, which may fractionate the Δ_{47} values away from the inorganic calcite values. Most biogenic material, including past work on coccolithophores (Tripati et al., 2010), does not show any vital effect offsets in biogenic Δ_{47} (i.e. it falls within the 95% confidence limits of the inorganic calcite Δ_{47} – temperature relationship), even when the bulk isotopic composition experiences considerable offsets driven by vital effects. However, some studies have shown that certain groups show offset Δ_{47} – temperature relationship when compared to the inorganic calcite line (molluscs and brachiopods – Henkes et al., 2013; shallow water corals – Saenger et al., 2012). It is feasible that the additional Δ_{47}- $U^{k'}_{37}$ SSTs offset is caused by a coccolithophore vital effect.

One mechanism that could drive Δ_{47} offsets due to vital effects in coccolithophores is pH. Some research has shown that pH ranges found in the ocean (7.6 – 8.6 – Stoll et al., 2012) does not cause additional fractionation of Δ_{47} (Tripati et al., 2010). However, the full effects of higher or lower pH on Δ_{47} are not yet fully understood, although initial studies indicate that Δ_{47} increases with both these cases (Guo et al., 2012; Hill et al., 2013; Kluge et al., in prep-b). Coccolithophores precipitate their coccolith plates from an internal vesicle, which can have different pH to the surrounding water (Stoll et al., 2012). The exact pH of the vesicle is not well constrained, although some research has suggested the pH can be as low as 6.4 – 7.2, or 7.6 – 8.3 or higher in some instances (Anning et al., 1996; Stoll et al., 2012). A combination of vesicle pH and cell size is known to induce a 'vital effect' fractionation of up to 5 ‰ in the $\delta^{18}O$ and $\delta^{13}C$ values (Ziveri et al., 2003). The possibility that vital effects might drive an additional fractionation in Δ_{47}, is potentially supported by work by Bolton and Stoll (2012), who show that there is a sudden spread in the amount of stable

isotope fractionation between different size coccolith(ophores) between 7.0 and 5.0 Ma. This coincides well with the interval where Δ_{47} was measured at Site U1338. In addition, the comparison of planktic foraminiferal and bulk $\delta^{18}O$ and $\delta^{13}C$ in sections 5.5.2 and 5.5.3 (specifically Figures 5.17 and 5.19) show that the bulk $\delta^{18}O$ and $\delta^{13}C$ values are generally offset to higher $\delta^{18}O$ and lower $\delta^{13}C$ compared to the planktic foraminiferal isotopic values. It is conceivable that the same mechanism that drives the fractionation in the conventional stable isotopes on the Site U1338 samples may also drive fractionation in the Δ_{47}.

Despite the large offset seen in this study between Δ_{47} and $U^{k'}_{37}$ inferred SSTs, Δ_{47} measurements on coccolith-rich sediments still have potential as a SST proxy. In the case of Site U1338, removal of the small (< 2 μm) non-coccolith fragments, and concentration of a narrow range of coccolith plates will reduce the influence of the non-coccolith calcite on the overall Δ_{47} value. Considering the conventional stable isotope fractionation seen between narrow size fractions by Bolton and Stoll (2012), isolating a narrow size fraction would be advisable, as this may also allow any vital effects on Δ_{47} to be reduced or at least constrained. The microfiltration technique proposed by Minoletti et al. (2009), which is also applied by Rousselle et al. (2013), would be a feasible methodology to apply to isolate a narrow size fraction. Finally, a better fundamental understanding of the potential coccolithophore vital effects on Δ_{47} is required, as the results from this study suggest that there is a vital effect driving higher Δ_{47} values than otherwise expected. It is also worth noting, that due to the measurement error associated with Δ_{47}, this proxy will mainly be suitable for studying large long-term shifts in temperature, or large absolute temperature differences between regions.

5.5.2. Productivity and Upwelling – Inferences from Sedimentation Rates and $\delta^{13}C$ Records

The late Miocene to early Pliocene Biogenic Bloom is generally thought to have occurred between 8.0 and 4.5 Ma throughout the Atlantic, Indian and Pacific Oceans in both upwelling and oligotrophic regions (Hermoyian and Owen, 2001; Grant and Dickens, 2002; Diester-Haass et al., 2005; see section 2.1.2). The driving force of the Biogenic Bloom has not yet been completely determined (Diester-Haass et al., 2006). Although primary surface water productivity is known to dominate the present-day equatorial Pacific upwelling region (Palike et al., 2010), the exact extent and duration of the Biogenic Bloom at Site U1338 has not yet been established. The next paragraphs investigates the nature of the sedimentary deposition cycles at Site U1338 and discuss what this implies about the timing and duration of the Biogenic Bloom at Site U1338. The latter part of this section explores the proposed mechanisms that could have caused the Biogenic Bloom in more detail. This section also includes a detailed discussion of the available sea surface and deep-water carbonate $\delta^{13}C$ records from Site U1338 to see what these imply about the surface water nutrient distribution and the cause of the Biogenic Bloom.

The high-resolution SEM and EDS images (Figure 5.10 and 5.12) show that in addition to the main two components (biogenic SiO_2 and $CaCO_3$), there is also some marine barite present (Figure 5.12 a, b, c and d). XRF measurements on the U1338 core splice indicate that there is $BaSO_4$ present throughout the late Miocene and early Pliocene (ranging from 0.5 to 2 weight %) (Lyle et al., 2012). The small size (1 – 2 μm) and euhedral to sub-spherical shape of crystals (Figure

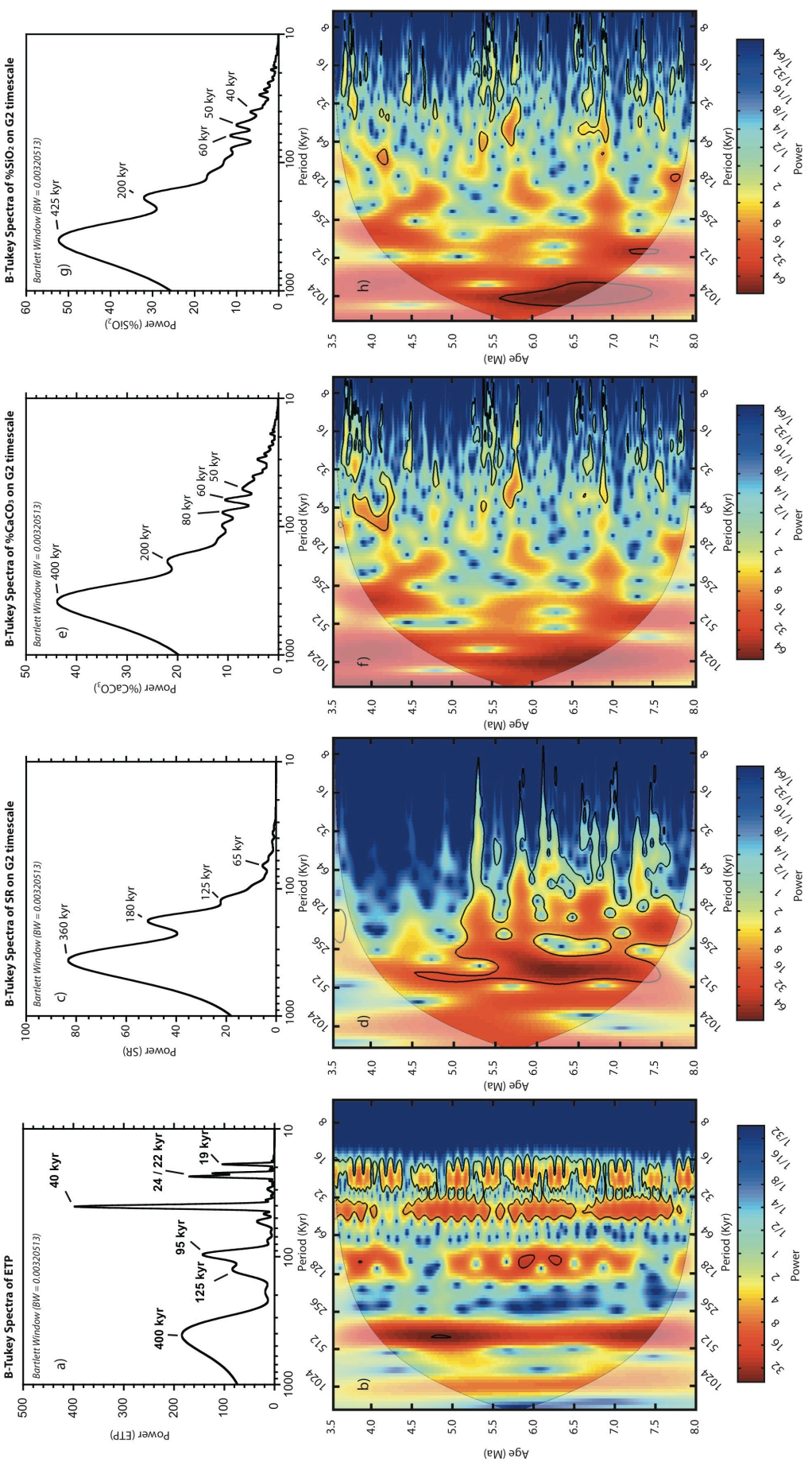
B-Tukey Spectra of ETP
Bartlett Window (BW = 0.00320513)
a)
400 kyr
125 kyr
95 kyr
40 kyr
24 / 22 kyr
19 kyr
Power (ETP)
B-Tukey Spectra of SR on G2 timescale
Bartlett Window (BW = 0.00320513)
c)
360 kyr
180 kyr
125 kyr
65 kyr
Power (SR)
B-Tukey Spectra of %CaCO3 on G2 timescale
Bartlett Window (BW = 0.00320513)
e)
400 kyr
200 kyr
80 kyr
60 kyr
50 kyr
Power (%CaCO3)
B-Tukey Spectra of %SiO2 on G2 timescale
Bartlett Window (BW = 0.00320513)
g)
425 kyr
200 kyr
60 kyr
50 kyr
40 kyr
Power (%SiO2)
b)
d)
f)
h)
Age (Ma)
Period (Kyr)
Power

Figure 5.16.

Overview of the B-Tukey and wavelet analyses of the external radiative forcing (ETP - a and b), and sedimentation rates (c and d), $\%CaCO_{3\_BULK/XRF}$ (e and f) and $\%SiO_{2\_XRF}$ (g and h) from Site U1338.

The sedimentation rates (c and d), $\%CaCO_{3\_BULK/XRF}$ (e and f) and $\%SiO_{2\_XRF}$ (g and h) from Site U1338 all show strong power around the 400 and 200 kyr bandwidths. The 400 kyr power is likely a response to long-term eccentricity forcing (a and b), however there is no external forcing in the 200 kyr band width.

The B-Tukey spectrum was calculated using Analyseries (Paillaird et al., 1996 - version 2.0.4.2), using a Bartlett window (bandwidth = 0.00320513). The wavelet analysis was calculated in Matlab using the Torrence and Compo, 1998 protocol, republished by Grinsted et al., 2004.

The $\%CaCO_{3\_BULK/XRF}$ and $\%SiO_{2\_XRF}$ records are published in Lyle and Backman, 2013; Lyle et al., 2012.

5.12.a and b) indicates the barite is marine barite, rather than hydrothermal or diagenetic barite (Paytan et al., 2002). Marine barite is precipitated in the upper water column during the degradation of organic material, potentially aided by zooplankton and/or bacteria (Griffith and Paytan, 2012). The presence of marine barite in the U1338 sediments supports the claim that the main flux to the seafloor consisted of biogenic (and not, for instance, terrestrial) material, as marine barite forms organic-rich fluxes in the water column. The SEM images of the fine fraction also show that the $CaCO_3$ and SiO_2 components in the sediment are predominantly biogenic in origin (Figure 5.10 and 5.12). Overall, the SEM study supports the claim that the $CaCO_3$ and SiO_2 sedimentation in the equatorial Pacific region during the late Miocene to early Pliocene is driven predominantly by biogenic cycles in surface water productivity (Lyle et al., 2012; Lyle and Backman, 2013).

Comparing the dominant variability of the sedimentation rates (SR_{U1338}) reconstructed for Site U1338 using the high-resolution age model (Chapter 4), together with the $CaCO_3$ and SiO_2 records (Lyle and Backman, 2013; Lyle et al., 2012) could help constrain the duration of the Biogenic Bloom at Site U1338. The SR_{U1338}, $\%CaCO_{3\_BULK/XRF}$ and $\%SiO_{2\_BULK}$ are analysed using the B-Tukey power series and the wavelet analysis shown in Figure 5.16. The SR spectrum has an interesting cyclic variability, as do the $\%CaCO_{3\_BULK/XRF}$ and $\%SiO_{2\_BULK}$ spectra. The SR_{U1338} B-Tukey spectrum shows a high power at ~ 380 and 180 kyr), whereas the $\%CaCO_{3\_BULK/XRF}$ and $\%SiO_{2\_BULK}$ have strong power around 400 and 425 kyr respectively, as well as a peak around 200 kyr. The SR_{U1338} wavelet (Figure 5.16 d) shows a strong response to both the ~ 400 and 200 kyr forcing, possibly combined with some minor forcing at the shorter-term eccentricity

scale, around 125 and 90 kyr. The $\%CaCO_{3\_BULK/XRF}$ (Figure 5.16 f) and $\%SiO_{2\_BULK}$ (Figure 5.16 h) wavelet analyses are remarkably similar to each other, although their wavelets do not show as strong or continuous a power in the ~400 kyr band as the SR_{U1338} wavelet. However, the high power in the 200-kyr band is similar in all three wavelets ($\%CaCO_{3\_BULK/XRF,}$ $\%SiO_{2\_BULK}$ and SR_{U1338}). This high power cannot be immediately linked to any Milankovitch forcing shown in the wavelet of the predicted external forcing (Figure 5.16 b). This raises interesting questions about the forcing that drives sedimentation rates in this region. The similarity in the wavelets from SR_{U1338}, $\%CaCO_{3\_BULK/XRF}$ and $\%SiO_{2\_BULK}$ supports the claim that that there is strong biogenic control on the sedimentation rates.

Considering that the deposition and preservation of biogenic sediments in this region is mainly controlled by primary productivity, the strong power around 400 kyr in all three records (SR_{U1338}, $\%CaCO_{3\_BULK/XRF}$ and $\%SiO_{2\_BULK}$) indicates that there is a strong long-term eccentricity based forcing on productivity. Furthermore, the 200 kyr power in the U1338 sedimentary records suggest that productivity may be driven by a strong 'unknown' forcing centred around 200 kyr. This 200-kyr power could reflect a non-linear climate response to external radiative forcing, for instance a double a short-term eccentricity cycle, or reflect forcing through another mechanism. A potential forcing that could have caused the 200-kyr-power band in the SR_{U1338} and $\%CaCO_{3\_BULK/XRF}$ and $\%SiO_{2\_BULK}$ records is the bloom of opportunistic species to low eccentricity intervals (Rickaby et al., 2007). Rickaby et al. (2007) proposed that during a low eccentricity orbit (e.g. more circular – see section 4.2.1), a more continuous level of light intensity throughout the year might enhance the coccolithophore season length, and result in blooms of opportunistic coccolithophore species. Beltran et

al. (2014) have proposed that a coccolithophore acme (intervals with a monospecific dominance of a specific coccolithophore species) around 8.6 Ma at Site U1338 could be related to this low-eccentricity forcing. It is possible that the 200-kyr cyclicity seen in the SR_{U1338}, $\%CaCO_{3\_BULK/XRF}$ and $\%SiO_{2\_BULK}$ records is a non-linear response to this forcing as well.

The high power in the 400 and 200 kyr bands is not equally strong throughout the SR_{U1338}, $\%CaCO_{3\_BULK/XRF}$ and $\%SiO_{2\_BULK}$ wavelets. The high power in the 400-kyr band decreases in power after 5.5 – 5.0 Ma in all three wavelets. The power in the 200-kyr band greatly decreases in the SR_{U1338} wavelet after 5.0 Ma, although there is some power in that band again around 4.5 Ma. The $\%CaCO_{3\_BULK/XRF}$ and $\%SiO_{2\_BULK}$ wavelets also show a reduction of power in the 200-kyr band between 5.5 and 5.0 Ma, which recovers around 4.5 Ma. The reduction in power in both the 400 and 200 kyr bands after about 5.5 Ma could either indicate that preservation at Site U1338 decreases, or that primary productivity above Site U1338 is reduced after 5.5 Ma. CCD reconstructions indicate that the CCD remains deep around 5.5 Ma (Palike et al., 2012), which therefore is unlikely to have driven the reduction in sedimentation rates after 5.5 Ma. Reduction in surface water productivity could be a reflection of Site U1338 leaving the main productivity zone of ± 2 ° around the equator (Palike et al., 2010), or an indication that productivity decreased overall after 5.5 Ma, signifying the end of the Biogenic Bloom at Site U1338. Past reconstructions of sedimentation rates at other sites experiencing this Biogenic Bloom have displayed high sedimentation rates up till 4.0 Ma, although initial decreases were seen around 5.0 Ma (Pisias et al., 1995; Grant and Dickens, 2002). Considering the timing of the decrease in wavelet power, the reduction in sedimentation

rates at Site U1338 most likely reflects a combination of both the site leaving the equatorial main productivity zone and of the end of the Biogenic Bloom.

The mechanisms driving the Biogenic Bloom and widespread high sedimentation rates are not yet fully understood, but would require an increase in nutrient influx into the surface waters. A change in the global distribution patter of nutrients through the reallocation of nutrients from one region or ocean basin to surface regions through changing circulation patterns and increased upwelling has been proposed as one mechanism to cause widespread productivity (Pisias et al., 1995; Grant and Dickens, 2002). An alternative mechanism that has been proposed is an increase in the overall nutrient influx into the ocean, either through increased chemical weathering or by an increased dust flux into the surface ocean (Pisias et al., 1995; Hermoyian and Owen, 2001; Diester-Haass et al., 2006). Both these mechanisms are applicable to Site U1338, as the site lies in the present day equatorial upwelling region (Palike et al., 2010) and increased aridity on the North and South American interiors (Filippelli, 1997; Lyle et al., 2008) could provide a dust source. The uplift of the Himalayas around 10 – 8 Ma is connected to intensification of the Indian and Asian monsoon systems and the intensification of the trade winds (Filippelli, 1997; An et al., 2001), and the increased erosion during uplift could have provided an additional source of dust (Filippelli, 1997). Increased nutrient flux to the surface region due to increased upwelling has also been proposed for the equatorial Pacific region. Further restriction of the Central American Seaway (CAS) has been linked to increased upwelling and a shallower thermocline (Pisias et al., 1995; Grant and Dickens, 2002). However, modelling and proxy studies have

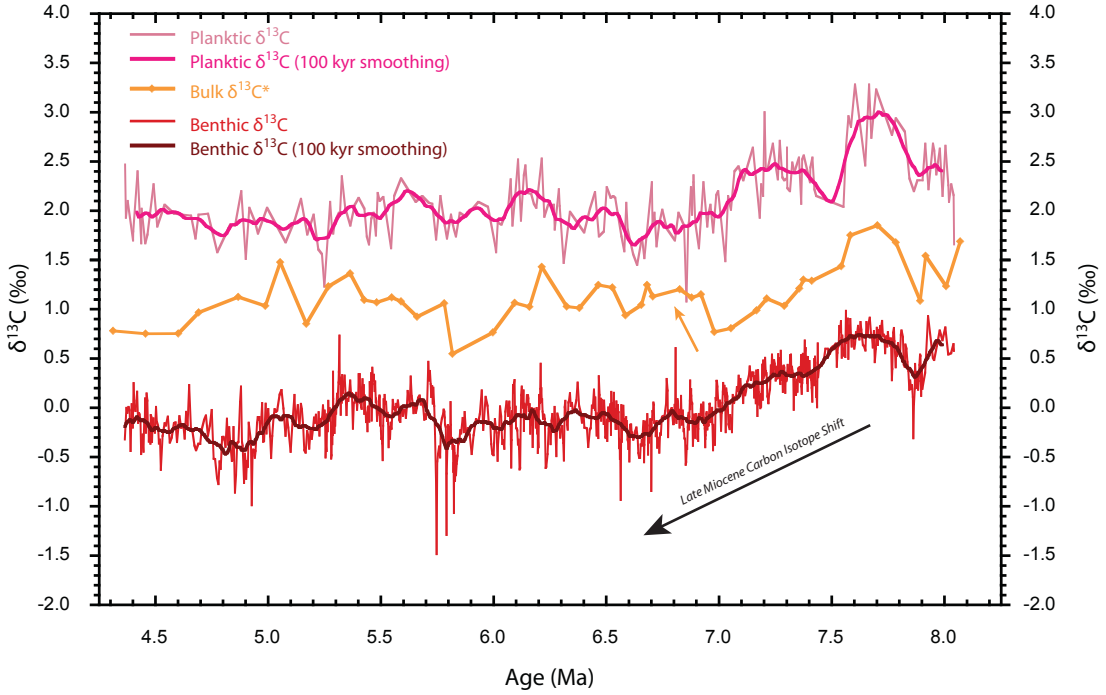

Figure 5.17. Overview of the planktic (pink) and benthic (red) foraminiferal and bulk sediment (orange – from *Rousselle et al., 2013) $\delta^{13}C$ records from Site U1338. To highlight the long-term trend, the planktic and benthic foraminiferal $\delta^{13}C$ records have been plotted with a 100-kyr smoothed record. A black arrow marks the LMCIS and an orange arrow denotes the point where the bulk $\delta^{13}C$ trend diverges from the planktic and benthic foraminiferal $\delta^{13}C$ (around 7.0 Ma).

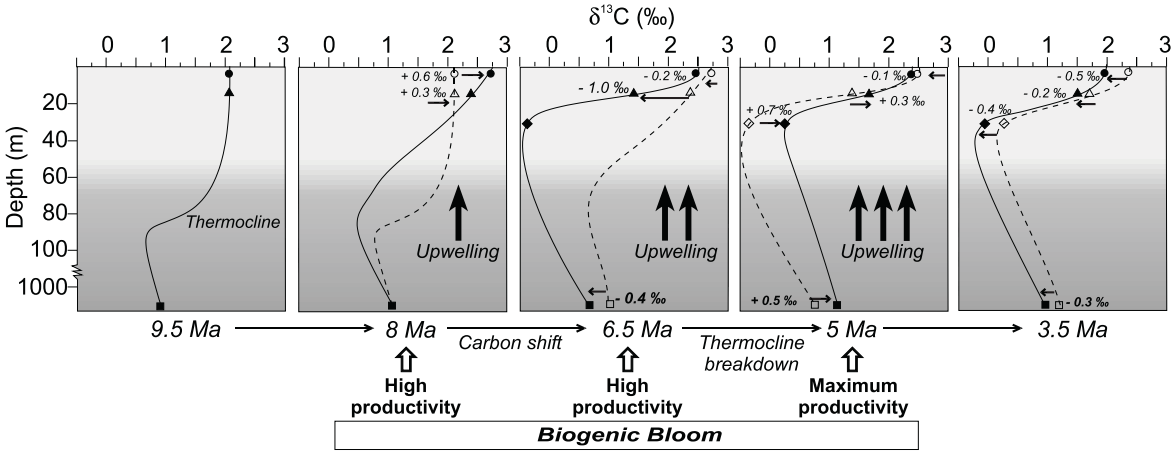

Figure 5.18. Schematic from Grant and Dickens (2002) of the interaction of the Biogenic Bloom, upwelling and the changes in the $\delta^{13}C$ values from bulk (circle -with a 1 ‰ addition to correct for the vital effects on coccolith $\delta^{13}C$ – see Grant and Dickens, 2002 for more information), planktic mixed (triangle), planktic thermocline (diamond) and benthic foraminiferal $\delta^{13}C$ (square). In each figure, the solid line denotes the current thermocline for the image time period. The dashed line denotes the thermocline from the earlier image time period.

indicated that the thermocline is deeper in the eastern equatorial Pacific when the CAS is open (Zhang et al., 2012; LaRiviere et al., 2012).

Because carbon isotopes in biogenic material, particularly in planktic and benthic foraminifera, reflect the local $\delta^{13}C_{DIC}$, looking at surface to deep $\Delta\delta^{13}C$ gradients can be used to deconvolve changes in surface productivity versus changes in global reservoir $\delta^{13}C$, as well as help reconstruct water-mass distribution in the surface waters (see section 3.2.1.2 in chapter 3). The initial comparison of benthic and planktic foraminiferal $\delta^{13}C$ in section 3.6.1 (chapter 3) suggested that the covariance in the oldest section of the record, identified as the late Miocene carbon isotope shift, reflects an oceanic reservoir-wide change in $\delta^{13}C$. Here we look in more detail at the different trends in the bulk (Rousselle et al., 2013), planktic and benthic foraminiferal $\delta^{13}C$ records between 8.0 and 4.4 Ma to see whether this gives more insight into changes in productivity at Site U1338 (Figure 5.17). This overview reveals a 2.0 to 2.5 ‰ offset between the more positive planktic and more negative benthic foraminifera, reflecting the preferential uptake of ^{12}C during organic matter formation in the surface regions (pink and red records – Figure 5.17). The bulk $\delta^{13}C$ also shows an offset from the other records, placing it ~ 1 ‰ lower than the planktic foraminiferal $\delta^{13}C$ and ~ 1 ‰ higher than the benthic foraminiferal $\delta^{13}C$ (orange record – Figure 5.17). This offset is counterintuitive, as the coccolithophores that dominate the bulk $\delta^{13}C$ live in a similar environment as the planktic foraminiferal $\delta^{13}C$, so would be expected to have a similar, if not slightly higher $\delta^{13}C$ value. The placement of the bulk $\delta^{13}C$ between the planktic and benthic foraminiferal calcite is most likely an effect of strong vital effects that fractionate coccolith calcite $\delta^{13}C$ and $\delta^{18}O$ by up to 5 ‰ (Ziveri et al., 2003; discussed in section 5.5.1.2. above). However it could

also partially be due to the presence of the small (< 2 μm), potentially early-diagenetic particles (see Figure 5.10 and discussion in section 5.5.1.2) that may have deep-sea $\delta^{13}C$ values. Although the recent work by Bolton and Stoll (2012) showed these vital effects did not emerge until the late Miocene, past studies comparing bulk – planktic and benthic foraminiferal $\delta^{13}C$ during the Biogenic Bloom have assumed these vital effects are constant as long as the coccolithophore assemblage did not change during the studied interval (Grant and Dickens, 2002; Ziveri et al., 2003). With this assumption, some studies have applied a correction factor to bring the bulk and planktic foraminiferal $\delta^{13}C$ together (Grant and Dickens, 2002), thereby enabling them to reconstruct the thermocline using $\delta^{13}C$ gradients at different stages during the Biogenic Bloom. Although the coccolith assemblages at Site U1338 remain fairly comparable between 8.0 and 4.4 Ma (Palike et al., 2010; Rousselle et al., 2013) and a study by Beltran et al. (2014) showed that comparable bulk to planktic $\delta^{13}C$ offsets existed between 8.9 and 8.4 Ma, no correction was applied to the current data. Instead, the trends and relative changes, rather than the absolute values are compared.

From 8.0 to 7.0 Ma, the trends and relative changes in the bulk, planktic and benthic foraminiferal $\delta^{13}C$ agree well, showing a broad maximum, followed by a negative shift of ~ 1.5 ‰ in the planktic and benthic foraminiferal records, and ~ 1 ‰ in the bulk record starting at 7.6 Ma (Figure 5.17). After 7.0 Ma, the bulk record returns to more positive values, whereas the planktic and benthic foraminiferal records continue decreasing until 6.6 Ma. The bulk record remains positive until around 4.7 Ma, with the exception of a brief interval between 6.1 and 5.7 Ma. The benthic and planktic foraminiferal records initially both remain

quite stable, until the benthic foraminiferal record increases between 5.8 and 5.2 Ma, followed by a return to pre-5.8 Ma values. Between 5.8 – 5.2 Ma, the temporary convergence of the planktic and benthic foraminiferal $\delta^{13}C$ could indicate an interval of decreased surface water productivity. In the intervals before 5.8 and after 5.2 Ma, the $\Delta\delta^{13}C$ between benthic and planktic foraminiferal calcite is larger, possibly signifying intervals of higher primary productivity in the surface realms.

The fact that all three records show the same shape during the first part of the LMCIS, between 8.0 and 7.0 Ma suggests that all three records strongly reflect a change in the $\delta^{13}C$ of the overall oceanic reservoir. Unlike other bulk-planktic-benthic foraminiferal $\delta^{13}C$ comparisons in the western Pacific where the bulk $\delta^{13}C$ does not shift to negative values until 5.5 Ma (Grant and Dickens, 2002), the bulk $\delta^{13}C$ at Site U1338 follows the same decreasing pattern as the planktic and benthic foraminiferal $\delta^{13}C$ records until 7.0 Ma, after which the bulk $\delta^{13}C$ diverges to more positive values than the benthic and planktic foraminiferal $\delta^{13}C$ records. This divergence could be driven by two mechanisms. Firstly, the positive trend of the bulk record starts at 7.0 Ma, and continues until 4.7 Ma, which coincides with the interval in which vital effects on coccolithophores could first develop (Bolton and Stoll (2012). The positive $\delta^{13}C$ shift in bulk carbonate may be a reflection of these emergent vital effects (see Figure 5.17). A detailed study of coccolith size distribution and assemblages at Site U1338 would be needed to determine this relationship. However, as Beltran et al. (2014) found similar offsets between 8.9 and 8.4 Ma, it is unlikely that these offsets developed much in the following interval. A second explanation could be that an increased stratification of water masses with different $\delta^{13}C$ due to upwelling, coupled with

increased productivity, would cause the bulk $\delta^{13}C$ (reflecting uppermost water layer) to become more positive, whereas the mixed layer planktic foraminiferal $\delta^{13}C$ (reflecting lower water mass) either decreases or remain unchanged (Figure 5.18) (Grant and Dickens, 2002). If this mechanism is correct, an interval of increased upwelling between 7.0 and 4.7 Ma is expected, which would agree well with the published ages of the Biogenic Bloom. The reduction in productivity suggested by the planktic – benthic foraminiferal $\Delta\delta^{13}C$ between 5.8 and 5.2 Ma does not agree with constant productivity between 7.0 and 4.7 Ma; however, overall the 7.0 – 4.7 Ma interval agrees well with the timing of the high-sedimentation rates discussed earlier. This overlap of the Biogenic Bloom with the potential upwelling interval between 7.0 and 4.7 Ma, suggests that the biogenic bloom was driven by the upwelling of nutrient-rich waters, as opposed to an increase in nutrient input from terrestrial sources. However, this study cannot exclude the influence of an additional nutrient influx from dust, which is conceivable, as regional studies have shown an increase in aeolian dust input into the eastern equatorial Pacific between ~ 8 and 5 Ma (Hovan, 1995).

5.5.3. Equatorial Pacific Climate Evolution and state of El-Niño-Southern Oscillation

Figure 5.19 provides an overview of the various $\delta^{18}O$ records and temperature records available at Site U1338. Bulk and 2 – 5 μm fraction $\delta^{18}O$ show higher values than the planktic foraminiferal $\delta^{18}O$ lower values than the benthic foraminiferal $\delta^{18}O$. This offset is similar to the offset found between the

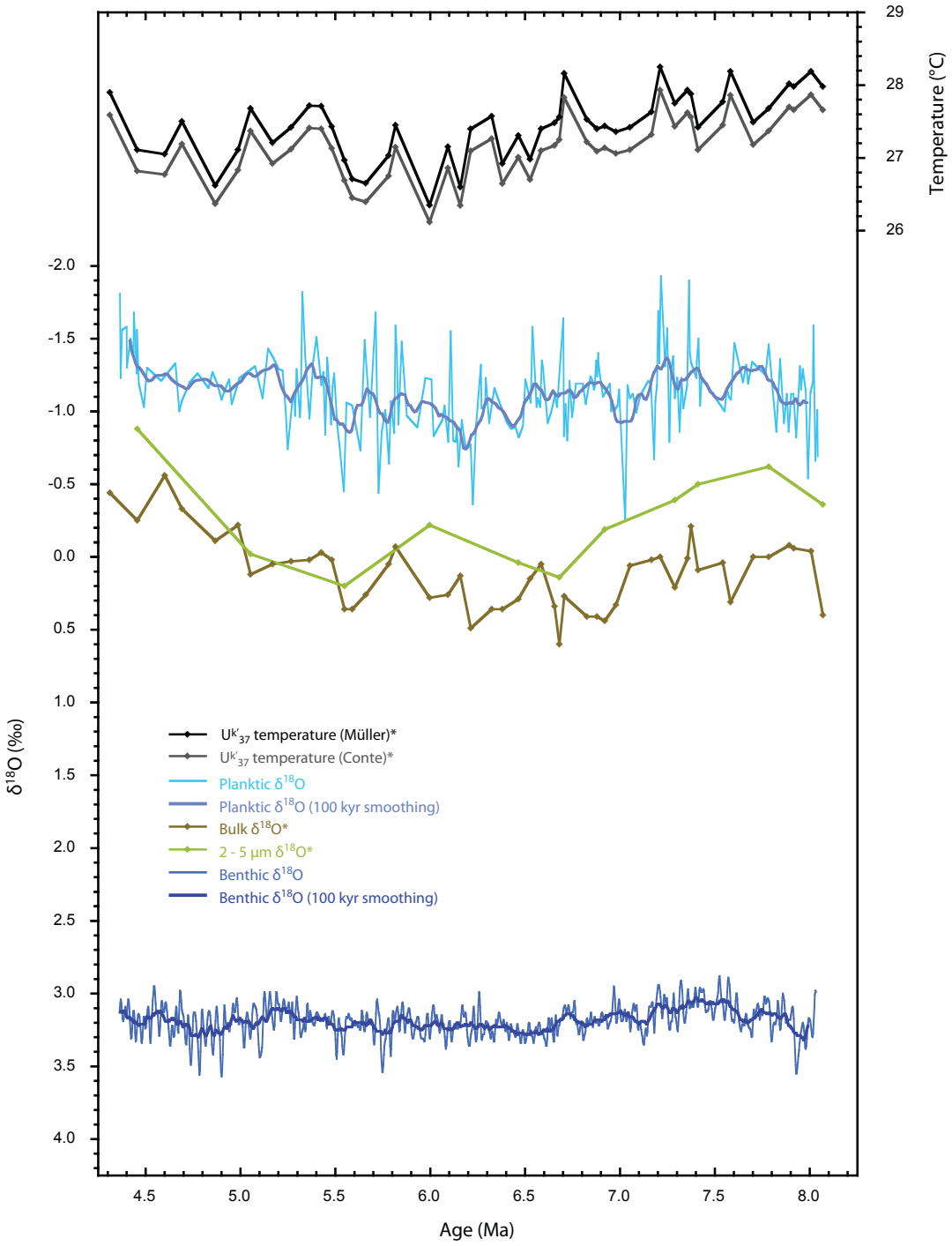

Figure 5.19. Overview of the planktic (light blue) and benthic (dark blue) foraminiferal, together with the bulk and 2 – 5 µm sediment (brown and green – from *Rousselle et al., 2013 $\delta^{18}O$ records from Site U1338. The $U^{k'}_{37}$ SST reconstructions from Rousselle et al. (2013) have also been plotted (black for Müller et al., 1998 calibration; grey for Conte et al., 2006 calibration – both from Rousselle et al., 2013). To highlight the long-term trends, the planktic and benthic foraminiferal $\delta^{18}O$ records have been plotted with a 100-kyr smoothed record.

bulk $\delta^{13}C$ and planktic and benthic foraminiferal $\delta^{13}C$ records, and is most likely caused by a combination of the same mechanisms as the $\delta^{13}C$ offset: mixing with bottom water calcite fragments (Figure 5.10), and the known offsets seen in bulk calcite samples (Ziveri et al., 2003). The planktic and benthic foraminiferal $\delta^{18}O$ show an offset of ~ 4.3 ‰, which would equate to a temperature difference of ~ 17.2 °C. (Figure 5.19) The planktic foraminiferal $\delta^{18}O$ record is far more variable than the benthic foraminiferal $\delta^{18}O$, which reflects the more variable temperature and salinity conditions generally found in the surface environment (Katz et al., 2010). Using the average Mg/Ca_{GS} SSTs for U1338 (25.3 °C), this temperature offset implies that bottom water temperatures could be as high as 6.9 °C. There are no independent bottom water estimates for Site U1338, however the benthic foraminiferal Mg/Ca temperatures average at about 5 – 6 °C at Site 806 in the Western Equatorial Pacific (Lear et al., 2002), and the U1338 benthic foraminiferal $\delta^{18}O$ is 0.52 ‰ / 2.1 °C higher than the benthic foraminiferal $\delta^{18}O$ from Site 806 (see Table 5.6). This would suggest bottom water temperatures of around 3 – 4 °C at Site U1338, which is much cooler than suggested by the benthic – planktic foraminiferal $\Delta\delta^{18}O$ gradient (Figure 5.19). A number of factors could have reduced the benthic – planktic foraminiferal $\Delta\delta^{18}O$ gradient. Firstly, as the SEM images presented in Chapter 3 (Figure 3.6) show, the preservation of the planktic foraminifera is not perfect, which could mean that the absolute planktic foraminiferal $\delta^{18}O$ is lower than when originally precipitated. Generally, the lack of correlation in long-term trend between the planktic and benthic foraminiferal $\delta^{18}O$ records also supports the suggestion that the temporal trends in planktic foraminiferal $\delta^{18}O$ might not be as affected as the absolute values. Apart from preservation, differences in bottom and surface

water salinity could also have reduced the surface to deep $\delta^{18}O$ gradient. Surface water salinity is likely to be higher than in the deep waters, which would mean the planktic foraminiferal $\delta^{18}O$ will be relatively enriched with ^{18}O and thereby decrease the difference between planktic and benthic foraminiferal $\delta^{18}O$ calcite (Rohling and Bigg, 1988).

Taking into account the above caveats on planktic foraminiferal $\delta^{18}O$ records, comparison between the $U^{k'}_{37}$ SST records and planktic foraminiferal $\delta^{18}O$ could help deconvolve the contributions of temperature, global ice volume and salinity change to the planktic foraminiferal $\delta^{18}O$ records (Figure 5.19). Generally, between 7.2 and 4.4 Ma, the $U^{k'}_{37}$ and planktic foraminiferal $\delta^{18}O$ show remarkably similar trends. Between 7.2 and 6.1 Ma, $U^{k'}_{37}$ SSTs decrease by ~ 2 °C at the same time as planktic foraminiferal $\delta^{18}O$ increases by ~ 0.5 ‰, which equates to an approximate 2 °C temperature decrease. Between 6.1 and 4.4 Ma, $U^{k'}_{37}$ temperatures increase again by 2 °C overall. This coincides with a 0.8 ‰ decrease in planktic foraminiferal $\delta^{18}O$, equivalent to a 3.2 °C increase in temperature. The inferred temperature change is comparable between 7.2 and 6.1 Ma, however, between 6.1 and 4.4 Ma, the planktic foraminiferal $\delta^{18}O$ inferred temperature increase is slightly larger than the increase seen in $U^{k'}_{37}$. The decrease in planktic foraminiferal $\delta^{18}O$ that cannot be attributed to temperature change could be due to a decrease in regional salinity, or it could reflect a decrease in global ice volume. Both mechanisms would drive a decrease in the surface seawater $\delta^{18}O$ at Site U1338, which would be reflected in the planktic foraminiferal $\delta^{18}O$. The benthic foraminiferal $\delta^{18}O$ shows a slight long-term decrease in from 4.7 to 4.4 Ma, so a decrease in global ice volume is feasible. Proximal studies from offshore Antarctica focussing on the dynamic behaviour of

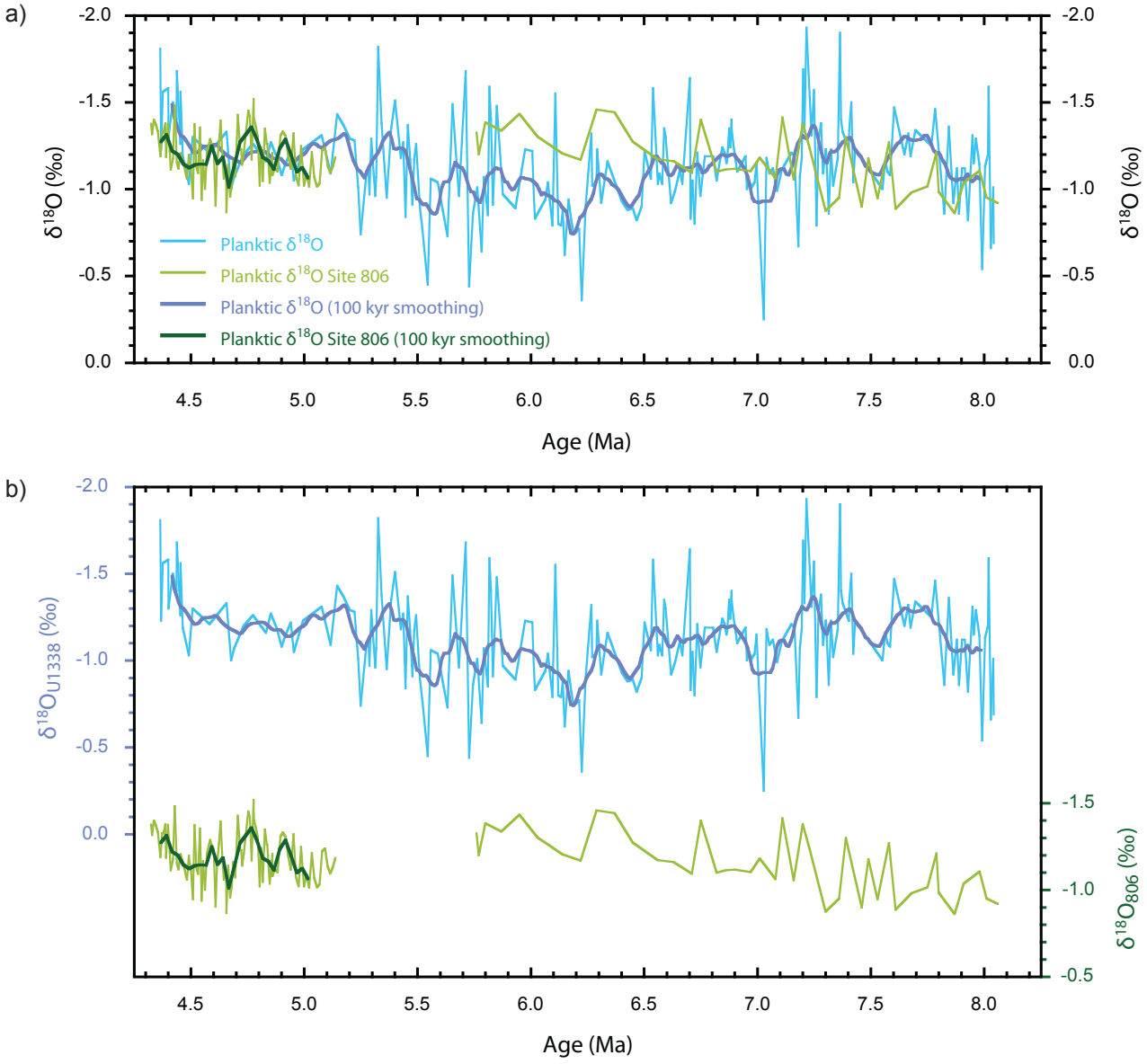

Figure 5.20. Planktic foraminiferal δ¹⁸O records from IODP Site U1338 and ODP Site 806 in the western equatorial Pacific (*Globigerinoides sacculifer* record from Nathan and Leckie, 2009 between 8 and 5.7 Ma, and from Wara et al., 2005 between 5.2 and 4.4 Ma). The planktic foraminiferal δ¹⁸O records are shown on a) the same and b) offset axes. The key for both a) and b) are shown in a).

the Eastern and Western Antarctic ice sheets show that both ice sheets experienced variation in size during this interval (McKay et al., 2009; Cook et al., 2013). Variation in global ice volume will be discussed in more detail when discussing deep-sea conditions in Chapter 6. A final mechanism that could explain the additional warming seen in the planktic foraminiferal $\delta^{18}O$ record could be increased distribution of heat in the mixed layer and a potential deepening of the thermocline. As the planktic foraminifera probably lived slightly deeper in the mixed layer than the alkenone producers, a deeper thermocline with more homogenous temperature distribution in the mixed layer could cause an additional increase of planktic foraminiferal $\delta^{18}O$ temperature on top of the warming trend seen in the $U^{k'}_{37}$ record. Unfortunately, Mg/Ca_{GS} ratios were not measured in this interval, so it is not possible to see whether the Mg/Ca_{GS} and $U^{k'}_{37}$ temperatures converge at this time.

The El-Niño phase of ENSO is associated with warm sea surface conditions in both the west and east of the equatorial Pacific (Figure 5.1; section 5.1). Overall, the warming trend seen at Site U1338 in the eastern equatorial Pacific between 6.1 and 4.4 Ma could suggest the establishment of permanent El Niño like conditions after 6.1 Ma (Figure 5.19). Figure 5.20 compares the planktic foraminiferal $\delta^{18}O$ records from Site U1338 to planktic foraminiferal $\delta^{18}O$ records from Site 806 (5.2 – 4.4 Ma: Wara et al., 2005; 8.0 – 5.2 Ma: Nathan and Leckie, 2009) in the western equatorial Pacific. Between 8.0 and 6.5 Ma, there is very good agreement between the Site 806 and U1338 planktic foraminiferal $\delta^{18}O$ records (Figure 5.20 a). When looking at the records with offset axes, the 806-planktic foraminiferal $\delta^{18}O$ shows a slight decreasing trend from 8.0 to 5.7 Ma (Figure 5.20 b). The U1338-planktic foraminiferal $\delta^{18}O$ initially shows a slight

decreasing trend between 8.0 and 7.2 Ma, followed by the increasing trend from 7.2 to 6.1 Ma (Figure 5.20 b). However, the two planktic foraminiferal $\delta^{18}O$ records do not diverge in absolute values until after 6.5 Ma. The correlation between the 806 and U1338 records between 8.0 and 6.5 Ma could indicate similar mixed layer temperatures across much of the equatorial Pacific. This lower east-west temperature gradient (Figure 5.20) implies a permanent El Niño-like state before 6.5 Ma, and agrees with thermocline reconstructions at Site 806 that imply a permanent El Niño state between 9.6 and 6.5 Ma (Nathan and Leckie, 2009). The subtle opposing trend in the planktic foraminiferal $\delta^{18}O$ records between 7.2 and 6.5 Ma could indicate an interval of transition from a permanent El Niño state at 7.2 Ma, to a permanent La Nina-like state by 6.5 Ma, which lasts until at least 5.7 Ma, as suggested by the divergence of the two planktic foraminiferal $\delta^{18}O$ records (Figure 5.20 b). There is a gap in the Site 806 records between 5.7 and 5.2 Ma, however between 5.2 and 4.4 Ma the correlation between the two planktic foraminiferal $\delta^{18}O$ is very good, again suggesting a return to a permanent El Niño state.

Figure 5.21 provides an overview of the $\delta^{13}C$, planktic foraminiferal $\delta^{18}O$ and $U^{k'}_{37}$ SST records from three sites respectively from the western (ODP Site 806), eastern (IODP Site U1338) and far eastern (Site 1241) equatorial Pacific (Figure 5.22). Comparing the multi-proxy records from these three locations in the equatorial Pacific enables a regional picture of the state of ENSO during the late Miocene and earliest Pliocene to be established. A regional comparison also allows the relationship between the state of ENSO and the Biogenic Bloom at Site U1338 to be discussed. The comparison of $U^{k'}_{37}$ temperatures from Site U1338 (Rousselle et al., 2013) and Site 1241 in the far eastern Pacific (Seki et al., 2012)

show that temperatures were uniform across the eastern Pacific between 8.0 and 6.9 Ma (Figure 5.21 a). After 6.9 Ma the temperature between the Far East and more central region diverge, with Site U1338 remaining between 1 and 2 °C cooler until the end of the record at 4.4 Ma. This most likely partially reflects the movement of Site 1241 further into the eastern equatorial warm pool (Figure 5.22), but also potentially reflects the development of cooler currents around Site U1338. The changes in temperature gradient in the eastern Pacific fit well with the inferred ENSO state from the west-east $\delta^{18}O$ gradient (permanent El Niño – 8.0 to 7.2 Ma; weakening El Niño – 7.2 to 6.5 Ma; permanent La Niña – 6.5 to 5.7 Ma; permanent El Niño – 5.2 – 4.4 Ma) (Figure 5.21 b).

Overall, the combined Site 1241, U1338 and 806 data indicate that El Niño dominated the early late Miocene, but that La Niña developed fully from 6.5 Ma and lasted potentially up to ~ 5.7 to 5.5 Ma, after which El Niño dominated again. The domination of El Niño state in the early Pliocene fits with past reconstructions suggesting that the early Pliocene was a period of permanent El Niño (Wara et al., 2005; Lawrence et al., 2006; Groeneveld et al., 2006; Steph et al., 2006; Dekens et al., 2008; Ford et al., 2012; Seki et al., 2012). Evidence of El Niño variability in varved evaporite deposits from ~ 5.6 Ma, could indicate that the permanent El Niño state was established in the latest Miocene (Galeotti et al., 2010). Some studies have suggested that the El Niño state of the early Pliocene also dominated the whole late Miocene (LaRiviere et al., 2012). However, the increase in temperature and $\delta^{18}O$ gradients from 6.5 to ~ 5.7 Ma seen in this study's comparison of planktic foraminiferal $\delta^{18}O$ and alkenone data, suggest that there was a distinct period of La Niña-like conditions throughout much of the Messinian stage. An interval of La Niña-like conditions would furthermore fit

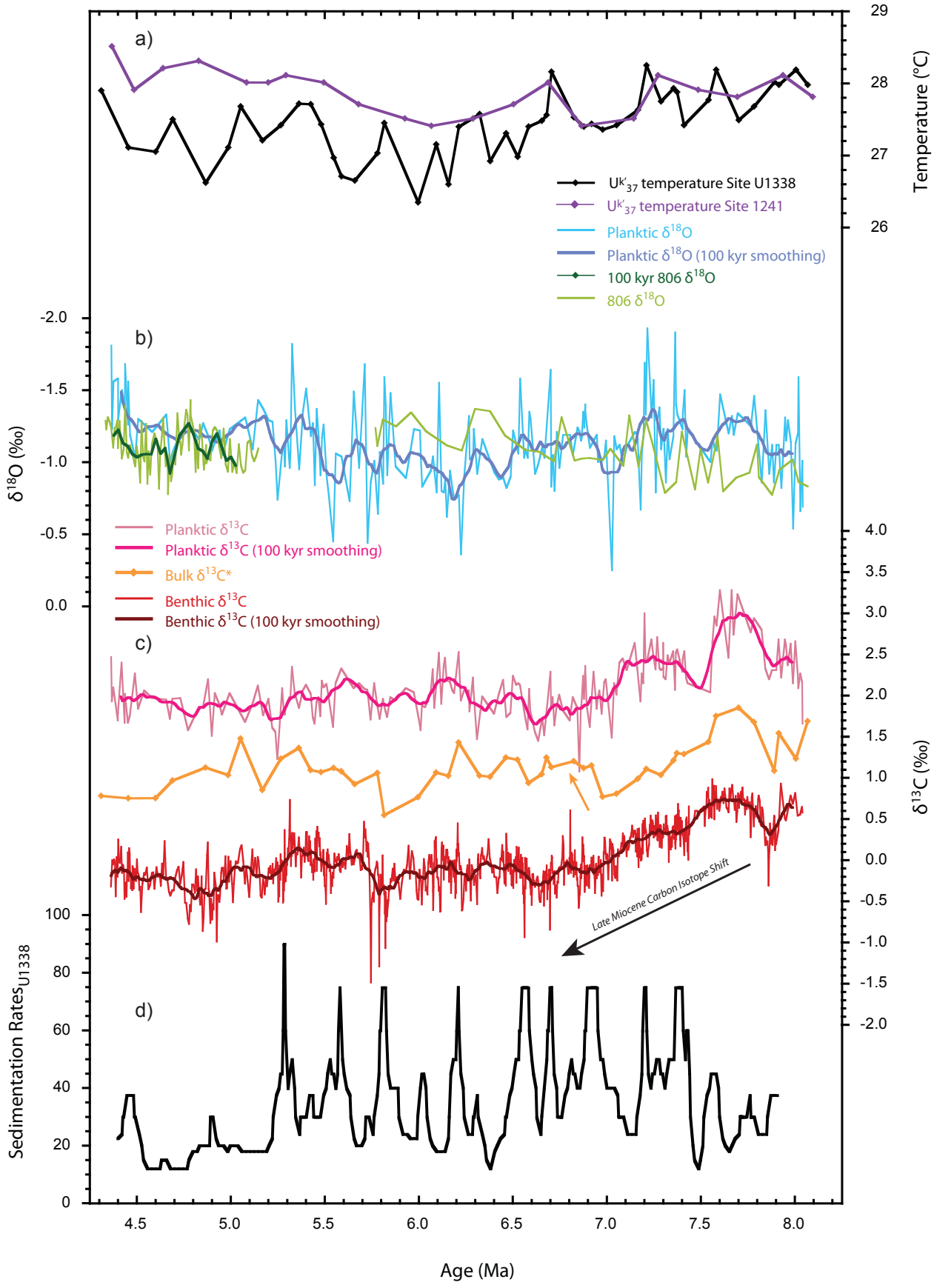
a)
b)
c)
d)
$U^{k'}_{37}$ temperature Site U1338
$U^{k'}_{37}$ temperature Site 1241
Planktic $\delta^{18}O$
Planktic $\delta^{18}O$ (100 kyr smoothing)
100 kyr 806 $\delta^{18}O$
806 $\delta^{18}O$
Planktic $\delta^{13}C$
Planktic $\delta^{13}C$ (100 kyr smoothing)
Bulk $\delta^{13}C$*
Benthic $\delta^{13}C$
Benthic $\delta^{13}C$ (100 kyr smoothing)
Late Miocene Carbon Isotope Shift
Temperature (°C)
$\delta^{18}O$ (‰)
$\delta^{13}C$ (‰)
Sedimentation Rates$_{U1338}$
Age (Ma)

Figure 5.21. Overview of data compilation from ODP Site 1241 in the far eastern, IODP Site U1338 in the eastern and ODP Site 806 in the western equatorial Pacific.

a) Shows the $U^{k'}_{37}$ records from Site 1241 (Seki et al., 2012) and Site U1338 (Rousselle et al., 2013).

b) Shows the planktic foraminiferal $\delta^{18}O$ records from Site U1338 (this study) and Site 806 (Wara et al., 2005; Nathan and Leckie, 2009).

c) Shows the planktic and benthic foraminiferal (this study) and bulk $\delta^{13}C$ (Rousselle et al., 2013) records from Site U1338. The LMCIS is marked with a black arrow and the bulk $\delta^{13}C$ divergence from the foraminiferal $\delta^{13}C$ ~ 7.0 Ma is marked with an orange arrow.

d) Shows the reconstructed sedimentation rates from Site U1338 (this study – Chapter 3).

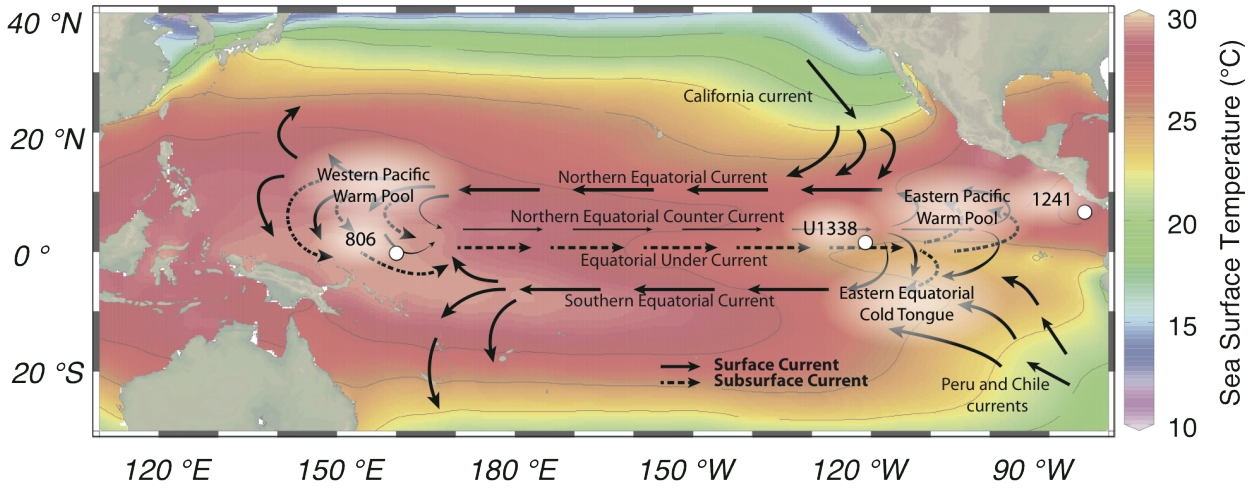

Figure 5.22. Overview of the modern sea surface distribution (Locarnini et al., 2009), together with the modern sea surface currents (Pisias et al., 1995) and the locations of IODP Site U1338, ODP Site 806 and ODP Site 1241 in the equatorial Pacific.

well with the conclusions regarding productivity and upwelling based on the U1338 bulk, planktic and benthic foraminiferal $\delta^{13}C$ and sedimentation rates discussed above (Figure 5.21 c and d respectively; section 5.5.2). The divergence in trends between the bulk and planktic/benthic foraminiferal $\delta^{13}C$ between ~ 7.0 and 4.9 Ma (Figure 5.21 c) could reflect upwelling and a shallower thermocline in the eastern equatorial, both characteristics of La Niña. Likewise, the duration of the Biogenic Bloom at Site U1338, suggested by high-sedimentation rates between ~ 7.5 and 5.0 Ma (Figure 5.21 d), would overlap well with the main period of La Niña suggested by the combined results above.

A La Niña period in the late Miocene could be driven by a number of factors. La Niña is associated with strengthened trade winds compared to El Niño intervals. The Himalayan uplift (10 – 8 Ma) has been linked to the intensification of the trade winds due to strengthening of atmospheric Walker and Hadley Cell circulation (Filippelli, 1997; An et al., 2001). In addition, a study on aeolian deposits in eastern equatorial Pacific near Site U1338 indicated an intensification of trade winds between 8 and 5 Ma (Hovan, 1995). In the present day, the eastern equatorial region is dominated by the Eastern Equatorial Cold Tongue, which is made up by a combination of the cool Equatorial Undercurrent (EUC) and the Peru and Chile currents (PCC) (Pisias et al., 1995; Rousselle et al., 2013). The movement of these currents into the eastern equatorial Pacific is partially due to the circulation of the Walker and Hadley Cells (Pisias et al., 1995). The characteristic La-Niña SST cooling and thermocline shoaling in the eastern equatorial Pacific is most likely an indication of the first appearance of the EUC and PCC, and the development of the (proto-) Eastern Equatorial Cold Tongue around 6.5 Ma (Figure 5.22).

Modelling studies have also indicated that a deeper Central American Seaway (CAS) would lead to a deeper thermocline in the eastern equatorial Pacific (Zhang et al., 2012). The La Niña interval between 6.5 and 5.7 Ma, with cooler SSTs and a shallower thermocline in the eastern equatorial Pacific, could therefore also be a response to an increased shoaling of the CAS. Although the exact timing of CAS closure is not yet well constrained (see section 2.1.1 in Chapter 2), intervals of CAS shoaling have been suggested between 6.6 and 6.0 Ma (Billups, 2002) and between 6.0 and 5.0 Ma (Lear et al., 2003). Other authors have suggested that the state of ENSO in the equatorial Pacific could also be related to the restriction of the Indonesian Throughflow (ITF) (Cane and Molnar, 2001). A more open ITF would allow warmer surface waters to move more freely, thereby creating a more uniform distribution of warm waters in the equatorial Pacific, characteristic of an El Niño-like phase (Cane and Molnar, 2001; Molnar and Cane, 2002). Therefore, the La Niña-like phase between 6.5 and 5.7 Ma could also be due to a phase of further restriction of the ITF. Overall, a combination of increased CAS shoaling and potentially further restriction of the ITF, coupled with trade wind intensification could have driven the La Niña-like interval and Biogenic Bloom at Site U1338 between 6.5 and ~5.7 Ma.

5.6. Conclusions

Sea surface temperature (SST) reconstructions using planktic foraminiferal Mg/Ca_{GS} values show that average SSTs at Site U1338 average ~ 25 °C, which is ~ 2 °C cooler than published $U^{k'}_{37}$ SSTs from the same site, which measure ~ 27

°C (Rousselle et al., 2013). Novel clumped isotope Δ_{47} temperatures are far lower than reasonable for SSTs: the Δ_{47} temperature for the 2 – 5 μm fraction are ~ 10 – 15 °C. Results also do not show an increase of temperature with decreasing size fraction. The lower temperatures are most likely due to the presence of only around 50% coccolith calcite in the 2 – 5 μm sediment fraction, as shown by the EDS maps. However, this is insufficient to explain the complete temperature offset between the Δ_{47} and $U^{k'}_{37}$ temperatures. Moderate or moderate to poor preservation of the coccolith calcite, particularly the presence of secondary overgrowth, could have further contributed to the Δ_{47} and $U^{k'}_{37}$ SST offset. However, the size of the offset may suggest that there are additional preservation or vital effects that would further contribute to decreasing the clumped isotope Δ_{47} temperatures. An offset in the pH of the calcifying vesicle could be a source of a Δ_{47} vital effect.

The presence of marine barite, combined with the common variability in the sedimentation rates, $\%CaCO_3$ and $\%SiO_2$ content suggest that primary productivity is the dominant control on sedimentary deposition at Site U1338. The reduction in power of the wavelet analyses of the sedimentation rate, $\%CaCO_3$ and $\%SiO_2$ from Site U1338 indicates that the Biogenic Bloom dominates between 8.0 and 5.5 Ma, possibly extending in a reduced extent to 4.5 Ma. The presence of a positive shift in the bulk $\delta^{13}C$ record between 7.0 and 4.7 Ma, at the same time as planktic and benthic foraminiferal $\delta^{13}C$ co-vary, suggest that the thermocline might be shallower during this interval. The combination of potential upwelling and high sedimentation rates suggest that the nutrient influx driving the Biogenic Bloom could be supplied by cool nutrient rich deep-water

upwelling, although an additional nutrient input through aeolian dust deposits cannot be excluded.

The planktic foraminiferal $\delta^{18}O$ records show similar amounts of cooling (~ 2 °C) as $U^{k'}_{37}$ SSTs between 7.2 and 6.1 Ma at Site U1338. Between 6.1 and 4.4 Ma, both planktic foraminiferal $\delta^{18}O$ and $U^{k'}_{37}$ show an increase of respectively 3 °C and 2 °C. The 1 °C offset in temperature increase could be due to a decrease in global ice volume leading into the Pliocene warm period. Combined planktic foraminiferal $\delta^{18}O$ from Sites U1338 and 806, together with $U^{k'}_{37}$ SSTs from Sites U1338 and 1241 suggest that an El Niño state dominated the equatorial Pacific between 8.0 and 7.2 Ma, which then transitioned into a dominant La Niña state by 6.5 Ma. The La Niña state dominated until 5.7 Ma, where it most likely transitioned back into El Niño by 5.2 Ma. The second El Niño phase lasted until the end of the record, which agrees with much published work on the dominance of El Niño during the Pliocene warm period. The presence of the La Niña state, with cooler SSTs and a shallower thermocline, between 6.5 and 5.7 Ma, with transitioning periods before and after, is most likely a response to strengthened trade winds, the shoaling of the Central American Seaway or further restriction of the Indonesian Throughflow. Increased trade winds would have led more vigorous surface water circulation and thermocline shoaling, and driven the emergence of the Eastern Equatorial Cold Tongue during the La Niña stage. The presence of a shallower thermocline in the eastern equatorial Pacific between at least 6.7 and 5.7 Ma would overlap well with the main interval of the Biogenic Bloom at Site U1338.

Chapter 6.

Evolution of Late Miocene to Early Pliocene Climate: changes in Background Climate Sensitivity and the origins of the Carbon Isotope Shift and the Messinian Salinity Crisis

6.1. Introduction and Approach

Constraining background climate variability is important to improve our understanding of how the Earth's climate system responds to external forcing during different climatic states. The long-term (>10^3 years) response of the overall Earth's climate is often investigated by reconstructing Earth system sensitivity. Earth system sensitivity is defined as the long-term (>10^3 year)

response of mean global temperature to a doubling of CO_2 (Pagani et al., 2009), and importantly, incorporates both the fast (e.g. atmospheric water vapour concentrations) and slow (continental ice sheets and carbon cycle) feedbacks that can affect the temperature changes that occur in response to external radiative forcing (Royer et al., 2012; Rohling et al., 2012). Another approach to approximate the long-term climate response to external radiative forcing is to investigate the response of individual long-term feedback systems of the Earth's climate, such as the cryosphere and the carbon cycle, to external radiative forcing. The combined response of long-term feedback systems to external radiative forcing will be referred to as Earth system response.

The late Miocene to early Pliocene was one of the more stable periods of the Cenozoic. This stable climate period is an ideal interval to study the response of the cryosphere and carbon cycle to changes in external radiative forcing in an interval when the climate system did not undergo any large perturbations in either feedback system. For both the cryosphere and carbon cycle, an increased sensitivity to solar forcing should be reflected by increased variability within each component. As the $\delta^{18}O$ from benthic foraminiferal calcite strongly relates to glacio-eustatic and ice volume variations (see section 3.2.1.1), high-resolution records of this proxy can be used to investigate changes in variability, and therefore sensitivity of the cryosphere to external radiative forcing. Similarly, benthic foraminiferal $\delta^{13}C$, which reflects changes in the oceanic reservoir $\delta^{13}C_{DIC}$ (see section 3.2.1.2), can be used to look at the changes in variability and sensitivity of the carbon cycle in response to changes in solar insolation. Combining the response of the cryosphere and carbon cycle to solar insolation

will help approximate the overall response of the Earth's climate system (Earth system response) to radiative forcing during the late Miocene and early Pliocene.

The cryosphere and carbon cycle sensitivity and Earth system response reconstructions can also be coupled with reconstructions of changes in global ice volume and inter-oceanic-basin $\delta^{13}C$ gradients, to help deconvolve global climate trends during the late Miocene and early Pliocene. Superimposed on the climatic stability of the late Miocene and early Pliocene, a number of regional and global climatic perturbations occurred, of which the origins are not always fully understood (see also section 2.1.2). During the Messinian Salinity Crisis (MSC - 5.95-5.33 Ma), which was a regional threshold event that may have affected the formation of deep water in the North Atlantic (Vidal et al., 2002), the present-day Mediterranean basin was isolated from the Atlantic Ocean and became an enclosed and desiccated basin (see section 6.2.3). A combination of tectonic uplift and glacio-eustatic fall caused the isolation of the Mediterranean from the Atlantic (Krijgsman et al., 1999); however, the relative contribution of the two mechanisms is unclear. Closer inspection of the variations in ice volume in the late Miocene using multi-site high-resolution $\delta^{18}O$ records could help further constrain the role of glacio-eustacy in the MSC. Finally, a global perturbation in foraminiferal $\delta^{13}C$ record that is not yet well understood is a negative shift in foraminiferal $\delta^{13}C$, which is referred to as the late Miocene Carbon Isotope Shift (LMCIS) (see section 6.2.4). The mechanism that caused the negative $\delta^{13}C$ shift has been attributed to both the synchronous late Miocene biogenic bloom (Diester-Haass et al., 2006) and to a change in the $\delta^{13}C$ of the oceanic reservoir (Hodell and Venz-Curtis, 2006). By looking at the sensitivity of the carbon cycle

to external forcing, as well as at a compilation of multiple $\delta^{13}C$ records, the origin of the LMCIS may be partially uncovered.

The objectives of this chapter are threefold. The first objective is to reconstruct changes in cryosphere and carbon cycle sensitivity and particularly Earth system response to external radiative forcing during the late Miocene and early Pliocene (see section 6.4.1). The second objective is to investigate variations in global ice volume during the late Miocene and early Pliocene and to further constrain the role of glacio-eustacy at the onset and termination of the Messinian Salinity Crisis (MSC). The final objective is to investigate changes in inter-ocean $\delta^{13}C$ gradients and to explore the origins of the late Miocene Carbon Isotopes Shift (LMCIS)

To achieve the first objective, changes in background cryosphere and carbon cycle sensitivity to external radiative forcing are first estimated by comparing spectral analyses (B-Tukey and wavelet) of the benthic foraminiferal $\delta^{18}O$ (cryosphere) and $\delta^{13}C$ (carbon cycle) records from Site U1338 and Site 982 to spectral analyses of predicted external forcing. The overall Earth system response is then inferred by combining the cryosphere and carbon cycle sensitivities.

To estimate variations in global ice volume, an eight-site compilation of benthic foraminiferal $\delta^{18}O$ from the Atlantic, Southern and Pacific Oceans is coupled with the reconstructed cryosphere sensitivity and published near-field ice records (see section 6.4.2). The importance of glacio-eustacy in the onset and termination of the MSC is explored using three high-resolution benthic foraminiferal $\delta^{18}O$ records, combined with cryosphere sensitivity and near-field ice proxy records (see section 6.4.2.1).

The evolution of inter-basin $\delta^{13}C$ gradients throughout the late Miocene and early Pliocene is investigated using a multi-site $\delta^{13}C$ compilation. The implications of the changes in inter-basin $\delta^{13}C$ gradient are discussed in the context of changes in the state of deep-water circulation (see section 6.4.3). The origins of the LMCIS are explored by combining the multi-site $\delta^{13}C$ compilation, the carbon cycle sensitivity reconstruction and a conceptual carbon-cycle box model (see section 6.4.3.1).

6.2. Background and Previous Work

6.2.1. Geological Setting and Site Selection

Eight sites were selected for the global compilation of benthic foraminiferal $\delta^{18}O$ and $\delta^{13}C$ records between 8.0 and 3.5 Ma (Table 6.1; Figure 6.1). Where possible, sites were chosen with high-resolution, continuous benthic foraminiferal stable isotope records that cover the whole interval were chosen. In the Pacific Ocean, the U1338 $\delta^{18}O$ and $\delta^{13}C$ records produced in this study (see Chapters 3 and 4) are supplemented with stable isotope records from ODP Sites 846 (Shackleton et al., 1995b), 849 (Mix et al., 1995; Hodell and Venz-Curtis, 2006) and 806 (Nathan and Leckie, 2009) (see Table 6.1). Sites U1338 and 849 are the only two sites that have continuous records over the whole interval, and, of these two, Site U1338 is the only record with a sufficiently high-resolution temporal sampling to all Milankovitch-scale cyclicity. The Site 846 records only

Overview of ODP, IODP and other sites								
Site name	*Location*	*Water Depth*	*Longitude*	*Latitude*	*Age Range in this study*	*Sampling Resolution*	*Astronomical Scale and Reference*	*Reference*
ODP Site 982	North Atlantic	1145 m	15°52.001'W	57°30.992'N	3.3 to 8.3 Ma (5.0 Myr)	3.6 kyr	4.6 - 8.0 Ma = La93 (orbitally tuned in Hodell et al., 2001) 3.5 - 4.6 Ma = Berger and Loutre, 1991 (orbitally tuned in Shackleton et al., 1995a)	Hodell et al., 2001; Hodell & Venz-Curtis, 2006
ODP Site 926	Equatorial Atlantic	3598 m	42°54'W	3°42'N	4.9 to 7.4 Ma (2.5 Myr)	4.7 kr	La93 (orbitally tuned in Shackleton and Hall, 1997)	Shackleton & Hall, 1997
Combined ODP Sites 704/1090	Southern Ocean (Atlantic)	2532 m	7°25'E	47°53'S	3.0 to 8.5 Ma (5.5 Myr)	10 kyr	Berger and Loutre, 1991 (orbitally tuned in Shackleton et al., 1995a)	Hodell and Venz, 1992; Müller et al., 1991
		3702 m	8°540E	42°55'S				Venz & Hodell, 2002
MV0502-4JC	Southern Ocean (Pacific)	4286 m	148°08'W	50°20'S	3.5 to 7.5 Ma (5.0 Myr)	33 kyr	Berger and Loutre, 1991 (orbitally tuned in Shackleton et al., 1995a)	Waddell et al., 2009
ODP Site 806	Western equatorial Pacific	2521 m	159°21.7'E	0°19.1'N	5.7 to 8.5 Ma (2.7 Myr)	61 kyr	Berger and Loutre, 1991 (orbitally tuned in Shackleton et al., 1995a)	Nathan & Leckie, 2009
ODP Site 846	Eastern equatorial Pacific	3296 m	90°49.07'W	3°5.80'S	3.0 to 6.1 Ma (3.1 Myr)	3.6 kyr	Berger and Loutre, 1991 (orbitally tuned in Shackleton et al., 1995a)	Shackleton et al., 1995b
ODP Site 849	Eastern equatorial Pacific	3850 m	110°31'W	0°11'N	3.0 to 8.5 Ma (5.5 Myr)	10 kyr	Berger and Loutre, 1991 (orbitally tuned in Shackleton et al., 1995a)	Mix et al., 1995; Hodell & Venz-Curtis, 2006
IODP Site U1338	Eastern equatorial Pacific	4200 m	117°58.178'W	2°30.469'N	3.5 to 8.0 Ma (4.5 Myr)	3.4 kyr	4.6 - 8.0 Ma = La93 (orbitally tuned in Hodell et al., 2001) 3.5 - 4.6 Ma = Berger and Loutre, 1991 (orbitally tuned in Shackleton et al., 1995a)	This study

Table 6.1. Overview of information about the ODP, IODP and other sites used in the compilation of the $\delta^{18}O$ and $\delta^{13}C$ records.

extend to 6 Ma; however, it has a comparable sampling resolution to Site U1338. The 806 records only cover the interval between 8 and 5.7 Ma, with low sampling resolution (~ 60 kyr), however the 806 isotope records are the only record available across this interval in the western Pacific. Comparing the four Pacific sites will help constrain how homogeneous the Pacific deep waters were during the early Pliocene and late Miocene. North Atlantic ODP Site 982 (Hodell et al., 2001; Hodell and Venz-Curtis, 2006) and equatorial Atlantic ODP Site 926 (Shackleton and Hall, 1997) were chosen to represent the Atlantic basin. The latitudinal and water-depth difference between these two Atlantic sites will allow the ventilation of North Atlantic Deep Water in the Atlantic basin to be assessed. Finally, to represent the Southern Ocean, a combined record from ODP Sites 704 and 1090 (Hodell and Venz-Curtis, 2006) was chosen in the Atlantic sector, and MV0502-4JC (Waddell et al., 2009) was chosen in the Pacific sector. The temporal resolution of the Southern Ocean records is low, however it will allow the evolution of the southern component deep water to be assessed.

The Site U1338 stable isotope records were correlated directly to the Site 982 (see Chapter 4), placing the U1338 records on the 982 age model (See section 4.2.2 for a more detailed discussion). Between 4.6 and 3.5 Ma, the Site 982 age model was placed on the astronomical age model from Shackleton et al. (1995a) (based on the astronomical timescale of Berger and Loutre, 1991). From 8.0 and 4.6 Ma, the Site 982 records were astronomically tuned to the La93 solution (Lascar et al., 1993; see section 4.2.1 in Chapter 4). Sites 849 and 704/1090 were chosen because Hodell and Venz-Curtis (2006) correlated these records to Site 982 isotope records, thereby placing the records on the Shackleton et al. (1995a) timescale. Equatorial Atlantic Site 926 was orbitally

tuned (Shackleton and Hall, 1997) to the La93 astronomical solution (Laskar et al., 1993). The MV0502-4JC chronology is not well constrained (Waddell et al., 2009): age constraints were obtained by using the late Pliocene $\delta^{13}C$ shift at 2.75 from Hodell and Venz-Curtis (2006) and by correlating the late Miocene carbon isotope shift from MV0502-4JC to the LMCIS at Site 704/1090. Waddell et al., (2009) thereby placed the MV0502-4JC records on the Shackleton et al. (1995a) timescale.

The high-resolution stable isotope results from Sites U1338, 982 and 926 have all been placed on the astronomical timescale of La93, which, up to 10 Ma, is essentially indistinguishable from the more recent La2004 astronomical solution (Laskar et al., 2004) used in the creation of the Neogene timescale ANTS2004 (Lourens et al., 2004) (see discussion 4.2.1 in Chapter 4). The high-resolution records from Site 846 are based on the Shackleton et al. (1995a) timescale, which was created by orbitally tuning high-resolution density GRAPE measurements to the astronomical solution from Berger and Loutre (1991). Hodell et al. (2001) suggests that there is a discrepancy of up to 1 obliquity cycle (~ 40 kyr) in the latest Miocene between ages assigned to specific interglacial/glacial cycles on the Shackleton et al. (1995b) and Shackleton and Hall (1997) age models. For this reason, in analyses requiring high-resolution isotope records, only the records on the Shackleton and Hall (1997) timescale in the late Miocene were used. When reconstructing changes in background variability across the late Miocene to early Pliocene (see sections 6.4.1), only the stable isotope records from Sites U1338 and 982 were used, as these were the only two records with complete high-resolution coverage between 8.0 and 3.5 Ma. When investigating the role of glacio-eustatic changes in the Messinian

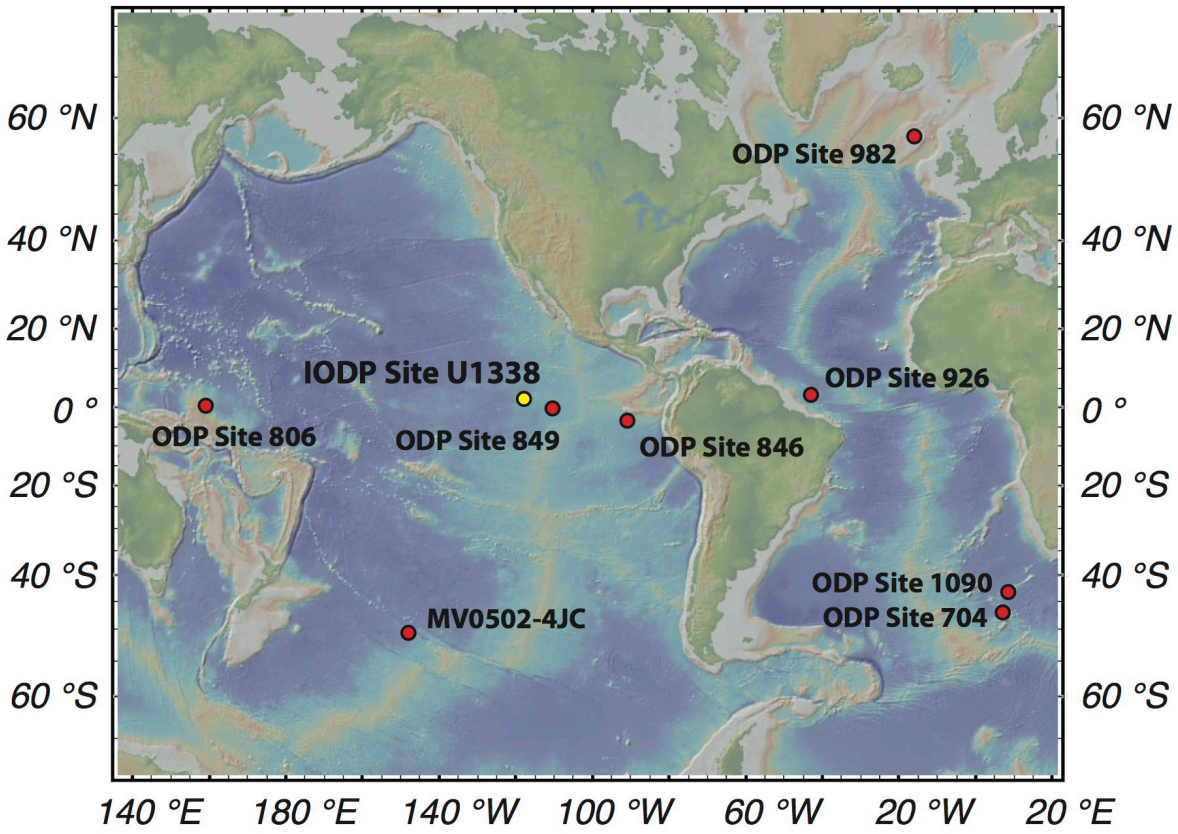

Figure 6.1.

Overview of the location of the ODP, IODP and other sites used in the compilation of the $\delta^{18}O$ and $\delta^{13}C$ records. Records produced in this study are highlighted in yellow.

Salinity Crisis (see sections 6.4.2), Sites 982, 926 and U1338 were used, as these records are all on the Shackleton and Hall (1997) timescale in this interval. For the discussions looking at global and regional long-term patterns in $\delta^{18}O$ and $\delta^{13}C$, the possible offset between the Berger and Loutre (1991) and La93 (Laskar et al., 1993) astronomical solutions in the latest Miocene does not play a major role. This means that the records on the Shackleton et al. (1995a) and Shackleton and Hall (1997) age models can be compared directly to each other when looking at long-term trends.

6.2.2. Climate variability in the late Miocene to early Pliocene

Past studies that have applied spectral analysis to high-resolution benthic foraminiferal isotopes highlighted the 41 kyr obliquity cycle as the predominant forcing of both carbon and oxygen isotope records throughout the late Miocene and the early Pliocene (Shackleton et al., 1995b; Mix et al., 1995; Shackleton and Hall, 1997; Hodell et al., 2001) (see section 4.2.1 for more information on orbital cycles). Some studies have also indicated the presence of long- and short-term eccentricity forcing in both carbon (400, 125 and 95 kyr periodicity – Shackleton and Hall, 1997) and oxygen records (100 kyr cycles – Mix et al., 1995). Mix et al., (1995) also found very minor precession control on benthic foraminiferal oxygen records in the early Pliocene (23 kyr). Pisias et al. (1995) investigated changes in dominant forcing of oxygen isotopes for the past 6 Ma using evolutionary spectra and found that obliquity variation was present throughout,

although no significant coherence with obliquity forcing was found before 4.6 and 4.3 Ma. Pisias et al. (1995) also reported reduced solar forcing overall between 4.6 and 4.3 Ma. Low frequency variance was present throughout the oxygen record, which did not show significant covariance with solar insolation. There was no evidence for 100 kyr short-term eccentricity forcing prior to 4.6 Ma, which they attribute to a lower sensitivity of the climate to external radiative forcing prior to 4.6 Ma in the benthic foraminiferal $\delta^{13}O$ (Pisias et al., 1995). No previous studies have investigated changes in variability in benthic foraminiferal $\delta^{13}C$ records during this interval, or changes in variability in benthic foraminiferal $\delta^{18}O$ records between 8.5 and 6.0 Ma.

6.2.3. Messinian Salinity Crisis

The Messinian Salinity Crisis (MSC) is an interesting climatic interval towards the end of the late Miocene during which the Mediterranean basin was isolated from the Atlantic ocean between 5.96 and 5.33 Ma (see also section 2.1.2, Chapter 2). The onset and termination of the MSC were driven by a combination of tectonic uplift and sea level fall (Krijgsman et al., 1999), although the relative role of each component is still debated (see also section 2.1.2, Chapter 2). One hypothesis is that tectonic uplift of the Mediterranean Sill closed the gateways connecting the Mediterranean and Atlantic. Alternatively, a large drop in global sea level, driven by ice volume fluctuations (glacio-eustacy), caused the Atlantic Ocean to fall below the level of the Mediterranean Sill, thereby isolating the two basins from each other (Krijgsman et al., 1999).

Past investigations into Messinian glacio-eustacy could not establish a direct causal relationship between the onset of the MSC and global sea level fall (Hodell et al., 1994). The two largest glacial stages TG20 (5.76 Ma) and TG22 (5.81 Ma) both occur after the main onset of the MSC at 5.96 Ma, but before the complete isolation at 5.56 Ma (Vidal et al., 2002). Therefore sea level lowering was probably not the main controlling factor causing either the initial or full isolation (Vidal et al., 2002). Although the end of the MSC and interglacial stage TG5 (5.33 Ma) may coincide, the amplitude of the sea level rise associated with TG5 is still uncertain (Vidal et al., 2002). Although the onset of the MSC was probably predominantly driven by tectonic uplift, there is still uncertainty surrounding the exact role of glacio-eustatic change during the MSC. The high-resolution benthic foraminiferal $\delta^{18}O$ records discussed in section 6.4.2.1 explore this topic in more detail.

The effect of the MSC on global climate is still debated, although some authors have suggested that the cessation of a high-density saline water influx into the Atlantic could have reduced the amount of North Atlantic Deep Water formation during the MSC (Vidal et al., 2002). However, if the strength of NADW decreased during the MSC, the overall thermohaline circulation would slow down and the $\delta^{13}C$ gradient between the Atlantic and the Pacific would increase. An increasing $\delta^{13}C$ gradient was not seen in the inter-basinal $\delta^{13}C$ reconstructions in Hodell and Venz-Curtis (2006). The compilations of benthic $\delta^{13}C$ produced in this chapter will be used to investigate this question. This discussion can be found in section 6.4.3.

6.2.4. Late Miocene Carbon Isotope Shift

First identified by Keigwin (1979), the late Miocene Carbon Isotope Shift (LMCIS) has been used to describe the 1 ‰ long-term negative shift seen in a number of low-resolution benthic foraminiferal $\delta^{13}C$ records between ~ 8 and 6.5 Ma (Haq et al., 1980). The late Miocene biogenic bloom, a long period of high productivity lasting approximately between 8 and 4.5 Ma, occurs around the same time as the LMCIS (Diester-Haass et al., 2004; see also section 5.5.2 in Chapter 5). In particular, the peak of the biogenic bloom (~ 7.6 – 6 Ma) occurs almost simultaneously with the LMCIS (Lyle et al., 1995; Diester-Haass et al., 2006). The LMCIS has been linked to both the increased surface water productivity (Diester-Haass et al., 2006) and to a long-term change in the $\delta^{13}C$ value of the oceanic reservoir (Hodell et al., 1994). As discussed in more detail in section 3.2.1.2, an increase in surface water productivity could lead to a negative shift in benthic foraminiferal $\delta^{13}C$ (Maslin and Swann, 2005). However, if the LMCIS reflects the biogenic bloom peak between ~ 7.6 and 6.0 Ma (Diester-Haass et al., 2006), this bloom would only cause a negative shift in benthic, and not planktic foraminiferal $\delta^{13}C$ records. A change in the overall oceanic $\delta^{13}C$ signature would affect both surface and deep-water $\delta^{13}C$ records in equal measure in all oceanic basins (Hodell et al., 1994). The compilation of multiple $\delta^{13}C$ records from the Atlantic, Southern Ocean and Pacific basins, discussed in section 6.2.1, should help establish the size, duration and range in shape of the LMCIS and maybe shed light on the driving force behind the shift.

6.3. Data Analysis Techniques

In order to facilitate the major discussion topics in this synthesis chapter, this section explores the techniques applied to the previously discussed stable isotope (see Chapter 3) and wavelet (see Chapter 4) results.

6.3.1. Earth System Response to Radiative Forcing

During intervals of increased cryosphere and carbon cycle sensitivity to external radiative forcing, higher variability is expected in benthic foraminiferal $\delta^{18}O$ (cryosphere) and $\delta^{13}C$ (carbon cycle) records. As discussed in section 4.3.3, wavelet analyses of a time series will show higher power in bandwidths that have higher variability. Therefore, in the benthic foraminiferal $\delta^{18}O$ and $\delta^{13}C$ records wavelets, higher variability in the original $\delta^{18}O$ and $\delta^{13}C$ records will correspond to higher power. Associating variability in the benthic foraminiferal $\delta^{18}O$ solely with cryosphere variability does assume that there is only minimal temperature influence on the benthic foraminiferal $\delta^{18}O$ records. The effects and caveats of this assumption will be considered further in the discussions in sections 6.4.1 and 6.4.2. The benthic foraminiferal isotope records were mainly chosen because the records are sufficiently high-resolution to resolve Milankovitch-scale cyclicity, including precession. Secondly, as discussed in detail in Chapter 3, the benthic foraminifera were generally well preserved at Site U1338, which implies that the primary signal in the benthic foraminiferal isotope records have only been minimally affected.

To reconstruct cryosphere and carbon cycle sensitivity, firstly, the spectral analyses (B-Tukey and wavelet) of the high-resolution benthic foraminiferal stable isotope records from Sites U1338 and 982 are compared to the predicted external forcing to determine the dominant variation in these records, and to determine any correspondence to a specific orbital forcing (Figure 6.2). As is discussed more thoroughly in section 6.4.1.1, obliquity is the predominant external forcing in the late Miocene to early Pliocene. Cryosphere and carbon cycle sensitivity is then determined using the combined information from wavelets of $\delta^{18}O$ and $\delta^{13}C$ records respectively. Firstly, a simplified obliquity forcing was reconstructed based on the external forcing wavelet (orange bar - Figure 6.3.a, 6.4.a and 6.5.a). The $\delta^{18}O$ and $\delta^{13}C$ wavelet responses to obliquity are reconstructed using records for both Site U1338 and 982 ($\delta^{18}O$: black bar in Figure 6.3.b; $\delta^{13}C$: black bar in Figure 6.4.b). By reconstructing the responses for both sites, the inherent record-noise at either site can be more easily distinguished from the true signal.

To assess the sensitivity of the cryosphere and the carbon cycle, the simplified obliquity forcing is then compared to the respective combined 982-U1338 $\delta^{18}O$ and $\delta^{13}C$ responses. The cryosphere/carbon cycle are considered to be sensitive to external forcing when obliquity forcing is present and recorded in the $\delta^{18}O/\delta^{13}C$ records ($\delta^{18}O$: blue bar in Figure 6.3.c; $\delta^{13}C$: red bar in Figure 6.4.c). The cryosphere/carbon cycle are considered to be insensitive when obliquity forcing is present, but there is no visible or strong response in the $\delta^{18}O/\delta^{13}C$ records. For intervals where obliquity forcing is low or absent, a best-guess cryosphere and carbon cycle sensitivity was inferred based on the pre- and

succeeding intervals. Such intervals are marked with a dotted pattern, and the interpretation in these intervals should be treated with caution.

The overall Earth system response is defined here as the combined cryosphere ($\delta^{18}O$) and carbon cycle ($\delta^{13}C$) response and inferred sensitivity to external radiative forcing. In Figure 6.5, the Earth system response (green bar) is reconstructed by comparing the reconstructed obliquity forcing (orange bar) to the $\delta^{18}O$ and $\delta^{13}C$ responses (black bars) and inferred cryosphere (blue bar) and carbon cycle sensitivities (red bar). Similar to the process of reconstructing the cryosphere and carbon cycle sensitivities, the Earth system response is considered responsive when there is obliquity forcing present, but there is no visible or strong response in either the inferred cryosphere or carbon cycle sensitivities. For intervals where obliquity forcing is low or absent, a best-guess Earth system response was inferred based on the pre- and succeeding intervals. Such intervals are marked with a dotted pattern, and the interpretation in these intervals should be treated with caution.

6.3.2. Global Trends in Benthic Foraminiferal $\delta^{18}O$ and $\delta^{13}C$

In order to look at global long-term trends in both global ice volume and the carbon cycle, multi-site $\delta^{18}O$ and $\delta^{13}C$ records were compiled (see section 6.4.2 and 6.4.3). Because there are considerable differences in water-depth

between the sites, every $\delta^{18}O$ and $\delta^{13}C$ record from each site was normalised. An average of these normalised $\delta^{18}O$ and $\delta^{13}C$ records was then taken to help visibly constrain global trends. This normalisation process was particularly important for comparison of the $\delta^{18}O$ records, as inter-site differences in water-depth complicates direct comparison between the $\delta^{18}O$ records, as the temperature offset causes considerable offsets in $\delta^{18}O$.

Each $\delta^{18}O$ and $\delta^{13}C$ record was normalised by subtracting the dataset mean from each data point, and then dividing the data point by the dataset standard deviation. An overview of all the normalised $\delta^{18}O$ and $\delta^{13}C$ records, and the resulting normalised average is shown in Figure 6.7 ($\delta^{18}O$) and appendix Figure 6.7.A ($\delta^{13}C$). It is worth noting that no steps were taken to remove biases due to differences in sampling resolution between the various records. As a result, the high-resolution records have a greater influence on the normalised average than lower resolution records. As there are high-resolution records present in both the North Atlantic and the Pacific, these basins should be reasonably well represented. However, the Southern Ocean records are considerably lower resolution (see Table 6.1), and therefore, the Southern Ocean may be somewhat under-represented in the overall average.

6.4. Discussion

6.4.1. Changes in Background Climate Variability: Implications for Cryosphere and Carbon Cycle Sensitivities and Earth System Response

6.4.1.1. Dominant orbital forcing on $\delta^{18}O$ and $\delta^{13}C$

The spectral analyses (B-Tukey and wavelet) of the benthic foraminiferal stable isotope records from Sites U1338 and 982 are compared to the predicted external forcing to determine whether the dominant variation in the stable isotope records is in response to a specific solar forcing. Figure 6.2 shows the predicted eccentricity (i), obliquity (j), precession (k) and combined solar forcing (ETP – l) calculated for the interval 8.0 – 3.5 Ma using the La2004 solution (Laskar et al., 2004) (see section 4.2.1 in chapter 4). The B-Tukey and wavelet analyses of the combined ETP are also shown (Figure 6.2 g and h). The ETP B-Tukey and wavelet analyses (Figure 6.2 g and h) shows the strongest forcing is found in the bandwidths associated with obliquity, particularly around 41 kyr, but also with a minor peak around 55 kyr. This is almost continuous throughout the record, with the exception to intervals around 6.4 Ma, around 5.4 Ma, and between 4.5 and 4.0 Ma. ETP also shows power in both long and short-term eccentricity. Long-term eccentricity (425 kyr) is present throughout the whole record, whereas short-term eccentricity (135 and 99 kyr) is high between 7.3

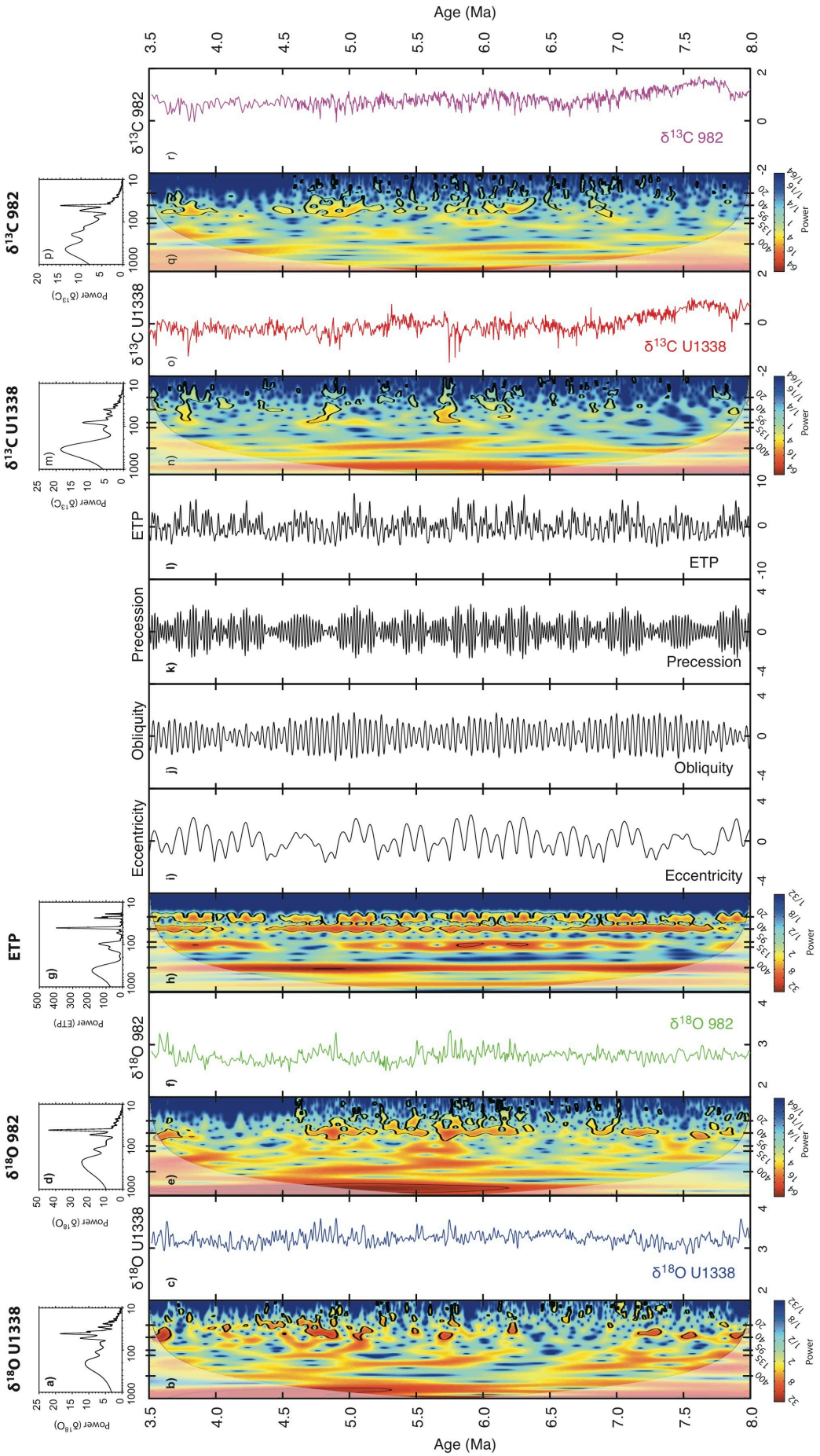
Age (Ma)
δ13C 982
δ13C U1338
ETP
Precession
Obliquity
Eccentricity
δ18O 982
δ18O U1338
Power
Power (δ13C)
Power (ETP)
Power (δ18O)

Figure 6.2.

Overview of external radiative forcing (ETP), and records from Sites U1338 and 982.

a), b) and c) show the B-Tukey (a) and wavelet analyses (b) on the benthic foraminiferal $\delta^{18}O$ records (c) from Site U1338. The highest power can be found in the obliquity bandwidth around 40 kyr.

d), e) and f) show the B-Tukey (d) and wavelet analyses (e) on the benthic foraminiferal $\delta^{18}O$ records (f) from Site 982 (Hodell et al., 2001). The highest power can be found in the obliquity bandwidth around 40 kyr.

g), h) and l) show the B-Tukey (g) and wavelet analyses (h) on the predicted external forcing (ETP – l) for the interval 8.0 – 3.5 Ma. The ETP is a combination of the eccentricity (i), obliquity (j) and precession (k) solutions calculated using the La2004 solution in Analyseries (Paillaird et al., 1996 - version 2.0.4.2; Laskar et al., 2004).

m), n) and o) show the B-Tukey (m) and wavelet analyses (n) on the benthic foraminiferal $\delta^{13}C$ records (o) from Site U1338. The highest power can be found in the obliquity bandwidth around 40 kyr.

p), q) and r) show the B-Tukey (p) and wavelet analyses (q) on the benthic foraminiferal $\delta^{13}C$ records (r) from Site 982 (Hodell et al., 2001). The highest power can be found in the obliquity bandwidth around 40 kyr.

All B-Tukey spectra were calculated using Analyseries (Paillaird et al., 1996 - version 2.0.4.2), using a Bartlett window (bandwidth = 0.00320513). All wavelet analyses were calculated in Matlab using the Torrence and Compo, 1998 protocol, republished by Grinsted et al., 2004.

and 5.5 Ma and 4.4 and 3.3 Ma. ETP also displays power in the precession bandwidths (23 – 21 kyr; 19 kyr) throughout most of the record.

Comparing the spectral analyses on the high resolution, continuous benthic foraminiferal isotope records from Sites U1338 (Figure 6.2. a, b, m and n) and 982 (Figure 6.2. d, e, p and q) to the predicted ETP (Figure 6.2. g and h), it is apparent that obliquity is the dominant forcing on the variability of the $\delta^{18}O$ and $\delta^{13}C$ foraminiferal records from both deep-sea sites. This agrees with published data that shows obliquity as the main forcing during the late Miocene and early Pliocene (Shackleton et al., 1995b; Hodell et al., 2001). High power in the 40 kyr bandwidth is particularly apparent in both the $\delta^{18}O$ wavelets (Figure 6.2. a, b, d and e). Both $\delta^{18}O$ records show a response around 50 kyr, although the 982 $\delta^{18}O$ wavelet do not show the same 30 kyr response as that present in the U1338 $\delta^{18}O$ wavelet. Lourens et al. (2010) attributes the 30 kyr power in their late Pliocene record to a non-linear climate response to obliquity. The results from the U1338 $\delta^{18}O_{CM}$ spectral analyses suggest that this non-linear response may already have been present in the early Pliocene to late Miocene. However, as the results are not reproduced at Site 982, it is possible that the 30 kyr response in the U1338 B-Tukey spectrum reflects minor issues with the age model, where sediment intervals may be compressed in age, thereby artificially compressing the 40 kyr signal to 30 kyr. The $\delta^{13}C$ wavelets from U1338 and 982 also have high power in the 40 kyr bandwidth (Figure 6.2. m, n, p and q), although less than that shown in the $\delta^{18}O$ wavelets. In fact, the spectral analyses from the U1338 $\delta^{13}C_{CM}$ show higher power in the 80 kyr band than in the 41 kyr band (Figure 6.2. m and n). This 80 kyr band could still be related to obliquity forcing, as it could reflect a double obliquity cycle.

In terms of longer-term trends, the $\delta^{13}C$ spectra from Site U1338 and 982 show a strong response to the 425 kyr long-term eccentricity cycle, however, there is no evidence for the shorter-term eccentricity forcing seen in the ETP being reflected in the $\delta^{13}C$ isotope records (Figure 6.2. m, n, p and q). The $\delta^{18}O$ spectra from Site U1338 and 982 possibly show a minor response to the short-term eccentricity forcing (Figure 6.2. a, b, d and e), however, the power is located around 125 and 80 kyr, not around the 135 and 99 kyr bands seen in ETP (Figure 6.2. g and h). Lourens et al. (2010) suggests that power in the 125 and 80 kyr bands can also reflect a double or triple 41 kyr obliquity cycles, so this power may just be an additional indication of the dominance of obliquity forcing during the late Miocene to early Pliocene climate. Interestingly, the $\delta^{18}O$ spectra from Site U1338 and 982 (Figure 6.2. a, b, d and e) also show a high power around the 200 – 250 kyr bandwidth, which is not reflected in the ETP forcing (Figure 6.2. g and h).

Overall, comparing the B-Tukey and wavelet analyses from U1338 and 982 to ETP suggest that obliquity was the predominant forcing during the early Pliocene to late Miocene. The ETP wavelet (Figure 6.2.h) shows high power during periods where there is a greater and more rapid change from a lower to a higher tilt and vice versa. This strong obliquity forcing indicates that high-latitude climate variations are an important driver of global climate at this time, as a greater change in tilt (e.g. a greater obliquity forcing) affects the seasonal contrast at high latitudes far more than at low latitudes.

6.4.1.2. Cryosphere sensitivity

Comparing the response of the combined $\delta^{18}O$ records (Site U1338 and 982 – Figure 6.3.b) to obliquity forcing in the ETP (Figure 6.3.a) shows that the response of the cryosphere to obliquity forcing is not always constant (Figure 6.3.c). Overall, the U1338 $\delta^{18}O_{CM}$ wavelet shows a weaker and less continuous response to obliquity than the 982 $\delta^{18}O$ wavelet, reflecting the lower variability, and therefore lower signal-to-noise ratio in the U1338 $\delta^{18}O_{CM}$ record compared to the 982 $\delta^{18}O$ record (Figure 6.2 c and f). However overall, the $\delta^{18}O$ response is high before ~ 7.0 Ma, between 6.3 and 4.7 Ma and between 3.7 Ma to the end of the record (Figure 6.3 b). During these intervals, the U1338 $\delta^{18}O_{CM}$ varies by around 0.5 ‰. The intervals in which there is less variation in the U1338 $\delta^{18}O_{CM}$ record less (variation of only 0.3 ‰), overlap well with the intervals where the response to obliquity forcing is reduced, particularly between 7.0 to 6.3 Ma and 4.7 to 3.7 Ma (Figure 6.3 b). The obliquity forcing is fairly strong throughout the record, with the exception of 6.7 to 6.5 Ma, 5.7 to 5.4 Ma and 4.4 to 3.7 Ma (Figure 6.3 a). Generally the obliquity forcing and $\delta^{18}O$ response agrees well, particularly between 6.3 and 4.7 Ma, suggesting that the cryosphere is sensitive to external radiative forcing (Figure 6.3 c). However, between 7.0 and 6.3 Ma and 4.7 and 3.7 Ma, the $\delta^{18}O$ response is absent for a longer period than the interval of reduced forcing. This implies that the cryosphere overall is less sensitive to external radiative forcing in these intervals, as it does not recover as quickly as the increase observed in the obliquity forcing (Figure 6.3 c). Pisias et al. (1995) compared evolutionary spectra of benthic foraminiferal $\delta^{18}O$, and suggested that the $\delta^{18}O$ did not show sensitivity to obliquity forcing before 4.6 Ma. The absence of obliquity forcing reported by Pisias et al. (1995) prior to 4.7 Ma could be

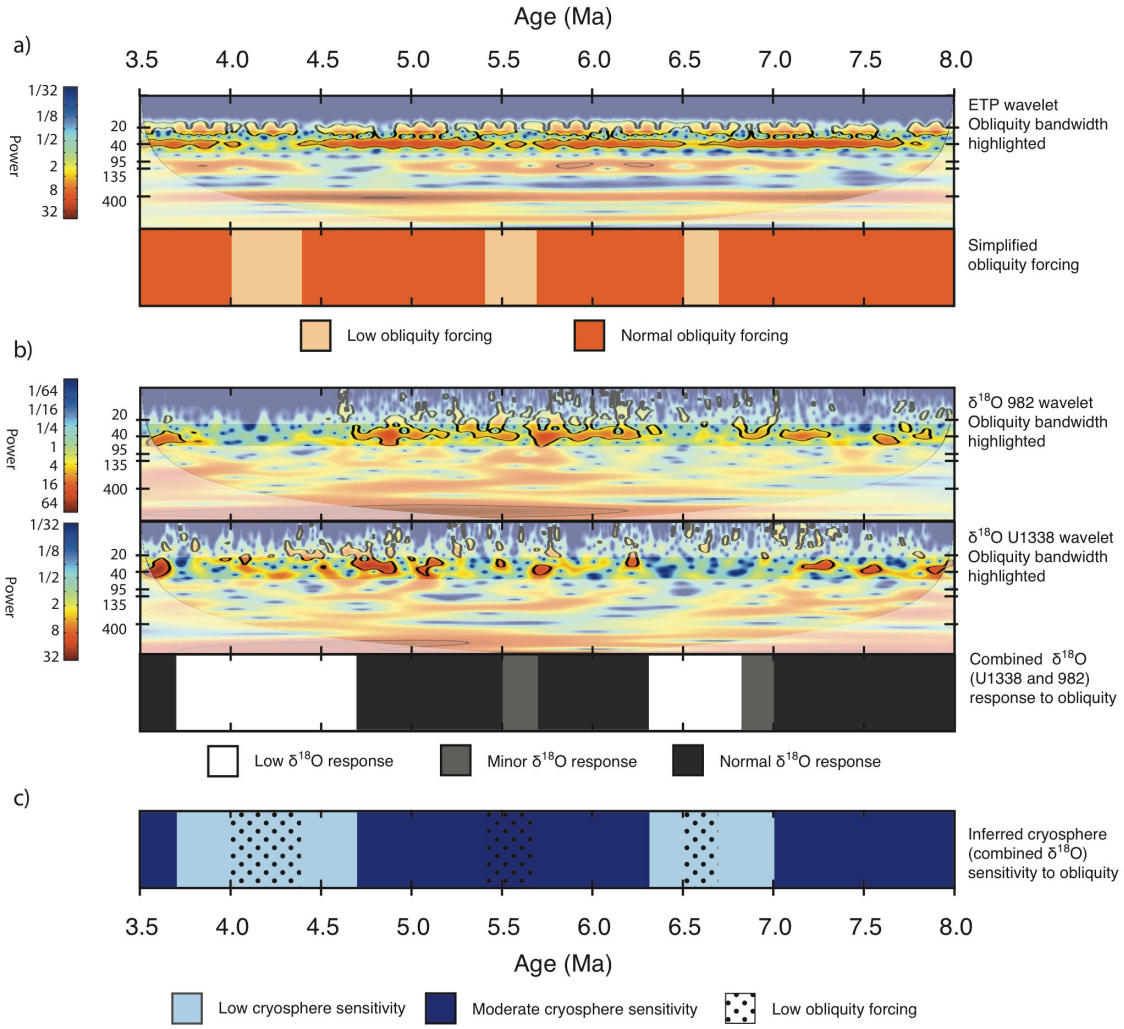

Figure 6.3.

Inferring cryosphere sensitivity by comparing the combined $\delta^{18}O$ response from Sites U1338 and 982 to the obliquity forcing.

a) Shows the original ETP wavelet, with the obliquity bandwidth highlighted. The simplified obliquity forcing is shown below.

b) Shows the original wavelets of the benthic foraminiferal $\delta^{18}O$ records from Sites U1338 and 982, with the obliquity bandwidth highlighted. The combined response of the $\delta^{18}O$ records in the obliquity bandwidth is shown below.

c) Shows the inferred cryosphere sensitivity based on comparing the combined $\delta^{18}O$ response (b) to the simplified obliquity forcing (a). Moderate sensitivity is defined as intervals when the obliquity forcing is reflected in the combined $\delta^{18}O$ response, whereas low sensitivity is defined as intervals when the combined $\delta^{18}O$ response shows low or no response to obliquity forcing. In intervals with low obliquity forcing, the sensitivity is inferred from the intervals before and after the low forcing.

because they used evolutionary spectra, which can mask the power in the higher frequencies if a too large a window is used (see section 4.3.3). It is important to note that in this cryosphere sensitivity reconstruction, the variability in the benthic foraminiferal $\delta^{18}O$ records is considered solely as ice sheet variation. A caveat of this assumption is that it ignores any influence that short-term fluctuations in temperature may have on the benthic foraminiferal $\delta^{18}O$ record. 0.3 to 0.5 ‰ change in benthic foraminiferal $\delta^{18}O$ could also equate to a change in bottom water temperatures (BWT) of 1.3 to 2.2 °C (see section 3.2.1.1 for temperature to ‰ relationship). BWT changes of 1 to 2 °C are feasible considering changes in BWT reconstructed from benthic foraminiferal Mg/Ca ratios for the past 200 kyr (2 – 3 °C – Martin et al., 2002) and 1.5 Myr (1 – 3 °C – Elderfield et al., 2012). The relative influence of temperature and ice volume on benthic $\delta^{18}O$ will be considered further in section 6.4.2.

6.4.1.3. Carbon cycle sensitivity

As with the combined $\delta^{18}O$ records, the combined $\delta^{13}C$ response (Site U1338 and 982 – Figure 6.4 b) to obliquity forcing in the ETP (Figure 6.4 a) is not always constant (Figure 6.4 c). In general, the power of $\delta^{13}C$ response to obliquity forcing is far less compared to the power in the combined $\delta^{18}O$ records, (Figure 6.4 b). This weaker response reflects the lower short-term variability in both the U1338 and 982 benthic foraminiferal $\delta^{13}C$ records (Figure 6.2 o and r). The $\delta^{13}C$ response from U1338 is far less continuous than the 982 wavelet. Also, the U1338 $\delta^{13}C$ response extends into the 80 kyr band, which is not seen in the 982 $\delta^{13}C$ response. Generally between 6.3 and 3.5 Ma, the degree of obliquity

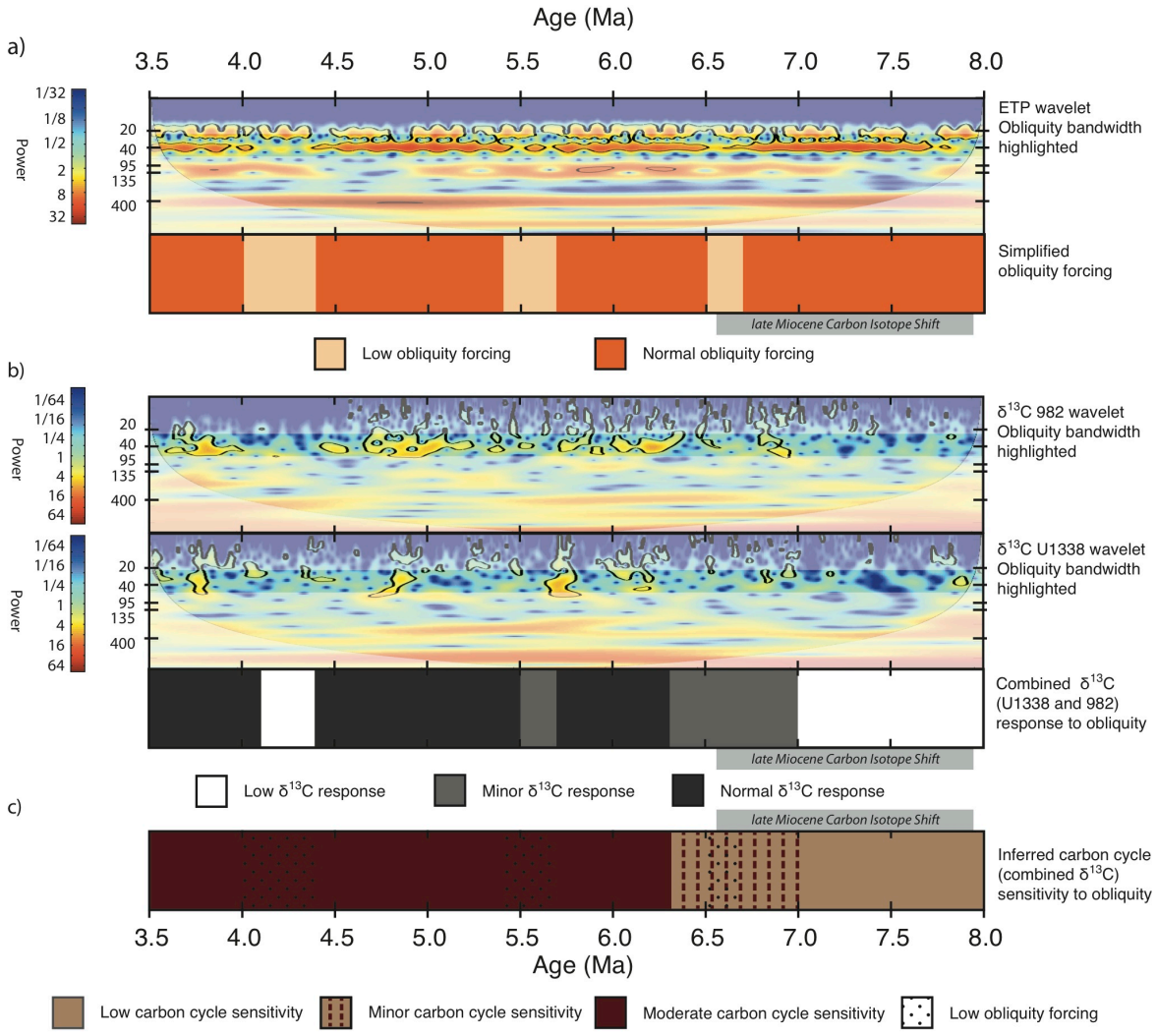

Figure 6.4.

Inferring carbon cycle sensitivity by comparing the combined $\delta^{13}C$ response from Sites U1338 and 982 to the obliquity forcing.

a) Shows the original ETP wavelet, with the obliquity bandwidth highlighted. The simplified obliquity forcing is shown below.

b) Shows the original wavelets of the benthic foraminiferal $\delta^{13}C$ records from Sites U1338 and 982, with the obliquity bandwidth highlighted. The combined response of the $\delta^{13}C$ records in the obliquity bandwidth is shown below.

c) Shows the inferred carbon cycle sensitivity based on comparing the combined $\delta^{13}C$ response (b) to the simplified obliquity forcing (a). Moderate sensitivity is defined as intervals when the obliquity forcing is reflected in the combined $\delta^{13}C$ response, whereas low sensitivity is defined as intervals when the combined $\delta^{13}C$ response shows low or no response to obliquity forcing. In intervals with low obliquity forcing, the sensitivity is inferred from the intervals before and after the low forcing.

forcing (Figure 6.4 a) corresponds well will the $\delta^{13}C$ response level (Figure 6.4 b), suggesting the carbon cycle is sensitive to external radiative forcing during the early Pliocene and much of the late Miocene (Figure 6.4 c). Because the response in the combined $\delta^{13}C$ record is not particularly high, this suggests that even though the carbon cycle seems to be sensitive to external radiative forcing, the coupling is not strong. The greater response to external forcing in the $\delta^{18}O$ record compared to $\delta^{13}C$ record is probably caused by a direct response in the $\delta^{18}O$ to obliquity forced glacial-interglacial variations in ice volume, whereas $\delta^{13}C$ changes through a series of feedbacks that vary in response to the interglacial/glacial cycles.

There is no correlation between obliquity and $\delta^{13}C$ before 7.0 Ma, and the degree of correlation is minimal between 7.0 and 6.3 Ma (Figure 6.4 a and b). This indicates that the coupling of the carbon cycle to external radiative forcing broke down during the LMCIS (Figure 6.4 c). The low carbon cycle sensitivity between 8.0 and 7.0 Ma (Figure 6.4 c) incidentally coincides with a period where the cryosphere responds more strongly to obliquity (Figure 6.3 c). The moderate response of the carbon cycle to external forcing is restored after the end of the LMCIS (Figure 6.4 c). The low sensitivity of the carbon cycle to obliquity between 8.0 and 7.0 Ma indicates that a process independent of solar forcing may have perturbed the carbon system during the LMCIS. The lack of response to obliquity forcing in the $\delta^{13}C$ record prior to LMCIS might also indicate that a low latitude external forcing, such as eccentricity, might be the main forcing driving the LMCIS. There is evidence for power in the 400 kyr bandwidth throughout the whole LMCIS, although part of this period is overlapped by the cone of influence where results should be treated cautiously (see section 4.3.3 for definition of

cone of influence). The low sensitivity to obliquity during the LMCIS will be considered in more detail when discussing the driving forces of the LMCIS in section 6.4.3.1.

6.4.1.4. Earth System Response

Combining the reconstructed cryosphere (Figure 6.5 b) and carbon cycle (Figure 6.5 c) sensitivities to obliquity forcing (Figure 6.5 a) allows the Earth system response (response of the major long-term climate system to external radiative forcing) to be inferred. This reconstruction indicates that generally the Earth system response (Figure 6.5 d) was moderate between 6.3 – 4.7 Ma and after 3.7 Ma. Between 4.7 and 3.7 Ma, the cryosphere responded less strongly, whereas the carbon cycle response correlated well with obliquity forcing. The combined Earth system response to solar forcing is lower between 7.0 and 6.3 Ma (Figure 6.5 c). Before 7.0 Ma the carbon cycle shows low sensitivity to external forcing, however this is likely caused by the perturbation that drove the LMCIS, as the cryosphere responds well to external forcing during this interval. No evidence was found for amplified response to external radiative forcing, which implies that there was no high sensitivity during this interval. The absence of high sensitivity intervals, coupled with the dominance of moderate to low sensitivity of the climate to external radiative forcing, could have greatly contributed to the overall stability of late Miocene to early Pliocene climate. In section 6.4.2 and 6.4.3, the reconstructed cryosphere and carbon cycle sensitivity and Earth system response are coupled with a detailed compilation of the

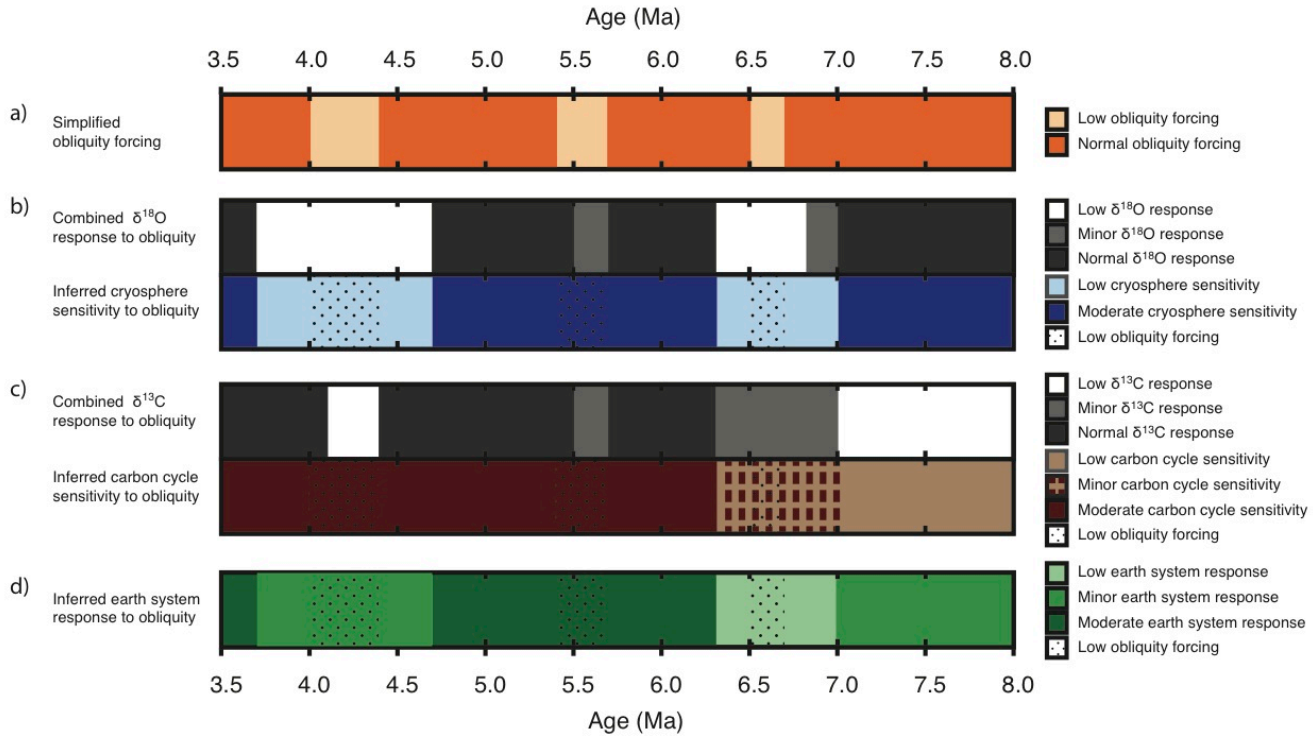

Figure 6.5

Inferring overall Earth system response to obliquity forcing, by combining the inferred cryosphere (Figure 4.19) and carbon cycle (Figure 4.20) sensitivity.

a) Shows the simplified obliquity forcing.

b) Shows the combined response of the $\delta^{18}O$ records in the obliquity bandwidth, coupled with the inferred cryosphere sensitivity to obliquity forcing.

c) Shows the combined response of the $\delta^{13}C$ records in the obliquity bandwidth, coupled with the inferred carbon cycle sensitivity to obliquity forcing.

d) Shows the inferred Earth system response to obliquity forcing, based on combining the cryosphere (b) and carbon cycle (c) sensitivities to obliquity forcing. A moderate response is defined as intervals when both the cryosphere and carbon cycle are sensitive to obliquity forcing, whereas a low response is defined as intervals when neither components are sensitive to external forcing. The intervals defined as having a minor response reflect times when only one component was sensitive to obliquity forcing. During intervals with low obliquity forcing, the overall response is inferred from the intervals before and after the low forcing.

benthic foraminiferal $\delta^{18}O$ and $\delta^{13}C$ records from the various DSDP, ODP and IODP sites discussed in section 6.2.1. These compilations enable a detailed investigation of the influence of regional and global climate perturbations on the stable isotope records, and help with discussions concerning the origins of climatic perturbations during the late Miocene and early Pliocene, such as the Messinian Salinity Crisis (section 6.4.2.1) and the LMCIS (section 6.4.3.1).

6.4.2. Global ice volume variations and implications for glacio-eustatic control of the Messinian Salinity Crisis

Figure 6.6 a shows the benthic foraminiferal $\delta^{18}O$ from three eastern equatorial Pacific Sites U1338, 849 and 846, and a western equatorial Pacific, Site 806. The Site U1338 stable isotope records are clearly the first high-resolution records in this region that extend back to 8.0 Ma. The $\delta^{18}O$ records from Sites U1338 and 849 are very similar between 5.0 and 3.5 Ma. The Site 846 $\delta^{18}O$, which is a shallower site in a slightly more isolated basin east of the East Pacific Rise, is considerably more variable (Figure 6.1): the higher variability could reflect local temperature changes and the shallower water depth may also explain the offset to more negative $\delta^{18}O$ values (Figure 6.6 a). Between 8.0 and 5.0 Ma, the U1338 and 849 $\delta^{18}O$ records still show similar long-term trends, although Site 849 shows more variation, probably because of the lower sampling resolution of the record (see Table 6.1 and section 6.2.1). An offset between the U1338 and 849 records between 7 and 5 Ma of up to 0.3 ‰ (~ 1 °C) could

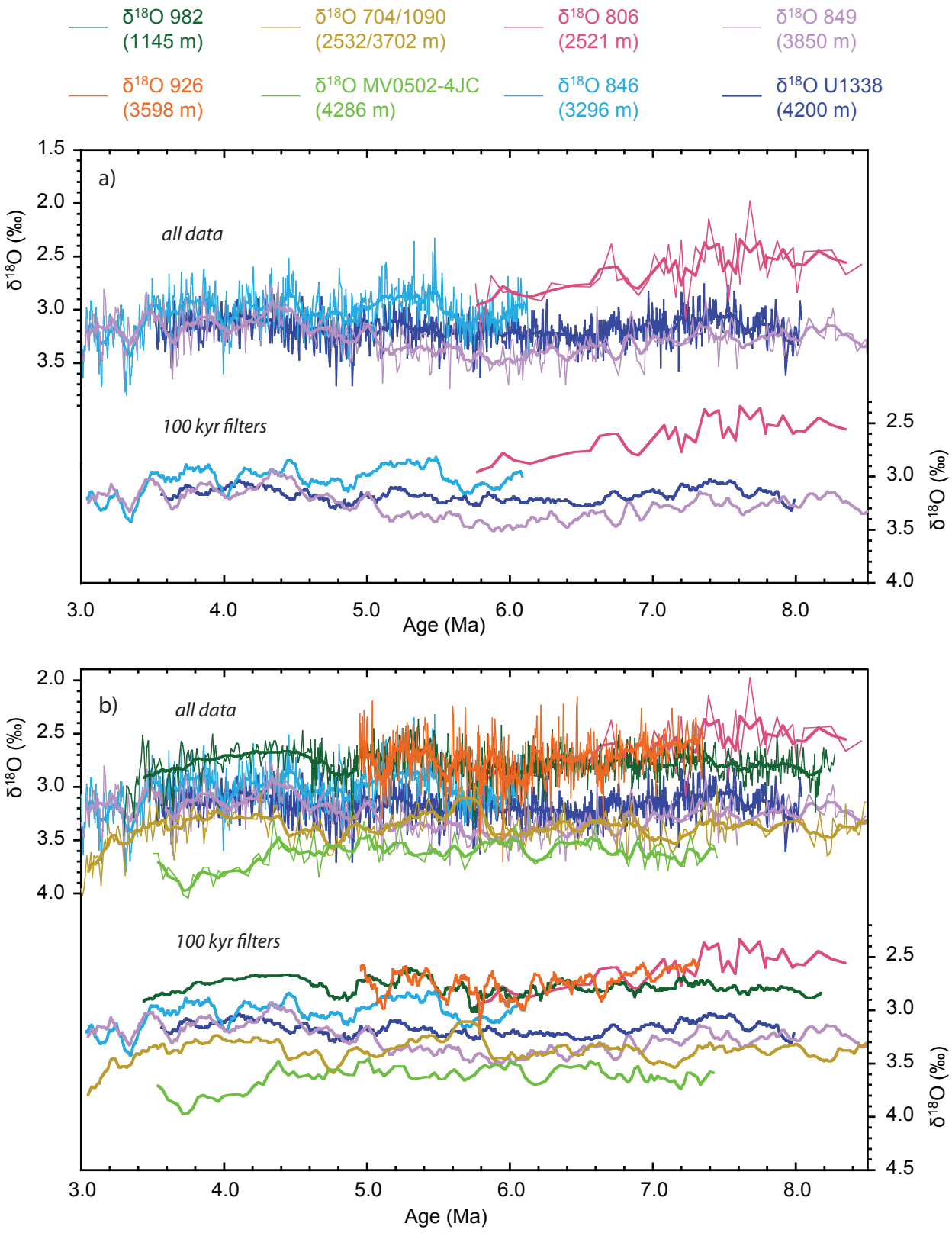
δ18O 982 (1145 m)
δ18O 704/1090 (2532/3702 m)
δ18O 806 (2521 m)
δ18O 849 (3850 m)
δ18O 926 (3598 m)
δ18O MV0502-4JC (4286 m)
δ18O 846 (3296 m)
δ18O U1338 (4200 m)
a)
all data
100 kyr filters
δ18O (‰)
Age (Ma)
b)
all data
100 kyr filters
δ18O (‰)
Age (Ma)

Figure 6.6.

Overview of the (a) Pacific only and (b) all eight $\delta^{18}O$ records used for the global compilation of $\delta^{18}O$ records.

a) Shows the three eastern Pacific (Site U1338, 849 and 846) and single western Pacific (Site 806) $\delta^{18}O$ records. The upper four records show each $\delta^{18}O$ record in full resolution and with a 100 kyr filter. The lower four records show the 100 kyr filters alone to highlight long-term trends.

b) Shows the four Pacific, two Atlantic (Sites 982 and 926) and two Southern Ocean (Atlantic sector combined Site 704/1090; Pacific sector Site MV0502-4JC) $\delta^{18}O$ records. The upper eight records show each $\delta^{18}O$ record in full resolution and with a 100-kyr filter. The lower four records show the 100-kyr filters alone to highlight long-term trends.

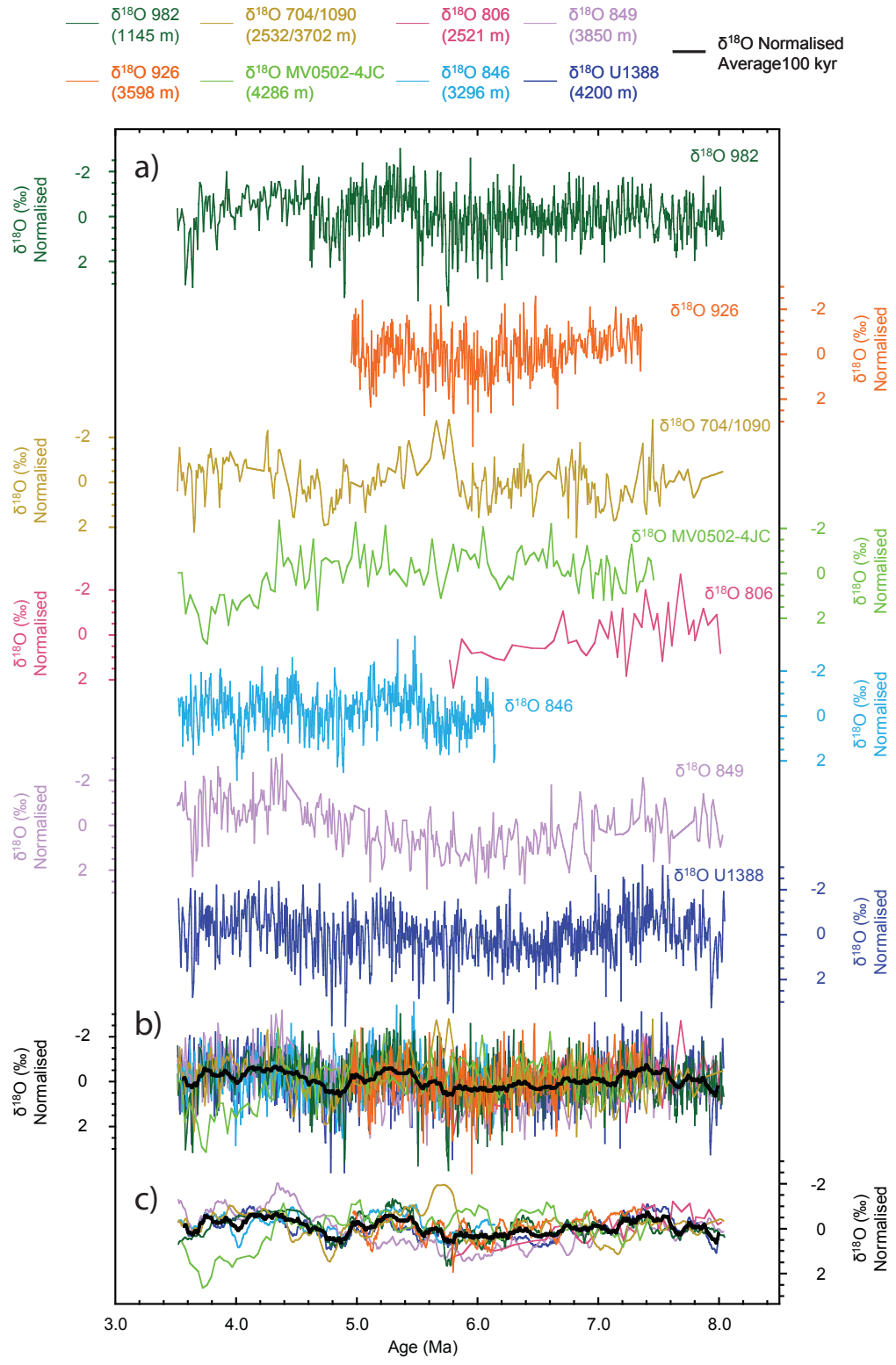

Figure 6.7.

Overview of the (a) individual normalised $\delta^{18}O$ records from the eight sites used in the multi-site compilation, (b) all full-resolution normalised $\delta^{18}O$ records plotted with the averaged 100-kyr filter; and (c) the individual 100-kyr filtered normalised $\delta^{18}O$ records plotted with the averaged 100-kyr filter.

indicate a difference in overlying water mass at the two sites, although the $\delta^{13}C$ records suggest that the water mass is fairly homogenous in the deep Pacific (see Figure 6.12 and section 6.4.3 discussion). Alternatively, the $\delta^{18}O$ offset could also be caused by a difference in temperature at the two sites; however, as U1338 is the deeper site, it is unexpected for this deeper site to have higher temperatures than the shallower Site 849. The western Site 806 $\delta^{18}O$ record is approximately 0.5 ‰ more negative than the eastern Pacific sites (Figure 6.6 a). This probably reflects an east to west Pacific temperature gradient in the deep waters. In the modern ocean, the temperature difference is less than 0.5 °C (east Pacific = 1.45 °C; west Pacific = 1.87 °C; Locarnini et al., 2010). The observed 0.5 ‰ difference, if due to temperature alone, is equivalent to ~ 2 °C. This implies that there was a greater than modern bottom water temperature gradient between the eastern and western Pacific, assuming that diagenetic overprinting is minimal at both sites.

Figure 6.6 b shows the four Pacific sites combined with two Atlantic site (ODP 982 and 926) and two Southern Ocean sites (Atlantic side: combined record from ODP Sites 704 and 1090; Pacific side: site MV0502-4JC). The gradients between the different sites are partially expected. The Southern Ocean Sites (704/1090; MV0502-4JC) show the highest $\delta^{18}O$, representing the coldest temperatures. The north Atlantic sites (982 and 926) show comparable values, implying fairly uniform temperature gradients from the north to the equatorial Atlantic, despite the large depth difference of almost 2.5 km between the two sites. This suggests that the North Atlantic Deep Water, of which the Site 982 $\delta^{18}O$ record is most likely a representative end member, extends to the deep ocean at the equator in the Atlantic. The east Pacific sites show $\delta^{18}O$ values in

between the Atlantic and Southern Ocean $\delta^{18}O$ values, whereas the west Pacific Site 806 $\delta^{18}O$ is more similar to the Atlantic $\delta^{18}O$, which is most likely an effect of warm bottom water conditions in the western equatorial Pacific (Lear et al., 2003).

Long-term global trends are difficult to discern in the benthic foraminiferal $\delta^{18}O$ data, as there are considerable differences in absolute values between the eight sites due to temperature and water depth differences (Figure 6.6 b). Taking an average of the normalised $\delta^{18}O$ records (see section 6.3.2) helps to highlight any globally synchronous trends. These long-term trends could reflect both long-term changes in temperature and/or global variations in ice volume. The average normalised record is more heavily influenced by the higher resolution records, particularly from Sites 982, 926, 846 and U1338, so the contribution of the Southern Ocean is underestimated (Figure 6.7). However, a number of distinct variations are visible in the combined records. Firstly, between 8 and 7 Ma, the long-term $\delta^{18}O$ is generally quite low, coupled with distinct short-term fluctuations. This broad minimum is followed by an interval with some of the highest $\delta^{18}O$ values between ~ 7 and 5.9 Ma. This interval also represents a period of relative long-term stability and a reduction in the amount of distinct short-term variability. Between 5.9 and 4.9 Ma, there is another broad minimum, again coupled with intervals of distinct variability in the short-term (obliquity cycle scale), followed by a brief (~ 100 to 200 kyr) interval of increased $\delta^{18}O$. The final 1.5 Myr of the record (~ 4.8 – 3.5 Ma) is characterised by a return to lower $\delta^{18}O$ values. Overall, there is less distinct short-term variability in this section of the record, although this could be a symptom of the lower temporal resolution of the 982 and U1338 records in this interval.

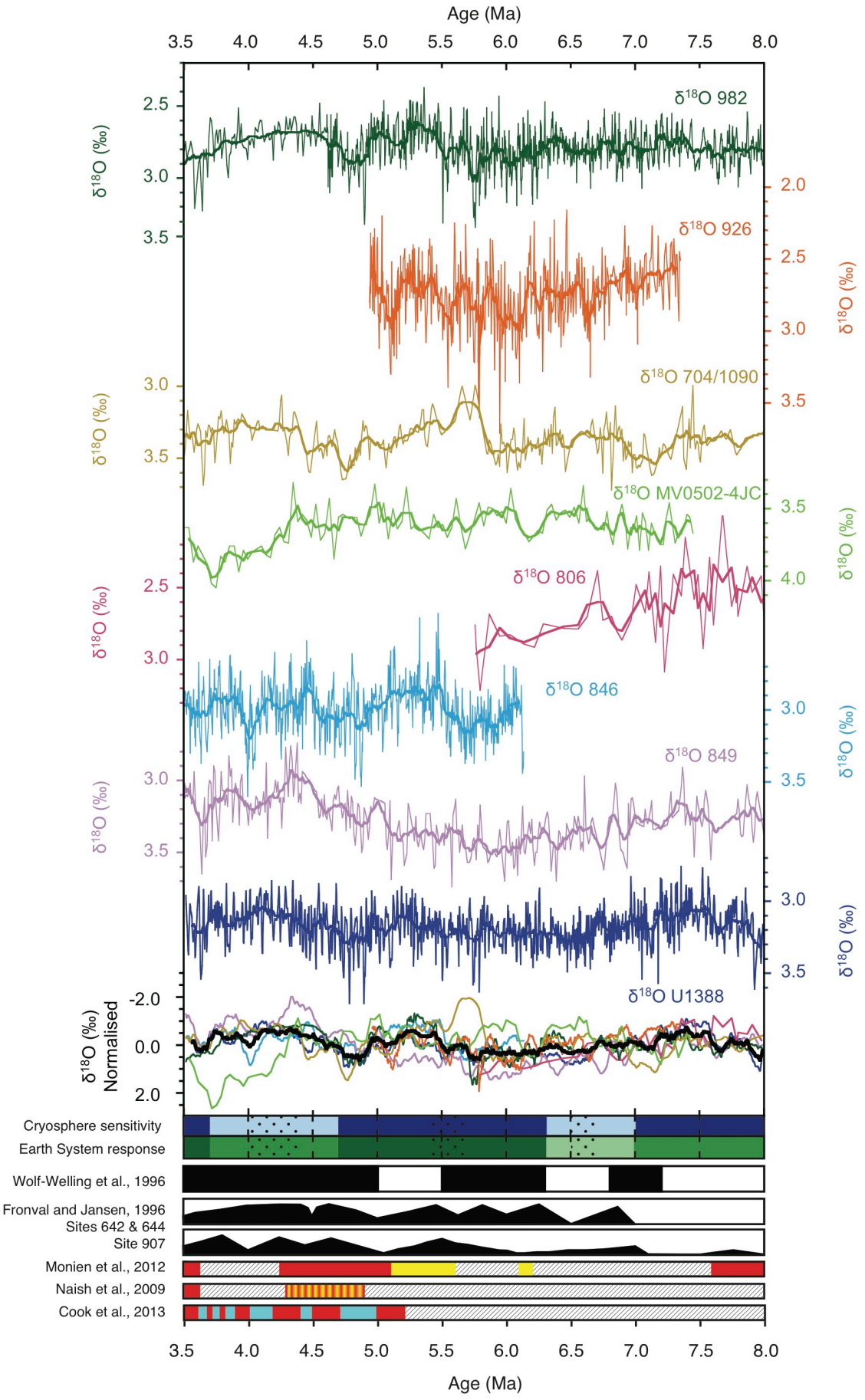
Age (Ma)
3.5 4.0 4.5 5.0 5.5 6.0 6.5 7.0 7.5 8.0
δ18O 982
δ18O 926
δ18O 704/1090
δ18O MV0502-4JC
δ18O 806
δ18O 846
δ18O 849
δ18O U1388
δ18O (‰)
δ18O (‰) Normalised
Cryosphere sensitivity
Earth System response
Wolf-Welling et al., 1996
Fronval and Jansen, 1996
Sites 642 & 644
Site 907
Monien et al., 2012
Naish et al., 2009
Cook et al., 2013
Age (Ma)

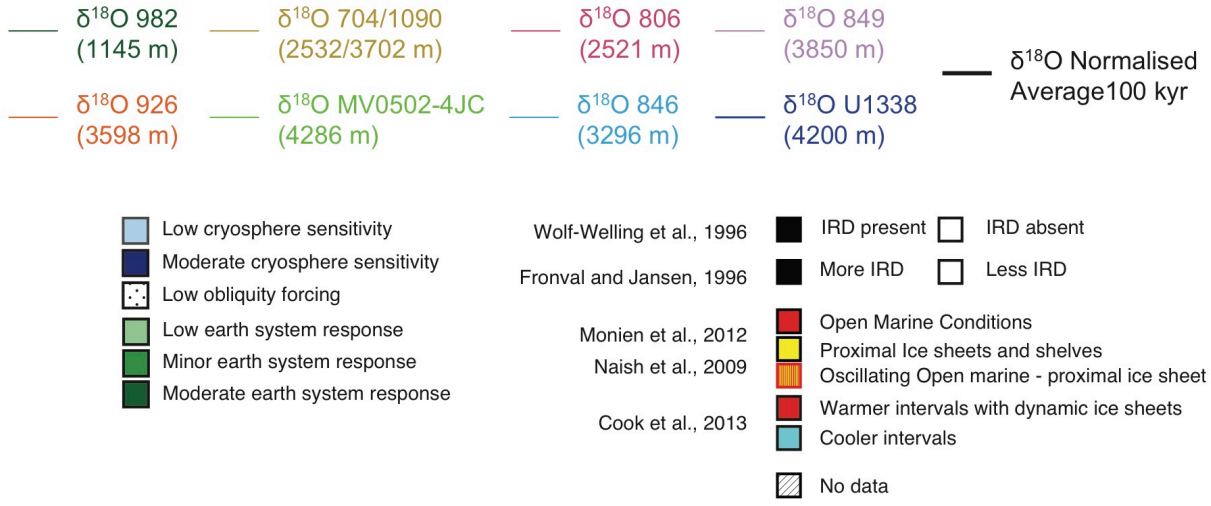

Figure 6.8.

Overview of the eight original full-resolution $\delta^{18}O$ records from the eight sites used in the multi-site compilation, with the normalised individual 100-kyr filtered $\delta^{18}O$ records and an averaged 100-kyr filter of all normalised data.

Plotted below are the reconstructed cryosphere and Earth system response, together with proximal ice proxy records from both the Northern and Southern hemispheres, shown in more detail in Figure 6.9.

Figure 6.8 shows all individual $\delta^{18}O$ records on offset axes together with the normalised $\delta^{18}O$ average, and reconstructed cryosphere sensitivity and Earth system response reconstructions and published ice proxy records. The early minimum in $\delta^{18}O$ between 8 and 7 Ma occurs during a period where the cryosphere sensitivity is moderate, although the overall Earth system response is somewhat reduced. Similarly, the second minimum between 5.7 and 4.9 Ma occurs during an interval of moderate cryosphere sensitivity and Earth system response. Figure 6.9 shows reconstructions based on records proximal to Greenland (Jansen and Sjøholm, 1991; Fronval and Jansen, 1996; Wolf-Welling et al., 1996), and the West (WAIS) (Naish et al., 2009; McKay et al., 2009; Talarico and Sandroni, 2009; Monien et al., 2012) and East (EAIS) (Cook et al., 2013) Antarctic Ice Sheets over the past 8 Myr. Records from the WAIS suggest that there were proximal ice to open marine conditions prevailing before 7.6 Ma, implying a decrease in overall ice volume (McKay et al., 2009; Monien et al., 2012). This interval coincides with an interval of more negative average benthic foraminiferal $\delta^{18}O$ (potentially decreased ice volume or increased temperature) and increased short-term variability in the $\delta^{18}O$ records with clear obliquity driven cycles. The interval prior to 7.0 Ma is also one of the warmest periods of the late Miocene, as seen from sea surface temperature records (Figure 6.10; see also section 5.5.1 and 5.5.3 in Chapter 5). Between 7.0 and 5.7 Ma the increased $\delta^{18}O$ coincides with an increase in ice rafted debris (IRD) around Greenland (Fronval and Jansen, 1996; Wolf-Welling et al., 1996). There is some evidence that the WAIS was also alternating between warmer and colder conditions around 6.2 – 6.1 Ma, with extended ice shelves but not fully glacial conditions. These ice records coincide with an interval of cooling in the SST records (Figure

6.10) and suggest that the increased $\delta^{18}O$ seen in the average normalised records (Figure 6.8) reflects a cooler period with increased ice volume in both the Northern and Southern Hemispheres between ~ 7 and 5.7 Ma.

A further two periods (5.7 to 5.0 Ma and 4.9 to 3.5 Ma) show lower $\delta^{18}O$ and high cryosphere sensitivity coinciding with evidence for dynamic variability in the WAIS and EAIS (Figure 6.9). Naish et al. (2009) also present evidence during these time periods for obliquity-driven glacial-interglacial variation in sedimentary cycles from the AND-1B core in the Ross Sea. A lower-resolution study on the same core suggests dynamic ice shelf conditions (5.7 to 5.1 Ma) developed into full-scale open marine conditions (5.1 to 4.25 Ma) (Monien et al., 2012). Evidence from IODP Site U1361, offshore of East Antarctica, shows repeated intervals of glacial retreat of the EAIS during warmer intervals throughout the early Pliocene (Cook et al., 2013). The intervals of lower $\delta^{18}O$ also coincide with a warming trend in the SST (Figure 6.8 and 6.10). Interestingly, evidence from deep-sea sites off Greenland, show the presence of IRD throughout this interval, of a similar strength as the colder interval between 7.0 and 5.9 Ma (Fronval and Jansen, 1996; Wolf-Welling et al., 1996). This could suggest that the ice volume in the Northern Hemisphere (either as small ice sheets or as mountain glaciers) was not experiencing any decrease, unlike that seen in the Southern Hemisphere (Figure 6.9). The low $\delta^{18}O$ interval between 4.7 and 3.7 Ma is an interval where the cryosphere sensitivity shows low sensitivity to external forcing (Figure 6.3). However, obliquity scale cyclicity is reported in proximal Antarctic records for this interval (Naish et al., 2009; Figure 6.8). The reduced temporal sampling in the U1338 and 982 $\delta^{18}O$ records between 4.7 and 3.5 Ma may have masked the true cryosphere sensitivity.

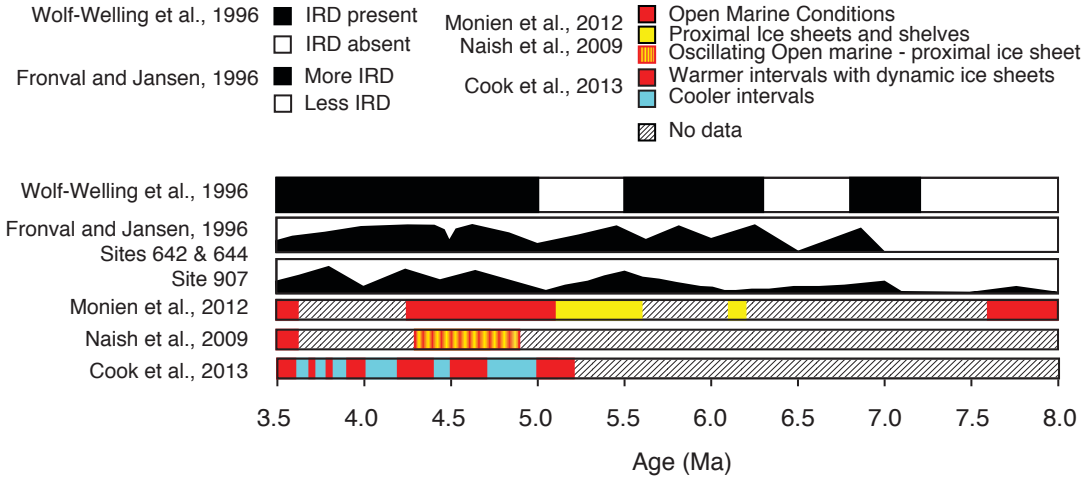

Figure 6.9.

Shows an overview of the various proximal ice proxy records from the Northern Hemisphere (Wolf-Welling et al., 1996; Fronval and Jansen, 1996), Western Antarctic Ice Sheet (Naish et al., 2009; Monien et al., 2012) and Eastern Antarctic Ice Sheet (Cook et al., 2013).

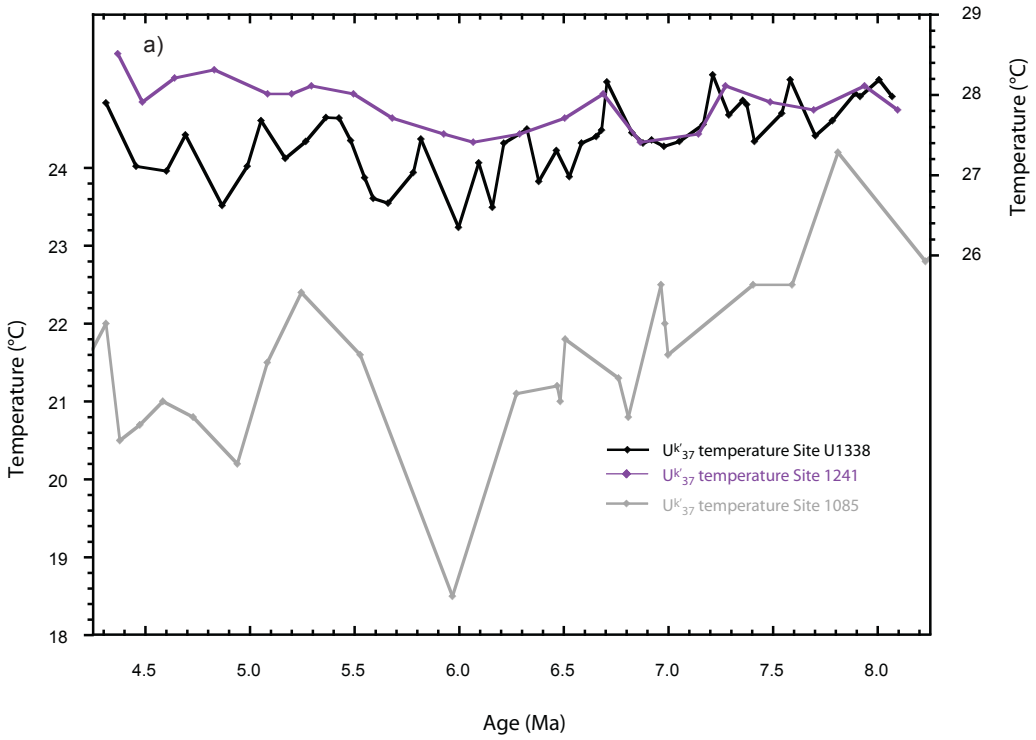

Figure 6.10.

Overview of alkenone $U^{k'}_{37}$ based SST records from Site U1338 in the eastern equatorial Pacific (Rousselle et al., 2013), Site 1241 in the far eastern equatorial Pacific (Seki et al., 2012), and Site 1085 in the South Atlantic (Rommerskirchen et al., 2011).

The intervals of decreased $\delta^{18}O$ (8 - 7 Ma, 6 - 5 Ma and after 4.9 Ma) coincide well with evidence for dynamic ice sheet variation in both the WAIS and EAIS (see Figure 6.8 and 6.9). These intervals also coincide with intervals where El Niño-like conditions are implied for the equatorial Pacific from multi-proxy surface water records, discussed in Chapter 5 (Figure 6.10; see sections 5.5.1 and 5.5.3). This suggests that there is a link between globally warmer surface water conditions and increased dynamism in Southern Hemisphere ice sheet extent, and supports the suggestion that warm sea surface temperatures act as the driving force for glacial retreats in EAIS during the Pliocene (Cook et al., 2013). The current record of ice sheet dynamism in the late Miocene is limited. However, as there is evidence for open marine to proximal ice shelf conditions around the WAIS in the earliest and latest sections of the late Miocene (Monien et al., 2012), it is feasible that the same relationship holds during the warm El Niño intervals in the late Miocene (Figure 6.10). The fact that IRD in the Northern Hemisphere does not change much in the late Miocene and early Pliocene suggests that SST variations do not govern the ice volume extent in that region.

6.4.2.1. Extent of Glacio-Eustatic Control on the Messinian Salinity Crisis (MSC)

Figure 6.11 shows the three high-resolution records that cover the Messinian Salinity Crisis, including Atlantic sites 982 and 926, and Pacific Site U1338. The Messinian Salinity Crisis (MSC) occurred during a period of

increased climate sensitivity. In terms of long-term trends, the onset occurs during some of the highest $\delta^{18}O$ values seen in this interval, which coincide with the lowest amplitude variation seen in the benthic foraminiferal $\delta^{18}O$ records and evidence from Antarctica for more stable conditions (Monien et al., 2012) (see discussion in section 6.4.2). The termination of the MSC occurs at the start of the broad $\delta^{18}O$ minimum between 5.7 and 5.0 Ma, which coincides with evidence for dynamic variation in the Antarctic ice sheet (Monien et al., 2012; Cook et al., 2013) and higher amplitude variation in the benthic foraminiferal $\delta^{18}O$ records (see discussion in section 6.4.2). Looking at the short-term variation, there is a $\delta^{18}O$ maximum stage, identified as TG32 in U1338 (see Figure 4.15 in Chapter 4) occurring in all three records around 5.96 Ma at the onset of the MSC (red line and band – Figure 6.11). The extent of change during the $\delta^{18}O$ maximum at 5.96 Ma differs per record: ~ 0.3 ‰ at Site U1338; ~ 0.5 ‰ at Site 926; ~ 0.3 ‰ at Site 982. All three records also show that a $\delta^{18}O$ minimum occurs at the termination of the MSC at ~ 5.33 Ma (green line and band – Figure 6.11). The extent of the change seen during the $\delta^{18}O$ minimum at 5.33 Ma varies from ~0.2 ‰ at Site U1338, and ~ 0.3 ‰ at Sites 926 and 982.

Although there is clear evidence for a $\delta^{18}O$ maximum, which could be a glacial stage, at the onset of the MSC and a $\delta^{18}O$ minimum, potentially an interglacial stage, at the termination, the importance of glacio-eustacy in controlling the exact timing of the MSC is not certain. Krijgsman et al. (1999) showed that the internal desiccation cycles seen in the Mediterranean Sea during the MSC are driven by precession, and therefore most likely controlled by hydrological cycles on continental Africa. However, the exact extent of glacio-eustatic control on the onset and termination of the MSC has not yet been

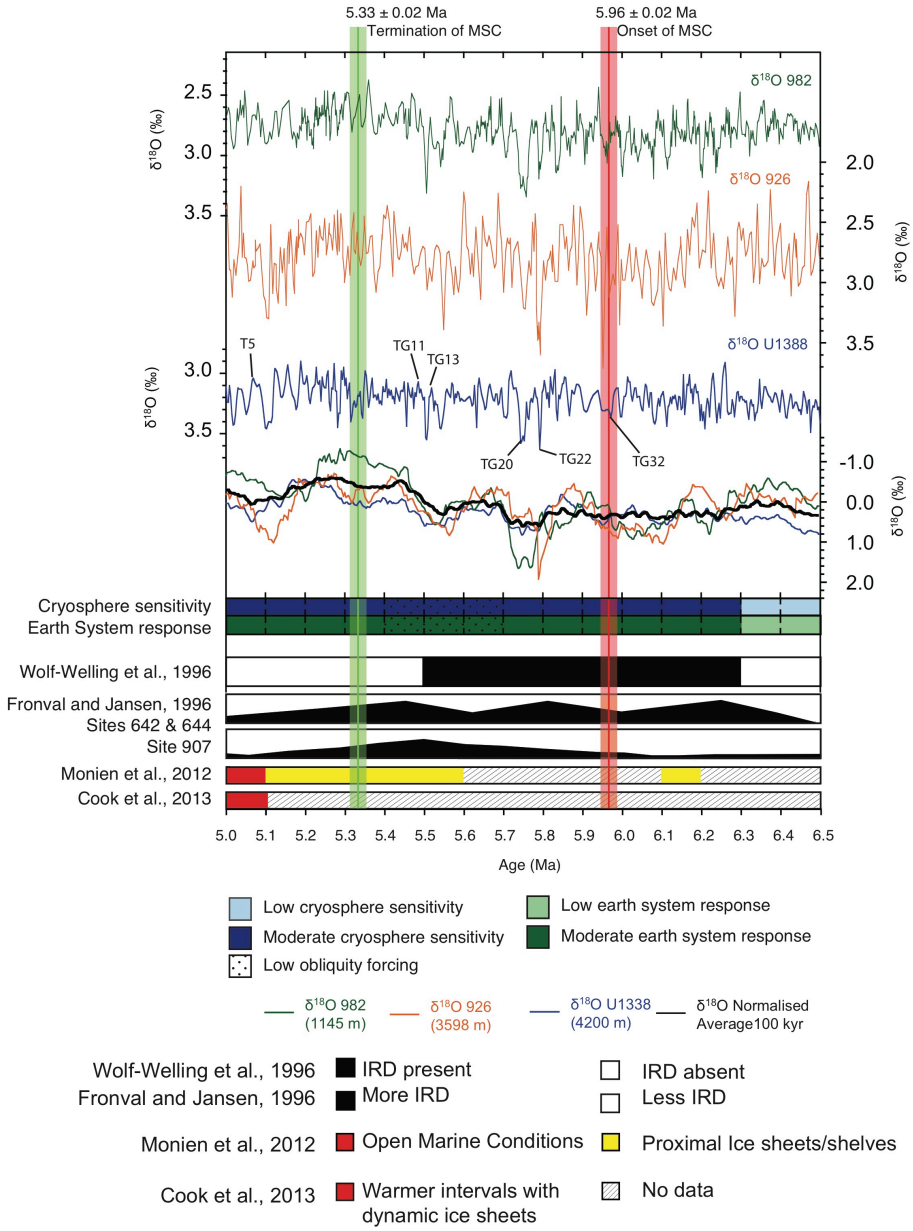

Figure 6.11.

Overview of the three high-resolution benthic foraminiferal $\delta^{18}O$ records from Sites 982 (green), 926 (orange) and U1338 (blue) with the normalised 100-kyr filtered average from each site, together with the 100-kyr average of all normalised records. Plotted below are the cryosphere sensitivity and Earth system response, together with relevant proximal ice proxies from offshore Greenland (Wolf-Welling et al., 1996; Fronval and Jansen, 1996) and Antarctica (Monien et al., 2012; Cook et al., 2013). The onset of the Messinian Salinity Crisis (MSC) is indicated with error at 5.96 ± 0.02 Ma with a red line and band. The termination is highlighted with error at 5.33 ± 0.02 Ma with a green line and band. Glacial and interglacial stages of interest that are discussed in text are also labelled.

constrained. It is difficult to assess the amount of sea level change that occurred based on solely benthic foraminiferal $\delta^{18}O$, as this is both controlled by changes in seawater $\delta^{18}O$ (e.g. variations in global ice volume) and changes in water temperatures. However, assuming the whole $\delta^{18}O$ change is due to ice volume change, the Pleistocene relationship between $\delta^{18}O$ and meters sea level change of 0.011 ‰/m from Fairbanks and Matthews (1978) can be applied to obtain a maximum estimate of sea level change. The range of 0.3 to 0.5 ‰ for the onset and 0.2 to 0.3 ‰ for the termination would equate to ~ 27 – 45 m sea level change at the start of the MSC around 5.96 Ma and ~ 20 – 27 m change at 5.33 Ma. If temperature change were taken into account in these calculations, these estimates would be lower. As previously discussed in section 6.4.1.2, 0.2 to 0.5 ‰ change in benthic foraminiferal $\delta^{18}O$ could reflect a 0.9 to 2.2 °C change in bottom water temperatures, which is not an unreasonable temperature change on a glacial-interglacial timescale (Elderfield et al., 2012).

An additional factor that should be considered when calculating the change in sea level potentially associated with the benthic foraminiferal $\delta^{18}O$ is the effect of latitudinal temperature gradient on the fractionation of $\delta^{18}O$ between water, water vapour and ice (see Figure 3.1). The Fairbanks and Matthews (1978) equation is based on Pleistocene data, when the latitudinal temperature gradient was greater than in the late Miocene. Biome reconstructions covering the middle to late Miocene show that the Tortonian (11.61 – 7.25 Ma) latitudinal temperature gradient was shallower than modern (Pound et al., 2011), although Messinian (7.25 – 5.33 Ma) gradients were closer to modern (Pound et al., 2012). The difference in latitudinal temperature gradient is important, as the gradient determines the amount of ^{16}O enrichment in atmospheric water vapour that

occurs with latitude due to the Rayleigh distillation (Ruddiman et al., 2001; see Figure 3.1 and discussion in section 3.2.1.1 in Chapter 3). With a shallower gradient, the atmospheric water vapour ^{16}O enrichment will be reduced compared to the Pleistocene, which will mean that the ^{18}O enrichment in oceanic $\delta^{18}O$ will be smaller for the same amount of ice volume/sea level change. Therefore the maximum sea level change could be greater than that estimated using the Fairbanks and Matthews (1978) equation, assuming no temperature influence on the benthic foraminiferal $\delta^{18}O$. Without additional high-resolution temperature control to constrain the deep-sea temperature control on the benthic foraminiferal $\delta^{18}O$ records, the extent of sea level change implied by benthic foraminiferal $\delta^{18}O$ cannot be constrained more narrowly than discussed above.

The onset of the MSC occurs during some of the highest $\delta^{18}O$ values (i.e. lowest temperatures and highest global ice volume) seen in the benthic foraminiferal $\delta^{18}O$ records. Despite the high $\delta^{18}O$ values, the TG20 and TG22 $\delta^{18}O$ isotope maxima (around 5.75 and 5.8 Ma) are far larger than TG32 (Figure 6.11), which suggests that tectonic uplift was the main driver in the isolation of the Mediterranean Sea from the Atlantic Ocean. The termination $\delta^{18}O$ minimum is likewise pre- and succeeded by larger $\delta^{18}O$ minima (TG11 and TG13 around 5.5 Ma; T5 around 5.1 Ma in Figure 6.11). However, the termination $\delta^{18}O$ minimum occurs during the peak of the long-term $\delta^{18}O$ minimum, which together with the dynamic ice-sheet variation implied from proximal ice sheet records (Naish et al., 2009; Cook et al., 2013) could indicated a long-term minimum in global ice volume. TG11/13 and T5 respectively occur during an interval of decreasing and increasing long-term $\delta^{18}O$, thereby implying that global ice volume would have

been smaller than that found around the time of the termination $\delta^{18}O$ minimum. In addition, the data reported by Naish et al. (2009) suggest that obliquity driven collapses of the WAIS were occurring as early as 4.9 Ma. Although the Naish study does not extend as far back as the MSC, it is possible that similar obliquity-driven interglacial-glacial cycles were present at the MSC termination. Overall, the evidence suggests glacio-eustacy could be a dominant factor in controlling the timing of the termination of the MSC, although a temperature component of the termination $\delta^{18}O$ minimum cannot be excluded.

6.4.3. Oceanic $\delta^{13}C$ gradients and Oceanic Circulation

Figure 6.12 a shows the benthic foraminiferal $\delta^{13}C$ records from three eastern equatorial Pacific sites (U1338, 849 and 846) and single western equatorial Pacific site (806). Similar to the $\delta^{18}O$ records, the benthic foraminiferal $\delta^{13}C$ records from eastern Pacific sites U1338 and 849 are very uniform between 8.0 and 3.5 Ma. The Site 846 $\delta^{13}C$ is generally slightly more negative than the $\delta^{13}C$ records from Sites U1338 and 849, which again may reflect that the location of Site 846 is in a more isolated basin east of the East Pacific Rise (Figure 6.1). Site 806 also shows very comparable $\delta^{13}C$ values to the eastern Pacific sites, which indicates that the deep-sea water mass in the Pacific was fairly homogeneous. In addition, the comparable $\delta^{13}C$ values across the Pacific also indicate that the $\delta^{18}O$ difference seen between the eastern and western sites in Figure 6.6 a, is caused by different water temperatures, rather than a different water mass overlying the different sites (see section 6.4.2).

As well as the Pacific $\delta^{13}C$ records, Figure 6.12 b also shows the two Atlantic (ODP 982 and 926) and Southern Ocean $\delta^{13}C$ records (combined $\delta^{13}C$ record from ODP 704 and 1090; site MV0502-4JC). It is clear there are distinct differences in $\delta^{13}C$ between the Atlantic, Southern Ocean and Pacific sites. The large negative shift in $\delta^{13}C$ is seen in all records in the oldest part of the compilation, broadly speaking between ~ 7.6 and 6.6. Ma. As previously discussed (sections 3.5.2 and 5.5.2), this shift matches the extent and duration of the late Miocene Carbon Isotope Shift (Keigwin, 1979). The fact that all eight $\delta^{13}C$ records shown in Figure 6.12 b all show a negative shift of ~ 1 ‰ is further evidence that the cause of the shift is a change in the $\delta^{13}C$ of the global oceanic carbon reservoir, as suggested by Hodell and Venz-Curtis, 2006. The underlying causes of such a large change to the $\delta^{13}C$ signature of the oceanic carbon reservoir are discussed in section 6.4.3.1.

Figure 6.12 b also shows that the relationship between the absolute $\delta^{13}C$ values from the different sites is different before and after the LMCIS. Before the LMCIS, the Atlantic 982 and Southern Ocean 704/1090 $\delta^{13}C$ records have similar high values, with the Pacific sites having distinctly lower $\delta^{13}C$ values. The modern distribution of $\delta^{13}C$ in the ocean, with values around 0.8 ‰ in the North Atlantic, progressively getting lower, reaching about 0.4 ‰ in the Southern Ocean, and then finally decreasing to around – 0.4 ‰ in the Pacific (Kroopnick, 1985) is approximately present from the end of the LMCIS (6.6 Ma) onwards (Figure 6.12 b). The pattern of decreasing $\delta^{13}C$, observed in transverses of the Atlantic and Southern Oceans and the Pacific basins represents 'water-mass aging', as the water mass builds up more ^{12}C from respired organic matter as it travels further from the source region (Broecker and Peng, 1982; see section

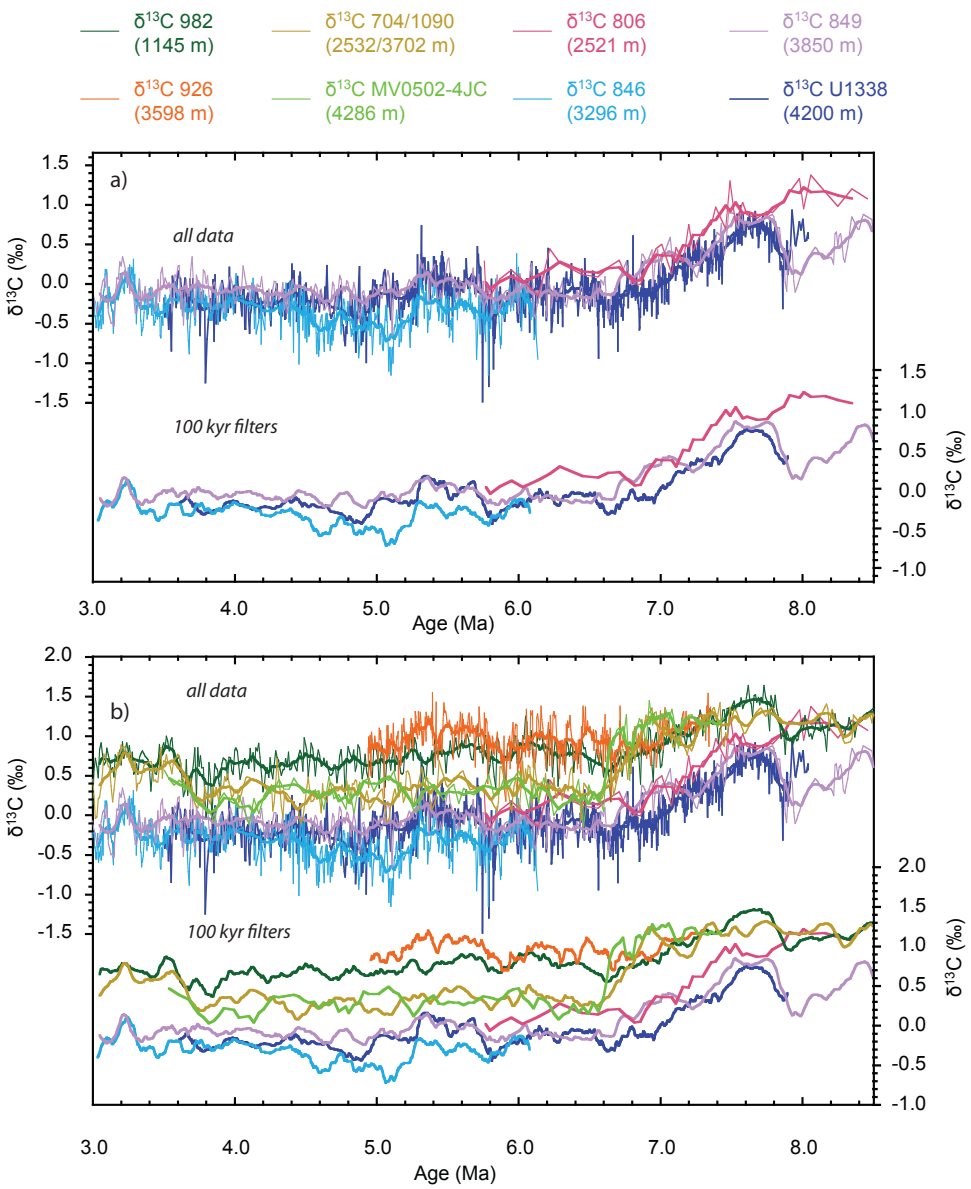

Figure 6.12.

Overview of the (a) Pacific only and (b) all eight $\delta^{13}C$ records used for the global compilation of $\delta^{13}C$ records.

a) Shows the three eastern Pacific (Site U1338, 849 and 846) and single western Pacific (Site 806) $\delta^{13}C$ records. The upper four records show each $\delta^{13}C$ record in full resolution and with a 100-kyr filter. The lower four records show the 100 kyr filters alone to highlight long-term trends.

b) Shows the four Pacific, two Atlantic (Sites 982 and 926) and two Southern Ocean (Atlantic sector combined Site 704/1090; Pacific sector Site MV0502-4JC) $\delta^{13}C$ records. The upper eight records show each $\delta^{13}C$ record in full resolution and with a 100-kyr filter. The lower four records show the 100-kyr filters alone to highlight long-term trends.

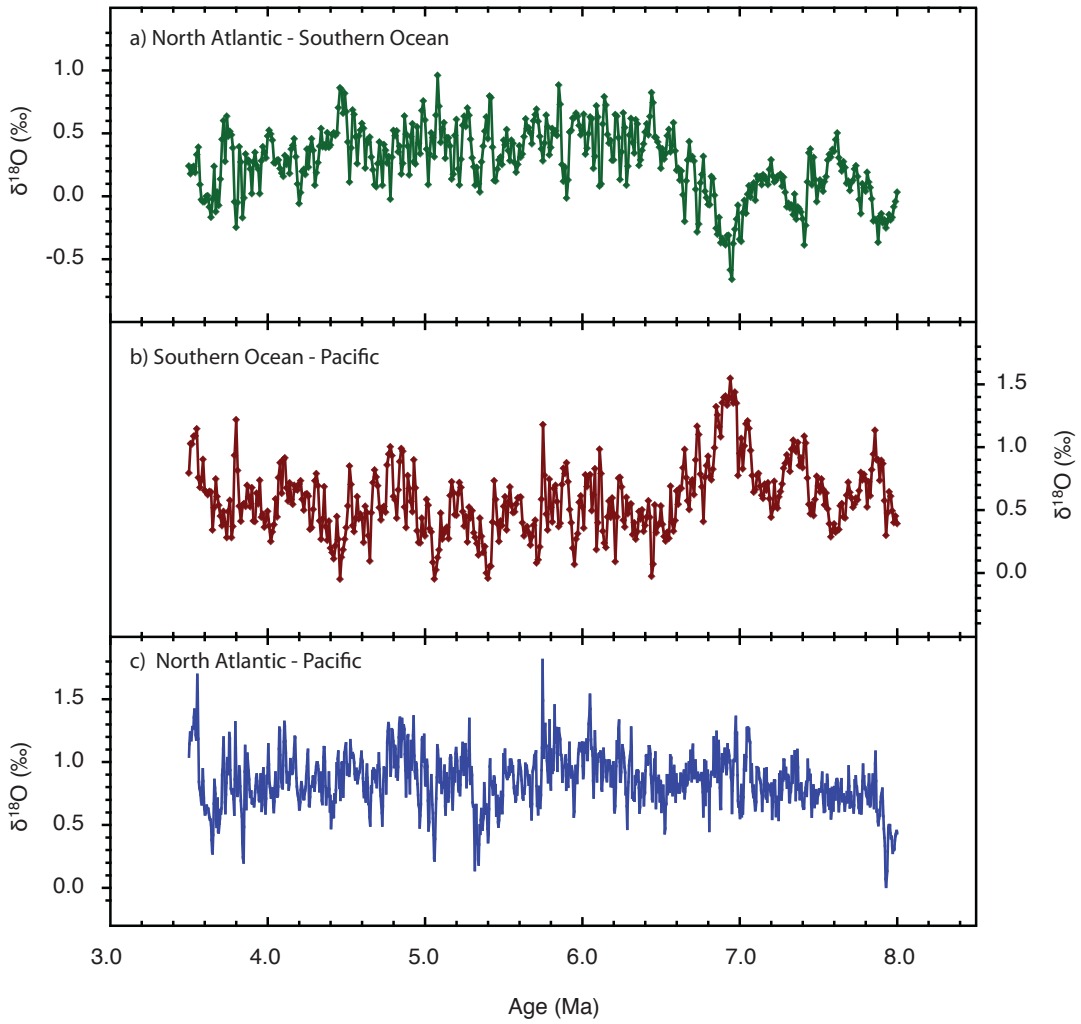

Figure 6.13.

Overview of the inter-oceanic-basin $\delta^{13}C$ gradients.

a) North Atlantic – Southern Ocean $\delta^{13}C$ gradient. Calculated by subtracting the combined Site 704/1090 $\delta^{13}C$ record from the Site 982 $\delta^{13}C$ record.

b) Southern Ocean – Pacific $\delta^{13}C$ gradient. Calculated by subtracting the Site U1338 $\delta^{13}C$ record from the combined Site 704/1090 $\delta^{13}C$ record.

c) North Atlantic – Pacific $\delta^{13}C$ gradient. Calculated by subtracting the U1338 $\delta^{13}C$ record from the Site 982 $\delta^{13}C$ record.

3.2.1.2). Additional factors that can alter benthic foraminiferal $\delta^{13}C$ are a change in the $\delta^{13}C_{DIC}$ of the source water, or a change in the productivity in the overlying surface waters (see section 3.2.1.2). A reduction in the amount of sea-air exchange in the source region of deep-water formation could drive the $\delta^{13}C_{DIC}$ of the source region to more negative values (Hodell and Venz-Curtis, 2006). Similarly, a more negative benthic foraminiferal $\delta^{13}C$ could reflect an increase in productivity in the overlying surface waters (Maslin and Swann, 2005).

The Atlantic – Southern Ocean – Pacific gradient of decreasing benthic foraminiferal $\delta^{13}C$ values consistent with the suggestion that the modern oceanic circulation pattern (with deep-water formed in the North Atlantic, travelling through the Southern Ocean and into the Pacific where it finally upwells) was established by the late Miocene (see section 2.1.1) (Wright et al., 1991; Hodell and Venz-Curtis, 2006; Klevenz et al., 2008). The gradients prior to the LMCIS are difficult to assess, as the $\delta^{13}C$ compilation does not extend much earlier than 8.0 Ma. However, around 8.0 Ma, the $\delta^{13}C$ values from the north Atlantic and Southern Oceans are more comparable, implying that the ventilation of NADW was enhanced and more vigorous than the modern and extended far into the Southern Ocean (Wright et al., 1991; Hodell and Venz-Curtis, 2006). Neodymium isotope (ε_{Nd}) records from Walvis Ridge ODP Sites 1262, 1263 and 1264 indicate that NADW export into the South Atlantic intensified around 10 Ma, and remains strong until around 5.4 Ma, when it starts to decrease (Thomas and Via, 2007; Klevenz et al., 2008). During and following the LMCIS, the difference between the Atlantic and Pacific $\delta^{13}C$ remains unchanged, which would concur with the NADW export retaining its strength, as seen in the ε_{Nd} records. However, after the LMCIS, the Southern Ocean $\delta^{13}C$ records fall between the Atlantic and Pacific

$\delta^{13}C$, which could imply a less vigorous NADW export between 7.0 and 4.0 Ma. This contradicts the ε_{Nd} records from Walvis Ridge, which show increasing influence of NADW in the South Atlantic up to ~ 5.4 Ma (Klevenz et al., 2008)

Figure 6.13 shows an overview of the absolute $\delta^{13}C$ gradients between a) the North Atlantic and Southern Ocean, b) Southern Ocean and the Pacific and c) North Atlantic and Pacific. Between 6.6 and 4.5 Ma, the gradients between the North Atlantic, Southern Ocean and Pacific are fairly constant, and supports the modern, interglacial-like circulation pattern suggested by Hodell and Venz-Curtis (2006). However, as mentioned above, the Walvis Ridge ε_{Nd} records see no change in NADW export. This could indicate that additional factors, such as a decrease in the $\delta^{13}C_{DIC}$ value of the source water in the Southern Ocean due to a reduction in the amount of air-sea exchange (Hodell and Venz-Curtis, 2006), are affecting the Southern Ocean benthic foraminiferal $\delta^{13}C$ records. The discrepancy between the ε_{Nd} and $\delta^{13}C$ records is most pronounced between approximately 7.0 and 4.5 Ma. This partially coincides with the interval of higher long-term benthic foraminiferal $\delta^{18}O$ between 7.0 and 5.7 Ma (see section 6.4.2). If this increased average benthic foraminiferal $\delta^{18}O$ is reflecting increased ice volume around Antarctica, it is possible that extended sea ice in the Southern Ocean may have been present during the same interval. As sea ice would have limited air-sea exchange, it could have increased the Southern Ocean source water $\delta^{13}C_{DIC}$.

Interestingly, there is a brief interval between ~ 5.9 and 5.3 Ma where the Pacific $\delta^{13}C$ record rapidly reaches far more negative values than both the Southern Ocean and the Atlantic (Figure 6.13.c). As this gradient is based on the $\delta^{13}C$ from Site U1338, the increase in gradient could reflect a more local control on the Site U1338 $\delta^{13}C$ record, for instance a decrease in benthic foraminiferal

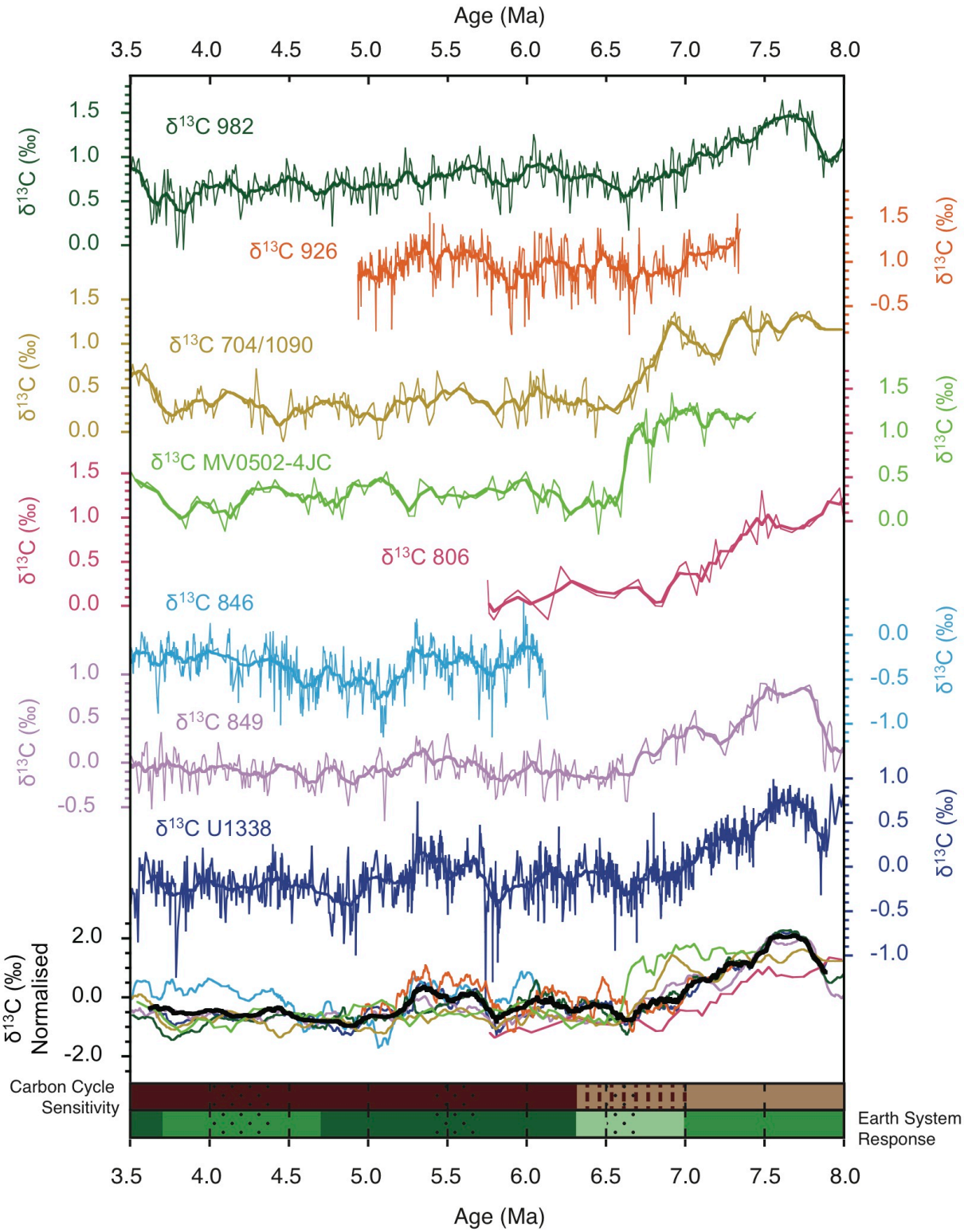
Age (Ma)
3.5 4.0 4.5 5.0 5.5 6.0 6.5 7.0 7.5 8.0
δ13C 982
δ13C 926
δ13C 704/1090
δ13C MV0502-4JC
δ13C 806
δ13C 846
δ13C 849
δ13C U1338
δ13C (‰)
δ13C (‰) Normalised
Carbon Cycle Sensitivity
Earth System Response

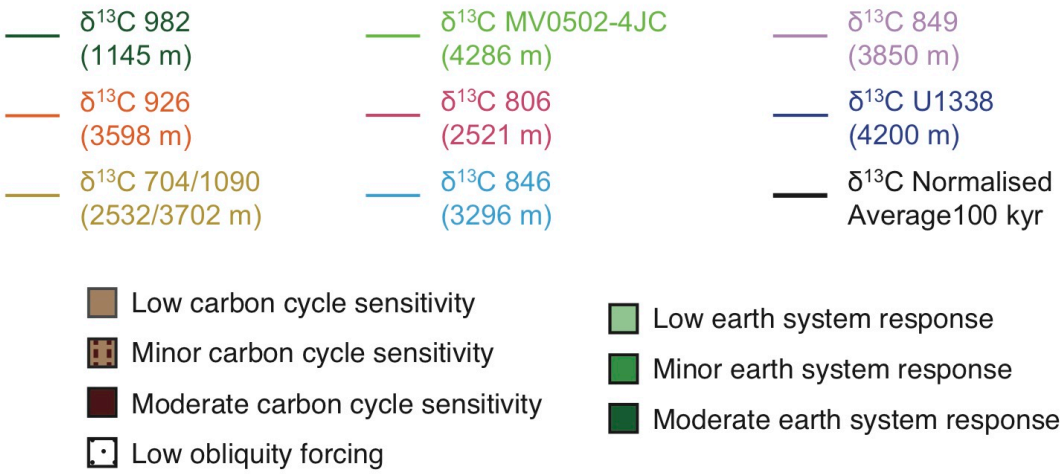

Figure 6.14.

Overview of the eight original full-resolution $\delta^{13}C$ records from the eight sites used in the multi-site compilation, with the normalised individual 100-kyr filtered $\delta^{13}C$ records and an averaged 100-kyr filter of all normalised data.

Plotted below are the reconstructed cryosphere and Earth system response.

$\delta^{13}C$ in response to increased surface water productivity, especially as the $\delta^{13}C$ record from Site 849 does not show as strong a decrease in $\delta^{13}C$ (Figure 6.12). However, the ε_{Nd} records from Walvis Ridge indicate that the peak export in NADW occurred around 5.4 Ma (Klevenz et al., 2008). The reduced North Atlantic to Pacific gradient could also reflect a peak in export of NADW. The interval of decreasing North Atlantic to Pacific gradient also overlaps with the MSC. Some authors have suggested that the isolation of the Mediterranean basin from the Atlantic could have slowed NADW export because of a reduced influx of saline waters into the Atlantic (Billups, 2002; Vidal et al., 2002). This contradicts the inferred peak in NADW export from the reduced North Atlantic to Pacific gradient. Considering that a peak in NADW export is also reflected in Southern Atlantic ε_{Nd} records (Klevenz et al., 2008), it is feasible to suggest that the MSC does not have any significant influence on deep ocean circulation.

From ~ 4.5 Ma until the end of the compilation, the gradient between the North Atlantic and Southern Ocean decreases, simultaneously with an increase in the Southern Ocean to Pacific gradient (Figure 6.13 a and b). The gradient between the North Atlantic and the Pacific remains unchanged (Figure 6.13 c). These changes in gradient after 4.5 Ma could imply that the ventilation of the Atlantic with NADW slowly increased further, thereby homogenising North Atlantic and Southern Ocean $\delta^{13}C$ values. An increase in NADW ventilation of the Atlantic basin between 4.5 and 3.5 Ma is also supported by the Walvis Ridge ε_{Nd} records, which show an increase in NADW export between 4.5 and 3.6 Ma following an interval of decreasing NADW influence between 5.5 and 4.5 Ma (Klevenz et al., 2008).

6.4.3.1. Origins of the Late Miocene Carbon Isotope Shift

As is clearly visible from Figure 6.12 b and Figure 6.14 overview, the LMCIS was globally synchronous. All six benthic foraminiferal isotope records that cover the interval between 8 and 6 Ma, record a negative $\delta^{13}C$ shift of around 1 ‰. The exact size and duration of the shift at each site is shown in Table 6.2. The two Southern Ocean sites (704/1090; MV0502-4JC) show a distinctly different shape to the LMCIS, with the negative $\delta^{13}C$ shift starting later (between 7.3 and 7.2 Ma) compared to the Atlantic (982) and Pacific (806, U1338 and 849) $\delta^{13}C$ shifts, which start earlier between 7.6 and 7.5 Ma. The LMCIS ends around 6.8 to 6.6 Ma in all records. The widespread biogenic bloom seen in all major oceanic basins between 8 and 4 Ma has been proposed as a mechanism for causing the negative shift in benthic foraminiferal $\delta^{13}C$. However, as briefly discussed in Chapter 3 and 5 (sections 3.5.2 and 5.5.2), the similarity in the shape and size of shift in the planktic and benthic foraminiferal $\delta^{13}C$ records (both ~ 1 ‰ shift) at Site U1338 between ~ 8 and 6.6 Ma suggests that the LMCIS is driven by a change in global reservoir $\delta^{13}C$ (Figures 3.4 and 5.16). A change in oceanic reservoir $\delta^{13}C$ would be consistent with the fact that the negative $\delta^{13}C$ shift is permanent, as the pre-7.5 Ma, more positive $\delta^{13}C$ values of the planktic or the benthic foraminiferal records do not recur in either record.

The processes that could be responsible for a negative 1 ‰ shift in the oceanic reservoir $\delta^{13}C$ can be assessed using a simple carbon box model, which describes the ocean as a surface ocean reservoir, and a deep ocean reservoir, each with a number of incoming and outgoing fluxes with distinct $\delta^{13}C$ values

Overview of Late Miocene Carbon Isotope Shift at relevant sites				
Site	*Carbon Shift*	*Size of Shift*	*Start*	*End*
U1338	0.75 to - 0.25 ‰	1.00 ‰	7.6 Ma	6.6 Ma
849	0.84 to - 0.13 ‰	0.97 ‰	7.6 Ma	6.6 Ma
806	1.03 to 0.04 ‰	0.99 ‰	7.5 Ma	6.8 Ma
982	1.47 to 0.54 ‰	0.93 ‰	7.6 Ma	6.6 Ma
704/1090	1.28 to 0.28 ‰	1.00 ‰	7.3 Ma	6.5 Ma
MC0502-4JC	1.24 to 0.18 ‰	1.06 ‰	7.2 Ma	6.5 Ma

Table 6.2.

Overview of the size and duration of the late Miocene Carbon Isotope Shift at the relevant deep-sea sites.

(Figure 6.15a; adapted from Broecker and Peng, 1982; Kump, 1991; Kump and Arthur, 1999). The surface ocean reservoir has carbon fluxes exchanging with the atmosphere (CO_2 gas exchange – F_{atm}) and a carbon flux from the continents from the combined riverine/weathering flux (F_w). There is also an internal ocean flux coming from the deep ocean reservoir through the process of upwelling (F_{upw}). The surface ocean reservoir is also where all primary productivity in the ocean takes place. The export from the primary production (both inorganic biogenic calcite and organic matter) is the main outgoing flux from the surface ocean, which can be split into internal fluxes to the deep ocean reservoir, and fluxes out of the ocean reservoir into sediments. Part of the organic and the inorganic matter resulting from the surface water primary productivity is exported as internal ocean fluxes of inorganic (F^i_{down}) and organic carbon (F^o_{down}) to the deep ocean reservoir. The F^i_{down} and F^o_{down} fluxes include processes such as water mass sinking/downwelling, and the sinking and dissolution of biogenic inorganic calcite and the respiration of organic matter, which releases this carbon into the deep ocean reservoir. The remaining inorganic and organic carbon that is not dissolved or respired as it sinks through the water column can be seen as a burial flux from the surface ocean reservoir to the sediments (F^i_{burial} and F^o_{burial}). Each reservoir and flux described above has its own distinct $\delta^{13}C$ value (see Table 6.3 for an overview of the different reservoirs and fluxes with their respective $\delta^{13}C$ values). A change in the size or characteristic flux $\delta^{13}C$ of either an incoming or outgoing flux could cause a long-term change in oceanic $\delta^{13}C$ value. Kump (1991) suggests that the exchanging fluxes between the surface and deep-water reservoirs cannot cause long-term (e.g. steady state or longer than 10^5 yr) changes to the reservoir value of the

whole $\delta^{13}C$. He suggests that when looking at long-term changes, a carbon box model consisting solely of the surface ocean reservoir can be used, with incoming atmosphere and weathering fluxes, and the outgoing burial fluxes (Kump, 1991). As the LMCIS is a long-term and permanent change to oceanic $\delta^{13}C$, such a simplified model is valid for this study (Figure 6.15.b). Using this model, the LMCIS could have been driven by 1) a change in ratio or the associated $\delta^{13}C$ fractionation of the organic to inorganic matter burial ratio; 2) a change in the amount or associated $\delta^{13}C$ fractionation of air-sea CO_2 exchange; 3) a change in the size or associated $\delta^{13}C$ fractionation of the continental flux.

Scenario 1: Change in size and/or $\delta^{13}C$ of organic matter burial flux. The difference between oceanic $\delta^{13}C$ and the $\delta^{13}C$ of the combined burial fluxes of inorganic and organic matter is mainly controlled by the burial amount and $\delta^{13}C$ value of the organic matter. When marine organic matter is formed in the surface regions, it preferentially uptakes ^{12}C, thereby leaving the surface waters and the inorganic calcite that precipitates from it enriched in ^{13}C. The characteristic $\delta^{13}C$ of buried organic matter (δ^{o}_{burial}) is controlled by the original seawater $\delta^{13}C$ ($\delta^{13}C$ of dissolved inorganic carbon = δ_{DIC}) and the fractionation of carbon into organic matter (Δ_{org}). In the modern ocean, Δ_{org} lies between – 18 and – 30 ‰ (Zeebe and Wolf-Gladrow, 2001). Kump and Arthur (1999) suggest that an approximation for average Δ_{org} can be obtained by looking at the relevant atmospheric CO_2 concentration, with lower CO_2 leading to a less negative Δ_{org}. Using late Miocene atmospheric CO_2 concentrations (alkenones = 250 ppmv, Tipple and Pagani, 2010; Stomatal indices = 300 ppmv, Kürschner et al., 2008;

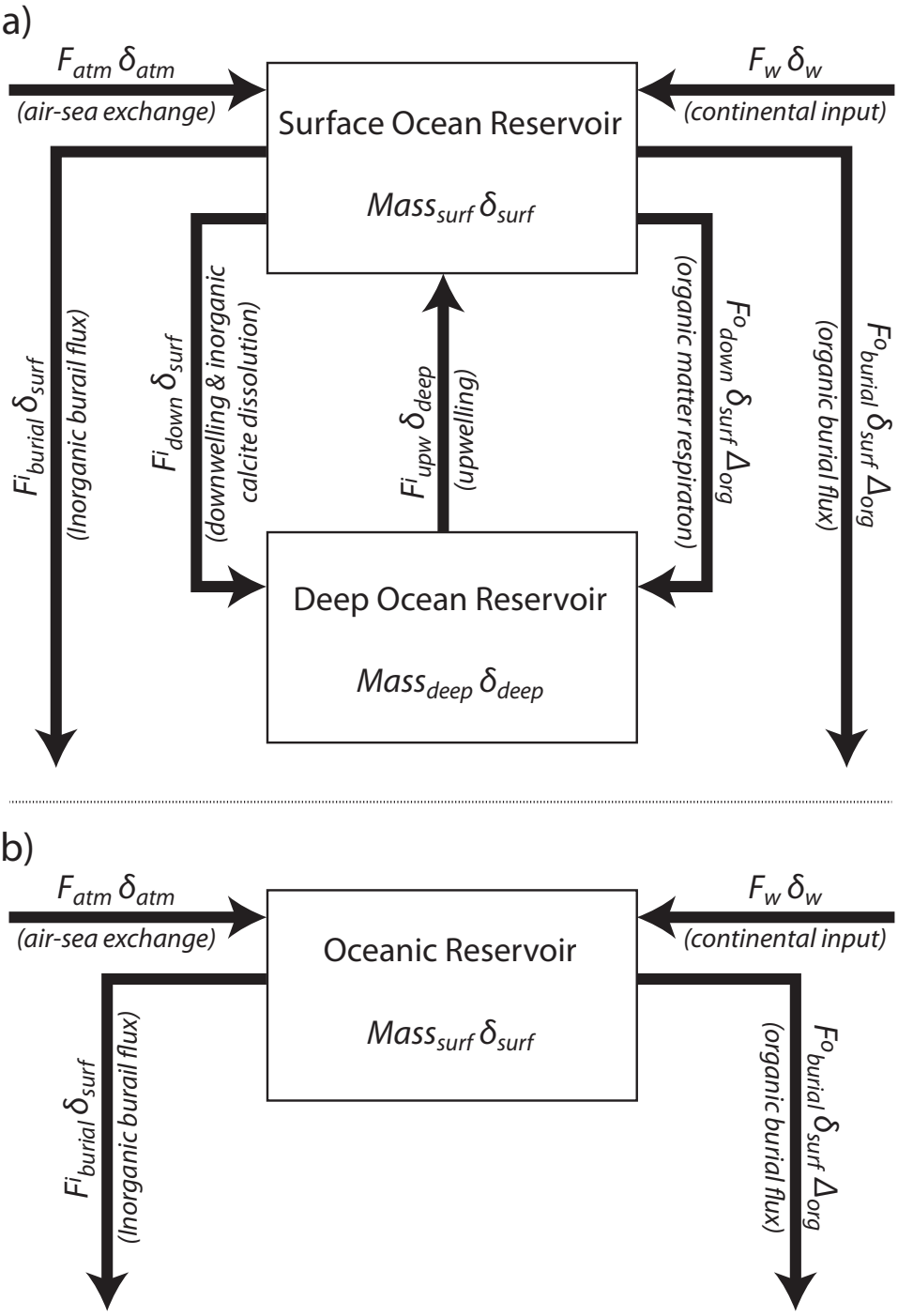

Figure 6.15.

Overview of the simplified carbon box models adapted from Broecker and Peng (1982), Kump (1991), Kump and Arthur (1999). For an overview of the different fluxes see Table 6.3.

a) Simple box model, describing fluxes in and out of the surface and deep ocean reservoir.

b) Further simplified box model with the oceanic reservoir simplified to a single reservoir.

Overview of Simplified Carbon Model Fluxes and $\delta^{13}C$ values			
Type	*Corresponding $\delta^{13}C$*	*Input / Output*	*Flux*
F^{i}_{burial}	δ_{surf}	Surface Reservoir Output	Inorganic burial flux
F^{i}_{down}	δ_{surf}	Surface Reservoir Output / Deep Reservoir Input	Downwelling and inorganic calcite dissolution flux
F^{i}_{upw}	δ_{deep}	Deep Reservoir Output / Surface Reservoir Input	Upwelling flux
F^{o}_{burial}	$\delta_{surf}\ \Delta_{org}$	Surface Reservoir Output	Organic burial flux
F^{o}_{down}	$\delta_{surf}\ \Delta_{org}$	Surface Reservoir Output / Deep Reservoir Input	Organic matter respiration
F_{atm}	δ_{atm}	Surface Reservoir Input	Air-Sea CO_2 exchange flux
F_{w}	δ_{w}	Surface Reservoir Input	Continental input flux

Table 6.3.

Overview of the fluxes in and out off the simplified carbon box models shown in Figure 6.15.

see also section 2.1.1 in Chapter 2), the Δ_{org} during the LMCIS could have been between – 24 to – 25 ‰ (Kump and Arthur, 1991). However, to cause the LMCIS, the Δ_{org} would have had to become less negative during the shift, and there is no drop in atmospheric CO_2 visible in the proxy records that could have driven this (see Figure 2.1), which makes a change in Δ_{org} an unlikely driving force of the LMCIS. A negative ocean reservoir $\delta^{13}C$ shift could also be caused by a reduction in the relative amount of organic matter compared to the amount of inorganic matter buried in ocean sediments. Figure 6.16 compares shipboard $\%CaCO_3$ and %total organic carbon (%TOC) records from Site U1338. There is no visible change in the ratio of organic to inorganic matter burial across the interval of the LMCIS (Figure 6.16), which again makes it unlikely that a reduction in organic matter burial caused the LMCIS.

Scenario 2: Change in size and/or $\delta^{13}C$ of air-sea CO_2 flux. The exchange of CO_2 between the surface-ocean and atmosphere leaves the seawater enriched in ^{13}C by an average fractionation of – 9 ‰ (δ_{atm}) (Broecker and Peng, 1982). The δ_{atm} is temperature dependent, and can range from – 7.6 ‰ at 30 °C to -10.6 ‰ at 0 °C (Broecker and Peng, 1980). A reduction in the δ_{atm} due to increasing temperatures could have caused a negative seawater $\delta^{13}C$ shift. However, SST records show that SSTs were in fact either unchanged or decreasing across the LMCIS (Figure 6.10; Billups et al., 2008), which would drive an increase in the air-sea carbon fractionation. Hodell and Venz-Curtis (2006) suggested that the LMCIS could occur because of a reduction in the amount of air-sea CO_2 exchange in the Southern Ocean due to the presence of widespread ice sheet cover, which

would increase the amount of ^{12}C retained in the ocean. However, the multi-site $\delta^{13}C$ reconstruction of Waddell et al. (2009) indicates that vertical mixing in the Southern Ocean was good, and that there was no stratification during the LMCIS. Proximal ice sheet reconstructions off Antarctica suggest that there were ice shelf conditions, rather than fully glacial conditions dominating the WAIS at least up to 7.6 Ma (Monien et al., 2012 – Figure 6.9). In addition, the evidence for IRD in the Greenland-Norwegian Sea increases around about 7.2 Ma (Fronval and Jansen, 1996; Wolf-Welling et al., 1996), which indicates more sea ice coverage in the Northern Hemisphere. Although there is no strong evidence in either hemisphere for widespread ice shelves that could have completely stopped atmosphere-ocean exchange, the presence of sea ice at this time could have partially reduced the atmosphere-ocean flux and contributed to the LMCIS.

Scenario 3: Change in continental/weathering flux or $\delta^{13}C$. The final process that could have driven the LMCIS is either an increase in the amount of the terrestrial weathering flux, or the $\delta^{13}C$ value of the terrestrial flux becoming more negative. Terrestrial flux is a complicated flux that consists of multiple continental influxes into the ocean from rivers. Silicate and carbonate weathering contribute a considerable amount to the terrestrial flux into the ocean reservoir; however, the average $\delta^{13}C$ of this flux is around 0‰, so any change in this flux is unlikely to change the overall $\delta^{13}C$ of the oceanic reservoir. An increase in weathering of organic rich rocks, which would have a very negative $\delta^{13}C$ signature, could cause the overall continental weathering flux to contribute more ^{12}C to the oceanic reservoir. As briefly discussed in Chapter 5,

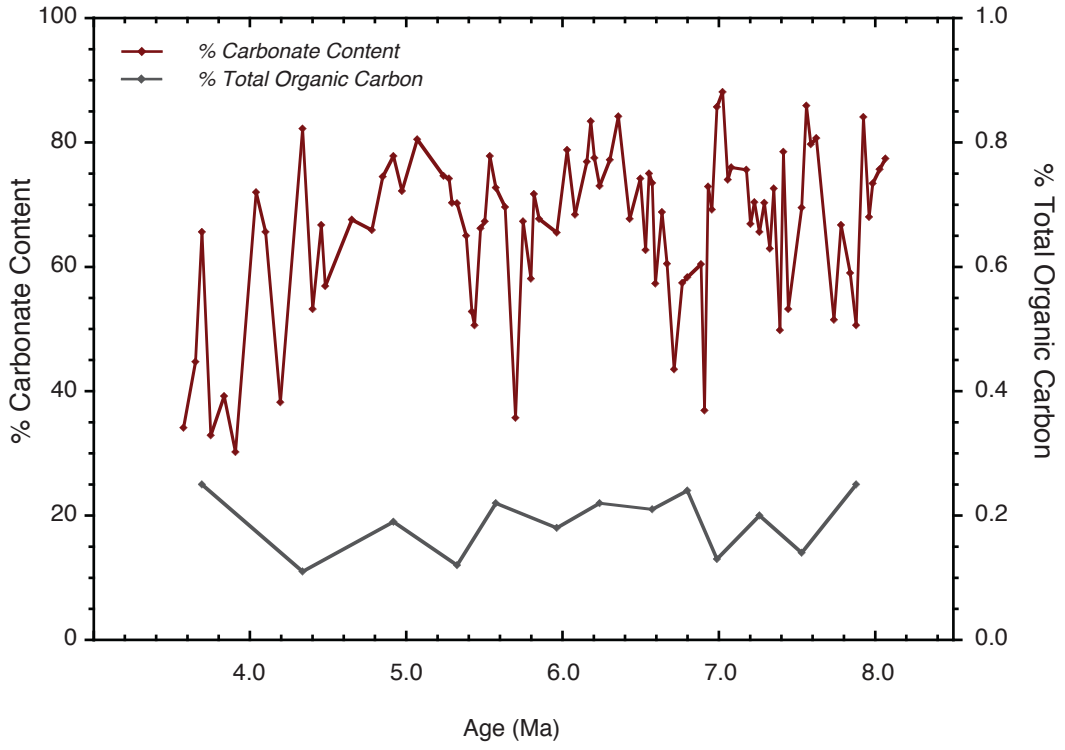

Figure 6.16.

Overview of the % Carbonate Content and the % Total Organic Carbon produced for hole U1338A, as part of the preliminary report (Expedition 320/321 Scientists, 2010).

increased uplift, and therefore a likely increase in weathering, occurred in the late Miocene (see section 5.5.2). Significant increases in Himalayan uplift have been placed between 10 and 8 Ma, which would increase the overall weathering flux, including the amount of organic-rich rock weathering, into the ocean (An et al., 2001). Filipelli (1997) proposes that a global increase in Ge/Si ratios in opaline diatoms between 8 and 6 Ma suggests an increase in chemical weathering during this interval. It is possible that this overall increase weathering could have led to an increased contribution of organic-rich rock weathering flux into the ocean, thereby potentially contributing to the LMCIS. Another component of the continental flux into the ocean reservoir is the volcanic/metamorphic flux, which is generally considered to have a $\delta^{13}C$ value of – 5 ‰. Based on calculated oceanic ridge spreading rates in Westerhold et al. (2012), there are peaks in spreading rates around 7.6, 7.4 and particularly at 7.0 Ma. It could be that this contributed a source of ^{12}C-enriched carbon to the oceanic reservoir.

Around the same time as the LMCIS, there was a large shift in the global vegetation patterns from a C_3-pathway dominated vegetation (e.g. trees) to a C_4-pathway dominated vegetation (e.g. grasses) occurred between 8 and 6 Ma (Pagani et al., 1999b). Although the causes of the C_3-C_4 shift are still debated (Cerling et al., 1997; Pagani et al., 1999b), the widespread increase in global aridity, coupled with low atmospheric CO_2 levels, have been suggested as the main cause of the C_4 expansion (Pagani et al., 1999b). The expansion of C_4-grasses was first recognised as a positive shift of up to 10 ‰ in mammalian tooth enamel (Cerling et al., 1997). The positive shift of around 10 – 14 ‰ has also been recorded in palaeosols (Behrensmeyer et al., 2007), and is attributed

to the expansion of C_4 plants, which have a more positive $\delta^{13}C$ (average – 10 to – 14 ‰) compared to C_3 plants (average – 22 to – 30 ‰) (Cerling et al., 1997). The exact change in the amount of C_3 and C_4 plants is not known (Kump and Arthur, 1999). Some estimates indicate that there was a 60 – 70 % expansion of C_4 plants (Behrensmeyer et al., 2007). Possibly, the initial decrease of C_3 plants may have provided an increased supply of ^{12}C-enriched dissolved organic carbon in the soil ($soil_{DOC}$) to the riverine input into the oceanic reservoir, thereby driving the LMCIS. Kump and Arthur (1999) suggest the shift in ratio of C_3:C_4 vegetation, could have altered the Δ_{org} by + 5 ‰, reducing it to – 20 ‰. Using a adapted version of the Kump (1991) model discussed at the beginning of this section, Kump and Arthur (1999) suggest that a + 5 ‰ change in Δ_{org} driven by the C_4 expansion, would have led to a – 1 ‰ excursion in the inorganic carbonate burial $\delta^{13}C$ value. The extent of this – 1 ‰ excursion may well account for the size of the LMCIS. Kump and Arthur (1999) noted that the excursion returns to pre-excursion values once the + 5 ‰ change in Δ_{org} was removed. However, Kump and Arthur (1999) also report that as the C_4 excursion would have been permanent, it is therefore feasible that the change in Δ_{org} would also have been permanent, which is a scenario that would concur with the permanent nature of the LMCIS change in oceanic $\delta^{13}C$.

As the above discussion has shown, there are a number of processes that could have led to the late Miocene carbon isotope shift in the oceanic reservoir. The most likely process is a change in the amount or $\delta^{13}C$ value from the terrestrial/continental flux, particularly in response to the C_3 to C_4 vegetation

shift. A reduction in the air-sea exchange could have also contributed further enrichment in ^{12}C, and could be a reason for the shape difference in the LMCIS between the Southern Ocean $\delta^{13}C$ records and $\delta^{13}C$ records from the North Atlantic and Pacific. However, the combined $\delta^{18}O$ wavelets from Sites U1338 and 982 show a strong response to obliquity during the LMCIS (Figure 6.4.1.4). Coupled with proximal Antarctic records that indicate that there were obliquity-scale interglacial-glacial stages present in the early Pliocene (Naish et al., 2009), it is feasible that any contribution to the LMCIS through reduced air-sea CO_2 exchange would have shown a response to obliquity forcing in the $\delta^{13}C$ record. This is not reflected in the combined $\delta^{13}C$ wavelets, which indicate that the LMCIS was an interval of reduced carbon cycle sensitivity to obliquity forcing (see Figure 6.4 and 6.5). The low carbon cycle sensitivity during the LMCIS would be in agreement with a forcing driven by a continental influx, such as increased volcanic or vegetation input. What is clear from the above discussion is that the exact impact of the C_4 grass expansion on the $\delta^{13}C$ of the continental flux into the ocean needs to be explored further. A better grasp of the absolute change in continental biomass and the associated change in $\delta^{13}C$ would help towards quantifying the influence of the C_4 expansion on the oceanic reservoir. In addition, modelling the carbon cycle in the late Miocene may bring new insights to the cause of the LMCIS: for instance, applying an intermediate complexity carbon-cycle box model, such as the LOSCAR model (Zeebe, 2012), or exploring the possibilities of expanding simple box models to include more detailed expressions of terrestrial vegetation and weathering processes, could provide more insight into LMCIS.

6.5. Conclusions

The combined spectral analyses of $\delta^{18}O$ and $\delta^{13}C$ from Sites U1338 and 982 show that obliquity is the dominant forcing on both the cryosphere and carbon cycle during the late Miocene and early Pliocene. The carbon cycle also shows a strong response to the 425 kyr long-term eccentricity, whereas the cryosphere shows a strong response in the 200 – 250 kyr bandwidth.

The wavelet analyses of $\delta^{18}O$ and $\delta^{13}C$ from Sites U1338 and 982 provide the first confirmation that the cryosphere and carbon cycle response to obliquity forcing is not continuous between 8.0 and 3.5 Ma. Earth system response was moderate between 6.3 – 4.7 Ma and after 3.7 Ma, although the response was reduced from 7.0 and 6.3 Ma. The carbon cycle shows very low sensitivity to external forcing before 6.3 Ma, which coincides with the LMCIS. Overall, the Earth system response reconstructions imply that the moderate to low sensitivity to radiative forcing, coupled with the absence of high sensitivity intervals, contributed to late Miocene to early Pliocene climate stability.

Global trends in ice volume were distinguished combining normalised global benthic foraminiferal $\delta^{18}O$ records, cryosphere sensitive reconstructions and published ice proxy records. Overall, long-term $\delta^{18}O$ is low from 8 to 7, 5.7 to 4.9 and 4.85 to 3.5 Ma with distinct short-term obliquity-driven variations superimposed. The low $\delta^{18}O$ intervals after 5.0 Ma agree with published ice proxy records that report obliquity-driven collapses of WAIS (Naish et al., 2009). The presence of dominant obliquity in the low-$\delta^{18}O$ intervals prior to 5.0 Ma, suggests that obliquity-driven oscillations in the Antarctic ice sheet were present throughout much of the late Miocene. Low $\delta^{18}O$ intervals are characterised by

dynamic variation of the Antarctic ice sheet, high cryosphere sensitivity, and warmer SSTs. The high $\delta^{18}O$ interval between 7.0 and 5.7 Ma is characterised by the lowest SSTs, more ice around Antarctica and more ice rafted debris (IRD) off Greenland. The IRD levels from Greenland remain fairly constant between 7.0 and 3.5 Ma, which may suggest that the decreases in $\delta^{18}O$ seen after 5.7 Ma mainly reflect changes in Antarctic ice sheets.

Combined high-resolution benthic foraminiferal $\delta^{18}O$ records from Site U1338 (this study – Pacific) and Sites 926 and 982 (Atlantic) indicate that a $\delta^{18}O$ maximum, potentially a glacial stage, occurred at the onset of the Messinian Salinity Crisis (MSC), and that a $\delta^{18}O$ minimum, potentially an interglacial stage, occurred at the termination. If the benthic $\delta^{18}O$ change is solely due to ice volume and no temperature effects are considered, the glacial stage would be equivalent to a sea level decrease of ~ 27 – 45 m at the onset, and the interglacial stage would equate to ~ 20 -27 m rise at the termination. The influence of glacio-eustacy on the onset of the MSC was minimal, as there are far larger glacial stages shortly after TG32. However, the termination interglacial occurs at the peak in minimum long-term $\delta^{18}O$, which would have been during the lowest global ice volume of the latest Miocene. This suggests that glacio-eustacy could have played an important role in the exact timing of the MSC termination.

The multi-site compilation of benthic foraminiferal $\delta^{13}C$ records collated in this chapter is compared to published ε_{Nd} records. The comparisons suggest that the modern deep ocean circulation pattern dominated for much of the latest Miocene and early Pliocene, with increased export of NADW into the Atlantic basin. A reduction in gradient between the Atlantic and Southern Ocean after ~ 4.5 Ma suggest that the ventilation of the Southern Ocean with North Atlantic

Deep Water may have increased further after 4.5 Ma. Furthermore, a decreasing North Atlantic to Pacific $\delta^{13}C$ gradient between 5.9 to 5.3 Ma would suggest increased export of NADW during the MSC, and therefore imply that the MSC does not significantly influence deep water circulation.

The compilation of $\delta^{13}C$ records also shows that the late Miocene Carbon Isotope Shift is present and fairly synchronous in all three major oceanic basins between ~ 7.6 and 6.6 Ma. The Southern Ocean $\delta^{13}C$ records show a distinctly different $\delta^{13}C$ compared to the North Atlantic and Pacific $\delta^{13}C$ records. The cause of the LMCIS is most likely a shift in the oceanic reservoir $\delta^{13}C$. Evaluation of a carbon box model suggests that the driving force of the negative shift in oceanic reservoir $\delta^{13}C$ is a change to the continental flux. A continental driving force of the LMCIS would also explain the reduced sensitivity seen in the carbon-cycle sensitivity reconstruction. An increase in oceanic spreading rates around 7.6, 7.4 and 7.0 Ma could have contributed more ^{12}C to the oceanic reservoir. However, the expansion of the C_4 grasses in the terrestrial realm is possibly a more likely driver of the LMCIS. The distinct shape of the LMCIS in the Southern Ocean could be related to an additional flux, such as a change in the air-sea CO_2 exchange.

Chapter 7.

Summary and Outlook

7.1. Thesis Outcomes and Conclusions

The main aims of this PhD project were twofold. Firstly, to investigate the state and evolution of background climate variability during the late Miocene and early Pliocene, and to use this detailed understanding to investigate changes in the response of the major Earth systems (Earth system response) to external radiative forcing during an extended period of climatic stability. Secondly, this project aimed to study the evolution of late Miocene to early Pliocene climate, by focussing on the following three significant 'climatic case studies': the state of the El-Niño-Southern-Oscillation, the role of glacio-eustacy in the Messinian Salinity Crisis, and finally the forcing behind the late Miocene Carbon Isotope Shift.

The thesis aims were achieved by combining multi-proxy geochemistry records and complementary spectral analyses from the deep-sea pelagic sediments from the recently drilled IODP Site U1338 in the eastern equatorial

Pacific, and comparing these to published records. The records produced in this thesis include benthic foraminiferal $\delta^{18}O$ and $\delta^{13}C$ records (8.0 – 3.5 Ma; ~ 3.5 kyr sampling resolution), planktic foraminiferal $\delta^{18}O$ and $\delta^{13}C$ (8.0 – 4.4 Ma; ~ 16 kyr sampling resolution) and Mg/Ca ratios (6.5 – 5.5 Ma), and novel clumped isotope Δ_{47} measurements on coccolith-rich sediment fractions (~ 6.0 and 5.0 Ma).

The main scientific outcomes from this PhD project can be divided into four main themes: 1) original data contribution and proxy development; 2) equatorial Pacific sea surface conditions and state of the El-Niño-Southern Oscillation; 3) evolution of background climate variability and Earth system response during an interval of comparative climate stability; 4) origins of climatic perturbations. Outcomes from theme 1 are relevant to both aims; outcomes discussed in theme 3 are related to the first aim, and the outcomes presented in themes 2 and 4 are relevant to answering the second aim.

Theme 1 outcomes: Original data contribution and proxy development.

The planktic and high-resolution benthic foraminiferal $\delta^{18}O$ and $\delta^{13}C$ records produced at Site U1338 are the first high-resolution continuous records that cover the interval between 8.0 and 3.5 Ma from the eastern equatorial Pacific. SEM and sedimentary properties suggest that the benthic and planktic foraminiferal $\delta^{18}O$ and $\delta^{13}C$ records reflect changes in primary, palaeoceanographical factors, which makes the records suitable for application in palaeoceanographical and palaeoclimatological reconstructions (Chapter 3).

A stratigraphic correlation between the benthic foraminiferal $\delta^{18}O$ and $\delta^{13}C$ from Sites U1338 and 982 provide a strong high-resolution astronomically based age model for Site U1338 sediments between 8.0 and 3.5 Ma. In addition to identifying 30 Shackleton-scheme marine isotope stages (MIS) between 6.4 and 3.5 Ma, 11 new MIS were preliminarily identified between 7.4 and 7.1 Ma in the benthic foraminiferal $\delta^{18}O$ records from Sites U1338 and 982 (Chapter 4).

The first application of 'clumped isotope' Δ_{47} measurements on coccolith-rich size fractions from U1338 sediments were used as a possible independent sea surface temperature (SST) proxy. However, the Δ_{47} values gave temperatures in the eastern equatorial Pacific of ~ 10 – 15 °C, which is unexpectedly cold. The presence of ~ 50 % non-coccolith calcite, which potentially originates in cold deep-waters, can partially explain the low temperatures. However, additional factors are required to fully explain the offset, such as moderate coccolith preservation and potential vital effects. This pilot study suggests that previously unknown vital effects may increase Δ_{47} in coccolith calcite. These vital effects could be driven by regulated pH in the calcifying vesicle of the coccolith (Chapter 5).

Theme 2 outcomes: Evolution of the equatorial Pacific in the late Miocene and early Pliocene – reconciling ENSO state and the Biogenic Bloom.

Combined planktic foraminiferal $\delta^{18}O$ from Site U1338 with published planktic foraminiferal $\delta^{18}O$ and alkenone SSTs from other sites in the eastern and western equatorial Pacific, suggest El Niño conditions dominated in the Pacific region between 8.0 and 7.2 Ma and after 5.2 Ma. The equatorial Pacific transitioned into a La Niña-like state by 6.5 Ma, which lasted until 5.7 Ma. This is

expected to be a response to strengthening trade winds, the shoaling of the Central American Seaway and potentially restriction of the Indonesian Throughflow. Changes in boundary conditions would have driven vigorous surface water circulation and thermocline shoaling in the eastern equatorial Pacific and signify the first appearance of surface water circulation patterns comparable to those observed in the modern day (Chapter 5).

The benthic and planktic foraminiferal $\delta^{13}C$ and sedimentation rates from Site U1338 combined with published bulk carbonate $\delta^{13}C$ from the same site, show that the Biogenic Bloom and the La-Nina-like conditions dominated Site U1338 and the equatorial Pacific at the same time. The overlap of the Biogenic Bloom with La-Niña conditions suggests that the upwelling of nutrient-rich waters to the mixed layer drove the Biogenic Bloom at Site U1338, although additional nutrient input through aeolian dust deposits cannot be excluded (Chapter 5).

Theme 3 outcomes: Evolution of background climate and Earth system sensitivity during an interval of comparative climatic stability.

Wavelet analyses of the benthic foraminiferal $\delta^{18}O$ and $\delta^{13}C$ from Sites U1338 and 982 show that Earth system response was not constant through time. Earth system response was moderate between 6.3 to 4.7 Ma and after 3.7 Ma. Overall response was lower between 7.0 and 6.3 Ma (Chapter 6).

Inferred global ice volume from the benthic foraminiferal multi-site $\delta^{18}O$ compilation was low between 8.0 – 7.0 Ma, 5.7 – 4.9 and 4.85 – 3.5 Ma, with distinct obliquity-driven short-term variations superimposed during these intervals. These intervals coincided with increased cryosphere sensitivity,

increased SSTs, and evidence for obliquity-scale variation of the West Antarctic Ice Sheet (WAIS – Naish et al., 2009). The presence of high power in the obliquity bandwidth during earlier intervals of low $\delta^{18}O$, high cryosphere sensitivity and higher SSTs, suggest that obliquity-driven oscillations in the Antarctic ice sheet were present throughout the late Miocene. Higher $\delta^{18}O$ dominated between 7.0 and 5.7 Ma, and coincided with lower cryosphere sensitivity, lower SSTs and more ice around Antarctica and IRD appearing in the Greenland Sea (Chapter 6).

Overall, the combination of the cryosphere sensitivity and the benthic foraminiferal multi-site $\delta^{18}O$ compilation and published records suggest that the ice sheets were far more stable and less sensitive to obliquity forcing during intervals of increased ice volume and lower SSTs, than during intervals of lower global ice volume and higher SSTs (Chapter 6).

The benthic foraminiferal multi-site $\delta^{13}C$ compilation shows that inter-basin $\delta^{13}C$ gradients resembled a modern, interglacial-like deep ocean circulation pattern dominated for much of the latest Miocene and early Pliocene. A reduction in the Atlantic – Southern Ocean gradient after ~ 4.5 Ma suggests the ventilation of the Southern Ocean with North Atlantic Deep Water may have slowly increased after 4.5 Ma (Chapter 6).

Theme 4 outcomes: Exploring the origins of climatic perturbations – the Messinian Salinity Crisis and the late Miocene Carbon Isotope Shift.

The high-resolution benthic foraminiferal $\delta^{18}O$ from Site U1338, combined with published benthic foraminiferal $\delta^{18}O$ records from the Atlantic and Pacific (Sites 926 and 982) show that $\delta^{18}O$ maximum TG32 occurred at the onset of the Messinian Salinity Crisis (MSC) and that an $\delta^{18}O$ minimum stage occurred at the

termination. Although TG32 occurs at the onset of the MSC, the influence of glacio-eustacy was most likely minimal, as there are far larger glacial stages (TG20 and TG22) shortly after TG32. The MSC termination $\delta^{18}O$ minimum is also surrounded by larger $\delta^{18}O$ minima (TG11/13 and T5); however, the termination $\delta^{18}O$ minimum occurs at the long-term minimum in $\delta^{18}O$, which coincided with the lowest global ice volume of the latest Miocene. This suggests that glacio-eustacy could have played an important role in the exact timing of the MSC termination (Chapter 6).

The benthic foraminiferal multi-site $\delta^{13}C$ compilation shows that the timing, size and duration of the LMCIS are broadly similar between the three basins, although the Southern Ocean $\delta^{13}C$ records have a distinctive shape. The compiled $\delta^{13}C$ data suggests the LMCIS is driven by a negative shift in the $\delta^{13}C$ of the whole oceanic reservoir. An increase in the size or $\delta^{13}C$ of the continental flux into the ocean is the most likely forcing of the negative shift, as this would also explain the low carbon cycle sensitivity to obliquity forcing during the LMCIS. Three pulses of increased sea floor spreading between 7.6 and 7.0 Ma, or more likely the 60 – 70 % expansion of C_4 grasses on the continents, could have driven a change in the continental flux. The distinct shape of the LMCIS in the Southern Ocean could be related to a change in the CO_2 exchange flux between the surface ocean and the atmosphere in this region (Chapter 6).

7.2. Wider Implications

This study has shown that the stable climate interval between the late Miocene to early Pliocene displayed considerable variability, both in terms of short-term fluctuations, as well as considerable differences in the overall long-term climate state. This variability occurred despite stable CO_2 concentrations which were similar to pre-industrial levels and which were low in comparison to much of the Cenozoic. On the one hand, much of the late Miocene to early Pliocene interval was dominated by globally warm conditions and a dominant El-Niño state in the Pacific region. This concurred with high cryosphere sensitivity, low global ice volume and very dynamic short-term variations in ice sheet extent before 7.0 Ma and after 5.7 Ma. In contrast, the most stable conditions occurred between ~ 7.0 and 5.7 Ma, when more La Niña-like conditions dominated the Pacific. This is also the interval with the highest global ice volume levels, low cryosphere sensitivity and lower SSTs.

Overall, the outcomes from this study suggest and support that in climate periods with low atmospheric CO_2, the continental ice sheets on Antarctica can remain sensitive to external forcing and display dynamic fluctuations of ice sheet retreat and growth. The sensitivity to external forcing and dynamism in ice volume variation may be strongly linked to SST variation. For future climate change studies, the late Miocene in particular, with both the reduced-sensitivity-La-Niña-like and increased-sensitivity-El-Niño-like intervals, could be an

interesting case study to investigate the effect of changing SSTs on ice volume variability during an interval of comparatively constant CO_2. Furthering the understanding of the role of SSTs in controlling ice volume fluctuations could also contribute to predictions of future climate variation.

7.3. Future Considerations

The results and discussions in this thesis have emphasised new research directions in palaeoclimate and palaeoceanography, and some interesting avenues that could lead to the greater integration of terrestrial and marine palaeoclimate research.

Future methodological developments:

Stratigraphic correlation is a powerful tool that enables direct inter-site comparison and age model generation. The Match autocorrelation method from Lisiecki and Lisiecki (2002) is useful for correlating multiple records, although it is limited by the lack of any error assessment. An estimation of alignment error is possible using the Monte-Carlo autocorrelation method (Maliverno 2012). As high-resolution geochemical proxy records are more frequently generated, and a wealth of published material is more readily available in online databases, facilitating correlation and comparison between these many records is very valuable. Advancing and "ground truthing" autocorrelation methods could provide valuable fundamental methodological development that could assist the

integrated multi-site, multi-proxy synthesis projects that are ideal for answering large outstanding global climate questions. An integrated study comparing the alignments from different auto-correlation methods, and potentially developing a means of user-friendly error estimation, would prove to be a very valuable tool.

The field of 'clumped isotope' thermometry is an upcoming and developing field. Although the study presented in Chapter 5 was not successful in achieving an applicable palaeo SST proxy, it raised some potentially interesting questions about the role of vital effects on Δ_{47}. Overall, there is a great scope for developing the application of Δ_{47} measurements on coccolith-rich sediments as a SST proxy. Firstly, accurate control of the size fraction separation, in particular to remove any small calcite fragments that possibly precipitated after deposition in bottom water conditions, would potentially enhance the accuracy of the Δ_{47} SSTs. Secondly, the fractionation of Δ_{47} into coccolith calcite should be studied further, particularly by inspecting any potential vital effects due to vesicle pH. These considerations should improve the application of Δ_{47} as an independent temperature proxy to palaeoclimate problems.

Palaeoclimate and palaeoceanography developments:

Late Miocene $\delta^{18}O$ stack: the development of ocean drilling, and the recovery of continuous and near complete sediment records from many ODP and IODP expeditions means there is now a wealth of high-resolution isotope data available for the late Miocene. In this study, 30 MIS were identified based on the Shackleton scheme up to 6.4 Ma. In addition, 16 new stages were identified between 7.4 and 6.9 Ma. The compilation of a late Miocene stack of $\delta^{18}O$ similar to the Lisiecki and Raymo (2005) Plio-Pleistocene stack, may aid the identification

of additional stages between 6.9 and 6.4 Ma, tie the newly identified stages from this study into the Shackleton-scheme, and identify global stages further back into the late Miocene record. Better constraining the isotope stratigraphy in the late Miocene would facilitate any study using isotopic correlation as a method for age model generation or inter-site comparison.

Independent temperature control on the MSC: As discussed in Chapter 6, there was both a glacial and interglacial stage present at the onset and the termination of the MSC, respectively. Due to the long-term trend in low $\delta^{18}O$ around the time of the termination interglacial, it is feasible that the timing of the termination was driven by glacio-eustatic variation. However, the biggest caveat of these estimates is that the benthic foraminiferal $\delta^{18}O$ reflect both changes in temperature and global ice volume. Further work incorporating an independent temperature proxy across the onset and termination of the MSC could significantly improve estimates of ice volume and glacio-eustatic change. Combining high-resolution benthic foraminiferal Mg/Ca and Li/Ca is a potential option for obtaining benthic foraminiferal water temperatures to couple with an existing high-resolution $\delta^{18}O$ records.

Carbon modelling the LMCIS: as also discussed in Chapter 6, due to the complicated nature of the terrestrial weathering input into the ocean, an integrated effort combining modelling with both terrestrial and marine proxies is needed to try to constrain the exact nature of the change in terrestrial input into the oceanic reservoir. Potential exploration of the terrestrial flux and oceanic reservoir through intermediate complexity carbon models, such as LOSCAR (Zeebe, 2012), could help elucidate how exactly the LMCIS occurred.

7.4. Final Remarks

The work resulting from this PhD study has provided new insights detailing the change in variability and the evolution of late Miocene and early Pliocene climate. It has highlighted that, despite being a period of comparative stability in the overall Cenozoic, the late Miocene and early Pliocene climate still displayed considerable short-term dynamic fluctuations. The fact that a stable climate still displays rapid variations in ice volume suggests that the late Miocene and early Pliocene remains a unique interval in Earth history to study the amplitude and forcing of short-term climate variability. Further study is expected to improve our knowledge of natural variation of the Earth's climate when in a near-equilibrium state, which is an essential pre-requisite to model current and future perturbation of the system through anthropogenic activities.

Acronym List

%CF	percentage coarse fraction
%FF	weight % fine fraction
AABW	Antarctic Bottom Water
BB	Biogenic Bloom
BSE	back-scattered electron
BSE-TOPO	back-scattered electron topography mode
BWT	bottom water temperatures
CAS	Central American Seaway
CCD	calcite compensation depth
CCSF-A	core composite depth below sea floor (uncorrected for expansion)
DI	deionised
DIC	dissolved inorganic carbon
DSDP	Deep Sea Drilling Programme
EAIS	East Antarctic Ice Sheet
EECT	Eastern Equatorial Cold Tongue
ENSO	El-Niño-Southern-Oscillation
EP	early Miocene
EPWP	Eastern Pacific Warm Pool

ESR	Earth System Response
ETP	eccentricity tilt precession (equal weighting)
EUC	Equatorial Undercurrent
GRA	gamma ray attenuation
GRAPE	gamma ray attenuation porosity evaluator
ICL	Imperial College London
ICM	Imperial Carrera Marble standard
ICP-OES	inductively coupled plasma optical emissions spectroscopy
IODP	Integrated Ocean Drilling Programme
IRD	ice rafted debris
IS	prefix for isotope-based tie points used in G2 Match alignment
ITCZ	Intertropical Convergence Zone
ITF	Indonesian Throughflow
LM	late Miocene
LMCIS	late Miocene Carbon Isotope Shift
LOSCAR	Long-Term Ocean-atmosphere-Sediment Carbon cycle reservoir model
MIS	marine isotope stage
MSC	Messinian Salinity Crisis
NADW	North Atlantic Deep Water
NEC	Northern Equatorial Current
NECC	North Equatorial Counter Current
NW	North West
ODP	Ocean Drilling Programme
PCC	Peru and Chile currents
PEAT	Pacific Equatorial Age Transect
RLM	reflective light microscope
SE	South East

SE	secondary electron
SEC	Southern Equatorial Current
SEM	Scanning electron microscopy
SR	sedimentation rates
SST	sea surface temperatures
TOC	Total Organic Carbon
TP	prefix for first-order tie points used in the G1 Match alignment
UCL	University College London
URF	universal reference frame
VP	variable pressure
VPDB	Vienna Peedee Belemnite standard
VSMOW	Vienna Standard Mean Ocean Water
WAIS	West Antarctic Ice Sheet
WMA	weighted moving average
WPWP	Western Pacific Warm Pool
XRF	X-Ray fluorescence

References

Adelseck, C.G., Geehan, G.W., and Roth, P.H. (1973), 'Experimental evidence for selective dissolution and overgrowth of calcareous nannofossil during diagenesis', *Geological Society of America Bulletin*, *Vol. 84* (8), p.2755-2762

Alexander, M.A., Blade, I., Newman, M., Lanzante, J.R., Lau, N.C., and Scott, J.D. (2002), 'The atmospheric bridge: The influence of ENSO tele-connections on air-sea interaction over the global oceans', *Journal of Climate*, *Vol. 15* (16), p.2205-2231.

An, Z.S., Kutzbach, J.E., Prell, W.L., and Porter, S.C. (2001), 'Evolution of Asian monsoons and phased uplift of the Himalayan Tibetan plateau since Late Miocene times', *Nature*, *Vol. 411* (6833), p.62-66.

Anning, T., Nimer, N., Merrett, M.J., and Brownlee, C. (1996), 'Costs and benefits of calcification in coccolithophorids', *Journal of Marine Systems*, *Vol. 9* (1-2), p.45-56.

Antonov, J.I., Seidov, D., Boyer, T.P., Locarnini, R.A., Mishonov, A.V., Garcia, H.E., Baranova, O.K., Zweng, M.M., and Johnson, D.R. (2010), World Ocean Atlas 2009, Volume 2: Salinity. , in *NOAA Atlas NESDIS 69*, edited by Levitus, S., p. 184 pp, Government Printing Office, Washington, D.C.

Backman, J., and Moran, K. (2009), 'Expanding the Cenozoic paleoceanographic record in the Central Arctic Ocean: IODP Expedition 302 Synthesis', *Central European Journal of Geosciences*, *Vol. 1* (2), p.157-175.

Barker, S., Greaves, M., and Elderfield, H. (2003), 'A study of cleaning procedures used for foraminiferal Mg/Ca paleothermometry', *Geochemistry Geophysics Geosystems*, *Vol. 4*.

Be, A.W.H. (1980), 'Gametogenic calcification in a spinose planktonic foraminifer, Globigerinoides-sacculifer (Brady)', *Marine Micropaleontology*, *Vol. 5* (3), p.283-310.

Be, A.W.H., Spero, H.J., and Anderson, O.R. (1982), 'Effect of symbiont elimination and reinfection on the life processes of the planktonic foraminifer *Globigerinoides- sacculifer*', *Marine Biology*, *Vol. 70* (1), p.73-86

Beerling, D.J., and Royer, D.L. (2011), 'Convergent Cenozoic CO2 history', *Nature Geoscience*, *Vol. 4* (7), p.418-420.

Beerling, D.J., Taylor, L.L., Bradshaw, C.D.C., Lunt, D.J., Valdes, P.J., Banwart, S.A., Pagani, M., and Leake, J.R. (2012), 'Ecosystem CO2 starvation and terrestrial silicate weathering: mechanisms and global-scale quantification during the late Miocene', *Journal of Ecology*, *Vol. 100* (1), p.31-41.

Behrensmeyer, A.K., et al. (2007), 'The structure and rate of late Miocene expansion of C-4 plants: Evidence from lateral variation in stable isotopes in paleosols of the Siwalik Group, northern Pakistan', *Geological Society of America Bulletin*, *Vol. 119* (11-12), p.1486-1505.

Beltran, C., Rousselle, G., Backman, J., Wade, B.S., and Sicre, M.A. (2014), 'Paleoenvironmental conditions for the development of calcareous nannofossil acme during the late Miocene in the Eastern Equatorial Pacific', *Paleoceanography*, *Vol.*, p.n/a-n/a.

Berger, A., and Loutre, M.F. (1991), 'Insolation values for the climate of the last 10000000 years, *Quaternary Science Reviews*, *Vol. 10* (4), p.297-317.

Bernasconi., e.a. (in prep), 'Inter-lab clumped isotope calibration study, *Vol.*

Berner, R.A. (2004), 'A model for calcium, magnesium and sulfate in seawater over Phanerozoic time', *American Journal of Science*, *Vol. 304* (5), p.438-453.

Bickert, T., Cordes, R., and Wefer, G. (1994), 'Late Pliocene to mid-Pleistocene (2.6-1.0 Ma) carbonate dissolution in the western equatorial Atlantic: Results of ODP Leg 154, Ceara Rise', in *Proceedings of the Ocean Drilling Program, Scientific Results*, edited by Shackleton, N.J., Curry, W.B., Richter, C. and Bralower, T.J.

Billups, K. (2002), 'Late Miocene through early Pliocene deep water circulation and climate change viewed from the sub-Antarctic South Atlantic', *Palaeogeography Palaeoclimatology Palaeoecology*, *Vol. 185* (3-4), p.287-307.

Billups, K., and Schrag, D.P. (2002), 'Paleotemperatures and ice volume of the past 27 Myr revisited with paired Mg/Ca and O-18/O-16 measurements on benthic foraminifera', *Paleoceanography*, *Vol. 17* (1).

Billups, K., Kelly, C., and Pierce, E. (2008), 'The late Miocene to early Pliocene climate transition in the Southern Ocean', *Palaeogeography Palaeoclimatology Palaeoecology*, *Vol. 267* (1-2), p.31-40.

Billups, K., Ravelo, A.C., and Zachos, J.C. (1998), 'Early Pliocene climate: A perspective from the western equatorial Atlantic warm pool', *Paleoceanography*, *Vol. 13* (5), p.459-470.

Blechschmidt, G. (1979), 'Biostratigraphy of Calcareous Nannofossils: Leg 47B, Deep Sea Drilling Project', in *Initial Reports of the Deep Sea Drilling Project*, edited by Laughter, F.H. and Fagerberg, E.M.

Bolton, C.T., Stoll, H.M., and Mendez-Vicente, A. (2012), 'Vital effects in coccolith calcite: Cenozoic climate-pCO(2) drove the diversity of carbon acquisition strategies in coccolithophores?', *Paleoceanography*, *Vol. 27*.

Bown, P.R., and Dunkley Jones, T. (2012), 'Calcareous nannofossils from the Paleogene equatorial Pacific (IODP Expedition 320 Sites U1331-1334)', *Journal of Nannoplankton Research*, *Vol. 32* (2), p.3-51

Bown, P.R., et al. (2008), 'A Paleogene calcareous microfossil Konservat-Lagerstatte from the Kilwa Group of coastal Tanzania', *Geological Society of America Bulletin*, *Vol. 120* (1-2), p.3-12

Boyle, E.A., and Keigwin, L.D. (1985), 'Comparison of Atlantic and Pacific paleochemical records for the last 215,000 years – changes in deep ocean circulation and chemical inventories', *Earth and Planetary Science Letters*, *Vol. 76* (1-2), p.135-150.

Broecker, W.S. (1991), 'The Great Ocean Conveyor', *Oceanography*, *Vol. 4* (2), p.79-89

Broecker, W.S., and Peng, T.-H. (1985), *Tracers in the Sea*, Lamont-Doherty Earth Observatory, Palisades, N.Y.

Bryden, H.L., and Brady, E.C. (1985), 'Diagnostic model of the 3-dimensional circulation in the equatorial Pacific Ocean', *Journal of Physical Oceanography*, *Vol. 15* (10), p.1255-1273.

Cande, S.C., and Kent, D.V. (1995), 'Revised calibration of the geomagnetic polarity timescale for the late Cretaceous and Cenozoic', *Journal of Geophysical Research-Solid Earth*, *Vol. 100* (B4), p.6093-6095.

Cane, M.A., and Molnar, P. (2001), 'Closing of the Indonesian seaway as a precursor to east African aridircation around 3-4 million years ago', *Nature*, *Vol. 411* (6834), p.157-162

Cerling, T.E., Harris, J.M., MacFadden, B.J., Leakey, M.G., Quade, J., Eisenmann, V., and Ehleringer, J.R. (1997), 'Global vegetation change through the Miocene/Pliocene boundary', *Nature*, *Vol. 389* (6647), p.153-158.

Cole, J.M., Rasbury, E.T., Hanson, G.N., Montanez, I.P., and Pedone, V.A. (2005), 'Using U-Pb ages of Miocene tufa for correlation in a terrestrial succession, Barstow Formation, California', *Geological Society of America Bulletin*, *Vol. 117* (3-4), p.276-287.

Conte, M.H., Sicre, M.A., Ruhlemann, C., Weber, J.C., Schulte, S., Schulz-Bull, D., and Blanz, T. (2006), 'Global temperature calibration of the alkenone unsaturation index (U(37)(K ')) in surface waters and comparison with surface sediments', *Geochemistry Geophysics Geosystems*, *Vol. 7*.

Cook, C.P., van de Flierdt, T., Williams, T., Hemming, S.R., Iwai, M., Kobayashi, M., et al. (2013), 'Dynamic behaviour of the East Antarctic ice sheet during Pliocene warmth', *Nature Geosci*, *Vol. 6* (9), p.765-769.

Davies, R., Cartwright, J., Pike, J., and Line, C. (2001), 'Early Oligocene initiation of North Atlantic Deep Water formation', *Nature*, *Vol. 410* (6831), p.917-920

de Villiers, S., Greaves, M., and Elderfield, H. (2002), 'An intensity ratio calibration method for the accurate determination of Mg/Ca and Sr/Ca of marine carbonates by ICP-AES', *Geochemistry Geophysics Geosystems*, *Vol. 3*.

Dekens, P.S., Lea, D.W., Pak, D.K., and Spero, H.J. (2002), 'Core top calibration of Mg/Ca in tropical foraminifera: Refining paleotemperature estimation', *Geochemistry Geophysics Geosystems*, *Vol. 3*.

Dekens, P.S., Ravelo, A.C., McCarthy, M.D., and Edwards, C.A. (2008), 'A 5 million year comparison of Mg/Ca and alkenone paleothermometers', *Geochemistry Geophysics Geosystems*, *Vol. 9*.

Dennis, K.J., Affek, H.P., Passey, B.H., Schrag, D.P., and Eiler, J.M. (2011), 'Defining an absolute reference frame for 'clumped' isotope studies of CO2', *Geochimica Et Cosmochimica Acta*, *Vol. 75* (22), p.7117-7131.

Dennis, K.J., and Schrag, D.P. (2010), 'Clumped isotope thermometry of carbonatites as an indicator of diagenetic alteration', *Geochimica Et Cosmochimica Acta*, *Vol. 74* (14), p.4110-4122.

Denniston, R.F., Asmerom, Y., Polyalk, V.Y., McNeill, D.F., Klaus, J.S., Cole, P., and Budd, A.F. (2008), 'Caribbean chronostratigraphy refined with U-Pb dating of a Miocene coral', *Geology*, *Vol. 36* (2), p.151-154.

Dickens, G.R., and Owen, R.M. (1994), 'Late Miocene – Early Pliocene manganese redirection in the central Indian Ocean – expansion of the intermediate water oxygen minimum zone', *Paleoceanography*, *Vol. 9* (1), p.169-181

Dickens, G.R., and Owen, R.M. (1999), 'The Latest Miocene-Early Pliocene biogenic bloom: a revised Indian Ocean perspective', *Marine Geology*, *Vol. 161* (1), p.75-91

Diester-Haass, L., Billups, K., and Emeis, K.C. (2005), 'In search of the late Miocene-early Pliocene "biogenic bloom"' in the Atlantic Ocean (Ocean Drilling Program Sites 982, 925, and 1088)', *Paleoceanography*, *Vol. 20* (4)

Diester-Haass, L., Billups, K., and Emeis, K.C. (2006), 'Late Miocene carbon isotope records and marine biological productivity: Was there a (dusty) link?', *Paleoceanography*, *Vol. 21* (4).

Diester-Haass, L., Meyers, P.A., and Bickert, T. (2004), 'Carbonate crash and biogenic bloom in the late Miocene: Evidence from ODP Sites 1085, 1086, and 1087 in the Cape Basin, southeast Atlantic Ocean', *Paleoceanography*, *Vol. 19* (1).

Diester-Haass, L., Meyers, P.A., and Vidal, L. (2002), 'The late Miocene onset of high productivity in the Benguela Current upwelling system as part of a global pattern', *Marine Geology*, *Vol. 180* (1-4), p.87-103.

Drury, A.J., John, C.M., and Jourdan, A.L. (2012), 'Constraining late Miocene seawater composition: a multiproxy approach', *Proceedings of the 22nd Annual V.M. Goldschmidt Conference*, *Vol.*

Duplessy, J.C., Lalou, C., and Vinot, A.C. (1970), 'Differential isotopic fractionation in benthic foraminifera and paleotemperatures reassessed', *Science*, *Vol. 168* (3928), p.250-&.

Edgar, K.M., Pälike, H., and Wilson, P.A. (2013), 'Testing the impact of diagenesis on the δ18O and δ13C of benthic foraminiferal calcite from a sediment burial depth transect in the equatorial Pacific', *Paleoceanography*, *Vol. 28* (3), p.468-480.

Eiler, J.M. (2007), '"Clumped-isotope" geochemistry - The study of naturally-occurring, multiply-substituted isotopologues', *Earth and Planetary Science Letters*, *Vol. 262* (3-4), p.309-327.

Eiler, J.M. (2011), 'Paleoclimate reconstruction using carbonate clumped isotope thermometry', *Quaternary Science Reviews*, *Vol. 30* (25-26), p.3575-3588.

Eiler, J.M., and Schauble, E. (2004), '(OCO)-O-18-C-13-O-16 in Earth's atmosphere', *Geochimica Et Cosmochimica Acta*, *Vol. 68* (23), p.4767-4777.

Elderfield, H., and Ganssen, G. (2000), 'Past temperature and delta O-18 of surface ocean waters inferred from foraminiferal Mg/Ca ratios', *Nature*, *Vol. 405* (6785), p.442-445.

Elderfield, H., Ferretti, P., Greaves, M., Crowhurst, S., McCave, I.N., Hodell, D., and Piotrowski, A.M. (2012), 'Evolution of Ocean Temperature and Ice Volume Through the Mid-Pleistocene Climate Transition', *Science*, *Vol. 337* (6095), p.704-709

Elderfield, H., Greaves, M., Barker, S., Hall, I.R., Tripati, A., Ferretti, P., Crowhurst, S., Booth, L., and Daunt, C. (2010), 'A record of bottom water temperature and seawater delta O-18 for the Southern Ocean over the past 440 kyr based on Mg/Ca of benthic foraminiferal Uvigerina spp', *Quaternary Science Reviews*, *Vol. 29* (1-2), p.160-169.

Elderfield, H., Vautravers, M., and Cooper, M. (2002), 'The relationship between shell size and Mg/Ca, Sr/Ca, delta O-18, and delta C-13 of species of planktonic foraminifera', *Geochemistry Geophysics Geosystems*, *Vol. 3*

Emiliani, C. (1954), 'Depth habitats of some species of pelagic foraminifera as indicated by oxygen isotope ratios', *American Journal of Science*, *Vol. 252*, p.149-158.

Epstein, S., Buchsbaum, R., Lowenstam, H.A., and Urey, H.C. (1953), 'Revised carbonate-water isotopic temperature scale', *Geological Society of America Bulletin*, *Vol. 64* (11), p.1315-1326.

Expedition 320/321 Scientists (2010), 'Site U1338', in *Proceedings of the Integrated Ocean Drilling Program*, edited by Palike, H., Lyle, M., Nishi, H., Raffi, I., Gamage, K., Klaus, A. and Scientists, E.

Fairbanks, R.G., and Matthews, R.K. (1978), 'Marine oxygen isotope record in Pleistocene coral, Barbados, West-Indies', *Quaternary Research*, *Vol. 10* (2), p.181-196.

Fantle, M.S., and DePaolo, D.J. (2006), 'Sr isotopes and pore fluid chemistry in carbonate sediment of the Ontong Java Plateau: Calcite recrystallization rates and evidence for a rapid rise in seawater Mg over the last 10 million years', *Geochimica Et Cosmochimica Acta*, *Vol. 70* (15), p.3883-3904.

Farrell, J.W., Raffi, I., Janecek, T.R., Murray, D.W., Levitan, M., Dadey, K.A., Emeis, K.C., Lyle, M., Flores, J.A., and Hovan, S. (1995), 'Late Neogen Sedimentation Patterns in the Eastern Equatorial Pacific Ocean', in *Proceedings of the Ocean Drilling Program, Scientific Results*, edited by Pisias, N.G., Mayer, L.A., Janecek, T.R., Palmer-Julson, A. and van Andel, T.H.

Filippelli, G.M. (1997), 'Intensification of the Asian monsoon and a chemical weathering event in the late Miocene early Pliocene: Implications for late Neogene climate change', *Geology*, *Vol. 25* (1), p.27-30.

Flower, B.P., and Kennett, J.P. (1993), 'Middle Miocene ocean-climate transition – high-resolution oxygen and carbon isotopic records from deep-sea drilling project Site 588A, southwest Pacific', *Paleoceanography*, *Vol. 8* (6), p.811-843.

Ford, H.L., Ravelo, A.C., and Hovan, S. (2012), 'A deep Eastern Equatorial Pacific thermocline during the early Pliocene warm period', *Earth and Planetary Science Letters*, *Vol. 355*, p.152-161.

Fox, L.R., and Wade, B.S. (2013), 'Systematic taxonomy of early-middle Miocene planktonic foraminifera from the equatorial Pacific Ocean: Integrated Ocean Drilling Program, Site U1338' , *Journal of Foraminiferal Research*, *Vol. 43* (4), p.374-405

Fronval, T., and Jansen, E. (1996), 'Late Neogene Paleoclimates and Paleoceanography in the Iceland-Norwegian Sea: Evidence from the Iceland and Vøring Plateaus', in *Proceedings of the Ocean Drilling Program, Scientific Results*, edited by Thiede, J., Myhre, A.M., Firth, J.V., Johson, G.I. and Ruddiman, W.F.

Galeotti, S., von der Heydt, A., Huber, M., Bice, D., Dijkstra, H., Jilbert, T., Lanci, L., and Reichart, G.J. (2010), 'Evidence for active El Nino Southern Oscillation variability in the Late Miocene greenhouse climate', *Geology*, *Vol. 38* (5), p.419-422.

Ghosh, P., Adkins, J., Affek, H., Balta, B., Guo, W.F., Schauble, E.A., Schrag, D., and Eller, J.M. (2006), '(13)C-(18)O bonds in carbonate minerals: A new kind of paleothermometer', *Geochimica Et Cosmochimica Acta*, *Vol. 70* (6), p.1439-1456.

Goddard, L., Mason, S.J., Zebiak, S.E., Ropelewski, C.F., Basher, R., and Cane, M.A. (2001), 'Current approaches to seasonal-to-interannual climate predictions', *International Journal of Climatology*, *Vol. 21* (9), p.1111-1152.

Grant, K.M., and Dickens, G.R. (2002), 'Coupled productivity and carbon isotope records in the southwest Pacific Ocean during the late Miocene-early Pliocene biogenic bloom', *Palaeogeography Palaeoclimatology Palaeoecology*, *Vol. 187* (1-2), p.61-82.

Grauel, A.L., Schmid, T.W., Hu, B., Bergami, C., Capotondi, L., Zhou, L.P., and Bernasconi, S.M. (2013), 'Calibration and application of the 'clumped isotope' thermometer to foraminifera for high-resolution climate reconstructions', *Geochimica Et Cosmochimica Acta*, *Vol. 108*, p.125-140.

Griffith, E.M., and Paytan, A. (2012), 'Barite in the ocean - occurrence, geochemistry and palaeoceanographic applications', *Sedimentology*, *Vol. 59* (6), p.1817-1835.

Grinsted, A., Moore, J.C., and Jevrejeva, S. (2004), 'Application of the cross wavelet transform and wavelet coherence to geophysical time series', *Nonlinear Processes in Geophysics*, *Vol. 11* (5-6), p.561-566.

Groeneveld, J., Nuernberg, D., Tiedemann, R., Reichart, G.-J., Steph, S., Reuning, L., Crudeli, D., and Mason, P. (2008), 'Foraminiferal Mg/Ca increase in the Caribbean during the pliocene: Western Atlantic Warm Pool formation, salinity influence, or diagenetic overprint?', *Geochemistry Geophysics Geosystems*, *Vol. 9*.

Groeneveld, J., Steph, S., Tiedemann, R., Garbe-Schönberg, D., Nürnberg, D., and Sturm, A. (2006), 'Pliocene Mixed-Layer Oceanography for Site 1241 using Combined Mg/Ca and δ18O Analyses of Globigerinoides sacculifer', *Proceedings of the Ocean Drilling Program, Scientific Results*, *Vol. 202*.

Guo, W.F., Kim, S.-T., Yuan, J., Farquhar, J., and Passey, B.H. (2012), '13C-18O bonds in dissolved inorganic carbon: Toward a better understanding of clumped isotope thermometer in biogenic carbonates', *Proceedings of the 22nd Annual V.M. Goldschmidt Conference*, *Vol.*

Haq, B.U., Worsley, T.R., Burckle, L.H., Douglas, R.G., Keigwin, L.D., Opdyke, N.D., Savin, S.M., Sommer, M.A., Vincent, E., and Woodruff, F. (1980), 'Late Miocene marine carbon isotopic shift and synchroneity of some phytoplanktonic of some phytoplanktonic biostratigraphic events', *Geology*, *Vol. 8* (9), p.427-431.

Hastings, D.W., Russell, A.D., and Emerson, S.R. (1998), 'Foraminiferal magnesium in Globeriginoides sacculifer as a paleotemperature proxy', *Paleoceanography*, *Vol. 13* (2), p.161-169.

Haug, G.H., and Tiedemann, R. (1998), 'Effect of the formation of the Isthmus of Panama on Atlantic Ocean thermohaline circulation', *Nature*, *Vol. 393* (6686), p.673-676.

Haug, G.H., Tiedemann, R., Zahn, R., and Ravelo, A.C. (2001), 'Role of Panama uplift on oceanic freshwater balance', *Geology*, *Vol. 29* (3), p.207-210.

Hayashi, H., Idemitsu, K., Wade, B.S., Idehara, Y., Kimoto, K., Nishi, H., and Matsui, H. (2013), 'Middle Miocene to Pleistocene planktonic foraminiferal biostratigraphy in the eastern equatorial Pacific Ocean', *Paleontological Research*, *Vol. 17* (1), p.91-109.

Hays, J.D., Imbrie, J., and Shackleton, N.J. (1976), 'Variations in Earths orbit – pacemaker of ice ages', *Science*, *Vol. 194* (4270), p.1121-1132.

Haywood, A.M., and Valdes, P.J. (2004), 'Modelling Pliocene warmth: contribution of atmosphere, oceans and cryosphere', *Earth and Planetary Science Letters*, *Vol. 218* (3-4), p.363-377.

Haywood, A.M., Dekens, P., Ravelo, A.C., and Williams, M. (2005), 'Warmer tropics during the mid-Pliocene? Evidence from alkenone paleothermometry and a fully coupled ocean-atmosphere GCM', *Geochemistry Geophysics Geosystems*, *Vol. 6*.

Hemleben, C., and Kitazato, H. (1995), 'Deep-sea foraminifera under long-term observation in the laboratory', *Deep-Sea Research Part I-Oceanographic Research Papers*, *Vol. 42* (6), p.827-832

Henkes, G.A., Passey, B.H., Wanamaker, A.D., Grossman, E.L., Ambrose, W.G., and Carroll, M.L. (2013), 'Carbonate clumped isotope compositions of modern marine mollusk and brachiopod shells', *Geochimica Et Cosmochimica Acta*, *Vol. 106*, p.307-325.

Herbert, T.D., Schuffert, J.D., Thomas, D., Lange, C., Weinheimer, A., Peleo-Alampay, A., and Herguera, J.C. (1998), 'Depth and seasonality of alkenone production along the California margin inferred from a core top transect', *Paleoceanography*, *Vol. 13* (3), p.263-271.

Hermoyian, C.S., and Owen, R.M. (2001), 'Late miocene-early pliocene biogenic bloom: Evidence from low-productivity regions of the Indian and Atlantic Oceans', *Paleoceanography*, *Vol. 16* (1), p.95-100

Hilgen, F.J. (1991), 'Extension of the astronomically calibrated (polarity) time scale to the Miocene Pliocene boundary', *Earth and Planetary Science Letters*, *Vol. 107* (2), p.349-368.

Hill, P.S., Tripati, A.K., and Schauble, E.A. 'Theoretical constraints on the effects of pH, salinity, and temperature on clumped isotope signatures of dissolved inorganic carbon species and precipitating carbonate minerals', *Geochimica Et Cosmochimica Acta*, *Vol.* (0).

Hodell, D.A., and Venz-Curtis, K.A. (2006), 'Late Neogene history of deep-water ventilation in the Southern Ocean', *Geochemistry Geophysics Geosystems*, *Vol. 7*.

Hodell, D.A., and Venz, K.A. (1992), 'Toward a high-resolution stable isotopic record of the Southern Ocean during the Plio-Pleistocene (4.8 to 0.8 Ma)', in *The Antarctic Paleoenvironment: A Perspective on Global Change Part I* edited by Kennett, J.P. and Warnke, D.A.

Hodell, D.A., Benson, R.H., Kent, D.V., Boersma, A., and Bied, K.R.E. (1994), 'Magnetostratigraphic, biostratigraphic and stable-isotope stratigraphy of an upper Miocene drill core from the Sale-Briqueterie (Northwestern Morocco) – a high-resolution chronology for the Messinian stage', *Paleoceanography*, *Vol. 9* (6), p.835-855.

Hodell, D.A., Curtis, J.H., Sierro, F.J., and Raymo, M.E. (2001), 'Correlation of late Miocene to early Pliocene sequences between the Mediterranean and North Atlantic', *Paleoceanography*, *Vol. 16* (2), p.164-178.

Holbourn, A., Kuhnt, W., Schulz, M., and Erlenkeuser, H. (2005), 'Impacts of orbital forcing and atmospheric carbon dioxide on Miocene ice-sheet expansion', *Nature*, *Vol. 438* (7067), p.483-487.

Holbourn, A., Kuhnt, W., Schulz, M., Flores, J.A., and Andersen, N. (2007), 'Orbitally-paced climate evolution during the middle Miocene "Monterey" carbon-isotope excursion', *Earth and Planetary Science Letters*, *Vol. 261* (3-4), p.534-550.

Hovan, S. (1995), 'Late Cenozoic Atmospheric Circulation Intensity and Climatic History Recorded By Eolian Deposition in the Eastern Equatorial Pacific Ocean, Leg 138', *Proceedings of the Ocean Drilling Program, Scientific Results*, *Vol. 138*.

Hover, V.C., Walter, L.M., and Peacor, D.R. (2001), 'Early marine diagenesis of biogenic aragonite and Mg-calcite: new constraints from high-resolution STEM and AEM analyses of modern platform carbonates', *Chemical Geology*, *Vol. 175* (3-4), p.221-248

Huntington, K.W., et al. (2009), 'Methods and limitations of 'clumped' CO2 isotope (Delta(47)) analysis by gas-source isotope ratio mass spectrometry', *Journal of Mass Spectrometry*, *Vol. 44* (9), p.1318-1329.

IODP-MI (2011), 'IODP Depth Scales Terminology Version 2.0, *Vol.*

James, R.H., and Austin, W.E.N. (2008), 'Biogeochemical controls on palaeoceanographic environmental proxies: a review', in *Biogeochemical Controls on Palaeoceanographic Environmental Proxies*, edited by Austin, W.E.N. and James, R.H., Geological Society, London.

Jansen, E., and Raymo, M.E. (1996), 'Leg 162: New Frontiers on Past Climates', in *Proceedings of the Ocean Drilling Program, Initial Reports*, edited by Jansen, E., Raymo, M.E., Blum, P. and 162', S.S.P.E.

Jansen, E., and Sjoholm, J. (1991), 'Reconstruction of glaciation over the past 6 Myr from ice-borne deposits in the Norwegian Sea', *Nature*, *Vol. 349* (6310), p.600-603.

John, C.M., Drury, A.J., and Jourdan, A.L. (2012), 'Invited: A Triple-Proxy Approach to Reconstructing Seawater δ18O', *Proceedings of the 22nd Annual V.M. Goldschmidt Conference*, *Vol.*

John, C.M., Karner, G.D., Browning, E., Leckie, R.M., Mateo, Z., Carson, B., and Lowery, C. (2011), 'Timing and magnitude of Miocene eustasy derived from the mixed siliciclastic-carbonate stratigraphic record of the northeastern Australian margin', *Earth and Planetary Science Letters*, *Vol. 304* (3-4), p.455-467.

Katz, M.E., Cramer, B.S., Franzese, A., Honisch, B., Miller, K.G., Rosenthal, Y., and Wright, J.D. (2010), 'Traditional and emerging geochemical proxies

in foraminifera', *Journal of Foraminiferal Research*, *Vol. 40* (2), p.165-192.

Keigwin, L.D. (1979), 'Late Cenozoic stable isotope stratigraphy and paleoceanography of DSDP sites from the east equatorial and central north Pacific Ocean', *Earth and Planetary Science Letters*, *Vol. 45* (2), p.361-382.

Kennett, J.P., and Srinivasan, M.S. (1983), *Neogene Planktonic Foraminifera*, Hutchinson Ross Publishing Company, Stroudsburg, Pennsylvania.

Kim, S.T., Mucci, A., and Taylor, B.E. (2007), 'Phosphoric acid fractionation factors for calcite and aragonite between 25 and 75 degrees C: Revisited', *Chemical Geology*, *Vol. 246* (3-4), p.135-146.

Klevenz, V., Vance, D., Schmidt, D.N., and Mezger, K. (2008), 'Neodymium isotopes in benthic foraminifera: Core-top systematics and a down-core record from the Neogene south Atlantic', *Earth and Planetary Science Letters*, *Vol. 265* (3-4), p.571-587.

Kluge, T., John, C.M., and Davis, S. (2013), 'Constraints for the Clumped Isotope Application in Diagenetic Environments Involving High Salt Concentrations', *Proceedings of the 23rd Annual V.M. Goldschmidt Conference*,

Kluge, T., John, C.M., and Kele, S. (in prep b), 'The effect of carbonate speciation on 13C-18O clumping as derived from hydrothermal vent calcites'

Kluge, T., John, C.M., Jourdan, A.L., and Crawshaw, J. (in prep a), 'High-temperature calibration of the carbonate clumped isotope thermometer for subsurface applications,

Kozdon, R., Kelly, D.C., Kitajima, K., Strickland, A., Fournelle, J.H., and Valley, J.W. (2013), 'In situ delta O-18 and Mg/Ca analyses of diagenetic and planktic foraminiferal calcite preserved in a deep-sea record of the Paleocene-Eocene thermal maximum', *Paleoceanography*, *Vol. 28* (3), p.517-528

Krijgsman, W., Hilgen, F.J., Raffi, I., Sierro, F.J., and Wilson, D.S. (1999), 'Chronology, causes and progression of the Messinian salinity crisis', *Nature*, *Vol. 400* (6745), p.652-655.

Krijgsman, W., Stoica, M., Vasiliev, I., and Popov, V.V. (2010), 'Rise and fall of the Paratethys Sea during the Messinian Salinity Crisis', *Earth and Planetary Science Letters*, *Vol. 290* (1-2), p.183-191.

Kroopnick, P.M. (1985), 'The distribution of C-13 of sigma-CO2 in the world oceans', *Deep-Sea Research Part a-Oceanographic Research Papers*, *Vol. 32* (1), p.57-84.

Kuiper, K.F., Hilgen, F.J., Steenbrink, J., and Wijbrans, J.R. (2004), 'Ar-40/Ar-39 ages of tephras intercalated in astronomically tuned Neogene sedimentary sequences in the eastern Mediterranean', *Earth and Planetary Science Letters*, *Vol. 222* (2), p.583-597.

Kump, L.R. (1991), 'Interpreting carbon-isotope excursions – Strangelove oceans', *Geology*, *Vol. 19* (4), p.299-302.

Kump, L.R., and Arthur, M.A. (1999), 'Interpreting carbon-isotope excursions: carbonates and organic matter', *Chemical Geology*, *Vol. 161* (1-3), p.181-198.

Kurschner, W.M., Kvacek, Z., and Dilcher, D.L. (2008), 'The impact of Miocene atmospheric carbon dioxide fluctuations on climate and the evolution of terrestrial ecosystems', *Proceedings of the National Academy of Sciences of the United States of America*, *Vol. 105* (2), p.449-453.

LaRiviere, J.P., Ravelo, A.C., Crimmins, A., Dekens, P.S., Ford, H.L., Lyle, M., and Wara, M.W. (2012), 'Late Miocene decoupling of oceanic warmth and atmospheric carbon dioxide forcing', *Nature*, *Vol. 486* (7401), p.97-100.

Larsen, H.C., et al. (1994), '7-million years of glaciation in Greenland', *Science*, *Vol. 264* (5161), p.952-955.

Laskar, J. (1999), 'The limits of Earth orbital calculations for geological time-scale use', *Philosophical Transactions of the Royal Society a-Mathematical Physical and Engineering Sciences*, *Vol. 357* (1757), p.1735-1759.

Laskar, J., Joutel, F., and Boudin, F. (1993), 'Orbital, precessional, and insolation quantities for the Earth from –20 Myr to +10 Myr', *Astronomy & Astrophysics*, *Vol. 270* (1-2), p.522-533.

Laskar, J., Robutel, P., Joutel, F., Gastineau, M., Correia, A.C.M., and Levrard, B. (2004), 'A long-term numerical solution for the insolation quantities of the Earth', *Astronomy & Astrophysics*, *Vol. 428* (1), p.261-285.

Lawrence, K.T., Liu, Z., and Herbert, T.D. (2006), 'Evolution of the Eastern Tropical Pacific Through Plio-Pleistocene Glaciation', *Science*, *Vol. 312* (5770), p.79-83.

Lea, D.W., Mashiotta, T.A., and Spero, H.J. (1999), 'Controls on magnesium and strontium uptake in planktonic foraminifera determined by live culturing', *Geochimica Et Cosmochimica Acta*, *Vol. 63* (16), p.2369-2379.

Lear, C.H., Mawbey, E.M., and Rosenthal, Y. (2010), 'Cenozoic benthic foraminiferal Mg/Ca and Li/Ca records: Toward unlocking temperatures and saturation states', *Paleoceanography*, *Vol. 25*.

Lear, C.H., Rosenthal, Y., and Wright, J.D. (2002), 'Benthic foraminiferal Mg/Ca paleothermometry and its application to Late Miocene changes in Atlantic circulation', *Geochimica Et Cosmochimica Acta*, *Vol. 66* (15A), p.A438-A438.

Lear, C.H., Rosenthal, Y., and Wright, J.D. (2003), 'The closing of a seaway: ocean water masses and global climate change', *Earth and Planetary Science Letters*, *Vol. 210* (3-4), p.425-436.

Lear, C.H., Wilson, P.A., Shackleton, N.J., and Elderfield, H. (2000), 'Palaeotemperature and ocean chemistry records for the Palaeogene from Mg/Ca and Sr/Ca in benthic foraminiferal calcite', *Gff*, *Vol. 122*, p.93-93.

Levitus, S. (Ed.) (2010), *World Ocean Atlas, 2009.*

Li, J., Wang, R., and Li, B. (2002), 'Variations of opal accumulation rates and paleoproductivity over the past 12 Ma at ODP Site 1143, southern South China Sea', *Chinese Science Bulletin*, *Vol. 47* (7), p.596-598

Lisiecki, L.E., and Herbert, T.D. (2007), 'Automated composite depth scale construction and estimates of sediment core extension', *Paleoceanography*, *Vol. 22* (4).

Lisiecki, L.E., and Lisiecki, P.A. (2002), 'Application of dynamic programming to the correlation of paleoclimate records', *Paleoceanography*, *Vol. 17* (4).

Lisiecki, L.E., and Raymo, M.E. (2005), 'A Pliocene-Pleistocene stack of 57 globally distributed benthic delta O-18 records', *Paleoceanography*, *Vol. 20* (1).

Locarnini, R.A., Mishonov, A. V., Antonov, J.I., Boyer, T.P., Garcia, H.E., Baranova, O.K., Zweng, M.M., and Johnson, D.R., (2010), World Ocean Atlas 2009, Volume 1: Temperature. , in *NOAA Atlas NESDIS 68*, edited by Levitus, S., p. 184 pp, Government Printing Office, Washington, D.C.

Lourens, L., Hilgen, F.J., Shackleton, N.J., Laskar, J., and Wilson, D. (2004), 'The Neogene Period', in *A Geologic Time Scale 2004*, edited by Gradstein, F.M., Ogg, J.G. and Smith, A.G., pp. 409-440, Cambridge University Press.

Lourens, L.J., Becker, J., Bintanja, R., Hilgen, F.J., Tuenter, E., van de Wal, R.S.W., and Ziegler, M. (2010), 'Linear and non-linear response of late Neogene glacial cycles to obliquity forcing and implications for the Milankovitch theory', *Quaternary Science Reviews*, *Vol. 29* (1-2), p.352-365.

Lyle, M. (2003), 'Neogene carbonate burial in the Pacific Ocean', *Paleoceanography*, *Vol. 18* (3).

Lyle, M., and Backman, J. (2013), 'Data report: calibration of XRF-estimated CaCO3 along the Site U1338 splice ', in *Proceedings of the Integrated Ocean Drilling Program, Scientific Results*, edited by Palike, H., Lyle, M., Nishi, H., Raffi, I., Gamage, K., Klaus, A. and Scientists, E.

Lyle, M., Barron, J., Bralower, T.J., Huber, M., Lyle, A.O., Ravelo, A.C., Rea, D.K., and Wilson, P.A. (2008), 'Pacific ocean and Cenozoic evolution of climate', *Reviews of Geophysics*, *Vol. 46* (2).

Lyle, M., Dadey, K.A., and Farrell, J.W. (1995), 'The Late Miocene (11-8 Ma) eastern Pacific carbonate crash: evidence for reorganisation of deep-water circulation by the closure of the Panama Gateway', in *Proceedings of the Ocean Drilling Program, Scientific Results*, edited by Pisias, N.G., Mayer, L.A., Janecek, T.R., Palmer-Julson, A. and van Andel, T.H.

Lyle, M., Olivarez Lyle, A., Gorgas, T., Holbourn, A., Westerhold, T., Hathorne, E., Kimoto, K., and Yamamoto, S. (2012), 'Data report: raw and normalized elemental data along the Site U1338 splice from X-ray fluoresence scanning', in *Proceedings of the Integrated Ocean Drilling Program, Scientific Results*, edited by Palike, H., Lyle, M., Nishi, H., Raffi, I., Gamage, K., Klaus, A. and Scientists, E.

Lyle, M., Pälike, H., Nishi, H., Raffi, I., Gamage, K., Klaus, A., and Scientists, E. (2010), 'The Pacific Equatorial Age Transect, IODP Expeditions 320 and 321: Building a 50-Million-Year-Long Environmental Record of the Equatorial Pacific Ocean', *Scientific Drilling*, *Vol. 9*.

Malinverno, A. (2013), 'Data report: Monte Carlo correlation of sediment records from core and downhole log measurements at Site U1337 and U1338 (IODP Expedition 321)', in *Proceedings of the Integrated Ocean Drilling Program*, edited by Palike, H., Lyle, M., Nishi, H., Raffi, I., Gamage, K., Klaus, A. and Scientists', E.

Marshall, J., and Speer, K. (2012), 'Closure of the meridional overturning circulation through Southern Ocean upwelling', *Nature Geoscience*, *Vol. 5* (3), p.171-180

Martin, E.E., and Scher, H. (2006), 'A Nd isotopic study of southern sourced waters and Indonesian Throughflow at intermediate depths in the Cenozoic Indian Ocean', *Geochemistry Geophysics Geosystems*, *Vol. 7*.

Martin, P.A., Lea, D.W., Rosenthal, Y., Shackleton, N.J., Sarnthein, M., and Papenfuss, T. (2002), 'Quaternary deep sea temperature histories derived from benthic foraminiferal Mg/Ca', *Earth and Planetary Science Letters*, *Vol. 198* (1-2), p.193-209

Martinson, D.G., Menke, W., and Stoffa, P. (1982), 'An inverse approach to signal correlation', *Journal of Geophysical Research*, *Vol. 87* (NB6), p.4807-4818.

Maslin, M., and Swann, G.A. (2005), 'Isotopes in Marine Sediments', in *Isotopes in Palaeoenvironmental Research*, edited by Leng, M.J., Springer, Dordrecht, the Netherlands.

Matson, S.D., and Fox, D.L. (2010), 'Stable isotopic evidence for terrestrial latitudinal climate gradients in the Late Miocene of the Iberian Peninsula', *Palaeogeography Palaeoclimatology Palaeoecology*, *Vol. 287* (1-4), p.28-44.

McKay, R., et al. (2009), 'The stratigraphic signature of the late Cenozoic Antarctic Ice Sheets in the Ross Embayment', *Geological Society of America Bulletin*, *Vol. 121* (11-12), p.1537-1561.

McKinney, C.R., McCrea, J.M., Epstein, S., Allen, H.A., and Urey, H.C. (1950), 'Improvements in Mass Spectrometers for the Measurement of Small Differences in Isotope Abundance Ratios', *The Review of Scientific Instruments*, *Vol. 21* (8).

Medina-Elizalde, M., Lea, D.W., and Fantle, M.S. (2008), 'Implications of seawater Mg/Ca variability for Plio-Pleistocene tropical climate reconstruction', *Earth and Planetary Science Letters*, *Vol. 269* (3-4), p.584-594.

Micheels, A., Bruch, A.A., Eronen, J., Fortelius, M., Harzhauser, M., Utescher, T., and Mosbrugger, V. (2011), 'Analysis of heat transport mechanisms from a Late Miocene model experiment with a fully-coupled atmosphere-ocean general circulation model', *Palaeogeography Palaeoclimatology Palaeoecology*, *Vol. 304* (3-4), p.337-350.

Milankovitch, M. (1941), 'Kanon der Erdbestrahlung und seine Anwendung aus das Eiszeitenproblem', *Royal Serbian Sciences, Special Publication*, *Vol. 33* (132), p.Republished as 'Canon of Insolation and Ice Age Problem' by the NSF in 1969.

Miller, K.G., Feigenson, M.D., Wright, J.D., and Clement, B.M. (1991), 'Miocene isotope reference section, Deep Sea Drilling Project Site 608: an evaluation of isotope and biostratigraphic resolution', *Paleoceanography*, *Vol. 6* (1), p.33-52.

Miller, K.G., Kominz, M.A., Browning, J.V., Wright, J.D., Mountain, G.S., Katz, M.E., Sugarman, P.J., Cramer, B.S., Christie-Blick, N., and Pekar, S.F. (2005), 'The phanerozoic record of global sea-level change', *Science*, *Vol. 310* (5752), p.1293-1298.

Minoletti, F., Hermoso, M., and Gressier, V. (2009), 'Separation of sedimentary micron-sized particles for palaeoceanography and calcareous nannoplankton biogeochemistry', *Nature Protocols*, *Vol. 4* (1), p.14-24.

Mix, A.C., Le, J., and Shackleton, N.J. (1995), 'Benthic Foraminiferal Stable Isotope Stratigraphy of Site 846', in *Proceedings of the Ocean Drilling Program, Scientific Results*, edited by Pisias, N.G., Mayer, L.A., Janecek, T.R., Palmer-Julson, A. and van Andel, T.H.

Molnar, P., and Cane, M.A. (2002), 'El Nino's tropical climate and teleconnections as a blueprint for pre-Ice Age climates', *Paleoceanography*, *Vol. 17* (2)

Monien, D., Kuhn, G., von Eynatten, H., and Talarico, F.M. (2012), 'Geochemical provenance analysis of fine-grained sediment revealing Late Miocene to recent Paleo-Environmental changes in the Western Ross Sea, Antarctica', *Global and Planetary Change*, *Vol. 96-97*, p.41-58.

Moore, D.M., and Reynolds Jr., R.C. (1997), *X-Ray Diffraction and the Identification and Analysis of Clay Minerals*.

Moore, T.C., and Lombari, G. (1981), 'Sea surface temperature changes in the north Pacific during the late Miocene', *Marine Micropaleontology*, *Vol. 6* (5-6), p.581-597.

Morkhoven, F.P.C.M., Berggren, W.A., and Edwards, A.S. (1986), *Cenozoic Cosmopolitan Deep-Water Benthic Foraminifera*, Elf Aquitaine, Pau.

Müller, D.W., Hodell, D.A., and Ciesielski (1991), 'Late Miocene to earliest Pliocene (9.8 - 4.5 Ma) paleoceanography of the subantarctic southeast Atlantic: Stable isotopic, sedimentologic, and microfossil evidence', *Proceedings of the Ocean Drilling Program, Scientific Results*, *Vol. 114*, p.459-474.

Muller, P.J., Kirst, G., Ruhland, G., von Storch, I., and Rosell-Mele, A. (1998), 'Calibration of the alkenone paleotemperature index U-37(K ') based on core-tops from the eastern South Atlantic and the global ocean (60 degrees N-60 degrees S)', *Geochimica Et Cosmochimica Acta*, *Vol. 62* (10), p.1757-1772.

Naish, T., et al. (2009), 'Obliquity-paced Pliocene West Antarctic ice sheet oscillations', *Nature*, *Vol. 458* (7236), p.322-U384.

Nathan, S.A., and Leckie, R.M. (2009), 'Early history of the Western Pacific Warm Pool during the middle to late Miocene (similar to 13.2-5.8 Ma): Role of sea-level change and implications for equatorial circulation', *Palaeogeography Palaeoclimatology Palaeoecology*, *Vol. 274* (3-4), p.140-159.

National Oceanic and Atmospheric Administration (2013), El Niño Theme Page - http://www.pmel.noaa.gov/tao/elnino/nino-home.html

Nurnberg, D. (1995), 'Magnesium in tests of Neogloboquadrina-pachyderma sinistral from high northern and southern latitudes', *Journal of Foraminiferal Research*, *Vol. 25* (4), p.350-368.

Nurnberg, D., Bijma, J., and Hemleben, C. (1996), 'Assessing the reliability of magnesium in foraminiferal calcite as a proxy for water mass temperatures', *Geochimica Et Cosmochimica Acta*, *Vol. 60* (5), p.803-814.

O'Connell, S., Wolf-Welling, T.C.W., Cremer, M., and Stein, R. (1996), 'Neogene Paleoceanography and Paleoclimate history from Fram Strait: changes in accumulation rates', in *Proceedings of the Ocean Drilling Program, Scientific Results*, edited by Thiede, J., Myhre, A.M., Firth, J.V., Johson, G.I. and Ruddiman, W.F.

Pagani, M., Arthur, M.A., and Freeman, K.H. (1999a), 'Miocene evolution of atmospheric carbon dioxide', *Paleoceanography*, *Vol. 14* (3), p.273-292.

Pagani, M., Caldeira, K., Berner, R., and Beerling, D.J. (2009), 'The role of terrestrial plants in limiting atmospheric CO2 decline over the past 24 million years', *Nature*, *Vol. 460* (7251), p.85-U94.

Pagani, M., Freeman, K.H., and Arthur, M.A. (1999b), 'Late Miocene atmospheric CO2 concentrations and the expansion of C-4 grasses', *Science*, *Vol. 285* (5429), p.876-879.

Pagani, M., Liu, Z.H., LaRiviere, J., and Ravelo, A.C. (2010), 'High Earth-system climate sensitivity determined from Pliocene carbon dioxide concentrations', *Nature Geoscience*, *Vol. 3* (1), p.27-30.

Paillard, D., Labeyrie, L., and Yiou, P. (1996), 'Macintosh program performs time-serires analysis', *Eos Trans. AGU*, *Vol. 77* (379).

Palike, H. (2005), Orbital Variation (Including Milankovitch Cycles), in *Encyclopedia of Geology*, edited by Selley, R.C., Cocks, L.R.M. and P.I.R., pp. 410-412, Elsevier, Oxford.

Palike, H., et al. (2012), 'A Cenozoic record of the equatorial Pacific carbonate compensation depth', *Nature*, *Vol. 488* (7413), p.609-+.

Palike, H., Lyle, M., Nishi, H., Raffi, I., Gamage, K., Klaus, A., and Scientists, E. (2010), 'Expedition 320/321 summary', in *Proceedings of the Integrated Ocean Drilling Program*, edited by Palike, H., Lyle, M., Nishi, H., Raffi, I., Gamage, K., Klaus, A. and Scientists, E.

Passey, B.H., and Henkes, G.A. (2012), 'Carbonate clumped isotope bond reordering and geospeedometry', *Earth and Planetary Science Letters*, *Vol. 351*, p.223-236.

Paytan, A., Mearon, S., Cobb, K.M., and Kastner, M. (2002), 'Origin of marine barite deposits: Sr and S isotope characterization', *Geology*, *Vol. 30* (8), p.747-750.

Pearson, P.N., and Burgess, C.E. (2008), 'Foraminifer test preservation and diagenesis: comparison of high latitude Eocene sites', in *Biogeochemical Controls on Palaeoceanographic Environmental Proxies*, edited by Austin, W.E.N. and James, R.H., pp. 59-72, Geological Society, London.

Pearson, P.N., and Palmer, M.R. (2000), 'Atmospheric carbon dioxide concentrations over the past 60 million years', *Nature*, *Vol. 406* (6797), p.695-699.

Pearson, P.N., Ditchfield, P.W., Singano, J., Harcourt-Brown, K.G., Nicholas, C.J., Olsson, R.K., Shackleton, N.J., and Hall, M.A. (2001), 'Warm tropical sea surface temperatures in the Late Cretaceous and Eocene epochs', *Nature*, *Vol. 413* (6855), p.481-487.

Pena, L.D., Calvo, E., Cacho, I., Eggins, S., and Pelejero, C. (2005), 'Identification and removal of Mn-Mg-rich contaminant phases on foraminiferal tests: Implications for Mg/Ca past temperature reconstructions', *Geochemistry Geophysics Geosystems*, *Vol. 6*

Pisias, N.G., Mayer, L.A., and Mix, A.C. (1995), 'Paleoceanography of the Eastern Equatorial Pacific during the Neogene: Synthesis of Leg 138 Drilling Results', in *Proceedings of the Ocean Drilling Program, Scientific Results*, edited by Pisias, N.G., Mayer, L.A., Janecek, T.R., Palmer-Julson, A. and van Andel, T.H.

Pound, M.J., Haywood, A.M., Salzmann, U., and Riding, J.B. (2012), 'Global vegetation dynamics and latitudinal temperature gradients during the Mid to Late Miocene (15.97-5.33 Ma)', *Earth-Science Reviews*, *Vol. 112* (1-2), p.1-22.

Pound, M.J., Haywood, A.M., Salzmann, U., Riding, J.B., Lunt, D.J., and Hunter, S.J. (2011), 'A Tortonian (Late Miocene, 11.61-7.25 Ma) global vegetation reconstruction', *Palaeogeography Palaeoclimatology Palaeoecology*, *Vol. 300* (1-4), p.29-45.

Prentice, K., Dunkley Jones, T., Lees, J.A., Young, J., Bown, P., Langer, G., Fearn, S., and EIMF (in prep), 'Trace metal distributions and preservation in fossil coccoliths determined by Secondary Ion Mass Spectrometry of single liths,

Reynolds, R.W., Smith, T.M., Liu, C., Chelton, D.B., Casey, K.S., and Schlax, M.G. (2007), 'Daily high-resolution-blended analyses for sea surface temperature', *Journal of Climate*, *Vol. 20* (22), p.5473-5496.

Rickaby, R.E.M., Bard, E., Sonzogni, C., Rostek, F., Beaufort, L., Barker, S., Rees, G., and Schrag, D.P. (2007), 'Coccolith chemistry reveals secular variations in the global ocean carbon cycle?', *Earth and Planetary Science Letters*, *Vol. 253* (1-2), p.83-95

Robin, G.D. (1988), 'The Antarctic ice-sheet, its history and response to sea-level and climatic changes over the past 100 million years', *Palaeogeography Palaeoclimatology Palaeoecology*, *Vol. 67* (1-2), p.31-50.

Rohling, E.J., and Bigg, G.R. (1998), 'Paleosalinity and delta O-18: A critical assessment', *Journal of Geophysical Research-Oceans*, *Vol. 103* (C1), p.1307-1318.

Rohling, E.J., et al. (2012), 'Making sense of palaeoclimate sensitivity', *Nature*, *Vol. 491* (7426), p.683-691.

Rommerskirchen, F., Condon, T., Mollenhauer, G., Dupont, L., and Schefuss, E. (2011), 'Miocene to Pliocene development of surface and subsurface temperatures in the Benguela Current system', *Paleoceanography*, *Vol. 26*.

Rosenthal, Y., Boyle, E.A., and Slowey, N. (1997), 'Temperature control on the incorporation of magnesium, strontium, fluorine, and cadmium into benthic foraminiferal shells from Little Bahama Bank: Prospects for thermocline paleoceanography', *Geochimica et Cosmochimica Acta*, *Vol. 61* (17), p.3633-3643.

Roth, P.H. (1973), 'Calcareous Nannofossils—Leg 17, Deep Sea Drilling Project', in *Initial Reports of the Deep Sea Drilling Project*, edited by Roth, P.H. and Herring, J.R.

Roth, P.H. (1983), 'Jurassic and Lower Cretaceous Calcareous Nannofossils in the Western North Atlantic (Site 534): Biostratigraphy, Preservation, and Some Observations on Biogeography and Paleoceanography', in *Initial Reports of the Deep Sea Drilling Project*, edited by Sheridan, R.E., et al.

Roth, P.H., and Thierstein, H.R. (1972), 'Calcareous Nannofossils - Leg 14 of the Deep Sea Drilling Project', in *Initial Reports of the Deep Sea Drilling Project*, edited by Hayes, D.E., Pimm, A.C., Beckman, J.P., Benson, W.E., PBerger, W.H., Roth, P.H., Supko, P.R. and von Rad, U.

Rousselle, G., Beltran, C., Sicre, M.A., Raffi, I., and De Rafelis, M. (2013), 'Changes in sea-surface conditions in the Equatorial Pacific during the middle Miocene-Pliocene as inferred from coccolith geochemistry', *Earth and Planetary Science Letters*, *Vol. 361*, p.412-421.

Royer, D.L., Pagani, M., and Beerling, D.J. (2012), 'Geobiological constraints on Earth system sensitivity to CO2 during the Cretaceous and Cenozoic', *Geobiology*, *Vol. 10* (4), p.298-310.

Ruddiman, W.F. (2001), *Earth's Climate, Past and Future*, W.H. Freeman.

Ryan, W.B.F., et al. (2009), 'Global Multi-Resolution Topography synthesis', *Geochemistry, Geophysics, Geosystems*, *Vol. 10* (3), p.Q03014.

Sadekov, A., Eggins, S.M., De Deckker, P., Ninnemann, U., Kuhnt, W., and Bassinot, F. (2009), 'Surface and subsurface seawater temperature reconstruction using Mg/Ca microanalysis of planktonic foraminifera Globigerinoides ruber, Globigerinoides sacculifer, and Pulleniatina obliquiloculata', *Paleoceanography*, *Vol. 24*

Saenger, C., Affek, H.P., Felis, T., Thiagarajan, N., Lough, J.M., and Holcomb, M. (2012), 'Carbonate clumped isotope variability in shallow water corals: Temperature dependence and growth-related vital effects', *Geochimica Et Cosmochimica Acta*, *Vol. 99*, p.224-242.

Schauble, E.A., Ghosh, P., and Eiler, J.M. (2006), 'Preferential formation of C-13-O-18 bonds in carbonate minerals, estimated using first-principles lattice dynamics', *Geochimica Et Cosmochimica Acta*, *Vol. 70* (10), p.2510-2529.

Schlitzer, R. (2010), Ocean Data View 4, http://odv.awi.de

Schmidt, D.N., Lazarus, D., Young, J.R., and Kucera, M. (2006), 'Biogeography and evolution of body size in marine plankton', *Earth-Science Reviews*, *Vol. 78* (3-4), p.239-266

Schmitz Jr., W.J. (1996), *On the World Ocean Circulation: Volume II - The Pacific and Indian Oceans / A Global Update*, Woods Hole Oceanographic Institution Technical Report.

Seki, O., Foster, G.L., Schmidt, D.N., Mackensen, A., Kawamura, K., and Pancost, R.D. (2010), 'Alkenone and boron-based Pliocene pCO(2) records', *Earth and Planetary Science Letters*, *Vol. 292* (1-2), p.201-211.

Seki, O., Schmidt, D.N., Schouten, S., Hopmans, E.C., Damste, J.S.S., and Pancost, R.D. (2012), 'Paleoceanographic changes in the Eastern Equatorial Pacific over the last 10 Myr', *Paleoceanography*, *Vol. 27*.

Sexton, P.F., and Wilson, P.A. (2009), 'Preservation of benthic foraminifera and reliability of deep-sea temperature records: Importance of sedimentation rates, lithology, and the need to examine test wall structure', *Paleoceanography*, *Vol. 24*.

Sexton, P.F., Wilson, P.A., and Pearson, P.N. (2006), 'Microstructural and geochemical perspectives on planktic foraminiferal preservation: "Glassy'' versus "Frosty"', *Geochemistry Geophysics Geosystems*, *Vol. 7*.

Shackleton, N.J., and Crowhurst, S. (1997), 'Sediment fluxes based on an orbitally tuned time scale 5 Ma to 14 Ma, Site 926', *Proceedings of the Ocean Drilling Program, Scientific Results*, *Vol. 154*, p.69-82.

Shackleton, N.J., and Hall, M.A. (1997), 'The Late Miocene Stable Isotope Record, Site 926', in *Proceedings of the Ocean Drilling Program, Scientific Results*, edited by Shackleton, N.J., Curry, W.B., Richter, C. and Bralower, T.J.

Shackleton, N.J., and Opdyke, N.D. (1973), 'Oxygen isotope and palaeomagnetic stratigraphy of Equatorial Pacific core V28-238: Oxygen isotope temperatures and ice volumes on a 105 year and 106 year scale', *Quaternary Research*, *Vol. 3* (1), p.39-55.

Shackleton, N.J., and Opdyke, N.D. (1977), 'Oxygen isotope and palaeomagnetic evidence for early northern hemisphere glaciation', *Nature*, *Vol. 270* (5634), p.216-219.

Shackleton, N.J., Crowhurst, S., Hagelberg, T., Pisias, N.G., and Schneider, D.A. (1995a), 'A New Late Neogene Time Scale: Application to Let 138 Sites', in *Proceedings of the Ocean Drilling Program, Scientific Results*, edited by Pisias, N.G., Mayer, L.A., Janecek, T.R., Palmer-Julson, A. and van Andel, T.H.

Shackleton, N.J., Hall, M.A., and Pate, D. (1995b), 'Pliocene Stable Isotope Stratigrahy of Site 846', in *Proceedings of the Ocean Drilling Program, Scientific Results*, edited by Pisias, N.G., Mayer, L.A., Janecek, T.R., Palmer-Julson, A. and van Andel, T.H.

Shackleton, N.J., Imbrie, J., and Hall, M.A. (1983), 'Oxygen and carbon isotope records of east Pacific core V19-30 – implications for the formation of deep-water in the late Pleistocene north Atlantic', *Earth and Planetary Science Letters*, *Vol. 65* (2), p.233-244.

Shipboard Scientific Party Expedition 162 (1996), 'Site 982', in *Proceedings of the Ocean Drilling Program, Initial Reports*, edited by Jansen, E., Raymo, M.E., Blum, P. and Shipboard Scientific Party Expedition 162

Spero, H.J. (1998), 'Life History and Stable Isotope Geochemistry of Planktonic Foraminifera', in *Isotope Paleobiology and Paleoecology*, edited by Norris, R.D. and Corfield, R.M.

Spero, H.J., and Lea, D.W. (1993), 'Intraspecific stable-isotope variability in the planktic foraminifera Globigerinoides-sacculifer – results from laboratory experiments', *Marine Micropaleontology*, *Vol. 22* (3), p.221-234.

Spero, H.J., and Williams, D.F. (1988), 'Extracting environmental information from planktonic foraminiferal delta-C-13 data', *Nature*, *Vol. 335* (6192), p.717-719.

Spero, H.J., Bijma, J., Lea, D.W., and Bemis, B.E. (1997), 'Effect of seawater carbonate concentration on foraminiferal carbon and oxygen isotopes', *Nature*, *Vol. 390* (6659), p.497-500.

Steph, S., Tiedemann, R., Groeneveld, J., Sturm, A., and Nürnberg, D. (2006), 'Pliocene changes in tropical East Pacific upper ocean stratification: response to tropical gateways?', *Proceedings of the Ocean Drilling Program, Scientific Results*, *Vol. 202*.

Stoll, H., Langer, G., Shimizu, N., and Kanamaru, K. (2012), 'B/Ca in coccoliths and relationship to calcification vesicle pH and dissolved inorganic carbon concentrations', *Geochimica Et Cosmochimica Acta*, *Vol. 80*, p.143-157.

Su, X., Baumann, K.-H., and Thiede, J. (2000), 'Calcareous nannofossils from Leg 168: Biochronology and Diagenesis', in *Proceedings of the Ocean Drilling Program, Scientific Results*, edited by Fisher, A., E.E., D. and Escutia, C.

Takahashi, T., Feely, R.A., Weiss, R.F., Wanninkhof, R.H., Chipman, D.W., Sutherland, S.C., and Takahashi, T.T. (1997), 'Global air-sea flux of CO2: An estimate based on measurements of sea-air pCO(2) difference', *Proceedings of the National Academy of Sciences of the United States of America*, *Vol. 94* (16), p.8292-8299.

Talarico, F.M., and Sandroni, S. (2009), 'Provenance signatures of the Antarctic Ice Sheets in the Ross Embayment during the Late Miocene to Early Pliocene: The ANDRILL AND-1B core record', *Global and Planetary Change*, *Vol. 69* (3), p.103-123.

Thiagarajan, N., Adkins, J., and Eiler, J. (2011), 'Carbonate clumped isotope thermometry of deep-sea corals and implications for vital effects', *Geochimica Et Cosmochimica Acta*, *Vol. 75* (16), p.4416-4425.

Thiede, J., and Myhre, A.M. (1996), 'The Paleoceanographic History of the North Atlantic-Arctic Gateways: Synthesis of the Leg 151 Drilling Results', *Proceedings of the Ocean Drilling Program, Scientific Results*, *Vol. 151*.

Thomas, D.J., and Via, R.K. (2007), 'Neogene evolution of Atlantic thermohaline circulation: Perspective from Walvis Ridge, southeastern Atlantic Ocean', *Paleoceanography*, *Vol. 22* (2)

Thunell, R., and Belyea, P. (1982), 'Neogene planktonic foraminiferal biogeography of the Atlantic ocean', *Micropaleontology*, *Vol. 28* (4), p.381-398.

Tipple, B.J., and Pagani, M. (2010), 'A 35 Myr North American leaf-wax compound-specific carbon and hydrogen isotope record: Implications for C-4 grasslands and hydrologic cycle dynamics', *Earth and Planetary Science Letters*, *Vol. 299* (1-2), p.250-262.

Torrence, C., and Compo, G.P. (1998), 'A practical guide to wavelet analysis', *Bulletin of the American Meteorological Society*, *Vol. 79* (1), p.61-78.

Trenberth, K.E. (1997), 'The definition of El Nino', *Bulletin of the American Meteorological Society*, *Vol. 78* (12), p.2771-2777.

Tripati, A.K., Eagle, R.A., Thiagarajan, N., Gagnon, A.C., Bauch, H., Halloran, P.R., and Eiler, J.M. (2010), 'C-13-O-18 isotope signatures and 'clumped isotope' thermometry in foraminifera and coccoliths', *Geochimica Et Cosmochimica Acta*, *Vol. 74* (20), p.5697-5717.

Tripati, A.K., Roberts, C.D., and Eagle, R.A. (2009), 'Coupling of CO2 and Ice Sheet Stability Over Major Climate Transitions of the Last 20 Million Years', *Science*, *Vol. 326* (5958), p.1394-1397.

Urey, H.C. (1947), 'The thermodynamic properties of isotopic substances', *Journal of the Chemical Society (Resumed)*, *Vol.* (0), p.562-581.

van Andel, T.H., Heath, G.R., and Moore, T.C. (1975), 'Cenozoic History and Paleoceanography of Central Equatorial Pacific Ocean', *Memoir of the Geological Society of America*, *Vol. 143*.

van de Flierdt, T., Frank, M., Halliday, A.N., Hein, J.R., Hattendorf, B., Günther, D., and Kubik, P.W. (2004), 'Deep and bottom water export from the Southern Ocean to the Pacific over the past 38 million years', *Paleoceanography*, *Vol. 19* (1), p.PA1020.

van der Laan, E., Gaboardi, S., Hilgen, F.J., and Lourens, L.J. (2005), 'Regional climate and glacial control on high-resolution oxygen isotope records from Ain el Beida (latest Miocene, northwest Morocco): A cyclostratigraphic analysis in the depth and time domain', *Paleoceanography*, *Vol. 20* (1).

Venz, K.A., and Hodell, D.A. (2002), 'New evidence for changes in Plio-Pleistocene deep water circulation from Southern Ocean ODP Leg 177 Site 1090', *Palaeogeography Palaeoclimatology Palaeoecology*, *Vol. 182* (3-4), p.197-220.

Via, R.K., and Thomas, D.J. (2006), 'Evolution of Atlantic thermohaline circulation: Early Oligocene onset of deep-water production in the North Atlantic', *Geology*, *Vol. 34* (6), p.441-444

Vidal, L., Bickert, T., Wefer, G., and Rohl, U. (2002), 'Late miocene stable isotope stratigraphy of SE Atlantic ODP Site 1085: Relation to Messinian events', *Marine Geology*, *Vol. 180* (1-4), p.71-85.

Wacker, U., Fiebig, J., and Schoene, B.R. (2013), 'Clumped isotope analysis of carbonates: comparison of two different acid digestion techniques', *Rapid Communications in Mass Spectrometry*, *Vol. 27* (14), p.1631-1642.

Waddell, L.M., Hendy, I.L., Moore, T.C., and Lyle, M.W. (2009), 'Ventilation of the abyssal Southern Ocean during the late Neogene: A new perspective from the subantarctic Pacific', *Paleoceanography*, *Vol. 24*.

Wade, B.S., Pearson, P.N., Berggren, W.A., and Palike, H. (2011), 'Review and revision of Cenozoic tropical planktonic foraminiferal biostratigraphy and calibration to the geomagnetic polarity and astronomical time scale', *Earth-Science Reviews*, *Vol. 104* (1-3), p.111-142.

Wang, R., Li, J., and Li, B. (2004), 'Data Report: Late Miocene-Quaternary Biogenic Opal Accumulation at ODP Site 1143, Southern South China Sea', in *Proceedings of the Ocean Drilling Program, Scientific Results*, edited by Prell, W.L., Wang, P., Blum, P., Rea, D.K. and Clemens, S.C.

Wang, Z., Schauble, E.A., and Eiler, J.M. (2004), 'Equilibrium thermodynamics of multiply substituted isotopologues of molecular gases', *Geochimica Et Cosmochimica Acta*, *Vol. 68* (23), p.4779-4797.

Wara, M.W., Ravelo, A.C., and Delaney, M.L. (2005), 'Permanent El Nino-like conditions during the Pliocene warm period', *Science*, *Vol. 309* (5735), p.758-761.

Weedon, G.P. (2005), *Time-series Analysis and Cyclostratigraphy: Examining Stratigraphic Records of Environmental Cycles*, Cambridge University Press.

Westerhold, T., Bickert, T., and Rohl, U. (2005), 'Middle to late Miocene oxygen isotope stratigraphy of ODP site 1085 (SE Atlantic): new constrains on miocene climate variability and sea-level fluctuations', *Palaeogeography Palaeoclimatology Palaeoecology*, *Vol. 217* (3-4), p.205-222.

Westerhold, T., Rohl, U., and Laskar, J. (2012), 'Time scale controversy: Accurate orbital calibration of the early Paleogene', *Geochemistry Geophysics Geosystems*, *Vol. 13*.

Wilkens, R.H., Dickens, G.R., Tian, J., Backman, J., and Scientists, E. (2013), 'Data report: revised composite depth scales for Sites U1336, U1337, and U1338', in *Proceedings of the Integrated Ocean Drilling Program, Scientific Results*, edited by Palike, H., Lyle, M., Nishi, H., Raffi, I., Gamage, K., Klaus, A. and Scientists, E.

Williams, M., Haywood, A.M., Taylor, S.P., Valdes, P.J., Sellwood, B.W., and Hillenbrand, C.-D. (2005), 'Evaluating the efficacy of planktonic foraminifer calcite d18O data for sea surface temperature reconstruction for the Late Miocene', *Geobios*, *Vol. 38* (6), p.843-863.

Wolf-Welling, T.C.W., Cremer, M., O'Connell, S., Winkler, A., and Thiede, J. (1996), 'Cenozoic Arctic Gateway paleoclimate variability: indications from changes in coarse-fractin composition', *Proceedings of the Ocean Drilling Program, Scientific Results*, *Vol. 151*.

Wolf, T.C.W., and Thiede, J. (1991), 'History of terrigenous sedimentation during the past 10 Myr in the north Atlantic (ODP Leg 104 and 105 and DSDP Leg 81), *Marine Geology*, *Vol. 101* (1-4), p.83-102.

Woodruff, F., and Savin, S.M. (1989), 'Miocene deep-water oceanography', *Paleoceanography*, *Vol. 4* (1), p.87-140.

Wright, J.D., and Miller, K.G. (1996), 'Control of North Atlantic deep water circulation by the Greenland-Scotland ridge', *Paleoceanography*, *Vol. 11* (2), p.157-170.

Wright, J.D., Miller, K.G., and Fairbanks, R.G. (1991), 'Evolution of modern deep-water circulation: evidence from the late Miocene southern ocean', *Paleoceanography*, *Vol. 6* (2), p.275-290.

Wright, J.D., Miller, K.G., and Fairbanks, R.G. (1992), 'Early and middle Miocene stable isotopes: implications for deep-water circulation and climate', *Paleoceanography*, *Vol. 7* (3), p.357-389.

Young, J.R., Geisen, M., and Probert, I. (2005), 'Review of selected aspects of coccolithophore biology with implications for paleobiodiversity estimation', *Micropaleontology*, *Vol. 51* (4), p.267-288

Zachos, J., Pagani, M., Sloan, L., Thomas, E., and Billups, K. (2001), 'Trends, rhythms, and aberrations in global climate 65 Ma to present', *Science*, *Vol. 292* (5517), p.686-693.

Zachos, J.C., Dickens, G.R., and Zeebe, R.E. (2008), 'An early Cenozoic perspective on greenhouse warming and carbon-cycle dynamics', *Nature*, *Vol. 451* (7176), p.279-283.

Zeebe, R.E. (2012), 'LOSCAR: Long-term Ocean-atmosphere-Sediment CArbon cycle Reservoir Model v2.0.4', *Geosci. Model Dev.*, *Vol. 5* (1), p.149-166.

Zeebe, R.E., and Wolf-Gladrow, D. (2001), *CO2 in Seawater: Equilibrium, Kinetics, Isotopes*, Elsevier.

Zhang, X., et al. (2012), 'Changes in equatorial Pacific thermocline depth in response to Panamanian seaway closure: Insights from a multi-model study', *Earth and Planetary Science Letters*, *Vol. 317*, p.76-84.

Ziveri, P., Stoll, H., Probert, I., Klass, C., Geisen, M., Ganssen, G., and Young, J. (2003), 'Stable isotope 'vital effects in coccolith calcite', *Earth and Planetary Science Letters*, *Vol. 210* (1-2), p.137-149.

Appendix A

A.1. Original Foraminiferal Isotope Data

Original foraminiferal planktic and benthic stable isotope data produced in this PhD study. Description of individual data columns can be found below.

- ***Data Point ID:*** The sample identity (ID) is given a prefix of 321-U1338 before the content to denote the expedition and site. Each cell denotes the hole-core-section-interval of the sample.
- ***Depth:*** in meters CCSF-A (core composite depth below sea floor) on Wilkens et al. (2013) splice.
- ***Age:*** in Ma. The generation of the age model is described in Chapter 4. The depth-age relationship for Site U1338 between 8.0 and 3.5 Ma is also provided in a table in Appendix B.1.
- ***Planktic Isotopes:***
    - ***$\delta^{13}C$ – original (replicates)*** and ***$\delta^{18}O$ – original (replicates):*** the columns in this section give replicate measurements (1st, 2nd and 3rd) of each sample for which the planktic foraminifera *Globigerinoides sacculifer* was measured for $\delta^{13}C$ and $\delta^{18}O$ respectively.

      Each replicate was corrected to VPDB using the offset between the known ($\delta^{13}C$ = 2.087 ‰; $\delta^{18}O$ = – 2.030 ‰) and average values calculated per run of Imperial Carrera Marble (ICM). All samples were run at Imperial College London (ICL). Analytical precision (1 standard deviation = 1 σ) based on repeat analyses of ICM is 0.04 ‰ for $\delta^{13}C$ and 0.07 ‰ for $\delta^{18}O$.

      NB: for samples B-10H-4-W 72/74 (97.82 m CCSF-A) and B-12H-1-W 112/124 (115.41 m CCSF-A) (highlighted in bold in table) a total of five and eight replicates were respectively measured. These measurements (listed in small table below) were used in any calculations of averages for the two respective samples (discussed below).

Sample 321-U1338B-10H-4-W 72/74 (97.82 m CCSF-A)					
Replicate	1st	2nd	3rd	4th	5th
$\delta^{13}C$	2.258	2.103	2.004	2.075	1.934
$\delta^{18}O$	-0.718	-0.600	-0.879	-1.684	-0.539

Sample 321-U1338B-12H-1-W 112/124 (115.41 m CCSF-A)								
Replicate	1st	2nd	3rd	4th	5th	6th	7th	8th
$\delta^{13}C$	2.077	1.808	1.838	2.182	1.817	1.808	2.057	1.943
$\delta^{18}O$	-1.138	-0.904	-0.876	-0.616	-0.941	-0.904	-1.127	-1.103

- ***$\delta^{13}C$ AVE*** and ***$\delta^{18}O$ AVE:*** these columns show the average of the replicates for each sample for which planktic foraminiferal $\delta^{13}C$ and $\delta^{18}O$ were measured. Values are reported against VPDB. The associated sample variability (1 standard deviation = 1 σ) based on repeat analyses of the same sample is better than 0.1 ‰ for $\delta^{13}C$ and $\delta^{18}O$.

- ***Benthic Isotopes:***
  - ***$\delta^{13}C$ – original (replicates)*** and ***$\delta^{18}O$ – original (replicates):*** show the replicate values (1st and 2nd) of samples for which benthic foraminiferal *Cibicidoides mundulus* $\delta^{13}C$ and $\delta^{18}O$ were measured. Each replicate was corrected to VPDB using the offset between the known ($\delta^{13}C$ = 2.087 ‰; $\delta^{18}O$ = – 2.030 ‰) and average values calculated per run of ICM.

    93% of the samples were run at ICL (denoted with italic 1), which have an analytical precision based on repeat analyses of ICM of 0.04 ‰ for $\delta^{13}C$ and 0.07 ‰ for $\delta^{18}O$ (1 standard deviation = 1 σ). 7% of the samples were run at University College London (UCL – denoted with italic 2), which have an analytical precision based on repeat analyses of ICM of 0.02 ‰ for $\delta^{13}C$ and 0.09 ‰ for $\delta^{18}O$ (1 standard deviation = 1 σ).

    NB: Replicates of ICM were run at both labs to ensure good inter-laboratory reproducibility. No offset was found between the known ICM values and the values measured at ICL or UCL:

    - Known ICM: $\delta^{13}C$ = 2.087 ± 0.029 ‰; $\delta^{18}O$ = – 2.030 ± 0.058 ‰
    - ICM at ICL: $\delta^{13}C$ = 2.092 ± 0.035 ‰; $\delta^{18}O$ = – 2.020 ± 0.065 ‰
    - ICM at UCL: $\delta^{13}C$ = 2.08 ± 0.02 ‰; $\delta^{18}O$ = – 2.00 ± 0.09 ‰

    All values are reported with 1 standard deviation = 1 σ.
  - ***$\delta^{13}C$ Average*** and ***$\delta^{18}O$ – average NON-EQUI:*** these columns show the average of the 1st, and 2nd replicates of each sample for which benthic foraminiferal $\delta^{13}C$ and $\delta^{18}O$ were respectively measured. Values are reported against VPDB, but not corrected to equilibrium.

    The associated sample variability (1 standard deviation = 1 σ) based on repeat analyses of the same sample is 0.08 ‰ for $\delta^{13}C$ and 0.07 ‰ for $\delta^{18}O$ for samples run at ICL (italic 1), and is 0.02 ‰ for $\delta^{13}C$ and 0.07 ‰ for $\delta^{18}O$ for samples run at UCL (italic 2).
  - ***$\delta^{18}O$ – Ave EQUI:*** this column denotes the data from ***$\delta^{18}O$ – average NON-EQUI*** corrected to equilibrium by the addition of 0.64 ‰ Shackleton et al., 1995b).
  - ***$\delta^{18}O$ – WMA EQUI:*** this column shows the weighted moving average values (1st and 5th point = 30%; 2nd and 4th point = 70%; 3rd point = 100%) of the data from ***$\delta^{18}O$ – Ave EQUI***.

Data Point ID	Depth	Age	Planktic Isotopes								Benthic Isotopes								
	In m		$\delta^{13}C$ - original (replicates)			$\delta^{13}C$	$\delta^{18}O$ - original (replicates)			$\delta^{18}O$	$\delta^{13}C$ - original (replicates)		$\delta^{13}C$	$\delta^{18}O$ - original (replicates)		$\delta^{18}O$ - average	$\delta^{18}O$ - Ave	$\delta^{18}O$ - WMA
321-U1338	CCSF-A	Ma	1st	2nd	3rd	AVE	1st	2nd	3rd	AVE	1st	2nd	Average	1st	2nd	NON-EQUI	EQUI	EQUI
B-5H-6-W 10/12	48.00	3.539									-0.181 *1*		-0.181 *1*	2.340 *1*		2.340 *1*	2.980	
B-5H-6-W 20/22	48.10	3.546									-0.414 *1*		-0.414 *1*	2.442 *1*		2.442 *1*	3.082	
B-5H-6-W 30/32	48.20	3.553									-0.249 *1*		-0.249 *1*	2.306 *1*		2.306 *1*	2.946	3.045
B-5H-6-W 40/42	48.30	3.559									-0.292 *1*		-0.292 *1*	2.474 *1*		2.474 *1*	3.114	3.119
B-5H-6-W 50/52	48.40	3.566									-0.306 *1*		-0.306 *1*	2.552 *1*		2.552 *1*	3.192	3.179
B-5H-6-W 60/62	48.50	3.573									-0.570 *1*		-0.570 *1*	2.761 *1*		2.761 *1*	3.401	3.197
B-5H-6-W 77/79	48.67	3.584									-0.258 *1*		-0.258 *1*	2.361 *1*		2.361 *1*	3.001	3.140
B-5H-6-W 88/90	48.78	3.554									-0.845 *1*		-0.845 *1*	2.432 *1*		2.432 *1*	3.072	3.117
B-5H-6-W 100/102	48.90	3.562									0.097 *1*		0.097 *1*	2.460 *1*		2.460 *1*	3.100	3.136
B-5H-6-W 110/112	49.00	3.568									-0.040 *1*		-0.040 *1*	2.649 *1*		2.649 *1*	3.289	3.212
B-5H-6-W 122/124	49.12	3.576									0.023 *1*		0.023 *1*	2.544 *1*		2.544 *1*	3.184	3.261
B-5H-6-W 130/132	49.20	3.588									-0.295 *1*		-0.295 *1*	2.780 *1*		2.780 *1*	3.420	3.277
B-5H-6-W 140/142	49.30	3.596									0.048 *1*		0.048 *1*	2.598 *1*		2.598 *1*	3.238	3.214
B-5H-6-W 148/150	49.38	3.603									0.160 *1*		0.160 *1*	2.455 *1*		2.455 *1*	3.095	3.108
B-5H-7-W 10/12	49.50	3.613									0.078 *1*		0.078 *1*	2.317 *1*		2.317 *1*	2.957	3.029
B-5H-7-W 20/22	49.60	3.617									0.063 *1*		0.063 *1*	2.250 *1*		2.250 *1*	2.890	3.072
B-5H-7-W 30/32	49.70	3.624									-0.046 *1*		-0.046 *1*	2.592 *1*		2.592 *1*	3.232	3.225
A-6H-3-W 54/56	49.80	3.631									-0.108 *1*		-0.108 *1*	2.915 *1*		2.915 *1*	3.555	3.376
A-6H-3-W 67/69	49.93	3.640									-0.286 *1*		-0.286 *1*	2.846 *1*		2.846 *1*	3.486	3.389
A-6H-3-W 80/82	50.06	3.648									-0.032 *1*		-0.032 *1*	2.706 *1*		2.706 *1*	3.346	3.259
A-6H-3-W 90/92	50.16	3.655									0.074 *1*		0.074 *1*	2.292 *1*		2.292 *1*	2.932	3.097
A-6H-3-W 100/102	50.26	3.656									0.050 *1*		0.050 *1*	2.267 *1*		2.267 *1*	2.907	3.054
A-6H-3-W 109/111	50.35	3.657									-0.057 *1*		-0.057 *1*	2.484 *1*		2.484 *1*	3.124	3.116
A-6H-3-W 123/125	50.49	3.662									-0.250 *1*		-0.250 *1*	2.731 *1*		2.731 *1*	3.371	3.202
A-6H-3-W 133/135	50.59	3.665									-0.298 *1*		-0.298 *1*	2.523 *1*		2.523 *1*	3.163	3.230
A-6H-3-W 140/142	50.66	3.668									-0.439 *1*		-0.439 *1*	2.571 *1*		2.571 *1*	3.211	3.222
A-6H-3-W 147/149	50.73	3.670									-0.356 *1*		-0.356 *1*	2.633 *1*		2.633 *1*	3.273	3.226

A-6H-4-W 10/12	50.86	3.674									-0.065	1		-0.065	1	2.486	1		2.486	1	3.126	3.240
A-6H-4-W 20/22	50.96	3.678									-0.202	1		-0.202	1	2.766	1		2.766	1	3.406	3.248
A-6H-4-W 41/43	51.17	3.685									-0.299	1		-0.299	1	2.549	1		2.549	1	3.189	3.226
A-6H-4-W 54/56	51.30	3.689									0.058	1		0.058	1	2.483	1		2.483	1	3.123	3.179
A-6H-4-W 60/62	51.36	3.691									-0.205	1		-0.205	1	2.629	1		2.629	1	3.269	3.113
A-6H-4-W 67/69	51.43	3.694									-0.013	1		-0.013	1	2.263	1		2.263	1	2.903	3.045
A-6H-4-W 80/82	51.56	3.693									-0.180	1		-0.180	1	2.343	1		2.343	1	2.983	3.028
A-6H-4-W 90/92	51.66	3.696									-0.109	1		-0.109	1	2.419	1		2.419	1	3.059	3.049
A-6H-4-W 100/102	51.76	3.698									-0.142	1		-0.142	1	2.513	1		2.513	1	3.153	3.092
A-6H-4-W 109/111	51.85	3.701									-0.136	1		-0.136	1	2.434	1		2.434	1	3.074	3.111
A-6H-4-W 118/120	51.94	3.703									-0.043	1		-0.043	1	2.481	1		2.481	1	3.121	3.121
B-6H-1-W 130/132	52.04	3.706									0.066	1		0.066	1	2.529	1		2.529	1	3.169	3.096
B-6H-1-W 140/142	52.14	3.708									-0.221	1		-0.221	1	2.447	1		2.447	1	3.087	3.047
B-6H-1-W 147/149	52.21	3.710									-0.243	1		-0.243	1	2.197	1		2.197	1	2.837	3.010
B-6H-2-W 10/12	52.34	3.715									-0.188	1		-0.188	1	2.405	1		2.405	1	3.045	3.033
B-6H-2-W 20/22	52.44	3.719									-0.439	1		-0.439	1	2.529	1		2.529	1	3.169	3.075
B-6H-2-W 30/32	52.54	3.722									-0.321	1		-0.321	1	2.436	1		2.436	1	3.076	3.090
B-6H-2-W 40/42	52.64	3.725									-0.287	1		-0.287	1	2.426	1		2.426	1	3.066	3.090
B-6H-2-W 54/56	52.78	3.730									-0.297	1		-0.297	1	2.414	1		2.414	1	3.054	3.085
B-6H-2-W 60/62	52.84	3.732									-0.184	1		-0.184	1	2.564	1		2.564	1	3.204	3.107
B-6H-2-W 70/72	52.94	3.740									-0.054	1		-0.054	1	2.329	1		2.329	1	2.969	3.097
B-6H-2-W 78/80	53.02	3.743									-0.274	1		-0.274	1	2.635	1		2.635	1	3.275	3.101
B-6H-2-W 88/90	53.12	3.747									-0.314	1		-0.314	1	2.259	1		2.259	1	2.899	3.092
B-6H-2-W 98/100	53.22	3.751									-0.187	1		-0.187	1	2.560	1		2.560	1	3.200	3.108
B-6H-2-W 110/112	53.34	3.756									-0.648	1		-0.648	1	2.537	1		2.537	1	3.177	3.120
B-6H-2-W 122/124	53.46	3.762									-0.247	1		-0.247	1	2.321	1		2.321	1	2.961	3.126
B-6H-2-W 132/134	53.56	3.766									-0.109	1		-0.109	1	2.692	1		2.692	1	3.332	3.119
B-6H-2-W 140/142	53.64	3.769									-0.180	1		-0.180	1	2.359	1		2.359	1	2.999	3.095
B-6H-2-W 149/151	53.73	3.773									-0.142	1		-0.142	1	2.364	1		2.364	1	3.004	3.084
B-6H-3-W 10/12	53.84	3.777									-0.181	1		-0.181	1	2.570	1		2.570	1	3.210	3.084

B-6H-3-W 20/22	53.94	3.783									-0.219 *1*		-0.219 *1*	2.364 *1*		2.364 *1*	3.004	3.080
B-6H-3-W 30/32	54.04	3.787									-0.192 *1*		-0.192 *1*	2.487 *1*		2.487 *1*	3.127	3.084
B-6H-3-W 40/42	54.14	3.793									-1.243 *1*		-1.243 *1*	2.362 *1*		2.362 *1*	3.002	3.083
B-6H-3-W 60/62	54.34	3.804									-0.698 *1*		-0.698 *1*	2.550 *1*		2.550 *1*	3.190	3.140
B-6H-3-W 79/81	54.53	3.815									-0.452 *1*		-0.452 *1*	2.443 *1*		2.443 *1*	3.083	3.157
B-6H-3-W 88/90	54.62	3.820									-0.302 *1*		-0.302 *1*	2.798 *1*		2.798 *1*	3.438	3.176
B-6H-3-W 100/102	54.74	3.830									-0.188 *1*		-0.188 *1*	2.191 *1*		2.191 *1*	2.831	3.157
B-6H-3-W 110/112	54.84	3.836									-0.453 *1*		-0.453 *1*	2.672 *1*		2.672 *1*	3.312	3.214
B-6H-3-W 122/124	54.96	3.844									0.054 *1*		0.054 *1*	2.656 *1*		2.656 *1*	3.296	3.247
B-6H-3-W 132/134	55.06	3.856									-0.721 *1*		-0.721 *1*	2.722 *1*		2.722 *1*	3.362	3.255
B-6H-3-W 140/142	55.14	3.863									0.114 *1*		0.114 *1*	2.443 *1*		2.443 *1*	3.083	3.196
B-6H-3-W 149/151	55.23	3.870									-0.500 *1*		-0.500 *1*	2.510 *1*		2.510 *1*	3.150	3.141
B-6H-4-W 10/12	55.34	3.879									-0.322 *1*		-0.322 *1*	2.555 *1*		2.555 *1*	3.195	3.105
B-6H-4-W 20/22	55.44	3.888									-0.271 *1*		-0.271 *1*	2.264 *1*		2.264 *1*	2.904	3.094
B-6H-4-W 30/32	55.54	3.896									-0.465 *1*		-0.465 *1*	2.554 *1*		2.554 *1*	3.194	3.115
B-6H-4-W 40/42	55.64	3.905									-0.270 *1*		-0.270 *1*	2.559 *1*		2.559 *1*	3.199	3.126
B-6H-4-W 50/52	55.74	3.913									0.008 *1*	0.073 *1*	0.040 *1*	2.364 *1*	2.489 *1*	2.427 *1*	3.067	3.127
B-6H-4-W 60/62	55.84	3.921									-0.052 *1*		-0.052 *1*	2.447 *1*		2.447 *1*	3.087	3.126
B-6H-4-W 70/72	55.94	3.930									-0.211 *1*		-0.211 *1*	2.549 *1*		2.549 *1*	3.189	3.146
B-6H-4-W 80/82	56.04	3.938									-0.079 *1*		-0.079 *1*	2.532 *1*		2.532 *1*	3.172	3.144
B-6H-4-W 88/90	56.12	3.945									-0.110 *1*		-0.110 *1*	2.518 *1*		2.518 *1*	3.158	3.138
B-6H-4-W 100/102	56.24	3.955									-0.355 *1*		-0.355 *1*	2.330 *1*		2.330 *1*	2.970	3.134
B-6H-4-W 110/112	56.34	3.963									0.209 *1*		0.209 *1*	2.695 *1*		2.695 *1*	3.335	3.166
B-6H-4-W 122/124	56.46	3.973									-0.297 *1*		-0.297 *1*	2.474 *1*		2.474 *1*	3.114	3.144
B-6H-4-W 132/134	56.56	3.978									-0.134 *1*		-0.134 *1*	2.546 *1*		2.546 *1*	3.186	3.103
B-6H-4-W 140/142	56.64	3.983									-0.142 *1*		-0.142 *1*	2.236 *1*		2.236 *1*	2.876	3.059
B-6H-4-W 149/151	56.73	3.989									-0.034 *1*		-0.034 *1*	2.462 *1*		2.462 *1*	3.102	3.080
B-6H-5-W 10/12	56.84	3.997									-0.319 *1*		-0.319 *1*	2.581 *1*		2.581 *1*	3.221	3.110
B-6H-5-W 20/22	56.94	3.998									-0.019 *1*		-0.019 *1*	2.408 *1*		2.408 *1*	3.048	3.114
B-6H-5-W 30/32	57.04	4.004									-0.361 *1*		-0.361 *1*	2.495 *1*		2.495 *1*	3.135	3.074

B-6H-5-W 40/42	57.14	4.010									0.012	1			0.012	1	2.409	1			2.409	1	3.049	3.050
B-6H-5-W 50/52	57.24	4.015									0.034	1			0.034	1	2.207	1			2.207	1	2.847	3.071
B-6H-5-W 60/62	57.34	4.021									-0.039	1	0.227	1	0.094	1	2.494	1	2.889	1	2.691	1	3.331	3.153
B-6H-5-W 70/72	57.44	4.026									-0.068	1			-0.068	1	2.553	1			2.553	1	3.193	3.197
B-6H-5-W 80/82	57.54	4.032									-0.217	1			-0.217	1	2.643	1			2.643	1	3.283	3.185
B-6H-5-W 88/90	57.62	4.036									-0.067	1			-0.067	1	2.402	1			2.402	1	3.042	3.113
B-6H-5-W 100/102	57.74	4.043									-0.246	1			-0.246	1	2.387	1			2.387	1	3.027	3.073
B-6H-5-W 110/112	57.84	4.051									-0.401	1			-0.401	1	2.436	1			2.436	1	3.076	3.058
A-7H-1-W 148/150	57.89	4.054									-0.156	1			-0.156	1	2.442	1			2.442	1	3.082	3.051
A-7H-2-W 10/12	58.01	4.062									-0.070	1			-0.070	1	2.392	1			2.392	1	3.032	3.034
A-7H-2-W 20/22	58.11	4.069									-0.066	1			-0.066	1	2.315	1			2.315	1	2.955	3.038
A-7H-2-W 30/32	58.21	4.075									-0.567	1			-0.567	1	2.432	1			2.432	1	3.072	3.058
A-7H-2-W 40/42	58.31	4.082									-0.570	1			-0.570	1	2.564	1			2.564	1	3.204	3.061
A-7H-2-W 50/52	58.41	4.083									-0.192	1			-0.192	1	2.292	1			2.292	1	2.932	3.014
A-7H-2-W 56/58	58.47	4.087									-0.135	1	-0.200	1	-0.168	1	2.393	1	2.258	1	2.326	1	2.966	2.965
A-7H-2-W 70/72	58.61	4.095									-0.118	1			-0.118	1	2.260	1			2.260	1	2.900	2.972
A-7H-2-W 79/81	58.70	4.100									-0.456	1			-0.456	1	2.315	1			2.315	1	2.955	3.069
A-7H-2-W 89/91	58.80	4.105									-0.623	1			-0.623	1	2.663	1			2.663	1	3.303	3.185
A-7H-2-W 100/102	58.91	4.111									-0.364	1			-0.364	1	2.762	1			2.762	1	3.402	3.222
A-7H-2-W 109/111	59.00	4.116									-0.327	1			-0.327	1	2.471	1			2.471	1	3.111	3.147
A-7H-2-W 121/123	59.12	4.123									-0.103	1			-0.103	1	2.323	1			2.323	1	2.963	3.051
A-7H-2-W 130/132	59.21	4.128									-0.181	1			-0.181	1	2.304	1			2.304	1	2.944	2.999
A-7H-2-W 140/142	59.31	4.134									-0.036	1			-0.036	1	2.461	1			2.461	1	3.101	2.998
A-7H-2-W 148/150	59.39	4.138									-0.259	1			-0.259	1	2.280	1			2.280	1	2.920	2.985
A-7H-3-W 10/12	59.51	4.145									-0.372	1			-0.372	1	2.358	1			2.358	1	2.998	2.981
A-7H-3-W 20/22	59.61	4.151									-0.058	1			-0.058	1	2.300	1			2.300	1	2.940	2.991
A-7H-3-W 30/32	59.71	4.156									-0.077	1			-0.077	1	2.403	1			2.403	1	3.043	3.035
A-7H-3-W 40/42	59.81	4.162									-0.130	1			-0.130	1	2.455	1			2.455	1	3.095	3.082
A-7H-3-W 54/56	59.95	4.169									-0.238	1			-0.238	1	2.484	1			2.484	1	3.124	3.091
A-7H-3-W 60/62	60.01	4.173									-0.428	1			-0.428	1	2.537	1			2.537	1	3.177	3.072

A-7H-3-W 70/72	60.11	4.181								-0.188	1			-0.188	1	2.183	1			2.183	1	2.823	3.061
A-7H-3-W 80/82	60.21	4.187								-0.222	1			-0.222	1	2.523	1			2.523	1	3.163	3.108
A-7H-3-W 89/91	60.30	4.194								-0.179	1	-0.494	1	-0.337	1	2.511	1	2.774	1	2.643	1	3.283	3.154
A-7H-3-W 100/102	60.41	4.201								-0.281	1			-0.281	1	2.471	1			2.471	1	3.111	3.164
A-7H-3-W 109/111	60.50	4.213								-0.397	1			-0.397	1	2.495	1			2.495	1	3.135	3.132
A-7H-3-W 121/123	60.62	4.223								-0.132	1			-0.132	1	2.489	1			2.489	1	3.129	3.080
A-7H-3-W 130/132	60.71	4.230								-0.093	1			-0.093	1	2.385	1			2.385	1	3.025	3.057
A-7H-3-W 140/142	60.81	4.238								-0.289	1			-0.289	1	2.246	1			2.246	1	2.886	3.060
A-7H-4-W 4/6	60.95	4.250								-0.267	1			-0.267	1	2.677	1			2.677	1	3.317	3.100
A-7H-4-W 10/12	61.01	4.255								-0.525	1			-0.525	1	2.413	1			2.413	1	3.053	3.110
A-7H-4-W 20/22	61.11	4.264								-0.080	1			-0.080	1	2.417	1			2.417	1	3.057	3.111
A-7H-4-W 30/32	61.21	4.272								-0.312	1			-0.312	1	2.528	1			2.528	1	3.168	3.084
A-7H-4-W 40/42	61.31	4.280								-0.162	1			-0.162	1	2.449	1			2.449	1	3.089	3.051
A-7H-4-W 50/52	61.41	4.289								-0.108	1			-0.108	1	2.241	1			2.241	1	2.881	3.014
A-7H-4-W 60/62	61.51	4.297								-0.001	1			-0.001	1	2.401	1			2.401	1	3.041	3.025
A-7H-4-W 70/72	61.61	4.305								-0.220	1			-0.220	1	2.418	1			2.418	1	3.058	3.088
A-7H-4-W 80/82	61.71	4.314								-0.360	1			-0.360	1	2.520	1			2.520	1	3.160	3.156
A-7H-4-W 90/92	61.81	4.322								-0.387	1			-0.387	1	2.691	1			2.691	1	3.331	3.208
A-7H-4-W 100/102	61.91	4.331								-0.231	1			-0.231	1	2.437	1			2.437	1	3.077	3.198
A-7H-4-W 107/109	61.98	4.336								-0.401	1			-0.401	1	2.722	1			2.722	1	3.362	3.141
B-7H-1-W 110/112	62.06	4.343								-0.127	1			-0.127	1	2.300	1			2.300	1	2.940	3.058
B-7H-1-W 118/120	62.14	4.348								-0.071	1			-0.071	1	2.187	1			2.187	1	2.827	3.043
B-7H-1-W 130/132	62.26	4.356								-0.444	1			-0.444	1	2.616	1			2.616	1	3.256	3.091
B-7H-1-W 140/142	62.36	4.362								-0.433	1			-0.433	1	2.545	1			2.545	1	3.185	3.121
B-7H-1-W 145/147	62.41	4.366	2.473		2.473	-1.810		-1.810															
B-7H-1-W 149/151	62.45	4.368	1.932		1.932	-1.229		-1.229		-0.321	1			-0.321	1	2.447	1			2.447	1	3.087	3.105
B-7H-2-W 10/12	62.56	4.371								-0.001	1			-0.001	1	2.325	1			2.325	1	2.965	3.088
B-7H-2-W 20/22	62.66	4.377	2.100		2.100	-1.560		-1.560		-0.052	1			-0.052	1	2.513	1			2.513	1	3.153	3.121
B-7H-2-W 30/32	62.76	4.382								0.004	1	0.013	1	0.009	1	2.449	1	2.760	1	2.605	1	3.245	3.163
B-7H-2-W 40/42	62.86	4.386								-0.025	1			-0.025	1	2.481	1			2.481	1	3.121	3.156

B-7H-2-W 50/52	62.96	4.391									-0.439 *1*		-0.439 *1*	2.564 *1*		2.564 *1*	3.204	3.130
B-7H-2-W 60/62	63.06	4.396									0.036 *1*		0.036 *1*	2.312 *1*		2.312 *1*	2.952	3.128
B-7H-2-W 70/72	63.16	4.401	1.695			1.695	-1.578			-1.578								
B-7H-2-W 72/74	63.18	4.402	1.788			1.788	-1.297			-1.297	-0.199 *1*		-0.199 *1*	2.567 *1*		2.567 *1*	3.207	3.144
B-7H-2-W 80/82	63.26	4.404									0.249 *1*		0.249 *1*	2.718 *1*		2.718 *1*	3.358	3.137
B-7H-2-W 88/90	63.34	4.407									0.007 *1*		0.007 *1*	2.177 *1*		2.177 *1*	2.817	3.077
B-7H-2-W 100/102	63.46	4.412									-0.035 *1*		-0.035 *1*	2.524 *1*		2.524 *1*	3.164	3.070
B-7H-2-W 110/112	63.56	4.417									0.072 *1*		0.072 *1*	2.314 *1*		2.314 *1*	2.954	3.117
B-7H-2-W 118/120	63.64	4.420	2.404			2.404	-1.502			-1.502	0.163 *1*		0.163 *1*	2.690 *1*		2.690 *1*	3.330	3.230
B-7H-2-W 130/132	63.76	4.424									-0.153 *1*		-0.153 *1*	2.708 *1*		2.708 *1*	3.348	3.291
B-7H-2-W 140/142	63.86	4.427									-0.054 *1*		-0.054 *1*	2.693 *1*		2.693 *1*	3.333	3.297
B-7H-2-W 148/150	63.94	4.430									-0.068 *1*		-0.068 *1*	2.607 *1*		2.607 *1*	3.247	3.231
B-7H-3-W 10/12	64.06	4.434									-0.135 *1*		-0.135 *1*	2.494 *1*		2.494 *1*	3.134	3.153
B-7H-3-W 20/22	64.16	4.437	1.672			1.672	-1.404			-1.404								
B-7H-3-W 22/24	64.18	4.438	2.015			2.015	-1.678			-1.678	-0.471 *1*		-0.471 *1*	2.407 *1*		2.407 *1*	3.047	3.101
B-7H-3-W 30/32	64.26	4.441									-0.385 *1*		-0.385 *1*	2.419 *1*		2.419 *1*	3.059	3.115
B-7H-3-W 40/42	64.36	4.444									-0.272 *1*		-0.272 *1*	2.514 *1*		2.514 *1*	3.154	3.187
B-7H-3-W 50/52	64.46	4.447									-0.386 *1*		-0.386 *1*	2.706 *1*		2.706 *1*	3.346	3.281
B-7H-3-W 60/62	64.56	4.451									-0.444 *1*		-0.444 *1*	2.727 *1*		2.727 *1*	3.367	3.350
B-7H-3-W 70/72	64.66	4.454	1.682			1.682	-1.264			-1.264								
B-7H-3-W 72/74	64.68	4.455	1.674			1.674	-1.564			-1.564	-0.093 *1*	-0.166 *1*	-0.129 *1*	2.815 *1*	2.674 *1*	2.745 *1*	3.385	3.356
B-7H-3-W 80/82	64.76	4.457									-0.114 *1*		-0.114 *1*	2.776 *1*		2.776 *1*	3.416	3.307
B-7H-3-W 87/89	64.83	4.455									0.096 *1*		0.096 *1*	2.463 *1*		2.463 *1*	3.103	3.214
B-7H-3-W 99/101	64.95	4.458									-0.253 *1*		-0.253 *1*	2.538 *1*		2.538 *1*	3.178	3.156
B-7H-3-W 110/112	65.06	4.461									0.147 *1*		0.147 *1*	2.386 *1*		2.386 *1*	3.026	3.138
B-7H-3-W 122/124	65.18	4.464	1.763			1.763	-1.192			-1.192	0.073 *1*		0.073 *1*	2.604 *1*		2.604 *1*	3.244	3.147
B-7H-3-W 130/132	65.26	4.466									-0.173 *1*		-0.173 *1*	2.568 *1*		2.568 *1*	3.208	3.147
B-7H-3-W 140/142	65.36	4.469									-0.160 *1*		-0.160 *1*	2.293 *1*		2.293 *1*	2.933	3.145
B-7H-3-W 148/150	65.44	4.471									-0.440 *1*	-0.247 *1*	-0.343 *1*	2.709 *1*	2.687 *1*	2.698 *1*	3.338	3.194
B-7H-4-W 10/12	65.56	4.474									-0.209 *1*		-0.209 *1*	2.517 *1*		2.517 *1*	3.157	3.270

B-7H-4-W 22/24	65.68	4.478									-0.364 *1*		-0.364 *1*	2.753 *1*		2.753 *1*	3.393	3.336
B-7H-4-W 30/32	65.76	4.480									-0.075 *1*		-0.075 *1*	2.900 *1*		2.900 *1*	3.540	3.369
B-7H-4-W 40/42	65.86	4.483									-0.102 *1*		-0.102 *1*	2.443 *1*		2.443 *1*	3.083	3.338
B-7H-4-W 50/52	65.96	4.485									-0.347 *1*		-0.347 *1*	2.979 *1*		2.979 *1*	3.619	3.286
B-7H-4-W 60/62	66.06	4.488									-0.140 *1*		-0.140 *1*	2.366 *1*		2.366 *1*	3.006	3.193
B-7H-4-W 72/74	66.18	4.491	2.274			2.274	-1.026			-1.026	-0.107 *1*		-0.107 *1*	2.412 *1*		2.412 *1*	3.052	3.164
B-7H-4-W 80/82	66.26	4.494									-0.203 *1*		-0.203 *1*	2.617 *1*		2.617 *1*	3.257	3.182
B-7H-4-W 87/89	66.33	4.497									-0.253 *1*		-0.253 *1*	2.592 *1*		2.592 *1*	3.232	3.222
B-7H-4-W 100/102	66.46	4.501									0.009 *1*		0.009 *1*	2.652 *1*		2.652 *1*	3.292	3.216
B-7H-4-W 109/111	66.55	4.504									-0.144 *1*		-0.144 *1*	2.471 *1*		2.471 *1*	3.111	3.159
B-7H-4-W 122/124	66.68	4.508	1.772	1.907		1.840	-1.187	-1.420		-1.303	-0.187 *1*		-0.187 *1*	2.485 *1*		2.485 *1*	3.125	3.115
B-7H-4-W 129/131	66.75	4.515									-0.363 *1*		-0.363 *1*	2.378 *1*		2.378 *1*	3.018	3.134
B-7H-4-W 140/142	66.86	4.520									-0.324 *1*		-0.324 *1*	2.500 *1*		2.500 *1*	3.140	3.205
B-7H-4-W 147/149	66.93	4.523									-0.631 *1*		-0.631 *1*	2.910 *1*		2.910 *1*	3.550	3.249
B-7H-5-W 10/12	67.06	4.531									-0.287 *1*		-0.287 *1*	2.491 *1*		2.491 *1*	3.131	3.174
B-7H-5-W 22/24	67.18	4.540	2.063			2.063	-1.264			-1.264	-0.157 *1*		-0.157 *1*	2.369 *1*		2.369 *1*	3.009	3.077
B-7H-5-W 30/32	67.26	4.545									-0.179 *1*		-0.179 *1*	2.221 *1*		2.221 *1*	2.861	3.023
B-7H-5-W 40/42	67.36	4.552									-0.089 *1*		-0.089 *1*	2.571 *1*		2.571 *1*	3.211	3.093
B-7H-5-W 50/52	67.46	4.564									-0.352 *1*		-0.352 *1*	2.410 *1*		2.410 *1*	3.050	3.151
B-7H-5-W 60/62	67.56	4.573									-0.300 *1*		-0.300 *1*	2.785 *1*		2.785 *1*	3.425	3.180
B-7H-5-W 72/74	67.68	4.583	1.967			1.967	-1.212			-1.212	-0.157 *1*		-0.157 *1*	2.357 *1*		2.357 *1*	2.997	3.136
B-7H-5-W 80/82	67.76	4.589									-0.147 *1*		-0.147 *1*	2.425 *1*		2.425 *1*	3.065	3.106
B-7H-5-W 88/90	67.84	4.596									-0.348 *1*		-0.348 *1*	2.539 *1*		2.539 *1*	3.179	3.092
B-7H-5-W 100/102	67.96	4.606									-0.086 *1*		-0.086 *1*	2.368 *1*		2.368 *1*	3.008	3.112
B-7H-5-W 110/112	68.06	4.615									-0.203 *1*		-0.203 *1*	2.510 *1*		2.510 *1*	3.150	3.178
B-7H-5-W 122/124	68.18	4.625									-0.195 *1*		-0.195 *1*	2.619 *1*		2.619 *1*	3.259	3.253
B-7H-5-W 130/132	68.26	4.631									-0.312 *1*		-0.312 *1*	2.833 *1*		2.833 *1*	3.473	3.300
B-7H-5-W 140/142	68.36	4.637									-0.041 *1*		-0.041 *1*	2.568 *1*		2.568 *1*	3.208	3.289
B-7H-5-W 149/151	68.45	4.643									-0.181 *1*		-0.181 *1*	2.545 *1*		2.545 *1*	3.185	3.260
B-7H-6-W 10/12	68.56	4.650									0.231 *1*		0.231 *1*	2.758 *1*		2.758 *1*	3.398	3.221

B-7H-6-W 22/24	68.68	4.658	1.951			1.951	-1.328			-1.328	-0.208	1			-0.208	1	2.458	1			2.458	1	3.098	3.192
B-7H-6-W 30/32	68.76	4.664									-0.242	1			-0.242	1	2.374	1			2.374	1	3.014	3.155
B-7H-6-W 40/42	68.86	4.670									-0.421	1	-0.343	1	-0.382	1	2.843	1	2.767	1	2.805	1	3.445	3.141
B-7H-6-W 50/52	68.96	4.677	1.716			1.716	-1.004			-1.004	-0.432	1			-0.432	1	2.202	1			2.202	1	2.842	3.102
A-8H-1-W 130/132	69.08	4.691	1.955			1.955	-1.065			-1.065	-0.365	1			-0.365	1	2.519	1			2.519	1	3.159	3.113
A-8H-1-W 140/142	69.18	4.700									-0.367	1			-0.367	1	2.484	1			2.484	1	3.124	3.160
A-8H-1-W 147/149	69.25	4.705									-0.224	1			-0.224	1	2.588	1			2.588	1	3.228	3.223
A-8H-2-W 10/12	69.38	4.716									-0.126	1			-0.126	1	2.801	1			2.801	1	3.441	3.254
A-8H-2-W 20/22	69.48	4.725									-0.078	1			-0.078	1	2.354	1			2.354	1	2.994	3.282
A-8H-2-W 30/32	69.58	4.733	1.967			1.967	-1.204			-1.204	-0.283	1			-0.283	1	2.792	1			2.792	1	3.432	3.332
A-8H-2-W 40/42	69.68	4.741									-0.161	1	-0.199	1	-0.180	1	2.860	1	3.012	1	2.936	1	3.576	3.330
A-8H-2-W 50/52	69.78	4.750									-0.021	1			-0.021	1	2.464	1			2.464	1	3.104	3.257
A-8H-2-W 60/62	69.88	4.758									-0.516	1			-0.516	1	2.495	1			2.495	1	3.135	3.194
A-8H-2-W 68/70	69.96	4.765									-0.522	1			-0.522	1	2.493	1			2.493	1	3.133	3.201
A-8H-2-W 80/82	70.08	4.775	1.584			1.584	-1.261			-1.261	-0.709	1			-0.709	1	2.716	1			2.716	1	3.356	3.317
A-8H-2-W 91/93	70.19	4.784									-0.775	1			-0.775	1	2.677	1			2.677	1	3.317	3.429
A-8H-2-W 100/102	70.28	4.792									-0.543	1			-0.543	1	3.153	1			3.153	1	3.793	3.472
A-8H-2-W 109/111	70.37	4.799									-0.621	1			-0.621	1	2.776	1			2.776	1	3.416	3.367
A-8H-2-W 121/123	70.49	4.796									-0.296	1			-0.296	1	2.372	1			2.372	1	3.012	3.238
A-8H-2-W 130/132	70.58	4.801									-0.295	1			-0.295	1	2.446	1			2.446	1	3.086	3.177
A-8H-2-W 140/142	70.68	4.807									-0.330	1			-0.330	1	2.730	1			2.730	1	3.370	3.239
A-8H-2-W 147/149	70.75	4.811									-0.396	1			-0.396	1	2.538	1			2.538	1	3.178	3.297
A-8H-3-W 10/12	70.88	4.818									-0.111	1			-0.111	1	2.891	1			2.891	1	3.531	3.316
A-8H-3-W 19/21	70.97	4.823									-0.371	1			-0.371	1	2.549	1			2.549	1	3.189	3.253
A-8H-3-W 30/32	71.08	4.828									-0.198	1			-0.198	1	2.520	1			2.520	1	3.160	3.191
A-8H-3-W 39/41	71.17	4.832	1.864			1.864	-1.163			-1.163	-0.349	1			-0.349	1	2.470	1			2.470	1	3.110	3.132
A-8H-3-W 54/56	71.32	4.840									-0.540	1			-0.540	1	2.501	1			2.501	1	3.141	3.135
A-8H-3-W 60/62	71.38	4.843									-0.527	1			-0.527	1	2.425	1			2.425	1	3.065	3.179
A-8H-3-W 67/69	71.45	4.846									-0.197	1			-0.197	1	2.671	1			2.671	1	3.311	3.278
A-8H-3-W 80/82	71.58	4.853	1.804	1.893		1.848	-1.279	-1.252		-1.265	-0.860	1			-0.860	1	2.769	1			2.769	1	3.409	3.352

A-8H-3-W 89/91	71.67	4.857									-0.680 *1*		-0.680 *1*	2.856 *1*		2.856 *1*	3.496	3.363
A-8H-3-W 99/101	71.77	4.862									-0.225 *1*	-0.493 *1*	-0.359 *1*	2.501 *1*	2.640 *1*	2.570 *1*	3.210	3.278
A-8H-3-W 108/110	71.86	4.867									-0.259 *1*	-0.431 *1*	-0.345 *1*	2.509 *1*	2.653 *1*	2.581 *1*	3.221	3.187
A-8H-3-W 121/123	71.99	4.874									0.059 *1*		0.059 *1*	2.351 *1*		2.351 *1*	2.991	3.143
A-8H-3-W 130/132	72.08	4.881	2.197			2.197	-1.182			-1.182	0.216 *1*		0.216 *1*	2.530 *1*		2.530 *1*	3.170	3.182
A-8H-3-W 138/140	72.16	4.885									-0.349 *1*		-0.349 *1*	2.699 *1*		2.699 *1*	3.339	3.228
A-8H-3-W 144/146	72.22	4.889									-0.385 *1*		-0.385 *1*	2.620 *1*		2.620 *1*	3.260	3.298
A-8H-4-W 10/12	72.38	4.895									-0.764 *1*		-0.764 *1*	2.513 *1*		2.513 *1*	3.153	3.389
A-8H-4-W 20/22	72.48	4.897									-0.466 *1*		-0.466 *1*	3.155 *1*		3.155 *1*	3.795	3.511
A-8H-4-W 30/32	72.58	4.900	1.512			1.512	-1.081			-1.081	-0.556 *1*		-0.556 *1*	2.942 *1*		2.942 *1*	3.582	3.563
A-8H-4-W 40/42	72.68	4.903									-0.721 *1*		-0.721 *1*	2.843 *1*		2.843 *1*	3.483	3.533
A-8H-4-W 50/52	72.78	4.907									-0.575 *1*	-0.504 *1*	-0.540 *1*	3.000 *1*	2.831 *1*	2.915 *1*	3.555	3.409
A-8H-4-W 60/62	72.88	4.910									-0.599 *1*		-0.599 *1*	2.637 *1*		2.637 *1*	3.277	3.280
A-8H-4-W 67/69	72.95	4.912									-0.152 *1*		-0.152 *1*	2.241 *1*		2.241 *1*	2.881	3.170
A-8H-4-W 80/82	73.08	4.917	2.026			2.026	-1.136			-1.136								
A-8H-4-W 92/94	73.20	4.921									-0.346 *1*		-0.346 *1*	2.735 *1*		2.735 *1*	3.375	3.170
A-8H-4-W 100/102	73.28	4.924									-0.989 *1*		-0.989 *1*	2.383 *1*		2.383 *1*	3.023	3.179
A-8H-4-W 108/110	73.36	4.931									-0.487 *1*		-0.487 *1*	2.756 *1*		2.756 *1*	3.396	3.212
A-8H-4-W 119/121	73.47	4.934									-0.424 *1*		-0.424 *1*	2.392 *1*		2.392 *1*	3.032	3.203
A-8H-4-W 130/132	73.58	4.938									-0.444 *1*	-0.416 *1*	-0.430 *1*	2.785 *1*	2.528 *1*	2.657 *1*	3.297	3.252
A-8H-4-W 139/141	73.67	4.941	1.890			1.890	-1.217			-1.217	-0.507 *1*		-0.507 *1*	2.646 *1*		2.646 *1*	3.286	3.256
A-8H-4-W 148/150	73.76	4.944									-0.438 *1*		-0.438 *1*	2.755 *1*		2.755 *1*	3.395	3.253
A-8H-5-W 10/12	73.88	4.948									-0.311 *1*		-0.311 *1*	2.317 *1*		2.317 *1*	2.957	3.225
A-8H-5-W 20/22	73.98	4.951									-0.083 *1*	-0.232 *1*	-0.158 *1*	2.749 *1*	2.676 *1*	2.712 *1*	3.352	3.215
A-8H-5-W 30/32	74.08	4.955	1.779	1.756		1.767	-1.058	-1.036		-1.047	-0.094 *1*		-0.094 *1*	2.722 *1*		2.722 *1*	3.362	3.164
A-8H-5-W 40/42	74.18	4.958									-0.124 *1*		-0.124 *1*	2.200 *1*		2.200 *1*	2.840	3.095
A-8H-5-W 48/50	74.26	4.961									-0.093 *1*		-0.093 *1*	2.389 *1*		2.389 *1*	3.029	3.067
A-8H-5-W 57/59	74.35	4.964									-0.233 *1*		-0.233 *1*	2.584 *1*		2.584 *1*	3.224	3.100
A-8H-5-W 68/70	74.46	4.967									-0.136 *1*		-0.136 *1*	2.420 *1*		2.420 *1*	3.060	3.121
A-8H-5-W 80/82	74.58	4.971									0.048 *1*		0.048 *1*	2.561 *1*		2.561 *1*	3.201	3.098

A-8H-5-W 90/92	74.68	4.975														-0.344	*1*			2.352	*1*			2.352	*1*	2.992	3.062
A-8H-5-W 100/102	74.78	4.983														-0.336	*1*			2.322	*1*			2.322	*1*	2.962	3.089
A-8H-5-W 114/116	74.92	4.989														0.042	*2*			2.566	*2*			2.566	*2*	3.206	3.154
A-8H-5-W 121/123	74.99	4.992													-0.179	-0.260	*1*			2.573	*1*	2.850	*1*	2.711	*1*	3.351	3.200
A-8H-5-W 130/132	75.08	4.995	2.031				-1.227									-0.065	*1*			2.488	*1*			2.488	*1*	3.128	3.197
A-8H-5-W 140/142	75.18	5.001														-0.013	*1*			2.443	*1*			2.443	*1*	3.083	3.173
A-8H-5-W 148/150	75.26	5.004														-0.132	*1*			2.685	*1*			2.685	*1*	3.325	3.183
A-8H-6-W 10/12	75.38	5.010														-0.290	*1*			2.409	*1*			2.409	*1*	3.049	3.220
A-8H-6-W 20/22	75.48	5.014														-0.510	*2*			2.675	*2*			2.675	*2*	3.315	3.293
A-8H-6-W 30/32	75.58	5.019														-0.287	*1*			2.821	*1*			2.821	*1*	3.461	3.328
A-8H-6-W 40/42	75.68	5.023														-0.102	*1*			2.719	*1*			2.719	*1*	3.359	3.300
A-8H-6-W 50/52	75.78	5.028														-0.015	*1*			2.480	*1*			2.480	*1*	3.120	3.214
A-8H-6-W 60/62	75.88	5.034														-0.041	*1*			2.497	*1*			2.497	*1*	3.137	3.163
A-8H-6-W 68/70	75.96	5.040														-0.025	*1*			2.483	*1*			2.483	*1*	3.123	3.145
B-8H-4-W 50/52	76.18	5.055														0.181	*1*			2.606	*1*			2.606	*1*	3.246	3.142
B-8H-4-W 60/62	76.28	5.067														-0.007	*1*			2.386	*1*			2.386	*1*	3.026	3.113
B-8H-4-W 72/74	76.40	5.077	1.683				-1.307									-0.284	*1*			2.471	*1*			2.471	*1*	3.111	3.105
B-8H-4-W 80/82	76.48	5.084														-0.082	*1*			2.443	*1*			2.443	*1*	3.083	3.147
B-8H-4-W 87/89	76.55	5.090														-0.200	*1*			2.544	*1*			2.544	*1*	3.184	3.244
B-8H-4-W 99/101	76.67	5.100														-0.447	*2*			2.842	*2*			2.842	*2*	3.482	3.346
B-8H-4-W 110/112	76.78	5.109														-0.136	*1*			2.756	*1*			2.756	*1*	3.396	3.356
B-8H-4-W 122/124	76.90	5.117	1.902				-1.086									0.130	*1*			2.778	*1*			2.778	*1*	3.418	3.266
B-8H-4-W 130/132	76.98	5.122														-0.180	*1*			2.311	*1*			2.311	*1*	2.951	3.117
B-8H-4-W 140/142	77.08	5.129														-0.049	*1*			2.331	*1*			2.331	*1*	2.971	3.050
B-8H-4-W 148/150	77.16	5.134														0.027	*1*			2.393	*1*			2.393	*1*	3.033	3.066
B-8H-5-W 10/12	77.28	5.142														-0.188	*1*			2.577	*1*			2.577	*1*	3.217	3.123
B-8H-5-W 22/24	77.40	5.146	2.122				-1.435									0.039	*1*			2.523	*1*			2.523	*1*	3.163	3.118
B-8H-5-W 30/32	77.48	5.150														-0.015	*1*			2.442	*1*			2.442	*1*	3.082	3.071
B-8H-5-W 40/42	77.58	5.156														-0.174	*1*			2.266	*1*			2.266	*1*	2.906	3.035
B-8H-5-W 49/51	77.67	5.161														-0.427	*1*			2.422	*1*			2.422	*1*	3.062	3.067

B-8H-5-W 60/62	77.78	5.167									-0.455	*1*			-0.455	*1*	2.527	*1*			2.527	*1*	3.167	3.142
B-8H-5-W 72/74	77.90	5.173	1.756			1.756	-1.367			-1.367	-0.234	*1*			-0.234	*1*	2.572	*1*			2.572	*1*	3.212	3.212
B-8H-5-W 80/82	77.98	5.178									-0.283	*1*			-0.283	*1*	2.682	*1*			2.682	*1*	3.322	3.209
B-8H-5-W 88/90	78.06	5.182									-0.105	*1*	-0.724	*1*	-0.415	*1*	2.600	*1*	2.536	*1*	2.568	*1*	3.208	3.142
B-8H-5-W 100/102	78.18	5.189									-0.211	*1*			-0.211	*1*	2.225	*1*			2.225	*1*	2.865	3.064
B-8H-5-W 110/112	78.28	5.195									-0.316	*1*			-0.316	*1*	2.438	*1*			2.438	*1*	3.078	3.037
B-8H-5-W 122/124	78.40	5.201	1.891	1.944	2.059	1.965	-1.257	-1.490	-1.116	-1.287	-0.196	*1*			-0.196	*1*	2.456	*1*			2.456	*1*	3.096	3.050
B-8H-5-W 130/132	78.48	5.204									-0.100	*1*			-0.100	*1*	2.356	*1*			2.356	*1*	2.996	3.091
B-8H-5-W 140/142	78.58	5.209									-0.151	*1*			-0.151	*1*	2.505	*1*			2.505	*1*	3.145	3.137
B-8H-5-W 148/150	78.66	5.213									-0.070	*1*			-0.070	*1*	2.641	*1*			2.641	*1*	3.281	3.169
B-8H-6-W 10/12	78.78	5.219									-0.173	*1*			-0.173	*1*	2.499	*1*			2.499	*1*	3.139	3.164
B-8H-6-W 22/24	78.90	5.223	1.610			1.610	-1.282			-1.282	-0.227	*1*			-0.227	*1*	2.458	*1*			2.458	*1*	3.098	3.121
B-8H-6-W 30/32	78.98	5.225									-0.045	*1*			-0.045	*1*	2.506	*1*			2.506	*1*	3.146	3.066
B-8H-6-W 40/42	79.08	5.228									-0.280	*1*			-0.280	*1*	2.300	*1*			2.300	*1*	2.940	3.035
B-8H-6-W 50/52	79.18	5.231									-0.115	*1*			-0.115	*1*	2.304	*1*			2.304	*1*	2.944	3.027
B-8H-6-W 60/62	79.28	5.235									-0.159	*1*			-0.159	*1*	2.606	*1*			2.606	*1*	3.246	3.055
B-8H-6-W 72/74	79.40	5.239	1.559			1.559	-1.009			-1.009	-0.178	*1*			-0.178	*1*	2.235	*1*			2.235	*1*	2.875	3.087
B-8H-6-W 80/82	79.48	5.241									-0.114	*1*			-0.114	*1*	2.571	*1*			2.571	*1*	3.211	3.125
B-8H-6-W 88/90	79.56	5.244									-0.097	*1*			-0.097	*1*	2.632	*1*			2.632	*1*	3.272	3.131
B-8H-6-W 100/102	79.68	5.243									0.024	*1*			0.024	*1*	2.320	*1*			2.320	*1*	2.960	3.109
B-8H-6-W 110/112	79.78	5.246									-0.081	*1*			-0.081	*1*	2.490	*1*			2.490	*1*	3.130	3.104
B-8H-6-W 122/124	79.90	5.249	1.228			1.228	-0.742			-0.742	-0.130	*1*			-0.130	*1*	2.432	*1*			2.432	*1*	3.072	3.114
B-8H-6-W 130/132	79.98	5.251									-0.027	*1*			-0.027	*1*	2.622	*1*			2.622	*1*	3.262	3.126
A-9H-1-W 140/142	80.05	5.253									-0.101	*1*			-0.101	*1*	2.386	*1*			2.386	*1*	3.026	3.081
A-9H-1-W 148/150	80.13	5.255									-0.502	*1*			-0.502	*1*	2.390	*1*			2.390	*1*	3.030	3.036
A-9H-2-W 10/12	80.25	5.258									-0.392	*1*			-0.392	*1*	2.327	*1*			2.327	*1*	2.967	3.060
A-9H-2-W 20/22	80.35	5.260									-0.440	*1*			-0.440	*1*	2.370	*1*			2.370	*1*	3.010	3.145
A-9H-2-W 30/32	80.45	5.263									-0.066	*1*			-0.066	*1*	2.953	*1*			2.953	*1*	3.593	3.229
A-9H-2-W 40/42	80.55	5.265									-0.238	*1*			-0.238	*1*	2.439	*1*			2.439	*1*	3.079	3.218
A-9H-2-W 50/52	80.65	5.268									0.070	*1*			0.070	*1*	2.495	*1*			2.495	*1*	3.135	3.156

A-9H-2-W 60/62	80.75	5.270									-0.131 *1*		-0.131 *1*	2.572 *1*		2.572 *1*	3.212	3.093
A-9H-2-W 70/72	80.85	5.273									-0.005 *1*		-0.005 *1*	2.196 *1*		2.196 *1*	2.836	3.065
A-9H-2-W 80/82	80.95	5.275	2.088			2.088	-1.093			-1.093								
A-9H-2-W 90/92	81.05	5.278									-0.080 *1*		-0.080 *1*	2.570 *1*		2.570 *1*	3.210	3.089
A-9H-2-W 100/102	81.15	5.279									-0.030 *1*		-0.030 *1*	2.437 *1*		2.437 *1*	3.077	3.159
A-9H-2-W 109/111	81.24	5.281									-0.515 *1*		-0.515 *1*	2.540 *1*		2.540 *1*	3.180	3.279
A-9H-2-W 121/123	81.36	5.282									-0.481 *1*		-0.481 *1*	2.950 *1*		2.950 *1*	3.590	3.371
A-9H-2-W 130/132	81.45	5.283	1.811			1.811	-1.119			-1.119	-0.263 *1*		-0.263 *1*	2.787 *1*		2.787 *1*	3.427	3.389
A-9H-2-W 140/142	81.55	5.285									-0.191 *1*		-0.191 *1*	2.608 *1*		2.608 *1*	3.248	3.358
A-9H-2-W 148/150	81.63	5.286									-0.369 *1*		-0.369 *1*	2.686 *1*		2.686 *1*	3.326	3.325
A-9H-3-W 10/12	81.75	5.286									-0.147 *1*		-0.147 *1*	2.765 *1*		2.765 *1*	3.405	3.339
A-9H-3-W 20/22	81.85	5.287									-0.277 *1*		-0.277 *1*	2.569 *1*		2.569 *1*	3.209	3.333
A-9H-3-W 30/32	81.95	5.288	1.773			1.773	-0.971			-0.971	0.366 *1*		0.366 *1*	2.907 *1*		2.907 *1*	3.547	3.286
A-9H-3-W 40/42	82.05	5.290									0.090 *1*		0.090 *1*	2.450 *1*		2.450 *1*	3.090	3.156
A-9H-3-W 54/56	82.19	5.291									-0.194 *1*		-0.194 *1*	2.298 *1*		2.298 *1*	2.938	3.052
A-9H-3-W 61/63	82.26	5.292									0.008 *1*		0.008 *1*	2.281 *1*		2.281 *1*	2.921	3.001
A-9H-3-W 70/72	82.35	5.293									-0.255 *1*		-0.255 *1*	2.510 *1*		2.510 *1*	3.150	3.011
A-9H-3-W 80/82	82.45	5.296	1.893			1.893	-1.294			-1.294	-0.044 *1*		-0.044 *1*	2.334 *1*		2.334 *1*	2.974	3.019
A-9H-3-W 90/92	82.55	5.297									-0.181 *1*		-0.181 *1*	2.274 *1*		2.274 *1*	2.914	3.023
A-9H-3-W 100/102	82.65	5.299									-0.004 *1*		-0.004 *1*	2.569 *1*		2.569 *1*	3.209	3.046
A-9H-3-W 109/111	82.74	5.301									-0.058 *1*		-0.058 *1*	2.297 *1*		2.297 *1*	2.937	3.073
A-9H-3-W 120/122	82.85	5.303									0.033 *1*		0.033 *1*	2.495 *1*		2.495 *1*	3.135	3.127
A-9H-3-W 130/132	82.95	5.304									0.141 *1*		0.141 *1*	2.582 *1*		2.582 *1*	3.222	3.169
A-9H-3-W 137/139	83.02	5.305									0.107 *1*		0.107 *1*	2.600 *1*		2.600 *1*	3.240	3.182
A-9H-3-W 143/145	83.08	5.309									0.102 *1*		0.102 *1*	2.495 *1*		2.495 *1*	3.135	3.150
A-9H-4-W 10/12	83.25	5.312									0.257 *1*		0.257 *1*	2.416 *1*		2.416 *1*	3.056	3.179
A-9H-4-W 20/22	83.35	5.314	1.981			1.981	-0.955			-0.955	0.365 *1*		0.365 *1*	2.498 *1*		2.498 *1*	3.138	3.266
A-9H-4-W 30/32	83.45	5.316									0.733 *1*		0.733 *1*	3.087 *1*		3.087 *1*	3.727	3.362
A-9H-4-W 40/42	83.55	5.318	1.945			1.945	-1.068			-1.068	0.244 *1*		0.244 *1*	2.599 *1*		2.599 *1*	3.239	3.351
A-9H-4-W 50/52	83.65	5.320									0.305 *1*		0.305 *1*	2.616 *1*		2.616 *1*	3.256	3.300

A-9H-4-W 60/62	83.75	5.322																													
A-9H-4-W 70/72	83.85	5.324																													
A-9H-4-W 80/82	83.95	5.326	2.352																												
A-9H-4-W 90/92	84.05	5.328																													
A-9H-4-W 100/102	84.15	5.331																													
A-9H-4-W 109/111	84.24	5.335																													
A-9H-4-W 120/122	84.35	5.339																													
A-9H-4-W 130/132	84.45	5.342	2.034																												
A-9H-4-W 140/142	84.55	5.345																													
A-9H-4-W 148/150	84.63	5.348																													
A-9H-5-W 10/12	84.75	5.352																													
A-9H-5-W 20/22	84.85	5.361																													
A-9H-5-W 30/32	84.95	5.365	1.853																												
A-9H-5-W 40/42	85.05	5.369																													
A-9H-5-W 48/50	85.13	5.372																													
A-9H-5-W 58/60	85.23	5.376																													
A-9H-5-W 70/72	85.35	5.381																													
A-9H-5-W 80/82	85.45	5.384	2.055																												
A-9H-5-W 90/92	85.55	5.388																													
A-9H-5-W 100/102	85.65	5.391																													
A-9H-5-W 109/111	85.74	5.394																													
A-9H-5-W 120/122	85.85	5.398																													
A-9H-5-W 130/132	85.95	5.401	2.134																												
A-9H-5-W 140/142	86.05	5.404																													
A-9H-5-W 148/150	86.13	5.402																													
A-9H-6-W 10/12	86.25	5.405																													
A-9H-6-W 20/22	86.35	5.408																													
A-9H-6-W 30/32	86.45	5.411																													
A-9H-6-W 40/42	86.55	5.411																													
A-9H-6-W 50/52	86.65	5.414																													

-0.070	*1*																														
0.297	*1*																														
0.052	*1*																														
0.331	*1*																														
0.149	*1*																														
0.221	*1*																														
0.327	*1*																														
0.147	*1*																														
-0.075	*1*																														
0.088	*1*																														
0.068	*1*																														
0.149	*1*																														
0.277	*1*																														
0.123	*1*																														
0.149	*1*																														
-0.212	*1*																														
0.049	*1*																														
0.056	*1*																														
0.118	*1*																														
0.116	*1*																														
0.152	*1*																														
-0.021	*1*																														
0.073	*1*																														
0.108	*1*	0.045	*1*																												
0.341	*1*																														
0.217	*1*																														
0.341	*1*																														
0.048	*1*																														
0.056	*1*																														
0.008	*1*																														

2.638	*1*																														
2.571	*1*																														
2.626	*1*																														
2.693	*1*																														
2.516	*1*																														
2.573	*1*																														
2.480	*1*																														
2.841	*1*																														
2.475	*1*																														
2.310	*1*																														
2.442	*1*																														
2.688	*1*																														
2.517	*1*																														
2.357	*1*																														
2.595	*1*																														
2.512	*1*																														
2.600	*1*																														
2.491	*1*																														
2.652	*1*																														
2.514	*1*																														
2.723	*1*																														
2.487	*1*																														
2.449	*1*																														
2.524	*1*	2.565	*1*																												
2.565	*1*																														
2.253	*1*																														
2.709	*1*																														
2.440	*1*																														
2.481	*1*																														
2.582	*1*																														

3.278																															
3.211																															
3.266																															
3.333																															
3.156																															
3.213																															
3.120																															
3.481																															
3.115																															
2.950																															
3.082																															
3.328																															
3.157																															
2.997																															
3.235																															
3.152																															
3.240																															
3.131																															
3.292																															
3.154																															
3.363																															
3.127																															
3.089																															
3.185																															
3.205																															
3.120																															
3.143																															
3.148																															
3.159																															
3.150																															

A-9H-6-W 60/62	86.75	5.416									-0.011 *1*		-0.011 *1*	2.496 *1*		2.496 *1*	3.136	3.159
A-9H-6-W 70/72	86.85	5.418									0.205 *1*		0.205 *1*	2.441 *1*		2.441 *1*	3.081	3.168
B-9H-4-W 30/32	86.93	5.420									0.288 *1*		0.288 *1*	2.667 *1*		2.667 *1*	3.307	3.180
B-9H-4-W 40/42	87.03	5.422									0.118 *1*	0.249 *1*	0.183 *1*	2.551 *1*	2.470 *1*	2.511 *1*	3.151	3.193
B-9H-4-W 50/52	87.13	5.423									0.057 *1*	0.170 *1*	0.114 *1*	2.505 *1*	2.418 *1*	2.462 *1*	3.102	3.203
B-9H-4-W 60/62	87.23	5.425									0.228 *1*		0.228 *1*	2.750 *1*		2.750 *1*	3.390	3.207
B-9H-4-W 72/74	87.35	5.427	2.023			2.023	-1.177			-1.177	-0.061 *1*		-0.061 *1*	2.484 *1*		2.484 *1*	3.124	3.182
B-9H-4-W 80/82	87.43	5.429									0.136 *1*	0.115 *1*	0.125 *1*	2.527 *1*	2.386 *1*	2.457 *1*	3.097	3.156
B-9H-4-W 88/90	87.51	5.430									0.087 *1*	-0.120 *1*	-0.016 *1*	2.640 *1*	2.418 *1*	2.529 *1*	3.169	3.143
B-9H-4-W 100/102	87.63	5.433									-0.049 *1*		-0.049 *1*	2.522 *1*		2.522 *1*	3.162	3.171
B-9H-4-W 110/112	87.73	5.435									-0.145 *1*		-0.145 *1*	2.495 *1*		2.495 *1*	3.135	3.197
B-9H-4-W 122/124	87.85	5.437	1.738			1.738	-1.266			-1.266	-0.106 *1*		-0.106 *1*	2.725 *1*		2.725 *1*	3.365	3.208
B-9H-4-W 130/132	87.93	5.439									0.065 *1*	-0.200 *1*	-0.067 *1*	2.554 *1*	2.410 *1*	2.482 *1*	3.122	3.189
B-9H-4-W 140/142	88.03	5.441									-0.238 *1*		-0.238 *1*	2.466 *1*		2.466 *1*	3.106	3.164
B-9H-4-W 148/150	88.11	5.442									-0.002 *1*		-0.002 *1*	2.608 *1*		2.608 *1*	3.248	3.158
B-9H-5-W 10/12	88.23	5.445									0.013 *1*		0.013 *1*	2.422 *1*		2.422 *1*	3.062	3.140
B-9H-5-W 22/24	88.35	5.447	1.662			1.662	-0.840			-0.840	-0.109 *1*		-0.109 *1*	2.601 *1*		2.601 *1*	3.241	3.122
B-9H-5-W 30/32	88.43	5.449									-0.141 *1*		-0.141 *1*	2.304 *1*		2.304 *1*	2.944	3.102
B-9H-5-W 40/42	88.53	5.451									0.260 *1*		0.260 *1*	2.514 *1*		2.514 *1*	3.154	3.146
B-9H-5-W 50/52	88.63	5.453									0.149 *1*		0.149 *1*	2.583 *1*		2.583 *1*	3.223	3.238
B-9H-5-W 60/62	88.73	5.455									0.082 *1*		0.082 *1*	2.680 *1*		2.680 *1*	3.320	3.297
B-9H-5-W 72/74	88.85	5.457	1.919			1.919	-1.366			-1.366	0.350 *1*	0.351 *1*	0.351 *1*	2.983 *1*	2.914 *1*	2.949 *1*	3.589	3.275
B-9H-5-W 80/82	88.93	5.459									-0.127 *1*		-0.127 *1*	2.216 *1*		2.216 *1*	2.856	3.167
B-9H-5-W 88/90	89.01	5.461									0.001 *1*		0.001 *1*	2.509 *1*		2.509 *1*	3.149	3.120
B-9H-5-W 100/102	89.13	5.463									0.406 *1*		0.406 *1*	2.467 *1*		2.467 *1*	3.107	3.120
B-9H-5-W 110/112	89.23	5.465									0.278 *1*		0.278 *1*	2.562 *1*		2.562 *1*	3.202	3.172
B-9H-5-W 122/124	89.35	5.467	1.984			1.984	-1.167			-1.167	0.207 *1*	0.370 *1*	0.289 *1*	2.548 *1*	2.508 *1*	2.528 *1*	3.168	3.176
B-9H-5-W 130/132	89.43	5.469									0.383 *1*	0.288 *1*	0.336 *1*	2.615 *1*	2.622 *1*	2.618 *1*	3.258	3.175
B-9H-5-W 140/142	89.53	5.471									0.175 *1*	0.307 *1*	0.241 *1*	2.281 *1*	2.476 *1*	2.379 *1*	3.019	3.173
B-9H-5-W 148/150	89.61	5.473									0.168 *1*	0.169 *1*	0.169 *1*	2.609 *1*	2.607 *1*	2.608 *1*	3.248	3.199

B-9H-6-W 10/12	89.73	5.475									0.268 *1*		0.268 *1*	2.682 *1*		2.682 *1*	3.322	3.199
B-9H-6-W 22/24	89.85	5.477	1.752			1.752	-0.914			-0.914	0.056 *1*		0.056 *1*	2.472 *1*		2.472 *1*	3.112	3.182
B-9H-6-W 30/32	89.93	5.479									0.205 *1*	-0.013 *1*	0.096 *1*	2.252 *1*	2.580 *1*	2.416 *1*	3.056	3.157
A-10H-1-W 108/110	90.01	5.481									0.038 *1*	0.090 *1*	0.064 *1*	2.775 *1*	2.581 *1*	2.678 *1*	3.318	3.143
A-10H-1-W 122/124	90.15	5.483									-0.132 *1*		-0.132 *1*	2.415 *1*		2.415 *1*	3.055	3.111
A-10H-1-W 130/132	90.23	5.485	2.184			2.184	-1.167			-1.167	-0.072 *1*		-0.072 *1*	2.359 *1*		2.359 *1*	2.999	3.105
A-10H-1-W 140/142	90.33	5.487									-0.019 *1*		-0.019 *1*	2.492 *1*		2.492 *1*	3.132	3.110
A-10H-1-W 148/150	90.41	5.489									0.012 *1*		0.012 *1*	2.658 *1*		2.658 *1*	3.298	3.136
A-10H-2-W 10/12	90.53	5.491									-0.054 *1*		-0.054 *1*	2.274 *1*		2.274 *1*	2.914	3.125
A-10H-2-W 20/22	90.63	5.493									0.095 *1*		0.095 *1*	2.622 *1*		2.622 *1*	3.262	3.143
A-10H-2-W 30/32	90.73	5.494	2.104			2.104	-1.262			-1.262	0.124 *1*		0.124 *1*	2.463 *1*		2.463 *1*	3.103	3.173
A-10H-2-W 40/42	90.83	5.496									0.114 *1*		0.114 *1*	2.582 *1*		2.582 *1*	3.222	3.213
A-10H-2-W 50/52	90.93	5.497									-0.178 *1*		-0.178 *1*	2.701 *1*		2.701 *1*	3.341	3.202
A-10H-2-W 60/62	91.03	5.499									-0.046 *1*		-0.046 *1*	2.456 *1*		2.456 *1*	3.096	3.195
A-10H-2-W 70/72	91.13	5.501									-0.236 *1*		-0.236 *1*	2.396 *1*		2.396 *1*	3.036	3.246
A-10H-2-W 80/82	91.23	5.502									-0.315 *1*		-0.315 *1*	2.888 *1*		2.888 *1*	3.528	3.368
A-10H-2-W 90/92	91.33	5.504									-0.306 *1*		-0.306 *1*	2.909 *1*		2.909 *1*	3.549	3.485
A-10H-2-W 100/102	91.43	5.506									-0.361 *1*		-0.361 *1*	2.822 *1*		2.822 *1*	3.462	3.528
A-10H-2-W 108/110	91.51	5.507									-0.532 *1*		-0.532 *1*	3.029 *1*		3.029 *1*	3.669	3.494
A-10H-2-W 121/123	91.64	5.509									-0.194 *1*	-0.171 *1*	-0.182 *1*	2.794 *1*	2.661 *1*	2.728 *1*	3.368	3.387
A-10H-2-W 130/132	91.73	5.511	2.139			2.139	-0.899			-0.899	0.086 *1*		0.086 *1*	2.585 *1*		2.585 *1*	3.225	3.274
A-10H-2-W 140/142	91.83	5.512									0.016 *1*	-0.202 *1*	-0.093 *1*	2.411 *1*	2.508 *1*	2.459 *1*	3.099	3.185
A-10H-2-W 148/150	91.91	5.516									0.131 *1*		0.131 *1*	2.590 *1*		2.590 *1*	3.230	3.156
A-10H-3-W 10/12	92.03	5.519									0.075 *1*	0.013 *1*	0.044 *1*	2.399 *1*	2.499 *1*	2.449 *1*	3.089	3.149
A-10H-3-W 20/22	92.13	5.521									0.044 *1*		0.044 *1*	2.491 *1*		2.491 *1*	3.131	3.180
A-10H-3-W 30/32	92.23	5.523	1.973			1.973	-0.758			-0.758	0.061 *1*		0.061 *1*	2.608 *1*		2.608 *1*	3.248	3.220
A-10H-3-W 40/42	92.33	5.526									-0.060 *1*		-0.060 *1*	2.711 *1*		2.711 *1*	3.351	3.261
A-10H-3-W 50/52	92.43	5.528									-0.133 *1*		-0.133 *1*	2.519 *1*		2.519 *1*	3.159	3.258
A-10H-3-W 60/62	92.53	5.530									-0.051 *1*		-0.051 *1*	2.721 *1*		2.721 *1*	3.361	3.257
A-10H-3-W 70/72	92.63	5.532									-0.168 *1*	-0.159 *1*	-0.164 *1*	2.566 *1*	2.438 *1*	2.502 *1*	3.142	3.257

A-10H-3-W 80/82	92.73	5.535									-0.401	1			-0.401	1	2.678	1			2.678	1	3.318	3.294
A-10H-3-W 90/92	92.83	5.537									-0.214	1	-0.172	1	-0.193	1	2.688	1	2.734	1	2.711	1	3.351	3.345
A-10H-3-W 100/102	92.93	5.539									-0.272	1			-0.272	1	2.730	1			2.730	1	3.370	3.405
A-10H-3-W 109/111	93.02	5.541									-0.315	1			-0.315	1	2.897	1			2.897	1	3.537	3.441
A-10H-3-W 122/124	93.15	5.544									-0.151	1			-0.151	1	2.783	1			2.783	1	3.423	3.438
A-10H-3-W 130/132	93.23	5.546	1.623			1.623	-0.447			-0.447	-0.215	1			-0.215	1	2.779	1			2.779	1	3.419	3.402
A-10H-3-W 140/142	93.33	5.548									-0.210	1			-0.210	1	2.727	1			2.727	1	3.367	3.334
A-10H-4-W 10/12	93.53	5.553									0.080	1			0.080	1	2.606	1			2.606	1	3.246	3.253
A-10H-4-W 20/22	93.63	5.555									0.037	1			0.037	1	2.499	1			2.499	1	3.139	3.185
A-10H-4-W 30/32	93.73	5.557									-0.012	1			-0.012	1	2.474	1			2.474	1	3.114	3.150
A-10H-4-W 40/42	93.83	5.559	2.149			2.149	-1.062			-1.062	0.056	1	-0.045	1	0.006	1	2.467	1	2.611	1	2.539	1	3.179	3.158
A-10H-4-W 50/52	93.93	5.561									-0.041	1	0.005	1	-0.018	1	2.475	1	2.513	1	2.494	1	3.134	3.167
A-10H-4-W 60/62	94.03	5.565									-0.045	1			-0.045	1	2.621	1			2.621	1	3.261	3.162
A-10H-4-W 70/72	94.13	5.569									0.040	1			0.040	1	2.445	1			2.445	1	3.085	3.145
A-10H-4-W 80/82	94.23	5.573									0.007	1			0.007	1	2.417	1			2.417	1	3.057	3.146
A-10H-4-W 90/92	94.33	5.576									0.075	1			0.075	1	2.649	1			2.649	1	3.289	3.171
A-10H-4-W 100/102	94.43	5.579									0.005	1			0.005	1	2.494	1			2.494	1	3.134	3.180
A-10H-4-W 108/110	94.51	5.582									-0.077	1	-0.159	1	-0.118	1	2.591	1	2.562	1	2.577	1	3.217	3.184
A-10H-4-W 121/123	94.64	5.586									-0.143	1			-0.143	1	2.477	1			2.477	1	3.117	3.180
A-10H-4-W 130/132	94.73	5.589	2.334			2.334	-1.036			-1.036	0.032	1	-0.089	1	-0.029	1	2.585	1	2.621	1	2.603	1	3.243	3.201
A-10H-4-W 139/141	94.82	5.592									0.000	1			0.000	1	2.567	1			2.567	1	3.207	3.213
A-10H-4-W 147/149	94.90	5.595									-0.082	1			-0.082	1	2.587	1			2.587	1	3.227	3.223
A-10H-5-W 10/12	95.03	5.599									-0.025	1			-0.025	1	2.590	1			2.590	1	3.230	3.220
A-10H-5-W 20/22	95.13	5.603									-0.062	1	0.015	1	-0.023	1	2.573	1	2.574	1	2.573	1	3.213	3.213
A-10H-5-W 30/32	95.23	5.611	2.251			2.251	-0.876			-0.876	-0.101	1	-0.106	1	-0.104	1	2.536	1	2.591	1	2.563	1	3.203	3.207
A-10H-5-W 40/42	95.33	5.616									0.008	1			0.008	1	2.544	1			2.544	1	3.184	3.216
A-10H-5-W 48/50	95.41	5.619									0.171	1			0.171	1	2.597	1			2.597	1	3.237	3.217
A-10H-5-W 58/60	95.51	5.623									0.112	1			0.112	1	2.664	1			2.664	1	3.304	3.240
A-10H-5-W 70/72	95.63	5.628									0.042	1			0.042	1	2.399	1			2.399	1	3.039	3.236
A-10H-5-W 80/82	95.73	5.632	2.173			2.173	-0.733			-0.733	0.318	1			0.318	1	2.917	1			2.917	1	3.557	3.231

A-10H-5-W 90/92	95.83	5.636									0.120	*1*			0.120	*1*	2.347	*1*			2.347	*1*	2.987	3.169
A-10H-5-W 100/102	95.93	5.641									0.031	*1*			0.031	*1*	2.452	*1*			2.452	*1*	3.092	3.146
A-10H-5-W 108/110	96.01	5.644									-0.055	*1*			-0.055	*1*	2.534	*1*			2.534	*1*	3.174	3.162
A-10H-5-W 117/119	96.10	5.649									0.029	*1*			0.029	*1*	2.577	*1*			2.577	*1*	3.217	3.217
A-10H-5-W 130/132	96.23	5.655	2.092			2.092	-1.493			-1.493	-0.052	*1*			-0.052	*1*	2.689	*1*			2.689	*1*	3.329	3.227
A-10H-5-W 139/141	96.32	5.659									0.003	*1*	0.003	*1*	0.003	*1*	2.610	*1*	2.470	*1*	2.540	*1*	3.180	3.195
A-10H-5-W 148/150	96.41	5.665									0.124	*1*	0.074	*1*	0.099	*1*	2.423	*1*	2.449	*1*	2.436	*1*	3.076	3.170
A-10H-6-W 10/12	96.53	5.671									0.098	*1*	0.152	*1*	0.125	*1*	2.492	*1*	2.610	*1*	2.551	*1*	3.191	3.170
A-10H-6-W 20/22	96.63	5.676									0.034	*1*			0.034	*1*	2.609	*1*			2.609	*1*	3.249	3.195
A-10H-6-W 30/32	96.73	5.683	2.150			2.150	-0.958			-0.958	0.054	*1*	0.041	*1*	0.047	*1*	2.583	*1*	2.396	*1*	2.489	*1*	3.129	3.205
A-10H-6-W 40/42	96.83	5.689									0.013	*1*			0.013	*1*	2.660	*1*			2.660	*1*	3.300	3.199
A-10H-6-W 50/52	96.93	5.694									-0.120	*1*			-0.120	*1*	2.506	*1*			2.506	*1*	3.146	3.191
B-10H-3-W 140/142	97.00	5.697									-0.067	*1*			-0.067	*1*	2.460	*1*			2.460	*1*	3.100	3.217
B-10H-3-W 148/150	97.08	5.701									-0.112	*1*			-0.112	*1*	2.722	*1*			2.722	*1*	3.362	3.280
B-10H-4-W 10/12	97.20	5.707									0.007	*1*			0.007	*1*	2.713	*1*			2.713	*1*	3.353	3.304
B-10H-4-W 22/24	97.32	5.713	2.075			2.075	-1.684			-1.684	0.466	*1*			0.466	*1*	2.747	*1*			2.747	*1*	3.387	3.254
B-10H-4-W 30/32	97.40	5.714									0.276	*1*			0.276	*1*	2.377	*1*			2.377	*1*	3.017	3.133
B-10H-4-W 40/42	97.50	5.719									0.373	*1*			0.373	*1*	2.386	*1*			2.386	*1*	3.026	3.055
B-10H-4-W 50/52	97.60	5.721									0.240	*1*			0.240	*1*	2.318	*1*			2.318	*1*	2.958	3.039
B-10H-4-W 60/62	97.70	5.724									0.109	*1*			0.109	*1*	2.500	*1*			2.500	*1*	3.140	3.080
B-10H-4-W 72/74	**97.82**	**5.728**	**2.258**	**2.103**	**2.004**	**2.075**	**-0.718**	**-0.600**	**-0.879**	**-0.884**	0.219	*1*			0.219	*1*	2.486	*1*			2.486	*1*	3.126	3.110
B-10H-4-W 80/82	97.90	5.731									0.043	*1*			0.043	*1*	2.475	*1*			2.475	*1*	3.115	3.134
B-10H-4-W 87/89	97.97	5.733									0.203	*1*			0.203	*1*	2.492	*1*			2.492	*1*	3.132	3.167
B-10H-4-W 99/101	98.09	5.737									0.030	*1*	0.003	*1*	0.016	*1*	2.589	*1*	2.570	*1*	2.580	*1*	3.220	3.257
B-10H-4-W 110/112	98.20	5.741									-0.266	*1*			-0.266	*1*	2.682	*1*			2.682	*1*	3.322	3.380
B-10H-4-W 122/124	98.32	5.745	1.711			1.711	-0.865			-0.865	-0.736	*1*			-0.736	*1*	3.025	*1*			3.025	*1*	3.665	3.493
B-10H-4-W 130/132	98.40	5.748									-1.486	*1*			-1.486	*1*	2.888	*1*			2.888	*1*	3.528	3.542
B-10H-4-W 140/142	98.50	5.751									-0.543	*1*			-0.543	*1*	2.869	*1*			2.869	*1*	3.509	3.519
B-10H-4-W 148/150	98.58	5.754									-0.468	*1*			-0.468	*1*	2.959	*1*			2.959	*1*	3.599	3.462
B-10H-5-W 10/12	98.70	5.758									-0.393	*1*			-0.393	*1*	2.558	*1*			2.558	*1*	3.198	3.386

B-10H-5-W 22/24	98.82	5.762									-0.502	1			-0.502	1	2.810	1			2.810	1	3.450	3.334
B-10H-5-W 30/32	98.90	5.764	2.146			2.146	-1.011			-1.011	-0.165	1			-0.165	1	2.608	1			2.608	1	3.248	3.280
B-10H-5-W 40/42	99.00	5.768									-0.108	1			-0.108	1	2.557	1			2.557	1	3.197	3.238
B-10H-5-W 50/52	99.10	5.776									-0.077	1			-0.077	1	2.621	1			2.621	1	3.261	3.195
B-10H-5-W 60/62	99.20	5.780									-0.018	1			-0.018	1	2.449	1			2.449	1	3.089	3.169
B-10H-5-W 72/74	99.32	5.783	1.851			1.851	-0.640			-0.640	-0.040	1			-0.040	1	2.522	1			2.522	1	3.162	3.170
B-10H-5-W 80/82	99.40	5.786									-0.099	1			-0.099	1	2.573	1			2.573	1	3.213	3.187
B-10H-5-W 87/89	99.47	5.788									-0.334	1	0.001	1	-0.167	1	2.450	1	2.671	1	2.560	1	3.200	3.216
B-10H-5-W 100/102	99.60	5.792									-0.194	1			-0.194	1	2.591	1			2.591	1	3.231	3.268
B-10H-5-W 110/112	99.70	5.790									-0.384	1			-0.384	1	2.652	1			2.652	1	3.292	3.372
B-10H-5-W 122/124	99.82	5.793	1.717			1.717	-1.068			-1.068	-1.291	1			-1.291	1	2.903	1			2.903	1	3.543	3.457
B-10H-5-W 130/132	99.90	5.795									-0.666	1			-0.666	1	3.095	1			3.095	1	3.735	3.426
A-11H-1-W 90/92	100.38	5.799									-0.177	1			-0.177	1	2.495	1			2.495	1	3.135	3.290
A-11H-1-W 100/102	100.48	5.800									-0.321	1			-0.321	1	2.298	1			2.298	1	2.938	3.161
A-11H-1-W 113/115	100.61	5.802									-0.383	1			-0.383	1	2.692	1			2.692	1	3.332	3.117
A-11H-1-W 121/123	100.69	5.803									-0.198	1	-0.466	1	-0.332	1	2.613	1	2.082	1	2.347	1	2.987	3.095
A-11H-1-W 130/132	100.78	5.804									-0.263	1			-0.263	1	2.464	1			2.464	1	3.104	3.094
A-11H-1-W 140/142	100.88	5.805									-0.191	1			-0.191	1	2.400	1			2.400	1	3.040	3.087
A-11H-1-W 148/150	100.96	5.806									-0.230	1			-0.230	1	2.558	1			2.558	1	3.198	3.122
A-11H-2-W 10/12	101.08	5.808									-0.260	1			-0.260	1	2.406	1			2.406	1	3.046	3.149
A-11H-2-W 20/22	101.18	5.809									0.057	1			0.057	1	2.611	1			2.611	1	3.251	3.177
A-11H-2-W 30/32	101.28	5.811	2.083	1.837		1.960	-0.846	-0.845		-0.845	-0.172	1			-0.172	1	2.613	1			2.613	1	3.253	3.172
A-11H-2-W 40/42	101.38	5.812									-0.403	1	-0.212	1	-0.307	1	2.391	1	2.413	1	2.402	1	3.042	3.167
A-11H-2-W 50/52	101.48	5.813									-0.339	1			-0.339	1	2.511	1			2.511	1	3.151	3.201
A-11H-2-W 59/61	101.57	5.814									-0.338	1			-0.338	1	2.699	1			2.699	1	3.339	3.249
A-11H-2-W 70/72	101.68	5.816									-0.307	1			-0.307	1	2.725	1			2.725	1	3.365	3.243
A-11H-2-W 81/83	101.79	5.817	1.877			1.877	-1.588			-1.588	-0.368	1			-0.368	1	2.476	1			2.476	1	3.116	3.161
A-11H-2-W 90/92	101.88	5.819									-0.418	1			-0.418	1	2.361	1			2.361	1	3.001	3.080
A-11H-2-W 100/102	101.98	5.820									-0.376	1			-0.376	1	2.390	1			2.390	1	3.030	3.058
A-11H-2-W 113/115	102.11	5.822									-0.649	1			-0.649	1	2.448	1			2.448	1	3.088	3.097

A-11H-2-W 121/123	102.19	5.823									-0.561	*1*			-0.561	*1*	2.512	*1*			2.512	*1*	3.152	3.143
A-11H-2-W 130/132	102.28	5.824	1.770	1.855		1.812	-1.571	-1.221		-1.396	-1.069	*1*			-1.069	*1*	2.614	*1*			2.614	*1*	3.254	3.173
A-11H-2-W 140/142	102.38	5.825									-0.389	*1*			-0.389	*1*	2.454	*1*			2.454	*1*	3.094	3.139
A-11H-2-W 148/150	102.46	5.826									-0.461	*1*			-0.461	*1*	2.587	*1*			2.587	*1*	3.227	3.081
A-11H-3-W 10/12	102.58	5.829									-0.743	*1*			-0.743	*1*	2.165	*1*			2.165	*1*	2.805	3.038
A-11H-3-W 20/22	102.68	5.831									-0.485	*1*			-0.485	*1*	2.400	*1*			2.400	*1*	3.040	3.111
A-11H-3-W 30/32	102.78	5.833	1.742			1.742	-0.911			-0.911	-0.684	*1*			-0.684	*1*	2.670	*1*			2.670	*1*	3.310	3.219
A-11H-3-W 40/42	102.88	5.834									-0.570	*1*			-0.570	*1*	2.838	*1*			2.838	*1*	3.478	3.292
A-11H-3-W 52/54	103.00	5.839									-0.487	*1*			-0.487	*1*	2.500	*1*			2.500	*1*	3.140	3.253
A-11H-3-W 60/62	103.08	5.843									-0.376	*1*			-0.376	*1*	2.594	*1*			2.594	*1*	3.234	3.188
A-11H-3-W 70/72	103.18	5.846									-0.349	*1*			-0.349	*1*	2.455	*1*			2.455	*1*	3.095	3.117
A-11H-3-W 81/83	103.29	5.850	1.984			1.984	-1.476			-1.476	-0.229	*1*			-0.229	*1*	2.436	*1*			2.436	*1*	3.076	3.091
A-11H-3-W 90/92	103.38	5.853									-0.260	*1*			-0.260	*1*	2.351	*1*			2.351	*1*	2.991	3.115
A-11H-3-W 103/105	103.51	5.863									-0.104	*1*			-0.104	*1*	2.585	*1*			2.585	*1*	3.225	3.183
A-11H-3-W 113/115	103.61	5.867									-0.249	*1*			-0.249	*1*	2.746	*1*			2.746	*1*	3.386	3.227
A-11H-3-W 121/123	103.69	5.872									-0.043	*1*			-0.043	*1*	2.483	*1*			2.483	*1*	3.123	3.204
A-11H-3-W 130/132	103.78	5.877	2.045	1.840		1.943	-1.176	-0.760		-0.968	-0.262	*1*			-0.262	*1*	2.542	*1*			2.542	*1*	3.182	3.157
A-11H-3-W 140/142	103.88	5.885									-0.220	*1*	-0.196	*1*	-0.208	*1*	2.418	*1*	2.455	*1*	2.437	*1*	3.077	3.137
A-11H-4-W 0/2	103.98	5.892									-0.276	*1*			-0.276	*1*	2.473	*1*			2.473	*1*	3.113	3.176
A-11H-4-W 10/12	104.08	5.898									-0.469	*1*			-0.469	*1*	2.660	*1*			2.660	*1*	3.300	3.230
A-11H-4-W 20/22	104.18	5.911									-0.280	*1*			-0.280	*1*	2.685	*1*			2.685	*1*	3.325	3.253
B-11H-1-W 110/112	104.32	5.923									-0.116	*1*			-0.116	*1*	2.564	*1*			2.564	*1*	3.204	3.225
B-11H-1-W 122/124	104.44	5.933	2.091			2.091	-0.893			-0.893	-0.149	*1*			-0.149	*1*	2.519	*1*			2.519	*1*	3.159	3.196
B-11H-1-W 130/132	104.52	5.940									-0.062	*1*			-0.062	*1*	2.498	*1*			2.498	*1*	3.138	3.206
B-11H-1-W 140/142	104.62	5.948									0.177	*1*			0.177	*1*	2.665	*1*			2.665	*1*	3.305	3.253
B-11H-1-W 148/150	104.70	5.955									-0.225	*1*			-0.225	*1*	2.675	*1*			2.675	*1*	3.315	3.296
B-11H-2-W 10/12	104.82	5.965									0.110	*1*			0.110	*1*	2.655	*1*			2.655	*1*	3.295	3.304
B-11H-2-W 22/24	104.94	5.975	2.036			2.036	-1.229			-1.229	0.021	*1*			0.021	*1*	2.730	*1*			2.730	*1*	3.370	3.273
B-11H-2-W 30/32	105.02	5.979									-0.159	*1*			-0.159	*1*	2.518	*1*			2.518	*1*	3.158	3.208
B-11H-2-W 40/42	105.12	5.986									-0.147	*1*			-0.147	*1*	2.484	*1*			2.484	*1*	3.124	3.175

B-11H-2-W 50/52	105.22	5.992											-0.420	1	-0.314	1	-0.367	1	2.560	1	2.369	1	2.465	1	3.105	3.199
B-11H-2-W 60/62	105.32	5.999											-0.467	1			-0.467	1	2.718	1			2.718	1	3.358	3.263
B-11H-2-W 72/74	105.44	6.007	1.654			1.654	-1.223			-1.223			-0.481	1			-0.481	1	2.721	1			2.721	1	3.361	3.285
B-11H-2-W 78/80	105.50	6.011	1.575			1.575	-1.042			-1.042			-0.354	1			-0.354	1	2.587	1			2.587	1	3.227	3.257
B-11H-2-W 87/89	105.59	6.007											-0.115	1			-0.115	1	2.537	1			2.537	1	3.177	3.196
B-11H-2-W 100/102	105.72	6.011											-0.220	1			-0.220	1	2.560	1			2.560	1	3.200	3.141
B-11H-2-W 110/112	105.82	6.014											-0.254	1			-0.254	1	2.368	1			2.368	1	3.008	3.092
B-11H-2-W 122/124	105.94	6.018	1.949	1.817		1.883	-0.774	-0.896		-0.835			-0.537	1			-0.537	1	2.445	1			2.445	1	3.085	3.087
B-11H-2-W 130/132	106.02	6.021											-0.352	1			-0.352	1	2.408	1			2.408	1	3.048	3.113
B-11H-2-W 140/142	106.12	6.024											-0.243	1			-0.243	1	2.617	1			2.617	1	3.257	3.153
B-11H-3-W 0/2	106.22	6.027											0.015	1			0.015	1	2.526	1			2.526	1	3.166	3.163
B-11H-3-W 11/13	106.33	6.031											-0.003	1	-0.174	1	-0.088	1	2.419	1	2.481	1	2.450	1	3.090	3.163
B-11H-3-W 22/24	106.44	6.035	1.864			1.864	-0.870			-0.870			-0.367	1			-0.367	1	2.581	1			2.581	1	3.221	3.178
B-11H-3-W 30/32	106.52	6.043											-0.326	1			-0.326	1	2.529	1			2.529	1	3.169	3.215
B-11H-3-W 40/42	106.62	6.047											-0.319	1	-0.514	1	-0.417	1	2.679	1	2.595	1	2.637	1	3.277	3.239
B-11H-3-W 50/52	106.72	6.053											-0.040	1			-0.040	1	2.692	1			2.692	1	3.332	3.224
B-11H-3-W 60/62	106.82	6.058											0.065	1			0.065	1	2.440	1			2.440	1	3.080	3.199
B-11H-3-W 72/74	106.94	6.064	2.027			2.027	-0.937			-0.937			-0.081	1			-0.081	1	2.487	1			2.487	1	3.127	3.193
B-11H-3-W 80/82	107.02	6.068											0.019	1			0.019	1	2.734	1			2.734	1	3.374	3.209
B-11H-3-W 88/90	107.10	6.072											0.063	1			0.063	1	2.476	1			2.476	1	3.116	3.197
B-11H-3-W 97/99	107.19	6.073											-0.001	1			-0.001	1	2.555	1			2.555	1	3.195	3.181
B-11H-3-W 110/112	107.32	6.077											-0.108	1			-0.108	1	2.484	1			2.484	1	3.124	3.177
B-11H-3-W 122/124	107.44	6.076	2.320			2.320	-1.041			-1.041			-0.182	1			-0.182	1	2.588	1			2.588	1	3.228	3.242
B-11H-3-W 130/132	107.52	6.077											-0.372	1			-0.372	1	2.611	1			2.611	1	3.251	3.321
B-11H-3-W 139/141	107.61	6.079											-0.606	1			-0.606	1	2.950	1			2.950	1	3.590	3.390
B-11H-3-W 148/150	107.70	6.080											-0.327	1			-0.327	1	2.700	1			2.700	1	3.340	3.406
B-11H-4-W 10/12	107.82	6.082											-0.036	1			-0.036	1	2.688	1			2.688	1	3.328	3.407
B-11H-4-W 22/24	107.94	6.084	1.845			1.845	-0.941			-0.941			-0.438	1	0.227	1	-0.105	1	2.847	1	2.931	1	2.889	1	3.529	3.395
B-11H-4-W 30/32	108.02	6.086											0.230	1			0.230	1	2.713	1			2.713	1	3.353	3.362
B-11H-4-W 40/42	108.12	6.087											0.032	1	0.276	1	0.154	1	2.530	1	2.694	1	2.612	1	3.252	3.303

B-11H-4-W 50/52	108.22	6.089									0.245	1			0.245	1	2.654	1			2.654	1	3.294	3.260
B-11H-4-W 60/62	108.32	6.093									0.281	1			0.281	1	2.507	1			2.507	1	3.147	3.234
B-11H-4-W 72/74	108.44	6.096	2.145			2.145	-0.788			-0.788	-0.123	1			-0.123	1	2.695	1			2.695	1	3.335	3.228
B-11H-4-W 80/82	108.52	6.097									0.011	1			0.011	1	2.494	1			2.494	1	3.134	3.198
B-11H-4-W 87/89	108.59	6.099									-0.205	1			-0.205	1	2.573	1			2.573	1	3.213	3.182
B-11H-4-W 100/102	108.72	6.102									-0.250	1	-0.173	1	-0.212	1	2.487	1	2.448	1	2.468	1	3.108	3.172
B-11H-4-W 110/112	108.82	6.106									-0.231	1			-0.231	1	2.566	1			2.566	1	3.206	3.206
B-11H-4-W 122/124	108.94	6.109	2.520			2.520	-1.553			-1.553	-0.371	1			-0.371	1	2.611	1			2.611	1	3.251	3.271
B-11H-4-W 130/132	109.02	6.111									-0.324	1			-0.324	1	2.685	1			2.685	1	3.325	3.333
B-11H-4-W 140/142	109.12	6.113									-0.418	1			-0.418	1	2.884	1			2.884	1	3.524	3.366
B-11H-4-W 148/150	109.20	6.115									-0.714	1	-0.537	1	-0.625	1	2.466	1	2.721	1	2.594	1	3.234	3.326
B-11H-5-W 10/12	109.32	6.118									-0.609	1			-0.609	1	2.717	1			2.717	1	3.357	3.275
B-11H-5-W 22/24	109.44	6.121	1.901			1.901	-0.800			-0.800	-0.062	1			-0.062	1	2.459	1			2.459	1	3.099	3.225
B-11H-5-W 30/32	109.52	6.123									0.126	1			0.126	1	2.620	1			2.620	1	3.260	3.227
B-11H-5-W 40/42	109.62	6.126									0.216	1			0.216	1	2.604	1			2.604	1	3.244	3.223
B-11H-5-W 50/52	109.72	6.128									0.085	1			0.085	1	2.611	1			2.611	1	3.251	3.220
B-11H-5-W 60/62	109.82	6.129									0.125	1			0.125	1	2.490	1			2.490	1	3.130	3.213
B-11H-5-W 72/74	109.94	6.132									0.000	1			0.000	1	2.586	1			2.586	1	3.226	3.214
B-11H-5-W 80/82	110.02	6.134	2.359			2.359	-0.788			-0.788	0.178	1			0.178	1	2.703	1			2.703	1	3.343	3.215
B-11H-5-W 88/90	110.10	6.136									-0.236	1			-0.236	1	2.394	1			2.394	1	3.034	3.212
B-11H-5-W 100/102	110.22	6.138									0.042	1			0.042	1	2.629	1			2.629	1	3.269	3.238
B-11H-5-W 110/112	110.32	6.141									-0.020	1	0.078	1	0.029	1	2.637	1	2.792	1	2.714	1	3.354	3.257
B-11H-5-W 122/124	110.44	6.142	2.463			2.463	-0.880			-0.880	0.018	1			0.018	1	2.595	1			2.595	1	3.235	3.249
B-11H-5-W 130/132	110.52	6.143									-0.080	1			-0.080	1	2.539	1			2.539	1	3.179	3.213
B-11H-5-W 140/142	110.62	6.145									0.001	1	-0.120	1	-0.060	1	2.519	1	2.579	1	2.549	1	3.189	3.195
B-11H-5-W 148/150	110.70	6.146									0.010	1			0.010	1	2.544	1			2.544	1	3.184	3.216
B-11H-6-W 10/12	110.82	6.148									0.181	1	0.071	1	0.126	1	2.577	1	2.615	1	2.596	1	3.236	3.249
B-11H-6-W 22/24	110.94	6.150	2.182			2.182	-0.616			-0.616	0.034	1			0.034	1	2.730	1			2.730	1	3.370	3.285
B-11H-6-W 30/32	111.02	6.151									0.077	1			0.077	1	2.576	1			2.576	1	3.216	3.264
B-11H-6-W 40/42	111.12	6.153									0.127	1			0.127	1	2.742	1			2.742	1	3.382	3.201

B-11H-6-W 50/52	111.22	6.155								0.126	*1*	0.067	*1*	0.096	*1*	2.269	*1*	2.300	*1*	2.285	*1*	2.925	3.140
B-11H-6-W 60/62	111.32	6.156								-0.033	*1*			-0.033	*1*	2.396	*1*			2.396	*1*	3.036	3.171
B-11H-6-W 72/74	111.44	6.158								0.024	*1*			0.024	*1*	2.822	*1*			2.822	*1*	3.462	3.257
B-11H-6-W 81/83	111.53	6.160								0.035	*1*			0.035	*1*	2.665	*1*			2.665	*1*	3.305	3.283
B-11H-6-W 88/90	111.60	6.161								0.002	*1*			0.002	*1*	2.664	*1*			2.664	*1*	3.304	3.230
B-11H-6-W 100/102	111.72	6.163								-0.261	*1*			-0.261	*1*	2.351	*1*			2.351	*1*	2.991	3.145
B-11H-6-W 110/112	111.82	6.165								-0.061	*1*			-0.061	*1*	2.497	*1*			2.497	*1*	3.137	3.113
B-11H-6-W 122/124	111.94	6.167	2.168				-0.937			-0.169	*1*			-0.169	*1*	2.503	*1*			2.503	*1*	3.143	3.089
B-11H-7-W 0/2	112.02	6.168				2.168	-0.937			-0.142	*1*	-0.202	*1*	-0.172	*1*	2.273	*1*	2.565	*1*	2.419	*1*	3.059	3.076
B-11H-7-W 10/12	112.12	6.170								-0.004	*1*			-0.004	*1*	2.319	*1*			2.319	*1*	2.959	3.078
A-12H-2-W 40/42	112.35	6.173								-0.399	*1*			-0.399	*1*	2.545	*1*			2.545	*1*	3.185	3.111
A-12H-2-W 50/52	112.45	6.175								-0.265	*1*			-0.265	*1*	2.569	*1*			2.569	*1*	3.209	3.151
A-12H-2-W 58/60	112.53	6.177								-0.113	*1*			-0.113	*1*	2.406	*1*			2.406	*1*	3.046	3.179
A-12H-2-W 72/74	112.67	6.179	2.075				-0.819			-0.068	*1*			-0.068	*1*	2.671	*1*			2.671	*1*	3.311	3.192
A-12H-2-W 80/82	112.75	6.180				2.075	-0.819			-0.011	*1*			-0.011	*1*	2.602	*1*			2.602	*1*	3.242	3.168
A-12H-2-W 90/92	112.85	6.182								-0.042	*1*			-0.042	*1*	2.360	*1*			2.360	*1*	3.000	3.128
A-12H-2-W 102/104	112.97	6.184								-0.036	*1*			-0.036	*1*	2.461	*1*			2.461	*1*	3.101	3.113
A-12H-2-W 113/115	113.08	6.186								-0.199	*1*			-0.199	*1*	2.526	*1*			2.526	*1*	3.166	3.123
A-12H-2-W 122/124	113.17	6.189	1.925	2.310	1.847	2.027	-0.737	-0.928	-0.549	-0.097	*1*			-0.097	*1*	2.521	*1*			2.521	*1*	3.161	3.147
A-12H-2-W 132/134	113.27	6.191								-0.003	*1*			-0.003	*1*	2.426	*1*			2.426	*1*	3.066	3.152
A-12H-2-W 140/142	113.35	6.193								-0.163	*1*			-0.163	*1*	2.653	*1*			2.653	*1*	3.293	3.190
A-12H-2-W 148/150	113.43	6.194								-0.259	*1*			-0.259	*1*	2.438	*1*			2.438	*1*	3.078	3.236
A-12H-3-W 10/12	113.55	6.196								-0.023	*1*			-0.023	*1*	2.785	*1*			2.785	*1*	3.425	3.316
A-12H-3-W 20/22	113.65	6.197								-0.458	*1*			-0.458	*1*	2.714	*1*			2.714	*1*	3.354	3.360
A-12H-3-W 30/32	113.75	6.199								-0.354	*1*			-0.354	*1*	2.801	*1*			2.801	*1*	3.441	3.358
A-12H-3-W 40/42	113.85	6.201								-0.401	*1*			-0.401	*1*	2.679	*1*			2.679	*1*	3.319	3.338
A-12H-3-W 52/54	113.97	6.203								-0.006	*1*			-0.006	*1*	2.472	*1*			2.472	*1*	3.112	3.340
A-12H-3-W 60/62	114.05	6.204								0.128	*1*			0.128	*1*	3.034	*1*			3.034	*1*	3.674	3.369
A-12H-3-W 70/72	114.15	6.203								-0.014	*1*			-0.014	*1*	2.625	*1*			2.625	*1*	3.265	3.353
A-12H-3-W 80/82	114.25	6.205								0.129	*1*			0.129	*1*	2.606	*1*			2.606	*1*	3.246	3.327

A-12H-3-W 90/92	114.35	6.206								-0.024	*1*	0.120	*1*	0.048	*1*	2.670	*1*	2.823	*1*	2.747	*1*	3.387	3.334
A-12H-3-W 100/102	114.45	6.207								0.252	*1*	0.134	*1*	0.193	*1*	2.617	*1*	2.628	*1*	2.623	*1*	3.263	3.378
B-12H-1-W 40/42	114.59	6.209								0.447	*1*			0.447	*1*	2.960	*1*			2.960	*1*	3.600	3.415
B-12H-1-W 50/52	114.69	6.211								0.146	*1*			0.146	*1*	2.722	*1*			2.722	*1*	3.362	3.371
B-12H-1-W 60/62	114.79	6.212								0.198	*1*			0.198	*1*	2.668	*1*			2.668	*1*	3.308	3.304
B-12H-1-W 72/74	114.91	6.214	2.529				-0.769			0.061	*1*			0.061	*1*	2.487	*1*			2.487	*1*	3.127	3.235
B-12H-1-W 80/82	114.99	6.215								0.085	*1*			0.085	*1*	2.630	*1*			2.630	*1*	3.270	3.230
B-12H-1-W 88/90	115.07	6.217								-0.038	*1*			-0.038	*1*	2.580	*1*			2.580	*1*	3.220	3.260
B-12H-1-W 100/102	115.19	6.219								-0.113	*1*			-0.113	*1*	2.647	*1*			2.647	*1*	3.287	3.282
B-12H-1-W 110/112	115.29	6.221								-0.069	*1*			-0.069	*1*	2.805	*1*			2.805	*1*	3.445	3.252
B-12H-1-W 122/124	**115.41**	**6.225**	**2.077**	**1.808**	**1.838**	**1.941**	**-1.138**	**-0.904**	**-0.876**	-0.075	*1*			-0.075	*1*	2.403	*1*			2.403	*1*	3.043	3.156
B-12H-1-W 130/132	115.49	6.227								-0.354	*1*	0.122	*1*	-0.116	*1*	2.418	*1*	2.408	*1*	2.413	*1*	3.053	3.083
B-12H-1-W 140/142	115.59	6.231								-0.455	*1*	-0.766	*1*	-0.610	*1*	2.467	*1*	2.186	*1*	2.327	*1*	2.967	3.095
B-12H-1-W 148/150	115.67	6.234								-0.598	*1*			-0.598	*1*	2.551	*1*			2.551	*1*	3.191	3.187
B-12H-2-W 10/12	115.79	6.238								-0.469	*1*			-0.469	*1*	2.810	*1*			2.810	*1*	3.450	3.282
B-12H-2-W 22/24	115.91	6.242	2.060			2.060	-0.896		-0.896	-0.210	*1*			-0.210	*1*	2.568	*1*			2.568	*1*	3.208	3.300
B-12H-2-W 30/32	115.99	6.245								-0.170	*1*			-0.170	*1*	2.786	*1*			2.786	*1*	3.426	3.247
B-12H-2-W 40/42	116.09	6.253								-0.370	*1*			-0.370	*1*	2.433	*1*			2.433	*1*	3.073	3.121
B-12H-2-W 50/52	116.19	6.257								-0.131	*1*			-0.131	*1*	2.307	*1*			2.307	*1*	2.947	3.055
B-12H-2-W 60/62	116.29	6.262								-0.063	*1*			-0.063	*1*	2.246	*1*			2.246	*1*	2.886	3.080
B-12H-2-W 72/74	116.41	6.267	2.064			2.064	-1.323		-1.323	-0.213	*1*			-0.213	*1*	2.761	*1*			2.761	*1*	3.401	3.208
B-12H-2-W 80/82	116.49	6.271	1.811			1.811	-1.018		-1.018	0.009	*1*			0.009	*1*	2.654	*1*			2.654	*1*	3.294	3.285
B-12H-2-W 88/90	116.57	6.274								-0.187	*1*			-0.187	*1*	2.734	*1*			2.734	*1*	3.374	3.313
B-12H-2-W 99/101	116.68	6.279								-0.492	*1*			-0.492	*1*	2.532	*1*			2.532	*1*	3.172	3.284
B-12H-2-W 109/111	116.78	6.284								-0.010	*1*	-0.107	*1*	-0.058	*1*	2.740	*1*	2.762	*1*	2.751	*1*	3.391	3.262
B-12H-2-W 122/124	116.91	6.289	2.355	2.088		2.222	-0.989	-1.101	-1.045	-0.118	*1*			-0.118	*1*	2.547	*1*			2.547	*1*	3.187	3.222
B-12H-2-W 129/131	116.98	6.293	2.052			2.052	-1.232		-1.232	-0.148	*1*	-0.121	*1*	-0.135	*1*	2.411	*1*	2.532	*1*	2.472	*1*	3.112	3.196
B-12H-2-W 139/141	117.08	6.297								-0.301	*1*			-0.301	*1*	2.617	*1*			2.617	*1*	3.257	3.191
B-12H-2-W 148/150	117.17	6.301								-0.223	*1*			-0.223	*1*	2.527	*1*			2.527	*1*	3.167	3.201
B-12H-3-W 10/12	117.29	6.306								-0.185	*1*			-0.185	*1*	2.579	*1*			2.579	*1*	3.219	3.215

B-12H-3-W 22/24	117.41	6.310	1.466			1.466	-0.916			-0.916	-0.417	1	-0.299	1	-0.358	1	2.584	1	2.593	1	2.588	1	3.228	3.223
B-12H-3-W 30/32	117.49	6.314									-0.534	1			-0.534	1	2.607	1			2.607	1	3.247	3.252
B-12H-3-W 40/42	117.59	6.316									0.006	1			0.006	1	2.577	1			2.577	1	3.217	3.287
B-12H-3-W 50/52	117.69	6.319									0.234	1	-0.093	1	0.070	1	2.921	1	2.671	1	2.796	1	3.436	3.317
B-12H-3-W 60/62	117.79	6.323									-0.112	1			-0.112	1	2.688	1			2.688	1	3.328	3.302
B-12H-3-W 72/74	117.91	6.327									-0.070	1			-0.070	1	2.557	1			2.557	1	3.197	3.268
B-12H-3-W 80/82	117.99	6.329									-0.172	1			-0.172	1	2.590	1			2.590	1	3.230	3.244
B-12H-3-W 88/90	118.07	6.332									-0.221	1			-0.221	1	2.642	1			2.642	1	3.282	3.263
B-12H-3-W 100/102	118.19	6.336									0.052	1			0.052	1	2.586	1			2.586	1	3.226	3.294
B-12H-3-W 110/112	118.29	6.335									0.068	1			0.068	1	2.786	1			2.786	1	3.426	3.327
B-12H-3-W 122/124	118.41	6.338	1.993			1.993	-1.159			-1.159	0.148	1			0.148	1	2.664	1			2.664	1	3.304	3.298
B-12H-3-W 130/132	118.49	6.342									0.019	1			0.019	1	2.691	1			2.691	1	3.331	3.254
B-12H-3-W 140/142	118.59	6.345									0.050	1			0.050	1	2.339	1			2.339	1	2.979	3.191
B-12H-3-W 147/149	118.66	6.347									0.054	1	-0.084	1	-0.015	1	2.726	1	2.693	1	2.710	1	3.350	3.181
B-12H-4-W 10/12	118.79	6.358									-0.015	1			-0.015	1	2.443	1			2.443	1	3.083	3.166
B-12H-4-W 22/24	118.91	6.368									0.076	1			0.076	1	2.531	1			2.531	1	3.171	3.182
B-12H-4-W 30/32	118.99	6.373									0.256	1			0.256	1	2.555	1			2.555	1	3.195	3.186
B-12H-4-W 40/42	119.09	6.380									0.021	1			0.021	1	2.609	1			2.609	1	3.249	3.201
B-12H-4-W 50/52	119.19	6.387									-0.046	1			-0.046	1	2.508	1			2.508	1	3.148	3.209
B-12H-4-W 60/62	119.29	6.393									-0.149	1			-0.149	1	2.564	1			2.564	1	3.204	3.218
B-12H-4-W 72/74	119.41	6.401	1.777			1.777	-0.929			-0.929	-0.068	1			-0.068	1	2.700	1			2.700	1	3.340	3.223
B-12H-4-W 80/82	119.49	6.407									-0.202	1			-0.202	1	2.474	1			2.474	1	3.114	3.226
B-12H-4-W 88/90	119.57	6.412									-0.203	1			-0.203	1	2.564	1			2.564	1	3.204	3.249
B-12H-4-W 100/102	119.69	6.415									-0.209	1			-0.209	1	2.766	1			2.766	1	3.406	3.269
B-12H-4-W 110/112	119.79	6.420									-0.424	1	-0.371	1	-0.398	1	2.546	1	2.693	1	2.620	1	3.260	3.266
B-12H-4-W 122/124	119.91	6.427	2.021			2.021	-0.878			-0.878	-0.220	1			-0.220	1	2.501	1			2.501	1	3.141	3.244
B-12H-4-W 130/132	119.99	6.431									-0.206	1			-0.206	1	2.668	1			2.668	1	3.308	3.241
B-12H-4-W 140/142	120.09	6.437									0.075	1	-0.031	1	0.022	1	2.658	1	2.547	1	2.602	1	3.242	3.253
B-12H-4-W 149/151	120.18	6.442									0.000	1			0.000	1	2.593	1			2.593	1	3.233	3.267
B-12H-5-W 10/12	120.29	6.447									0.159	1	0.211	1	0.185	1	2.665	1	2.687	1	2.676	1	3.316	3.286

B-12H-5-W 22/24	120.41	6.450	2.191			2.191	-0.886	-0.886	-0.019	1		-0.019	1	2.647	1		2.647	1	3.287		3.307
B-12H-5-W 30/32	120.49	6.453							0.106	1		0.106	1	2.705	1		2.705	1	3.345		3.303
B-12H-5-W 40/42	120.59	6.456							-0.137	1		-0.137	1	2.694	1		2.694	1	3.334		3.266
B-12H-5-W 50/52	120.69	6.459							-0.281	1		-0.281	1	2.475	1		2.475	1	3.115		3.214
B-12H-5-W 60/62	120.79	6.463							-0.057	1		-0.057	1	2.549	1		2.549	1	3.189		3.197
B-12H-5-W 72/74	120.91	6.467	1.737			1.737	-0.821	-0.821	-0.182	1		-0.182	1	2.551	1		2.551	1	3.191		3.224
B-12H-5-W 80/82	120.99	6.469							-0.307	1		-0.307	1	2.656	1		2.656	1	3.296		3.268
B-12H-5-W 87/89	121.06	6.467							0.320	1		0.320	1	2.717	1		2.717	1	3.357		3.273
B-12H-5-W 100/102	121.19	6.471							0.130	1		0.130	1	2.583	1		2.583	1	3.223		3.279
B-12H-5-W 110/112	121.29	6.473							-0.105	1		-0.105	1	2.498	1		2.498	1	3.138		3.308
B-12H-5-W 122/124	121.41	6.477							0.092	1		0.092	1	2.949	1		2.949	1	3.589		3.364
B-12H-5-W 130/132	121.49	6.479							-0.130	1		-0.130	1	2.727	1		2.727	1	3.367		3.365
B-12H-5-W 140/142	121.59	6.480							0.080	1		0.080	1	2.635	1		2.635	1	3.275		3.328
B-12H-5-W 147/149	121.66	6.482							-0.084	1		-0.084	1	2.629	1		2.629	1	3.269		3.278
B-12H-6-W 10/12	121.79	6.486							-0.022	1		-0.022	1	2.648	1		2.648	1	3.288		3.253
B-12H-6-W 22/24	121.91	6.489	1.794			1.794	-0.905	-0.905	-0.165	1		-0.165	1	2.565	1		2.565	1	3.205		3.242
B-12H-6-W 30/32	121.99	6.491							0.073	1		0.073	1	2.551	1		2.551	1	3.191		3.246
B-12H-6-W 40/42	122.09	6.493							-0.053	1		-0.053	1	2.709	1		2.709	1	3.349		3.267
B-12H-6-W 50/52	122.19	6.496							-0.297	1		-0.297	1	2.604	1		2.604	1	3.244		3.297
B-12H-6-W 60/62	122.29	6.498							-0.308	1		-0.308	1	2.650	1		2.650	1	3.290		3.338
B-12H-6-W 72/74	122.41	6.501	2.244			2.244	-1.220	-1.220	-0.145	1		-0.145	1	2.833	1		2.833	1	3.473		3.360
B-12H-6-W 80/82	122.49	6.503							-0.122	1		-0.122	1	2.746	1		2.746	1	3.386		3.340
B-12H-6-W 88/90	122.57	6.505							-0.337	1		-0.337	1	2.561	1		2.561	1	3.201		3.301
A-13H-1-W 117/119	122.64	6.507							-0.112	1		-0.112	1	2.614	1		2.614	1	3.254		3.279
A-13H-1-W 129/131	122.76	6.510							0.003	1		0.003	1	2.731	1		2.731	1	3.371		3.285
A-13H-1-W 140/142	122.87	6.513							-0.136	1		-0.136	1	2.587	1		2.587	1	3.227		3.280
A-13H-1-W 147/149	122.94	6.514							-0.094	2		-0.094	2	2.653	2		2.653	2	3.293		3.255
A-13H-2-W 10/12	123.07	6.516							0.018	1		0.018	1	2.597	1		2.597	1	3.237		3.233
A-13H-2-W 22/24	123.19	6.519	2.251	2.012		2.132	-1.210	-1.028	0.038	1		0.038	1	2.474	1		2.474	1	3.114		3.218
A-13H-2-W 30/32	123.27	6.521							-0.274	2		-0.274	2	2.725	2		2.725	2	3.365		3.204

A-13H-2-W 38/40	123.35	6.523									0.161 *1*		0.161 *1*	2.460 *1*		2.460 *1*	3.100	3.185
A-13H-2-W 50/52	123.47	6.525									-0.104 *1*		-0.104 *1*	2.450 *1*		2.450 *1*	3.090	3.200
A-13H-2-W 60/62	123.57	6.528									0.044 *2*		0.044 *2*	2.699 *2*		2.699 *2*	3.339	3.251
A-13H-2-W 72/74	123.69	6.530	2.152			2.152	-1.063			-1.063	-0.123 *1*		-0.123 *1*	2.670 *1*		2.670 *1*	3.310	3.304
A-13H-2-W 78/80	123.75	6.532									-0.030 *1*	0.043 *1*	0.006 *1*	2.724 *1*	2.692 *1*	2.708 *1*	3.348	3.323
A-13H-2-W 90/92	123.87	6.534									0.152 *2*		0.152 *2*	2.678 *2*		2.678 *2*	3.318	3.294
A-13H-2-W 100/102	123.97	6.537									0.001 *2*		0.001 *2*	2.629 *2*		2.629 *2*	3.269	3.257
A-13H-2-W 109/111	124.06	6.539									-0.159 *1*	-0.121 *1*	-0.140 *1*	2.459 *1*	2.517 *1*	2.488 *1*	3.128	3.243
A-13H-2-W 122/124	124.19	6.540	2.128			2.128	-1.577			-1.577	-0.027 *1*	-0.068 *1*	-0.048 *1*	2.694 *1*	2.599 *1*	2.647 *1*	3.287	3.257
A-13H-2-W 130/132	124.27	6.541									-0.031 *2*		-0.031 *2*	2.750 *2*		2.750 *2*	3.390	3.275
A-13H-2-W 140/142	124.37	6.543									-0.214 *1*		-0.214 *1*	2.500 *1*		2.500 *1*	3.140	3.307
A-13H-2-W 148/150	124.45	6.545									-0.013 *2*		-0.013 *2*	2.680 *2*		2.680 *2*	3.320	3.369
A-13H-3-W 10/12	124.57	6.547									-0.085 *2*		-0.085 *2*	3.017 *2*		3.017 *2*	3.657	3.430
A-13H-3-W 20/22	124.67	6.549									0.066 *1*		0.066 *1*	2.733 *1*		2.733 *1*	3.373	3.410
A-13H-3-W 30/32	124.77	6.547									-0.213 *2*		-0.213 *2*	2.719 *2*		2.719 *2*	3.359	3.324
A-13H-3-W 38/40	124.85	6.548									-0.032 *1*		-0.032 *1*	2.526 *1*		2.526 *1*	3.166	3.261
A-13H-3-W 52/54	124.99	6.550									-0.010 *1*		-0.010 *1*	2.491 *1*		2.491 *1*	3.131	3.279
A-13H-3-W 60/62	125.07	6.551									-0.003 *2*		-0.003 *2*	2.899 *2*		2.899 *2*	3.539	3.350
A-13H-3-W 70/72	125.17	6.552									0.029 *1*		0.029 *1*	2.713 *1*		2.713 *1*	3.353	3.362
A-13H-3-W 78/80	125.25	6.553									-0.045 *2*		-0.045 *2*	2.770 *2*		2.770 *2*	3.410	3.319
A-13H-3-W 90/92	125.37	6.555									-0.045 *1*		-0.045 *1*	2.465 *1*		2.465 *1*	3.105	3.228
A-13H-3-W 100/102	125.47	6.556									-0.312 *2*		-0.312 *2*	2.581 *2*		2.581 *2*	3.221	3.179
B-13H-1-W 50/52	125.57	6.557									-0.410 *1*		-0.410 *1*	2.463 *1*		2.463 *1*	3.103	3.152
B-13H-1-W 60/62	125.67	6.559									-0.325 *1*		-0.325 *1*	2.519 *1*		2.519 *1*	3.159	3.166
B-13H-1-W 72/74	125.79	6.560	1.832			1.832	-1.030			-1.030	-0.520 *1*		-0.520 *1*	2.548 *1*		2.548 *1*	3.188	3.172
B-13H-1-W 80/82	125.87	6.561									-0.368 *2*		-0.368 *2*	2.587 *2*		2.587 *2*	3.227	3.227
B-13H-1-W 88/90	125.95	6.562									-0.449 *1*		-0.449 *1*	2.452 *1*		2.452 *1*	3.092	3.305
B-13H-1-W 99/101	126.06	6.564									-0.936 *2*		-0.936 *2*	3.065 *2*		3.065 *2*	3.705	3.401
B-13H-1-W 110/112	126.17	6.565									-0.454 *2*		-0.454 *2*	2.743 *2*		2.743 *2*	3.383	3.368
B-13H-1-W 122/124	126.29	6.567	1.741			1.741	-1.089			-1.089	0.025 *1*		0.025 *1*	2.685 *1*		2.685 *1*	3.325	3.257

B-13H-1-W 130/132	126.37	6.568										-0.148	*1*			-0.148	*1*	2.269	*1*			2.269	*1*	2.909	3.115
B-13H-1-W 139/141	126.46	6.569										-0.344	*2*			-0.344	*2*	2.462	*2*			2.462	*2*	3.102	3.093
B-13H-1-W 147/149	126.54	6.570										-0.155	*1*			-0.155	*1*	2.436	*1*			2.436	*1*	3.076	3.151
B-13H-2-W 10/12	126.67	6.572										-0.223	*2*			-0.223	*2*	2.661	*2*			2.661	*2*	3.301	3.250
B-13H-2-W 22/24	126.79	6.574										-0.094	*1*			-0.094	*1*	2.764	*1*			2.764	*1*	3.404	3.285
B-13H-2-W 30/32	126.87	6.575										-0.071	*2*			-0.071	*2*	2.637	*2*			2.637	*2*	3.277	3.262
B-13H-2-W 41/43	126.98	6.576										-0.095	*1*	0.137	*1*	0.021	*1*	2.553	*1*	2.329	*1*	2.441	*1*	3.081	3.179
B-13H-2-W 51/53	127.08	6.578										-0.138	*2*	-0.092	*2*	-0.115	*2*	2.553	*2*	2.695	*2*	2.624	*2*	3.264	3.127
B-13H-2-W 60/62	127.17	6.579										-0.113	*1*			-0.113	*1*	2.215	*1*			2.215	*1*	2.855	3.124
B-13H-2-W 72/74	127.29	6.580	1.594	-1.032						-1.032		-0.168	*1*			-0.168	*1*	2.620	*1*			2.620	*1*	3.260	3.230
B-13H-2-W 80/82	127.37	6.582										-0.163	*2*	-0.132	*2*	-0.147	*2*	2.854	*2*	2.699	*2*	2.777	*2*	3.417	3.327
B-13H-2-W 88/90	127.45	6.583										-0.075	*2*	-0.167	*2*	-0.121	*2*	2.716	*2*	3.071	*2*	2.893	*2*	3.533	3.368
B-13H-2-W 99/101	127.56	6.584										-0.227	*1*			-0.227	*1*	2.532	*1*			2.532	*1*	3.172	3.314
B-13H-2-W 109/111	127.66	6.585										-0.095	*2*	-0.253	*2*	-0.174	*2*	2.553	*2*	2.699	*2*	2.626	*2*	3.266	3.284
B-13H-2-W 122/124	127.79	6.587										-0.161	*1*			-0.161	*1*	2.643	*1*			2.643	*1*	3.283	3.286
B-13H-2-W 130/132	127.87	6.588	2.080	-1.352						-1.352		-0.101	*2*	-0.091	*2*	-0.096	*2*	2.851	*2*	2.588	*2*	2.720	*2*	3.360	3.297
B-13H-2-W 140/142	127.97	6.590										-0.239	*2*			-0.239	*2*	2.646	*2*			2.646	*2*	3.286	3.041
B-13H-2-W 147/149	128.04	6.590										-0.135	*2*			-0.135	*2*	2.535	*2*			2.535	*2*	3.175	2.705
B-13H-3-W 10/12	128.17	6.592										-0.184	*2*	-0.233	*2*	-0.209	*2*	2.571	*2*	-1.991	*2*	0.290	*2*	0.930	2.479
B-13H-3-W 22/24	128.29	6.595	1.807	-1.302						-1.302		-0.321	*1*			-0.321	*1*	2.635	*1*			2.635	*1*	3.275	2.734
B-13H-3-W 30/32	128.37	6.596										-0.341	*2*			-0.341	*2*	2.716	*2*			2.716	*2*	3.356	3.062
B-13H-3-W 40/42	128.47	6.598										-0.419	*2*			-0.419	*2*	2.613	*2*			2.613	*2*	3.253	3.295
B-13H-3-W 50/52	128.57	6.599										-0.255	*2*			-0.255	*2*	2.629	*2*			2.629	*2*	3.269	3.308
B-13H-3-W 58/60	128.65	6.601										-0.544	*2*			-0.544	*2*	2.731	*2*			2.731	*2*	3.371	3.311
B-13H-3-W 72/74	128.79	6.606										-0.173	*1*			-0.173	*1*	2.731	*1*			2.731	*1*	3.371	3.305
B-13H-3-W 80/82	128.87	6.608										-0.199	*1*			-0.199	*1*	2.489	*1*			2.489	*1*	3.129	3.311
B-13H-3-W 88/90	128.95	6.610										-0.169	*2*			-0.169	*2*	2.743	*2*			2.743	*2*	3.383	3.352
B-13H-3-W 100/102	129.07	6.612										-0.275	*2*			-0.275	*2*	2.911	*2*			2.911	*2*	3.551	3.378
B-13H-3-W 110/112	129.17	6.615										-0.265	*2*	-0.237	*2*	-0.251	*2*	2.642	*2*	2.653	*2*	2.647	*2*	3.287	3.337
B-13H-3-W 122/124	129.29	6.619	1.342	1.787		1.565	-0.574	-1.272		-0.923		-0.286	*1*	-0.360	*1*	-0.323	*1*	2.546	*1*	2.667	*1*	2.607	*1*	3.247	3.251

B-13H-3-W 130/132	129.37	6.622									-0.306 *1*		-0.306 *1*	2.534 *1*		2.534 *1*	3.174	3.182
B-13H-3-W 140/142	129.47	6.626									-0.295 *1*		-0.295 *1*	2.420 *1*		2.420 *1*	3.060	3.173
B-13H-3-W 148/150	129.55	6.628									-0.239 *1*		-0.239 *1*	2.595 *1*		2.595 *1*	3.235	3.193
B-13H-4-W 10/12	129.67	6.632									-0.199 *2*		-0.199 *2*	2.695 *2*		2.695 *2*	3.335	3.198
B-13H-4-W 22/24	129.79	6.636	1.452			1.452	-0.995			-0.995	-0.308 *1*		-0.308 *1*	2.412 *1*		2.412 *1*	3.052	3.184
B-13H-4-W 30/32	129.87	6.639									-0.459 *1*		-0.459 *1*	2.498 *1*		2.498 *1*	3.138	3.194
B-13H-4-W 40/42	129.97	6.642									-0.510 *2*		-0.510 *2*	2.690 *2*		2.690 *2*	3.330	3.260
B-13H-4-W 50/52	130.07	6.651									-0.508 *1*		-0.508 *1*	2.613 *1*		2.613 *1*	3.253	3.325
B-13H-4-W 60/62	130.17	6.654									-0.372 *2*		-0.372 *2*	2.899 *2*		2.899 *2*	3.539	3.345
B-13H-4-W 72/74	130.29	6.658	1.735			1.735	-1.110			-1.110	-0.383 *1*		-0.383 *1*	2.608 *1*		2.608 *1*	3.248	3.274
B-13H-4-W 80/82	130.37	6.660									-0.274 *1*	-0.379 *1*	-0.327 *1*	2.437 *1*	2.603 *1*	2.520 *1*	3.160	3.185
B-13H-4-W 88/90	130.45	6.663									-0.382 *1*		-0.382 *1*	2.387 *1*		2.387 *1*	3.027	3.116
B-13H-4-W 100/102	130.57	6.667									-0.207 *1*		-0.207 *1*	2.502 *1*		2.502 *1*	3.142	3.125
B-13H-4-W 110/112	130.67	6.666									-0.163 *1*	-0.108 *1*	-0.136 *1*	2.426 *1*	2.536 *1*	2.481 *1*	3.121	3.205
B-13H-4-W 122/124	130.79	6.669	1.521			1.521	-1.031			-1.031	-0.554 *1*		-0.554 *1*	2.632 *1*		2.632 *1*	3.272	3.316
B-13H-4-W 130/132	130.87	6.671									-0.376 *2*		-0.376 *2*	3.017 *2*		3.017 *2*	3.657	3.390
B-13H-4-W 140/142	130.97	6.673									-0.258 *1*	-0.176 *1*	-0.217 *1*	2.686 *1*	2.635 *1*	2.661 *1*	3.301	3.351
B-13H-4-W 148/150	131.05	6.675									-0.146 *1*	-0.146 *1*	-0.146 *1*	2.613 *1*	2.609 *1*	2.611 *1*	3.251	3.249
B-13H-5-W 10/12	131.17	6.678									-0.149 *1*		-0.149 *1*	2.481 *1*		2.481 *1*	3.121	3.203
B-13H-5-W 20/22	131.27	6.681									-0.236 *1*		-0.236 *1*	2.374 *1*		2.374 *1*	3.014	3.223
B-13H-5-W 30/32	131.37	6.680									-0.132 *2*		-0.132 *2*	3.071 *2*		3.071 *2*	3.711	3.268
B-13H-5-W 40/42	131.47	6.682									-0.203 *1*		-0.203 *1*	2.357 *1*		2.357 *1*	2.997	3.225
B-13H-5-W 50/52	131.57	6.683									-0.065 *1*		-0.065 *1*	2.529 *1*		2.529 *1*	3.169	3.190
B-13H-5-W 60/62	131.67	6.684									-0.178 *1*		-0.178 *1*	2.555 *1*		2.555 *1*	3.195	3.167
B-13H-5-W 70/72	131.77	6.686									-0.475 *1*		-0.475 *1*	2.541 *1*		2.541 *1*	3.181	3.182
B-13H-5-W 80/82	131.87	6.688									-0.335 *1*		-0.335 *1*	2.569 *1*		2.569 *1*	3.209	3.169
B-13H-5-W 88/90	131.95	6.689									-0.354 *1*		-0.354 *1*	2.471 *1*		2.471 *1*	3.111	3.139
B-13H-5-W 99/101	132.06	6.691									-0.351 *1*		-0.351 *1*	2.477 *1*		2.477 *1*	3.117	3.117
B-13H-5-W 110/112	132.17	6.693									-0.255 *1*		-0.255 *1*	2.441 *1*		2.441 *1*	3.081	3.143
B-13H-5-W 118/120	132.25	6.692									-0.236 *1*	-0.326 *1*	-0.281 *1*	2.590 *1*	2.379 *1*	2.485 *1*	3.125	3.208

B-13H-5-W 130/132	132.37	6.693									-0.241	2			-0.241	2	2.851	2			2.851	2	3.491	3.252
B-13H-5-W 140/142	132.47	6.695									-0.116	1			-0.116	1	2.573	1			2.573	1	3.213	3.236
C-14H-1-W 140/142	132.78	6.699									-0.198	1			-0.198	1	2.370	1			2.370	1	3.010	3.188
C-14H-1-W 148/150	132.86	6.700									-0.845	1			-0.845	1	2.712	1			2.712	1	3.352	3.154
C-14H-2-W 10/12	132.98	6.702	2.285			2.285	-1.642			-1.642	-0.122	1			-0.122	1	2.394	1			2.394	1	3.034	3.119
C-14H-2-W 18/20	133.06	6.703									-0.121	1			-0.121	1	2.415	1			2.415	1	3.055	3.097
C-14H-2-W 30/32	133.18	6.705	1.848			1.848	-0.835			-0.835	-0.034	1			-0.034	1	2.484	1			2.484	1	3.124	3.079
C-14H-2-W 40/42	133.28	6.707									-0.047	1			-0.047	1	2.424	1			2.424	1	3.064	3.075
C-14H-2-W 50/52	133.38	6.709									0.053	1			0.053	1	2.429	1			2.429	1	3.069	3.078
C-14H-2-W 60/62	133.48	6.710									0.030	1			0.030	1	2.393	1			2.393	1	3.033	3.085
C-14H-2-W 68/70	133.56	6.712									-0.154	1			-0.154	1	2.558	1			2.558	1	3.198	3.100
C-14H-2-W 80/82	133.68	6.714	1.983			1.983	-1.052			-1.052	-0.140	1			-0.140	1	2.412	1			2.412	1	3.052	3.112
C-14H-2-W 90/92	133.78	6.715									-0.142	1			-0.142	1	2.431	1			2.431	1	3.071	3.127
C-14H-2-W 100/102	133.88	6.720									-0.289	2			-0.289	2	2.646	2			2.646	2	3.286	3.150
C-14H-2-W 110/112	133.98	6.722									-0.254	1			-0.254	1	2.410	1			2.410	1	3.050	3.143
C-14H-2-W 118/120	134.06	6.723	1.642			1.642	-0.801			-0.801	-0.135	1			-0.135	1	2.570	1			2.570	1	3.210	3.120
C-14H-2-W 130/132	134.18	6.726									-0.404	1			-0.404	1	2.397	1			2.397	1	3.037	3.074
C-14H-2-W 140/142	134.28	6.729									-0.303	1			-0.303	1	2.367	1			2.367	1	3.007	3.065
C-14H-2-W 148/150	134.36	6.730									-0.390	1			-0.390	1	2.415	1			2.415	1	3.055	3.074
C-14H-3-W 10/12	134.48	6.733									-0.313	2	-0.322	2	-0.317	2	2.535	2	2.588	2	2.562	2	3.202	3.108
C-14H-3-W 18/20	134.56	6.735	1.866			1.866	-1.215			-1.215	-0.454	1			-0.454	1	2.390	1			2.390	1	3.030	3.137
C-14H-3-W 30/32	134.68	6.738									-0.259	1			-0.259	1	2.567	1			2.567	1	3.207	3.162
C-14H-3-W 40/42	134.78	6.741									-0.273	1			-0.273	1	2.627	1			2.627	1	3.267	3.161
C-14H-3-W 50/52	134.88	6.745									-0.108	1			-0.108	1	2.400	1			2.400	1	3.040	3.145
C-14H-3-W 60/62	134.98	6.749	2.005			2.005	-0.961			-0.961	-0.093	1			-0.093	1	2.477	1			2.477	1	3.117	3.118
C-14H-3-W 80/82	135.18	6.755									-0.083	2			-0.083	2	2.571	2			2.571	2	3.211	3.086
C-14H-3-W 90/92	135.28	6.759									-0.097	1			-0.097	1	2.296	1			2.296	1	2.936	3.044
C-14H-3-W 100/102	135.38	6.762									-0.033	1			-0.033	1	2.356	1			2.356	1	2.996	3.061
C-14H-3-W 110/112	135.48	6.765									0.034	1			0.034	1	2.414	1			2.414	1	3.054	3.128
C-14H-3-W 118/120	135.56	6.768	1.824			1.824	-1.189			-1.189	0.293	1			0.293	1	2.801	1			2.801	1	3.441	3.201

C-14H-3-W 130/132	135.68	6.772									0.175	1			0.175	1	2.506	1			2.506	1	3.146	3.197
C-14H-3-W 140/142	135.78	6.775									-0.298	1			-0.298	1	2.439	1			2.439	1	3.079	3.186
C-14H-3-W 148/150	135.86	6.778									-0.026	1			-0.026	1	2.579	1			2.579	1	3.219	3.209
C-14H-4-W 10/12	135.98	6.782									-0.060	1			-0.060	1	2.662	1			2.662	1	3.302	3.266
C-14H-4-W 20/22	136.08	6.785									-0.032	1			-0.032	1	2.689	1			2.689	1	3.329	3.291
C-14H-4-W 30/32	136.18	6.789									-0.063	1			-0.063	1	2.659	1			2.659	1	3.299	3.283
C-14H-4-W 40/42	136.28	6.792									-0.014	1			-0.014	1	2.557	1			2.557	1	3.197	3.264
C-14H-4-W 50/52	136.38	6.791									-0.003	1			-0.003	1	2.664	1			2.664	1	3.304	3.247
C-14H-4-W 60/62	136.48	6.793									-0.123	1	0.027	1	-0.048	1	2.555	1	2.653	1	2.604	1	3.244	3.216
C-14H-4-W 80/82	136.68	6.799									-0.167	1			-0.167	1	2.486	1			2.486	1	3.126	3.188
C-14H-4-W 90/92	136.78	6.799									-0.165	1			-0.165	1	2.509	1			2.509	1	3.149	3.186
C-14H-4-W 100/102	136.88	6.801									-0.026	1	-0.084	1	-0.055	1	2.624	1	2.562	1	2.593	1	3.233	3.218
B-14H-1-W 140/142	136.90	6.802									-0.122	1			-0.122	1	2.638	1			2.638	1	3.278	3.251
B-14H-1-W 142/144	136.92	6.802									-0.142	1			-0.142	1	2.639	1			2.639	1	3.279	3.252
B-14H-1-W 148/150	136.98	6.804	1.702			1.702	-1.195			-1.195	0.030	1			0.030	1	2.597	1			2.597	1	3.237	3.294
B-14H-2-W 10/12	137.10	6.806									-0.077	1			-0.077	1	2.520	1			2.520	1	3.160	3.361
B-14H-2-W 22/24	137.22	6.809									0.605	1			0.605	1	3.213	1			3.213	1	3.853	3.413
B-14H-2-W 30/32	137.30	6.811									-0.070	2			-0.070	2	2.613	2			2.613	2	3.253	3.344
B-14H-2-W 40/42	137.40	6.811									-0.154	1			-0.154	1	2.454	1			2.454	1	3.094	3.263
B-14H-2-W 50/52	137.50	6.813									0.062	1			0.062	1	2.594	1			2.594	1	3.234	3.244
B-14H-2-W 60/62	137.60	6.815									0.121	1	0.054	1	0.088	1	2.754	1	2.625	1	2.690	1	3.330	3.284
B-14H-2-W 72/74	137.72	6.818									0.061	1			0.061	1	2.778	1			2.778	1	3.418	3.296
B-14H-2-W 80/82	137.80	6.821	1.981			1.981	-1.054			-1.054	-0.074	1			-0.074	1	2.486	1			2.486	1	3.126	3.234
B-14H-2-W 88/90	137.88	6.822									-0.024	2			-0.024	2	2.629	2			2.629	2	3.269	3.173
B-14H-2-W 100/102	138.00	6.825									-0.200	1			-0.200	1	2.354	1			2.354	1	2.994	3.139
B-14H-2-W 109/111	138.09	6.827									-0.041	1			-0.041	1	2.496	1			2.496	1	3.136	3.169
B-14H-2-W 122/124	138.22	6.830									0.029	1	-0.056	1	-0.014	1	2.705	1	2.705	1	2.705	1	3.345	3.205
B-14H-2-W 129/131	138.29	6.831									0.121	1			0.121	1	2.533	1			2.533	1	3.173	3.203
B-14H-2-W 139/141	138.39	6.834									-0.171	1			-0.171	1	2.549	1			2.549	1	3.189	3.196
B-14H-2-W 148/150	138.48	6.836									-0.143	1			-0.143	1	2.430	1			2.430	1	3.070	3.195

B-14H-3-W 10/12	138.60	6.838									-0.028	1			-0.028	1	2.778	1			2.778	1	3.418	3.210
B-14H-3-W 22/24	138.72	6.843									-0.238	1			-0.238	1	2.488	1			2.488	1	3.128	3.168
B-14H-3-W 30/32	138.80	6.845	1.849			1.849	-1.240			-1.240	-0.215	1			-0.215	1	2.420	1			2.420	1	3.060	3.125
B-14H-3-W 40/42	138.90	6.847									-0.310	1			-0.310	1	2.431	1			2.431	1	3.071	3.100
B-14H-3-W 50/52	139.00	6.850									-0.320	1			-0.320	1	2.529	1			2.529	1	3.169	3.138
B-14H-3-W 60/62	139.10	6.852									-0.578	1			-0.578	1	2.464	1			2.464	1	3.104	3.191
B-14H-3-W 72/74	139.22	6.855	1.083			1.083	-1.215			-1.215	-0.548	1			-0.548	1	2.709	1			2.709	1	3.349	3.243
B-14H-3-W 80/82	139.30	6.857									-0.385	1			-0.385	1	2.643	1			2.643	1	3.283	3.253
B-14H-3-W 88/90	139.38	6.859									-0.418	1			-0.418	1	2.552	1			2.552	1	3.192	3.233
B-14H-3-W 100/102	139.50	6.862									-0.198	1			-0.198	1	2.583	1			2.583	1	3.223	3.199
B-14H-3-W 110/112	139.60	6.864	1.841			1.841	-1.147			-1.147	-0.085	1			-0.085	1	2.525	1			2.525	1	3.165	3.175
B-14H-3-W 122/124	139.72	6.866	1.891			1.891	-1.171			-1.171	-0.052	1			-0.052	1	2.495	1			2.495	1	3.135	3.161
B-14H-3-W 130/132	139.80	6.868									-0.219	1			-0.219	1	2.531	1			2.531	1	3.171	3.142
B-14H-3-W 140/142	139.90	6.869									-0.325	1	0.127	1	-0.099	1	2.471	1	2.562	1	2.516	1	3.156	3.127
B-14H-3-W 148/150	139.98	6.870									-0.088	1			-0.088	1	2.368	1			2.368	1	3.008	3.144
B-14H-4-W 11/13	140.11	6.872									0.084	1	0.062	1	0.073	1	2.482	1	2.632	1	2.557	1	3.197	3.183
B-14H-4-W 22/24	140.22	6.874									0.278	1			0.278	1	2.783	1			2.783	1	3.423	3.246
B-14H-4-W 30/32	140.30	6.875	2.237			2.237	-1.348			-1.348	-0.014	1			-0.014	1	2.374	1			2.374	1	3.014	3.250
B-14H-4-W 40/42	140.40	6.877									0.138	2			0.138	2	2.911	2			2.911	2	3.551	3.242
B-14H-4-W 50/52	140.50	6.879									0.189	1			0.189	1	2.345	1			2.345	1	2.985	3.178
B-14H-4-W 60/62	140.60	6.878									0.123	1			0.123	1	2.522	1			2.522	1	3.162	3.154
B-14H-4-W 72/74	140.72	6.879									0.038	1	0.037	1	0.038	1	2.415	1	2.612	1	2.513	1	3.153	3.130
B-14H-4-W 80/82	140.80	6.880	1.962			1.962	-1.240			-1.240	0.051	1			0.051	1	2.485	1			2.485	1	3.125	3.152
B-14H-4-W 88/90	140.88	6.882									-0.063	1	0.145	1	0.041	1	2.448	1	2.532	1	2.490	1	3.130	3.165
B-14H-4-W 99/101	140.99	6.883									-0.111	2			-0.111	2	2.642	2			2.642	2	3.282	3.199
B-14H-4-W 110/112	141.10	6.884									-0.385	1			-0.385	1	2.469	1			2.469	1	3.109	3.221
B-14H-4-W 122/124	141.22	6.886	2.287			2.287	-1.397			-1.397	-0.307	1			-0.307	1	2.729	1			2.729	1	3.369	3.249
B-14H-4-W 130/132	141.30	6.887	2.356			2.356	-1.338			-1.338	-0.110	1			-0.110	1	2.557	1			2.557	1	3.197	3.232
B-14H-4-W 140/142	141.40	6.889									-0.068	1			-0.068	1	2.623	1			2.623	1	3.263	3.222
B-14H-4-W 147/149	141.47	6.890									-0.118	1			-0.118	1	2.438	1			2.438	1	3.078	3.205

B-14H-5-W 10/12	141.60	6.893									-0.147	2			-0.147	2	2.695	2			2.695	2	3.335	3.221
B-14H-5-W 22/24	141.72	6.895	1.875			1.875	-1.246			-1.246	-0.304	1			-0.304	1	2.555	1			2.555	1	3.195	3.212
B-14H-5-W 30/32	141.80	6.896									-0.189	1			-0.189	1	2.551	1			2.551	1	3.191	3.205
B-14H-5-W 40/42	141.90	6.898									-0.104	1			-0.104	1	2.531	1			2.531	1	3.171	3.183
B-14H-5-W 50/52	142.00	6.899									-0.064	1			-0.064	1	2.586	1			2.586	1	3.226	3.167
B-14H-5-W 59/61	142.09	6.901									-0.079	1			-0.079	1	2.449	1			2.449	1	3.089	3.161
B-14H-5-W 72/74	142.22	6.903									-0.189	1			-0.189	1	2.483	1			2.483	1	3.123	3.162
B-14H-5-W 80/82	142.30	6.904									-0.172	2			-0.172	2	2.690	2			2.690	2	3.330	3.155
B-14H-5-W 87/89	142.37	6.903									-0.106	1			-0.106	1	2.370	1			2.370	1	3.010	3.120
B-14H-5-W 99/101	142.49	6.905									-0.314	1			-0.314	1	2.415	1			2.415	1	3.055	3.109
B-14H-5-W 110/112	142.60	6.906									-0.206	1			-0.206	1	2.512	1			2.512	1	3.152	3.119
B-14H-5-W 124/126	142.74	6.908									-0.336	1			-0.336	1	2.559	1			2.559	1	3.199	3.155
B-14H-5-W 130/132	142.80	6.909									-0.214	1			-0.214	1	2.438	1			2.438	1	3.078	3.160
B-14H-5-W 140/142	142.90	6.910	1.615			1.615	-1.104			-1.104	-0.063	2			-0.063	2	2.653	2			2.653	2	3.293	3.166
B-14H-5-W 147/149	142.97	6.911									-0.089	1			-0.089	1	2.398	1			2.398	1	3.038	3.158
B-14H-6-W 9/11	143.09	6.913									-0.104	1			-0.104	1	2.578	1			2.578	1	3.218	3.162
B-14H-6-W 19/21	143.19	6.914									-0.109	1			-0.109	1	2.544	1			2.544	1	3.184	3.174
B-14H-6-W 29/31	143.29	6.916									-0.116	1			-0.116	1	2.439	1			2.439	1	3.079	3.186
B-14H-6-W 39/41	143.39	6.917									-0.086	2			-0.086	2	2.757	2			2.757	2	3.397	3.197
B-14H-6-W 50/52	143.50	6.918									-0.088	1			-0.088	1	2.384	1			2.384	1	3.024	3.181
B-14H-6-W 58/60	143.58	6.919									-0.012	1			-0.012	1	2.585	1			2.585	1	3.225	3.170
B-14H-6-W 69/71	143.69	6.921									0.032	1			0.032	1	2.556	1			2.556	1	3.196	3.151
B-14H-6-W 79/81	143.79	6.922									0.019	1			0.019	1	2.402	1			2.402	1	3.042	3.163
A-15H-2-W 30/32	143.85	6.923									-0.073	1			-0.073	1	2.573	1			2.573	1	3.213	3.177
A-15H-2-W 40/42	143.95	6.925									0.006	1			0.006	1	2.672	1			2.672	1	3.312	3.162
A-15H-2-W 50/52	144.05	6.927									-0.131	1	-0.039	1	-0.085	1	2.403	1	2.403	1	2.403	1	3.043	3.124
A-15H-2-W 60/62	144.15	6.929									-0.115	1			-0.115	1	2.302	1			2.302	1	2.942	3.110
A-15H-2-W 72/74	144.27	6.931	2.294			2.294	-1.148			-1.148	0.054	1			0.054	1	2.654	1			2.654	1	3.294	3.168
A-15H-2-W 82/84	144.37	6.932									-0.029	1	-0.202	1	-0.116	1	2.601	1	2.503	1	2.552	1	3.192	3.234
A-15H-2-W 90/92	144.45	6.934									-0.149	2	-0.198	2	-0.173	2	2.682	2	2.731	2	2.706	2	3.346	3.279

A-15H-2-W 100/102	144.55	6.935									-0.101	*1*			-0.101	*1*	2.627	*1*			2.627	*1*	3.267	3.275
A-15H-2-W 109/111	144.64	6.937									-0.211	*1*			-0.211	*1*	2.628	*1*			2.628	*1*	3.268	3.263
A-15H-2-W 122/124	144.77	6.939									-0.455	*1*	-0.345	*1*	-0.400	*1*	2.633	*1*	2.554	*1*	2.593	*1*	3.233	3.222
A-15H-2-W 130/132	144.85	6.941									-0.318	*1*			-0.318	*1*	2.584	*1*			2.584	*1*	3.224	3.193
A-15H-2-W 140/142	144.95	6.942									-0.278	*1*			-0.278	*1*	2.388	*1*			2.388	*1*	3.028	3.177
A-15H-2-W 148/150	145.03	6.944									-0.176	*2*	-0.188	*2*	-0.182	*2*	2.594	*2*	2.730	*2*	2.662	*2*	3.302	3.212
A-15H-3-W 10/12	145.15	6.946									-0.025	*1*	-0.097	*1*	-0.061	*1*	2.577	*1*	2.571	*1*	2.574	*1*	3.214	3.226
A-15H-3-W 22/24	145.27	6.948	1.836						-1.186		-0.045	*1*			-0.045	*1*	2.689	*1*			2.689	*1*	3.329	3.223
A-15H-3-W 30/32	145.35	6.949									-0.184	*1*			-0.184	*1*	2.406	*1*			2.406	*1*	3.046	3.172
A-15H-3-W 40/42	145.45	6.948									-0.220	*1*			-0.220	*1*	2.581	*1*			2.581	*1*	3.221	3.173
A-15H-3-W 52/54	145.57	6.950									-0.136	*1*			-0.136	*1*	2.427	*1*			2.427	*1*	3.067	3.188
A-15H-3-W 60/62	145.65	6.952									-0.184	*2*			-0.184	*2*	2.757	*2*			2.757	*2*	3.397	3.214
A-15H-3-W 72/74	145.77	6.954	1.970		-0.998				-0.998		-0.174	*1*			-0.174	*1*	2.532	*1*			2.532	*1*	3.172	3.184
A-15H-3-W 82/84	145.87	6.955									-0.046	*1*	-0.090	*1*	-0.068	*1*	2.396	*1*	2.413	*1*	2.404	*1*	3.044	3.153
A-15H-3-W 90/92	145.95	6.957									0.039	*1*			0.039	*1*	2.535	*1*			2.535	*1*	3.175	3.128
A-15H-3-W 100/102	146.05	6.958									0.022	*1*	0.062	*1*	0.042	*1*	2.549	*1*	2.523	*1*	2.536	*1*	3.176	3.117
A-15H-3-W 109/111	146.14	6.960									-0.143	*1*			-0.143	*1*	2.368	*1*			2.368	*1*	3.008	3.101
A-15H-3-W 122/124	146.27	6.962	2.055		-1.046		-1.046				-0.129	*1*	-0.161	*1*	-0.145	*1*	2.498	*1*	2.447	*1*	2.472	*1*	3.112	3.066
A-15H-3-W 130/132	146.35	6.966									-0.141	*2*			-0.141	*2*	2.500	*2*			2.500	*2*	3.140	3.003
A-15H-3-W 140/142	146.45	6.968									-0.092	*1*			-0.092	*1*	2.123	*1*			2.123	*1*	2.763	2.921
A-15H-4-W 0/2	146.55	6.970									0.019	*1*	-0.021	*1*	-0.001	*1*	2.220	*1*	2.204	*1*	2.212	*1*	2.852	2.903
A-15H-4-W 10/12	146.65	6.972									-0.168	*1*			-0.168	*1*	2.270	*1*			2.270	*1*	2.910	2.939
A-15H-4-W 22/24	146.77	6.974	1.784		-1.010		-1.010				-0.432	*1*			-0.432	*1*	2.511	*1*			2.511	*1*	3.151	3.033
A-15H-4-W 30/32	146.85	6.976									-0.174	*1*			-0.174	*1*	2.283	*1*			2.283	*1*	2.923	3.102
A-15H-4-W 42/44	146.97	6.978									-0.295	*2*			-0.295	*2*	2.725	*2*			2.725	*2*	3.365	3.190
A-15H-4-W 50/52	147.05	6.980									-0.370	*1*			-0.370	*1*	2.526	*1*			2.526	*1*	3.166	3.233
A-15H-4-W 60/62	147.15	6.982									-0.375	*2*			-0.375	*2*	2.682	*2*			2.682	*2*	3.322	3.241
A-15H-4-W 72/74	147.27	6.984									0.191	*1*	0.010	*1*	0.100	*1*	2.521	*1*	2.696	*1*	2.608	*1*	3.248	3.179
A-15H-4-W 82/84	147.37	6.987	2.161		-1.043		-1.043				0.080	*1*			0.080	*1*	2.361	*1*			2.361	*1*	3.001	3.131
A-15H-4-W 90/92	147.45	6.989									0.272	*1*			0.272	*1*	2.406	*1*			2.406	*1*	3.046	3.109

A-15H-4-W 100/102	147.55	6.991									0.252	*2*	0.294	*2*	0.273	*2*	2.678	*2*	2.637	*2*	2.658	*2*	3.298	3.098
A-15H-4-W 109/111	147.64	6.993									0.215	*1*			0.215	*1*	2.351	*1*			2.351	*1*	2.991	3.052
A-15H-4-W 122/124	147.77	6.996	2.199			2.199	-1.153			-1.153	0.092	*1*			0.092	*1*	2.260	*1*			2.260	*1*	2.900	3.012
A-15H-4-W 130/132	147.85	6.998									0.014	*1*			0.014	*1*	2.400	*1*			2.400	*1*	3.040	3.034
B-15H-2-W 10/12	147.90	6.999									0.046	*1*			0.046	*1*	2.446	*1*			2.446	*1*	3.086	3.090
B-15H-2-W 22/24	148.02	7.002									0.023	*1*			0.023	*1*	2.608	*1*			2.608	*1*	3.248	3.146
B-15H-2-W 30/32	148.10	7.004									0.072	*1*			0.072	*1*	2.404	*1*			2.404	*1*	3.044	3.167
B-15H-2-W 40/42	148.20	7.006									-0.062	*2*	-0.014	*2*	-0.038	*2*	2.680	*2*	2.629	*2*	2.655	*2*	3.295	3.189
B-15H-2-W 50/52	148.30	7.010									-0.253	*1*	-0.213	*1*	-0.233	*1*	2.559	*1*	2.513	*1*	2.536	*1*	3.176	3.191
B-15H-2-W 60/62	148.40	7.012									-0.053	*1*			-0.053	*1*	2.504	*1*			2.504	*1*	3.144	3.197
B-15H-2-W 72/74	148.52	7.015									0.049	*1*			0.049	*1*	2.617	*1*			2.617	*1*	3.257	3.183
B-15H-2-W 80/82	148.60	7.017									0.220	*2*	0.107	*2*	0.163	*2*	2.594	*2*	2.489	*2*	2.541	*2*	3.181	3.178
B-15H-2-W 88/90	148.68	7.019									0.251	*1*			0.251	*1*	2.400	*1*			2.400	*1*	3.040	3.160
B-15H-2-W 100/102	148.80	7.022									0.138	*2*			0.138	*2*	2.699	*2*			2.699	*2*	3.339	3.130
B-15H-2-W 110/112	148.90	7.025									0.224	*1*			0.224	*1*	2.352	*1*			2.352	*1*	2.992	3.086
B-15H-2-W 122/124	149.02	7.028	1.491			1.491	-0.248			-0.248	0.070	*1*			0.070	*1*	2.269	*1*			2.269	*1*	2.909	3.104
B-15H-2-W 130/132	149.10	7.030									-0.249	*1*			-0.249	*1*	2.628	*1*			2.628	*1*	3.268	3.166
B-15H-2-W 140/142	149.20	7.032									0.197	*2*			0.197	*2*	2.757	*2*			2.757	*2*	3.397	3.221
B-15H-2-W 148/150	149.28	7.034									0.149	*1*			0.149	*1*	2.419	*1*			2.419	*1*	3.059	3.210
B-15H-3-W 10/12	149.40	7.037									0.115	*2*			0.115	*2*	2.581	*2*			2.581	*2*	3.221	3.172
B-15H-3-W 22/24	149.52	7.040	2.154			2.154	-1.183			-1.183	-0.108	*1*	0.062	*1*	-0.023	*1*	2.488	*1*	2.617	*1*	2.553	*1*	3.193	3.149
B-15H-3-W 30/32	149.60	7.042									-0.166	*1*			-0.166	*1*	2.362	*1*			2.362	*1*	3.002	3.144
B-15H-3-W 40/42	149.70	7.045									-0.206	*1*	-0.177	*1*	-0.191	*1*	2.537	*1*	2.718	*1*	2.627	*1*	3.267	3.134
B-15H-3-W 50/52	149.80	7.047									-0.217	*2*			-0.217	*2*	2.500	*2*			2.500	*2*	3.140	3.123
B-15H-3-W 60/62	149.90	7.050									-0.075	*1*			-0.075	*1*	2.282	*1*			2.282	*1*	2.922	3.179
B-15H-3-W 72/74	150.02	7.053	2.010			2.010	-1.095			-1.095	-0.122	*1*			-0.122	*1*	2.684	*1*			2.684	*1*	3.324	3.280
B-15H-3-W 80/82	150.10	7.055									-0.111	*2*			-0.111	*2*	3.065	*2*			3.065	*2*	3.705	3.329
B-15H-3-W 88/90	150.18	7.057									-0.248	*1*			-0.248	*1*	2.481	*1*			2.481	*1*	3.121	3.269
B-15H-3-W 100/102	150.30	7.060									0.131	*1*			0.131	*1*	2.346	*1*			2.346	*1*	2.986	3.180
B-15H-3-W 110/112	150.40	7.062									0.022	*2*	0.072	*2*	0.047	*2*	2.664	*2*	2.757	*2*	2.711	*2*	3.351	3.132

B-15H-3-W 122/124	150.52	7.067										0.048	*1*			0.048	*1*	2.407	*1*			2.407	*1*	3.047		3.115
B-15H-3-W 130/132	150.60	7.069	2.398		2.398		-1.119		-1.119	0.090	*1*	0.077	*1*	0.084	*1*	2.419	*1*	2.209	*1*	2.314	*1*	2.954		3.077	
B-15H-3-W 140/142	150.70	7.073								0.111	*2*			0.111	*2*	2.661	*2*			2.661	*2*	3.301		3.075	
B-15H-3-W 148/150	150.78	7.075								0.128	*1*	0.078	*1*	0.103	*1*	2.041	*1*	2.197	*1*	2.119	*1*	2.759		3.073	
B-15H-4-W 10/12	150.90	7.079								0.210	*2*			0.210	*2*	2.730	*2*			2.730	*2*	3.370		3.104	
B-15H-4-W 22/24	151.02	7.084								0.171	*1*			0.171	*1*	2.374	*1*			2.374	*1*	3.014		3.075	
B-15H-4-W 30/32	151.10	7.086	2.447		2.447		-0.995		-0.995	0.324	*1*			0.324	*1*	2.395	*1*			2.395	*1*	3.035		3.101	
B-15H-4-W 40/42	151.20	7.090								0.130	*1*			0.130	*1*	2.357	*1*			2.357	*1*	2.997		3.136	
B-15H-4-W 50/52	151.30	7.093								0.293	*2*			0.293	*2*	2.854	*2*			2.854	*2*	3.494		3.217	
B-15H-4-W 60/62	151.40	7.096								0.171	*1*			0.171	*1*	2.487	*1*			2.487	*1*	3.127		3.224	
B-15H-4-W 72/74	151.52	7.100								0.205	*1*			0.205	*1*	2.557	*1*			2.557	*1*	3.197		3.217	
B-15H-4-W 80/82	151.60	7.108	2.306		2.306		-1.113		-1.113	0.048	*2*			0.048	*2*	2.569	*2*			2.569	*2*	3.209		3.213	
B-15H-4-W 88/90	151.68	7.111								0.205	*1*			0.205	*1*	2.601	*1*			2.601	*1*	3.241		3.246	
B-15H-4-W 100/102	151.80	7.116								0.065	*1*	0.188	*1*	0.127	*1*	2.590	*1*	2.708	*1*	2.649	*1*	3.289		3.283	
B-15H-4-W 110/112	151.90	7.120								0.171	*2*			0.171	*2*	2.664	*2*			2.664	*2*	3.304		3.321	
B-15H-4-W 122/124	152.02	7.125								0.262	*1*			0.262	*1*	2.742	*1*			2.742	*1*	3.382		3.342	
B-15H-4-W 130/132	152.10	7.129								0.272	*1*	0.292	*1*	0.282	*1*	2.810	*1*	2.689	*1*	2.750	*1*	3.390		3.319	
B-15H-4-W 140/142	152.20	7.133								0.326	*1*			0.326	*1*	2.595	*1*			2.595	*1*	3.235		3.278	
B-15H-4-W 148/150	152.28	7.136								0.420	*1*			0.420	*1*	2.506	*1*			2.506	*1*	3.146		3.261	
B-15H-5-W 10/12	152.40	7.141								0.280	*1*			0.280	*1*	2.725	*1*			2.725	*1*	3.365		3.253	
B-15H-5-W 22/24	152.52	7.146								0.358	*1*			0.358	*1*	2.692	*1*			2.692	*1*	3.332		3.220	
B-15H-5-W 30/32	152.60	7.150	2.638		2.638		-1.214		-1.214	0.322	*1*			0.322	*1*	2.322	*1*			2.322	*1*	2.962		3.149	
B-15H-5-W 40/42	152.70	7.154								0.359	*1*			0.359	*1*	2.545	*1*			2.545	*1*	3.185		3.105	
B-15H-5-W 50/52	152.80	7.156								0.105	*1*			0.105	*1*	2.402	*1*			2.402	*1*	3.042		3.085	
B-15H-5-W 60/62	152.90	7.160								0.322	*1*			0.322	*1*	2.447	*1*			2.447	*1*	3.087		3.091	
B-15H-5-W 72/74	153.02	7.164	2.539	2.126	2.332	-1.074	-1.302	-1.074	-1.188	0.046	*1*			0.046	*1*	2.467	*1*			2.467	*1*	3.107		3.093	
B-15H-5-W 80/82	153.10	7.166								0.377	*1*			0.377	*1*	2.444	*1*			2.444	*1*	3.084		3.092	
B-15H-5-W 88/90	153.18	7.169								0.263	*2*			0.263	*2*	2.489	*2*			2.489	*2*	3.129		3.075	
B-15H-5-W 100/102	153.30	7.173								-0.084	*1*			-0.084	*1*	2.362	*1*			2.362	*1*	3.002		3.046	
B-15H-5-W 110/112	153.40	7.176								0.384	*1*			0.384	*1*	2.369	*1*			2.369	*1*	3.009		3.056	

B-15H-5-W 122/124	153.52	7.180	1.927			1.927	-0.671		-0.671	0.142	1	0.178	1	0.160	1	2.415	1	2.400	1	2.408	1	3.048		3.158		
B-15H-5-W 130/132	153.60	7.183								0.034	1			0.034	1	2.644	1			2.644	1	3.284		3.300		
B-15H-5-W 140/142	153.70	7.182								0.115	1			0.115	1	3.096	1			3.096	1	3.736		3.343		
B-15H-5-W 148/150	153.78	7.184								-0.006	2			-0.006	2	2.569	2			2.569	2	3.209		3.241		
B-15H-6-W 10/12	153.90	7.187	2.266			2.266	-1.069		-1.069	0.141	1			0.141	1	2.140	1			2.140	1	2.780		3.119		
A-16H-1-W 132/134	153.93	7.188								0.011	1			0.011	1	2.581	1			2.581	1	3.221		3.092		
A-16H-1-W 139/141	154.00	7.190								0.092	1			0.092	1	2.542	1			2.542	1	3.182		3.102		
A-16H-1-W 148/150	154.09	7.190								0.229	1			0.229	1	2.419	1			2.419	1	3.059		3.091		
A-16H-2-W 10/12	154.21	7.193								0.436	1			0.436	1	2.336	1			2.336	1	2.976		3.100		
A-16H-2-W 22/24	154.33	7.194								0.083	1			0.083	1	2.479	1			2.479	1	3.119		3.140		
A-16H-2-W 32/34	154.43	7.196	2.151			2.151	-1.177		-1.177	0.416	2			0.416	2	2.842	2			2.842	2	3.482		3.134		
A-16H-2-W 38/40	154.49	7.197								0.480	1			0.480	1	2.235	1			2.235	1	2.875		3.009		
A-16H-2-W 50/52	154.61	7.199								0.306	1			0.306	1	2.130	1			2.130	1	2.770		2.890		
A-16H-2-W 60/62	154.71	7.200								0.526	1	0.357	1	0.442	1	2.146	1	2.180	1	2.163	1	2.803		2.835		
A-16H-2-W 72/74	154.83	7.202	2.999			2.999	-1.689		-1.689	0.423	1			0.423	1	2.291	1			2.291	1	2.931		2.899		
A-16H-2-W 79/81	154.90	7.204								0.325	1			0.325	1	2.188	1			2.188	1	2.828		2.966		
A-16H-2-W 90/92	155.01	7.203								0.387	2			0.387	2	2.672	2			2.672	2	3.312		3.015		
A-16H-2-W 100/102	155.11	7.204								0.507	1			0.507	1	2.219	1			2.219	1	2.859		2.967		
A-16H-2-W 122/124	155.33	7.207	2.406			2.406	-1.331		-1.331	0.359	1			0.359	1	2.265	1			2.265	1	2.905		2.906		
A-16H-2-W 130/132	155.41	7.208								0.375	1			0.375	1	2.169	1			2.169	1	2.809		2.895		
A-16H-2-W 140/142	155.51	7.210								0.336	1			0.336	1	2.205	1			2.205	1	2.845		2.969		
A-16H-2-W 148/150	155.59	7.211								0.352	2			0.352	2	2.675	2			2.675	2	3.315		3.041		
A-16H-3-W 10/12	155.71	7.213								0.299	1			0.299	1	2.376	1			2.376	1	3.016		3.036		
A-16H-3-W 22/24	155.83	7.214								0.117	1			0.117	1	2.235	1			2.235	1	2.875		3.006		
A-16H-3-W 30/32	155.91	7.216	2.425			2.425	-1.927		-1.927	0.107	1			0.107	1	2.380	1			2.380	1	3.020		3.014		
A-16H-3-W 38/40	155.99	7.217								0.051	1			0.051	1	2.435	1			2.435	1	3.075		3.078		
A-16H-3-W 47/49	156.08	7.219								0.014	1	0.077	1	0.046	1	2.585	1	2.478	1	2.532	1	3.172		3.152		
A-16H-3-W 59/61	156.20	7.221								0.136	2			0.136	2	2.566	2			2.566	2	3.206		3.196		
A-16H-3-W 73/75	156.34	7.226								0.185	1			0.185	1	2.634	1			2.634	1	3.274		3.188		
A-16H-3-W 77/79	156.38	7.227								0.192	1			0.192	1	2.519	1			2.519	1	3.159		3.122		

A-16H-3-W 90/92	156.51	7.230									0.430	1			0.430	1	2.308	1			2.308	1	2.948	3.037
A-16H-3-W 100/102	156.61	7.232									0.306	1			0.306	1	2.322	1			2.322	1	2.962	2.980
A-16H-3-W 109/111	156.70	7.234									0.540	1			0.540	1	2.342	1			2.342	1	2.982	2.994
A-16H-3-W 122/124	156.83	7.238	2.680			2.680	-1.315			-1.315	0.356	1			0.356	1	2.293	1			2.293	1	2.933	3.054
A-16H-3-W 129/131	156.90	7.240									0.317	2			0.317	2	2.653	2			2.653	2	3.293	3.099
A-16H-3-W 140/142	157.01	7.243									0.367	1			0.367	1	2.520	1			2.520	1	3.160	3.082
A-16H-4-W 0/2	157.11	7.245									0.482	1			0.482	1	2.173	1			2.173	1	2.813	3.025
A-16H-4-W 10/12	157.21	7.247									0.446	1			0.446	1	2.466	1			2.466	1	3.106	2.997
A-16H-4-W 22/24	157.33	7.249	2.482			2.482	-1.573			-1.573	0.392	1			0.392	1	2.322	1			2.322	1	2.962	3.003
A-16H-4-W 32/34	157.43	7.252									0.276	1			0.276	1	2.346	1			2.346	1	2.986	3.052
A-16H-4-W 42/44	157.53	7.254									0.292	1			0.292	1	2.490	1			2.490	1	3.130	3.123
A-16H-4-W 50/52	157.61	7.256									0.417	1			0.417	1	2.610	1			2.610	1	3.250	3.209
A-16H-4-W 58/60	157.69	7.258									0.387	1			0.387	1	2.645	1			2.645	1	3.285	3.240
A-16H-4-W 72/74	157.83	7.261	2.325			2.325	-0.787			-0.787	0.298	1			0.298	1	2.661	1			2.661	1	3.301	3.233
A-16H-4-W 80/82	157.91	7.261									0.372	1			0.372	1	2.393	1			2.393	1	3.033	3.226
A-16H-4-W 90/92	158.01	7.263									0.544	1			0.544	1	2.692	1			2.692	1	3.332	3.261
A-16H-4-W 100/102	158.11	7.265									0.307	2			0.307	2	2.750	2			2.750	2	3.390	3.280
A-16H-4-W 109/111	158.20	7.267									0.505	1			0.505	1	2.571	1			2.571	1	3.211	3.239
A-16H-4-W 122/124	158.33	7.269	2.713			2.713	-1.275			-1.275	0.275	1	0.584	1	0.429	1	2.442	1	2.670	1	2.556	1	3.196	3.160
A-16H-4-W 130/132	158.41	7.271									0.495	1	0.017	1	0.256	1	2.338	1	2.355	1	2.346	1	2.986	3.120
A-16H-4-W 140/142	158.51	7.273									0.239	1			0.239	1	2.462	1			2.462	1	3.102	3.167
A-16H-4-W 148/150	158.59	7.275									0.816	1	0.340	1	0.578	1	3.021	1	2.390	1	2.706	1	3.346	3.227
A-16H-5-W 11/13	158.72	7.277									0.318	2			0.318	2	2.719	2			2.719	2	3.359	3.215
A-16H-5-W 22/24	158.83	7.279									0.281	1			0.281	1	2.413	1			2.413	1	3.053	3.101
A-16H-5-W 30/32	158.91	7.281	2.338			2.338	-1.384			-1.384	0.398	1			0.398	1	2.279	1			2.279	1	2.919	2.983
A-16H-5-W 42/44	159.03	7.283									0.160	1			0.160	1	2.199	1			2.199	1	2.839	2.934
A-16H-5-W 52/54	159.13	7.285									0.383	1	0.456	1	0.420	1	2.285	1	2.416	1	2.350	1	2.990	2.980
A-16H-5-W 62/64	159.23	7.287									0.428	1			0.428	1	2.392	1			2.392	1	3.032	3.075
A-16H-5-W 72/74	159.33	7.289	2.306			2.306	-1.089			-1.089	0.406	1			0.406	1	2.570	1			2.570	1	3.210	3.159
A-16H-5-W 82/84	159.43	7.291									0.273	2			0.273	2	2.695	2			2.695	2	3.335	3.183

A-16H-5-W 91/93	159.52	7.293											0.064	1	0.239	1	0.152	1	2.357	1	2.447	1	2.402	1	3.042		3.158
A-16H-5-W 101/103	159.62	7.296											0.316	1			0.316	1	2.458	1			2.458	1	3.098		3.153
A-16H-5-W 109/111	159.70	7.298											0.231	1	0.307	1	0.269	1	2.568	1	2.599	1	2.584	1	3.224		3.180
A-16H-5-W 122/124	159.83	7.301	2.329								-1.234		0.209	1	0.373	1	0.291	1	2.658	1	2.561	1	2.610	1	3.250		3.232
B-16H-2-W 122/124	159.85	7.301	2.642								-1.182		0.447	1	0.197	1	0.322	1	2.523	1	2.593	1	2.558	1	3.198		3.271
B-16H-2-W 130/132	159.93	7.303	2.231								-1.230		0.434	2			0.434	2	2.770	2			2.770	2	3.410		3.284
B-16H-2-W 140/142	160.03	7.305											0.405	1	0.342	1	0.373	1	2.673	1	2.613	1	2.643	1	3.283		3.253
B-16H-2-W 148/150	160.11	7.309											0.378	1			0.378	1	2.460	1			2.460	1	3.100		3.191
B-16H-3-W 9/11	160.22	7.311											0.321	1			0.321	1	2.556	1			2.556	1	3.196		3.120
B-16H-3-W 22/24	160.35	7.315	2.198								-0.856		0.361	1			0.361	1	2.413	1			2.413	1	3.053		3.036
B-16H-3-W 30/32	160.43	7.317											0.533	1			0.533	1	2.271	1			2.271	1	2.911		2.954
B-16H-3-W 40/42	160.53	7.318											0.424	1			0.424	1	2.194	1			2.194	1	2.834		2.891
B-16H-3-W 50/52	160.63	7.320											0.540	1			0.540	1	2.268	1			2.268	1	2.908		2.884
B-16H-3-W 59/61	160.72	7.322											0.323	1			0.323	1	2.191	1			2.191	1	2.831		2.915
B-16H-3-W 72/74	160.85	7.325	2.486								-1.233		0.417	1			0.417	1	2.378	1			2.378	1	3.018		2.954
B-16H-3-W 80/82	160.93	7.327											0.378	1			0.378	1	2.408	1			2.408	1	3.048		2.957
B-16H-3-W 87/89	161.00	7.329											0.350	1			0.350	1	2.215	1			2.215	1	2.855		2.951
B-16H-3-W 100/102	161.13	7.331											0.339	1			0.339	1	2.237	1			2.237	1	2.877		2.987
B-16H-3-W 110/112	161.23	7.332											-0.021	1			-0.021	1	2.507	1			2.507	1	3.147		3.088
B-16H-3-W 122/124	161.35	7.334	2.058	2.726		2.392		-0.803	-1.232				-1.017				0.272	1	2.591	1			2.591	1	3.231		3.176
B-16H-3-W 129/131	161.42	7.336											0.320	1			0.320	1	2.638	1			2.638	1	3.278		3.200
B-16H-3-W 140/142	161.53	7.338											0.125	1	0.186	1	0.156	1	2.401	1	2.569	1	2.485	1	3.125		3.174
B-16H-3-W 148/150	161.61	7.340											0.258	1			0.258	1	2.454	1			2.454	1	3.094		3.186
B-16H-4-W 10/12	161.73	7.342											0.130	2			0.130	2	2.587	2			2.587	2	3.227		3.221
B-16H-4-W 22/24	161.85	7.344											0.192	1			0.192	1	2.804	1			2.804	1	3.444		3.236
B-16H-4-W 30/32	161.93	7.346											0.286	1			0.286	1	2.433	1			2.433	1	3.073		3.176
B-16H-4-W 40/42	162.03	7.348											0.164	1			0.164	1	2.448	1			2.448	1	3.088		3.120
B-16H-4-W 50/52	162.13	7.350											0.274	1			0.274	1	2.407	1			2.407	1	3.047		3.093
B-16H-4-W 60/62	162.23	7.352											0.395	1			0.395	1	2.541	1			2.541	1	3.181		3.108
B-16H-4-W 72/74	162.35	7.355	2.538			2.538		-1.181			-1.181		0.398	1	0.413	1	0.405	1	2.459	1	2.416	1	2.438	1	3.078		3.083

B-16H-4-W 80/82	162.43	7.356																											
B-16H-4-W 88/90	162.51	7.358																											
B-16H-4-W 100/102	162.63	7.360																											
B-16H-4-W 110/112	162.73	7.362																											
B-16H-4-W 122/124	162.85	7.365	2.067			2.067		-1.899		-1.899	0.273	1	0.273	1	2.409	1	2.409	1					2.409	1	3.049	2.998			
B-16H-4-W 130/132	162.93	7.366									0.412	1	0.412	1	2.391	1	2.391	1					2.391	1	3.031	3.117			
B-16H-4-W 140/142	163.03	7.368									0.535	1	0.535	1	2.772	1	2.772	1					2.772	1	3.412	3.180			
B-16H-4-W 148/150	163.11	7.370									0.217	1	0.217	1	2.479	1	2.479	1					2.479	1	3.119	3.159			
B-16H-5-W 10/12	163.23	7.367									0.142	1	0.142	1	2.386	1	2.386	1					2.386	1	3.026	3.118			
B-16H-5-W 22/24	163.35	7.369	2.521			2.521		-1.397		-1.397	0.209	1	0.296	1	0.252	1	2.500	1	2.503	1			2.502	1	3.142	3.087			
B-16H-5-W 30/32	163.43	7.370									0.251	1	0.251	1	2.432	1	2.432	1					2.432	1	3.072	3.100			
B-16H-5-W 40/42	163.53	7.371									0.296	1	0.341	1	0.319	1	2.369	1	2.452	1			2.410	1	3.050	3.115			
B-16H-5-W 50/52	163.63	7.372									0.680	1	0.414	1	0.547	1	2.759	1	2.541	1			2.650	1	3.290	3.124			
B-16H-5-W 60/62	163.73	7.374									0.367	1			0.367	1	2.354	1					2.354	1	2.994	3.093			
B-16H-5-W 72/74	163.85	7.375	2.555			2.555		-1.330		-1.330	0.413	1			0.413	1	2.460	1					2.460	1	3.100	3.053			
B-16H-5-W 80/82	163.93	7.376									0.423	1			0.423	1	2.354	1					2.354	1	2.994	3.002			
B-16H-5-W 87/89	164.00	7.377									0.483	1			0.483	1	2.294	1					2.294	1	2.934	3.016			
B-16H-5-W 100/102	164.13	7.379									0.433	1			0.433	1	2.324	1					2.324	1	2.964	3.093			
B-16H-5-W 110/112	164.23	7.380									0.683	1			0.683	1	2.739	1					2.739	1	3.379	3.176			
B-16H-5-W 122/124	164.35	7.382									0.347	1			0.347	1	2.688	1					2.688	1	3.328	3.165			
B-16H-5-W 130/132	164.43	7.383									0.494	1	0.658	1	0.576	1	2.204	1	2.279	1			2.242	1	2.882	3.071			
B-16H-5-W 140/142	164.53	7.384									0.604	1			0.604	1	2.340	1					2.340	1	2.980	3.006			
B-16H-5-W 147/149	164.60	7.385									0.431	1			0.431	1	2.371	1					2.371	1	3.011	3.014			
B-16H-6-W 10/12	164.73	7.387									0.519	1			0.519	1	2.408	1					2.408	1	3.048	3.061			
B-16H-6-W 20/22	164.83	7.388									0.357	1			0.357	1	2.516	1					2.516	1	3.156	3.106			
B-16H-6-W 30/32	164.93	7.390									0.368	1	0.395	1	0.381	1	2.393	1	2.483	1			2.438	1	3.078	3.140			
B-16H-6-W 40/42	165.03	7.391									0.250	1			0.250	1	2.599	1					2.599	1	3.239	3.141			
B-16H-6-W 50/52	165.13	7.393									0.361	1			0.361	1	2.532	1					2.532	1	3.172	3.090			
B-16H-6-W 57/59	165.20	7.393									0.171	1			0.171	1	2.238	1					2.238	1	2.878	3.011			
B-16H-6-W 69/71	165.32	7.395									0.514	1			0.514	1	2.334	1					2.334	1	2.974	2.951			

B-16H-6-W 80/82	165.43	7.397									0.370 *1*		0.370 *1*	2.302 *1*		2.302 *1*	2.942	2.914
A-17H-2-W 29/31	165.52	7.398									0.408 *1*		0.408 *1*	2.204 *1*		2.204 *1*	2.844	2.897
A-17H-2-W 41/43	165.64	7.399									0.443 *1*		0.443 *1*	2.239 *1*		2.239 *1*	2.879	2.907
A-17H-2-W 50/52	165.73	7.401									0.348 *1*		0.348 *1*	2.296 *1*		2.296 *1*	2.936	2.964
A-17H-2-W 59/61	165.82	7.402									0.475 *1*		0.475 *1*	2.402 *1*		2.402 *1*	3.042	3.021
A-17H-2-W 69/71	165.92	7.403	2.287			2.287	-1.229			-1.229	0.335 *1*		0.335 *1*	2.554 *1*		2.554 *1*	3.194	3.051
A-17H-2-W 79/81	166.02	7.405	2.443			2.443	-1.338			-1.338	0.309 *1*		0.309 *1*	2.243 *1*		2.243 *1*	2.883	3.049
A-17H-2-W 89/91	166.12	7.407									0.330 *1*		0.330 *1*	2.464 *1*		2.464 *1*	3.104	3.074
A-17H-2-W 100/102	166.23	7.409									0.383 *1*	0.184 *1*	0.283 *1*	2.606 *1*	2.409 *1*	2.508 *1*	3.148	3.104
A-17H-2-W 108/110	166.31	7.410									0.202 *1*		0.202 *1*	2.489 *1*		2.489 *1*	3.129	3.125
A-17H-2-W 122/124	166.45	7.413									0.064 *1*		0.064 *1*	2.478 *1*		2.478 *1*	3.118	3.113
A-17H-2-W 131/133	166.54	7.414	2.544			2.544	-1.497			-1.497	0.352 *1*		0.352 *1*	2.461 *1*		2.461 *1*	3.101	3.063
A-17H-2-W 139/141	166.62	7.415									0.291 *1*		0.291 *1*	2.410 *1*		2.410 *1*	3.050	2.992
A-17H-2-W 147/149	166.70	7.419									0.309 *1*		0.309 *1*	2.135 *1*		2.135 *1*	2.775	2.923
A-17H-3-W 10/12	166.83	7.422									0.228 *1*		0.228 *1*	2.287 *1*		2.287 *1*	2.927	2.906
A-17H-3-W 22/24	166.95	7.423	2.225			2.225	-1.041			-1.041	0.494 *1*		0.494 *1*	2.297 *1*		2.297 *1*	2.937	2.934
A-17H-3-W 30/32	167.03	7.424									0.326 *1*		0.326 *1*	2.281 *1*		2.281 *1*	2.921	2.989
A-17H-3-W 42/44	167.15	7.426									0.451 *1*	0.586 *1*	0.518 *1*	2.503 *1*	2.468 *1*	2.486 *1*	3.126	3.031
A-17H-3-W 52/54	167.25	7.428									0.456 *1*		0.456 *1*	2.440 *1*		2.440 *1*	3.080	3.023
A-17H-3-W 60/62	167.33	7.430									0.267 *1*		0.267 *1*	2.308 *1*		2.308 *1*	2.948	2.982
A-17H-3-W 72/74	167.45	7.432	2.148			2.148	-1.232			-1.232	0.110 *1*		0.110 *1*	2.228 *1*		2.228 *1*	2.868	2.951
A-17H-3-W 80/82	167.53	7.433									0.162 *1*		0.162 *1*	2.346 *1*		2.346 *1*	2.986	2.979
A-17H-3-W 90/92	167.63	7.435									0.006 *1*		0.006 *1*	2.385 *1*		2.385 *1*	3.025	3.004
A-17H-3-W 100/102	167.73	7.436									0.653 *1*		0.653 *1*	2.502 *1*		2.502 *1*	3.142	3.006
A-17H-3-W 109/111	167.82	7.438									0.310 *1*		0.310 *1*	2.146 *1*		2.146 *1*	2.786	2.976
A-17H-3-W 122/124	167.95	7.443									0.414 *1*		0.414 *1*	2.399 *1*		2.399 *1*	3.039	3.005
A-17H-3-W 130/132	168.03	7.446									0.413 *1*		0.413 *1*	2.391 *1*		2.391 *1*	3.031	3.055
A-17H-3-W 140/142	168.13	7.450									0.328 *1*	0.545 *1*	0.437 *1*	2.473 *1*	2.663 *1*	2.568 *1*	3.208	3.115
A-17H-4-W 0/2	168.23	7.453									0.461 *1*		0.461 *1*	2.440 *1*		2.440 *1*	3.080	3.118
A-17H-4-W 10/12	168.33	7.462									0.482 *1*		0.482 *1*	2.521 *1*		2.521 *1*	3.161	3.105

A-17H-4-W 19/21	168.42	7.467									0.600	1			0.600	1	2.380	1			2.380	1	3.020	3.092
A-17H-4-W 30/32	168.53	7.482									0.545	1	0.655	1	0.600	1	2.361	1	2.502	1	2.431	1	3.071	3.111
A-17H-4-W 42/44	168.65	7.492									0.547	1			0.547	1	2.586	1			2.586	1	3.226	3.132
A-17H-4-W 50/52	168.73	7.499									0.587	1	0.626	1	0.606	1	2.514	1	2.483	1	2.498	1	3.138	3.127
A-17H-4-W 60/62	168.83	7.507									0.622	1			0.622	1	2.420	1			2.420	1	3.060	3.090
A-17H-4-W 70/72	168.93	7.515									0.546	1	0.706	1	0.626	1	2.396	1	2.465	1	2.431	1	3.071	3.052
A-17H-4-W 80/82	169.03	7.524									0.638	1			0.638	1	2.345	1			2.345	1	2.985	3.020
A-17H-4-W 90/92	169.13	7.520									0.569	1	0.732	1	0.651	1	2.361	1	2.449	1	2.405	1	3.045	2.987
A-17H-4-W 100/102	169.23	7.522									0.602	1			0.602	1	2.279	1			2.279	1	2.919	2.925
A-17H-4-W 108/110	169.31	7.525									0.417	1			0.417	1	2.236	1			2.236	1	2.876	2.863
A-17H-4-W 121/123	169.44	7.529									0.558	1			0.558	1	2.076	1			2.076	1	2.716	2.843
A-17H-4-W 130/132	169.53	7.532									0.614	1			0.614	1	2.207	1			2.207	1	2.847	2.907
B-17H-2-W 30/32	169.69	7.531									0.634	1			0.634	1	2.464	1			2.464	1	3.104	2.989
B-17H-2-W 40/42	169.79	7.534									0.829	1			0.829	1	2.484	1			2.484	1	3.124	3.039
B-17H-2-W 50/52	169.89	7.536									0.768	1			0.768	1	2.252	1			2.252	1	2.892	3.047
B-17H-2-W 60/62	169.99	7.538									0.858	1	0.709	1	0.784	1	2.493	1	2.511	1	2.502	1	3.142	3.056
B-17H-2-W 72/74	170.11	7.541									0.879	1			0.879	1	2.464	1			2.464	1	3.104	3.054
B-17H-2-W 81/83	170.20	7.543									0.710	1			0.710	1	2.335	1			2.335	1	2.975	3.049
B-17H-2-W 88/90	170.27	7.544									0.508	1			0.508	1	2.387	1			2.387	1	3.027	3.059
B-17H-2-W 100/102	170.39	7.547									0.732	1			0.732	1	2.487	1			2.487	1	3.127	3.127
B-17H-2-W 110/112	170.49	7.549									0.595	1			0.595	1	2.512	1			2.512	1	3.152	3.199
B-17H-2-W 122/124	170.61	7.552	2.037			2.037	-1.004			-1.004	0.599	1			0.599	1	2.815	1			2.815	1	3.455	3.228
B-17H-2-W 130/132	170.69	7.554									0.531	1			0.531	1	2.458	1			2.458	1	3.098	3.184
B-17H-2-W 140/142	170.79	7.556									0.582	1			0.582	1	2.415	1			2.415	1	3.055	3.127
B-17H-2-W 149/151	170.88	7.558									0.675	1			0.675	1	2.530	1			2.530	1	3.170	3.105
B-17H-3-W 10/12	170.99	7.561									0.515	1			0.515	1	2.362	1			2.362	1	3.002	3.107
B-17H-3-W 22/24	171.11	7.563	2.651			2.651	-1.161			-1.161	0.984	1			0.984	1	2.616	1			2.616	1	3.256	3.095
B-17H-3-W 30/32	171.19	7.565									0.660	1			0.660	1	2.370	1			2.370	1	3.010	3.015
B-17H-3-W 40/42	171.29	7.567									0.718	1			0.718	1	2.260	1			2.260	1	2.900	2.924
B-17H-3-W 50/52	171.39	7.569									0.857	1			0.857	1	2.113	1			2.113	1	2.753	2.864

B-17H-3-W 60/62	171.49	7.572															0.904	*1*			2.232	*1*			2.232	*1*			2.872	2.875
B-17H-3-W 72/74	171.61	7.574	2.956			2.956	-1.104			-1.104							0.497	*1*			2.347	*1*			2.347	*1*			2.987	2.906
B-17H-3-W 80/82	171.69	7.576															0.745	*1*			2.246	*1*			2.246	*1*			2.886	2.925
B-17H-3-W 88/90	171.77	7.578															0.833	*1*			2.277	*1*			2.277	*1*			2.917	2.935
B-17H-3-W 100/102	171.89	7.581															0.761	*1*			2.341	*1*			2.341	*1*			2.981	2.981
B-17H-3-W 110/112	171.99	7.583															0.901	*1*			2.315	*1*			2.315	*1*			2.955	3.050
B-17H-3-W 122/124	172.11	7.586	2.797	2.895		2.846	-0.952	-1.218		-1.085							0.723	*1*			2.646	*1*			2.646	*1*			3.286	3.135
B-17H-3-W 131/133	172.20	7.588															0.623	*1*			2.470	*1*			2.470	*1*			3.110	3.183
B-17H-3-W 140/142	172.29	7.590															0.715	*1*			2.626	*1*			2.626	*1*			3.266	3.203
B-17H-3-W 149/151	172.38	7.592													0.705	*1*	0.761	*1*	0.733	*1*	2.655	*1*	2.513	*1*	2.584	*1*			3.224	3.192
B-17H-4-W 10/12	172.49	7.596															0.734	*1*			2.434	*1*			2.434	*1*			3.074	3.191
B-17H-4-W 22/24	172.61	7.600															0.601	*1*			2.633	*1*			2.633	*1*			3.273	3.195
B-17H-4-W 30/32	172.69	7.603	3.284			3.284	-1.466			-1.466							0.649	*1*			2.595	*1*			2.595	*1*			3.235	3.168
B-17H-4-W 40/42	172.79	7.606															0.768	*1*			2.457	*1*			2.457	*1*			3.097	3.101
B-17H-4-W 50/52	172.89	7.609															0.754	*1*			2.318	*1*			2.318	*1*			2.958	3.039
B-17H-4-W 60/62	172.99	7.617															0.832	*1*			2.326	*1*			2.326	*1*			2.966	3.046
B-17H-4-W 72/74	173.11	7.623															0.695	*1*			2.504	*1*			2.504	*1*			3.144	3.108
B-17H-4-W 82/84	173.21	7.627															0.870	*1*			2.601	*1*			2.601	*1*			3.241	3.181
B-17H-4-W 88/90	173.27	7.631															0.793	*1*			2.517	*1*			2.517	*1*			3.157	3.218
B-17H-4-W 100/102	173.39	7.637															0.638	*1*			2.701	*1*			2.701	*1*			3.341	3.235
B-17H-4-W 110/112	173.49	7.642															0.627	*1*			2.518	*1*			2.518	*1*			3.158	3.226
B-17H-4-W 122/124	173.61	7.648	2.457			2.457	-1.204			-1.204					0.541	*1*	0.625	*1*	0.583	*1*	2.607	*1*	2.595	*1*	2.601	*1*			3.241	3.224
B-17H-4-W 130/132	173.69	7.655															0.870	*1*			2.576	*1*			2.576	*1*			3.216	3.201
B-17H-4-W 140/142	173.79	7.660															0.749	*1*			2.582	*1*			2.582	*1*			3.222	3.181
B-17H-4-W 149/151	173.88	7.665	3.266	3.291		3.279	-1.435	-1.213		-1.324							0.849	*1*			2.410	*1*			2.410	*1*			3.050	3.160
B-17H-5-W 10/12	173.99	7.670															0.914	*1*			2.567	*1*			2.567	*1*			3.207	3.174
B-17H-5-W 22/24	174.11	7.676	2.737			2.737	-1.195			-1.195							0.742	*1*			2.579	*1*			2.579	*1*			3.219	3.199
B-17H-5-W 30/32	174.19	7.680															0.736	*1*			2.558	*1*			2.558	*1*			3.198	3.224
B-17H-5-W 40/42	174.29	7.685															0.612	*1*			2.630	*1*			2.630	*1*			3.270	3.235
B-17H-5-W 51/53	174.40	7.688															0.780	*1*			2.595	*1*			2.595	*1*			3.235	3.255

B-17H-5-W 60/62	174.49	7.692									0.462	*1*			0.462	*1*	2.586	*1*			2.586	*1*	3.226		3.279					
B-17H-5-W 72/74	174.61	7.697	3.229		3.229		-1.339				0.597	*1*			0.597	*1*	2.775	*1*			2.775	*1*	3.415		3.274					
B-17H-5-W 81/83	174.70	7.701									0.812	*1*			0.812	*1*	2.615	*1*			2.615	*1*	3.255		3.218					
B-17H-5-W 94/96	174.83	7.705									0.636	*1*			0.636	*1*	2.356	*1*			2.356	*1*	2.996		3.147					
B-17H-5-W 102/104	174.91	7.709									0.786	*1*			0.786	*1*	2.508	*1*			2.508	*1*	3.148		3.129					
B-17H-5-W 112/114	175.01	7.711									0.567	*1*	0.894	*1*	0.730	*1*	2.490	*1*	2.494	*1*	2.492	*1*	3.132		3.146					
B-17H-5-W 122/124	175.11	7.715									0.828	*1*			0.828	*1*	2.600	*1*			2.600	*1*	3.240		3.155					
B-17H-5-W 130/132	175.19	7.717									0.667	*1*	0.733	*1*	0.700	*1*	2.470	*1*	2.487	*1*	2.478	*1*	3.118		3.130					
B-17H-5-W 140/142	175.29	7.721									0.821	*1*			0.821	*1*	2.378	*1*			2.378	*1*	3.018		3.102					
B-17H-5-W 150/152	175.39	7.724									0.881	*1*			0.881	*1*	2.536	*1*			2.536	*1*	3.176		3.084					
B-17H-6-W 10/12	175.49	7.727									0.730	*1*			0.730	*1*	2.393	*1*			2.393	*1*	3.033		3.071					
B-17H-6-W 20/22	175.59	7.731									0.742	*1*			0.742	*1*	2.378	*1*			2.378	*1*	3.018		3.094					
B-17H-6-W 30/32	175.69	7.734									0.729	*1*			0.729	*1*	2.492	*1*			2.492	*1*	3.132		3.144					
B-17H-6-W 40/42	175.79	7.737									0.553	*1*			0.553	*1*	2.682	*1*			2.682	*1*	3.322		3.178					
B-17H-6-W 50/52	175.89	7.741									0.714	*1*			0.714	*1*	2.531	*1*			2.531	*1*	3.171		3.148					
B-17H-6-W 60/62	175.99	7.744									0.724	*1*			0.724	*1*	2.343	*1*			2.343	*1*	2.983		3.107					
B-17H-6-W 70/72	176.09	7.747									0.684	*1*	0.562	*1*	0.623	*1*	2.435	*1*	2.427	*1*	2.431	*1*	3.071		3.113					
B-17H-6-W 80/82	176.19	7.751									0.768	*1*			0.768	*1*	2.607	*1*			2.607	*1*	3.247		3.151					
B-17H-6-W 94/96	176.33	7.755									0.731	*1*	0.615	*1*	0.673	*1*	2.562	*1*	2.532	*1*	2.547	*1*	3.187		3.156					
B-17H-6-W 102/104	176.41	7.758									0.787	*1*	0.621	*1*	0.704	*1*	2.492	*1*	2.448	*1*	2.470	*1*	3.110		3.113					
B-17H-6-W 110/112	176.49	7.761									0.673	*1*			0.673	*1*	2.399	*1*			2.399	*1*	3.039		3.051					
B-17H-6-W 121/123	176.60	7.764									0.738	*1*	0.523	*1*	0.631	*1*	2.358	*1*	2.338	*1*	2.348	*1*	2.988		3.015					
A-18H-2-W 60/62	176.68	7.763									0.703	*1*			0.703	*1*	2.332	*1*			2.332	*1*	2.972		3.017					
A-18H-2-W 73/75	176.81	7.767	2.767	2.770	2.769	-1.129	-1.364				0.279	*1*	-1.246		0.279	*1*	2.413	*1*			2.413	*1*	3.053		3.050					
A-18H-2-W 79/81	176.87	7.769									0.395	*1*			0.395	*1*	2.487	*1*			2.487	*1*	3.127		3.072					
A-18H-2-W 90/92	176.98	7.773									0.761	*1*			0.761	*1*	2.463	*1*			2.463	*1*	3.103		3.060					
A-18H-2-W 100/102	177.08	7.776									0.809	*1*			0.809	*1*	2.324	*1*			2.324	*1*	2.964		3.040					
A-18H-2-W 109/111	177.17	7.779									0.677	*1*			0.677	*1*	2.358	*1*			2.358	*1*	2.998		3.030					
A-18H-2-W 122/124	177.30	7.783	2.942		2.942	-1.465					0.424	*1*	-1.465		0.397	*1*	2.602	*1*	2.431	*1*	2.517	*1*	3.157		3.036					
A-18H-2-W 131/133	177.39	7.787									0.567	*1*			0.567	*1*	2.286	*1*			2.286	*1*	2.926		3.051					

A-18H-2-W 140/142	177.48	7.790									0.528 *1*		0.528 *1*	2.410 *1*		2.410 *1*	3.050	3.114
A-18H-2-W 149/151	177.57	7.793									0.655 *1*		0.655 *1*	2.640 *1*		2.640 *1*	3.280	3.216
A-18H-3-W 10/12	177.68	7.796									0.588 *1*		0.588 *1*	2.697 *1*		2.697 *1*	3.337	3.291
A-18H-3-W 22/24	177.80	7.800									0.526 *1*		0.526 *1*	2.761 *1*		2.761 *1*	3.401	3.294
A-18H-3-W 30/32	177.88	7.803									0.739 *1*		0.739 *1*	2.509 *1*		2.509 *1*	3.149	3.243
A-18H-3-W 38/40	177.96	7.806									0.821 *1*	0.748 *1*	0.785 *1*	2.657 *1*	2.451 *1*	2.554 *1*	3.194	3.208
A-18H-3-W 52/54	178.10	7.816									0.715 *1*		0.715 *1*	2.569 *1*		2.569 *1*	3.209	3.199
A-18H-3-W 60/62	178.18	7.819									0.441 *1*		0.441 *1*	2.559 *1*		2.559 *1*	3.199	3.206
A-18H-3-W 72/74	178.30	7.824	2.798			2.798	-0.860			-0.860	0.416 *1*		0.416 *1*	2.586 *1*		2.586 *1*	3.226	3.185
A-18H-3-W 79/81	178.37	7.827									0.641 *1*		0.641 *1*	2.545 *1*		2.545 *1*	3.185	3.132
A-18H-3-W 90/92	178.48	7.832									0.600 *1*		0.600 *1*	2.353 *1*		2.353 *1*	2.993	3.087
A-18H-3-W 100/102	178.58	7.836									0.466 *1*		0.466 *1*	2.361 *1*		2.361 *1*	3.001	3.104
A-18H-3-W 111/113	178.69	7.840									0.374 *1*		0.374 *1*	2.593 *1*		2.593 *1*	3.233	3.176
A-18H-3-W 122/124	178.80	7.845	2.333			2.333	-1.359			-1.359	0.153 *1*	0.214 *1*	0.183 *1*	2.649 *1*	2.722 *1*	2.686 *1*	3.326	3.230
A-18H-3-W 130/132	178.88	7.848									0.277 *1*		0.277 *1*	2.589 *1*		2.589 *1*	3.229	3.209
A-18H-3-W 140/142	178.98	7.853									0.190 *1*		0.190 *1*	2.496 *1*		2.496 *1*	3.136	3.123
A-18H-4-W 0/2	179.08	7.857									0.229 *1*		0.229 *1*	2.382 *1*		2.382 *1*	3.022	3.044
A-18H-4-W 10/12	179.18	7.860									0.106 *1*		0.106 *1*	2.225 *1*		2.225 *1*	2.865	3.006
A-18H-4-W 22/24	179.30	7.864	2.204			2.204	-0.922			-0.922	-0.309 *1*		-0.309 *1*	2.495 *1*		2.495 *1*	3.135	3.022
A-18H-4-W 29/31	179.37	7.866									0.036 *1*		0.036 *1*	2.368 *1*		2.368 *1*	3.008	3.052
A-18H-4-W 43/45	179.51	7.871									0.023 *1*	0.365 *1*	0.194 *1*	2.292 *1*	2.523 *1*	2.408 *1*	3.048	3.095
A-18H-4-W 50/52	179.58	7.873									0.444 *1*		0.444 *1*	2.565 *1*		2.565 *1*	3.205	3.149
A-18H-4-W 60/62	179.68	7.877									0.317 *1*		0.317 *1*	2.519 *1*		2.519 *1*	3.159	3.200
A-18H-4-W 72/74	179.80	7.881	2.306			2.306	-1.124			-1.124	0.201 *1*		0.201 *1*	2.677 *1*		2.677 *1*	3.317	3.219
A-18H-4-W 80/82	179.88	7.878									0.364 *1*		0.364 *1*	2.564 *1*		2.564 *1*	3.204	3.198
A-18H-4-W 93/95	180.01	7.882									0.240 *1*		0.240 *1*	2.449 *1*		2.449 *1*	3.089	3.176
A-18H-4-W 100/102	180.08	7.884									0.184 *1*		0.184 *1*	2.559 *1*		2.559 *1*	3.199	3.174
A-18H-4-W 109/111	180.17	7.886									0.271 *1*		0.271 *1*	2.565 *1*		2.565 *1*	3.205	3.183
A-18H-4-W 122/124	180.30	7.890	2.195	2.430		2.313	-0.733	-0.989		-0.861	0.435 *1*		0.435 *1*	2.554 *1*		2.554 *1*	3.194	3.186
A-18H-4-W 130/132	180.38	7.892									0.540 *1*		0.540 *1*	2.504 *1*		2.504 *1*	3.144	3.178

A-18H-4-W 140/142	180.48	7.894								0.525	*1*			0.525	*1*	2.558	*1*			2.558	*1*	3.198	3.184
A-18H-4-W 149/151	180.57	7.897								0.121	*1*			0.121	*1*	2.540	*1*			2.540	*1*	3.180	3.184
A-18H-5-W 10/12	180.68	7.900								0.417	*1*			0.417	*1*	2.589	*1*			2.589	*1*	3.229	3.170
A-18H-5-W 22/24	180.80	7.903	2.306		-1.118		-1.118	0.192	*1*			0.192	*1*	2.467	*1*			2.467	*1*	3.107	3.186
A-18H-5-W 72/74	181.30	7.915	2.685		-1.116		-1.116	0.359	*1*			0.359	*1*	2.433	*1*			2.433	*1*	3.073	3.249
A-18H-5-W 122/124	181.80	7.928						0.930	*1*			0.930	*1*	2.982	*1*			2.982	*1*	3.622	3.335
A-18H-5-W 130/132	181.88	7.930	2.217		-0.819		-0.819														
B-18H-3-W 148/150	182.64	7.949	2.680		-1.306		-1.306	0.532	*1*	0.488	*1*	0.510	*1*	2.644	*1*	2.700	*1*	2.672	*1*	3.312	3.336
B-18H-4-W 20/22	182.86	7.954	2.609		-1.151		-1.151	0.484	*1*			0.484	*1*	2.625	*1*			2.625	*1*	3.265	3.308
B-18H-4-W 60/62	183.26	7.964	2.369		-1.292		-1.292														
B-18H-4-W 70/72	183.36	7.967						0.627	*1*			0.627	*1*	2.531	*1*			2.531	*1*	3.171	3.270
B-18H-4-W 120/122	183.86	7.979	2.626		-1.144		-1.144	0.785	*1*			0.785	*1*	2.808	*1*			2.808	*1*	3.448	3.270
B-18H-5-W 20/22	184.36	7.992	2.152		-0.544		-0.544	0.684	*1*			0.684	*1*	2.514	*1*			2.514	*1*	3.154	3.252
B-18H-5-W 70/72	184.86	8.004	2.661		-1.133		-1.133	0.815	*1*			0.815	*1*	2.544	*1*			2.544	*1*	3.184	3.216
B-18H-5-W 120/122	185.36	8.017	2.259		-1.203		-1.203	0.542	*1*			0.542	*1*	2.717	*1*			2.717	*1*	3.357	3.167
B-18H-5-W 130/132	185.46	8.020	2.093		-1.594		-1.594														
B-18H-6-W 20/22	185.86	8.030	2.265		-0.656		-0.656	0.553	*1*			0.553	*1*	2.260	*1*			2.260	*1*	2.900	3.136
A-19H-1-W 147/149	186.32	8.041	2.157		-1.006		-1.006	0.646	*1*			0.646	*1*	2.488	*1*			2.488	*1*	3.128	
B-18H-6-W 70/72	186.36	8.042	1.657		-0.691		-0.691	0.791	*1*	0.361	*1*	0.576	*1*	2.783	*1*	2.682	*1*	2.733	*1*	3.373	

A.2. Benthic Foraminiferal Scanning Electron Images

Larger versions of the benthic foraminifera SEM images from Figure 3.5.

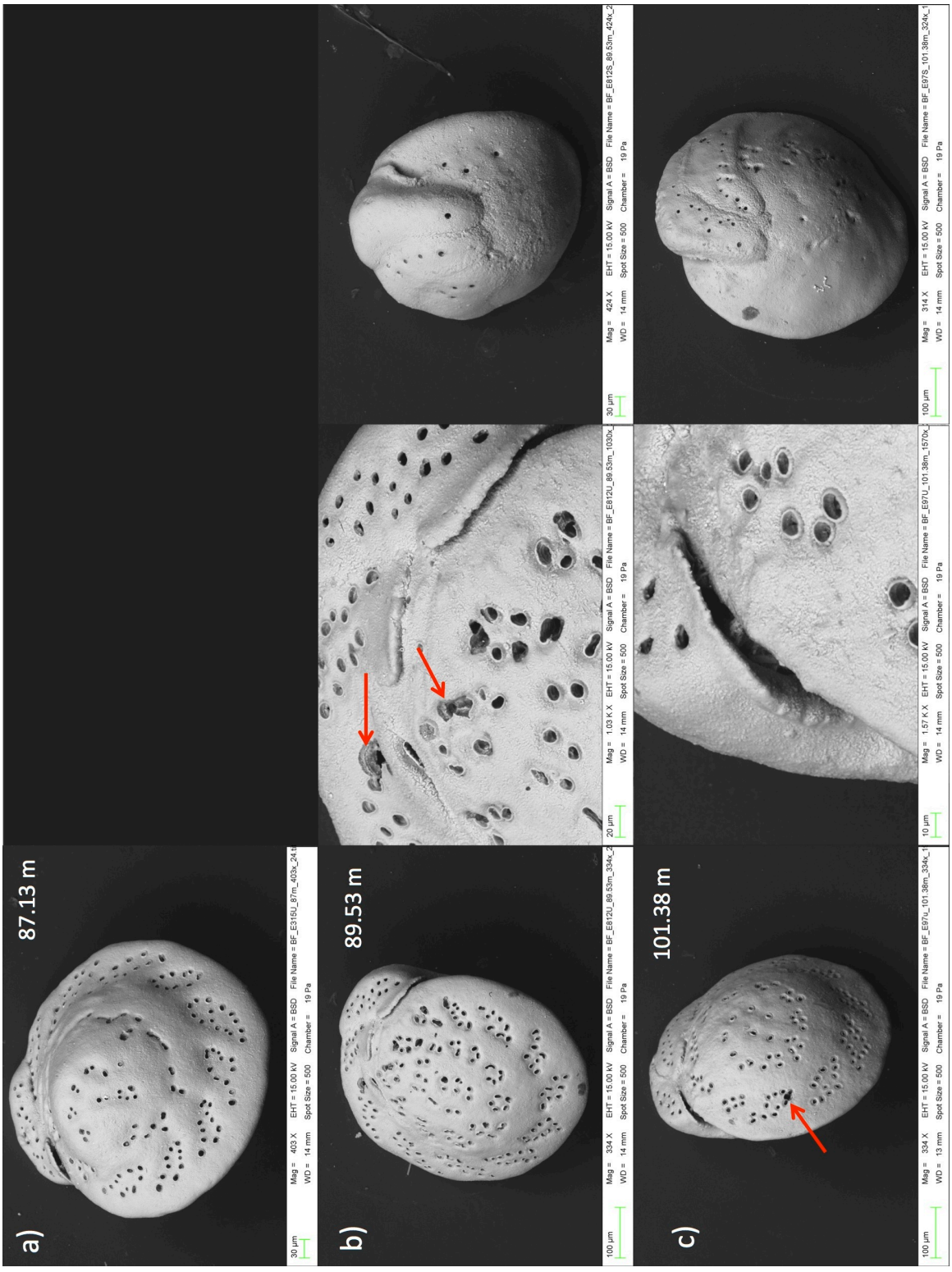

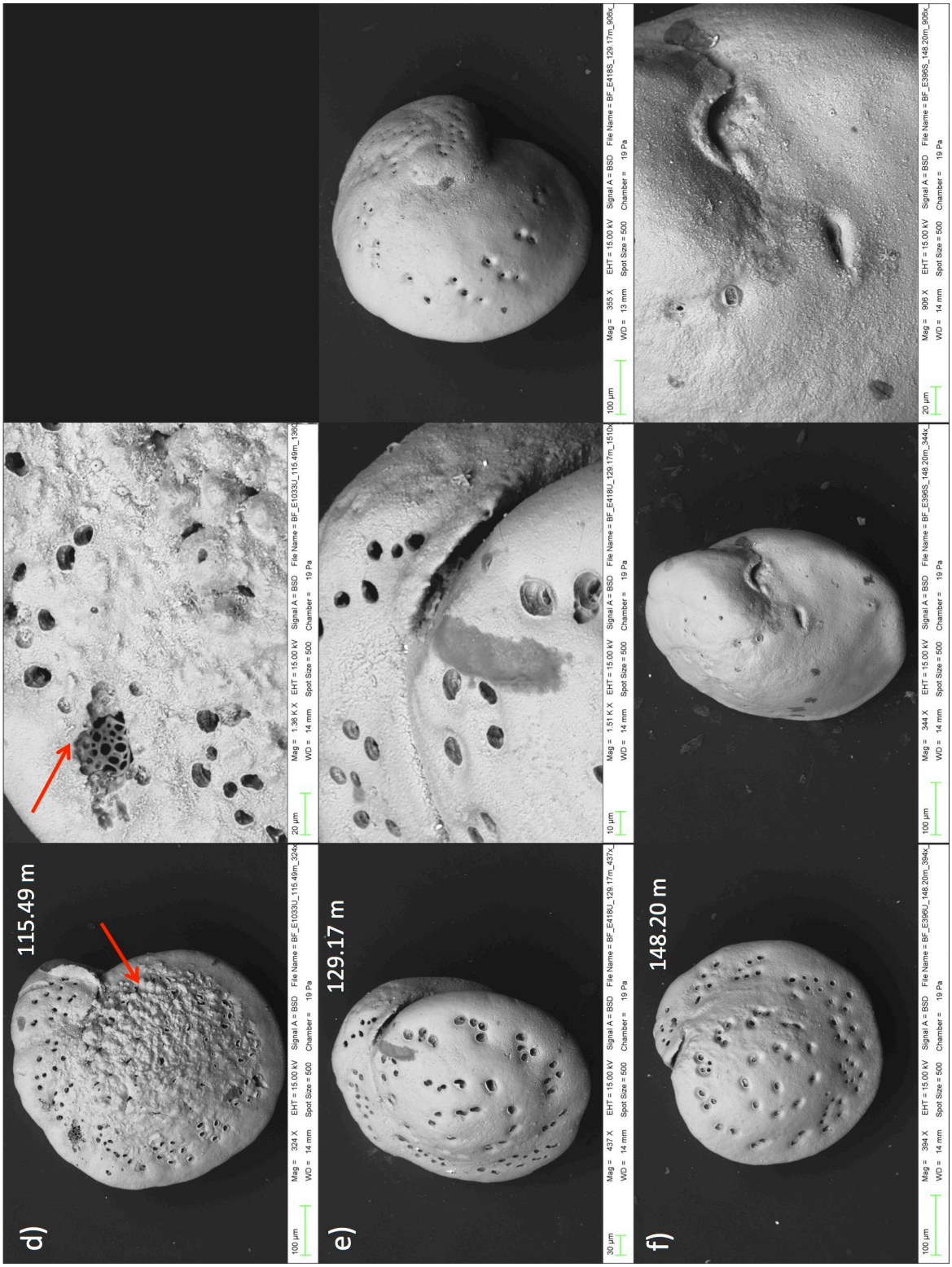
d)
115.49 m
e)
129.17 m
f)
148.20 m

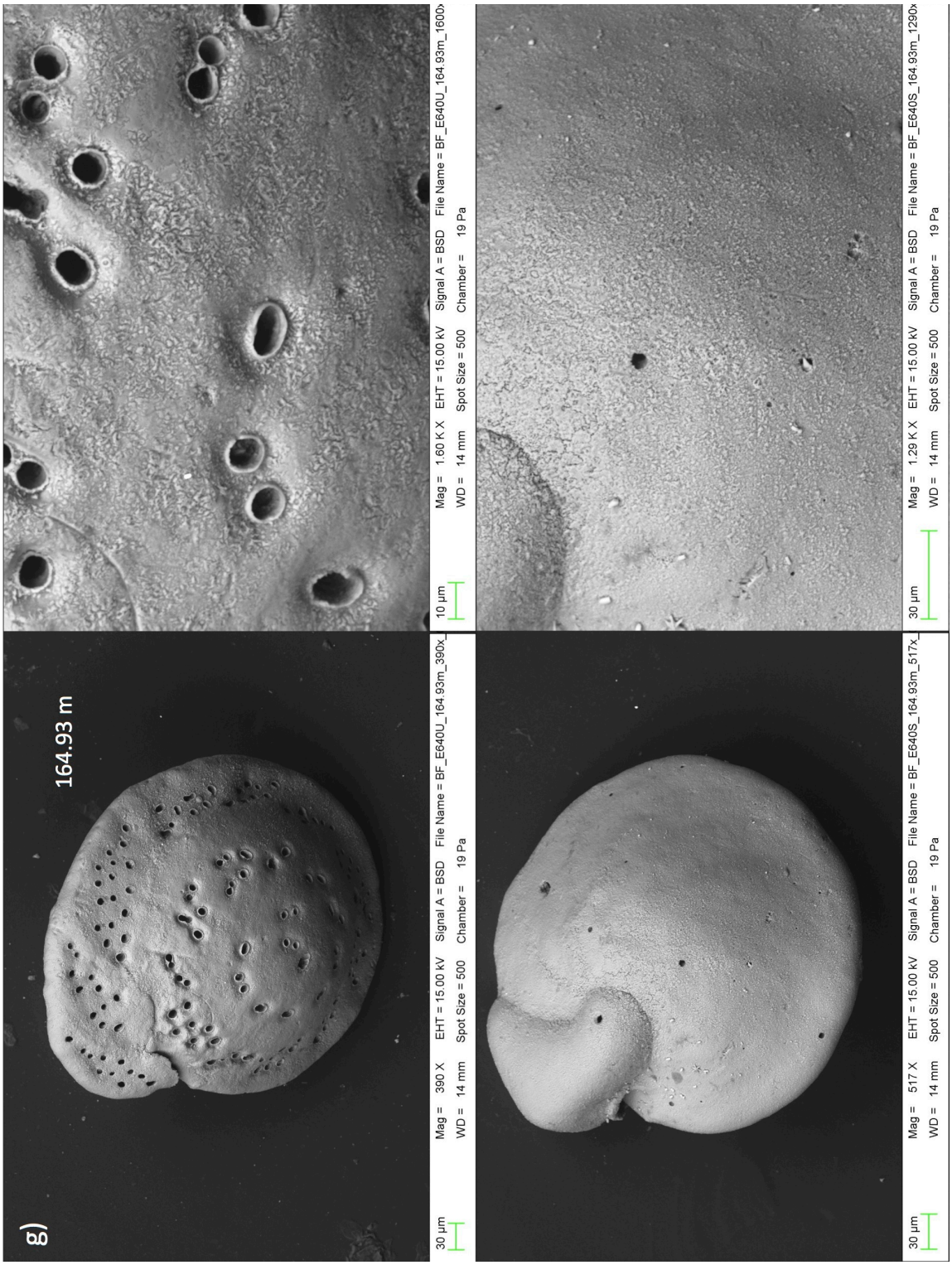
g)
164.93 m
30 µm
Mag = 390 X EHT = 15.00 kV Signal A = BSD File Name = BF_E640U_164.93m_390x_
WD = 14 mm Spot Size = 500 Chamber = 19 Pa
30 µm
Mag = 517 X EHT = 15.00 kV Signal A = BSD File Name = BF_E640S_164.93m_517x_
WD = 14 mm Spot Size = 500 Chamber = 19 Pa
10 µm
Mag = 1.60 K X EHT = 15.00 kV Signal A = BSD File Name = BF_E640U_164.93m_1600
WD = 14 mm Spot Size = 500 Chamber = 19 Pa
30 µm
Mag = 1.29 K X EHT = 15.00 kV Signal A = BSD File Name = BF_E640S_164.93m_1290
WD = 14 mm Spot Size = 500 Chamber = 19 Pa

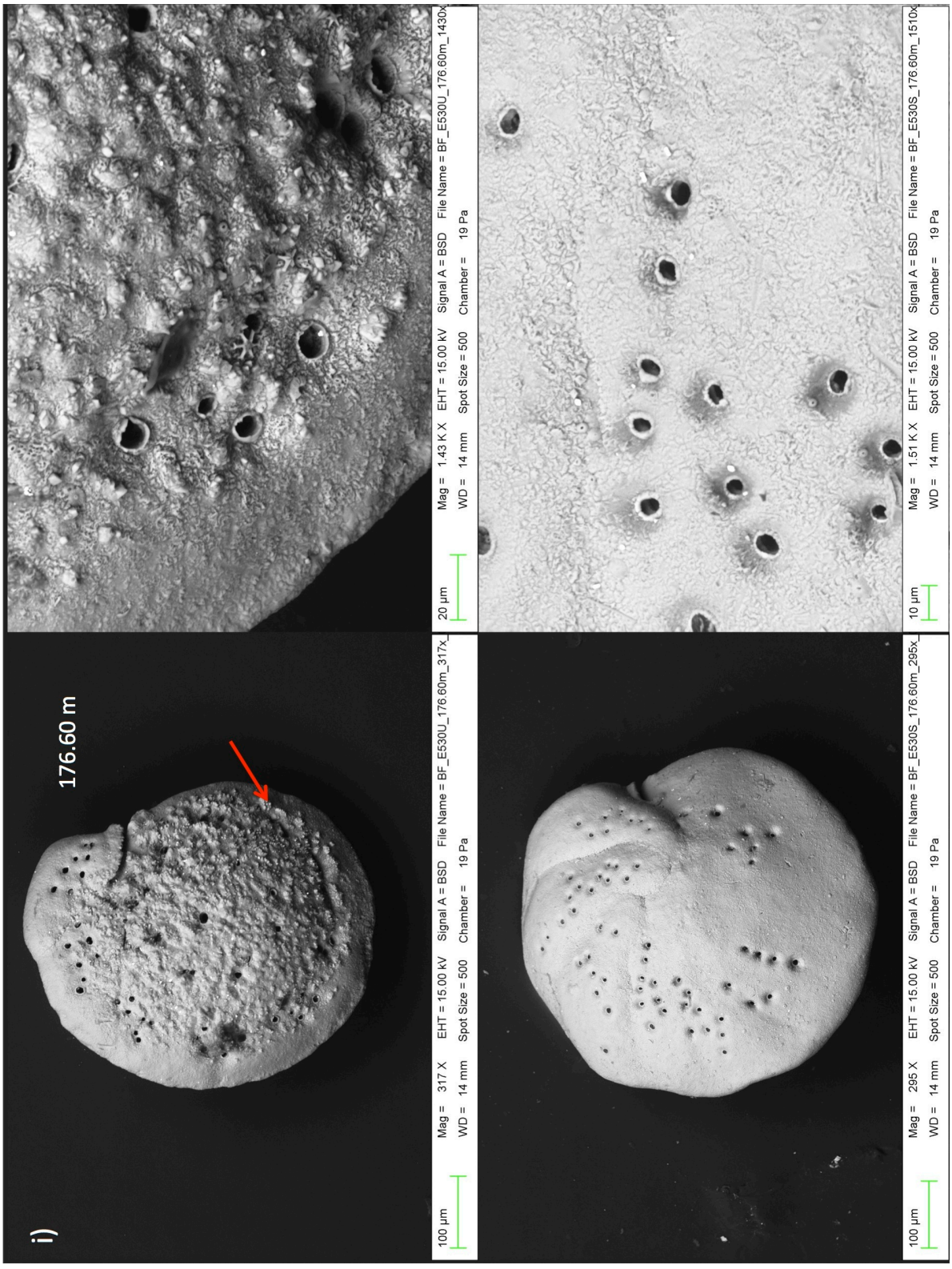
i)
176.60 m
100 µm
Mag = 317 X EHT = 15.00 kV Signal A = BSD File Name = BF_E530U_176.60m_317x_
WD = 14 mm Spot Size = 500 Chamber = 19 Pa
20 µm
Mag = 1.43 K X EHT = 15.00 kV Signal A = BSD File Name = BF_E530U_176.60m_1430x
WD = 14 mm Spot Size = 500 Chamber = 19 Pa
100 µm
Mag = 295 X EHT = 15.00 kV Signal A = BSD File Name = BF_E530S_176.60m_295x_
WD = 14 mm Spot Size = 500 Chamber = 19 Pa
10 µm
Mag = 1.51 K X EHT = 15.00 kV Signal A = BSD File Name = BF_E530S_176.60m_1510x
WD = 14 mm Spot Size = 500 Chamber = 19 Pa

A.3. Planktic Foraminiferal Scanning Electron Images

Larger versions of the planktic foraminifera SEM images from Figure 3.6 and 3.7.

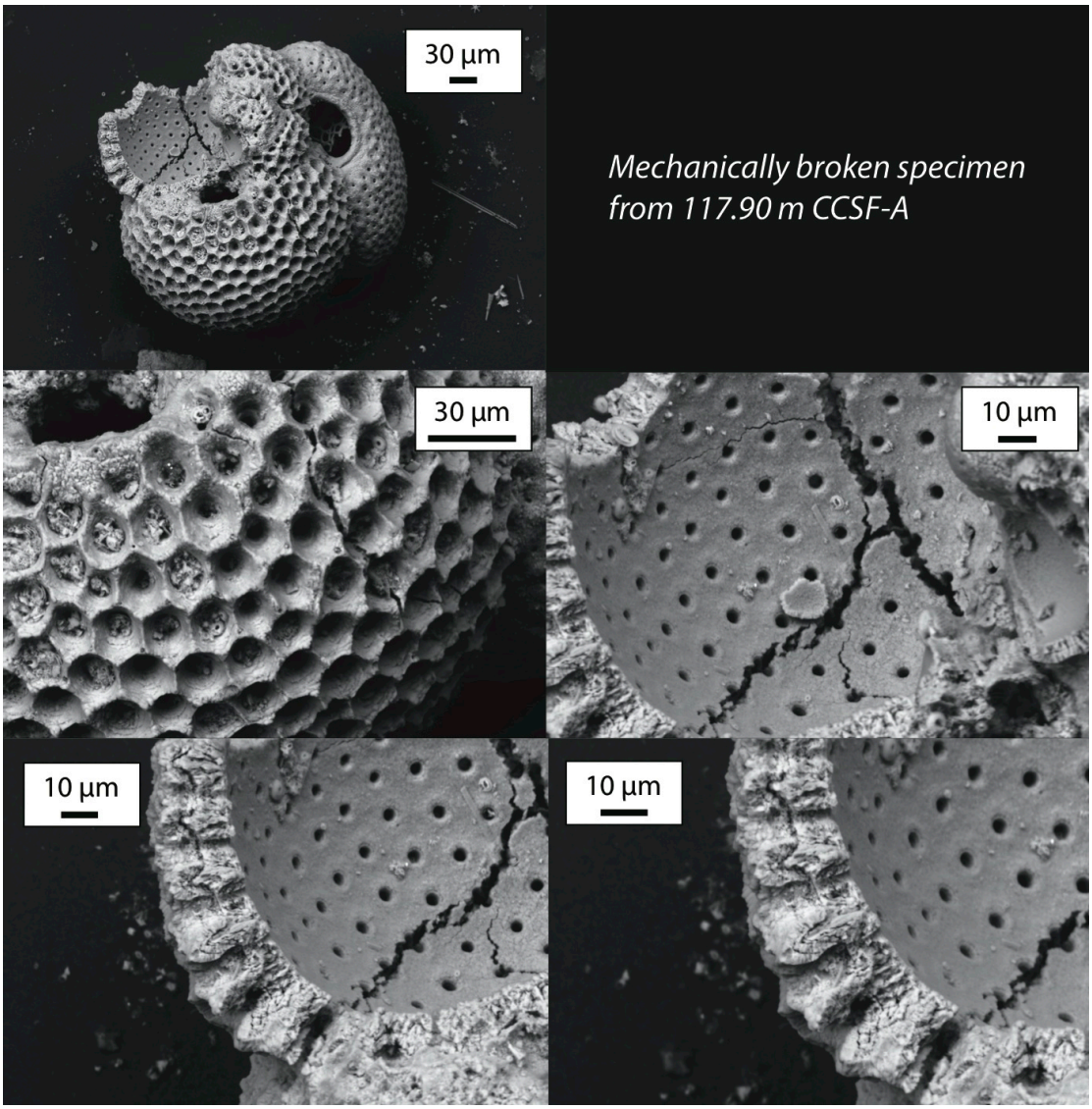

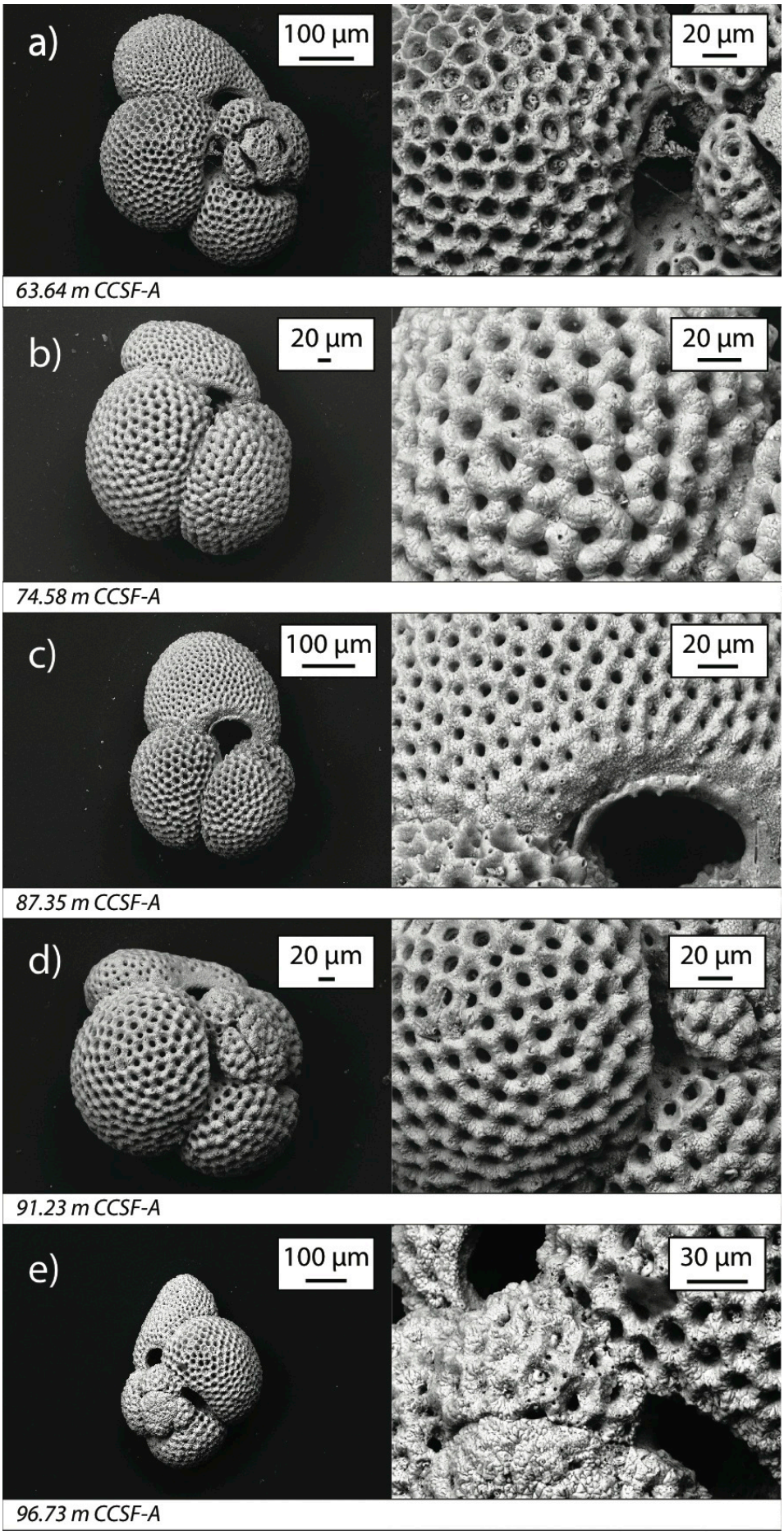
a)
100 µm
20 µm
63.64 m CCSF-A
b)
20 µm
20 µm
74.58 m CCSF-A
c)
100 µm
20 µm
87.35 m CCSF-A
d)
20 µm
20 µm
91.23 m CCSF-A
e)
100 µm
30 µm
96.73 m CCSF-A

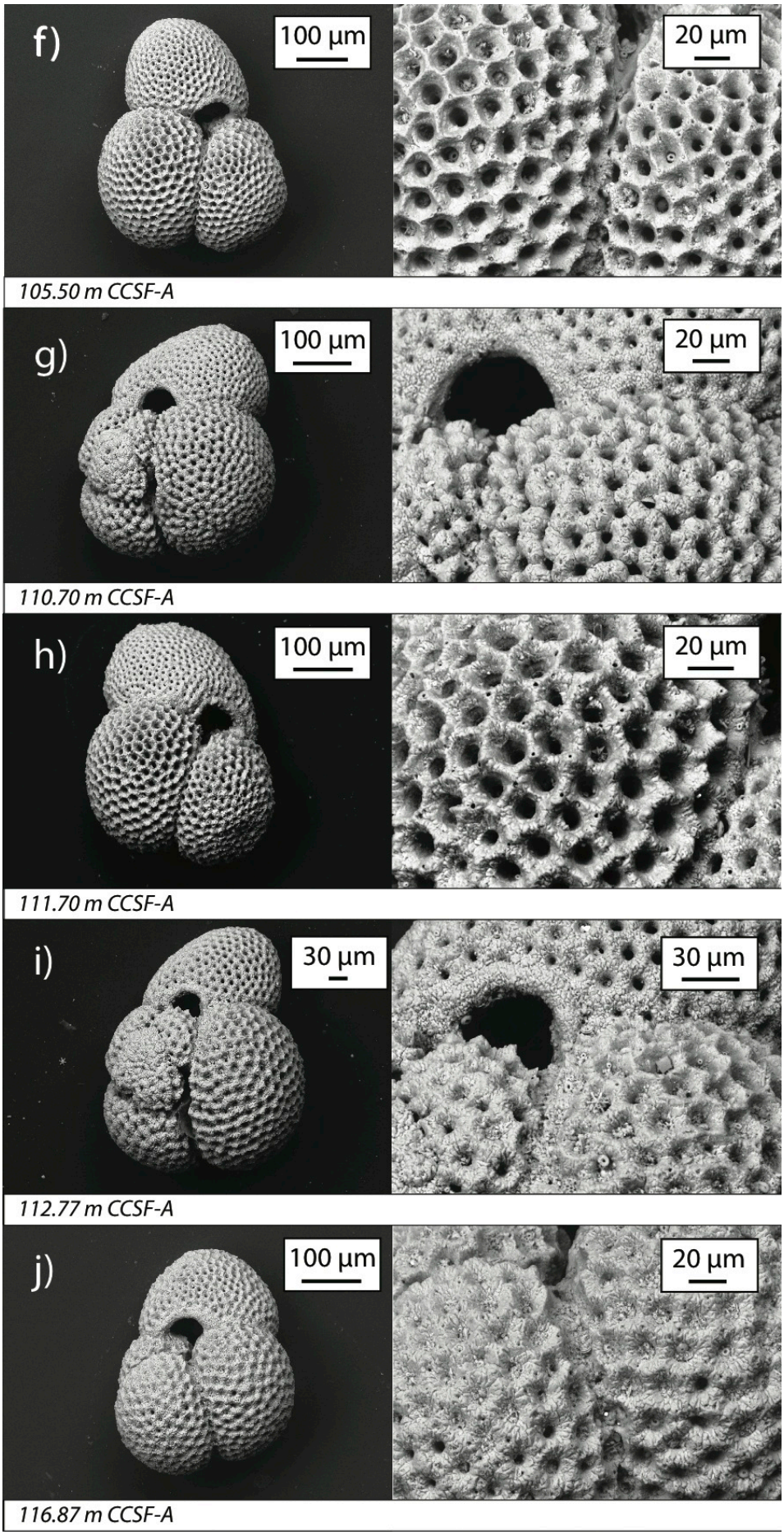
f)
100 µm
20 µm
105.50 m CCSF-A
g)
100 µm
20 µm
110.70 m CCSF-A
h)
100 µm
20 µm
111.70 m CCSF-A
i)
30 µm
30 µm
112.77 m CCSF-A
j)
100 µm
20 µm
116.87 m CCSF-A

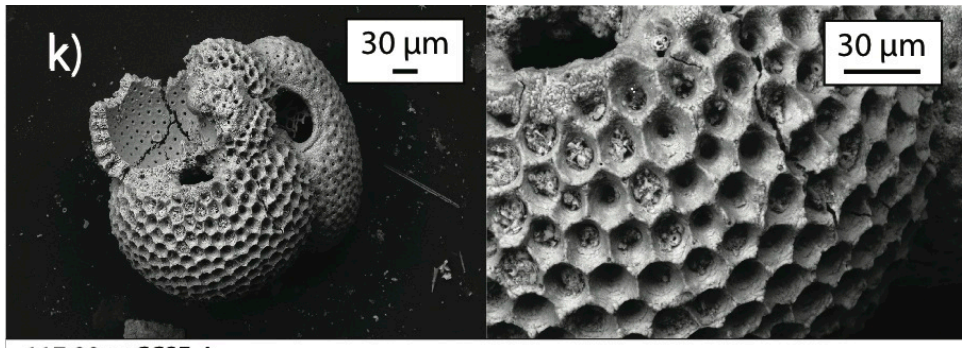

117.90 m CCSF-A

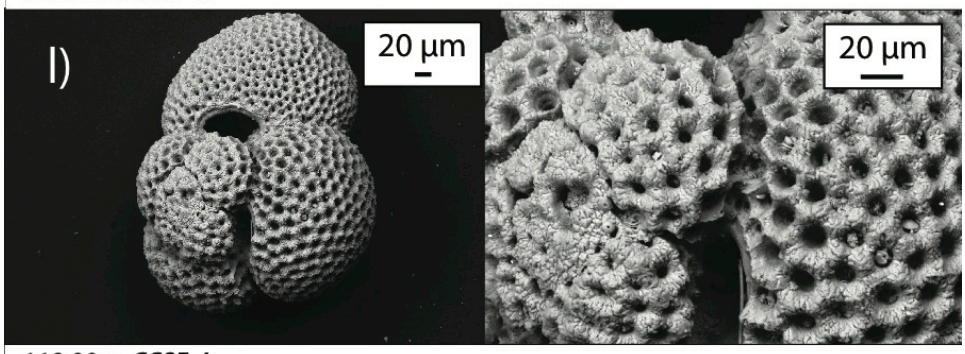

118.90 m CCSF-A

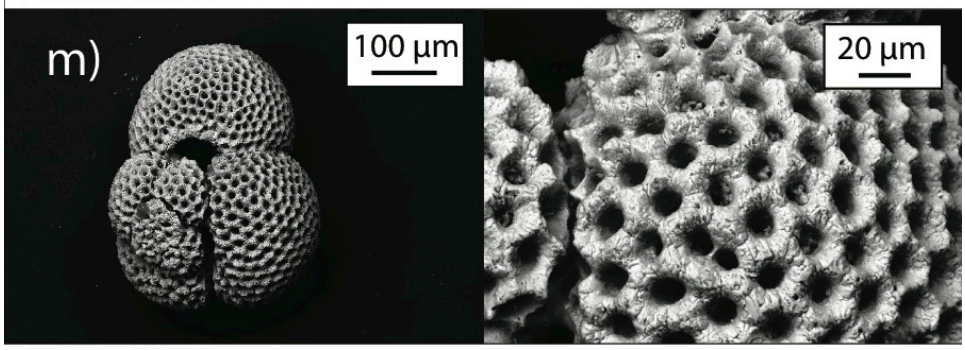

125.74 m CCSF-A

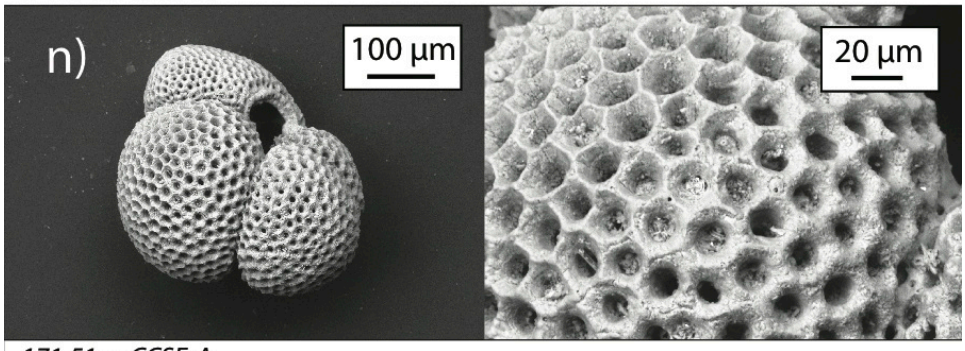

171.51 m CCSF-A

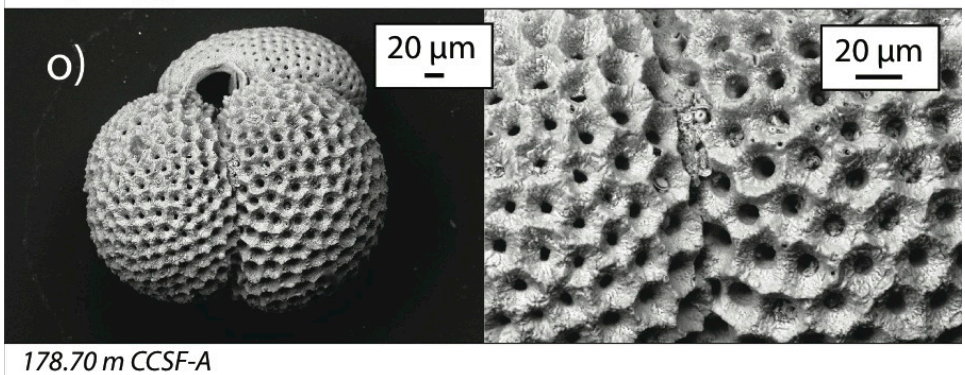

178.70 m CCSF-A

A.4. Data Compilation Site U1338

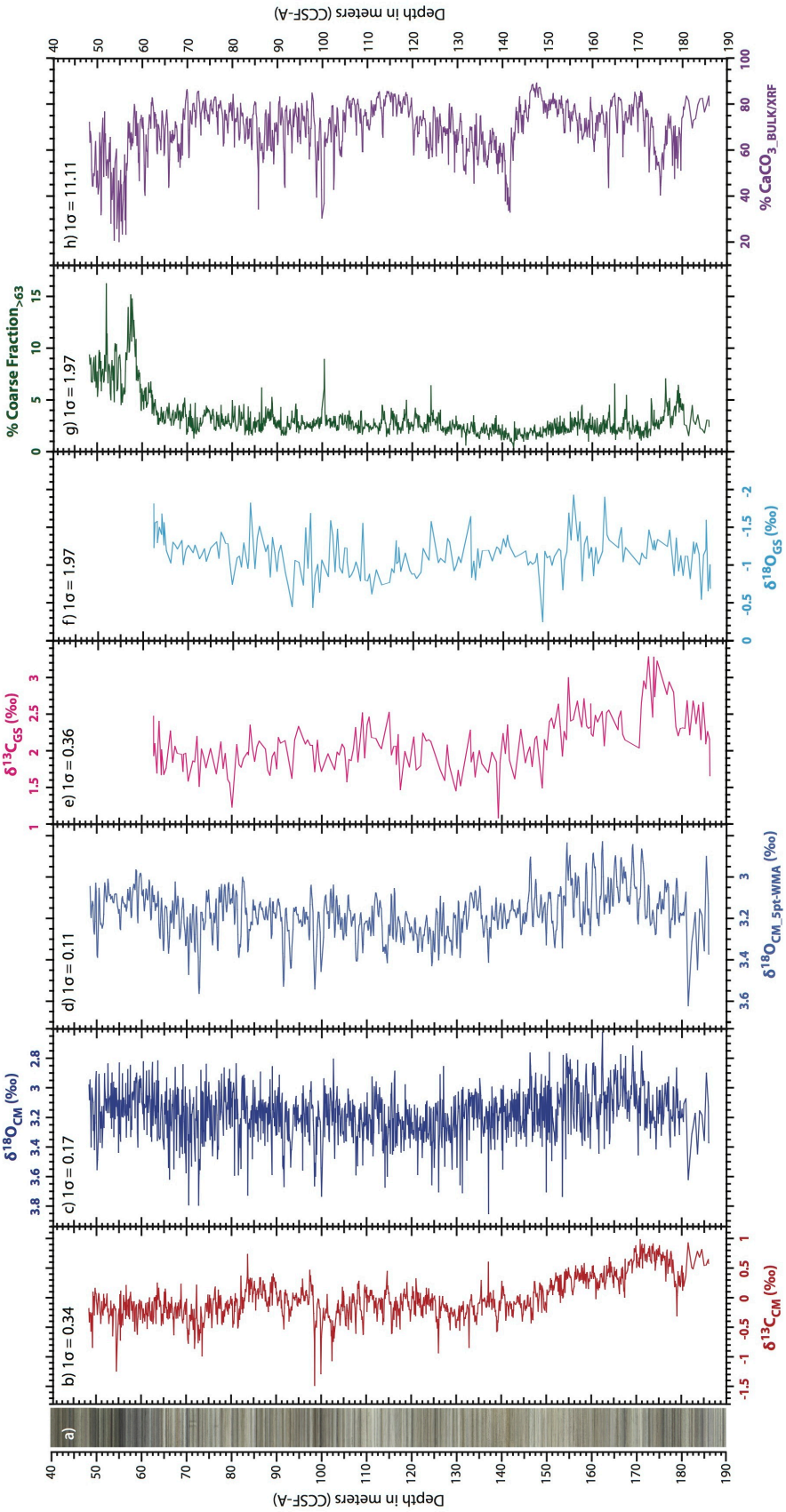

Overview of benthic foraminiferal stable isotopes and sediment properties from Site U1338. All data is plotted against depth in meters CCSF-A. 1σ is 1 standard deviation.

a) Core photo of the spliced section of U1338 (Wilkens et al., 2012).

b) $\delta^{13}C_{CM}$ record from Site U1338. Samples are taken every 10 cm between 48 and 181 m CCSF-A. Below 181 m samples were taken every 50 cm. Average = -0.01 ‰, 1σ = 0.34 ‰.

c) $\delta^{18}O_{CM}$ record from Site U1338. Samples are taken every 10 cm between 48 and 181 m CCSF-A. Below 181 m samples were taken every 50 cm. Average = 3.17 ‰, 1σ = 0.17 ‰.

a) 5 point weighted moving average (5pt WMA) of the $\delta^{18}O_{CM}$ record shown in b). The following weighting was applied to smooth the record = 1st point = 30%; 2nd point = 70%; 3rd point = 100%; 4th point = 70%; 5th point = 30%. Average = 3.17 ‰, 1σ = 0.11 ‰.

b) Planktic $\delta^{13}C_{GS}$ record from Site U1338. Samples are taken approximately every 50 cm between 62 and 186 m CCSF-A. Average = 2.09 ‰, 1σ = 0.36 ‰.

c) Planktic $\delta^{18}O_{GS}$ record from Site U1338. Samples are taken approximately every 50 cm between 62 and 186 m CCSF-A. Average = -1.14 ‰, 1σ = 0.26 ‰.

d) % coarse fraction (> 63 μm; $\%CF_{>63}$) record from Site U1338. Samples are taken every 10 cm between 48 and 181 m CCSF-A. Below 181 m samples were taken every 50 cm. Average = 3.23 %, 1σ = 1.97 %.

e) Carbonate content (weight% $CaCO_{3\_BULK/XRF}$) record from Site U1338. This record is a composite of $CaCO_3$ estimates from XRF measurements, and discrete measurements of $CaCO_3$ on bulk sediment samples (Lyle et al., 2012 and Lyle and Bachman, 2012 respectively). Data points were resamples from a larger dataset, at the same frequency as the original isotope records. Average = 69.78 %, 1σ = 11.11 %.

Appendix B

B.1. Second Generation G2 Match Age Model

Second generation G2 Match age model displayed as the original depth in m CCSF-A from Site U1338 and the equivalent 982 age from Hodell et al., 2001 and Hodell and Venz-Curtis, 2006.

Second Generation G2 Match Age Model	
U1338 depth *m CCSF-A*	***982 Age*** *kyr*
48.73	3550.00
48.86	3558.81
49.12	3580.84
49.38	3602.87
49.51	3611.68
49.65	3620.50
49.78	3629.31
49.91	3638.12
50.17	3651.34
50.30	3655.74
50.44	3660.15
50.57	3664.55
50.70	3668.96
50.83	3673.37
51.49	3690.99
52.14	3708.61
52.28	3713.02
52.41	3717.43
52.93	3739.46
53.46	3761.49
53.85	3779.11
54.12	3792.33
54.51	3814.36
54.64	3823.17
54.77	3831.98
55.04	3854.01
55.30	3876.04
55.56	3898.07
55.83	3920.10
56.09	3942.13
56.35	3964.16
56.48	3972.97
56.88	3995.00
57.27	4017.03
57.67	4039.06
57.80	4047.87
57.93	4056.68
58.32	4078.71
58.72	4100.74
59.11	4122.77
59.51	4144.80
59.90	4166.83
60.03	4175.64
60.17	4184.46
60.43	4206.49
60.69	4228.51
60.95	4250.54
61.22	4272.57
61.48	4294.60
61.74	4316.63
62.01	4338.66
62.14	4347.48
62.53	4369.50
62.79	4382.72
63.19	4400.35
63.72	4422.38
63.85	4426.78
63.98	4431.19
64.11	4435.59
64.77	4453.22
65.42	4470.84
66.08	4488.47
66.21	4492.87
66.74	4514.90
67.00	4528.12
67.13	4536.93
67.40	4558.96
67.66	4580.99
67.92	4603.02
68.19	4625.05
68.32	4633.86
68.45	4642.67
68.58	4651.49
68.71	4660.30
68.97	4682.33
69.24	4704.36

69.50	4726.39
69.76	4748.42
70.03	4770.45
70.42	4792.48
70.82	4814.50
71.08	4827.72
71.34	4840.94
71.60	4854.16
72.00	4876.19
72.26	4889.41
72.39	4893.81
72.52	4898.22
72.66	4902.62
72.79	4907.03
73.31	4929.06
73.45	4933.47
73.58	4937.87
73.71	4942.28
73.84	4946.68
73.97	4951.09
74.10	4955.50
74.23	4959.90
74.76	4981.93
75.15	4999.55
75.55	5017.18
75.81	5030.40
75.94	5039.21
76.21	5061.24
76.47	5083.27
76.73	5105.30
76.86	5114.11
77.00	5122.92
77.39	5144.95
77.78	5166.98
78.18	5189.01
78.44	5202.23
78.84	5219.85
78.97	5224.26
79.63	5241.88
80.15	5255.10
80.68	5268.32
81.07	5277.13
81.33	5281.53
81.73	5285.94
82.12	5290.35
82.39	5294.75
83.04	5307.97
83.70	5321.19
84.10	5330.00
84.23	5334.41
84.75	5356.44
85.28	5378.47
85.41	5382.87
86.07	5400.50
86.46	5409.31
87.12	5422.52
87.78	5435.74
88.43	5448.96
89.09	5462.18
89.75	5475.40
90.41	5488.61
90.67	5493.02
90.93	5497.43
91.20	5501.83
91.85	5515.05
92.25	5523.86
92.64	5532.67
93.04	5541.49
93.43	5550.30
93.96	5563.51
94.09	5567.92
94.22	5572.33
94.35	5576.73
94.48	5581.14
94.61	5585.54
95.14	5607.57
95.67	5629.60
96.06	5647.23
96.32	5660.45
96.72	5682.48
96.98	5695.69
97.38	5713.32
97.51	5717.72
97.64	5722.13
97.77	5726.53
97.90	5730.94
98.03	5735.35
98.16	5739.75
98.30	5744.16
98.43	5748.56
98.56	5752.97
99.08	5775.00
99.22	5779.41
99.61	5788.22
100.27	5797.03
100.93	5805.84
101.58	5814.65
102.24	5823.47
102.50	5827.87
102.90	5836.68
103.03	5841.09
103.42	5858.71
103.69	5871.93
103.82	5880.74
104.08	5902.77
104.34	5924.80
104.61	5946.83
104.87	5968.86

105.00	5977.67
105.13	5986.49
105.53	6004.11
105.66	6008.51
105.79	6012.92
105.92	6017.33
106.05	6021.73
106.45	6039.36
106.71	6052.57
106.97	6065.79
107.11	6070.20
107.37	6074.60
107.63	6079.01
107.89	6083.42
108.29	6092.23
108.82	6105.45
109.34	6118.66
109.74	6127.48
110.39	6140.69
110.66	6145.10
110.92	6149.50
111.18	6153.91
111.44	6158.32
111.71	6162.72
111.97	6167.13
112.23	6171.53
112.50	6175.94
113.15	6189.16
113.42	6193.56
114.07	6202.38
114.73	6211.19
114.99	6215.59
115.39	6224.41
115.52	6228.81
115.65	6233.22
116.05	6250.84
116.44	6268.47
116.84	6286.09
117.36	6308.12
117.49	6312.52
117.62	6316.93
118.28	6334.55
118.41	6338.96
118.68	6352.18
118.81	6360.99
118.94	6369.80
119.07	6378.61
119.20	6387.43
119.60	6409.46
119.99	6431.49
120.25	6444.70
120.39	6449.11
121.04	6466.73
121.57	6479.95

122.10	6493.17
122.62	6506.39
123.02	6515.20
123.41	6524.01
124.07	6537.23
124.72	6546.04
125.38	6554.85
126.04	6563.66
126.70	6572.48
127.35	6581.29
128.01	6590.10
128.27	6594.50
128.67	6603.32
129.20	6616.53
129.33	6620.94
129.46	6625.35
129.98	6647.38
130.12	6651.78
130.64	6665.00
131.30	6678.22
131.56	6682.62
132.22	6691.44
132.88	6700.25
133.14	6704.65
133.80	6717.87
134.19	6726.68
134.72	6739.90
134.85	6744.31
134.98	6748.71
135.11	6753.12
135.24	6757.52
135.38	6761.93
135.51	6766.34
135.64	6770.74
136.30	6788.37
136.69	6797.18
137.35	6810.40
137.74	6819.21
138.14	6828.02
138.66	6841.24
139.19	6854.46
139.58	6863.27
139.85	6867.67
140.50	6876.49
141.16	6885.30
141.42	6889.70
141.69	6894.11
142.34	6902.92
143.00	6911.73
143.66	6920.54
143.92	6924.95
144.18	6929.36
144.45	6933.76
144.71	6938.17

145.37	6946.98
145.63	6951.39
146.29	6964.60
146.95	6977.82
147.34	6986.63
147.73	6995.45
148.26	7008.66
148.79	7021.88
149.31	7035.10
149.84	7048.32
150.50	7065.94
150.63	7070.35
150.76	7074.75
150.89	7079.16
151.02	7083.56
151.55	7105.59
152.07	7127.62
152.60	7149.65
152.73	7154.06
152.86	7158.47
152.99	7162.87
153.65	7180.50
154.05	7189.31
154.31	7193.71
154.97	7202.52
155.62	7211.34
155.89	7215.74
156.28	7224.55
156.81	7237.77
157.20	7246.58
157.86	7259.80
158.52	7273.02
159.17	7286.24
159.57	7295.05
160.09	7308.27
160.49	7317.08
161.15	7330.30
161.80	7343.51
162.46	7356.73
163.12	7365.54
163.78	7374.36
164.43	7383.17
165.09	7391.98
165.75	7400.79
166.01	7405.20
166.67	7418.42
166.93	7422.82
167.19	7427.23

167.46	7431.63
167.85	7440.45
167.98	7444.85
168.25	7458.07
168.51	7480.10
168.77	7502.13
169.04	7515.35
169.17	7519.75
169.56	7528.56
169.96	7537.38
170.35	7546.19
170.74	7555.00
171.14	7563.81
171.53	7572.62
171.93	7581.44
172.45	7594.65
172.59	7599.06
172.98	7616.68
173.24	7629.90
173.64	7651.93
173.90	7665.15
174.29	7682.77
174.82	7704.80
174.95	7709.21
175.08	7713.61
175.22	7718.02
175.35	7722.43
175.48	7726.83
175.61	7731.24
175.74	7735.64
175.87	7740.05
176.00	7744.46
176.66	7762.08
176.79	7766.48
176.92	7770.89
177.06	7775.30
177.19	7779.70
177.32	7784.11
177.45	7788.51
177.98	7810.54
178.50	7832.57
179.03	7854.60
179.16	7859.01
179.82	7876.63
180.47	7894.26
181.00	7907.48

B.2. First Generation G1 U1338 and 982 benthic foraminiferal $\delta^{18}O$ and $\delta^{13}C$ alignment

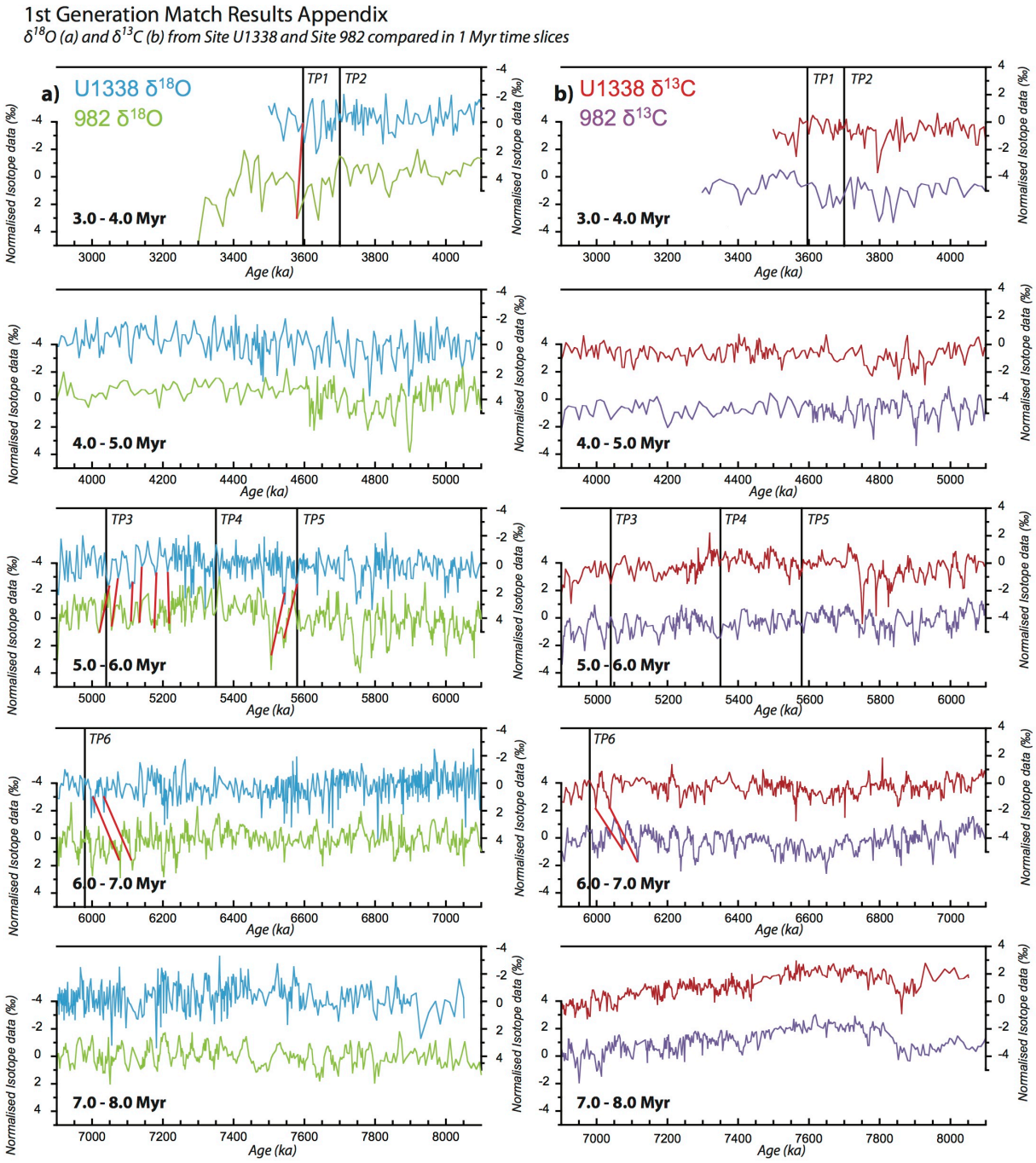

Overview of the benthic $\delta^{18}O$ (a) and $\delta^{13}C$ (b) from Sites U1338 and 982 aligned using the first-generation Match alignment to evaluate how well the records align in terms of short-term fluctuations. The positions of the tie points used to guide the alignment are highlighted with black lines.

Generally, the alignment is good throughout most of the record. The exceptions are highlighted using red lines. Here the location of TP1, 3, 5 and 6 respectively have seemingly forced an offset between isotopic events of a similar nature.

B.3. Second Generation G2 U1338 and 982 benthic foraminiferal $\delta^{18}O$ and $\delta^{13}C$ alignment

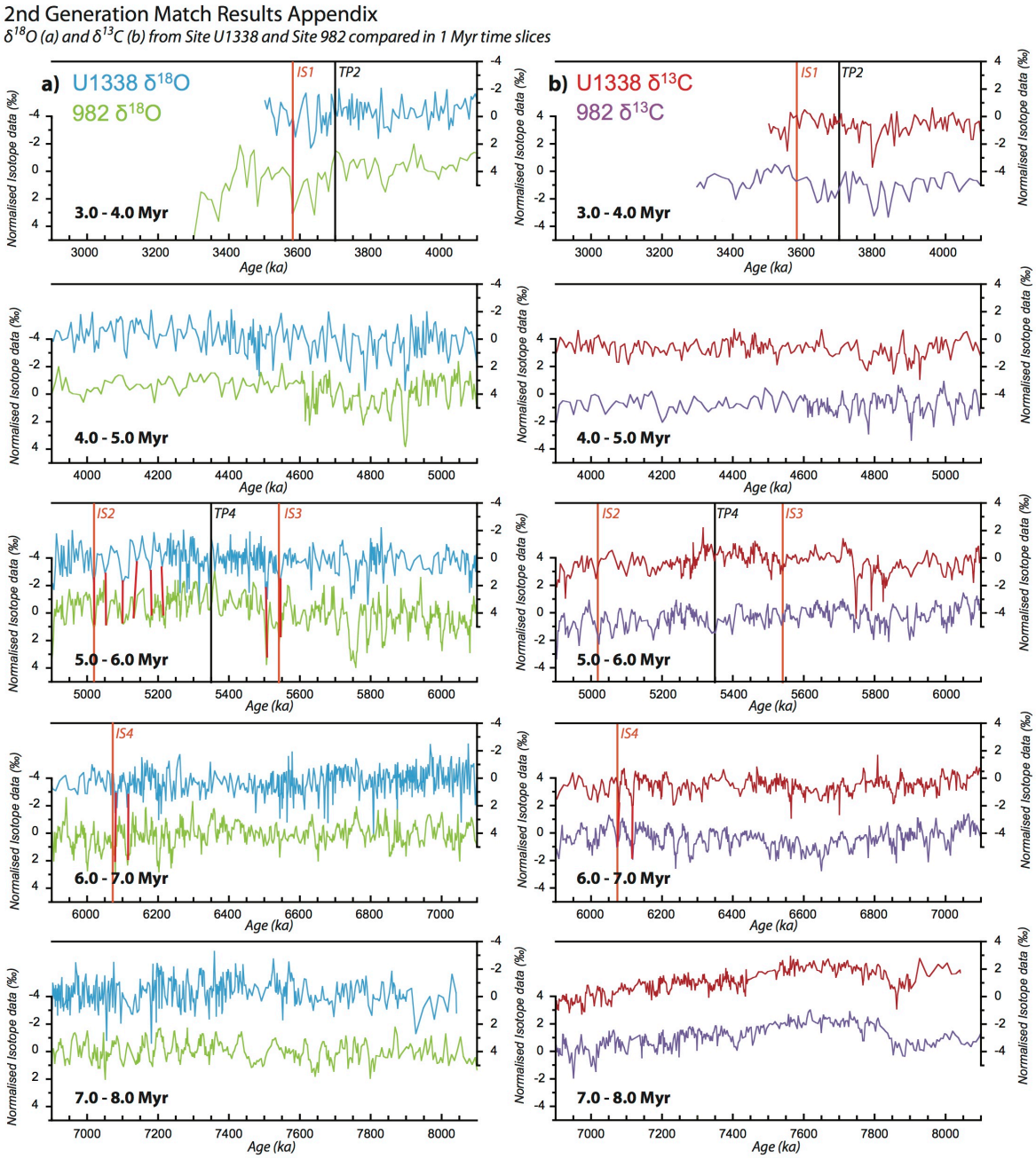

Overview of the benthic $\delta^{18}O$ (a) and $\delta^{13}C$ (b) from Sites U1338 and 982 aligned using the second-generation Match alignment to evaluate how well the records align in terms of short-term fluctuations. The positions of the tie points used to guide the alignment are highlighted with black and orange lines.

The red lines highlight the areas that were initially badly aligned in the second-generation Match alignment. Simply by adjusting 4 tie points, the alignment is much improved. Other areas that already had good alignment are now equally well aligned.

B.4. Resampled Site U1338 Benthic Foraminiferal $\delta^{18}O_{CM}$ Record

The 982 benthic foraminiferal $\delta^{18}O$ record from Hodell et al., 2001 was resampled at 2.5 kyr. To enable easy comparison after conversion from depth to age, the benthic foraminiferal $\delta^{18}O_{CM}$ record from Site U1338 was resampled at 3 kyr using Analyseries (Paillaird et al., 1996 - version 2.0.4.2). The Site U1338 resampled benthic foraminiferal $\delta^{18}O_{CM}$ data is listed in the ***Resampled U1338 $\delta^{18}O_{CM}$***. The 5-point weighted moving average (1st and 5th point = 30%; 2nd and 4th point = 70%; 3rd point = 100%) is applied to the resampled data in ***Resampled U1338 $\delta^{18}O_{CM}$***, and shown in ***Resampled U1338 $\delta^{18}O_{CM}$ WMA***.

Age (Ma)	Resampled U1338 $\delta^{18}O_{CM}$	Resampled U1338 $\delta^{18}O_{CM}$ WMA
3.515	2.96	
3.518	3.02	
3.521	3.10	3.08
3.524	3.14	3.14
3.527	3.18	3.19
3.530	3.24	3.25
3.533	3.34	3.30
3.536	3.37	3.30
3.539	3.26	3.25
3.542	3.16	3.16
3.545	3.05	3.09
3.548	3.02	3.05
3.551	3.04	3.05
3.554	3.07	3.06
3.557	3.08	3.08
3.560	3.09	3.10
3.563	3.11	3.13
3.566	3.18	3.18
3.569	3.24	3.22
3.572	3.28	3.25
3.575	3.25	3.24
3.578	3.22	3.23
3.581	3.20	3.25
3.584	3.29	3.29
3.587	3.39	3.33
3.590	3.37	3.34
3.593	3.31	3.30
3.596	3.24	3.24
3.599	3.18	3.18
3.602	3.11	3.12
3.605	3.06	3.06
3.608	3.01	3.01
3.611	2.96	2.97
3.614	2.93	2.95
3.617	2.90	2.97
3.620	3.01	3.04
3.623	3.17	3.17
3.626	3.31	3.31
3.629	3.46	3.42
3.632	3.54	3.49
3.635	3.52	3.51
3.638	3.50	3.49
3.641	3.45	3.43
3.644	3.39	3.34
3.647	3.25	3.21
3.650	3.01	3.08
3.653	2.92	3.02
3.656	3.02	3.07

3.659	3.20	3.16
3.662	3.33	3.23
3.665	3.21	3.24
3.668	3.22	3.23
3.671	3.24	3.23
3.674	3.17	3.24
3.677	3.35	3.27
3.680	3.29	3.26
3.683	3.19	3.21
3.686	3.16	3.13
3.689	3.05	3.07
3.692	2.96	3.03
3.695	3.04	3.05
3.698	3.12	3.08
3.701	3.09	3.11
3.704	3.13	3.11
3.707	3.14	3.07
3.710	2.95	3.02
3.713	2.93	3.01
3.716	3.06	3.05
3.719	3.15	3.09
3.722	3.10	3.10
3.725	3.07	3.08
3.728	3.06	3.07
3.731	3.06	3.08
3.734	3.11	3.09
3.737	3.13	3.10
3.740	3.03	3.10
3.743	3.20	3.10
3.746	3.03	3.08
3.749	3.01	3.09
3.752	3.18	3.12
3.755	3.18	3.13
3.758	3.12	3.12
3.761	3.00	3.11
3.764	3.15	3.12
3.767	3.24	3.12
3.770	3.02	3.09
3.773	3.01	3.07
3.776	3.10	3.08
3.779	3.18	3.10
3.782	3.07	3.09
3.785	3.04	3.08
3.788	3.11	3.07
3.791	3.07	3.06
3.794	3.02	3.06
3.797	3.06	3.07

3.800	3.11	3.10
3.803	3.16	3.14
3.806	3.18	3.15
3.809	3.15	3.15
3.812	3.12	3.14
3.815	3.10	3.16
3.818	3.21	3.22
3.821	3.38	3.25
3.824	3.27	3.20
3.827	3.05	3.09
3.830	2.88	3.03
3.833	3.02	3.06
3.836	3.21	3.17
3.839	3.31	3.26
3.842	3.30	3.29
3.845	3.30	3.30
3.848	3.30	3.31
3.851	3.32	3.32
3.854	3.35	3.32
3.857	3.32	3.28
3.860	3.20	3.21
3.863	3.10	3.15
3.866	3.11	3.13
3.869	3.14	3.14
3.872	3.16	3.16
3.875	3.17	3.17
3.878	3.19	3.16
3.881	3.14	3.11
3.884	3.04	3.05
3.887	2.94	3.01
3.890	2.98	3.02
3.893	3.08	3.08
3.896	3.18	3.14
3.899	3.20	3.18
3.902	3.20	3.19
3.905	3.19	3.17
3.908	3.15	3.14
3.911	3.10	3.11
3.914	3.07	3.09
3.917	3.08	3.08
3.920	3.08	3.09
3.923	3.11	3.11
3.926	3.14	3.14
3.929	3.18	3.16
3.932	3.18	3.18
3.935	3.18	3.18
3.938	3.17	3.17

3.941	3.17	3.16
3.944	3.16	3.14
3.947	3.12	3.11
3.950	3.06	3.07
3.953	3.01	3.05
3.956	3.02	3.08
3.959	3.15	3.15
3.962	3.28	3.22
3.965	3.29	3.24
3.968	3.21	3.21
3.971	3.13	3.17
3.974	3.14	3.14
3.977	3.16	3.10
3.980	3.01	3.04
3.983	2.93	3.02
3.986	3.06	3.06
3.989	3.14	3.12
3.992	3.20	3.15
3.995	3.16	3.14
3.998	3.07	3.11
4.001	3.08	3.10
4.004	3.12	3.09
4.007	3.09	3.07
4.010	3.04	3.02
4.013	2.93	2.99
4.016	2.92	3.03
4.019	3.16	3.12
4.022	3.30	3.21
4.025	3.23	3.24
4.028	3.22	3.24
4.031	3.26	3.21
4.034	3.18	3.16
4.037	3.05	3.10
4.040	3.04	3.05
4.043	3.03	3.04
4.046	3.04	3.05
4.049	3.06	3.06
4.052	3.08	3.07
4.055	3.08	3.07
4.058	3.06	3.05
4.061	3.03	3.03
4.064	2.99	3.01
4.067	2.97	3.00
4.070	3.02	3.03
4.073	3.09	3.08
4.076	3.16	3.11
4.079	3.15	3.09

4.082	3.01	3.04
4.085	2.95	2.98
4.088	2.96	2.95
4.091	2.93	2.93
4.094	2.91	2.93
4.097	2.92	2.96
4.100	2.98	3.03
4.103	3.15	3.15
4.106	3.31	3.26
4.109	3.36	3.31
4.112	3.36	3.29
4.115	3.20	3.21
4.118	3.08	3.11
4.121	3.01	3.03
4.124	2.96	2.99
4.127	2.95	2.98
4.130	2.99	3.00
4.133	3.07	3.01
4.136	3.02	3.00
4.139	2.93	2.98
4.142	2.96	2.97
4.145	2.99	2.97
4.148	2.97	2.97
4.151	2.95	2.98
4.154	3.00	3.01
4.157	3.05	3.04
4.160	3.08	3.07
4.163	3.10	3.09
4.166	3.11	3.11
4.169	3.12	3.12
4.172	3.15	3.12
4.175	3.13	3.07
4.178	2.98	3.00
4.181	2.86	2.96
4.184	2.96	3.00
4.187	3.10	3.08
4.190	3.19	3.17
4.193	3.24	3.22
4.196	3.27	3.23
4.199	3.22	3.21
4.202	3.17	3.18
4.205	3.12	3.14
4.208	3.12	3.13
4.211	3.13	3.13
4.214	3.13	3.13
4.217	3.13	3.13
4.220	3.13	3.12

4.223	3.12	3.11
4.226	3.08	3.08
4.229	3.04	3.04
4.232	3.00	2.99
4.235	2.95	2.96
4.238	2.90	2.96
4.241	2.97	3.00
4.244	3.08	3.09
4.247	3.20	3.17
4.250	3.28	3.20
4.253	3.18	3.16
4.256	3.06	3.11
4.259	3.05	3.07
4.262	3.06	3.07
4.265	3.07	3.09
4.268	3.11	3.11
4.271	3.15	3.13
4.274	3.15	3.13
4.277	3.12	3.12
4.280	3.09	3.08
4.283	3.03	3.02
4.286	2.95	2.97
4.289	2.90	2.94
4.292	2.94	2.96
4.295	3.00	2.99
4.298	3.04	3.02
4.301	3.05	3.05
4.304	3.05	3.06
4.307	3.08	3.08
4.310	3.11	3.11
4.313	3.15	3.16
4.316	3.20	3.21
4.319	3.26	3.25
4.322	3.31	3.26
4.325	3.25	3.23
4.328	3.16	3.19
4.331	3.11	3.19
4.334	3.24	3.20
4.337	3.31	3.19
4.340	3.11	3.10
4.343	2.93	2.99
4.346	2.86	2.94
4.349	2.91	2.98
4.352	3.10	3.08
4.355	3.24	3.16
4.358	3.21	3.19
4.361	3.17	3.16
4.364	3.11	3.11
4.367	3.05	3.06
4.370	2.99	3.04
4.373	3.04	3.07
4.376	3.14	3.13
4.379	3.21	3.17
4.382	3.22	3.19
4.385	3.15	3.17
4.388	3.16	3.15
4.391	3.15	3.11
4.394	3.00	3.09
4.397	3.06	3.11
4.400	3.20	3.15
4.403	3.30	3.14
4.406	2.96	3.08
4.409	2.97	3.04
4.412	3.12	3.05
4.415	3.01	3.10
4.418	3.18	3.19
4.421	3.34	3.27
4.424	3.35	3.31
4.427	3.33	3.30
4.430	3.25	3.24
4.433	3.16	3.17
4.436	3.09	3.12
4.439	3.06	3.12
4.442	3.15	3.18
4.445	3.32	3.27
4.448	3.37	3.33
4.451	3.39	3.32
4.454	3.27	3.26
4.457	3.15	3.19
4.460	3.09	3.15
4.463	3.15	3.14
4.466	3.20	3.15
4.469	3.04	3.16
4.472	3.27	3.21
4.475	3.21	3.27
4.478	3.41	3.33
4.481	3.35	3.34
4.484	3.36	3.30
4.487	3.24	3.22
4.490	3.03	3.16
4.493	3.13	3.16
4.496	3.25	3.20
4.499	3.24	3.24
4.502	3.28	3.23

4.505	3.21	3.20
4.508	3.12	3.15
4.511	3.12	3.11
4.514	3.07	3.09
4.517	3.05	3.11
4.520	3.12	3.19
4.523	3.37	3.30
4.526	3.47	3.34
4.529	3.30	3.29
4.532	3.15	3.19
4.535	3.09	3.11
4.538	3.05	3.05
4.541	3.00	3.00
4.544	2.94	2.95
4.547	2.88	2.95
4.550	2.96	2.99
4.553	3.09	3.07
4.556	3.19	3.12
4.559	3.15	3.13
4.562	3.09	3.13
4.565	3.09	3.15
4.568	3.21	3.22
4.571	3.35	3.29
4.574	3.37	3.29
4.577	3.24	3.23
4.580	3.11	3.14
4.583	3.01	3.07
4.586	3.03	3.05
4.589	3.06	3.07
4.592	3.11	3.11
4.595	3.16	3.13
4.598	3.15	3.12
4.601	3.10	3.10
4.604	3.05	3.07
4.607	3.02	3.06
4.610	3.07	3.08
4.613	3.12	3.12
4.616	3.16	3.16
4.619	3.20	3.20
4.622	3.23	3.24
4.625	3.28	3.30
4.628	3.39	3.35
4.631	3.43	3.36
4.634	3.32	3.32
4.637	3.22	3.26
4.640	3.20	3.22
4.643	3.20	3.23
4.646	3.28	3.28
4.649	3.36	3.30
4.652	3.33	3.29
4.655	3.22	3.22
4.658	3.11	3.14
4.661	3.06	3.09
4.664	3.03	3.10
4.667	3.15	3.17
4.670	3.30	3.25
4.673	3.40	3.27
4.676	3.21	3.18
4.679	3.00	3.06
4.682	2.88	2.98
4.685	2.96	2.99
4.688	3.06	3.05
4.691	3.14	3.11
4.694	3.15	3.13
4.697	3.14	3.14
4.700	3.14	3.16
4.703	3.18	3.19
4.706	3.24	3.24
4.709	3.30	3.30
4.712	3.36	3.34
4.715	3.41	3.35
4.718	3.35	3.30
4.721	3.19	3.21
4.724	3.04	3.15
4.727	3.11	3.17
4.730	3.27	3.27
4.733	3.42	3.38
4.736	3.48	3.46
4.739	3.53	3.49
4.742	3.53	3.46
4.745	3.38	3.36
4.748	3.21	3.25
4.751	3.11	3.16
4.754	3.12	3.13
4.757	3.13	3.13
4.760	3.13	3.13
4.763	3.13	3.15
4.766	3.16	3.19
4.769	3.24	3.24
4.772	3.32	3.29
4.775	3.35	3.33
4.778	3.33	3.40
4.781	3.45	3.49
4.784	3.71	3.56

4.787	3.62	3.53
4.790	3.40	3.40
4.793	3.22	3.24
4.796	3.05	3.13
4.799	3.05	3.11
4.802	3.12	3.15
4.805	3.27	3.22
4.808	3.32	3.26
4.811	3.22	3.30
4.814	3.34	3.34
4.817	3.48	3.36
4.820	3.36	3.33
4.823	3.19	3.25
4.826	3.17	3.18
4.829	3.15	3.15
4.832	3.12	3.13
4.835	3.12	3.12
4.838	3.13	3.13
4.841	3.11	3.15
4.844	3.14	3.20
4.847	3.31	3.27
4.850	3.36	3.35
4.853	3.41	3.40
4.856	3.46	3.42
4.859	3.44	3.38
4.862	3.28	3.31
4.865	3.21	3.25
4.868	3.21	3.19
4.871	3.14	3.13
4.874	3.05	3.09
4.877	3.04	3.10
4.880	3.16	3.16
4.883	3.28	3.23
4.886	3.30	3.25
4.889	3.23	3.26
4.892	3.18	3.32
4.895	3.46	3.44
4.898	3.71	3.54
4.901	3.56	3.57
4.904	3.50	3.52
4.907	3.52	3.42
4.910	3.34	3.28
4.913	3.01	3.14
4.916	2.98	3.08
4.919	3.12	3.13
4.922	3.27	3.19
4.925	3.29	3.23

4.928	3.12	3.22
4.931	3.31	3.21
4.934	3.10	3.20
4.937	3.22	3.23
4.940	3.29	3.26
4.943	3.35	3.26
4.946	3.18	3.22
4.949	3.08	3.21
4.952	3.34	3.21
4.955	3.28	3.17
4.958	2.93	3.10
4.961	3.02	3.07
4.964	3.18	3.10
4.967	3.14	3.13
4.970	3.09	3.13
4.973	3.16	3.12
4.976	3.12	3.08
4.979	3.00	3.04
4.982	2.97	3.03
4.985	3.05	3.08
4.988	3.16	3.16
4.991	3.29	3.21
4.994	3.25	3.21
4.997	3.12	3.18
5.000	3.10	3.17
5.003	3.24	3.18
5.006	3.24	3.19
5.009	3.10	3.19
5.012	3.19	3.23
5.015	3.34	3.31
5.018	3.43	3.37
5.021	3.42	3.37
5.024	3.34	3.31
5.027	3.21	3.23
5.030	3.12	3.17
5.033	3.13	3.14
5.036	3.13	3.13
5.039	3.13	3.15
5.042	3.16	3.18
5.045	3.22	3.23
5.048	3.29	3.28
5.051	3.34	3.31
5.054	3.31	3.30
5.057	3.27	3.26
5.060	3.22	3.21
5.063	3.14	3.14
5.066	3.06	3.09

5.069	3.04	3.07
5.072	3.07	3.07
5.075	3.09	3.08
5.078	3.11	3.09
5.081	3.10	3.10
5.084	3.09	3.11
5.087	3.13	3.15
5.090	3.19	3.20
5.093	3.27	3.28
5.096	3.36	3.35
5.099	3.45	3.41
5.102	3.46	3.44
5.105	3.43	3.43
5.108	3.40	3.42
5.111	3.40	3.40
5.114	3.41	3.37
5.117	3.36	3.28
5.120	3.12	3.15
5.123	2.96	3.04
5.126	2.97	2.99
5.129	2.99	3.00
5.132	3.04	3.05
5.135	3.11	3.11
5.138	3.19	3.16
5.141	3.20	3.18
5.144	3.18	3.16
5.147	3.14	3.12
5.150	3.08	3.06
5.153	2.99	3.01
5.156	2.93	2.99
5.159	3.01	3.02
5.162	3.09	3.07
5.165	3.14	3.13
5.168	3.18	3.17
5.171	3.20	3.20
5.174	3.23	3.24
5.177	3.30	3.25
5.180	3.27	3.22
5.183	3.17	3.15
5.186	3.02	3.05
5.189	2.90	2.99
5.192	2.99	3.00
5.195	3.08	3.04
5.198	3.09	3.07
5.201	3.07	3.07
5.204	3.02	3.08
5.207	3.10	3.12

5.210	3.21	3.17
5.213	3.25	3.19
5.216	3.17	3.18
5.219	3.12	3.14
5.222	3.11	3.10
5.225	3.09	3.06
5.228	2.95	3.04
5.231	3.07	3.05
5.234	3.09	3.08
5.237	3.06	3.10
5.240	3.23	3.11
5.243	3.03	3.10
5.246	3.10	3.10
5.249	3.12	3.10
5.252	3.12	3.08
5.255	3.02	3.06
5.258	2.98	3.10
5.261	3.24	3.16
5.264	3.31	3.20
5.267	3.12	3.16
5.270	3.13	3.10
5.273	2.92	3.06
5.276	3.14	3.12
5.279	3.15	3.21
5.282	3.45	3.31
5.285	3.33	3.31
5.288	3.33	3.23
5.291	2.98	3.11
5.294	3.05	3.05
5.297	2.95	3.02
5.300	3.10	3.06
5.303	3.04	3.10
5.306	3.21	3.13
5.309	3.14	3.16
5.312	3.08	3.21
5.315	3.40	3.27
5.318	3.35	3.30
5.321	3.26	3.29
5.324	3.23	3.27
5.327	3.28	3.25
5.330	3.26	3.24
5.333	3.18	3.21
5.336	3.19	3.20
5.339	3.15	3.23
5.342	3.33	3.26
5.345	3.37	3.24
5.348	3.12	3.16

5.351	2.98	3.08
5.354	3.02	3.07
5.357	3.13	3.13
5.360	3.28	3.19
5.363	3.22	3.18
5.366	3.11	3.14
5.369	3.04	3.12
5.372	3.20	3.15
5.375	3.18	3.17
5.378	3.18	3.19
5.381	3.22	3.20
5.384	3.17	3.21
5.387	3.25	3.22
5.390	3.23	3.22
5.393	3.26	3.20
5.396	3.11	3.17
5.399	3.15	3.14
5.402	3.15	3.13
5.405	3.05	3.13
5.408	3.20	3.14
5.411	3.13	3.15
5.414	3.18	3.16
5.417	3.14	3.17
5.420	3.21	3.19
5.423	3.19	3.19
5.426	3.25	3.19
5.429	3.12	3.17
5.432	3.16	3.18
5.435	3.19	3.18
5.438	3.23	3.19
5.441	3.15	3.17
5.444	3.14	3.15
5.447	3.15	3.14
5.450	3.07	3.17
5.453	3.23	3.22
5.456	3.44	3.24
5.459	3.08	3.20
5.462	3.13	3.17
5.465	3.18	3.16
5.468	3.20	3.18
5.471	3.12	3.19
5.474	3.29	3.20
5.477	3.16	3.19
5.480	3.19	3.16
5.483	3.10	3.13
5.486	3.07	3.12
5.489	3.16	3.13

5.492	3.13	3.15
5.495	3.18	3.18
5.498	3.22	3.23
5.501	3.20	3.32
5.504	3.53	3.42
5.507	3.55	3.45
5.510	3.45	3.40
5.513	3.20	3.28
5.516	3.18	3.19
5.519	3.12	3.17
5.522	3.18	3.20
5.525	3.31	3.23
5.528	3.23	3.25
5.531	3.26	3.27
5.534	3.26	3.30
5.537	3.35	3.36
5.540	3.45	3.41
5.543	3.46	3.42
5.546	3.41	3.39
5.549	3.34	3.33
5.552	3.26	3.26
5.555	3.16	3.19
5.558	3.13	3.16
5.561	3.16	3.16
5.564	3.18	3.17
5.567	3.20	3.16
5.570	3.08	3.14
5.573	3.10	3.15
5.576	3.25	3.17
5.579	3.17	3.18
5.582	3.20	3.18
5.585	3.15	3.17
5.588	3.17	3.19
5.591	3.23	3.20
5.594	3.21	3.22
5.597	3.22	3.22
5.600	3.23	3.22
5.603	3.23	3.22
5.606	3.22	3.22
5.609	3.21	3.21
5.612	3.20	3.20
5.615	3.19	3.21
5.618	3.22	3.23
5.621	3.27	3.23
5.624	3.25	3.22
5.627	3.10	3.23
5.630	3.28	3.25

5.633	3.45	3.25
5.636	3.11	3.19
5.639	3.04	3.12
5.642	3.11	3.12
5.645	3.17	3.16
5.648	3.21	3.21
5.651	3.25	3.25
5.654	3.30	3.26
5.657	3.28	3.25
5.660	3.19	3.20
5.663	3.12	3.15
5.666	3.09	3.13
5.669	3.14	3.15
5.672	3.19	3.18
5.675	3.22	3.20
5.678	3.23	3.21
5.681	3.17	3.20
5.684	3.17	3.20
5.687	3.26	3.21
5.690	3.24	3.21
5.693	3.15	3.19
5.696	3.12	3.20
5.699	3.28	3.26
5.702	3.36	3.32
5.705	3.36	3.35
5.708	3.37	3.32
5.711	3.33	3.25
5.714	3.06	3.14
5.717	3.02	3.06
5.720	2.98	3.04
5.723	3.08	3.07
5.726	3.13	3.10
5.729	3.12	3.13
5.732	3.12	3.15
5.735	3.17	3.19
5.738	3.24	3.27
5.741	3.35	3.38
5.744	3.58	3.48
5.747	3.56	3.54
5.750	3.52	3.54
5.753	3.56	3.49
5.756	3.42	3.42
5.759	3.24	3.36
5.762	3.36	3.33
5.765	3.38	3.31
5.768	3.24	3.28
5.771	3.21	3.24
5.774	3.24	3.21
5.777	3.18	3.18
5.780	3.12	3.17
5.783	3.19	3.19
5.786	3.21	3.26
5.789	3.31	3.36
5.792	3.63	3.43
5.795	3.45	3.38
5.798	3.16	3.26
5.801	3.13	3.15
5.804	3.06	3.12
5.807	3.12	3.13
5.810	3.21	3.17
5.813	3.16	3.19
5.816	3.28	3.17
5.819	3.03	3.14
5.822	3.12	3.12
5.825	3.17	3.10
5.828	3.05	3.09
5.831	2.97	3.13
5.834	3.30	3.21
5.837	3.39	3.26
5.840	3.18	3.25
5.843	3.21	3.20
5.846	3.15	3.15
5.849	3.09	3.11
5.852	3.08	3.07
5.855	3.03	3.06
5.858	3.04	3.09
5.861	3.15	3.16
5.864	3.26	3.23
5.867	3.35	3.27
5.870	3.25	3.24
5.873	3.14	3.19
5.876	3.16	3.16
5.879	3.17	3.15
5.882	3.13	3.13
5.885	3.09	3.11
5.888	3.09	3.10
5.891	3.10	3.11
5.894	3.12	3.14
5.897	3.18	3.18
5.900	3.24	3.23
5.903	3.30	3.28
5.906	3.31	3.30
5.909	3.32	3.31
5.912	3.31	3.30

5.915	3.28	3.28
5.918	3.25	3.25
5.921	3.22	3.23
5.924	3.20	3.20
5.927	3.18	3.19
5.930	3.17	3.17
5.933	3.16	3.16
5.936	3.15	3.16
5.939	3.14	3.17
5.942	3.19	3.20
5.945	3.25	3.24
5.948	3.30	3.28
5.951	3.31	3.30
5.954	3.31	3.31
5.957	3.31	3.31
5.960	3.30	3.31
5.963	3.30	3.31
5.966	3.31	3.32
5.969	3.33	3.33
5.972	3.36	3.32
5.975	3.31	3.28
5.978	3.19	3.22
5.981	3.15	3.17
5.984	3.13	3.14
5.987	3.12	3.14
5.990	3.12	3.18
5.993	3.26	3.25
5.996	3.36	3.30
5.999	3.36	3.31
6.002	3.27	3.27
6.005	3.19	3.22
6.008	3.19	3.17
6.011	3.16	3.13
6.014	3.03	3.09
6.017	3.07	3.08
6.020	3.07	3.10
6.023	3.18	3.15
6.026	3.23	3.18
6.029	3.17	3.17
6.032	3.12	3.15
6.035	3.12	3.15
6.038	3.20	3.17
6.041	3.19	3.19
6.044	3.19	3.22
6.047	3.26	3.25
6.050	3.30	3.27
6.053	3.31	3.25

6.056	3.18	3.19
6.059	3.09	3.15
6.062	3.11	3.15
6.065	3.21	3.19
6.068	3.28	3.21
6.071	3.16	3.21
6.074	3.16	3.24
6.077	3.33	3.30
6.080	3.40	3.36
6.083	3.42	3.38
6.086	3.38	3.35
6.089	3.27	3.30
6.092	3.21	3.25
6.095	3.27	3.23
6.098	3.19	3.20
6.101	3.17	3.19
6.104	3.15	3.19
6.107	3.23	3.25
6.110	3.32	3.30
6.113	3.44	3.33
6.116	3.28	3.31
6.119	3.26	3.27
6.122	3.20	3.23
6.125	3.25	3.22
6.128	3.19	3.21
6.131	3.21	3.21
6.134	3.18	3.22
6.137	3.24	3.23
6.140	3.30	3.24
6.143	3.19	3.24
6.146	3.20	3.24
6.149	3.30	3.23
6.152	3.28	3.22
6.155	3.01	3.20
6.158	3.34	3.21
6.161	3.23	3.19
6.164	3.09	3.14
6.167	3.10	3.09
6.170	3.01	3.08
6.173	3.16	3.12
6.176	3.13	3.15
6.179	3.25	3.16
6.182	3.12	3.15
6.185	3.09	3.13
6.188	3.16	3.14
6.191	3.15	3.19
6.194	3.24	3.25

6.197	3.39	3.30
6.200	3.26	3.33
6.203	3.39	3.35
6.206	3.32	3.36
6.209	3.46	3.36
6.212	3.29	3.31
6.215	3.21	3.28
6.218	3.25	3.26
6.221	3.36	3.25
6.224	3.18	3.18
6.227	3.05	3.11
6.230	3.00	3.09
6.233	3.12	3.15
6.236	3.29	3.26
6.239	3.41	3.32
6.242	3.32	3.33
6.245	3.25	3.31
6.248	3.37	3.27
6.251	3.20	3.18
6.254	3.03	3.08
6.257	2.95	2.99
6.260	2.91	3.00
6.263	3.02	3.09
6.266	3.31	3.21
6.269	3.34	3.30
6.272	3.33	3.32
6.275	3.33	3.30
6.278	3.22	3.28
6.281	3.27	3.28
6.284	3.36	3.28
6.287	3.26	3.25
6.290	3.16	3.21
6.293	3.15	3.19
6.296	3.23	3.19
6.299	3.19	3.20
6.302	3.19	3.20
6.305	3.22	3.21
6.308	3.22	3.22
6.311	3.24	3.24
6.314	3.23	3.27
6.317	3.32	3.30
6.320	3.38	3.31
6.323	3.25	3.28
6.326	3.22	3.26
6.329	3.27	3.27
6.332	3.26	3.30
6.335	3.39	3.33

6.338	3.33	3.33
6.341	3.32	3.28
6.344	3.24	3.22
6.347	3.05	3.18
6.350	3.22	3.20
6.353	3.29	3.21
6.356	3.20	3.19
6.359	3.11	3.15
6.362	3.11	3.13
6.365	3.14	3.14
6.368	3.17	3.16
6.371	3.19	3.19
6.374	3.20	3.20
6.377	3.23	3.22
6.380	3.24	3.22
6.383	3.20	3.20
6.386	3.16	3.18
6.389	3.17	3.19
6.392	3.21	3.22
6.395	3.26	3.25
6.398	3.32	3.26
6.401	3.23	3.23
6.404	3.14	3.20
6.407	3.19	3.22
6.410	3.27	3.27
6.413	3.36	3.32
6.416	3.37	3.32
6.419	3.29	3.29
6.422	3.23	3.24
6.425	3.17	3.21
6.428	3.19	3.22
6.431	3.29	3.24
6.434	3.27	3.26
6.437	3.24	3.25
6.440	3.24	3.26
6.443	3.27	3.27
6.446	3.31	3.29
6.449	3.30	3.30
6.452	3.34	3.29
6.455	3.27	3.25
6.458	3.15	3.21
6.461	3.19	3.21
6.464	3.24	3.24
6.467	3.33	3.26
6.470	3.23	3.28
6.473	3.22	3.31
6.476	3.49	3.34

6.479	3.32	3.34
6.482	3.27	3.30
6.485	3.28	3.26
6.488	3.22	3.25
6.491	3.24	3.26
6.494	3.30	3.28
6.497	3.28	3.32
6.500	3.41	3.34
6.503	3.36	3.33
6.506	3.24	3.31
6.509	3.33	3.29
6.512	3.26	3.27
6.515	3.26	3.25
6.518	3.17	3.21
6.521	3.25	3.20
6.524	3.10	3.21
6.527	3.29	3.25
6.530	3.33	3.28
6.533	3.31	3.29
6.536	3.20	3.28
6.539	3.29	3.30
6.542	3.33	3.32
6.545	3.46	3.34
6.548	3.19	3.32
6.551	3.40	3.29
6.554	3.24	3.25
6.557	3.15	3.23
6.560	3.19	3.25
6.563	3.39	3.27
6.566	3.34	3.26
6.569	3.04	3.22
6.572	3.29	3.20
6.575	3.23	3.20
6.578	3.07	3.22
6.581	3.36	3.25
6.584	3.28	3.28
6.587	3.30	3.28
6.590	3.23	3.26
6.593	3.23	3.26
6.596	3.32	3.28
6.599	3.27	3.30
6.602	3.33	3.31
6.605	3.37	3.32
6.608	3.22	3.34
6.611	3.43	3.36
6.614	3.45	3.36
6.617	3.27	3.31
6.620	3.23	3.23
6.623	3.15	3.17
6.626	3.10	3.17
6.629	3.22	3.21
6.632	3.29	3.24
6.635	3.28	3.22
6.638	3.11	3.18
6.641	3.10	3.17
6.644	3.21	3.21
6.647	3.31	3.28
6.650	3.30	3.33
6.653	3.47	3.33
6.656	3.26	3.26
6.659	3.10	3.18
6.662	3.10	3.15
6.665	3.14	3.21
6.668	3.37	3.28
6.671	3.40	3.29
6.674	3.20	3.26
6.677	3.12	3.22
6.680	3.33	3.22
6.683	3.16	3.20
6.686	3.18	3.18
6.689	3.11	3.17
6.692	3.24	3.18
6.695	3.22	3.18
6.698	3.08	3.15
6.701	3.17	3.12
6.704	3.08	3.10
6.707	3.08	3.09
6.710	3.05	3.08
6.713	3.14	3.10
6.716	3.07	3.12
6.719	3.20	3.14
6.722	3.12	3.12
6.725	3.12	3.10
6.728	3.02	3.08
6.731	3.08	3.09
6.734	3.14	3.12
6.737	3.11	3.15
6.740	3.23	3.17
6.743	3.18	3.15
6.746	3.07	3.13
6.749	3.12	3.13
6.752	3.17	3.13
6.755	3.18	3.11
6.758	2.99	3.06

6.761	2.98	3.05
6.764	3.03	3.10
6.767	3.30	3.18
6.770	3.27	3.21
6.773	3.11	3.20
6.776	3.18	3.21
6.779	3.28	3.25
6.782	3.32	3.28
6.785	3.29	3.28
6.788	3.23	3.26
6.791	3.27	3.23
6.794	3.20	3.21
6.797	3.14	3.19
6.800	3.21	3.22
6.803	3.23	3.28
6.806	3.42	3.32
6.809	3.41	3.32
6.812	3.15	3.29
6.815	3.29	3.28
6.818	3.37	3.26
6.821	3.20	3.22
6.824	3.09	3.18
6.827	3.15	3.17
6.830	3.28	3.19
6.833	3.18	3.20
6.836	3.12	3.21
6.839	3.33	3.21
6.842	3.18	3.18
6.845	3.07	3.14
6.848	3.11	3.13
6.851	3.13	3.17
6.854	3.27	3.21
6.857	3.26	3.23
6.860	3.21	3.21
6.863	3.18	3.18
6.866	3.15	3.16
6.869	3.10	3.17
6.872	3.26	3.19
6.875	3.25	3.20
6.878	3.13	3.18
6.881	3.16	3.18
6.884	3.20	3.20
6.887	3.27	3.22
6.890	3.18	3.22
6.893	3.27	3.21
6.896	3.19	3.19
6.899	3.14	3.16
6.902	3.16	3.14
6.905	3.09	3.13
6.908	3.16	3.14
6.911	3.16	3.16
6.914	3.16	3.18
6.917	3.21	3.18
6.920	3.19	3.18
6.923	3.15	3.16
6.926	3.17	3.15
6.929	3.07	3.17
6.932	3.25	3.21
6.935	3.29	3.24
6.938	3.25	3.24
6.941	3.17	3.22
6.944	3.26	3.21
6.947	3.16	3.20
6.950	3.18	3.19
6.953	3.26	3.18
6.956	3.10	3.15
6.959	3.16	3.12
6.962	3.05	3.07
6.965	3.10	3.01
6.968	2.83	2.95
6.971	2.90	2.97
6.974	3.06	3.04
6.977	3.16	3.14
6.980	3.23	3.20
6.983	3.29	3.20
6.986	3.12	3.17
6.989	3.09	3.11
6.992	3.14	3.07
6.995	2.94	3.04
6.998	3.02	3.06
7.001	3.17	3.11
7.004	3.12	3.16
7.007	3.24	3.19
7.010	3.17	3.19
7.013	3.19	3.19
7.016	3.21	3.18
7.019	3.10	3.16
7.022	3.25	3.13
7.025	2.99	3.11
7.028	3.04	3.13
7.031	3.34	3.17
7.034	3.14	3.19
7.037	3.20	3.18
7.040	3.16	3.16

7.043	3.11	3.14
7.046	3.19	3.13
7.049	3.00	3.16
7.052	3.21	3.23
7.055	3.54	3.26
7.058	3.11	3.23
7.061	3.09	3.17
7.064	3.26	3.13
7.067	3.04	3.11
7.070	3.05	3.08
7.073	3.15	3.07
7.076	2.91	3.09
7.079	3.27	3.12
7.082	3.12	3.10
7.085	3.03	3.08
7.088	3.02	3.08
7.091	3.06	3.15
7.094	3.37	3.23
7.097	3.31	3.25
7.100	3.15	3.22
7.103	3.18	3.20
7.106	3.20	3.20
7.109	3.22	3.23
7.112	3.25	3.25
7.115	3.28	3.28
7.118	3.30	3.30
7.121	3.32	3.33
7.124	3.36	3.35
7.127	3.39	3.35
7.130	3.33	3.31
7.133	3.23	3.26
7.136	3.17	3.24
7.139	3.28	3.27
7.142	3.36	3.29
7.145	3.33	3.26
7.148	3.12	3.18
7.151	3.07	3.12
7.154	3.13	3.09
7.157	3.06	3.09
7.160	3.09	3.09
7.163	3.10	3.09
7.166	3.10	3.08
7.169	3.07	3.06
7.172	3.01	3.06
7.175	3.03	3.12
7.178	3.20	3.21
7.181	3.57	3.27

7.184	3.07	3.21
7.187	3.12	3.13
7.190	3.06	3.08
7.193	3.09	3.04
7.196	3.02	3.00
7.199	2.84	2.96
7.202	3.04	2.94
7.205	2.90	2.94
7.208	2.85	2.96
7.211	3.13	2.99
7.214	2.94	3.02
7.217	3.05	3.08
7.220	3.17	3.13
7.223	3.22	3.17
7.226	3.21	3.14
7.229	3.02	3.06
7.232	2.96	3.01
7.235	2.97	3.01
7.238	3.03	3.04
7.241	3.21	3.06
7.244	2.93	3.04
7.247	3.04	3.03
7.250	2.98	3.06
7.253	3.14	3.13
7.256	3.28	3.20
7.259	3.23	3.24
7.262	3.24	3.25
7.265	3.32	3.24
7.268	3.20	3.20
7.271	3.05	3.19
7.274	3.28	3.19
7.277	3.29	3.15
7.280	2.98	3.06
7.283	2.88	3.00
7.286	3.01	3.04
7.289	3.17	3.11
7.292	3.24	3.16
7.295	3.08	3.17
7.298	3.20	3.20
7.301	3.24	3.24
7.304	3.36	3.26
7.307	3.22	3.22
7.310	3.16	3.15
7.313	3.08	3.05
7.316	2.90	2.96
7.319	2.88	2.92
7.322	2.89	2.91

7.325	3.01	2.94
7.328	2.87	2.98
7.331	3.05	3.06
7.334	3.23	3.13
7.337	3.18	3.18
7.340	3.14	3.20
7.343	3.34	3.20
7.346	3.14	3.17
7.349	3.07	3.13
7.352	3.14	3.07
7.355	3.08	3.01
7.358	2.76	2.97
7.361	2.96	3.00
7.364	3.21	3.06
7.367	3.08	3.10
7.370	3.09	3.10
7.373	3.12	3.08
7.376	3.01	3.08
7.379	3.10	3.09
7.382	3.16	3.09
7.385	3.00	3.09
7.388	3.10	3.09
7.391	3.18	3.06
7.394	2.95	3.00
7.397	2.89	2.96
7.400	2.93	2.97
7.403	3.10	3.02
7.406	3.00	3.06
7.409	3.13	3.09
7.412	3.12	3.09
7.415	3.10	3.05
7.418	2.91	2.98
7.421	2.91	2.96
7.424	2.96	2.97
7.427	3.09	2.99
7.430	2.92	2.99
7.433	2.97	2.99
7.436	3.07	2.98
7.439	2.91	2.97
7.442	2.95	2.98
7.445	3.04	3.02
7.448	3.07	3.08
7.451	3.17	3.12
7.454	3.15	3.13
7.457	3.09	3.12
7.460	3.11	3.12
7.463	3.14	3.12
7.466	3.14	3.11
7.469	3.08	3.08
7.472	3.03	3.06
7.475	3.04	3.05
7.478	3.05	3.06
7.481	3.07	3.08
7.484	3.11	3.11
7.487	3.16	3.15
7.490	3.20	3.18
7.493	3.21	3.18
7.496	3.17	3.16
7.499	3.13	3.13
7.502	3.09	3.10
7.505	3.06	3.08
7.508	3.07	3.06
7.511	3.05	3.04
7.514	3.00	3.02
7.517	3.02	2.99
7.520	2.96	2.93
7.523	2.85	2.88
7.526	2.77	2.88
7.529	2.95	2.94
7.532	3.11	3.01
7.535	2.98	3.04
7.538	3.10	3.06
7.541	3.06	3.06
7.544	3.03	3.09
7.547	3.12	3.14
7.550	3.27	3.18
7.553	3.22	3.18
7.556	3.09	3.14
7.559	3.08	3.11
7.562	3.16	3.07
7.565	3.01	2.99
7.568	2.83	2.92
7.571	2.85	2.89
7.574	2.95	2.91
7.577	2.91	2.94
7.580	2.97	2.99
7.583	3.02	3.06
7.586	3.22	3.14
7.589	3.19	3.18
7.592	3.23	3.19
7.595	3.11	3.18
7.598	3.19	3.19
7.601	3.26	3.20
7.604	3.21	3.18

7.607	3.12	3.12
7.610	3.03	3.05
7.613	2.96	3.00
7.616	2.97	3.00
7.619	3.03	3.04
7.622	3.12	3.11
7.625	3.18	3.16
7.628	3.22	3.19
7.631	3.18	3.22
7.634	3.24	3.24
7.637	3.31	3.26
7.640	3.27	3.25
7.643	3.18	3.22
7.646	3.19	3.21
7.649	3.23	3.21
7.652	3.23	3.22
7.655	3.22	3.22
7.658	3.22	3.19
7.661	3.16	3.16
7.664	3.08	3.14
7.667	3.15	3.15
7.670	3.21	3.18
7.673	3.22	3.21
7.676	3.21	3.22
7.679	3.22	3.23
7.682	3.26	3.24
7.685	3.25	3.24
7.688	3.23	3.25
7.691	3.25	3.28
7.694	3.35	3.30
7.697	3.36	3.29
7.700	3.22	3.22
7.703	3.08	3.14
7.706	3.07	3.11
7.709	3.14	3.13
7.712	3.17	3.15
7.715	3.20	3.14
7.718	3.08	3.12
7.721	3.06	3.10
7.724	3.14	3.08
7.727	3.04	3.07
7.730	3.03	3.09
7.733	3.12	3.13
7.736	3.26	3.18
7.739	3.23	3.17
7.742	3.07	3.13
7.745	3.03	3.11
7.748	3.17	3.14
7.751	3.22	3.15
7.754	3.14	3.13
7.757	3.05	3.07
7.760	2.99	3.02
7.763	2.99	3.02
7.766	3.04	3.05
7.769	3.11	3.07
7.772	3.10	3.06
7.775	3.00	3.04
7.778	2.99	3.03
7.781	3.08	3.04
7.784	3.08	3.05
7.787	2.97	3.06
7.790	3.09	3.12
7.793	3.26	3.21
7.796	3.32	3.29
7.799	3.35	3.33
7.802	3.38	3.31
7.805	3.24	3.26
7.808	3.17	3.22
7.811	3.20	3.20
7.814	3.21	3.20
7.817	3.20	3.21
7.820	3.21	3.21
7.823	3.22	3.19
7.826	3.19	3.16
7.829	3.09	3.10
7.832	3.00	3.05
7.835	3.01	3.07
7.838	3.13	3.13
7.841	3.25	3.21
7.844	3.31	3.25
7.847	3.26	3.24
7.850	3.18	3.18
7.853	3.11	3.10
7.856	3.01	3.03
7.859	2.91	3.00
7.862	3.07	3.02
7.865	3.02	3.05
7.868	3.07	3.10
7.871	3.18	3.16
7.874	3.23	3.20
7.877	3.25	3.20
7.880	3.13	3.19
7.883	3.17	3.18
7.886	3.20	3.18

7.889	3.19	3.18
7.892	3.16	3.18
7.895	3.19	3.18
7.898	3.21	3.18
7.901	3.15	3.15
7.904	3.10	3.12
7.907	3.09	3.10
7.910	3.09	3.09
7.913	3.08	3.11
7.916	3.13	3.17
7.919	3.27	3.27
7.922	3.40	3.39
7.925	3.53	3.49
7.928	3.61	3.55
7.931	3.57	3.55
7.934	3.52	3.52
7.937	3.48	3.48
7.940	3.43	3.43
7.943	3.39	3.39
7.946	3.35	3.35
7.949	3.31	3.31
7.952	3.28	3.28
7.955	3.26	3.26
7.958	3.23	3.23
7.961	3.21	3.21
7.964	3.19	3.20
7.967	3.19	3.22
7.970	3.25	3.26
7.973	3.32	3.32
7.976	3.38	3.37
7.979	3.43	3.38
7.982	3.38	3.36
7.985	3.31	3.31
7.988	3.24	3.24
7.991	3.17	3.20
7.994	3.16	3.17
7.997	3.17	3.17
8.000	3.17	3.18
8.003	3.18	3.19
8.006	3.21	3.22
8.009	3.25	3.25
8.012	3.29	3.29
8.015	3.33	3.30
8.018	3.31	3.27
8.021	3.20	3.19
8.024	3.09	3.09
8.027	2.98	3.01
8.030	2.92	2.98
8.033	2.98	2.99
8.036	3.03	
8.039	3.09	

Appendix C

C.1. Overview of Trace Element Data

Original foraminiferal planktic trace element data from *Globigerinoides sacculifer* produced in this PhD study. Description of the data columns can be found below.

- ***IODP Sample Name:*** the sample identity (ID) is given a prefix of 321-U1338 before the content to denote the expedition and site. Each cell denotes the hole-core-section-interval of the sample.
- ***Own Sample ID:*** the simplified sample identity (ID) given to each sample. GS# denotes the sample. The size fraction is indicated by A (250 – 355 μm), B (355 – 425 μm) and C (425 – 500 μm). The number following the size fraction letter denotes which replicate analysis it is.
- ***Depth:*** in meters CCSF-A (core composite depth below sea floor) on Wilkens et al. (2013) splice.
- ***Age:*** in Ma. The generation of the age model is described in Chapter 4. The depth-age relationship for Site U1338 between 8.0 and 3.5 Ma is also provided in a table in Appendix B.1.
- ***Size fraction:*** lists in μm from what size fraction the *Globigerinoides sacculifer* were selected.
- ***Size fraction Correction Factor:*** lists the correction factor applied by division to the Mg/Ca trace element data for measurements on the 355 – 425 μm and the 425 – 500 μm fraction.
- ***Closest Core Depth:*** relevant overlying water-column depth for each sample (Palike et al., 2012).
- ***Core depth Correction Factor:*** lists the correction factor in ° C applied within the Dekens et al. (2002) Mg/Ca to temperature calibration for *Globigerinoides sacculifer*.
- ***[Ca]:*** lists the calcium concentration in mol of each measurement.
- ***Fe/Ca; Al/Ca; Mn/Ca; Sr/Ca; Mg/Ca:*** uncorrected metal/Ca ratios (mmol/mol). Analytical precision based on standard replication (1 σ) is (in mmol/mol): Fe/Ca – 0.003; Al/Ca – 0.03; Mn/Ca – 0.001; Sr/Ca – 0.007; Mg/Ca – 0.02. Natural variability based on duplicated samples (1 σ) is (in mmol/mol): Fe/Ca – 0.002; Al/Ca – 0.23; Mn/Ca – 0.04; Sr/Ca – 0.01; Mg/Ca – 0.18.
- ***Mg/Ca size corrected:*** the Mg/Ca ratios after correction for size fraction (see column Size fraction Correction Factor). For size corrected samples the overall variability is 0.24 mmol/mol.
- ***Temp*** and ***Temp (Size):*** lists the temperature in °C based on the uncorrected Mg/Ca (***Temp***) and size corrected Mg/Ca (***Temp (Size)***) ratios using the Dekens et al., 2002 calibration.

IODP Sample Name Prefix 321-U1338	Own Sample ID	Depth m CCSF-A	Age Ma	Size fraction µm	Size fraction Correction Factor	Closest Core Depth	Core depth Correction Factor (°C)	[Ca] mol	Fe/Ca mmol/mol	Al/Ca mmol/mol	Mn/Ca mmol/mol	Sr/Ca mmol/mol	Mg/Ca mmol/mol	Mg/Ca size corrected mmol/mol	Temp. °C	Temp (Size) °C
A-10H-3-W 90/92	GS3-A1	92.83	5.537	250-355	1.00	3.97	3.43	23.61	0.05	0.06	0.73	1.08	2.65	2.65	25.32	25.32
A-10H-5-W 100/102	GS6-A1	95.93	5.641	250-355	1.00	3.96	3.43	30.56	0.02	-0.01	0.93	1.14	3.10	3.10	27.03	27.03
B-10H-4-W 130/132	GS7-A1	98.40	5.748	250-355	1.00	3.96	3.43	31.12	0.20	-0.10	0.72	1.13	2.30	2.30	23.72	23.72
B-10H-4-W 130/132	GS7-B1	98.40	5.748	355-425	1.13	3.96	3.43	57.35	0.03	0.13	1.03	1.15	2.80	2.47	25.92	24.54
B-10H-4-W 130/132	GS7-C1	98.40	5.748	425-500	1.25	3.96	3.43	48.25	0.01	0.05	0.84	1.14	3.13	2.51	27.15	24.68
B-10H-5-W 87/89	GS8-A1	99.47	5.788	250-355	1.00	3.96	3.43	27.62	0.16	-0.11	0.82	1.11	2.74	2.74	25.68	25.68
B-10H-5-W 87/89	GS8-B1	99.47	5.788	355-425	1.13	3.96	3.43	49.81	0.00	0.02	1.29	1.12	2.80	2.48	25.93	24.56
B-10H-5-W 87/89	GS8-C1	99.47	5.788	425-500	1.25	3.96	3.43	55.53	0.03	0.02	1.07	1.13	3.09	2.48	27.02	24.55
A-11H-1-W 148/150	GS9-A1	100.96	5.806	250-355	1.00	3.96	3.43	41.89	0.00	0.04	0.81	1.14	3.08	3.08	26.97	26.97
A-12H-2-W-80/82	GS19-A1	112.75	6.180	250-355	1.00	3.95	3.42	7.79	0.13	-0.19	0.35	1.01	2.31	2.31	23.79	23.79
A-12H-2-W-80/82	GS19-B1	112.75	6.180	355-425	1.13	3.95	3.42	51.77	0.00	0.15	0.87	1.05	3.04	2.68	26.80	25.43
A-12H-2-W-102/104	GS20-A1	112.97	6.184	250-355	1.00	3.94	3.42	39.74	0.01	0.04	1.02	1.08	2.65	2.65	25.31	25.31
A-12H-2-W-102/104	GS20-A2	112.97	6.184	250-355	1.00	3.94	3.42	35.34	0.01	0.04	1.06	1.06	2.90	2.90	26.30	26.30
A-12H-2-W-102/104	GS20-B1	112.97	6.184	355-425	1.13	3.94	3.42	4.75	0.46	-0.32	0.56	1.03	3.51	3.10	28.43	27.05
A-12H-2-W 140/142	GS12-A1	113.35	6.193	250-355	1.00	3.94	3.42	14.73	0.02	0.54	0.73	1.04	2.89	2.89	26.26	26.26
A-12H-2-W 140/142	GS12-A2	113.35	6.193	250-355	1.00	3.94	3.42	36.86	0.03	-0.02	0.82	1.02	2.53	2.53	24.78	24.78
A-12H-2-W 140/142	GS12-B1	113.35	6.193	355-425	1.13	3.94	3.42	10.91	0.34	-0.07	0.58	1.01	2.81	2.48	25.95	24.58
A-12H-2-W 140/142	GS12-C1	113.35	6.193	425-500	1.25	3.94	3.42	42.37	0.01	0.02	0.71	1.03	3.14	2.51	27.18	24.70
A-12H-3-W 10/12	GS13-B1	113.55	6.196	355-425	1.13	3.94	3.42	44.63	0.00	0.02	0.85	1.07	3.00	2.65	26.69	25.31
B-12H-1-W 110/112	GS15-B1	115.29	6.221	355-425	1.13	3.94	3.42	45.74	0.00	-0.03	1.14	1.07	3.04	2.68	26.81	25.44
B-12H-1-W 110/112	GS15-C1	115.29	6.221	425-500	1.25	3.94	3.42	36.70	0.04	0.01	0.91	1.05	3.71	2.97	29.02	26.54
B-12H-3-W 50/52	GS16-A1	117.69	6.319	250-355	1.00	3.94	3.42	56.57	-0.02	0.08	0.78	1.06	2.25	2.25	23.47	23.47
B-12H-4-W 130/132	GS17-A1	119.99	6.431	250-355	1.00	3.93	3.42	12.98	0.01	-0.16	0.50	1.03	2.20	2.20	23.21	23.21

C.2. Uncorrected Mg/Ca_{GS} and Sr/Ca_{GS} data with size corrected Mg/Ca_{GS} data

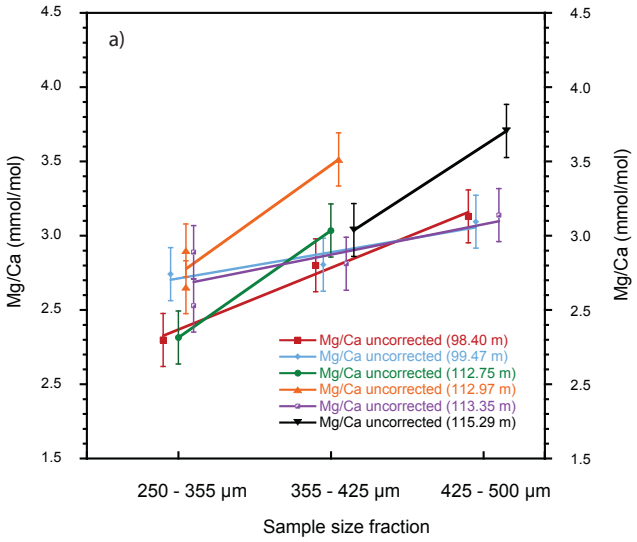

a) Shows original Mg/Ca ratios from the three different size fractions. Error bars are 0.18 mmol/mol (1 σ = 1 standard deviation).

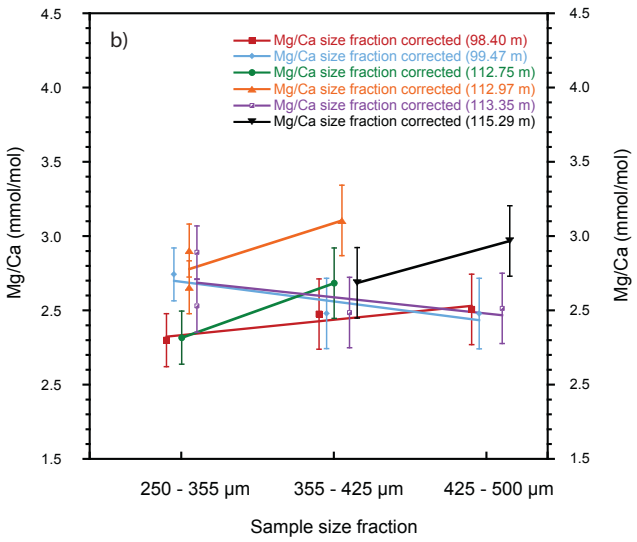

b) Shows Mg/Ca ratios after size fraction correction from the three different size fractions. The Mg/Ca ratios from the different size fractions from the same sample are now within error of each other. Error bars are 0.24 mmol/mol (1 σ) for data in the 355 – 500 µm size fractions and 0.18 mmol/mol (1 σ) for data in the 250 – 355 µm size fraction. 1 σ = 1 standard deviation.

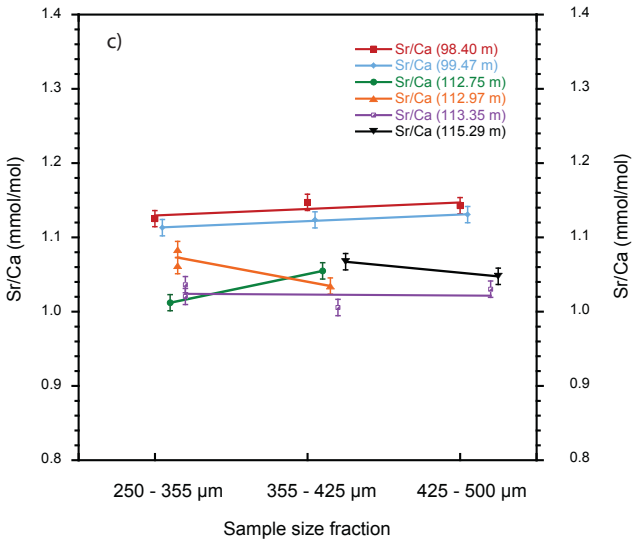

c) Shows original Sr/Ca ratios from the three different size fractions. Error bars are 0.01 mmol/mol (1 σ = 1 standard deviation).

C.3. Larger version Figure 5.9

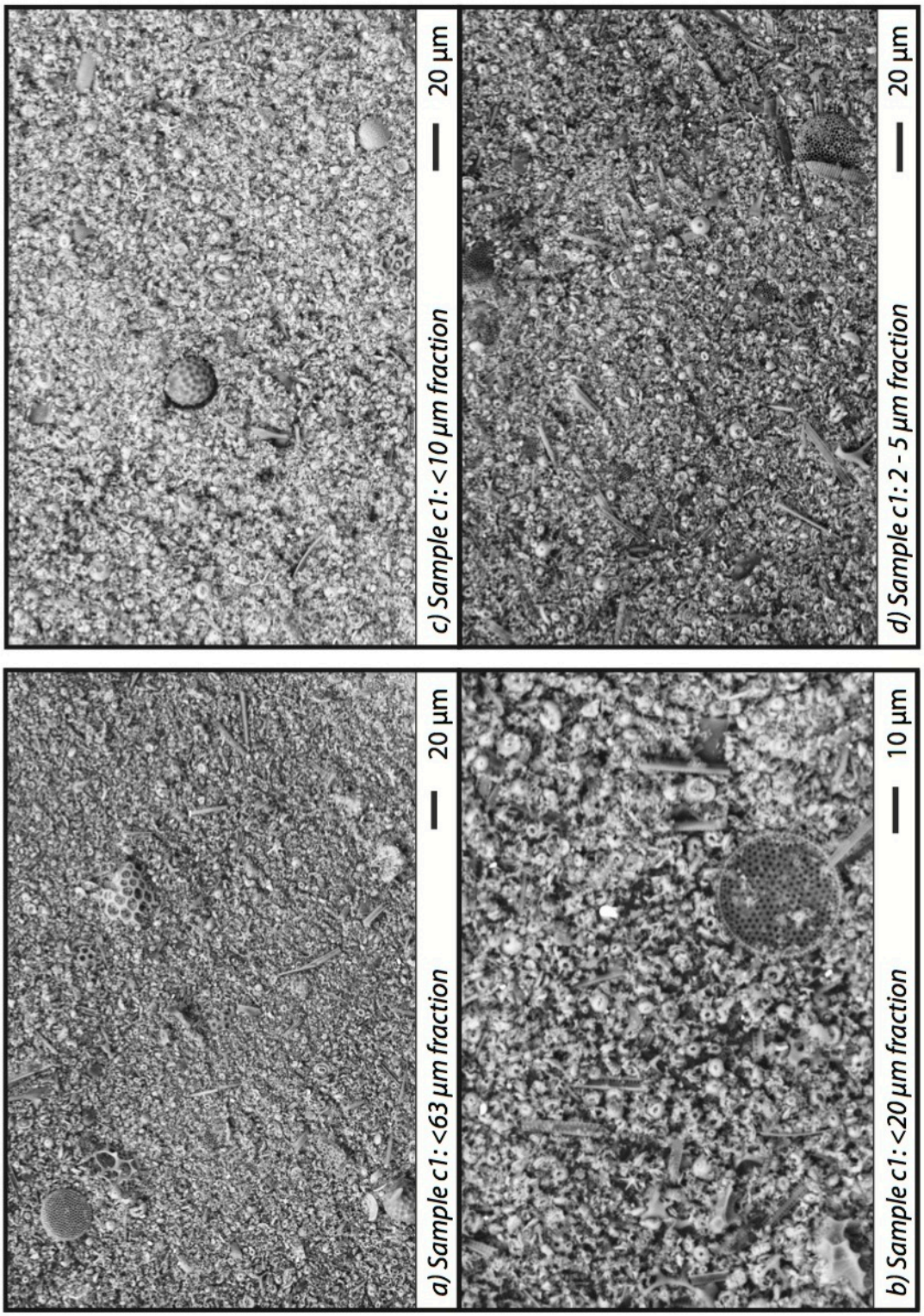

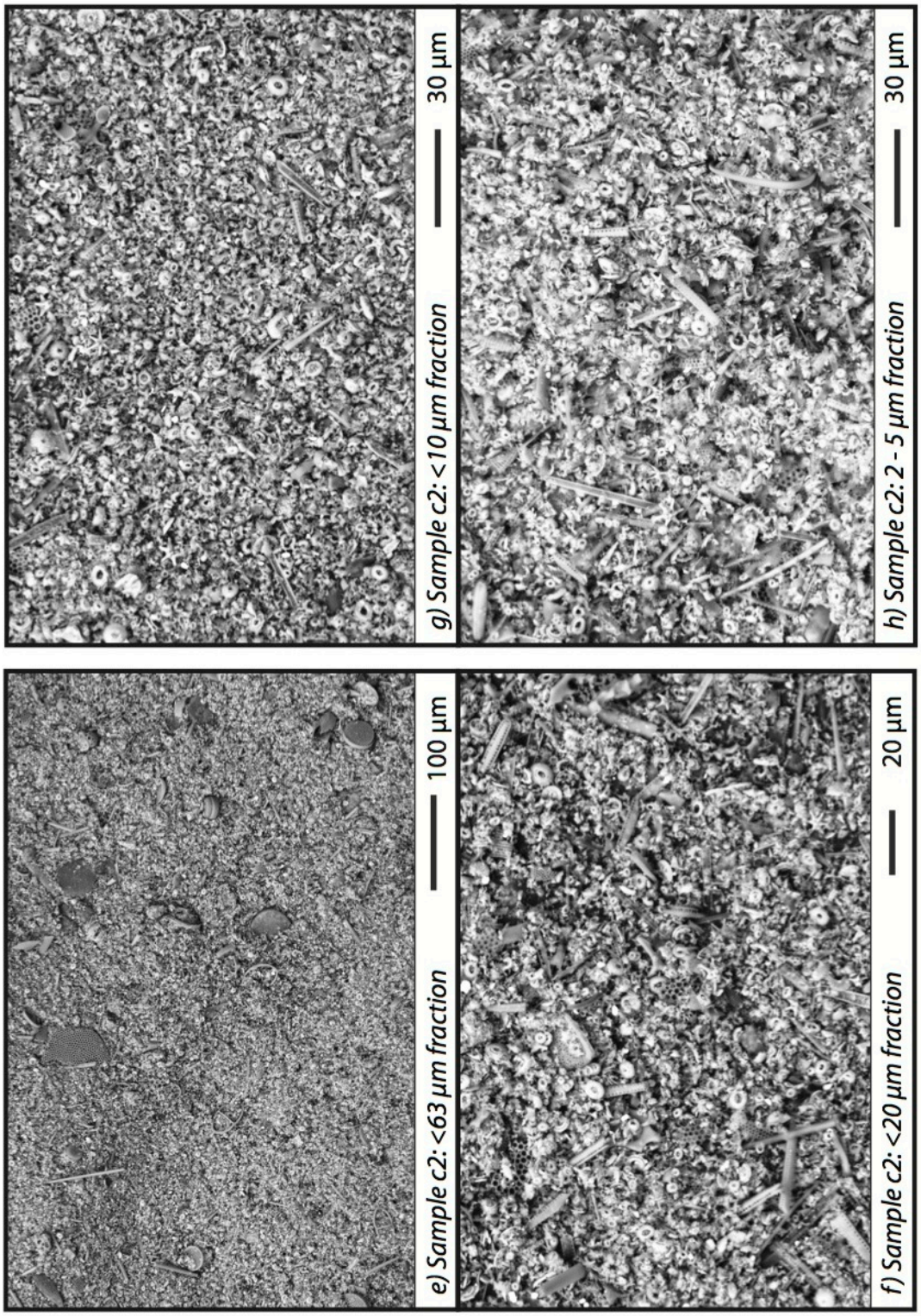
e) Sample c2: <63 µm fraction
100 µm
f) Sample c2: <20 µm fraction
20 µm
g) Sample c2: <10 µm fraction
30 µm
h) Sample c2: 2 - 5 µm fraction
30 µm

C.4. Larger version Figure 5.10

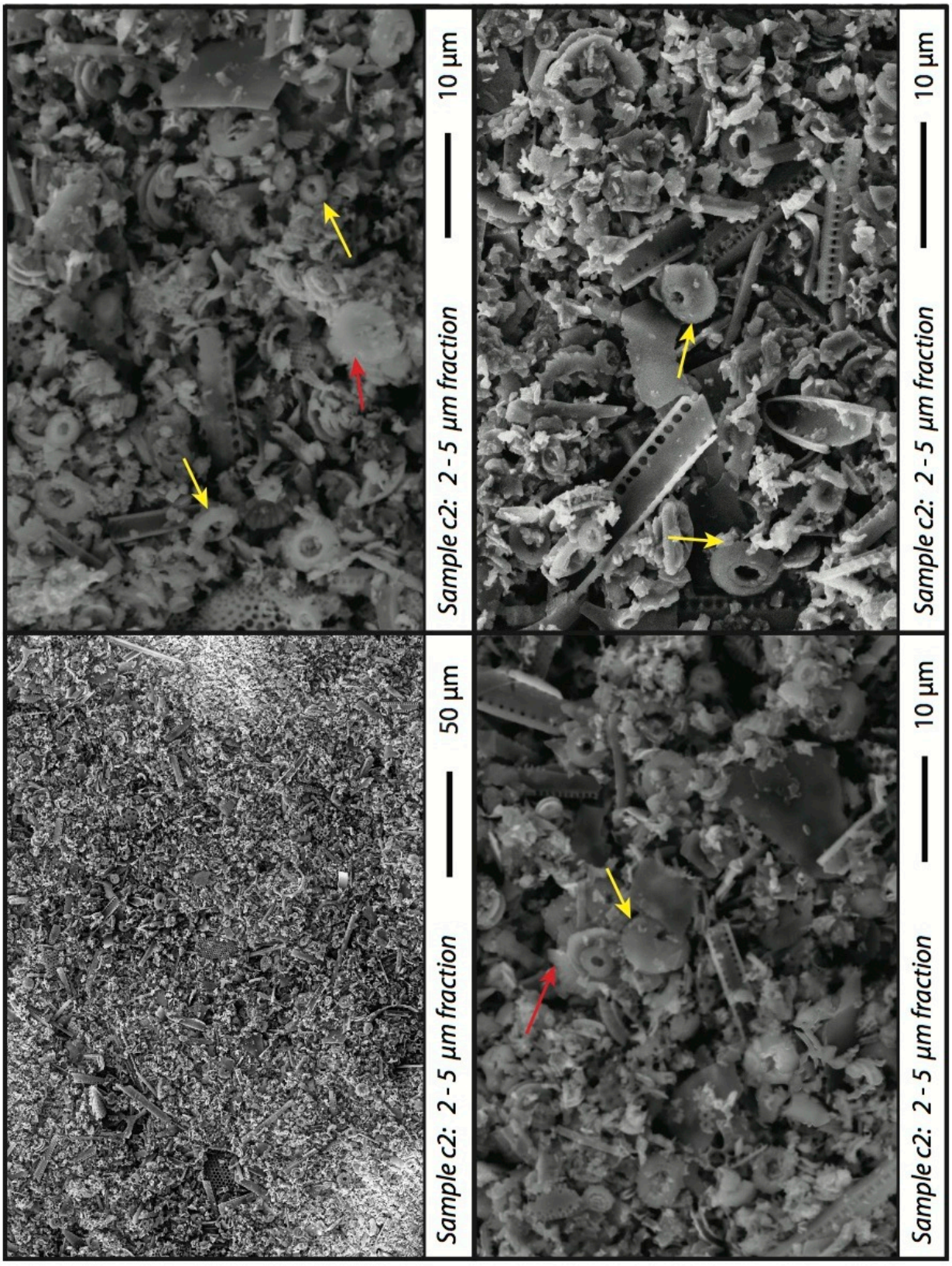

C.5. Larger version Figure 5.12

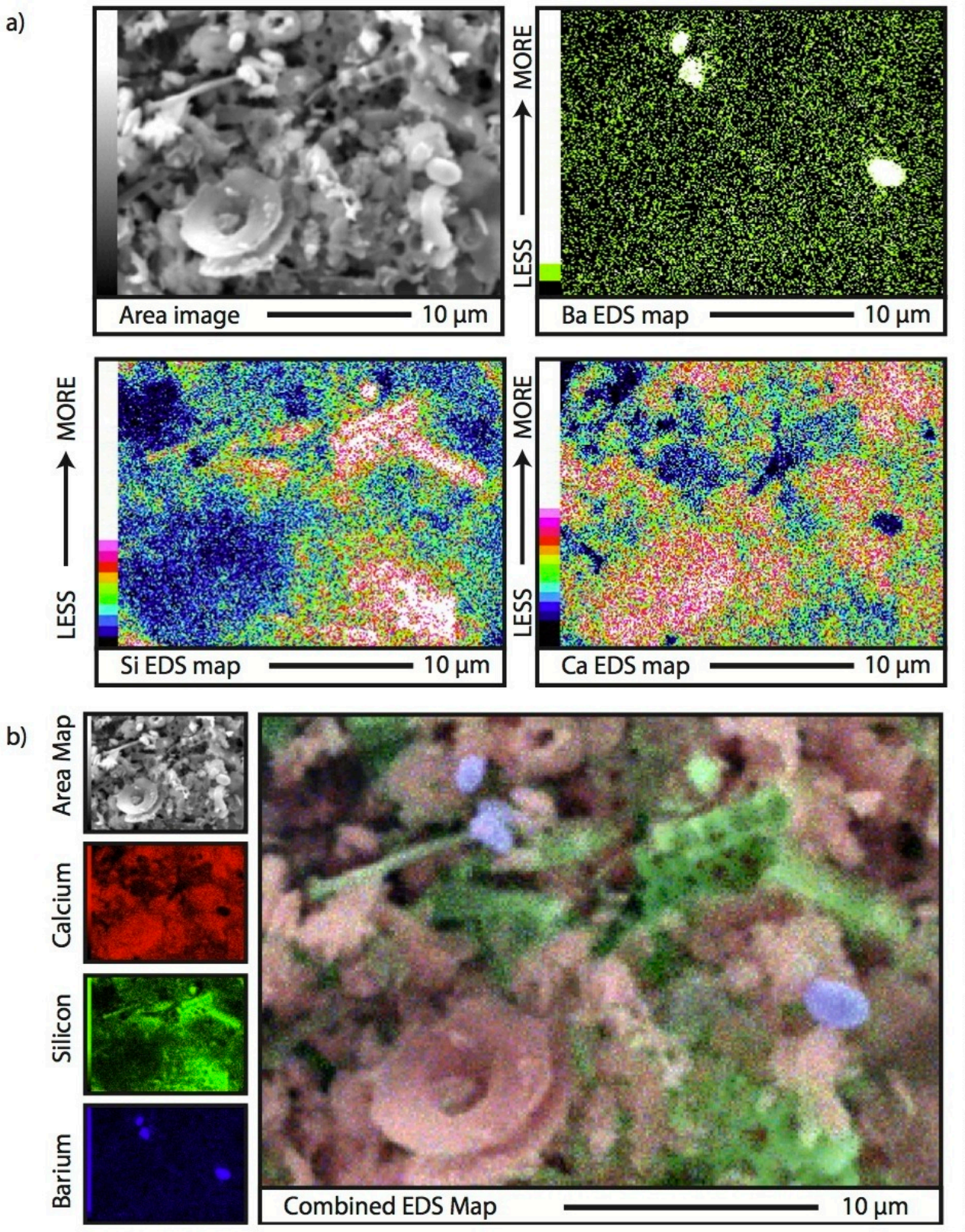

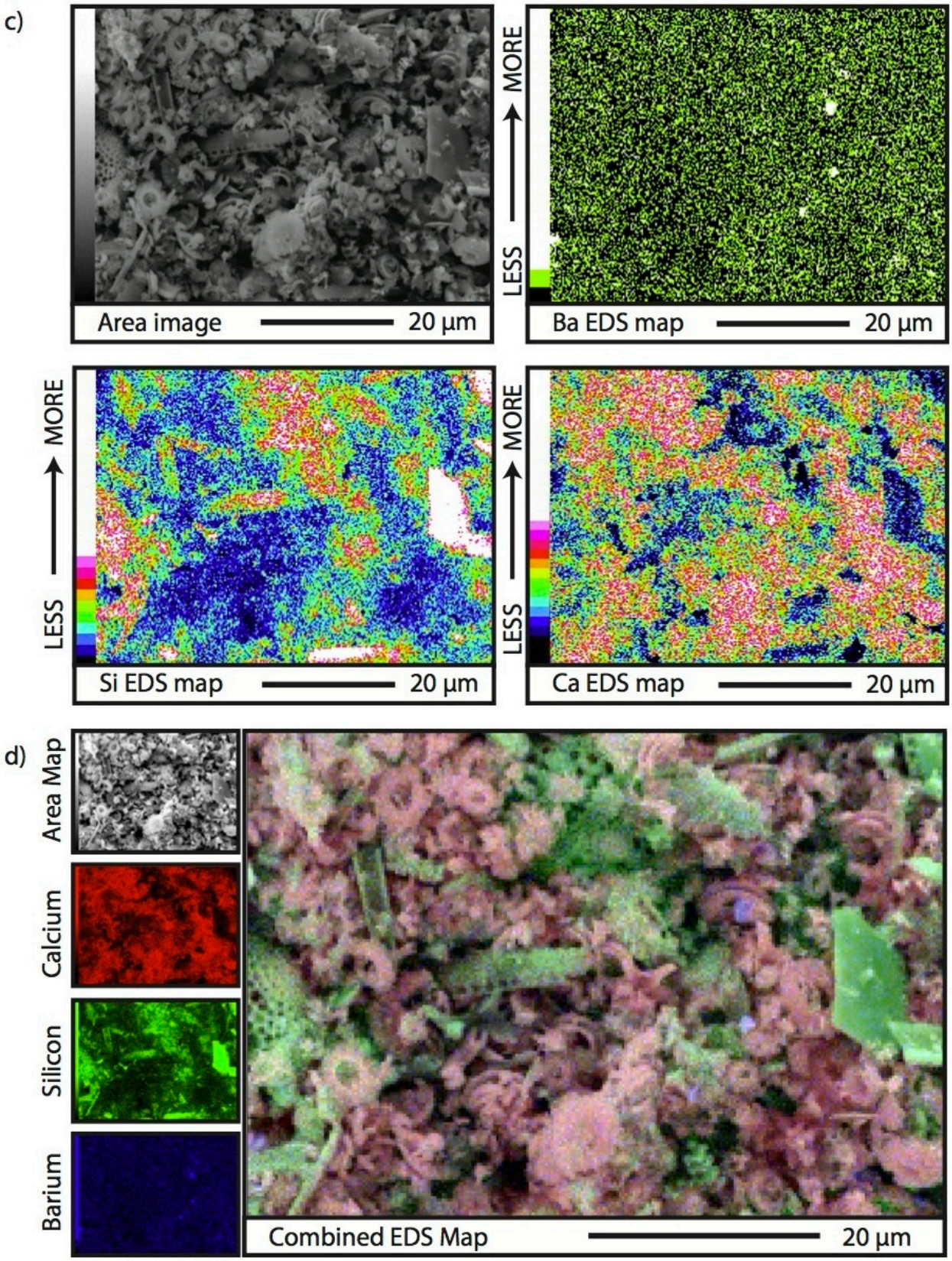
c)
Area image
20 µm
MORE
LESS
Ba EDS map
20 µm
MORE
LESS
Si EDS map
20 µm
MORE
LESS
Ca EDS map
20 µm
d)
Area Map
Calcium
Silicon
Barium
Combined EDS Map
20 µm

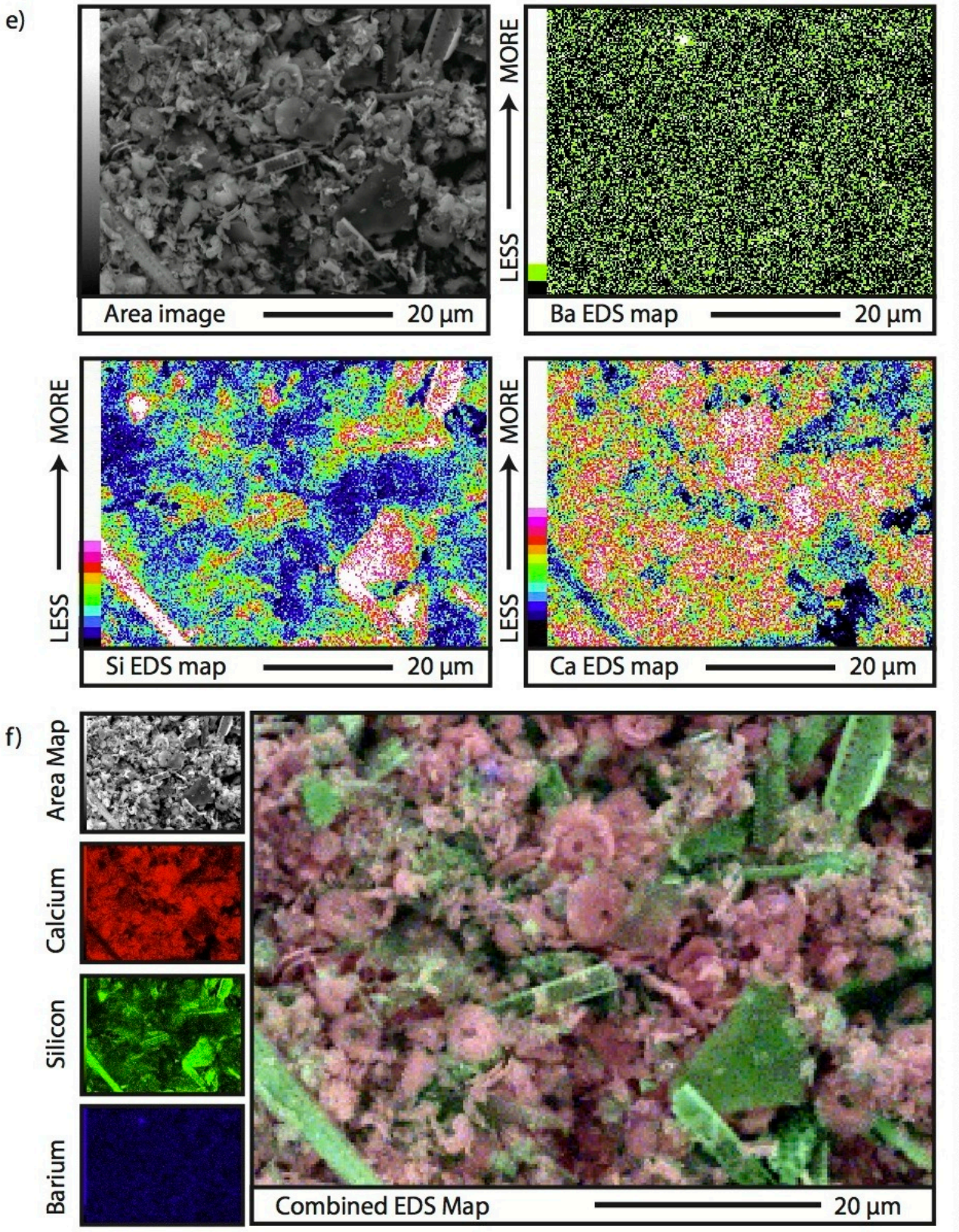
e)
Area image
20 µm
MORE
LESS
Ba EDS map
20 µm
MORE
LESS
Si EDS map
20 µm
MORE
LESS
Ca EDS map
20 µm
f)
Area Map
Calcium
Silicon
Barium
Combined EDS Map
20 µm

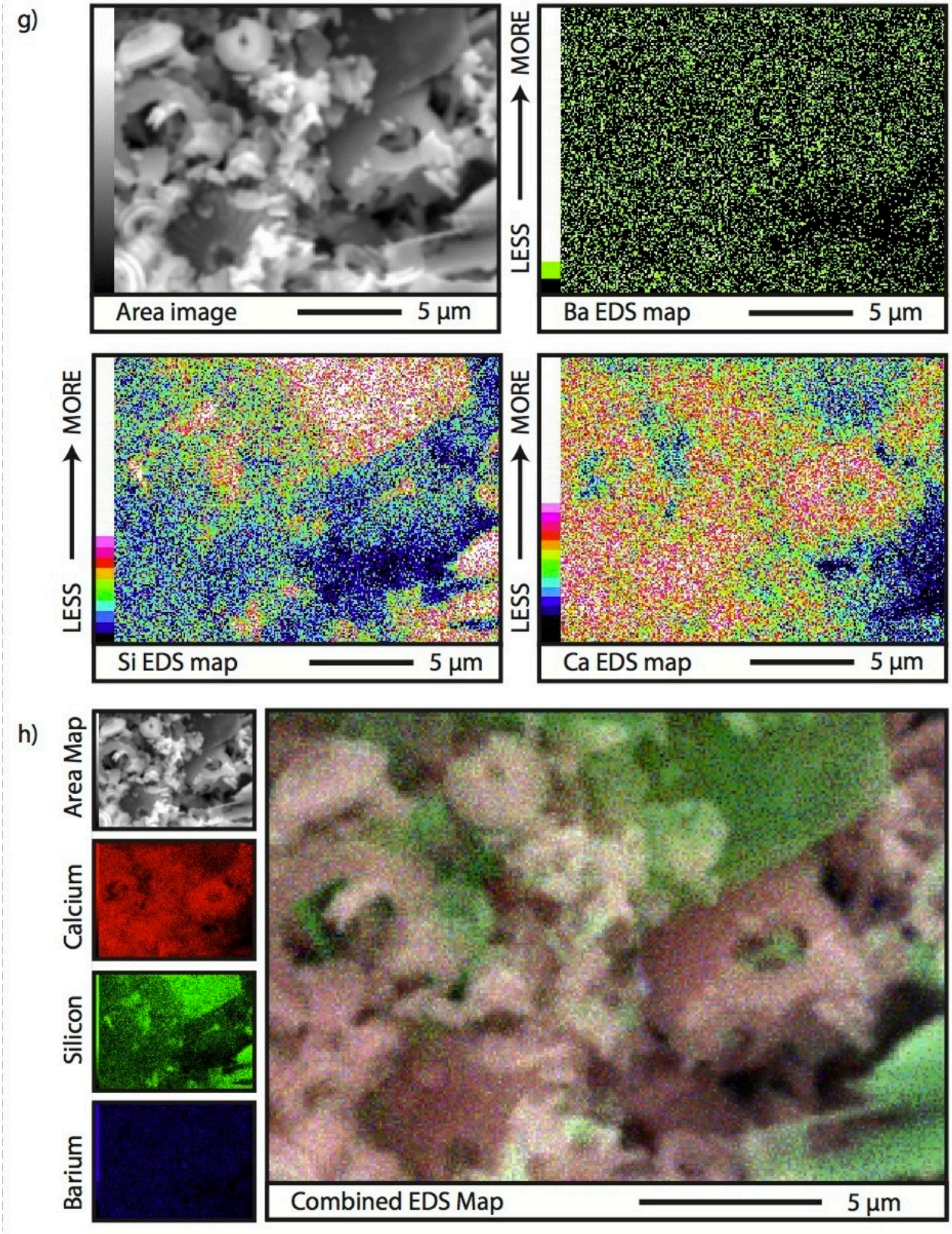
g)
Area image
5 µm
MORE
LESS
Ba EDS map
5 µm
MORE
LESS
Si EDS map
5 µm
MORE
LESS
Ca EDS map
5 µm
h)
Area Map
Calcium
Silicon
Barium
Combined EDS Map
5 µm

C.6. Larger version Figure 5.13

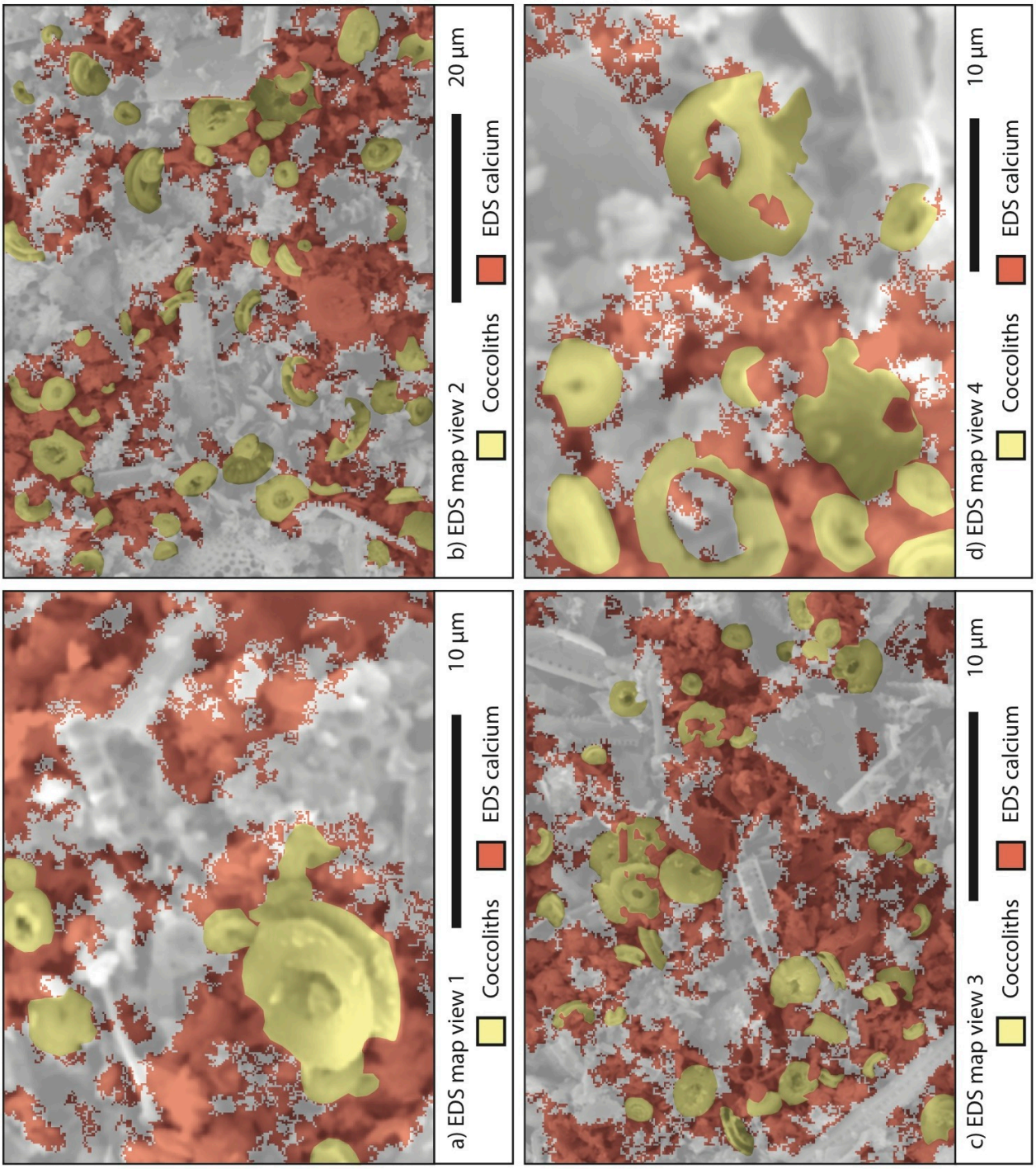

Appendix D

D.1. Normalised $\delta^{13}C$ data

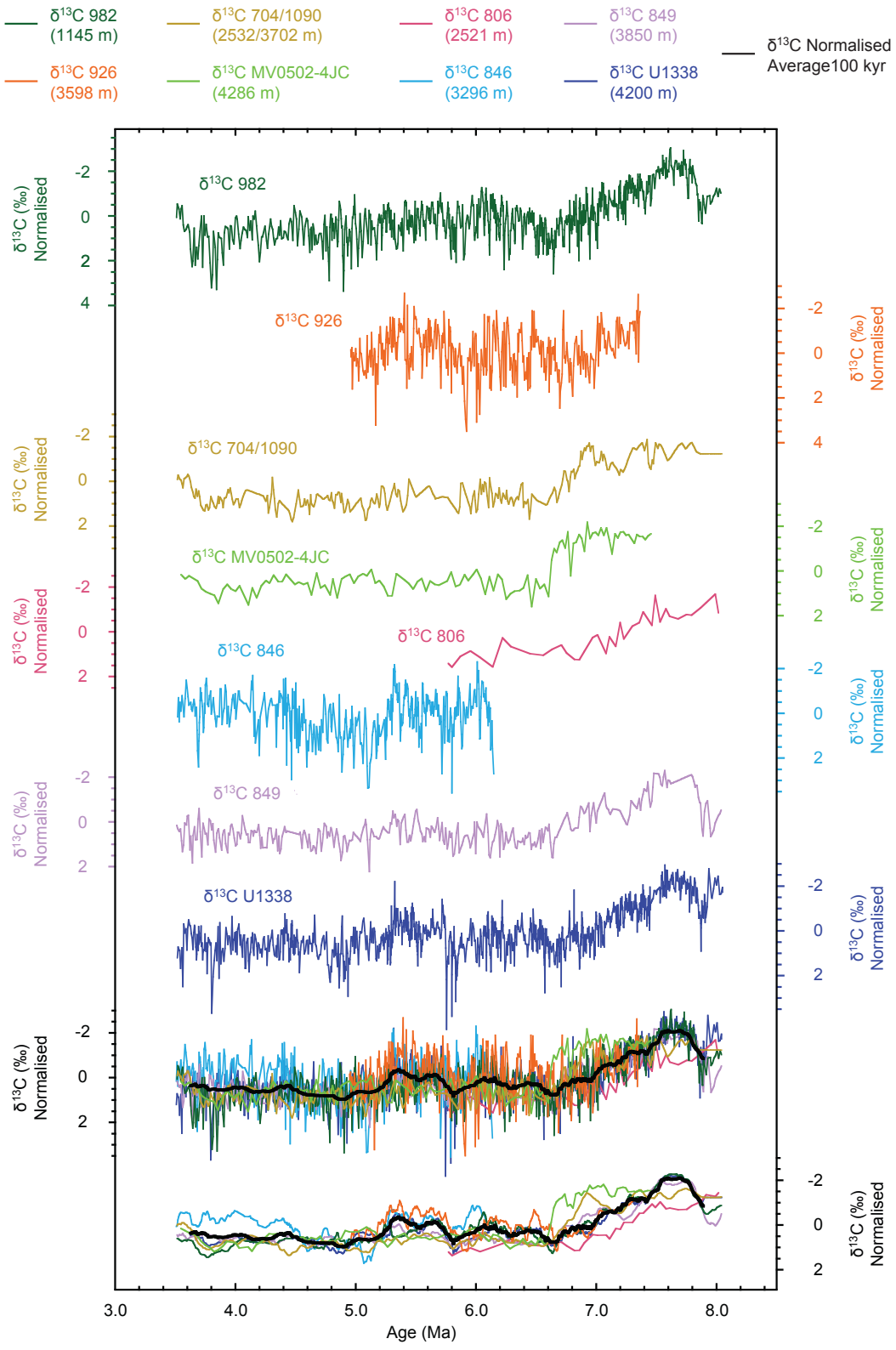

Figure 6.7.

Overview of the eight original full-resolution benthic foraminiferal $\delta^{13}C$ records from the eight sites used in the multi-site compilation, with the normalised individual 100-kyr filtered $\delta^{13}C$ records and an averaged 100-kyr filter of all normalised data.

Plotted below are the reconstructed cryosphere and Earth system sensitivity, together with proximal ice proxy records from both the Northern and Southern hemispheres, shown in more detail in Figure 6.9.